Core-Concrete Interactions Using Molten UO$_2$ With Zirconium on A Basaltic Basemat

The SURC–2 Experiment

Prepared by
E. R. Copus, R. E. Blose, J. E. Brockmann,
R. B. Simpson,.D. A. Lucero

Sandia National Laboratories
Operated by
Sandia Corporation

Prepared for
U.S. Nuclear Regulatory Commission

Core-Concrete Interactions Using Molten UO$_2$ With Zirconium on A Basaltic Basemat

The SURC-2 Experiment

Prepared by
E. R. Copus, R. E. Blose*, J. E. Brockmann,
R. B. Simpson, D. A. Lucero

Sandia National Laboratories
Albuquerque, NM 87185

*Ktech Corporation, Albuquerque, NM 87185

Abstract

An inductively heated experiment, SURC-2, using prototypic UO_2-ZrO_2 materials was executed as part of the Integral Core-Concrete Interactions Experiments Program. The purpose of this experimental program was to measure and assess the variety of source terms produced during core debris/concrete interactions. These source terms include thermal energy released to both the reactor basemat and the containment environment, as well as flammable gas, condensable vapor and toxic or radioactive aerosols generated during the course of a severe reactor accident. The SURC-2 experiment eroded a total of 35 cm of basaltic concrete during 160 minutes of sustained interaction using 203.9 kg of prototypic UO_2-ZrO_2 core debris material that included 18 kg of Zr metal and 3.4 kg of fission product simulants. The meltpool temperature ranged from 2400-1900°C during the first 50 minutes of the test followed by steady temperatures of 1750-1800°C during the middle portion of the test and increased temperatures of 1800-1900°C during the final 50 minutes of testing. The total erosion during the first 50 minutes was 15 cm with an additional 7 cm during the middle part of the test and 13 cm of ablation during the final 50 minutes. Comprehensive gas flowrates, gas compositions, and aerosol release rates were also measured during the SURC-2 test. When combined with the SURC-1 results, SURC-2 forms a complete data base for prototypic UO_2-ZrO_2 core debris interactions with concrete.

Contents

Contents (Concluded)

Figures

Figures (Continued)

Figures (Concluded)

Tables

Executive Summary

The SURC-1 and SURC-2 experiments form a major part of the core debris-concrete interactions data base. These tests were designed to assess the range of responses which are most likely during the initial two to ten hours of these ex-vessel events. The range of response was measured using an oxide debris of UO_2-ZrO_2 on both limestone and siliceous concretes. Also included were a Zr metallic component and a limited number of fission product simultants. Both tests sustained the core debris-concrete interaction for over two hours using an identical power input history of .2-.3 W/g.

The purpose of the SURC-2 experiment was to measure the source terms produced during core debris/concrete interactions with basaltic concrete. These source terms include thermal energy released to both the reactor basemat and the containment environment, as well as flammable gas, condensable vapor, and toxic or radioactive aerosols generated during the course of a severe nuclear reactor accident. The SURC-2 experiment was an integral effects test conducted as part of the Core Debris Interactions program and used the same geometry and instrumentation scheme as was used in the SURC-1 and SURC-4 tests. The basic geometry was a 40 cm diameter basaltic concrete basemat surrounded by an MgO annulus. A 280 kW induction power supply was used to heat a series of tungsten rings that were embedded in the oxide charge material. After 130 minutes of heating, the 203.9 kg oxide charge (69% UO_2 - 22% ZrO_2-9% Zr) became molten and began to attack the underlying concrete basemat. A total of 35 cm of basaltic concrete were then eroded during the following 150 minutes. During the first 100 minutes of erosion a net power of 76 kW was applied to the tungsten susceptors to sustain the interaction. After 100 minutes, the power was increased to a net power of 100 kW for the final 50 minutes. Comprehensive measurements of meltpool temperature, erosion distance, sidewall heat losses, total gas production, total aerosol production, gas composition, and aerosol composition were taken throughout the test using a computerized data acquisition system.

Four time periods during the test were of particular interest. These were the onset of gas release prior to melting, a period of rapid erosion following initial melt-concrete contact, slowed erosion after the Zr metal in the charge was chemically consumed, and increased erosion when the power was increased towards the end of test. During the 50 minutes prior to melt, the temperature of the oxide charge increased from 1300 K to 2600 K. The concrete basemat started to dehydrate during this time at an average rate of 4 cm/hr producing a reaction gas flow rate of 26 slpm. The composition of this initial effluent gas was 70 to 80% H_2 - 15% H_2O - 20% CO_2 and only light aerosols were present at levels less than 1 g/m^3. Concrete erosion began when the oxide charge became completely molten, and a protective ZrO_2 insulator board was breached. Meltpool temperatures at the onset of concrete attack were approximately 2700 K. These temperatures decreased to 2100 K as 15 cm of concrete were eroded over a period of 30 minutes. The reaction gas flow increased to 110 slpm and had a composition of 75% H_2 - 5% H_2O - 15% CO - 5% CO_2. Large amounts of aerosol were also produced at densities of 50-300 g/m^3 which had a composition rich in silicon, sodium, potassium, barium, molybdenum, and uranium. The size distribution of these aerosols ranged from 0.5 to 20 microns with a mass mean diameter at 3 microns. After 30 minutes of erosion the erosion rate slowed from 30 cm/hr to 5 cm/hr after all of the Zr metal became oxidized. The meltpool temperatures ranged from 2050 to 2100 K as an additional 5 cm of concrete were eroded over a period of 60 minutes. The reaction gas flow rate decreased to 20 slpm and had a composition of 70% H_2 - 5% H_2O - 15% CO - 10% CO_2. After 90 to 100 minutes, the net power to the charge material was increased from 70 to 100 kW. This resulted in increased erosion rates, increased gas release rates, and increased aerosol release rates. The meltpool temperature increased from 2050 to 2150 K during these final 50 to 60 minutes of the test as an additional 15 cm of concrete were eroded. The reaction gas flow rate increased from 15 to 40 slpm

and the gas composition was 75% H_2 - 5% H_2O - 15% CO - 5% CO_2. Aerosols registered constant levels of production at about 10 g/m^3.

After 280 minutes of heating and 150 minutes of continuous erosion, the SURC-2 melt penetrated the remaining 5 cm of concrete and ran out into the bottom of the containment vessel. Power to the test was shut down at this point and the test was terminated. The test was excellent in all respects and successfully met all of the test goals.

The results of the SURC-2 test with basaltic concrete generally confirm the observations made in the SURC-1 test with limestone concrete. Both tests had very similar charge compositions and nearly identical power histories. The key observations made during the tests were (1) high initial temperatures and erosion rates, (2) sustained interaction temperatures in excess of 2000 K, and (3) continuous release of gas and aerosols in large amounts. This test provides comprehensive, redundant, and well-characterized information on molten oxide interactions with basaltic concrete which is well-suited for code validation efforts.

The major conclusions from the test are that interaction temperatures remain at least 300 K above the concrete melting point, that zirconium chemistry drastically affects the ablation rate and the gas composition, and that silicate concrete chemistry seems to retain a substantial portion of the fission product simulants in the melt. The results of the SURC test provide a solid base for validation of the heat transfer, gas chemistry, and aerosol release models such as those found in the CORCON code and indicate that a relatively complete understanding now exists concerning the initial phases of core debris interactions with concrete when liquid water is not present. We feel that the understanding derived from the combined oxide and metal data base is reasonably adequate for current regulatory purposes. Future regulations or new reactor design efforts will be able to tap this technology base but may also suggest a new range of responses that need definition.

Acknowledgment

1.0 General

The Core Debris Interactions Program is intended to measure, model, and assess the thermal, gas evolution, and aerosol source terms produced during core debris-concrete interactions that might occur following a severe nuclear reactor accident. These source terms are the governing phenomena in any postaccident containment integrity analysis or risk evaluation. A matrix of tests is being conducted as part of the program. This matrix is designated as the SURC (SUSTAINED URANIA-CONCRETE) test series.

In addition to extending the existing data base to include more prototypic core debris-concrete interactions, [Blose et al., 1987], the SURC experiments are designed to provide information necessary to validate three important aspects of ex-vessel core debris-concrete interactions models. These are (1) heat transfer mechanisms, (2) gas release chemistry, and (3) vaporization release of aerosols. Both integral tests using UO_2-ZrO_2 materials (SURC-1, SURC-2,) as well as separate effects tests using Fe-Zr (SURC-3, SURC-4) have been conducted.

The SURC-1 and SURC-2 tests in the SURC series were designed to be integral tests using a 203.9 kg molten mixture of 69 w/o UO_2-22 w/o ZrO_2-9 w/o Zr over a 40 cm diameter concrete basemat formed from either limestone concrete (SURC-1) or basaltic concrete (SURC-2). The purpose of these tests was to study the protracted interaction of an oxidic meltpool on a range of concrete basemat materials. Before these tests were conducted the bulk of data available for evaluating the exvessel core concrete interaction was either from tests using metallic iron as the core debris simulant or from tests which lasted only a few minutes. The SURC-1 test sustained the oxide-concrete reaction for over 180 minutes as did the SURC-2 experiment. During the course of these tests it was our goal to measure all of the essential aspects of the core-concrete interaction; namely, melt temperatures, erosion rates, overall heat balance, thermal conduction into the concrete, gas release rates, gas release

chemistry, aerosol release rates and aerosol chemistry. The data return from both tests was excellent and provides comprehensive, redundant, and well characterized information on the oxide-concrete interaction which should be well suited for code validation efforts.

The SURC-2 experiment was conducted using the same geometry and instrumentation scheme as was used in SURC-1 [Copus et al., 1992] and in SURC-4 [Copus et al., 1989]. The basic geometry consisted of a 60 cm diameter interaction crucible with a 40 cm diameter basaltic concrete cylinder in the base of a magnesium oxide (MgO) annulus. A 10 cm thick, circular cover of MgO was fabricated and placed on top of the crucible. The interaction crucible and induction coil were housed in a sealed, water cooled, aluminum containment vessel. An overview photograph of this vessel and some of the rest of the test apparatus is shown in Figure 1.1. The vessel was 180 cm high, 120 cm in diameter and contained feedthroughs for the induction power leads, instrumentation leads, and an exhaust gas port connected to the flow and aerosol sampling instrumentation. The interaction crucible was instrumented with numerous thermocouple arrays cast into the concrete cylinder, MgO annulus and MgO cover. A 280 kW induction power supply and coil were used to heat and melt the 203.9 kg charge within the test article and to sustain the interaction for the duration of the experiment. Additionally, 3.4 kg of fission product simulants were added into the melt to study fission product release. Flow rates of generated gases were measured using a sharp edge concentric orifice, a laminar flow device and two dry gas clocks. Gaseous effluents produced during the experiment were monitored and sampled using an infrared gas analyzer, a mass spectrometer, and by an integral grab sample technique. Aerosols were captured on filters, cascade impactors and a cascade cyclone. Erosion characteristics were measured using type K, S, and C thermocouples. Three tungsten thermowells containing optical pyrometers were embedded in the charge in order
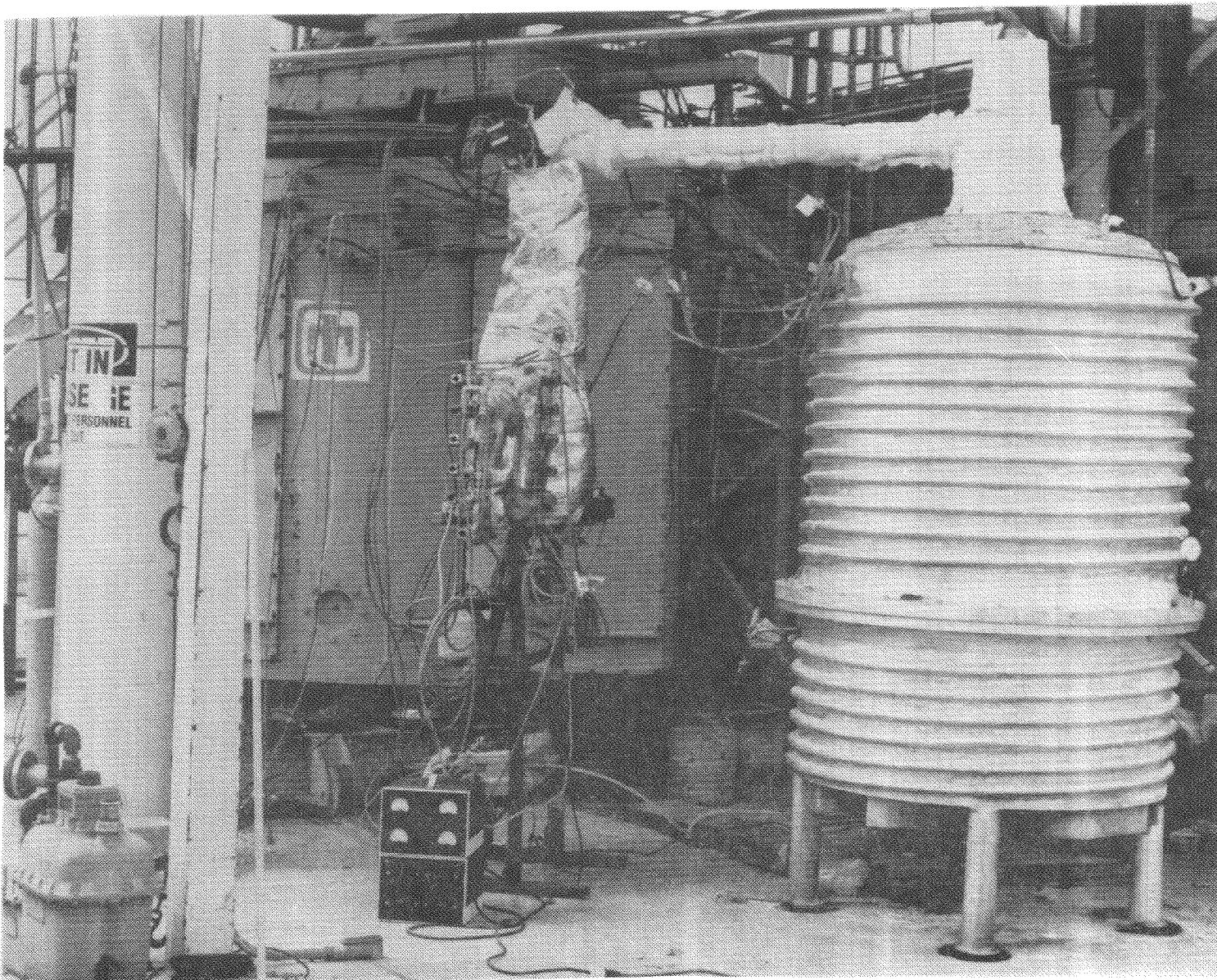
Figure 1.1 SURC-2 overview photograph

to define the meltpool temperature and overall heat balance. The apparatus was sealed and purged with argon gas in order to direct the majority of the reaction gas and aerosol effluents through a 5 cm diameter flow pipe. The SURC-2 test was run at local atmospheric pressure (.83 atm) and at an ambient temperature of 25°C.

2.0 Materials

The interaction crucible used in the SURC-2 experiment is of cylindrical geometry and is shown in Figure 2.1. The crucible consists of three major components; the lower crucible, upper crucible and cover. The annulus of the upper and lower crucible and the cover are cast using a MgO castable refractory material. Basaltic concrete is cast into the base of the lower crucible. A detailed description of the interaction crucible including dimensions and thermocouple locations will be discussed later in Section 3.2.

2.1 Magnesium Oxide (MgO) Castable Refractory

The annulus of the crucible was cast using an MgO castable material manufactured by Kaiser Refractories called K/R Cast-98. This material is a superior MgO castable produced from critically sized 97 w/o MgO periclase and bonded with a special chromate composition. K/R Cast-98 can be vibrated to exceptionally high densities. This material resists melt penetration and provides outstanding resistance to highly basic slags. This material also has excellent volume stability and is commonly used for crucibles in the steel industry. The chemical composition of K/R Cast-98 taken from manufacturer's specifications is shown in Table 2.1.

The MgO castable was mixed by placing a known mass of dry material into a clean paddle-type mixer. City drinking water was then added 5% by weight to the castable material and mixed for at least two minutes. Once a homogeneous mixture was achieved, the mix was carefully placed into the casting forms with small scoops and shovels. Two types of vibrators, operating at 10,000 to 12,000 vibrations/minute were used to densify the mix and remove entrained air. A pneumatically operated eccentric vibrator was attached to the brackets mounted to the steel casting forms. Another mechanical vibrator called a "stinger" was inserted directly into the mix to enhance densification.

After casting, the mix was cured at ambient temperature (15 to 35°C) for 24 hours. Then the forms were placed into an oven and initially heated at a rate of 40°C/hour to 265°C. The casting was held at temperature for 12 hours. The total curing cycle took 24 hours. During the baking period, two K-type thermocouples were connected to a strip chart recorder to monitor the curing temperature. One thermocouple measured the ambient oven temperature, the other thermocouple was cast into the annulus and measured the actual temperature of the annulus.

The thermal behavior of the K/R Cast-98 was characterized by thermal gravimetric analysis (TGA), shown in Figure 2.2.

This analysis was performed with a Dupont 790 thermal analysis apparatus with a 1870 K DTA cell and Model 950 TGA attachment.

The TGA was performed in dry air with a flowrate of 50 cc/min. The heating rate was 10°C/min from room temperature to 800°C. The sample had been air cured for 24 hours, baked at 200°C for 24 hours, then allowed to air cool for an additional 24 hours prior to thermal analysis. Weight losses indicated in the thermogram are attributed to the release of free and bound water. This sample shows a 4.0 weight-percent loss due to release of free and bound water between ambient temperature and 700°C. From 700°C to 1000°C, an additional 0.2 percent-weight loss was observed, which is probably due to the decomposition of brucite $(Mg(OH)_2)$.

UPPER CRUCIBLE

LOWER CRUCIBLE

100 cm

70 cm

40 cm

CONCRETE SLUG

40 cm

60 cm
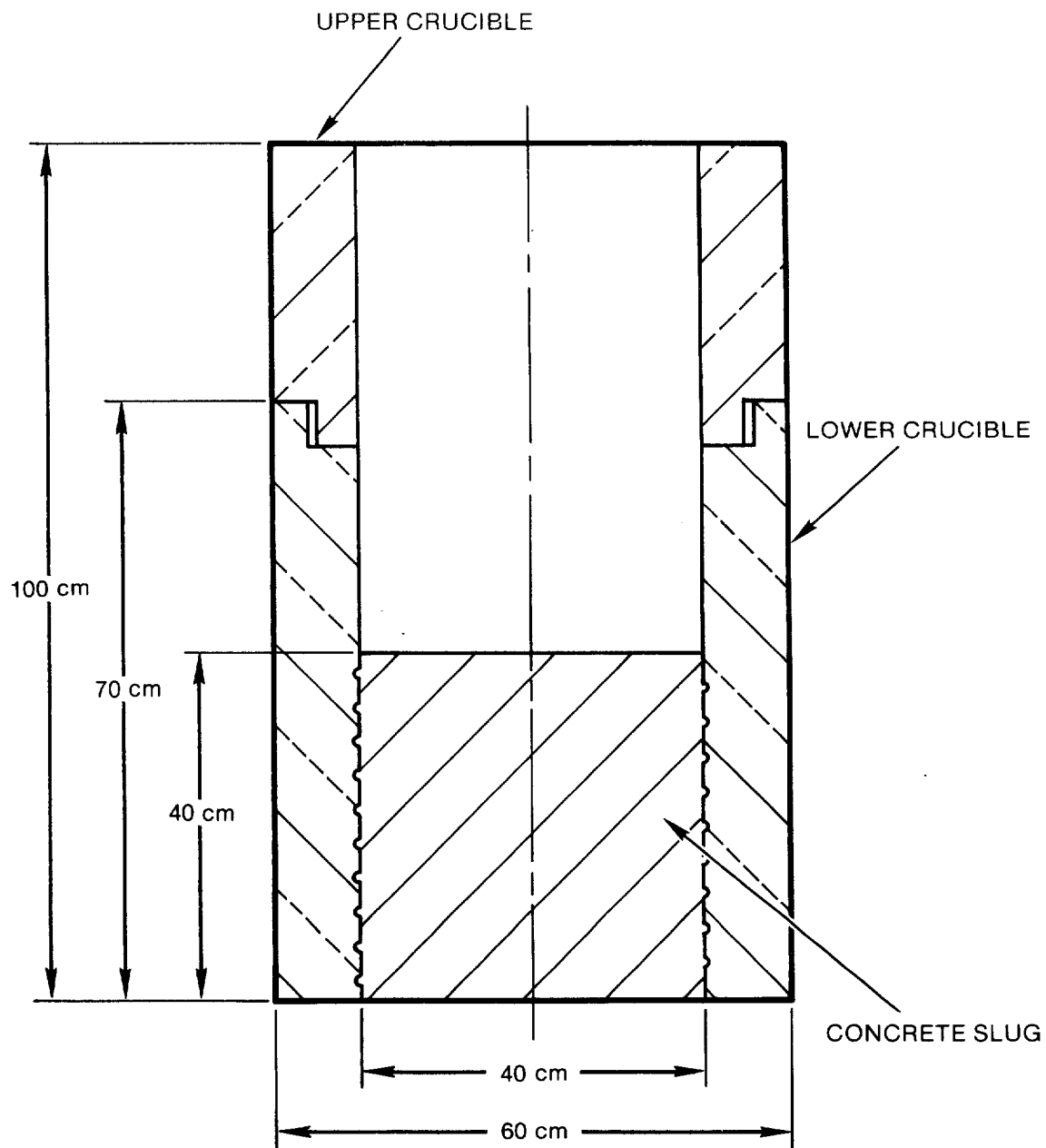
Figure 2.1 Interaction crucible, SURC-2 experiment

Table 2.1 Chemical composition of K/R Cast-98* MgO castable refractory

Oxide	Weight %
MgO	97.1
SiO_2	0.4
Al_2O_3	0.1
Fe_2O_3	0.3
CaO	1.0
Cr_2O_3	1.1

*K/R Cast-98 is a product of Kaiser Refractories, 300 Lakeside Drive, Oakland, CA 94643.

Data Obtained from Basic Ramming and Casting Mixes Bulletin Published by Kaiser Refractories.

Three 10.2-cm-diameter x 20.3-cm-long test cylinders were cast with the annulus to measure the compressive strength after baking. The strength for the three samples were 1600, 1771, and 2248 psi. These values are well within the acceptable limits for ensuring structural integrity during the test.

The thermal properties of the castable K/R Cast-98 have been extensively investigated. In addition to industry data, experiments were conducted at Sandia to study the thermal response of the MgO to intense heating conditions similar to those expected during an experiment. The results of these tests yield a value for specific heat and temperature dependent values for thermal conductivity.

The thermal property data for the MgO castable used to calculate sidewall heat fluxes are presented in the SURC-4 document [Copus et al., 1989] and shown below.

Density (kg/m^3)	2664
Specific Heat (J/kg K)	1250

Thermal Conductivity
$$(W/m\ K) = k = aT + b$$

where:

$$a = -5.0 \times 10^{-3}$$
$$b = 8.193$$
$$T = \text{Degrees K}$$

Another determination of the thermophysical properties and density of K/R Cast-98 was performed by Purdue University and is described in Appendix A of the SURC-4 document [Copus et al., 1989].

The data returned by Purdue is slightly different than that produced by Sandia. This data has been mentioned here because product literature data for these high temperature material properties are limited. This data provides an additional resource for the analysts.

2.2 Concrete Material

The base of the interaction crucible was constructed of basaltic concrete. This concrete was used because it is typical of that used in the construction of nuclear power plants. Materials making up this type of siliceous concrete are found throughout the United States. This concrete melts over a range of 1350-1650 K and typically liberates 1.5 weight-percent CO_2 gas and 5 weight-percent H_2O vapor when heated to melting [Powers et al., 1982].

The casting of the concrete was performed by mixing the concrete constituents in a clean paddle mixer. Once a homogeneous mixture had been achieved, the mix was carefully placed into casting forms and vibrated as previously described in Section 2.1.

7
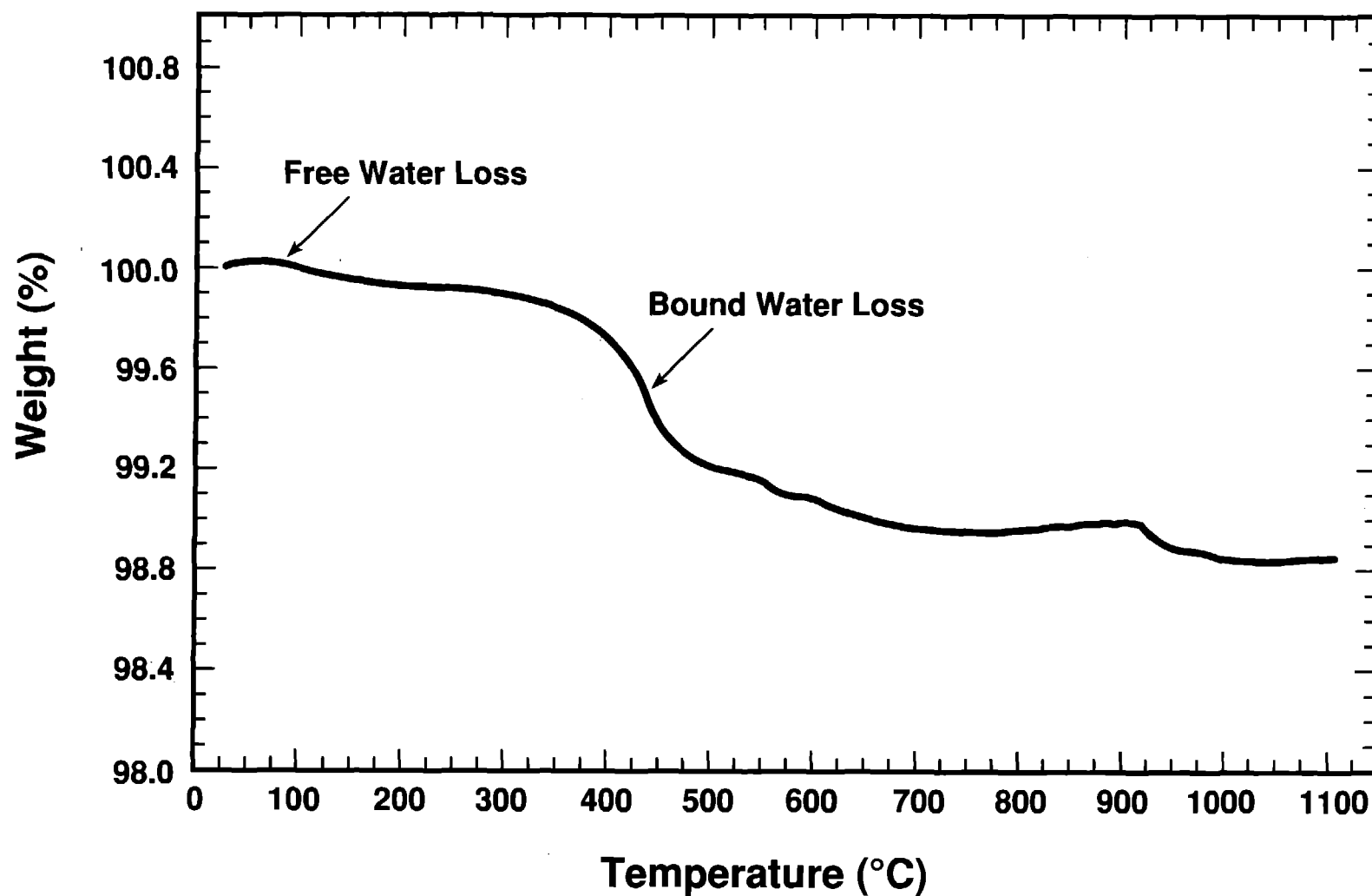
Figure 2.2 Thermogram (TGA) of MgO K/R Cast-98; air-cure 24 hours baked at 470 K for 24 hours, air cooled

Specifications for the concrete are listed in Table 2.2. Tables 2.3 and 2.4 summarize the engineering and chemical composition of the basaltic concrete. Tables 2.5 and 2.6 show comparisons of the size specifications and the distribution of sizes for the aggregate and sand actually used for the concrete.

Four 10.2 cm diameter x 20.3 cm long test cylinders were cast with the concrete slug to measure the compressive strength after 7, 14, 28, and 1070 (day of the experiment) days. The concrete cylinder was cured at ambient temperature conditions, nominally $20° \pm 10°C$. Compressive strengths are plotted against cure time in Figure 2.3. The strength for the compressive cylinder tested at 1070 days (not shown in the figure) was 41.4 MPa (6000 psi).

The thermal behavior of the concrete can be characterized by thermal gravimetric analysis (TGA), derivative thermogravimetric analysis (DTGA), and differential thermal analysis (DTA). Figure 2.4 shows a typical thermogram produced by TGA for basaltic concrete.

2.3 Charge Material

The charge material consisted of 203.9 kg of UO_2-ZrO_2 and Zr metal in the form of powder, crushed isostatic pressed cylinders and metal chips. The total mass and w/o of constituents in each of the material forms is presented in Table 2.7. The relative weight percentages of the individual constituents for the total charge were calculated to be 69.1 w/o UO_2, 22.6 w/o ZrO_2, and 8.3 w/o Zr metal. In order to produce a homogeneous mix, Zr metal chips were added to the crushed UO_2-ZrO_2 cylinder material to produce the desired ratios. Five tungsten plates were placed within the charge material to serve as susceptors to heat the material. The plates were spaced approximately 10 cm apart within the charge. A detailed description of the charge assembly is discussed in Section 3.4. The mass and ratio of charge constituents placed between the tungsten plates are shown in Figure 2.5. The density of the charge was calculated to be 3.6 g/cc.

2.4 Fission Product Simulants

In order to evaluate the transport of fission products during the melt-concrete interaction, various chemical species, listed in Table 2.8, were added to the charge prior to heating. These materials were added to the charge material as a homogeneous powdered mixture just below the third tungsten plate. The placement of the simulants corresponds to a location 53.8% of the charge height.

Table 2.2 Concrete specifications

1. Compressive strength after 90 day cure = 27.5 MPa minimum (3990 psi)

2. Slump = 5 cm

3. Cement = American Type II Portland Cement

4. Air content = 3 to 5% by volume

5. Air entraining agent per reference (a) below

6. Composition per reference (b) below

7. Aggregate size and size distribution per reference (c) below

8. Water reducing agent per reference (a) below

9. Mixing, forming, and placing per references (b,c,d,e) below

---

a. ASTM C-494-71, Standard Specification for Chemical Admixtures for Concrete, American Society for Testing and Materials, Philadelphia, PA.

b. ACTI 211. 1-74, Recommended Practices for Normal and Heavy Concrete, American Concrete Institute, Detroit, MI.

c. ASTM 33-74., Standard Specifications for Concrete Aggregates, American Society for Testing and Materials, Philadelphia, PA.

d. ACI 347-68, Recommended Practice for Working Concrete, American Concrete Institute, Detroit, MI.

e. ACI 315-74, Detailing Manual, American Concrete Institute, Detroit, MI.

Table 2.3 Engineering composition of basaltic concrete

Constituents[b]	Mass	Weight %
Aggregate[c]	42.3 kg	35.7
Sand	47.4 kg	40.1
Cement	19.4 kg	16.4
Water	9.3 kg	7.8
*AEA[a]	22.2 ml	-

*Air Entraining Agent

a. ASTM C-494-71, Standard Specification for Chemical Admixtures for Concrete, American Society for Testing and Materials, Philadelphia, PA.

b. ACTI 211. 1-74, Recommended Practices for Normal and Heavy Concrete, American Concrete Institute, Detroit, MI.

c. ASTM 33-74., Standard Specifications for Concrete Aggregates, American Society for Testing and Materials, Philadelphia, PA.

Table 2.4 Chemical composition of basaltic concrete constituents[a,b]

Oxide	Type 1 and 2 Cement (%)	Sand (%)	Basalt Aggregate[c]
Fe_2O_3	4.11	2.15	7.78
Cr_2O_3	0.011	0.042	0.06
MnO	0.08	0.02	0.08
TiO_2	0.2	0.18	1.82
K_2O	0.54	2.7	7.2
Na_2O	0.27	1.74	1.85
CaO	63.5	1.52	6.54
MgO	1.53	0.34	9.7
SiO_2	20.1	82.8	54.9
Al_2O_3	4.2	7.24	9.51
CO_2	ND	ND	< 0.02
H_2O	ND	0.1	0.1
SO_2	1.0	ND	ND

ND = Not Determined

a. ASTM C-494-71, Standard Specification for Chemical Admixtures for Concrete, American Society for Testing and Materials, Philadelphia, PA.

b. ACTI 211. 1-74, Recommended Practices for Normal and Heavy Concrete, American Concrete Institute, Detroit, MI.

c. ASTM 33-74., Standard Specifications for Concrete Aggregates, American Society for Testing and Materials, Philadelphia, PA.

Table 2.5 Comparison of specified and actual size distributions
for the fine and total aggregate

	Through the Screen Opening	
Screen Opening (cm)	Specified Weight % Passing Through the Screen	Observed Weight % Passing Through the Screen
A) Total Aggregate		
2.5	95-100	100
1.9	90-100	96.3
1.3	25-60	54.7
0.95	20-55	25.2
0.48	0-10	5.6
0.23	0-5	not measured
B) Fine Aggregate		
1.3	100	100
0.95	85-100	98.9
0.48	10-30	96.8
0.23	0-10	84.4
0.12	0-5	59.7

Table 2.6 Comparison of specified and actual size
distributions for the sand

Screen Opening (cm)	Weight % Passing Through the Screen	
	Specified	Observed
0.95	100	99.85
0.48	95-100	97.85
0.23	80-90	85.14
0.12	55-75	60.93
0.058	30-60	33.92
0.030	12-30	16.50
0.015	2-10	7.11
0.0076	-	3.06
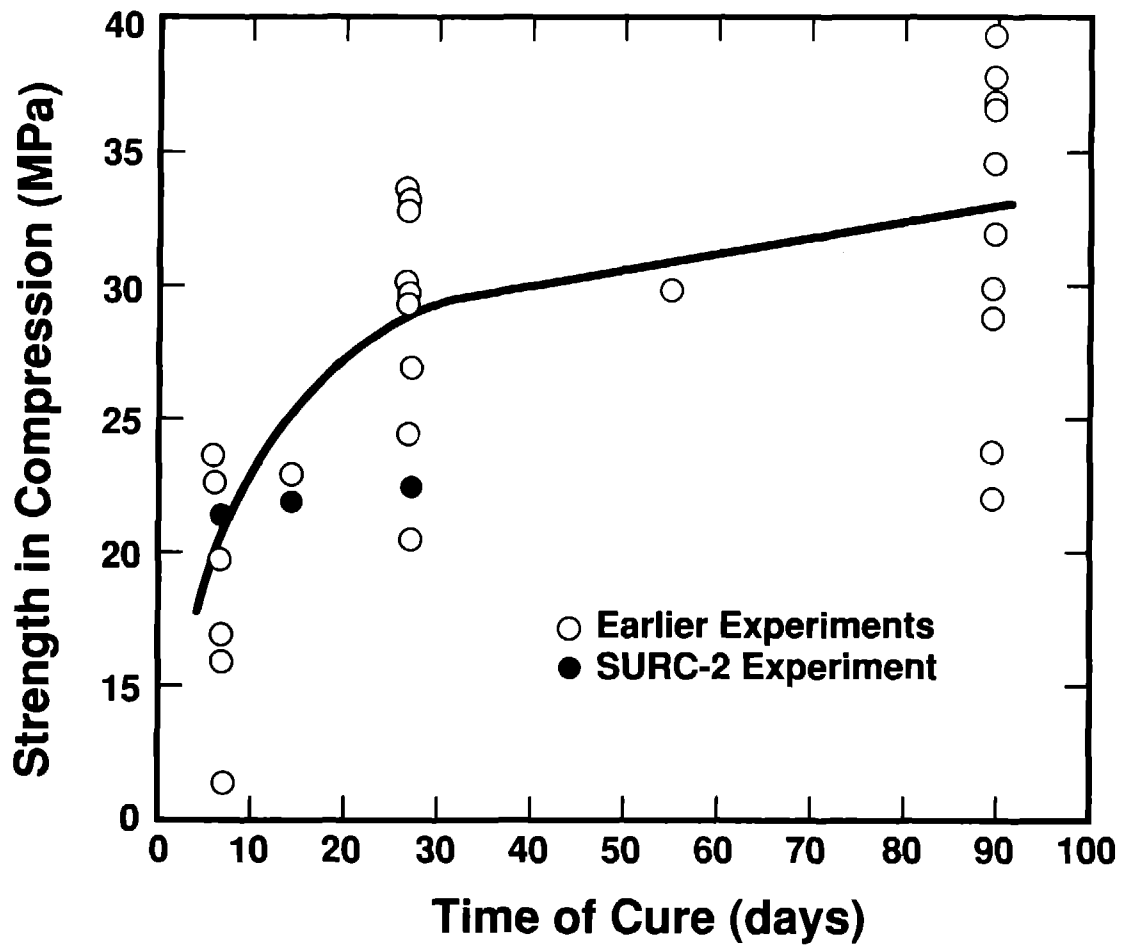
Figure 2.3   Compressive strength as a function of cure time for basaltic concrete

15
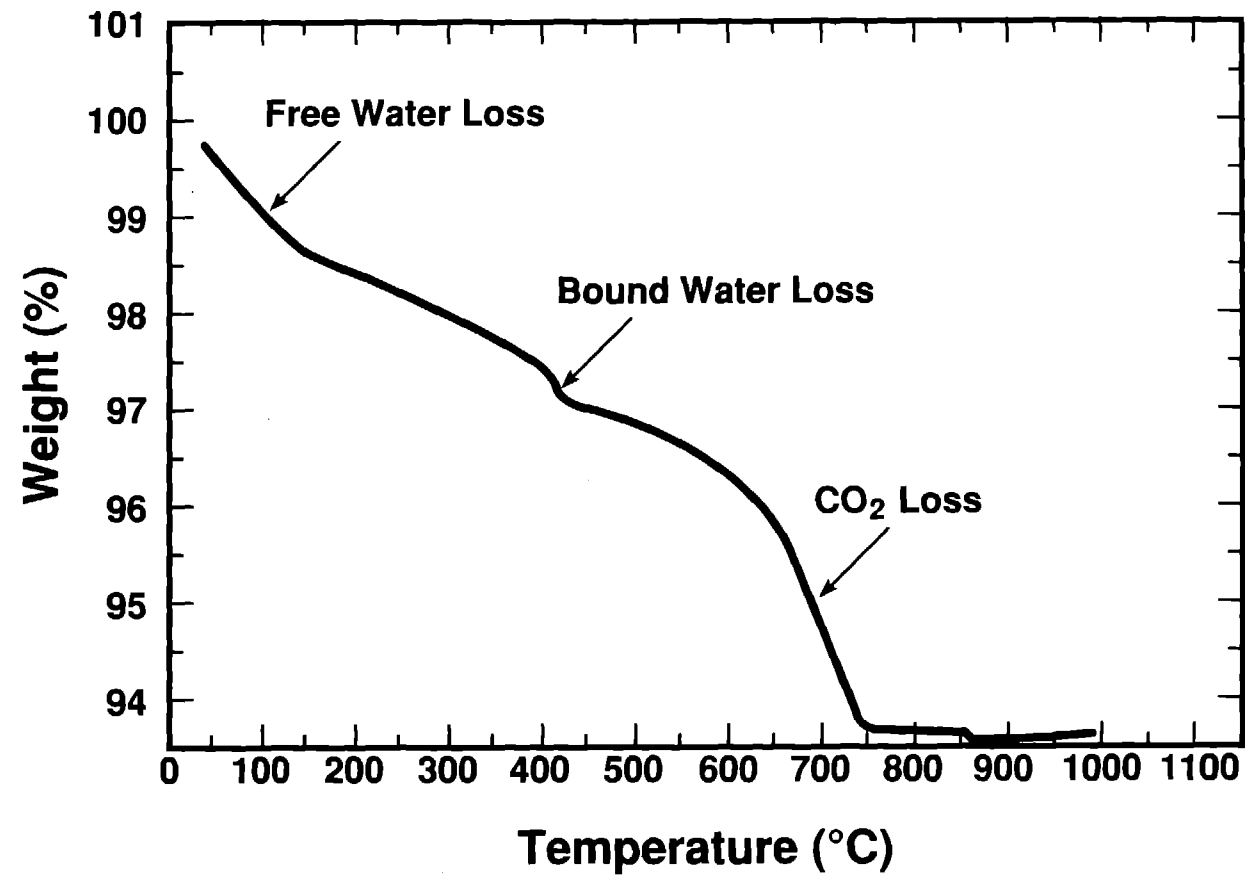
Figure 2.4 Thermogram (TGA) of basaltic concrete

Table 2.7 Mass and composition of charge material

Material	Composition (w/o)	Mass (g)
Crushed Isostatic Pressed Cylinders	63 UO_2 27 ZrO_2 10 Zr	36,969
Crushed Isostatic Pressed Cylinders	70 UO_2 30 ZrO_2	117,448
Powder	100 UO_2	33,079
Chips	100 Zr	13,000

Table 2.8 SURC-2 fission product simulants

Fission Product	Chemical Formula	Quantity (g)
Barium Molybdate	$BaMoO_4$	1000
Lanthanum Oxide	La_2O_3	750
Cerium Oxide	CeO_2	750
Niobium Oxide	Nb_2O_5	864
TOTAL		3364 g

FINE UO2 POWDER (33.1 kg) **ZrO2 BOARD** (2.5 CM) **TUNGSTEN PLATE SUSCEPTOR**

24.3 kg
64.2% UO2-27.5% ZrO2-8.2% Zr

27.5 kg
61.1% UO2-26.2% ZrO2-8.7% Zr

27.4 kg
61.1% UO2-26.2% ZrO2-12.8% Zr

25.2 kg
64.5% UO2-27.6% ZrO2-7.9% Zr

26.1 kg
64.6% UO2-27.7% ZrO2-7.7% Zr

37.0 kg
63.0% UO2-27.0% ZrO2-10.0% Zr

6 cm

11 cm

7.5 cm

11.5 cm

6 cm

10 cm

ZrO2 BOARD (1.3 CM)

BASALTIC CONCRETE
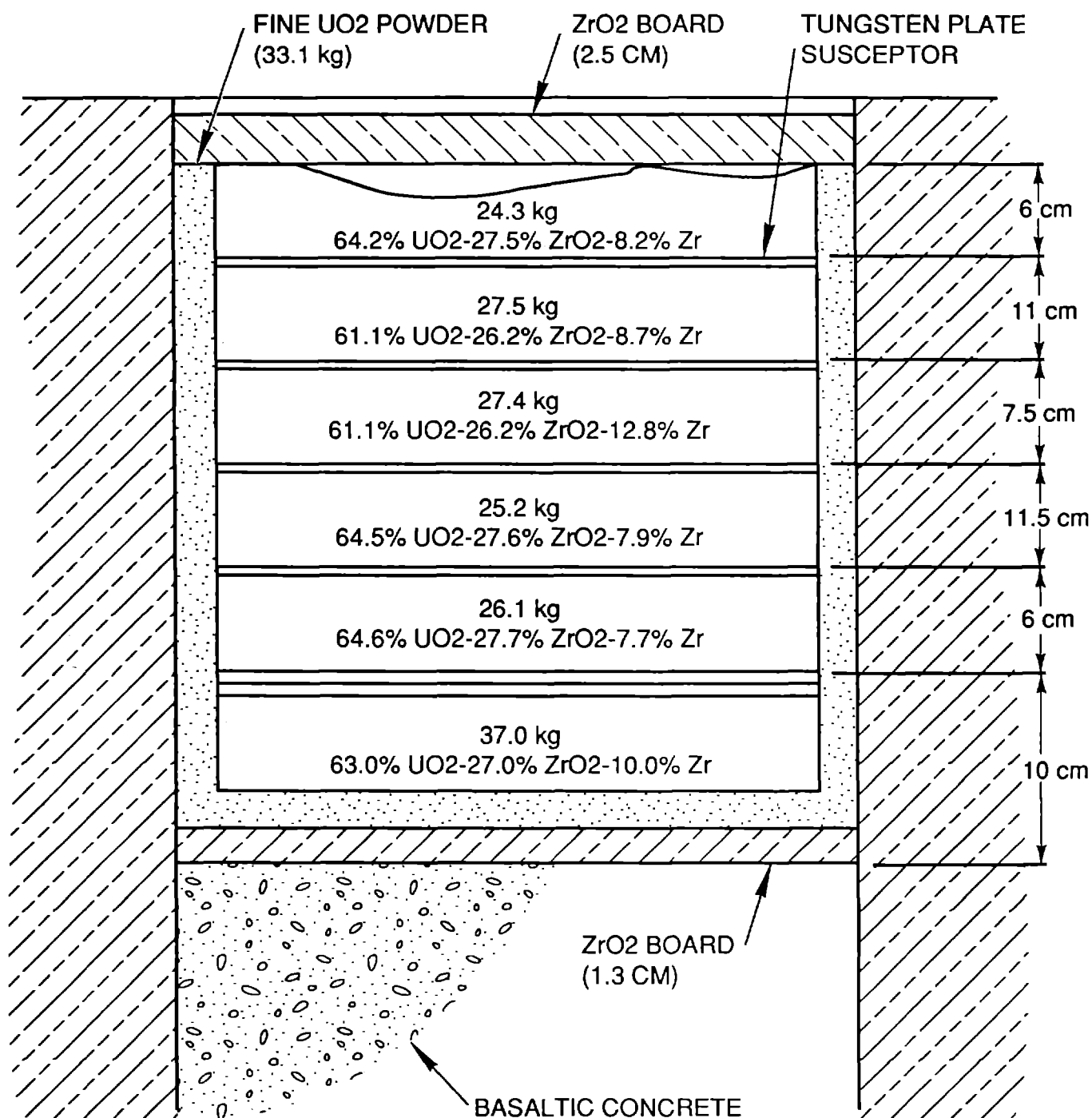
Figure 2.5 Mass and charge composition, SURC-2

3.0 Experimental Apparatus

The major components of the SURC-2 experimental apparatus are shown in Figure 3.1 and include a sealed, water-cooled, containment vessel, interaction crucible, and induction coil. These components are described in the following sections. The remainder of the SURC-2 apparatus including the exit flow piping and the gravel bed filter is described in Section 4.3.

3.1 Containment Vessel

An aluminum containment vessel was used in SURC-2 to ensure that nearly all of the reaction products would pass through the instrumented exit flow piping. A sectional view of the water cooled containment vessel is shown in Figure 3.2. The vessel was fabricated in two sections using 2.5 cm thick, weldable 6061-T6 aluminum alloy. The two sections were assembled using 24, 1.4 cm diameter hex head bolts and nuts securing the mating flanges. The flange of the lower section incorporated a double O-ring for sealing. The vessel was supported by four 10 cm diameter x 45.7 cm long legs welded to the bottom of the lower section. Basic features of the vessel are shown in Figure 3.2. The internal volume of the vessel was calculated to be approximately 2.0 m^3.

Aluminum (6061-T6) tubing 2.5 cm in diameter was welded to the outside and top of the vessel at a pitch of approximately 10 cm. This tubing was used to circulate a mixture of 50% by volume ethylene glycol in water used to cool the vessel during the experiment. The bottom of the vessel was cooled by means of three large reservoirs welded to the bottom of the vessel. The tubing and reservoirs were connected in series to form a single cooling circuit.

Bolted, flanged ports located in the lower section of the vessel were used to provide feedthroughs for power and instrumentation leads and for mounting fittings to connect a pressure transducer and tubing for supplying argon purge gas. Another port was fitted with a spring-loaded

safety diaphragm calibrated to open at 15 psig to eliminate the potential for overpressurization of the vessel. A 7.5 cm diameter flange port located in the base of the vessel was used as a feedthrough for all crucible thermocouple terminations. The sheaths and/or extension wires for all the thermocouples were pulled through a mating 90° flanged elbow. The elbow was filled with epoxy and allowed to cure, encapsulating the instrumentation leads and thermocouple sheaths. The elbow was then bolted to the flanged port, sealing the instrumentation cabling. A flanged port in the top of the vessel was fitted with a 5 cm O.D. x -157 cm wall x 1 m long, 304 stainless steel tube. This tube connected the interaction crucible with the flow system instrumented for sampling evolved gas and aerosols and measuring gas flowrate.

The inside floor of the lower vessel was lined with six inches of standard refractory MgO brick and back-filled with fine MgO powder. The perimeter of the floor was built-up with an extra layer of bricks six inches high and two inches thick. This was done to protect the vessel from melt attack should any molten material breach the interaction crucible during the experiment.

The vessel was pressure tested and certified to operate either in a partial vacuum or up to 20 psig.

3.2 Interaction Crucible

The interaction crucible for SURC-2 was designed to limit concrete erosion to the downward or axial direction. The materials used in the construction of the interaction crucible have been discussed in detail in Sections 2.1 and 2.2. The crucible used in SURC-2 was cylindrical and is shown in Figure 3.3. The main body of the crucible was cast in two sections--namely the upper and lower crucible. The overall dimensions of the crucible are 60 cm diameter x 100.0 cm high with a 40.0 cm diameter cavity 60.0 cm deep. Cast into the bottom of the lower
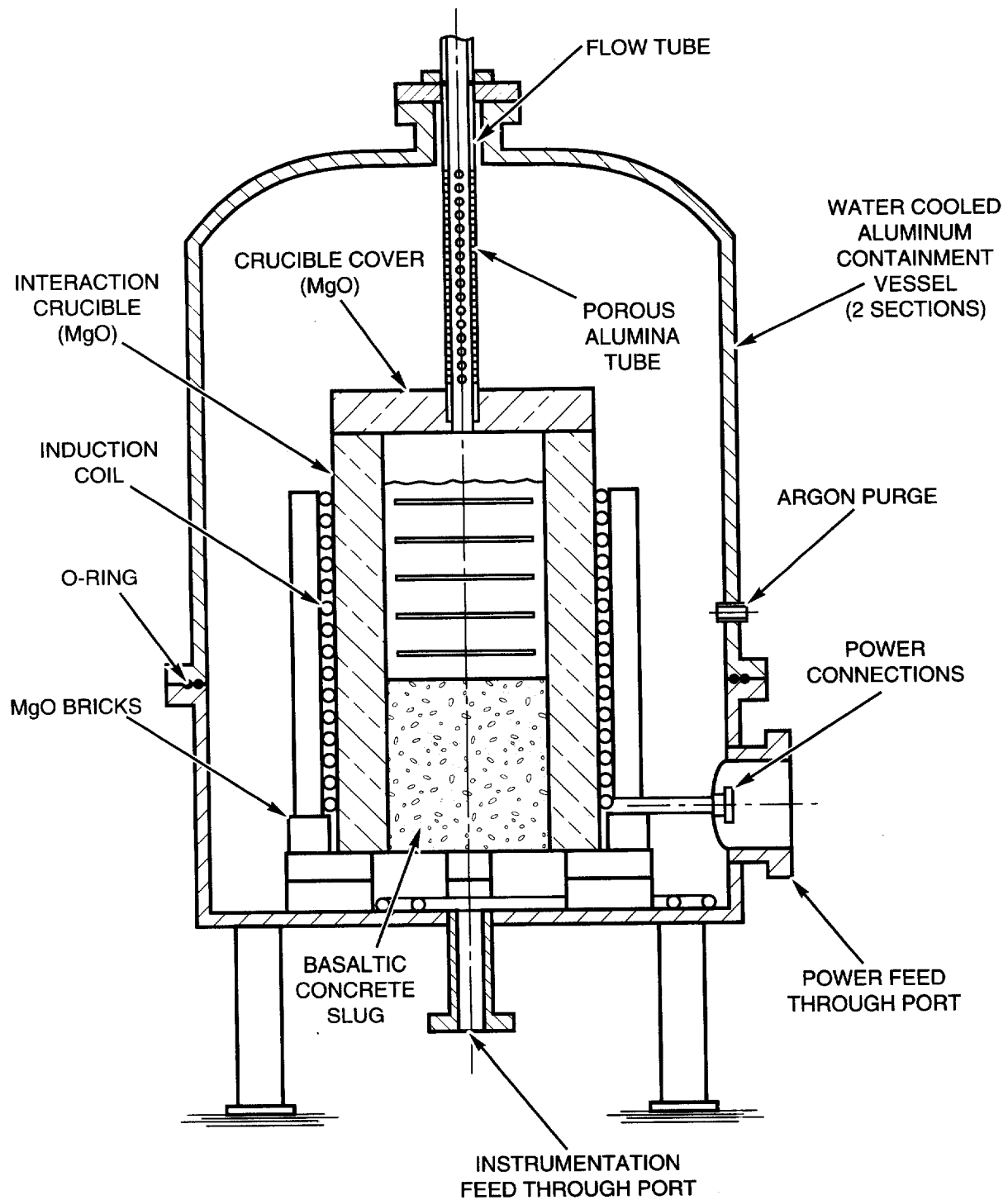
Figure 3.1 SURC-2 experimental apparatus

EXHAUST GAS & AEROSOL
PORT

UPPER
VESSEL
SECTION

FEED THROUGH
PORT

MgO BRICK
LINER

LOWER
VESSEL
SECTION

INSTRUMENTATION
PORT
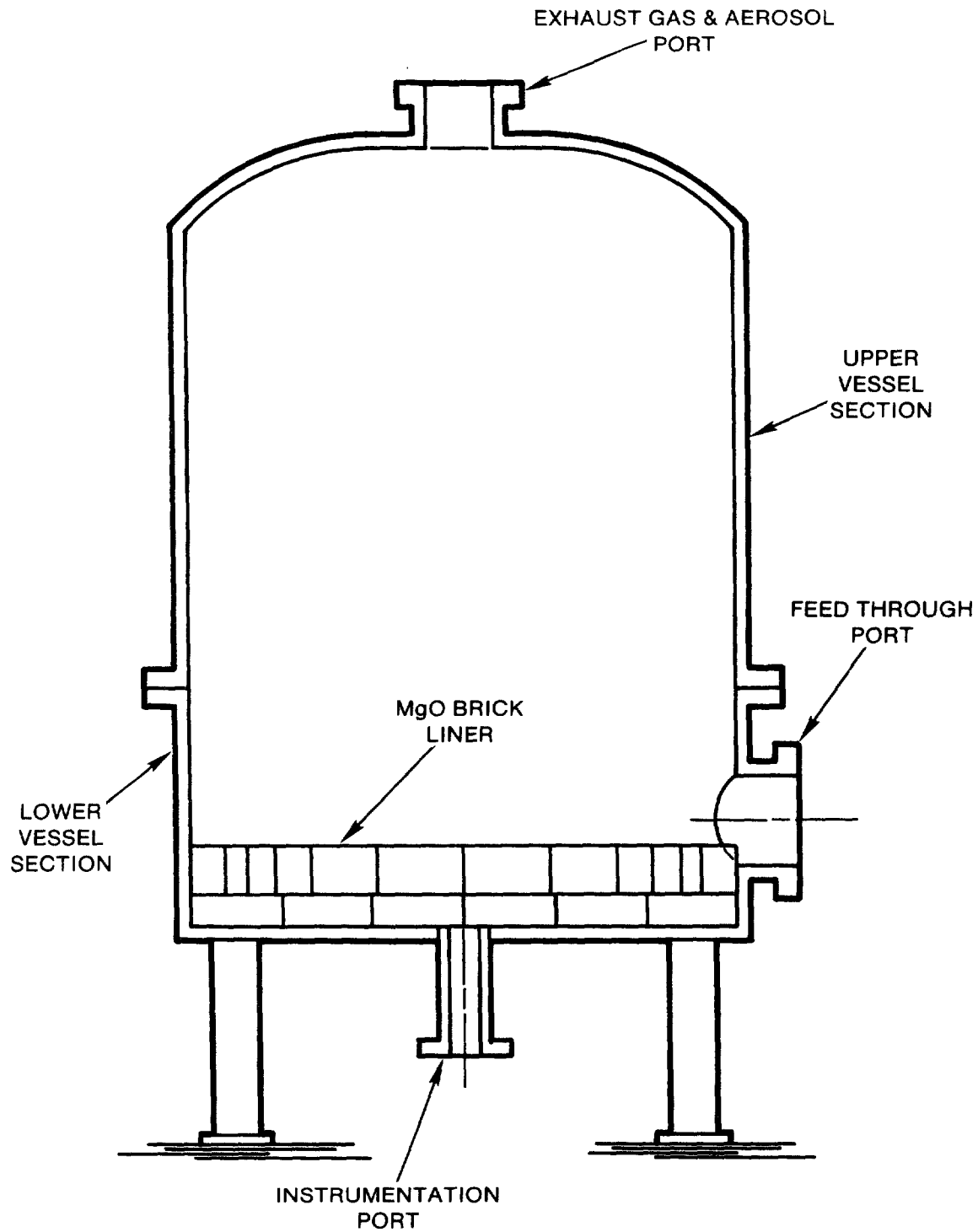
Figure 3.2 Sealed, water-cooled, containment vessel
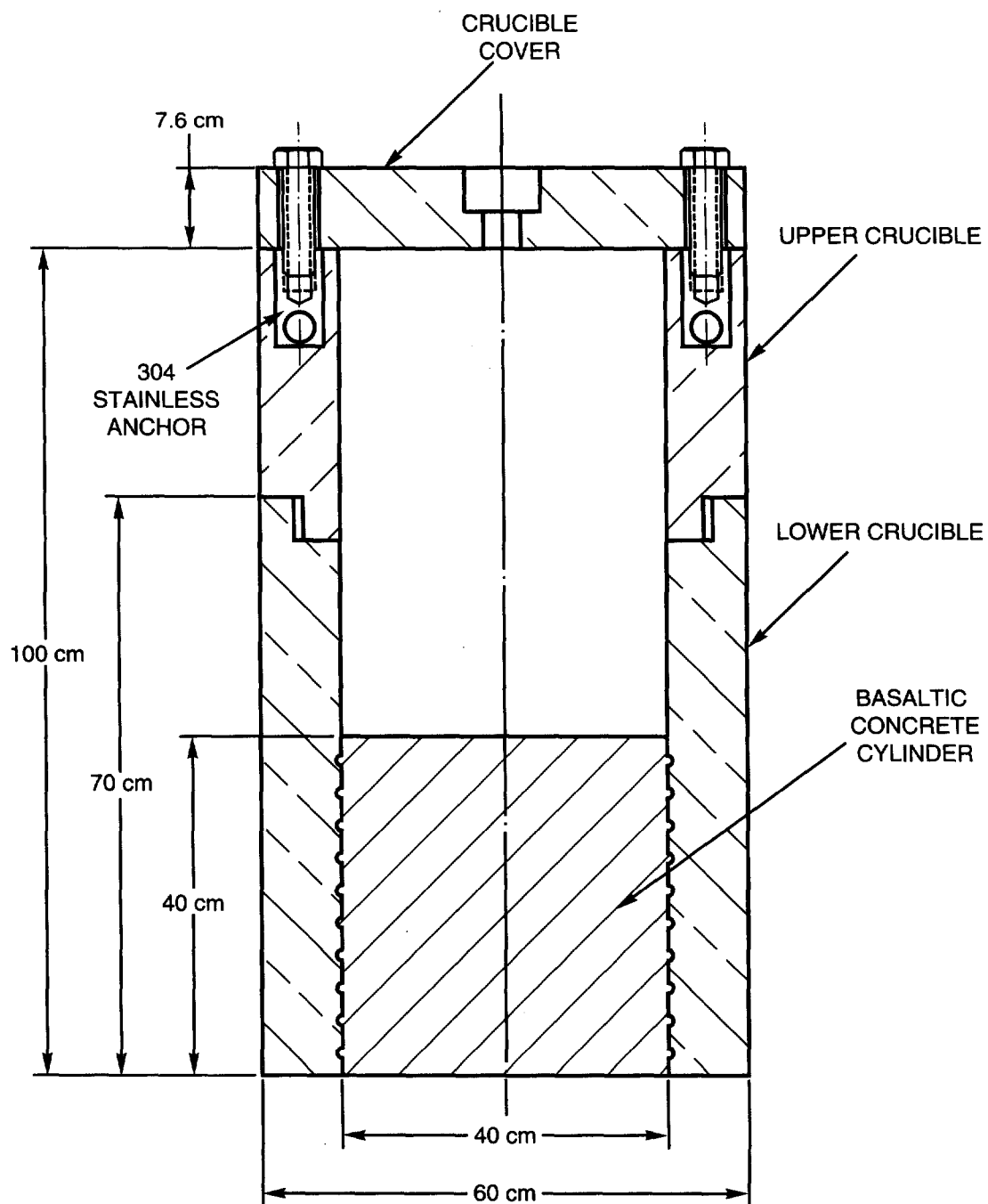
Figure 3.3 Interaction crucible, SURC-2

crucible was an instrumented basaltic concrete cylinder 40.0 cm diameter x 40.0 cm thick. The upper crucible was cast with an annular step and the lower crucible with a mating annular recess. The two crucible sections were assembled and sealed with Saureisen Cement No. 31.

The annulus of the upper and lower crucible and cover was cast using a reusable steel casting form constructed in a clam shell arrangement. Bolts were placed through the crucible cover and threaded into brass anchors cast into the upper crucible securing the cover. A detailed description of the casting forms and fabrication procedures is presented in Appendix B of the SURC-4 document [Copus et al., 1989].

Approximately 0.18 m^3 of MgO castable ceramic and 0.05 m^3 of basaltic concrete were required per crucible cast. The total estimated mass of the crucible was:

Annulus - MgO Castable
  Volume - 0.15 m^3 @ 2680 kg/m^3 = 402 kg

Cover - MgO Castable
  Volume - 0.03 m^3 @ 2680 kg/m^3 = 80 kg

Concrete Cylinder - Basaltic Concrete
  Volume - 0.05 m^3 @ 2400 kg/m^3 = 120 kg

TOTAL MASS   602 kg

The annulus, concrete cylinder, and crucible cover were instrumented with 117 type K thermocouples cast into the crucible in 16 arrays to measure thermal response. Figure 3.4 shows the relative thermocouple locations and the various arrays cast into the crucible. This figure also shows the nomenclature used to describe the locations of the thermocouples in cylindrical coordinates, specifically r, θ, z and t. Additionally, six type S and six type C thermocouples installed into six alumina tubes were cast into the basaltic concrete cylinder to measure melt temperature.

Seventy-two thermocouples were cast into the concrete in three arrays. The array containing thermocouples designated C1 through C24 was located on the axial centerline at one centimeter intervals (0, 1, 2, etc.). The array containing thermocouples designated C25 through C48 were located on a line parallel to the center axis at a radial distance of 10.0 cm. The third array designated by thermocouples C49 through C72 was located near the perimeter of the concrete cylinder at a radial distance of 18.0 cm. The depth of the thermocouples in the latter two arrays were identical to the axial array. The locations of the thermocouples cast into the concrete cylinder are tabulated in Table 3.1. The sheath of each thermocouple was bent at an angle of 90°, 10 sheath diameters from the tip. This was done to minimize the errors caused by heat conduction down the metal sheath. Installation of a typical thermocouple array is shown in Figure 3.5.

Six four-hole alumina tubes were cast into the concrete slug parallel to the axial centerline, 60 degrees apart at a radial distance of 14 cm. Installed in each tube were two type S and two type C thermocouples located at various depths from the surface of the concrete cylinder. These thermocouples were used to measure melt temperature and their locations are tabulated in Table 3.2. As the meltpool attacks the concrete, the alumina tubes are exposed to the meltpool and the embedded C and S type thermocouples then record the melt temperature. Figure 3.5 shows an installation of a typical alumina tube with the type S and type C thermocouples.

Thermocouples used to monitor sidewall temperatures in the MgO annulus of the crucible were installed into pre-cast MgO cylinders prior to casting as shown in Figure 3.6. The ends of the cylinders conformed to the curvature of the annulus of the casting forms providing a good fit. The cylinders were bolted to the inside diameter of the outer steel crucible form by threading a small hex head bolt into a small brass anchor
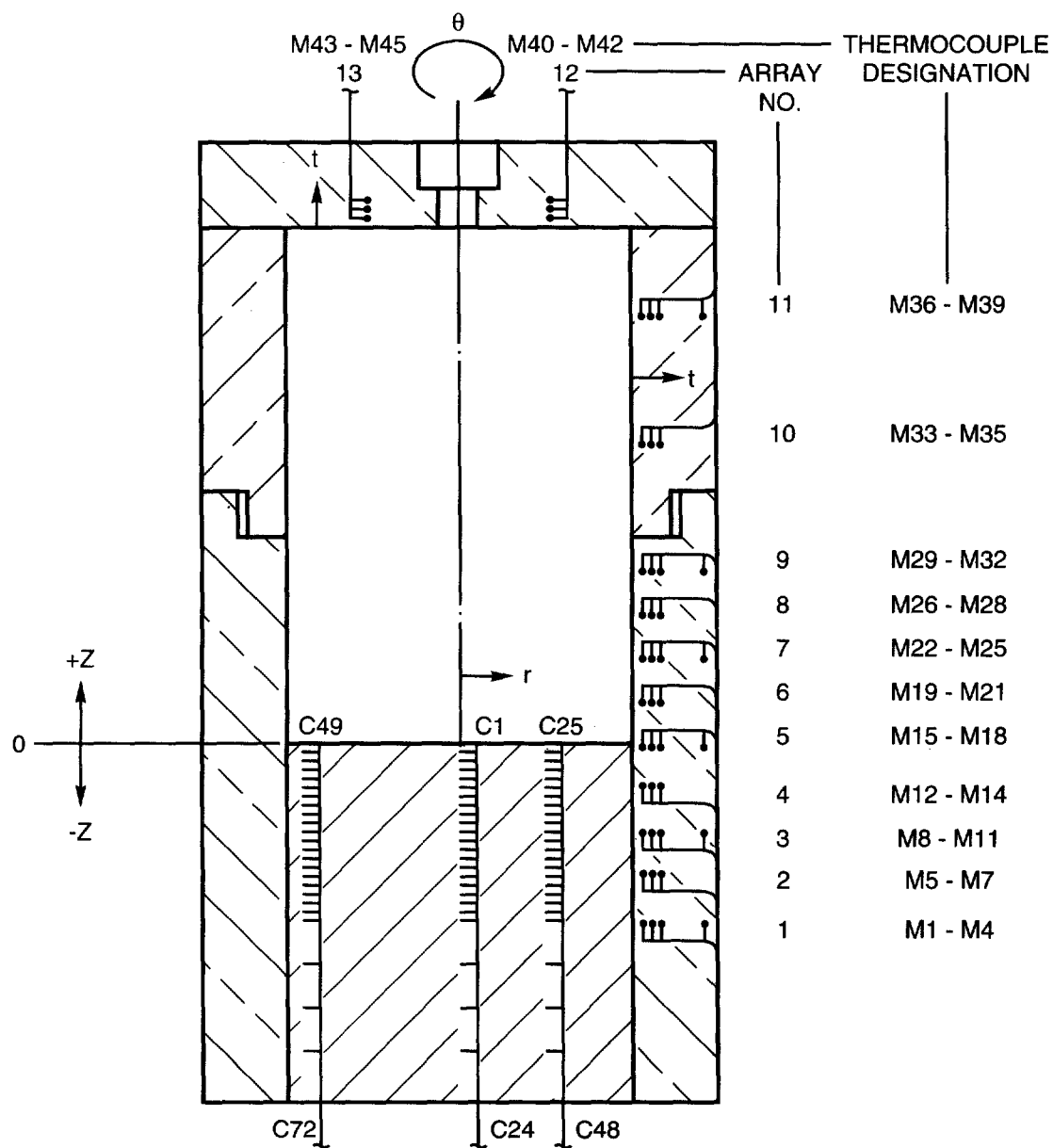
Figure 3.4 Relative thermocouple locations, SURC-2 crucible

Table 3.1 Location of thermocouples cast within the concrete
cylinder, SURC-2 (see Figure 3.4)

Thermocouple No.	r (cm)	θ (degree)	-z (cm)
C1	0	0	0
C2	0	0	1.0
C3	0	0	2.0
C4	0	0	3.0
C5	0	0	4.0
C6	0	0	5.0
C7	0	0	6.0
C8	0	0	7.0
C9	0	0	8.0
C10	0	0	9.0
C11	0	0	10.0
C12	0	0	11.0
C13	0	0	12.0
C14	0	0	13.0
C15	0	0	14.0
C16	0	0	15.0
C17	0	0	16.0
C18	0	0	17.0
C19	0	0	18.0
C20	0	0	19.0
C21	0.0	0	20.0
C22	0.0	0	25.0
C23	0.0	0	30.0
C24	0.0	0	35.0
C25	10.0	0	0.0
C26	10.0	0	1.0
C27	10.0	0	2.0
C28	10.0	0	3.0
C29	10.0	0	4.0
C30	10.0	0	5.0
C31	10.0	0	6.0
C32	10.0	0	7.0
C33	10.0	0	8.0
C34	10.0	0	9.0
C35	10.0	0	10.0
C36	10.0	0	11.0
C37	10.0	0	12.0
C38	10.0	0	13.0
C39	10.0	0	14.0
C40	10.0	0	15.0

Table 3.1 Location of thermocouples cast within the concrete
cylinder, SURC-2 (see Figure 3.4) (Continued)

Thermocouple No.	r (cm)	θ (degree)	-z (cm)
C41	10.0	0	16.0
C42	10.0	0	17.0
C43	10.0	0	18.0
C44	10.0	0	19.0
C45	10.0	0	20.0
C46	10.0	0	25.0
C47	10.0	0	30.0
C48	10.0	0	35.0
C49	18.0	180	0.0
C50	18.0	180	1.0
C51	18.0	180	2.0
C52	18.0	180	3.0
C53	18.0	180	4.0
C54	18.0	180	5.0
C55	18.0	180	6.0
C56	18.0	180	7.0
C57	18.0	180	8.0
C58	18.0	180	9.0
C59	18.0	180	10.0
C60	18.0	180	11.0
C61	18.0	180	12.0
C62	18.0	180	13.0
C63	18.0	180	14.0
C64	18.0	180	15.0
C65	18.0	180	16.0
C66	18.0	180	17.0
C67	18.0	180	18.0
C68	18.0	180	19.0
C69	18.0	180	20.0
C70	18.0	180	25.0
C71	18.0	180	30.0
C72	18.0	180	35.0
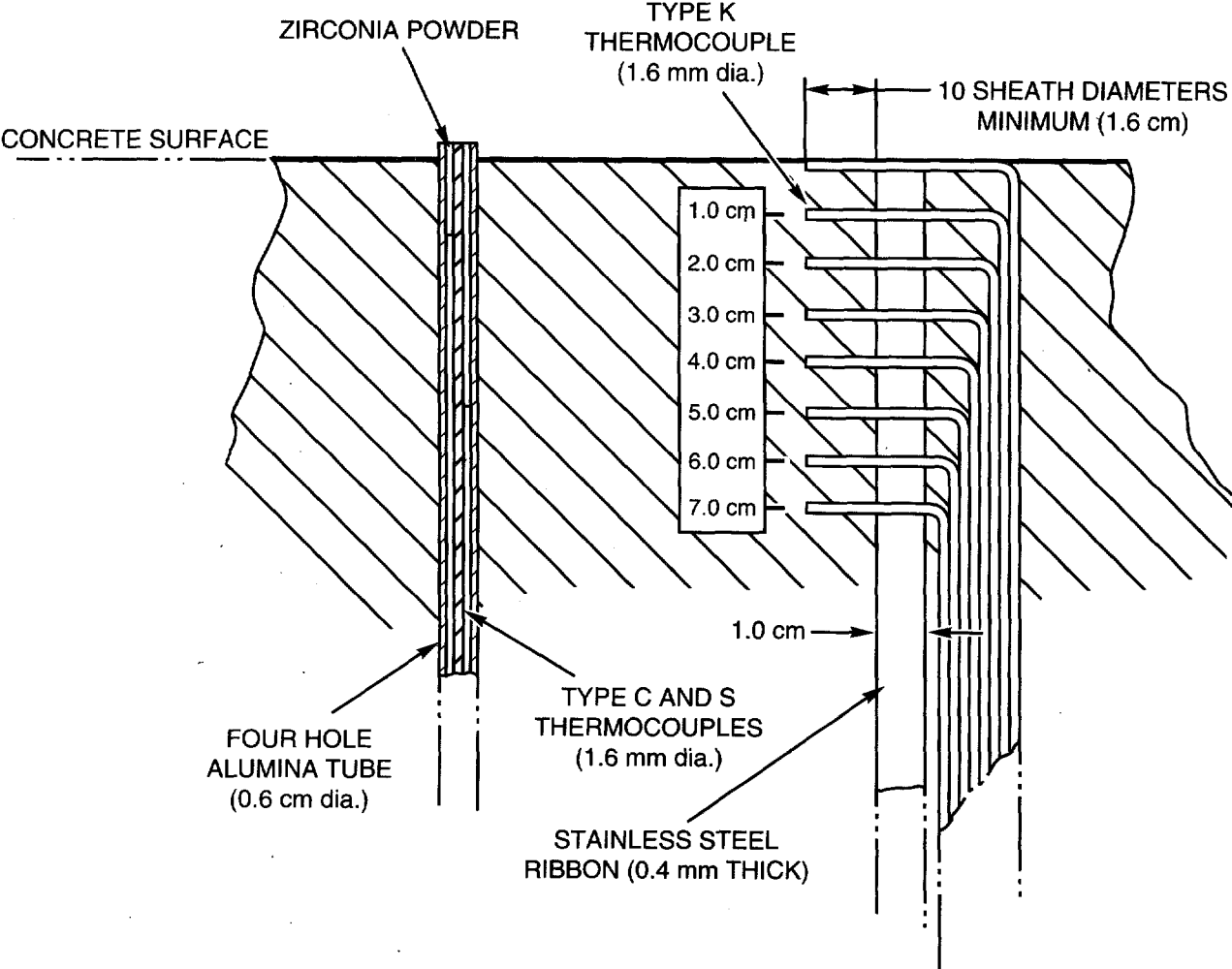
Figure 3.5 Typical thermocouple arrays cast into the concrete

Table 3.2 Location of thermocouples installed in the alumina
tubes and cast into the concrete cylinder, SURC-2

Tube Number	Thermocouple No.	Thermocouple Type	r (cm)	θ (degree)	-z (cm)
4	T4-1	C	14	180	1
1	T1-1	C	14	0	2
2	T2-1	C	14	60	2
5	T5-1	C	14	240	2
3	T3-1	C	14	120	3
6	T6-1	C	14	300	3
4	T4-2	C	14	180	4.5
1	T1-2	C	14	0	5
2	T2-2	C	14	60	5
5	T5-2	C	14	240	5
3	T3-2	C	14	120	7
6	T6-2	C	14	300	7
4	T4-3	S	14	180	10.5
5	T5-3	S	14	240	11.0
1	T1-3	S	14	0	12.0
2	T2-3	S	14	60	13
3	T3-3	S	14	120	13
6	T6-3	S	14	300	13
4	T4-4	S	14	180	15
1	T1-4	S	14	0	15.5
5	T5-4	S	14	240	18
2	T2-4	S	14	60	19
3	T3-4	S	14	120	19
6	T6-4	S	14	300	19
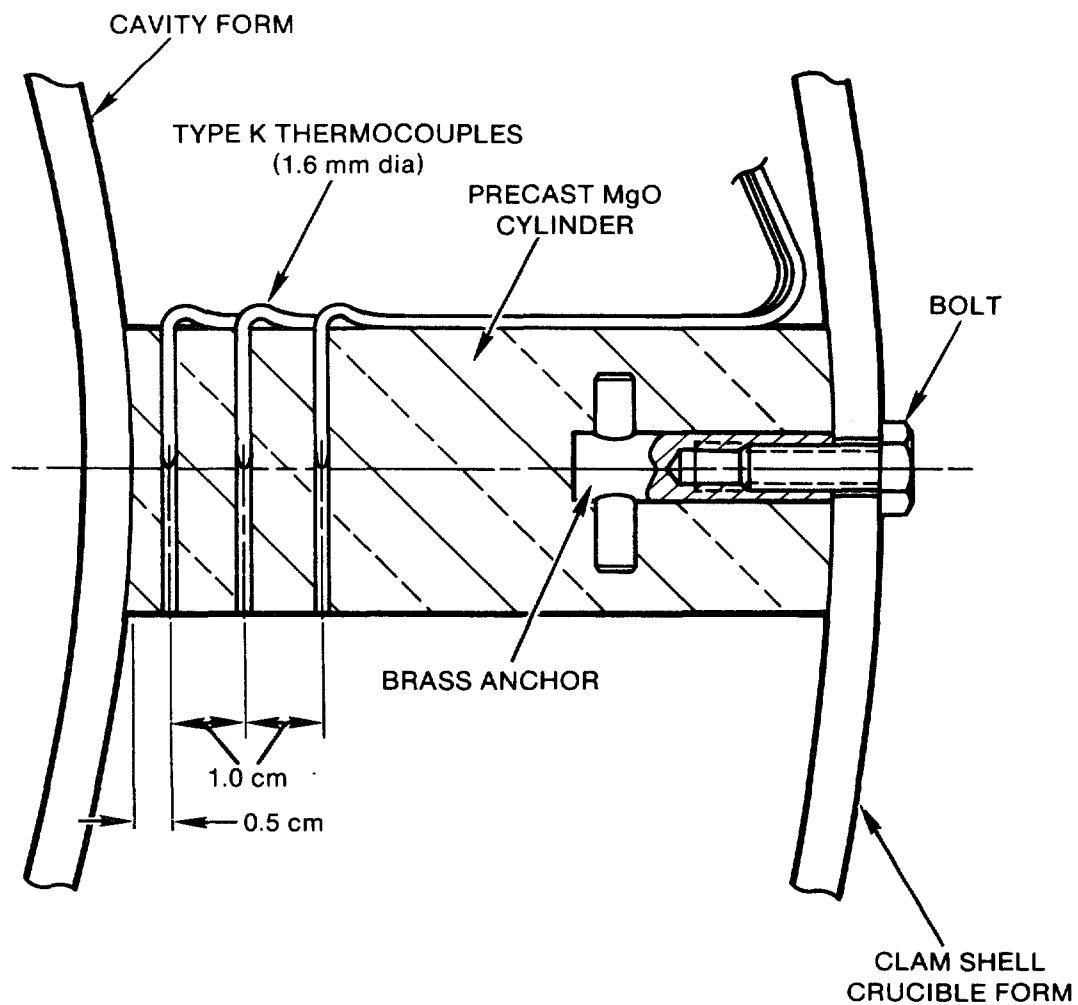
Figure 3.6 Thermocouple array installation, MgO annulus

cast into the MgO cylinders. This method for installation of sidewall thermocouples accurately positions the thermocouples which is critical for heat flux calculations. The thermocouple tips were oriented in a horizontal plane parallel to the base of the crucible and perpendicular to the thermal front. The specific locations of the sidewall thermocouples are tabulated in Table 3.3.

Two thermocouple arrays were cast into the crucible cover. Like the arrays cast into the annulus, the thermocouples were installed into pre-cast MgO cylinders. The locations of these thermocouples are listed in Table 3.4. The t dimension given in the table is referenced from the bottom face of the crucible cover.

3.3 Induction Coil

The induction coil used in the SURC-2 experiment was designed and built by Inductotherm Corporation. The coil was fabricated with 3.8 cm O.D. copper tubing having 20 turns with a pitch of 4.2 cm. The coil was supported by six equally spaced hard rock maple columns 7.5 cm x 5.5 cm x 100 cm long attached to the outside of the coil. The dimensions of the coil were 61 cm I.D. x 71 cm high. After the coil was placed around the crucible and centered on the oxide charge inside the aluminum containment vessel, fiber glass cloth was attached to the outside of the support columns. Fine MgO powder was placed between the crucible and coil and dry K/R Cast-98 was placed between the coil and fiber glass shroud. This was done to protect the coil from contact with debris, should the crucible fail.

3.4 Charge Assembly

The inductive ring susceptor technique was used to melt and sustain the molten state of the oxide meltpool. Basically, this technique uses embedded tungsten susceptors which are inductively heated using an external coil. The susceptor

assemblies draw power from the magnetic induction field. This energy heats the metallic susceptors which in turn heats the oxide charge materials via conduction and radiation heat transfer. The number and size of the susceptors determine the boundaries of the meltpool and the material and shape of the susceptors determine the heating efficiency. This technique was developed by E.R. Copus at Sandia National Laboratories and has been used to melt SiO_2, Al_2O_3, UO_2, and UO_2-ZrO_2 materials. Detailed information on the development of the inductive ring susceptor technique is reported by E.R. Copus [Copus, 1983] and experimental efforts using the technique are described by Copus [Bradley and Copus, 1986] and J.G. Gronager [Gronager et al., 1986].

The charge assembly for the SURC-2 test consisted of 3 elements: (1) the oxide melt material, (2) the ring susceptor assembly, and (3) the boundary insulation layer. A schematic depicting the layout of the charge assembly was previously shown in Figure 2.5. The oxide melt material in the SURC-2 experiment was formed from isostatically pressed cylinders of 63 w/o UO_2 - 27 w/o ZrO_2 - 10 w/o Zr. These cylinders were crushed into particulate form just prior to the execution of SURC-2. The particulate material was evenly distributed within the central charge volume which had dimensions of 52 cm (height) x 35.6 cm (diameter). The oxide melt material weighed 167.5 kg and had an approximate density of 3.6 g/cm^3.

The ring susceptor assembly for SURC-2 consisted of five tungsten rings, three tungsten guide rods, and fifteen tungsten spacers. All of the tungsten rings were 35.6 cm in diameter and had a central hole diameter of 7.6 cm. The top four rings had a thickness of 0.32 cm and were spaced as shown in Figure 2.5. The bottom ring had a thickness of 0.64 cm and was spaced 7.5 cm above the zirconia board insulation layer. Three guide rods were used to prevent skewed collapse during the melting and interaction phase of experiment. These rods were 1.3 cm

Table 3.3 Location of thermocouples cast within the MgO
sidewall, SURC-2 (see Figure 3.4)

Array No.	Thermocouple No.	t (cm)	θ (degree)	z (cm)
1	M1	0.5	0	-20.0
	M2	1.5	0	-20.0
	M3	2.5	0	-20.0
	M4	9.0	0	-20.0
2	M5	0.5	0	-15.0
	M6	1.5	0	-15.0
	M7	2.5	0	-15.0
3	M8	0.5	0	-10.0
	M9	1.5	0	-10.0
	M10	2.5	0	-10.0
	M11	9.0	0	-10.0
4	M12	0.5	90	- 5.0
	M13	1.5	90	- 5.0
	M14	2.5	90	- 5.0
5	M15	0.5	90	0.0
	M16	1.5	90	0.0
	M17	2.5	90	0.0
	M18	9.0	90	0.0
6	M19	0.5	165	+ 5.0
	M20	1.5	165	+ 5.0
	M21	2.5	165	+ 5.0
7	M22	0.5	165	+10.0
	M23	1.5	165	+10.0
	M24	2.5	165	+10.0
	M25	9.0	165	+10.0
8	M26	0.5	270	+15.0
	M27	1.5	270	+15.0
	M28	2.5	270	+15.0
9	M29	0.5	270	+20.0
	M30	1.5	270	+20.0
	M31	2.5	270	+20.0
	M32	9.0	270	+20.0
10	M33	0.5	0	+35.0
	M34	1.5	0	+35.0
	M35	2.5	0	+35.0
11	M36	0.5	0	+50.0
	M37	1.5	0	+50.0
	M38	2.5	0	+50.0
	M39	9.0	0	+50.0

Table 3.4 Location of thermocouples cast within the
crucible cover, SURC-2 (see Figure 3.6)

Array No.	Thermocouple No.	t (cm)	θ (degree)	z (cm)
12	M40	10.0	0	0.5
	M41	10.0	0	1.5
	M42	10.0	0	2.5
13	M43	10.0	180	0.5
	M44	10.0	180	1.5
	M45	10.0	180	2.5

in diameter and 40 cm in length. The tungsten spacers were 0.64 cm in diameter and 2.5 cm in length. Five spacers were placed in the bottom, middle, and top rings with 1 cm above and 1 cm below each ring so that none of the rings would touch each other during the test. The total tungsten ring assembly weighed approximately 50 kg.

The boundary insulation layer of the charge consisted of a zirconia insulating board placed on top and at the base of the charge and an annulus of fine uranium dioxide powder. The zirconia boards were 40 cm in diameter. A 1.3-cm-thick board was placed on top of the concrete cylinder. This was followed by a 1.3-cm-thick layer of fine UO_2 powder. The base of the charge was configured in this manner to minimize concrete dehydration during initial heating and prior to melt attack. As the charge was built up within the crucible, fine UO_2 powder was used between the crucible sidewall and charge material. The annular thickness of the powder was 2.5 cm and spanned the height of the charge of 52 cm. The average density of the UO_2 insulation boundary layer was 4.9 g/cm^3 and its total weight was 33.1 kg. The powder at the sidewalls sintered during the experiment providing an insulating skull preventing melt contact with the MgO crucible. A 2.5 cm zirconia board was placed on top of the charge. This was done to prevent heat losses. The total mass at the two zirconia boards used in the charge was 1.7 kg. The total mass of the charge including 3.4 kg of fission product simulants was 203.9 kg.

4.0 Instrumentation and Calibration

The HP 1000 data acquisition system used 197 data channels to record the results of the SURC-2 test. Of these, 162 were thermocouple channels. Seventy-two thermocouple channels were used to monitor axial erosion in the concrete. An additional 45 thermocouple channels were used to record temperatures in the crucible sidewalls and lid. Eleven thermocouples were located in the system to monitor the temperature of power supply water and effluent gases. Seven more thermocouples were used to monitor the temperature within the aerosol collection system, and the last 27 thermocouple channels were used to record the meltpool temperature.

Thirty-five data channels were voltage channels. Fourteen of these were used to monitor pressure and flow through the system. One was used to record the relative opacity of the gas stream. Five more were used to measure the induction coil power and coolant flow levels. Three channels were used to record the output from the optical pyrometer. Four were used to monitor the composition of the effluent gas and the last eight were used to record aerosol data. Each channel was recorded every ten seconds for the first 90 minutes of the test and every five seconds at times thereafter.

In addition to the HP 1000 data system, data were sampled and stored with the SEDS aerosol system (31 channels), the gas grab sample system (seven channels), the Infocon Mass Spectrometer (nine channels), and a video camera/recorder system.

4.1 Thermocouple and Pyrometer Instrumentation

Seventy-two thermocouples divided into three groups were cast into the concrete slug of the interaction crucible. The relative locations of the thermocouples were discussed in Section 3.2. One typical array of 24 type K thermocouples was located on the axial centerline. Thermocouples in this array were spaced 1 cm apart.

These thermocouples had a 0.16 cm diameter, stainless steel ungrounded sheaths. Six sets of two type S and two type C (Tungsten - 5% Rhenium vs. Tungsten 26% Rhenium) thermocouples were mounted in alumina tubes and cast into the concrete. The alumina tubes were 0.64 cm in diameter and contained four 0.2 cm diameter holes in which the thermocouples were installed. The type S thermocouples installed in the alumina tubes were 0.16 cm diameter, and had ungrounded, tantalum sheaths. The type C thermocouples also had a 0.16 cm, ungrounded, tantalum sheath. These alumina tube arrays were cast into the concrete slug on a radius of 14 cm from the axis and at 60 degrees. Theta for the angular orientation of these arrays is taken to be zero relative to the sidewall array located at $z = -20$ cm. Positive theta is clockwise looking down on the crucible from the top. The type S and the type C thermocouples were installed for measuring melt temperatures. These thermocouples also provided some data on the concrete thermal response prior to ablation which complimented data from the arrays of type K thermocouples.

The type K thermocouples were cast into the concrete primarily to measure the thermal response and to indicate the position of ablation front. The C and S types were installed into the four hole alumina protection tubes to measure melt pool temperature. Each of these thermocouple configurations was comprised of 0.254 mm wire junctions. The time constant for these metal sheathed thermocouples based on water studies published by the manufacturer is 0.3 sec [Omega Engineering Inc.].

The temperature range of the type K thermocouples is 273 K to 1523 K. The maximum limit of error using manufacturer's calibration data is ±9.4 K at 1523 K [Omega Engineering Inc.]. These thermocouples are primarily used to measure temperatures in the concrete and to indicate the position of the erosion front. The temperature measured by these thermocouples increases with the approach of the advancing melt

front. They rapidly fail after contact with the melt front by oxidation or dissolution of the sheath material and junction, thus, indicating the position of the ablation front.

The type C and S thermocouples installed in the four hole alumina tubes are used to indicate the temperature of the melt pool. The alumina tube protects the thermocouples long enough to obtain a reliable temperature reading for up to several minutes prior to failure. The sheath material and junction then fail by oxidation or dissolution into the melt pool.

The type C thermocouples were installed in the alumina tubes at concrete depths from $z = -1$ cm to -7 cm. This is the region where the initial melt pool temperatures will be the highest. These thermocouples have a range of 273 K to 2593 K. The maximum limit or error using the manufacturer's calibration is ± 25.9 K [Omega Engineering Inc.].

The type S thermocouples have a range of 273 K to 2033 K. The maximum limit of error using manufacturer's calibration is ± 5.1 K [Omega Engineering Inc.]. These thermocouples were installed in the alumina protection tubes at concrete depths ranging from $z = -10.5$ cm to 19 cm. At these depths, a sufficient amount of concrete will be taken into solution with the uranium dioxide to reduce the melt temperature of the pool to a range that can be measured by these thermocouples.

The tantalum sheath and junction of the type C thermocouples is not well suited to operate in a severe oxidizing environment. These thermocouples function best in an inert environment which extends their period of survival. As a result, these thermocouples will perform well installed in the bottom of the argon purged tungsten pyrotubes that will be discussed next. These thermocouples will provide a reliable secondary measurement of the charge temperature indicated by the fiber optic pyrometers focused at the bottom of the pyrotubes.

The S type junction functions better than the C type in an oxidizing environment, however, it does not have the temperature range of the C types. To get a reliable temperature measurement with these two types of thermocouples, they only need to survive contact with the melt pool for approximately 30 sec. Melt pool temperatures have been successfully measured using this technique in numerous sustained core/concrete experiments conducted in the past.

An additional 45 thermocouples were used to monitor the MgO sidewall and lid temperatures. Locations for these K-type devices are also described in Section 3.2. These type K thermocouples were identical in sheath material and diameter as those cast in the concrete.

In addition to the thermocouples, three fiber optic pyrometers manufactured by Micron Incorporated were used to measure the temperature of the oxidic debris. Fiber optic pyrometers were used because the focusing head and lens assembly were very compact and the fiber optic signal transmitted to the signal conditioner was not affected by the electric field caused by the induction power supply. These pyrometers provided virtually a noise-free output signal proportional to the temperature measured at their focal point. A schematic showing the hardware and instrumentation used in the pyrotube assembly is shown in Figure 4.1.1. Each of the pyrometers was attached to a closed end thick walled tungsten pyrotube measuring 2.5 cm O.D. and 1.3 cm I.D. The lengths varied so that the debris temperature could be measured at three different elevations. The length of the pyrotubes were 66, 76, and 81 cm long. The bottom of the pyrotubes were located 0, 5, and 15 cm above the 1.3 cm thick zirconia insulating board placed directly on the concrete. The three pyrotubes were precisely located in the center of the charge equally spaced on a 5.4 cm diameter bolt circle as shown in Figure 4.1.2. The tungsten tubes were connected to a stainless steel adapter using a stainless steel tube to pipe adapter as shown in Figure 4.1.3.
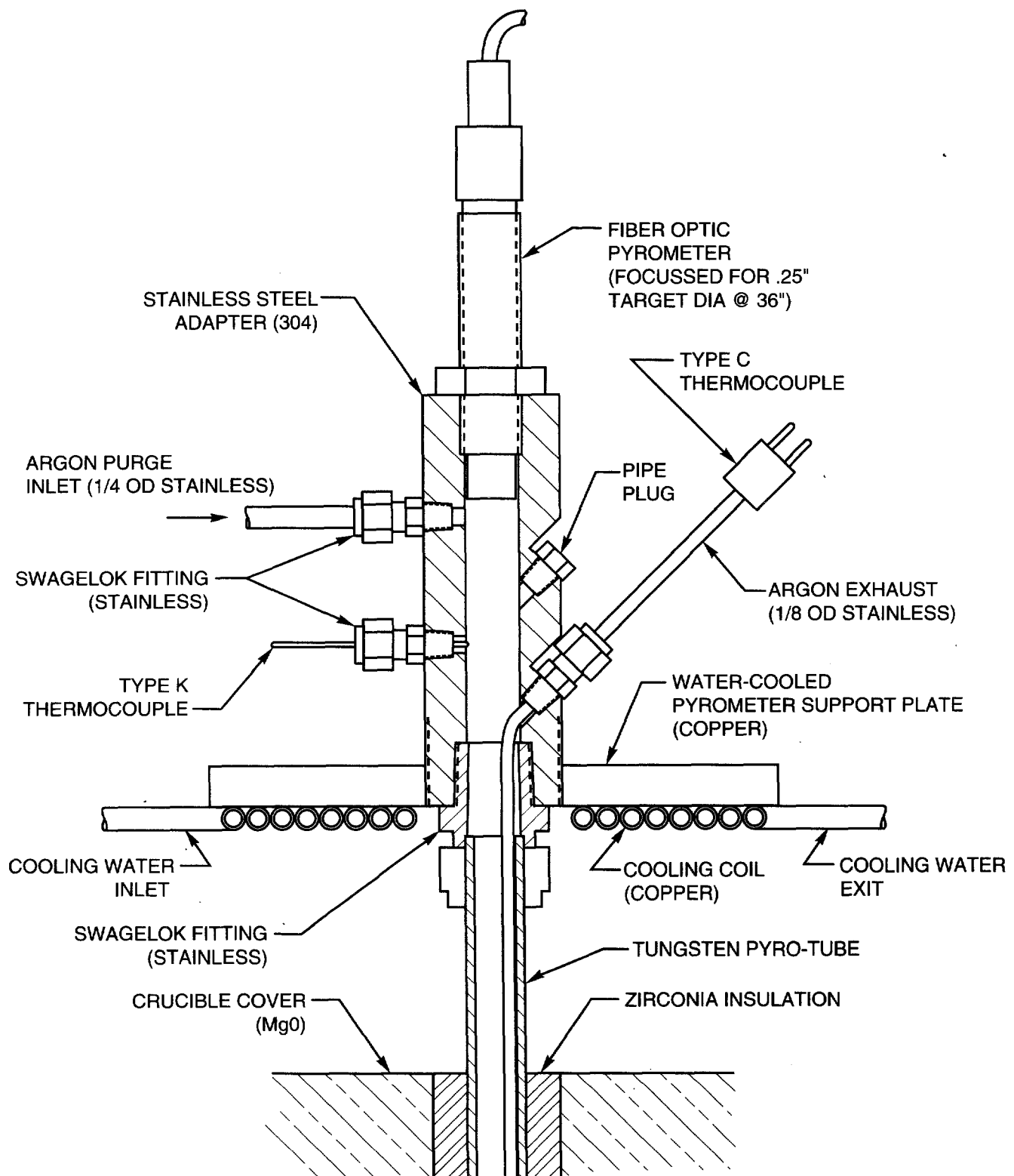
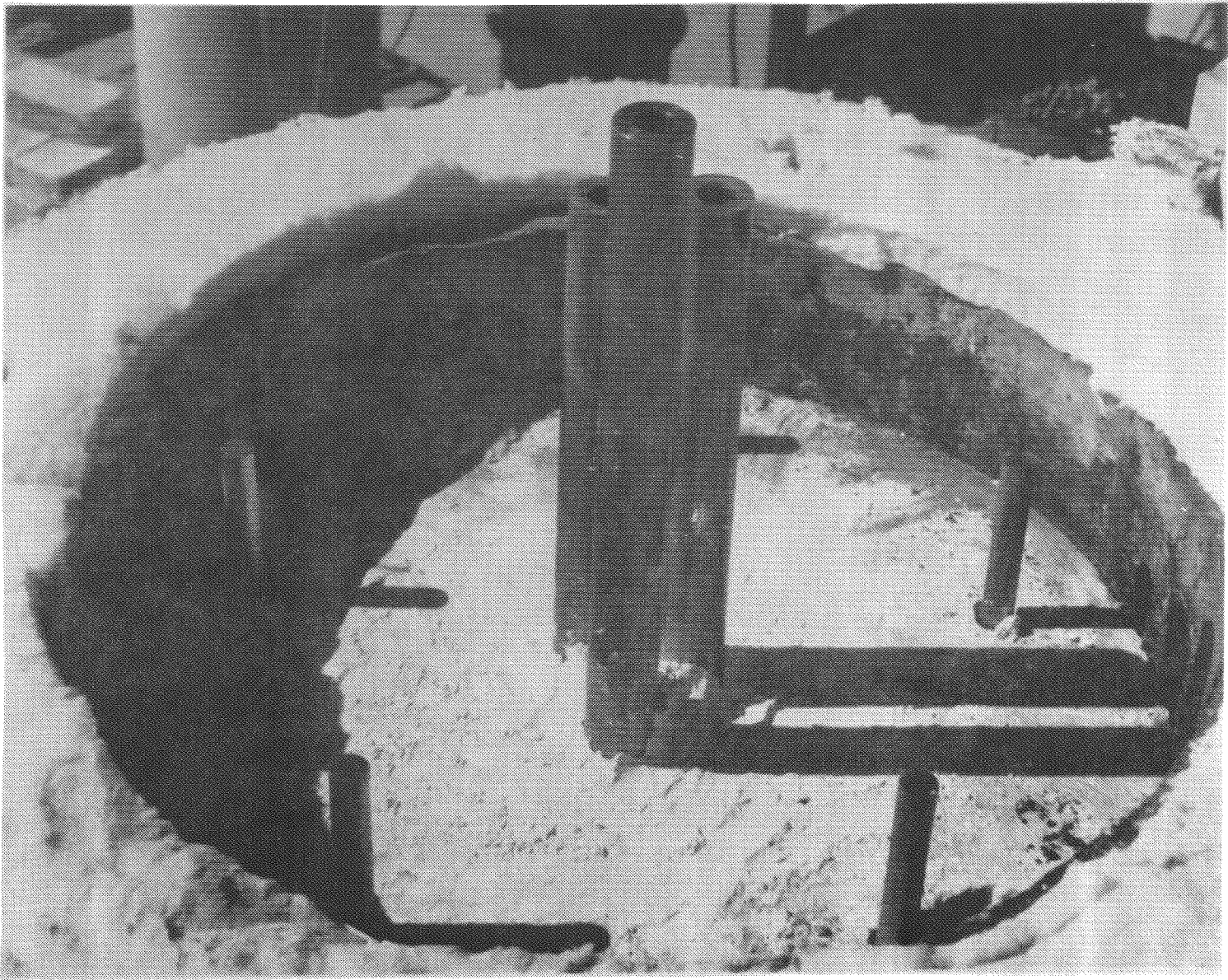Figure 4.1.1 Schematic of fiber optic pyrotube assembly

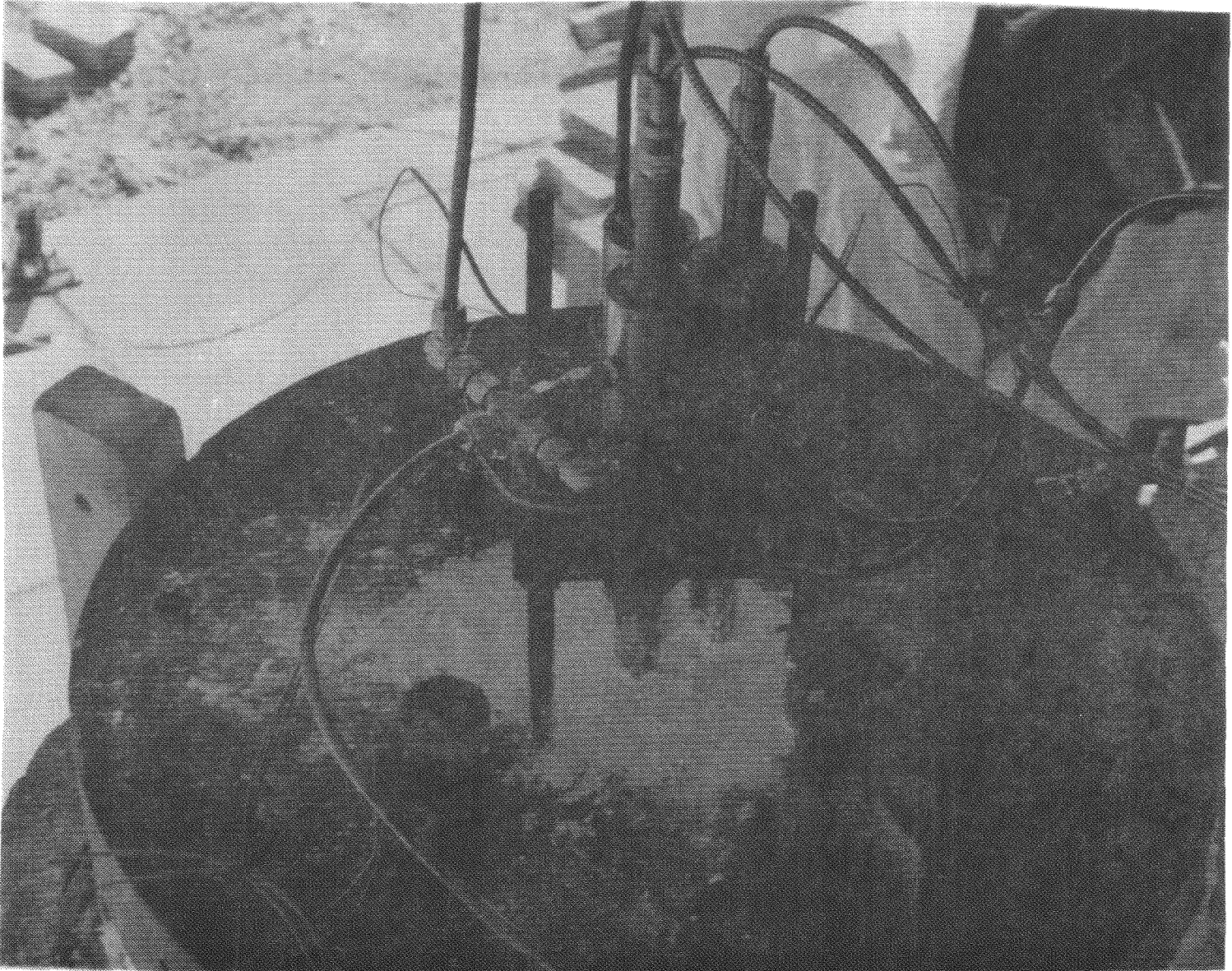Figure 4.1.2 Position of tungsten pyrotubes installed in the charge

Figure 4.1.3 Photo of the pyrotube assembly installed on the interaction crucible

Each of the three stainless steel adapters was threaded into a water cooled copper plate. This plate served to support the pyrotube assemblies and keep the pyrometer heads cool during the experiment. Installed into each adapter was a type K thermocouple to monitor pyrometer head temperature, a type C thermocouple installed inside a thin walled tantalum tube measuring 0.32 cm OD x 0.25 cm ID. The tantalum tube with the type C thermocouple installed was routed through a stainless steel Swageloc tube to pipe adapter located on the pyrotube adapter down to the bottom of the closed end tungsten pyrotube. The base of the tantalum tube (not including the thermocouple sheath) was bent at a right angle to keep the assembly adjacent to the inside diameter of the tungsten tube so as not to obstruct the focal area of the pyrometer. In order to keep the tantalum thermocouple sheaths from oxidizing during the experiment, argon was purged into the assembly very close to the lense of the pyrometer head. The tantalum tube served as the exhaust for the argon purge gas, thereby, constantly flooding the tungsten pyrotube and sheaths of the type C thermocouples with a flow of argon. This minimized the potential for oxidation and ultimate failure. The head of each pyrometer was threaded into the stainless steel adapter and secured with a lock nut. The 4 m fiber optic extension leads were routed to their respective electronic modules through a connector located in the side of the aluminum containment vessel. Figure 4.1.3 shows the installation of the pyro head assembly on the crucible cover.

Each pyrometer was calibrated prior to the experiment with a black body source and calibration standard. The calibration curves showing a plot of temperature as a function of voltage and resulting least squares fit is shown in Figures 4.1.4, 4.1.5, and 4.1.6. The heads were calibrated at a focal distance of 76 cm. Deviation from this focal length only affected the spot size measuring 0.64 cm in diameter. For the differences in focal lengths discussed, the change in spot size is negligible and well within the diameter of the tungsten pyrotubes.

4.2 Gas Analysis Instrumentation

Gas composition analysis for the SURC-2 test was done using three techniques: An Infocon Model IQ200 mass spectrometer, an Infrared Industries Series 700 CO/CO_2 detector, and integral grab samples. The first two techniques yield real-time data which is viewed on-line and stored on computer disks. The grab samples are stored and analyzed posttest using both gas chromatography and mass spectrometry. A schematic layout of the SURC-2 gas composition sampling apparatus is shown in Figure 4.2.1.

Three different sampling locations were utilized. Location No. 1 was downstream of the main exhaustline gravel filter. Location No. 2 was between the containment vessel and the gravel filter and location No. 3 was inside the aluminum containment vessel. All sample lines for gas collection were 6.4 mm (.250 in) O.D. stainless steel with Swageloc stainless steel fittings and Nupro plug valves. Inline filters used for SURC-2 were 0.3 micron Gelman HEPA filters with an element of acrylic copolymer.

Type K thermocouples were used to monitor sample gas temperatures at the flow pipe sample port and at the CO/CO_2 monitor. A stainless steel cold trap with a volume of 75 cm^3 and cooled with ice was used to prevent large amounts of water from fouling the analysis equipment. A single Gast diaphragm-type air pump was used to provide flow for the gas analysis system and flow indication for the system was measured by self-indicating rotameters. The CO/CO_2 supply was also monitored with a Dwyer 0-10 scfh air rotameter.

Samples from the grab sample system were analyzed by gas chromatography/mass spectrometry using a Tracor MT-150g gas chromatograph and a Finnigan Mat 271/45 mass spectrometer. The samples were contained in 150 cm^3 stainless steel bottles with 1/4 in. NPT solenoid valves for closures. All sample bottles were evacuated to a pressure of 100 mtorr

○ Calibration Data

--- Second Order Fit

Calibration Date 09-19-89
Head S/N 32209-3
Electronics S/N 28886-1
Cable #2

Second Order Equation
T = Temperature (C)
V = Voltage (V)

$T = -37.626057 \, (V)^2$
$+589.591125 \, (V)$
$+392.671631$

Standard Deviation = 10.159150
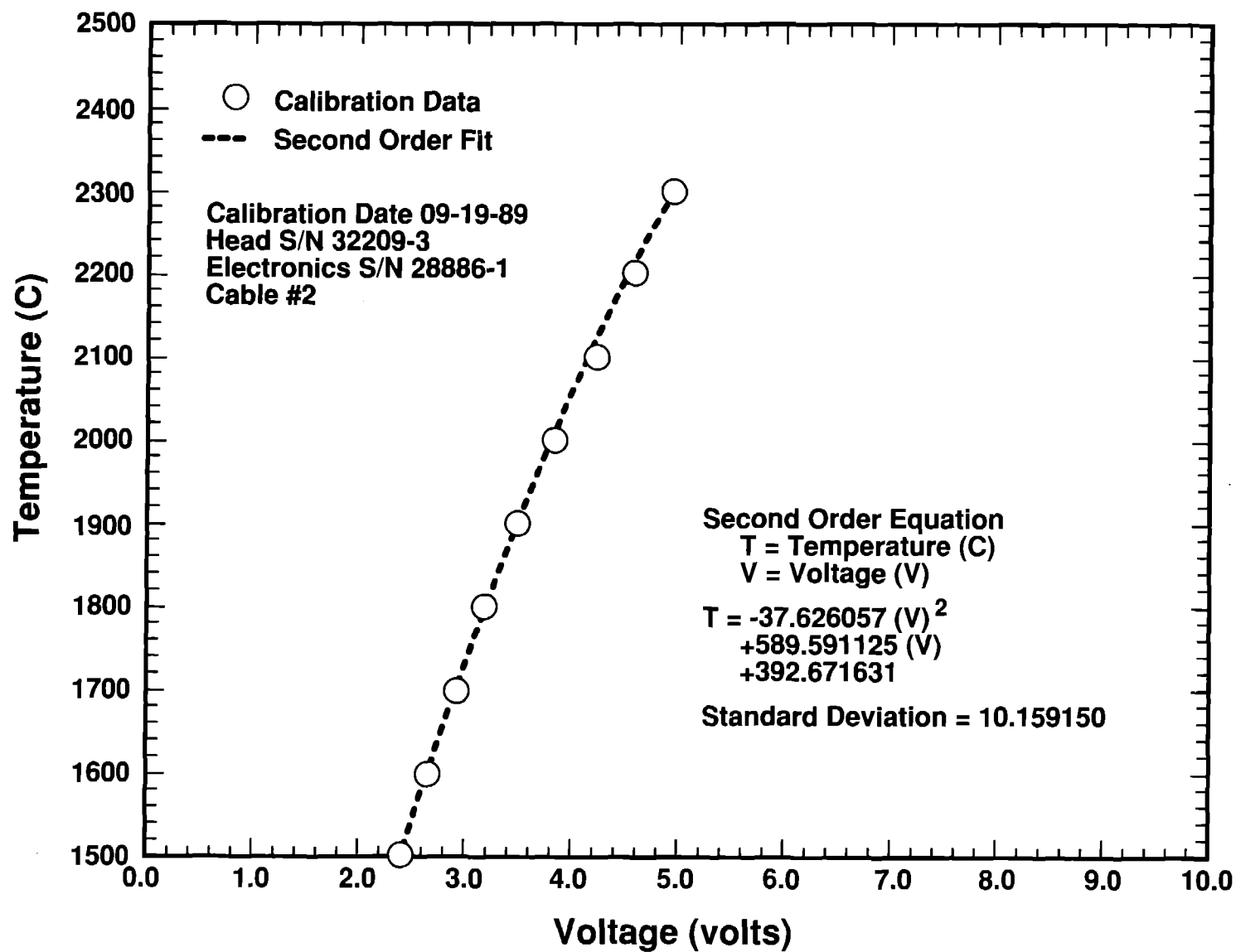
Figure 4.1.4 Micron fiber optic pyrometer calibration, pyrotube elevation Z = +15 cm

39
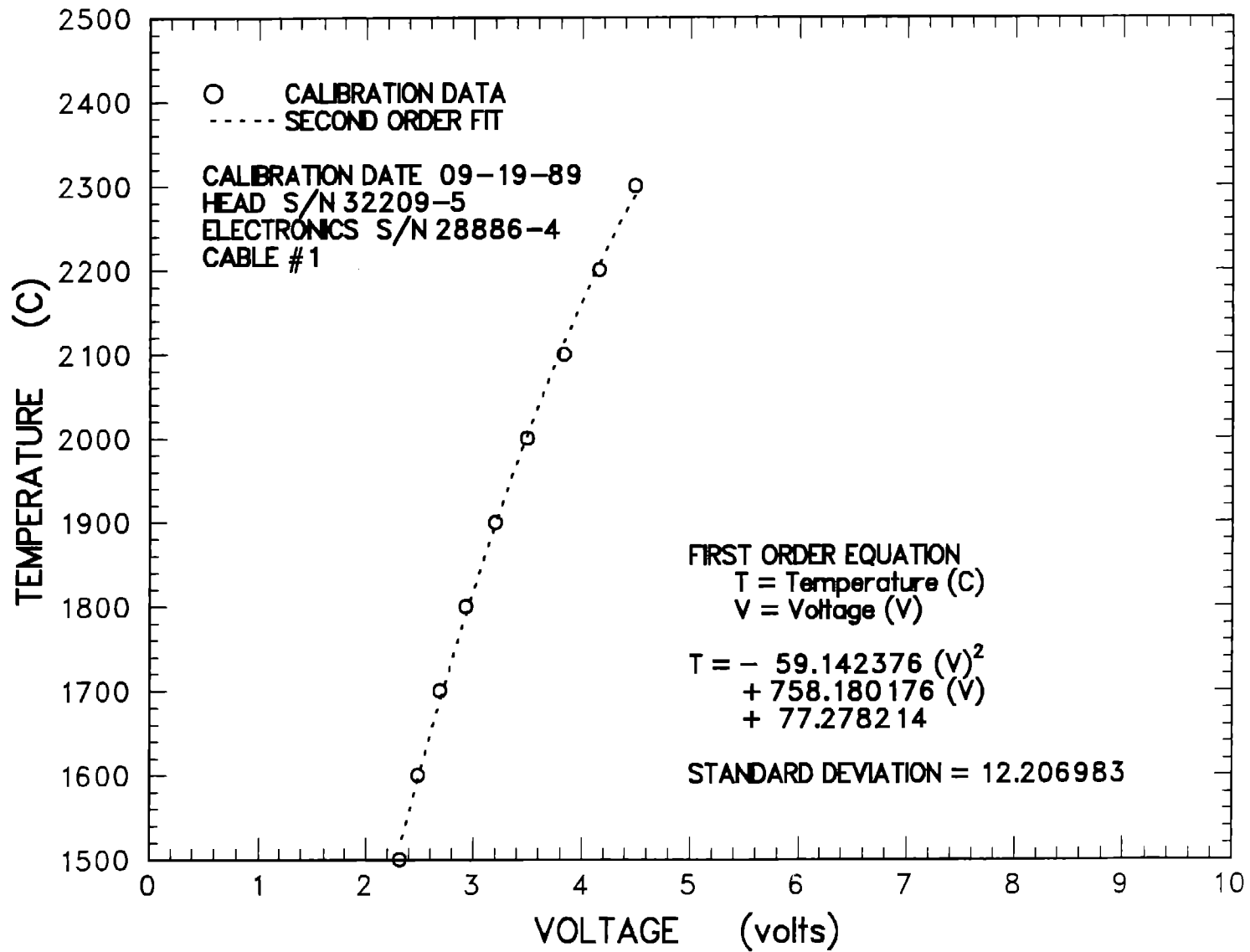
Figure 4.1.5 Micron fiber optic pyrometer calibration, pyrotube elevation Z = +0 cm

O   CALIBRATION DATA
- - - - SECOND ORDER FIT

CALIBRATION DATE 09-19-89
HEAD S/N 32209-6
ELECTRONICS S/N 28886-5
CABLE #3

SECOND ORDER EQUATION
T = Temperature (C)
V = Voltage (V)

$$T = - 390.812073 \ (V)^2$$
$$+ 3361.755127 \ (V)$$
$$- 4896.556152$$

STANDARD DEVIATION = 21.374634
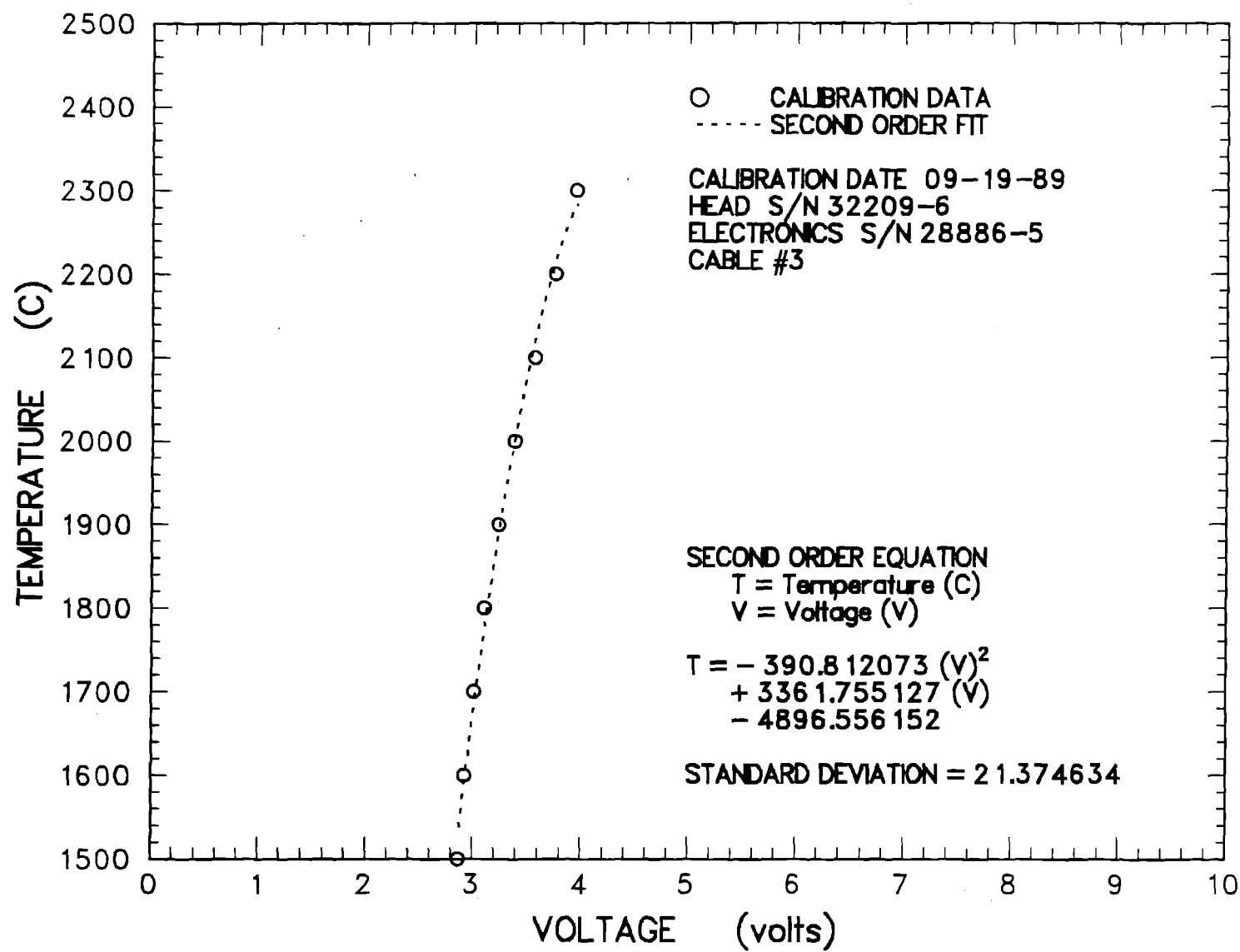
Figure 4.1.6 Micron fiber optic pyrometer calibration, pyrotube elevation Z = +5 cm
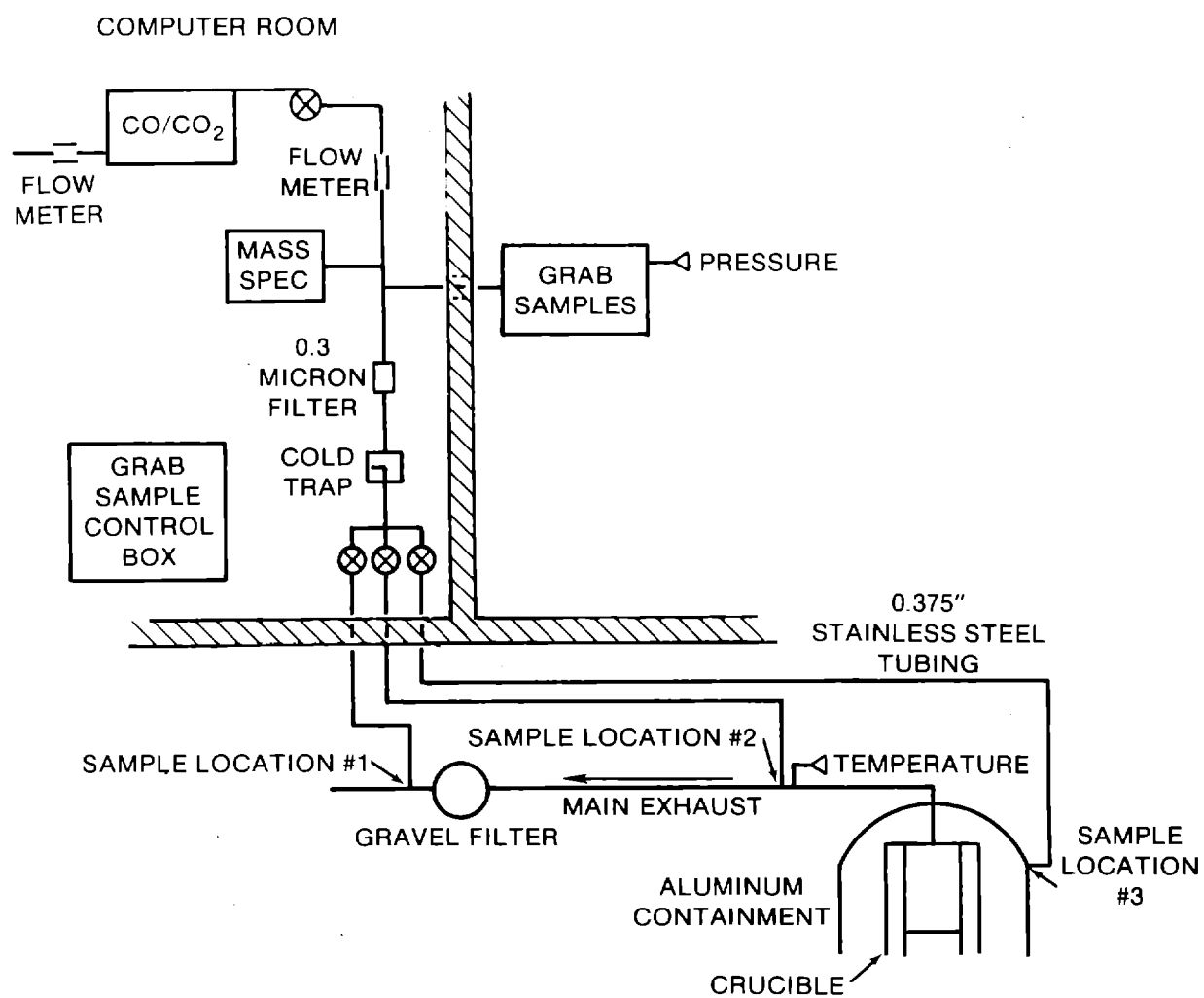
Figure 4.2.1 SURC-2 gas sampling schematic

immediately before the test and pressure transducer output was used to mark the time of sampling events by monitoring manifold pressure. The grab sample system samples were manually actuated and recorded. A remote control panel housed valve position indicator lights and two-position switches for controlling the valves used in acquiring the grab samples.

The CO/CO_2 analyzer operates on an infrared absorption technique using Infrared Industries Models 702 and 703 detectors (Figure 4.2.2). Carbon monoxide is monitored over a range of 0-50% and carbon dioxide is monitored over a range of 0-20%. Response time is 5 seconds for 90% of the reading with a sensitivity of $\pm$ 2%. Output for the detectors to the data acquisition system is 0-5 volts.

Another diagnostic tool for gas data used for the SURC-2 test was a quadripole residual gas analyzer, Infocon model IQ200 (Figure 4.2.3). This instrument was set up in the table display mode and controlled automatically with a Hewlett Packard 9826 computer for scanning specifically selected masses corresponding to the gas species of interest: H_2, H_2O, CO, O_2, Ar, and CO_2. A pressure converter manifold with a 10 torr orifice, 27 lpm vacuum pump, and 0.5 mm (0.020 in.) I.D. capillary tube provided the ability for continuous sampling from a pressure of up to 2 atmospheres at the sample source, down to 10 torr at the analyzer supply where the associated 150 lps turbo pump could maintain 10^{-6} torr at the analyzer head. A Faraday cup detector was used to produce the currents for analysis.

For data acquisition, the Hewlett Packard 1000 (right side--Figure 4.2.2) series computer system was used with acquisition rates of 15 seconds for the test warm-up and 5 seconds for the majority of the run where test events necessitated a faster rate. Data inputs from gas composition data were: temperature from the containment chamber thermocouple; temperature from the CO/CO_2 monitor thermocouple; percent CO as 0-5 volts

per 0-50%; and percent CO_2 as 0-5 volts per 0-20%.

Layout and Location

The location of the various support components and analysis equipment can be seen in Figure 4.2.1. The UO_2-ZrO_2 filters for the gas sample lines were mounted on the expansion chamber flange approximately 15 cm downstream from the end of the sample tube which was located inside the containment vessel. The HEPA filter and cold trap were located just upstream of the grab sample line approximately 8.5 m from the inter-action crucible. The diaphragm air pump and flowmeter were located at the CO/CO_2 monitor supply line. Temperature inside the containment vessel was measured by one of the type K thermocouples, while another type K thermo-couple measured the gas temperature at the CO/CO_2 monitor sample tee.

The grab sample system tied into the main gas line using a 6.4 mm (0.250 in.) O.D. stainless steel tube. Each sample line was teed to the main line with 3 cm of this tube. This equipment was located adjacent to the CO/CO_2 monitor and the mass spectrometer approximately 9.0 m from the SURC-2 containment chamber. The control panel for manual sample acquisition was located in the remote control center along with other instrumentation.

The CO/CO_2 instrument was located in the shielded computer room where it was connected to the main gas line by a 6.4 mm (.250 in.) O.D. UO_2-ZrO_2 tube. A diaphragm pump and flow-meter supplied the sample gas from the main gas stream for the infrared detectors. The distance upstream to the SURC-2 test article was 9.5 m (31 ft).

The Infocon mass spectrometer was also located in the shielded computer room and was connected to the main gas stream by a .5 mm (0.020 in.) I.D. capillary tube and was situated approxi-mately 10 m (33 ft) from the test vessel.
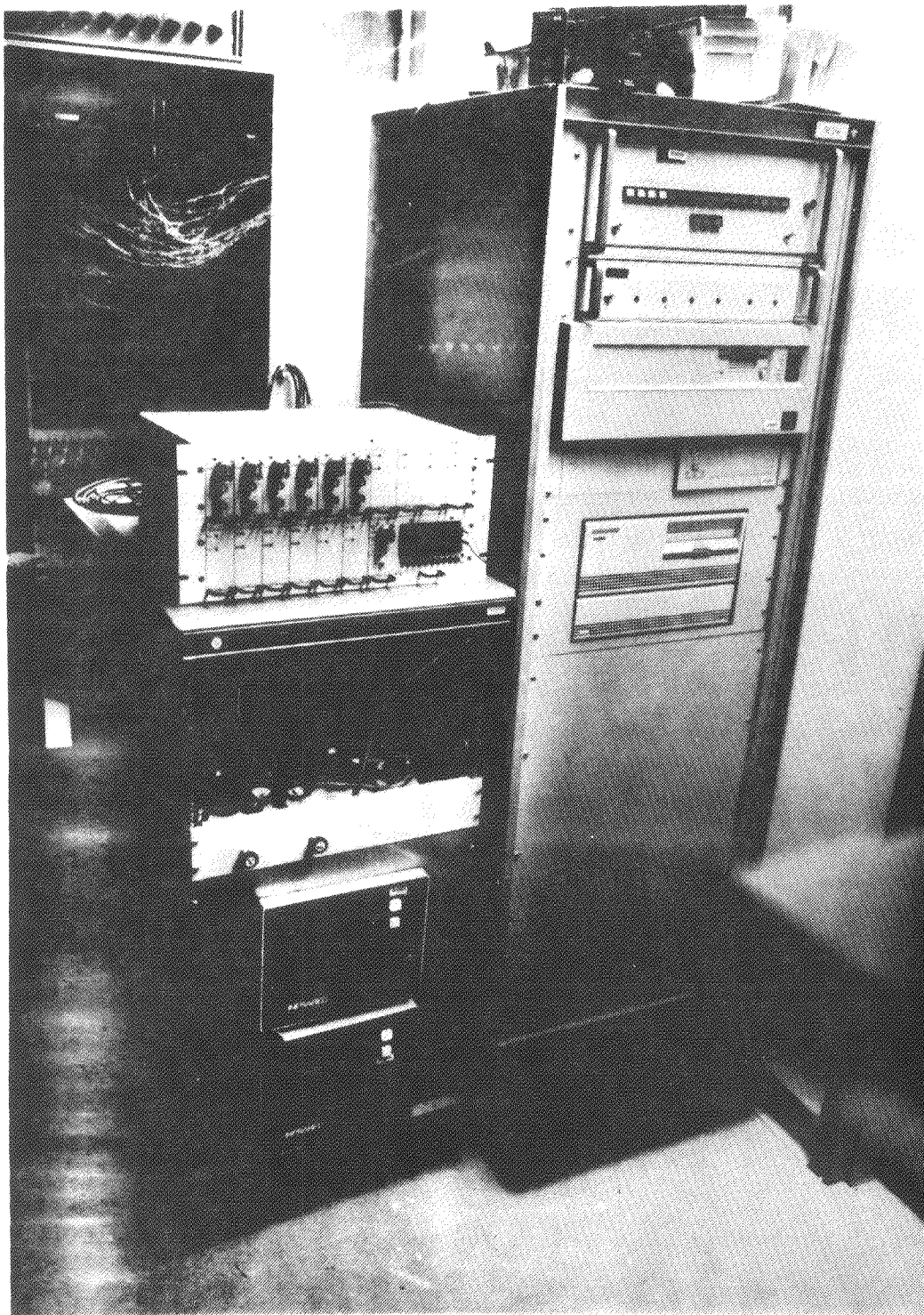
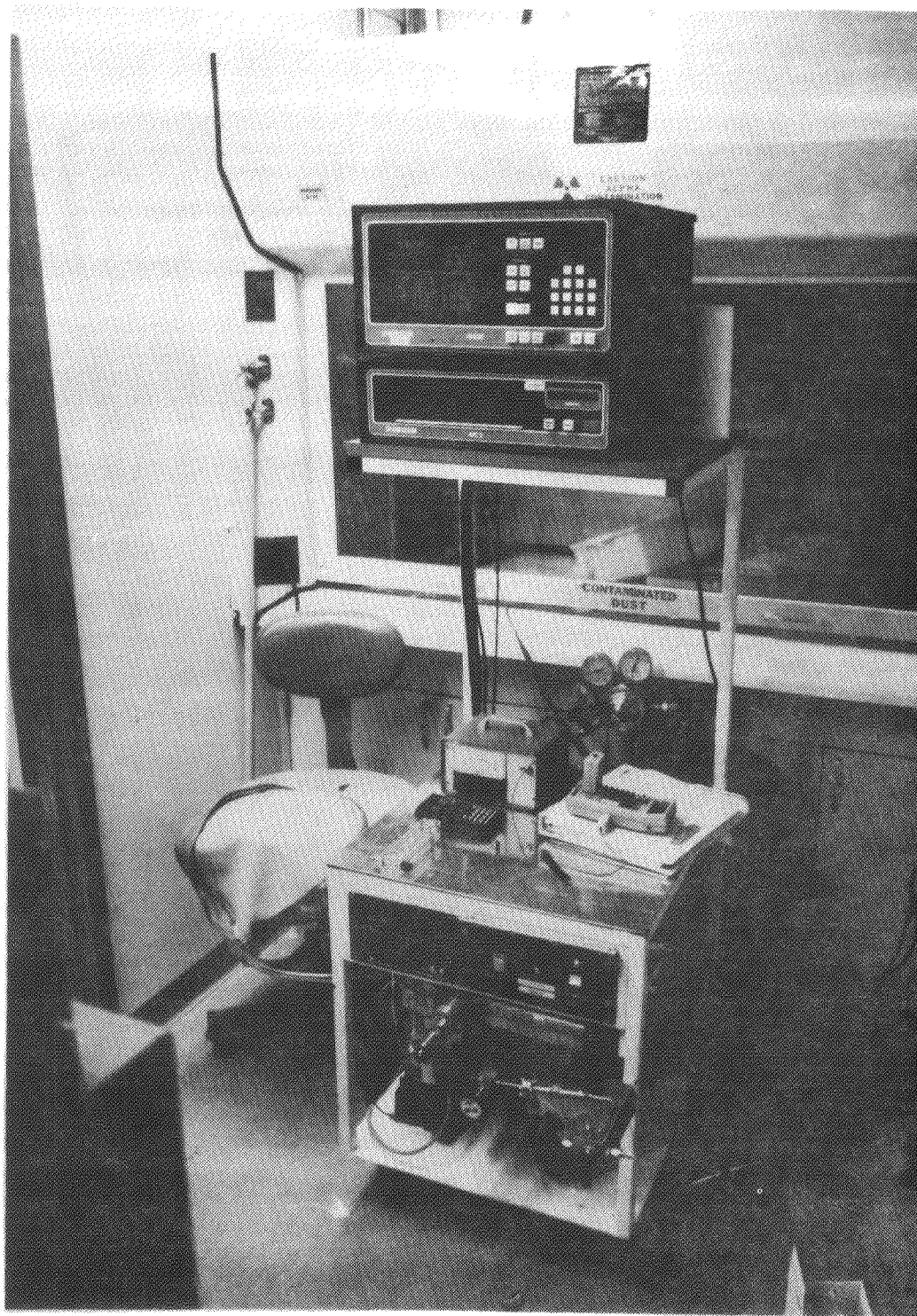Figure 4.2.2 CO/CO$_2$ monitor hardware

Figure 4.2.3 Mass spectrometer hardware

Calibrations

In-situ calibrations for the different gas sampling equipment were accomplished with primary standard calibration gas mixtures from Alphagaz. For the analysis, mixtures of 2.0% H_2, 25.1% CO, 10.0% CO_2, 62.9% Ar (Alphagaz Mix 1) and 45.0% CO, 15.0% CO_2, 40% N_2 (Alphagaz Mix 2) were analyzed in addition to the SURC-2 test samples. Results from these calibrations are listed on Table 4.2.1.

The CO/CO_2 analyzer was calibrated according to the operating reference manual using gas mixture Alphagaz Mix 2 as well as pure nitrogen. This calibration procedure was accomplished pretest. Following the test completion, the zero and full range were again checked to ensure that there was no significant drift.

After the test, the calibration procedure for the mass spectrometer was completed again and showed no significant drift. Operational checks of the support instrumentation included response of the thermocouples from below ambient to above ambient as compared with other type K thermocouples in the same environment. Flow measurements through the self-indicating rotameters were matched with several other similar flowmeters. Output from the pressure transducer was monitored while changing the grab sample manifold configuration from pressure to vacuum conditions.

4.3 Flow Device Instrumentation

Five different devices were used to measure the gas flow rate in SURC-2: A 1.02 cm orifice plate, a laminar flow element, a turbine meter, a Rockwell 415 gas clock, and a Rockwell 750 gas clock. Figure 4.3.1 shows a flow train schematic of the hardware for SURC-2.

The flow system consisted of a series of piping, tubing, and a gravel filter instrumented with a variety of devices for measuring gas flow rates. The flow system starts with an exhaust tube that is mounted in the top part of the containment vessel and is fit into the crucible cover. The tube material was 304 stainless steel having dimensions of 5.1 cm O.D. x 0.17 cm wall x 1.2 meters long. Several 0.32 cm diameter holes were drilled in the sidewall of the tubes in the section residing inside the containment vessel. These holes were used to provide a pathway for the argon gas used to purge the experimental chamber and provide background gas for gas composition measurements. A 5.1 cm diameter stainless steel vacuum tee was mounted to the top of the exhaust tube. The vertical flange of the tee was fitted with a 5.1 cm diameter ball valve used to deliver the zirconium metal. The horizontal flange of the tee was connected to a 5.1 cm O.D. x 0.17 cm wall x 1.8 meter long length of stainless steel tubing. The end of this tubing was fitted with a 5.1 cm O.D., stainless steel flanged cross. The centerline of all the flange ports on the cross were positioned in a parallel plane. The cross was used to mount an opacity meter and a nozzle for sampling the aerosol. The cross was adapted to a 2.0 meter section of 5.1 cm diameter 150 pound schedule 40 black steel pipe via a 5.1 cm bolted flange. A 1.02 cm diameter, sharp-edge, concentric orifice was mounted between two flanges 1.0 meters from the stainless steel cross. Two Validyne pressure transducers were connected in parallel across pressure taps machined in the flanges. Another pressure transducer was connected to the flange upstream of the orifice to measure gas flow pressure.

The section of pipe containing the orifice was connected to the top of a gravel filter with a 1.1 meter length of 5.1 cm black steel pipe using a combination of flanges and fittings. The gravel filter had an inside diameter of 25.4 cm and was filled with sand to a depth of 1 meter. The gravel filter was used to filter aerosols, preventing them from entering the laminar flow device and the two gas clocks located downstream. The filter was designed and tested to remove 99% of the aerosols at flow rates of 300 slpm with a backpressure of less than .25 psig.

Table 4.2.1 Results of grab sample analysis on calibrated gas using gas chromatography

SAMPLE #	CO(%)	CO_2(%)	N_2(%)	Ar(%)	H_2(%)
Alphagaz Mix 1	25.1	10.0	0.	62.9	2.0
Mass Spectrometer	22	9	N.D.*	68	1
Garb Sample	27.2	9.6	4.0	56.3	1.7
CO/CO_2 Monitor	23.4	10.0	N.D.	N.D.	N.D.
Alphagaz Mix 2	45.0	15.0	40.0	0.	0.
Grab Size	44.5	15.6	39.8	N.D.	0.2

*NOT DETECTED

Connected to the outlet of the gravel filter were two lengths of 2.54 cm schedule 40 black steel pipe, 50.8 cm long. A laminar flow element (LFE) was installed between the two pipe sections. The LFE was instrumented with a Validyne differential pressure transducer. The end of the flow train was terminated by two Rockwell gas clocks mounted in series. The gas clocks were connected using 2.5 cm schedule 40 black steel pipe fittings.

The principles of operation and pertinent equations for orifice plate flowmeters may be found in [Baker and Pouchot, 1983]. The orifice plate flowmeter is probably the most widely used flowmeter in service today. It is found mostly in field use and is simple, rugged, reliable, accurate, and inexpensive. Orifice plates used for gas measurement are considered to be accurate to 1-2% based on physical dimensions and published correction factors. It should be noted, however, that uncertainties in differential pressure (the measured parameter), temperature, line pressure, and gas density can easily overwhelm the uncertainty from the laboratory calibration. One disadvantage of the orifice plate is that a 10:1 change in differential pressure results from only a 3:1 change in flow due to the square root relationship between differential pressure and flow. Hence, 50% of expected full flow is measured in 20% of expected differential

pressure. This makes low flow rates difficult to measure accurately.

The orifice flowmeter used in the SURC-2 experiment had an opening of 1.02 cm and was mounted between flanges in a 5 cm I.D. pipe. This pipe was mounted to the SURC-2 containment vessel so that 80 cm of straight pipe preceded the flow device and at least 50 cm of straight pipe followed the device. Three Validyne pressure transducers were used in conjunction with the orifice plate. Two of these were used to record the differential pressures across the plate and had operational ranges of 0-2 psi and 0-5 psi. The third pressure transducer was used to measure the system pressure and had a range of 0-10 psig. All of these devices were calibrated as a set--both in the laboratory and at the test site--using several different gases and a range of flow rates. Results of the laboratory calibration are shown graphically in Figure 4.3.2.

The laminar flow element (LFE) is a group of capillary tubes bundled together to form a matrix such that the flow through each passage is laminar, even though the total flow upstream of the device may be turbulent. The LFE is not as sensitive to piping configuration as an orifice plate so that an inlet pipe length of one or two pipe diameters (instead of 5 or 10) is usually
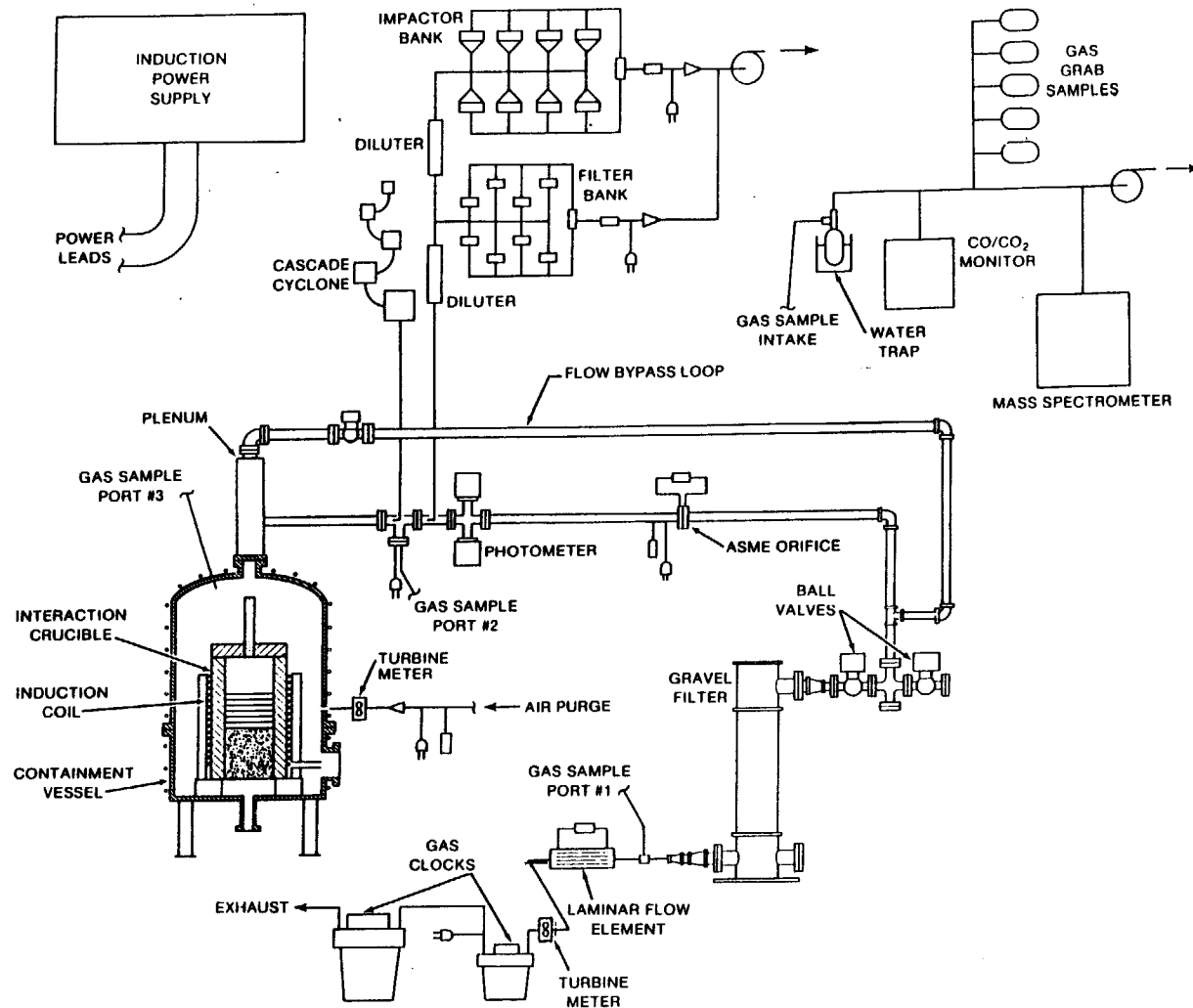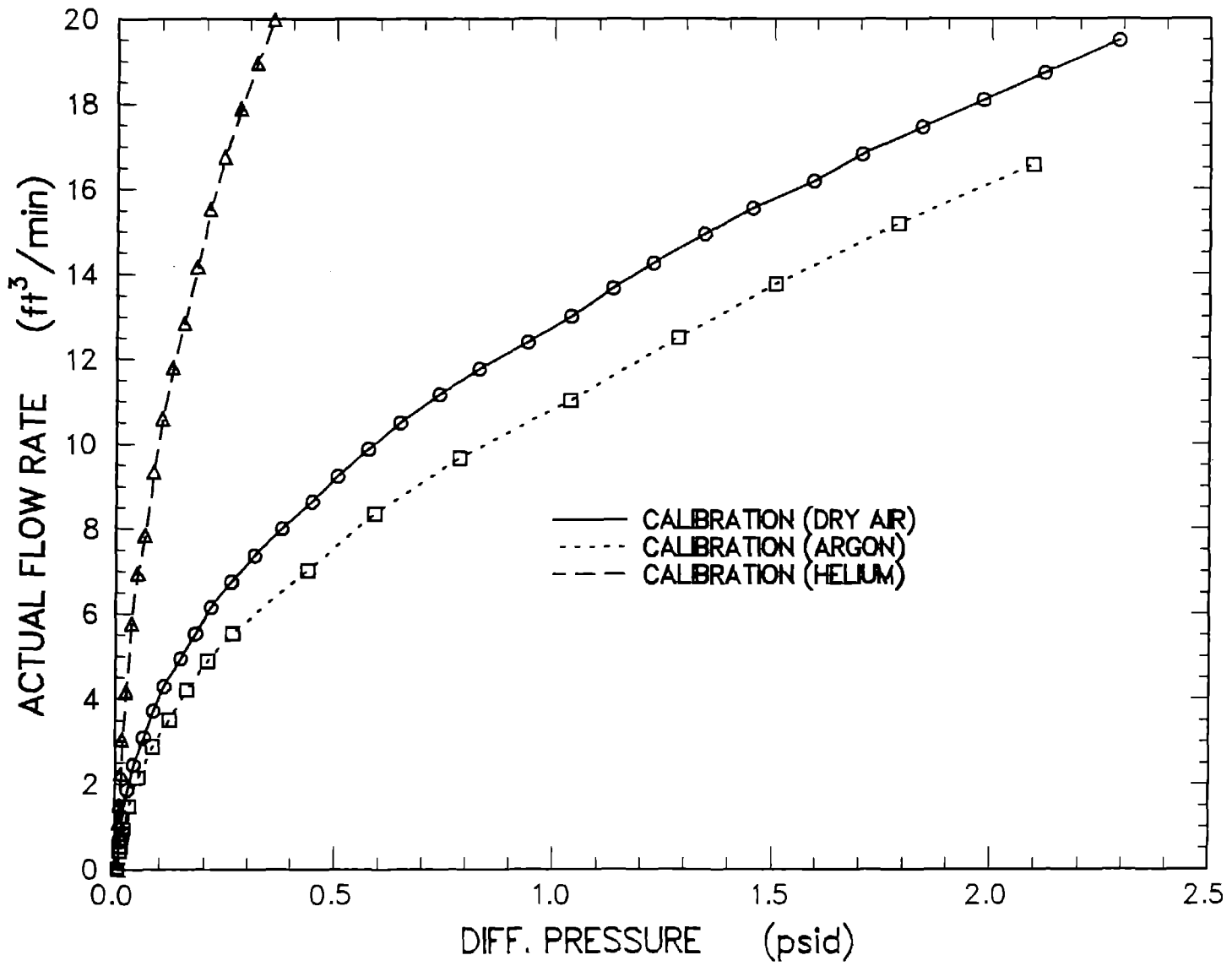
Figure 4.3.1 Flow train schematic

Figure 4.3.2 Orifice flowmeter calibration

sufficient to provide a satisfactory flow pattern. The equations governing the operation of LFE devices are given in Baker and Pouchot [1983]. One advantage of a LFE is that the relationship between differential pressure (the measured parameter) and flow is linear for the range of flows for which it is designed. Calibration of the device should be done against a primary standard and is a function of gas viscosity which is itself a function of gas composition. A potential disadvantage is that the small passages in the flow matrix are susceptible to plugging when the gas contains aerosols or water vapor.

The LFE used in the SURC-2 experiment was designed and built by Calibrating and Measuring Equipment (CME) and has a nameplate flow range of 0-300 slpm for air at standard conditions. The LFE is contained in a 50 cm pipe with an I.D. of 3.6 cm. Differential pressure is measured using a Validyne differential transducer with a range of 0-2 psi. The device was calibrated both in the laboratory and at the test site. Laboratory calibration (Figure 4.3.3) was done using a variety of gases with NBS-traceable critical orifices as the primary standard.

The turbine flow meter [Baker and Pouchot, 1983] consists of a freely rotating propeller mounted concentrically in a pipe. The force of the gas striking the propeller blades causes them to rotate at an angular velocity proportional to the gas velocity so that the volumetric gas flow is directly proportional to the rotational speed of the propeller. A magnetic pickup in the rotor causes a voltage to be generated in an external electrical coil. The magnitude of the voltage is then directly proportional to the volumetric flow rate for the designated flow range of the device. The output of the device is in actual liters per minute (ALPM) and must be corrected to standard conditions. Turbine flow meters must be calibrated to determine the coefficient of discharge but once this is done are considered to be accurate to about 1%. Some advantages of the turbine flowmeter are that it is insensitive to gas

composition and that it produces a linear response over its design flow range. Some disadvantages are that it is susceptible to drag if the gas contains aerosols or water and that the magnetic pickup can be affected by an induction or electrical field.

The turbine meter used in SURC-2 was made by Flow Technology, Inc., and was contained in a 50 cm long pipe with an I.D. of 1.3 cm. The operating range of the device is 0-280 slpm as indicated by a voltage output of 0-10 volts dc. The turbine meter was calibrated in the laboratory and at the test site using argon, He, air, and CO_2. Results of the laboratory calibration are shown in Figure 4.3.4.

The Rockwell gas clocks used in SURC-2 are dry gas meters. These devices have four bellows-type chambers that alternately fill and empty known volumes of gas. The slide valves that control the cycle are attached to mechanical counters that totalize the volume of gas that passes through the meter. These devices are very rugged and bulky and register the total volume in actual liters per minute (ALPM). They are impervious to the aerosol or water content in the gas and measure total volume independently without corrections for density or viscosity. Once the volume of the bellows is known, the accuracy of the gas clocks is within 1%. The major disadvantages of the dry gas meter are its size and lack of sensitivity to transient flow perturbations.

The Rockwell 415 gas clock has a stated operational range of 0-200 LPM at STP. The device has a sensitivity of 28.3 liters per cycle. The Rockwell 750 was also manufactured by Rockwell and has an operational range of 0-350 LPM at STP. The Rockwell 750 gas clock has a sensitivity of 283 liters per cycle. Both devices were calibrated in the laboratory and at the test site with different gases and a range of flow rates. The laboratory calibrations are shown in Figures 4.3.5 and 4.3.6.
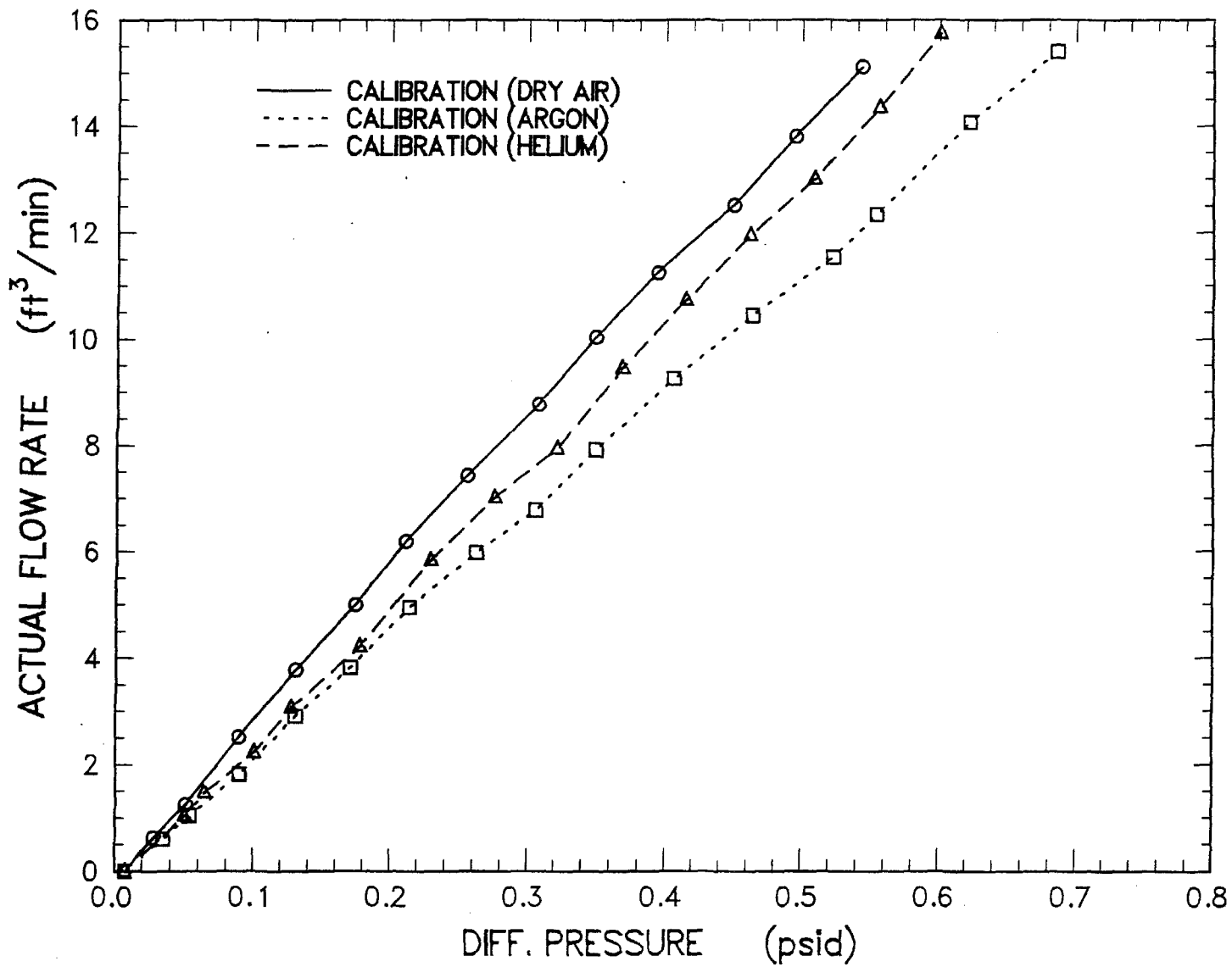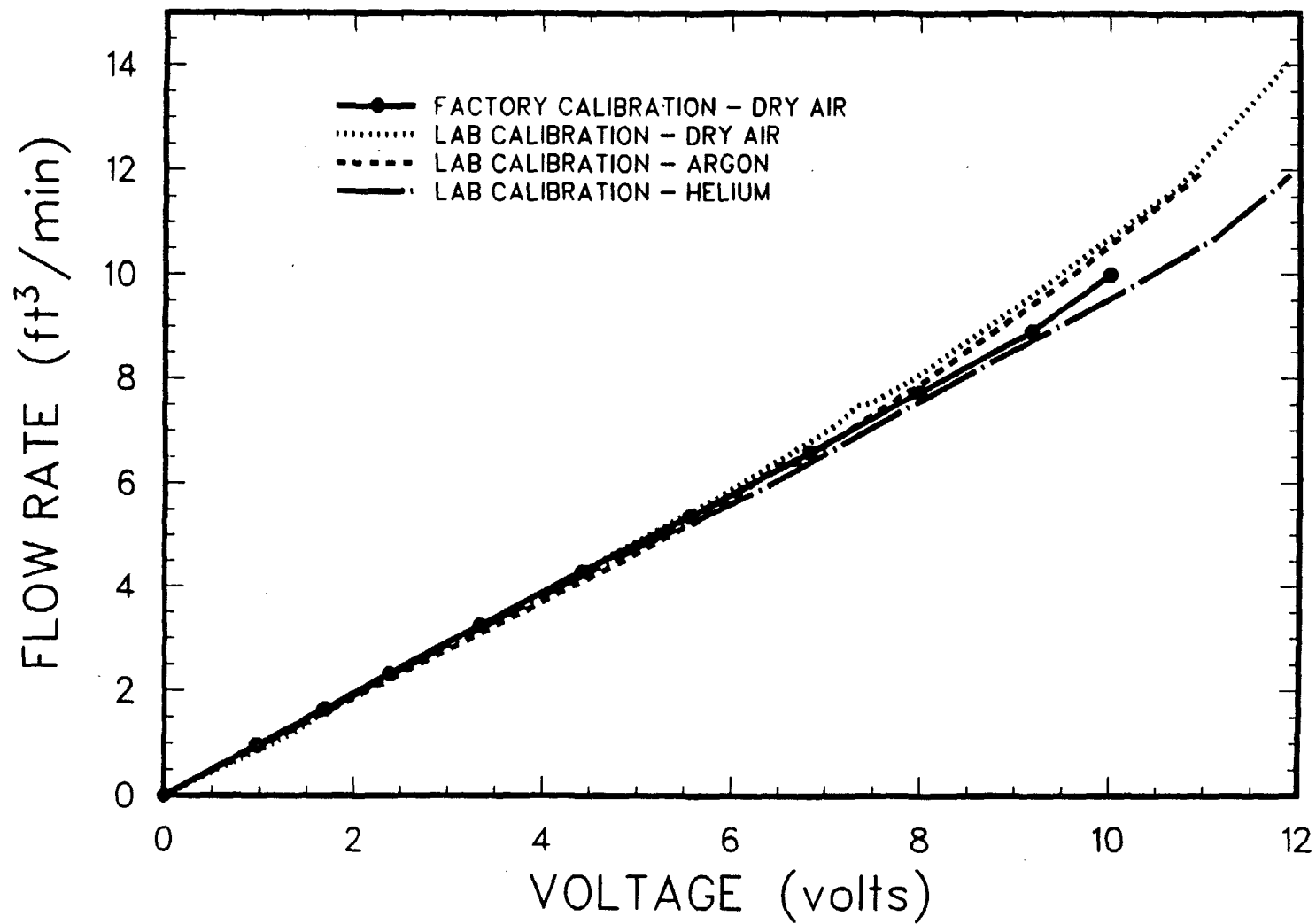
Figure 4.3.3 LFE flow rate calibration

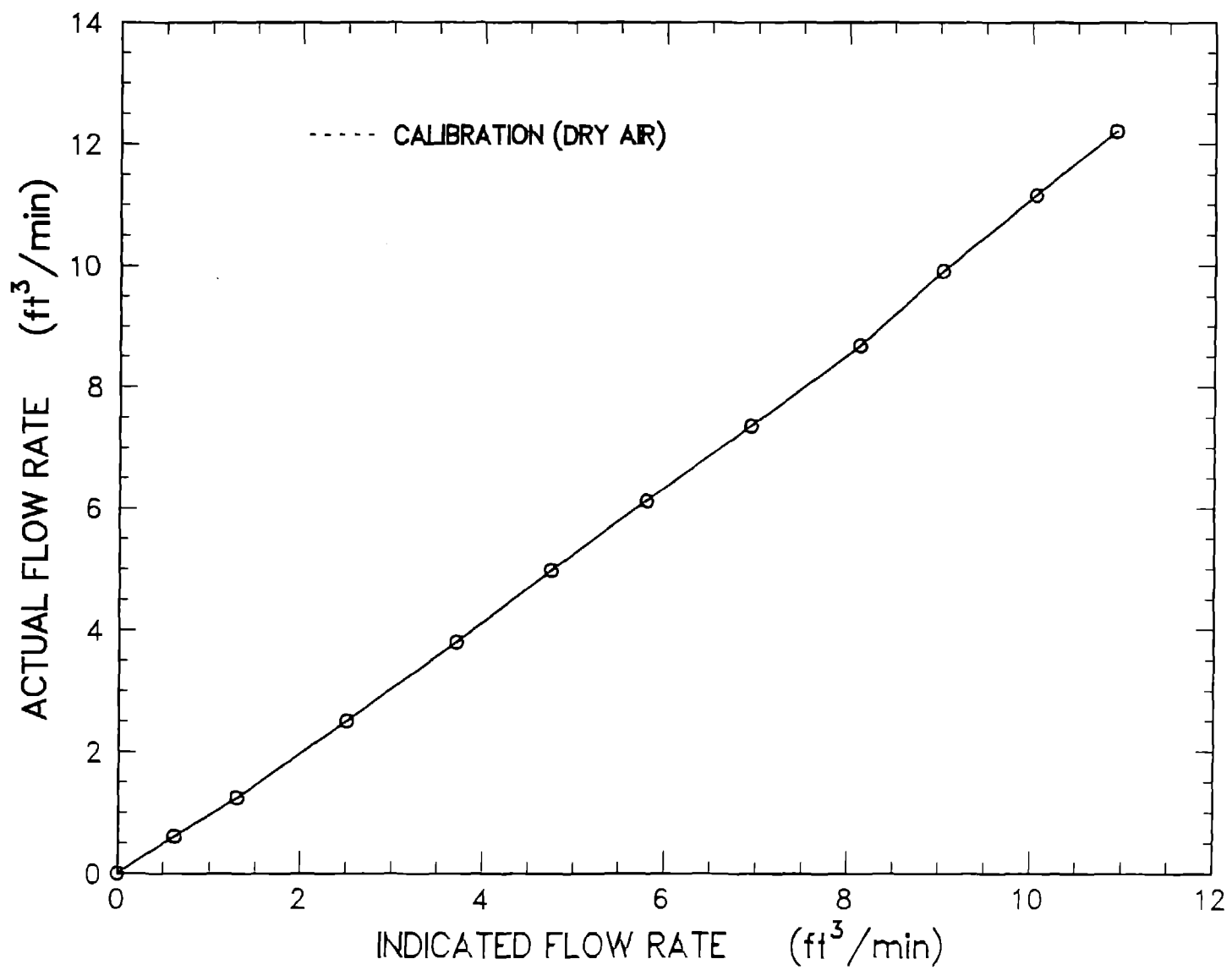Figure 4.3.4 Turbine meter calibration
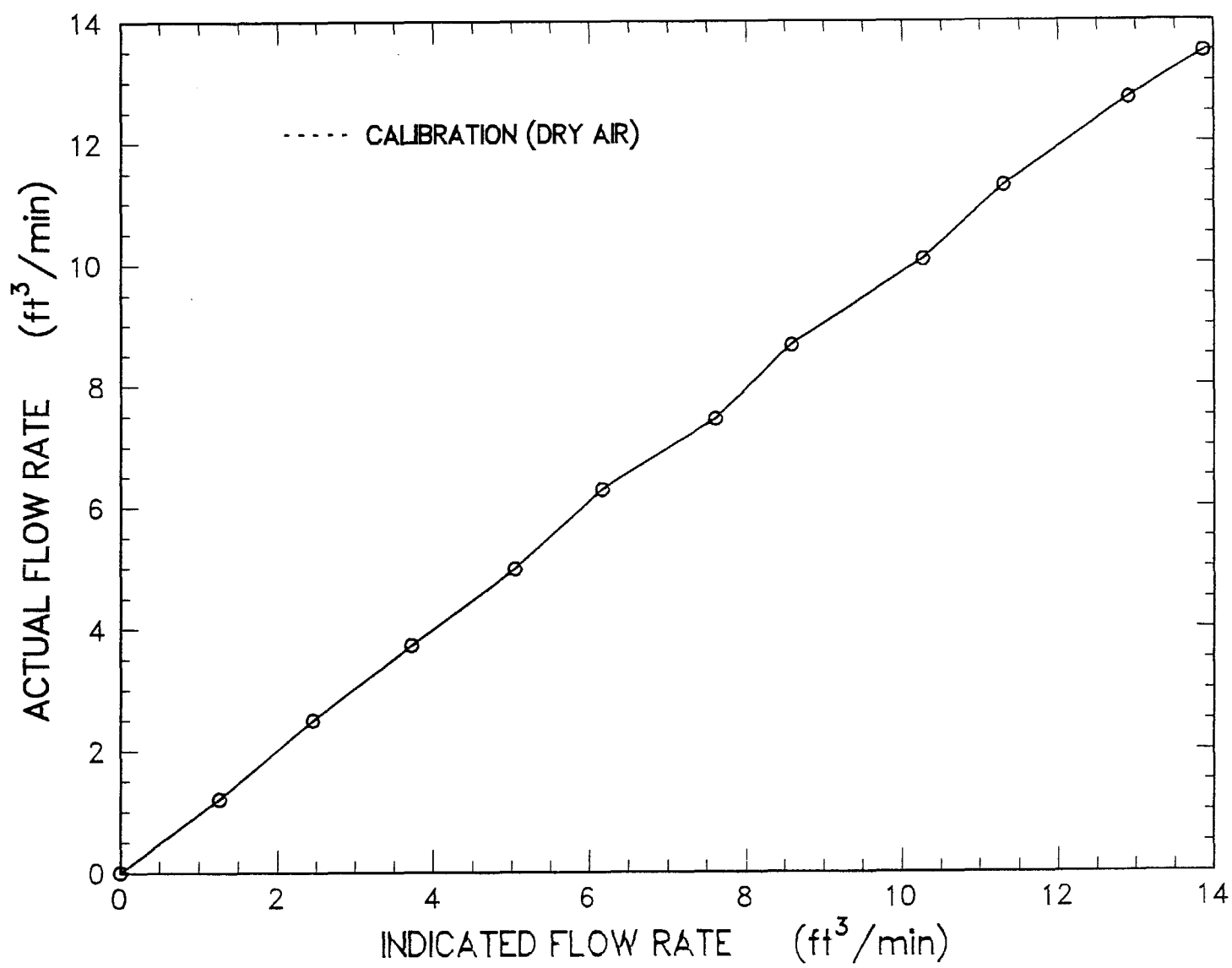
51

Figure 4.3.5 Rockwell 415 calibration

Figure 4.3.6 Rockwell 750 calibration

Instrumentation

After the experimental setup was completed for the SURC-2 test, an in-situ calibration was performed using argon. This was done to ensure that the laboratory calibrations were still valid, to evaluate the entire flow system, and to determine the system pressure as a function of flow rate. Results of the in-situ calibration for the orifice flowmeter, LFE, turbine meter, and system pressure are given in Table 4.3.1. In addition, a systems leak test was performed by valving off the flow train and pressurizing the crucible and containment vessel. A pressure decay chart for this procedure is given in Table 4.3.2. Based on the in-situ checks, the initial leak rate from the crucible was calculated to be 12 slpm at a system pressure of 1.0 psig or 7% of the 165 slpm flow rate.

4.4 Aerosol Instrumentation

The interaction of hot molten material with concrete produces an aerosol. In the context of nuclear reactor accidents, the aerosol produced by the interaction of molten core debris with concrete basemat material is a potential source of radionuclide release [Brockmann, 1987].

It is, therefore, important to characterize this aerosol with respect to its mass source rate, concentration, composition, and transport properties. The aerosol source term is defined as the mass source rate of aerosol generation, its composition, and its size distribution, as well as additional parameters such as the dynamic shape factor that aids in the description of the aerosol's transport behavior and the agglomeration shape factor which aids in the description of the aerosol's coagulation behavior. Measurements of the aerosol source term resulting from the melt/concrete interaction experiments provide a data base against which to test predictive models of aerosol release and formation [Powers et al., 1986].

The SURC-2 test contained aerosol instrumentation designed to provide data which would allow calculation of the aerosol source term.

Specific measurements were made in order to determine the aerosol mass generation rate, aerosol size distribution, and aerosol composition. Figure 4.4.1 is a flow chart illustrating how each of the three source term parameters mentioned above is determined. The aerosol mass generation source rate is the product of the melt/concrete gas evolution rate and the aerosol mass concentration in the evolved gas. The gas flow train described in Section 4.3 measures the gas evolution rate. The aerosol mass concentration is measured primarily by filter samples; however, impactor samples and an opacity meter provide additional means of aerosol mass concentration measurement. The size distribution of the sampled aerosol is primarily determined by cascade impactor samples. The cascade cyclone gives an additional means of determining the integral aerosol size distribution over an extended sampling time.

Aerosol composition is determined from elemental analysis of the aerosol collected on the filters. A size dependent aerosol composition is obtained from analysis of the aerosol collected by the cascade cyclone.

The sample extraction dilution system (SEDS) comprised of the filters, cascade impactors, cascade cyclone, and the necessary dilution systems and flow control is shown schematically in Figure 4.4.2. An aerosol sample is drawn into the SEDS through a gooseneck sample probe (from Andersen, Inc.). The probe has a nozzle with a 1/8-in. inside diameter opening located coaxially in the center of the exhaust line. The nozzle expands into a 5/8-in. inside diameter tube. The cyclone samples the undiluted aerosol. The primary dilution is performed on the sample and this is sampled by the filters. A secondary dilution is performed and this aerosol is sampled by the impactors.

Figure 4.4.3 is a more detailed schematic diagram of the SEDS showing the locations and connections of the dilution and gas flow control systems. The locations of the flow controlling

Table 4.3.1 In-situ calibration* for SURC-2 flow devices

750 Gas Clock Flow (SLPM)	Inlet Turbine Flow (SLPM)	Orifice Plate Flow (SLPM)	LFE Flow (SLPM)	System Pressure (psig)	Outlet Turbine Flow (SLPM)
268	255	257	264	2.0	255
186	193	181	185	1.1	188
132	144	132	132	.7	135
128	113	120	121	.6	125
91	85	89	88	.4	91
--	28	33	29	.1	28

*Calibration done with argon gas

Table 4.3.2 Pretest pressure decay and leakrate for SURC-2 containment vessel and flowtrain*

Time (min)	Pressure (psig)
0.	2.25
1.0	1.56
2.0	1.14
4.0	0.63
5.0	0.40
7.0	0.14

*Calibration with argon gas

Instrument **Measured Quantity** **Source Term Parameter**

```
┌─────────────────┐      ┌─────────────────┐      ┌─────────────────┐
│ Gas Flow Train  │ ───▶ │Gas Evolution Rate│      │  Aerosol Mass   │
└─────────────────┘      └─────────────────┘      │   Generation    │
                                                   │  Source Rate    │
┌─────────────────┐      ┌─────────────────┐      └─────────────────┘
│    Filters      │ ───▶ │  Aerosol Mass   │
└─────────────────┘      │  Concentration  │
                         └─────────────────┘
┌─────────────────┐
│  Opacity Meter  │                               ┌─────────────────┐
└─────────────────┘      ┌─────────────────┐      │  Aerosol Size   │
                         │  Aerosol Mass   │ ───▶ │  Distribution   │
┌─────────────────┐      │  Distribution   │      └─────────────────┘
│    Impactors    │      └─────────────────┘
└─────────────────┘                               ┌─────────────────┐
                                                   │    Aerosol      │
┌─────────────────┐      ┌─────────────────┐      │  Composition    │
│    Cyclone      │ ───▶ │   Elemental     │ ───▶ └─────────────────┘
└─────────────────┘      │  Composition    │
                         └─────────────────┘
```
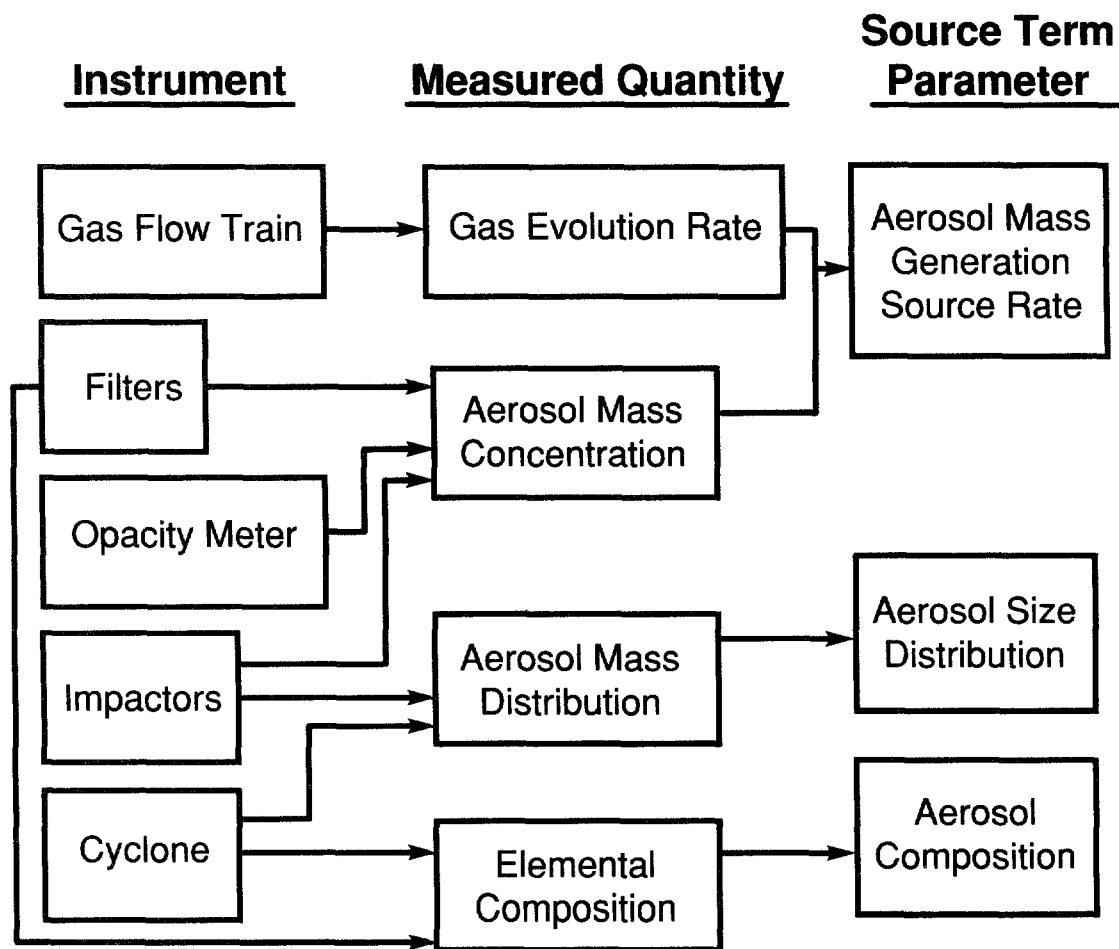
Figure 4.4.1 Flow chart illustrating how the source term parameters are determined from measurements made in the SURC-2 melt/concrete interaction test
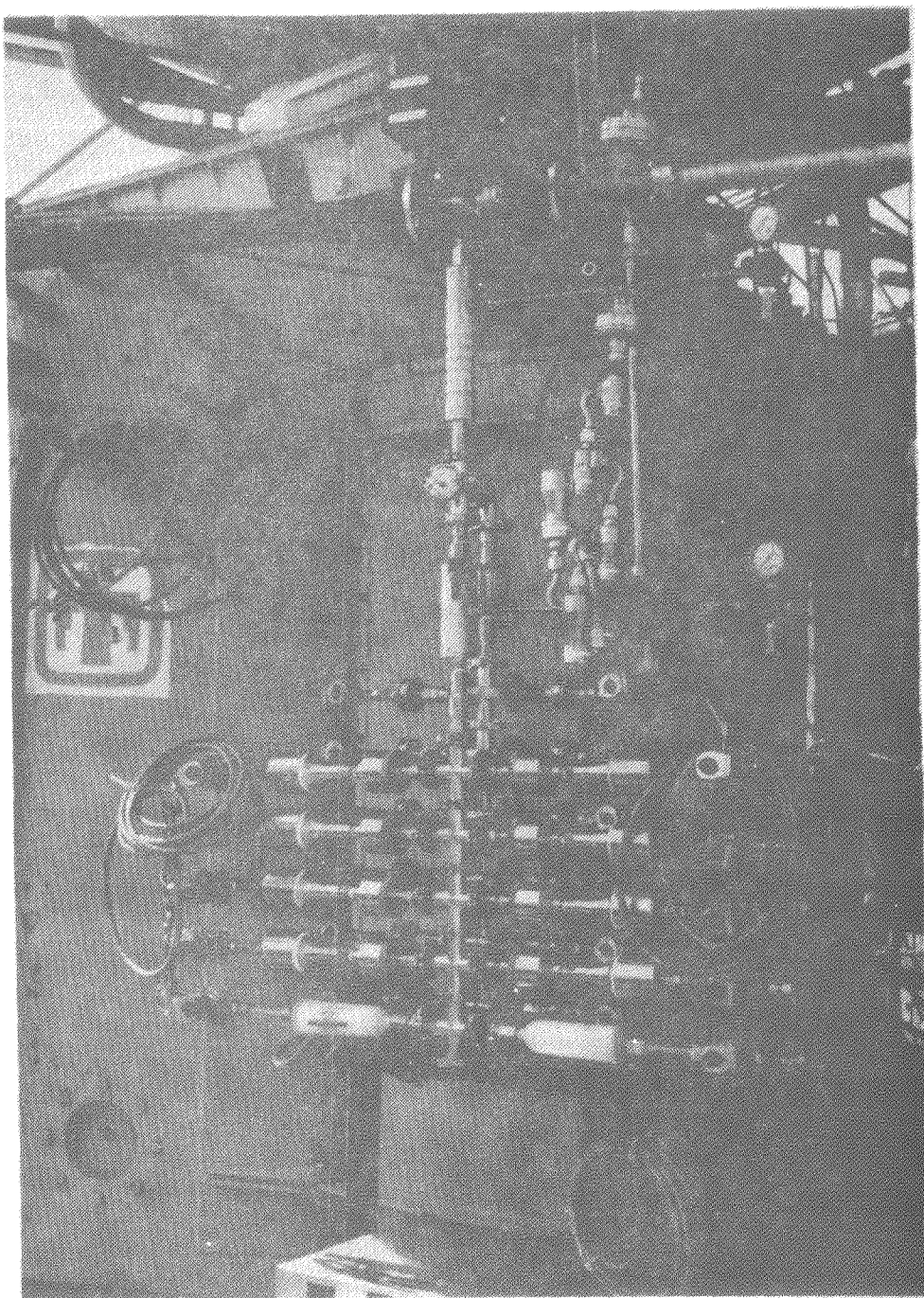
Figure 4.4.2 Photograph of the aerosol sampling instrumentation connected to the flow line
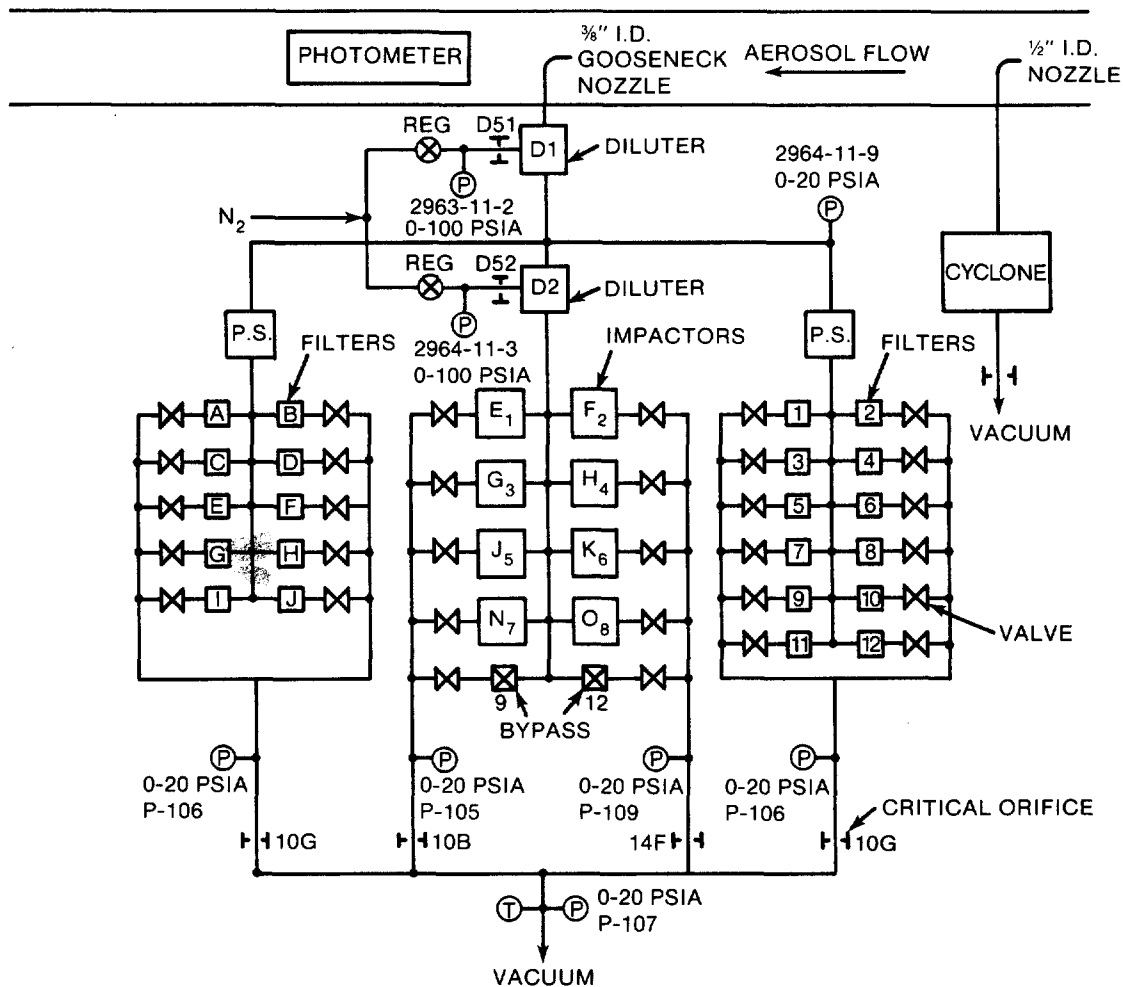
Figure 4.4.3 Schematic diagram of the sample extraction dilution system (SEDS) showing the locations of pressure transducers, thermocouples, and flow controlling orifices. The identifying designations of the orifices and thermocouples are also shown.

orifices, pressure transducers, and thermocouples are shown. Their alphanumeric identifications are also listed on the figure.

The flows are controlled by critical orifices manufactured by Millipore and calibrated at Sandia's Primary Standards Laboratory. Critical flow occurs when the ratio of upstream to downstream absolute pressure exceeds two. The equations governing flow through a critical orifice are [Holman, 1966]:

$$Q = Q_c \left[\frac{T}{T_c} \cdot \frac{MW_c}{MW} \right]^{1/2}$$

$$\dot{n} = \frac{PQ}{RT}$$

$$= \frac{PQ_c}{RT_c^{1/2}T^{1/2}} \left[\frac{MW_c}{MW} \right]^{1/2}$$

where Q is the volumetric flow rate of gas upstream of the orifice, T is the upstream temperature, P is the upstream pressure, MW is the molecular weight of the gas, ṅ is the molar flow rate, R is the universal gas constant, and the subscript c refers to the calibration conditions.

As shown in Figure 4.4.3 temperature and pressure upstream of the orifices are measured. Where the critical orifices are located away from any heated sections of the test apparatus, such as the cyclone and dilution gas supply system, ambient temperature is assumed.

Figure 4.4.4 shows photographs of the Millipore critical orifices and how they are mounted in a 3/8-in. Swageloc male-to-male connector.

The dilution flows and sample flows are turned on and off by remotely actuated valves manufactured by ASCO. The remotely actuated valves for the samplers are operated by the

Modicon Micro 84 programmable controller shown in Figure 4.4.5.

Dilution of the sample by the diluters D1 and D2 serves three purposes. The first is to reduce the high aerosol concentration to a level that is within the measurement range of the instrumentation (less than about 20 g/m³ for the filters and less than about 5 g/m³ for the impactors). The second is to cool the flow and to reduce the temperature variation of gas passing through the SEDS by the addition of the cooler dilution gas. The third is to reduce the variation in gas properties by the addition of a known dilution gas in high enough amounts to dominate the gas properties. Dilution can be used to inhibit further evolution of an aerosol size distribution resulting from coagulation and condensation [Brockmann et al., 1984]. In this application, however, the aerosol size distribution has evolved during transport through the crucible and exhaust line and is likely to have reached a point where the time scale of evolution is large compared to that of transport through the SEDS.

Figure 4.4.6 is a schematic diagram of the flow diluter designed for this test series. Figure 4.4.7 shows photographs of the assembled and disassembled diluter. The diluter consists of an aluminum outer tube 15 cm long and 6.35 cm in outside diameter and a 1.9 cm outside diameter sintered stainless steel inner tube. End caps hold the tubes in place. Dry dilution gas passed through a 1/4-in. Swageloc fitting in the outer tube to the annular plenum region between the two tubes. Gas passes through the porous walls of the inner tube diluting the aerosol sample flowing through it.

The total flow out of the diluter, QT, was measured and the dilution flow into the diluter, QD, was measured. The dilution ratio DR is then defined as QT divided by the difference between QT and QD. Some care in the magnitude of the dilution is necessary. The dilution ratio is calculated using the difference between
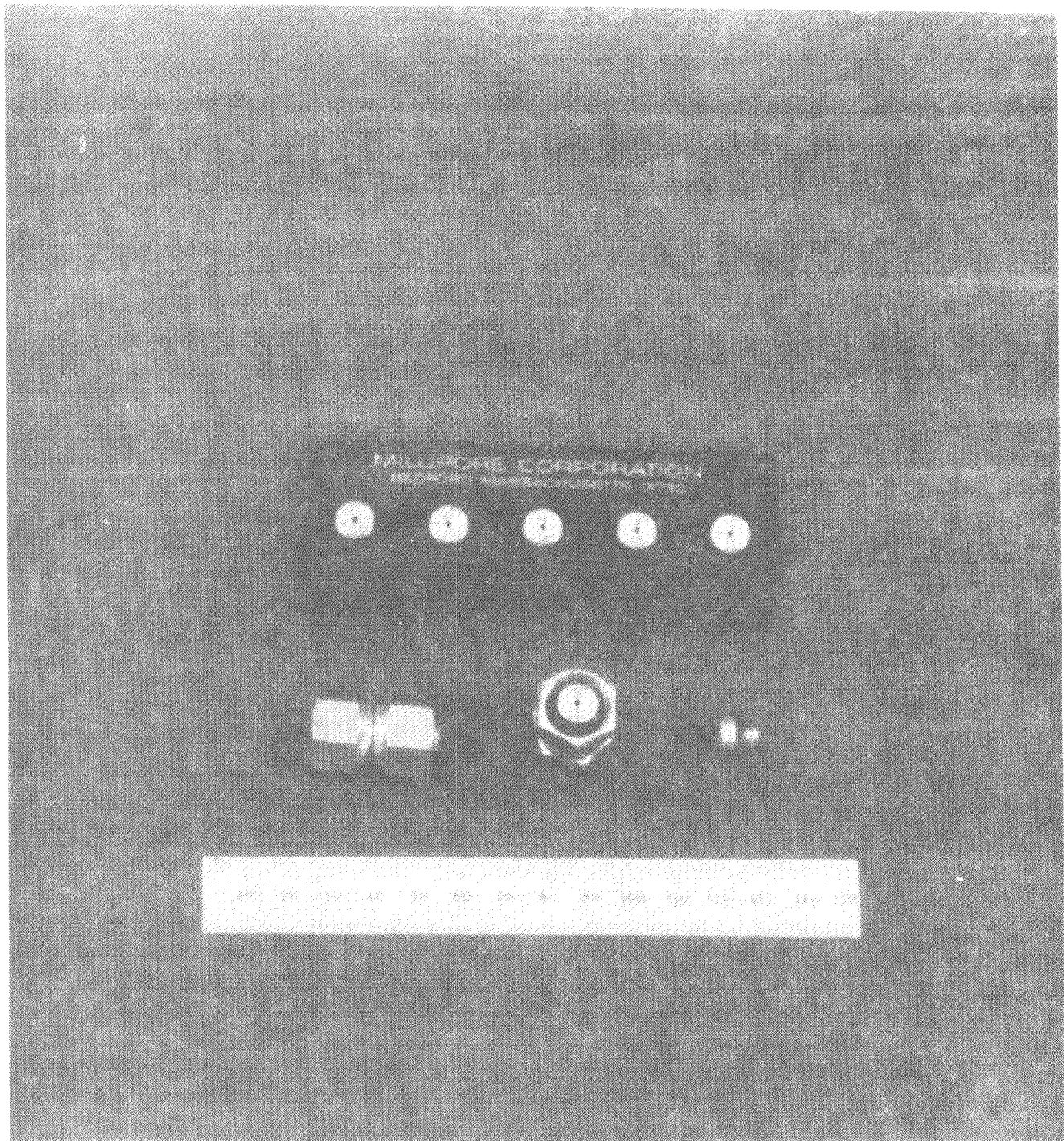
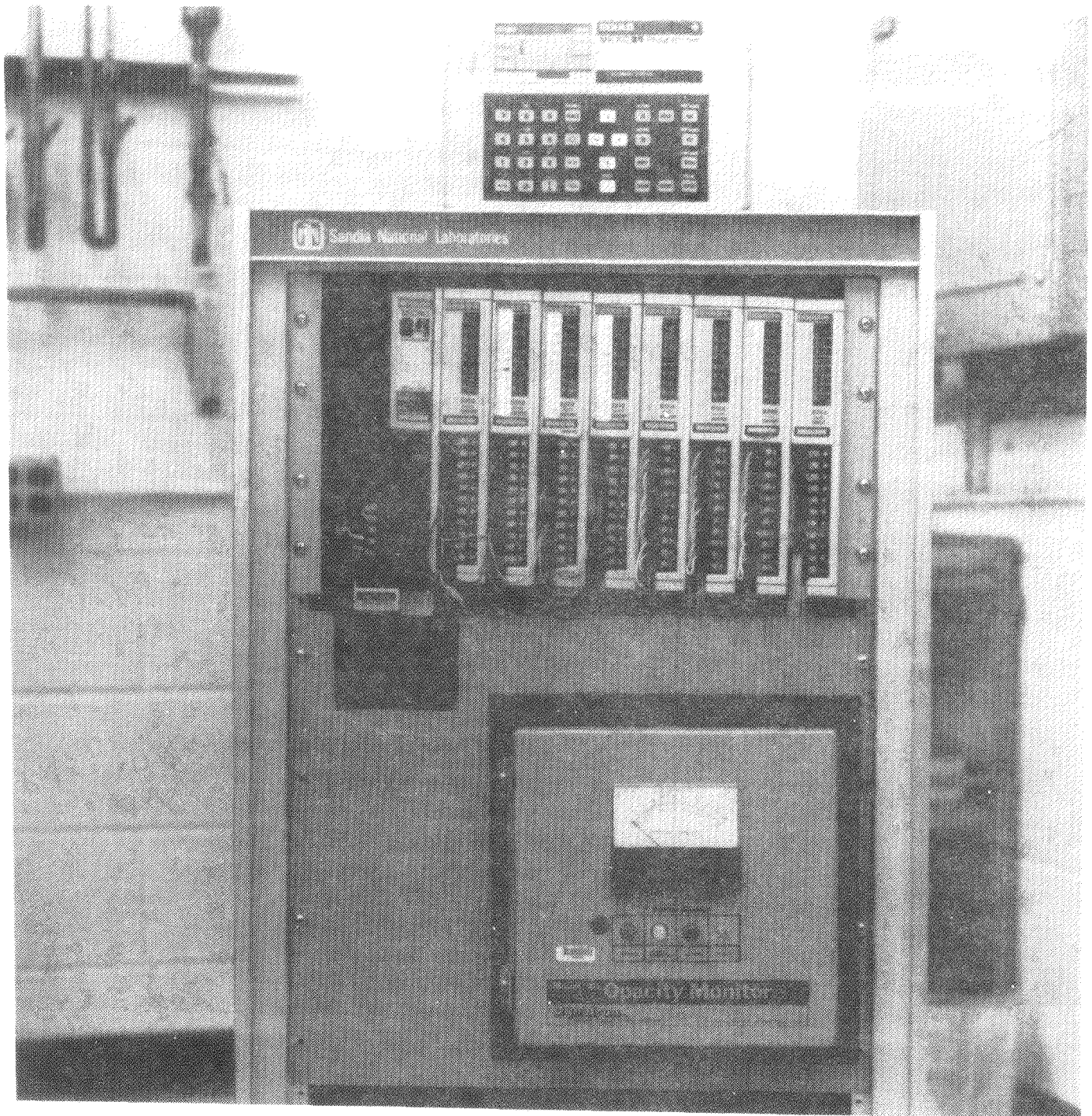Figure 4.4.4 Millipore critical orifices used to control the sample flows and dilution gas flows

Figure 4.4.5 Modicon Micro 84 programmable controller shown with the control/programming
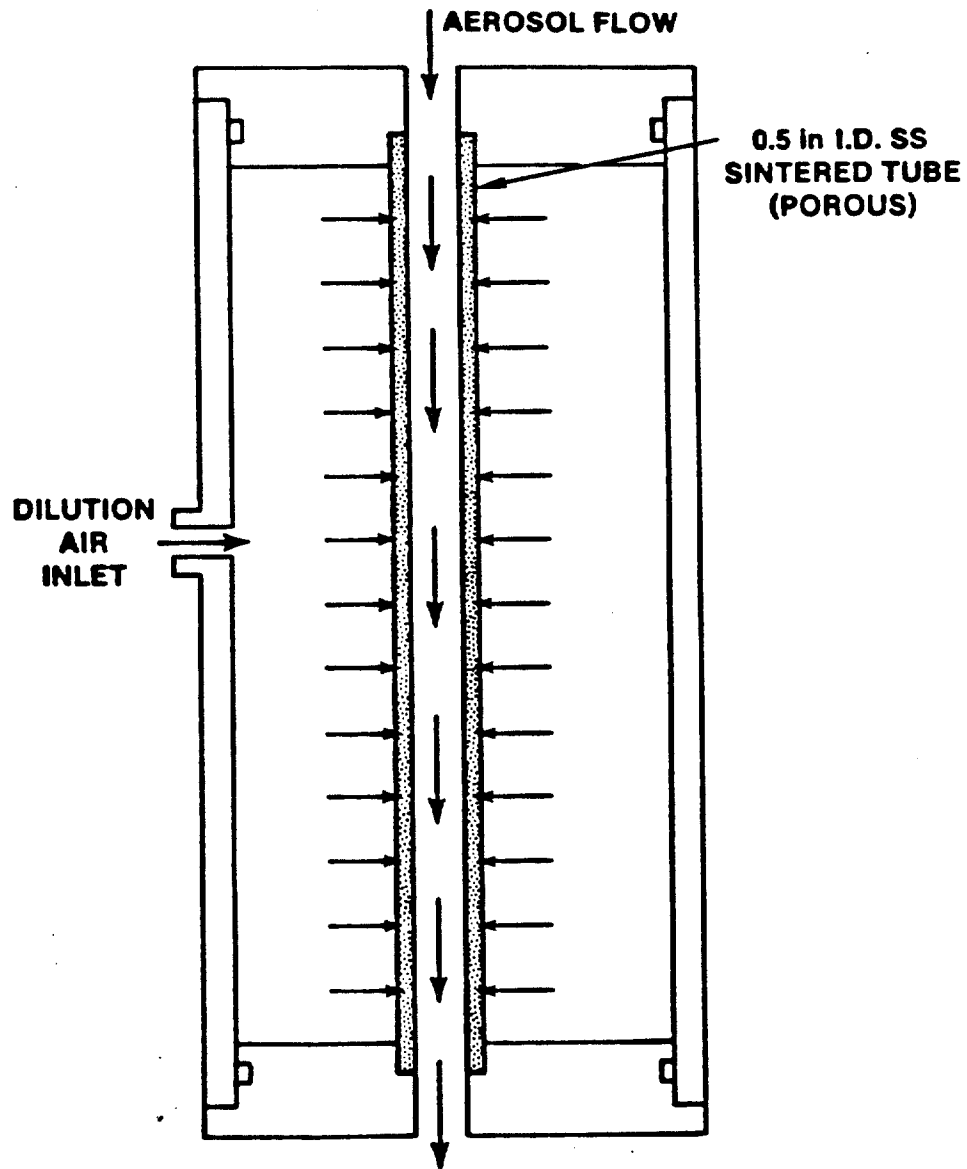unit sitting atop the switching section

AEROSOL FLOW

0.5 in I.D. SS SINTERED TUBE (POROUS)

DILUTION AIR INLET

Figure 4.4.6 Schematic diagram of flow diluter used in the sample extraction dilution system
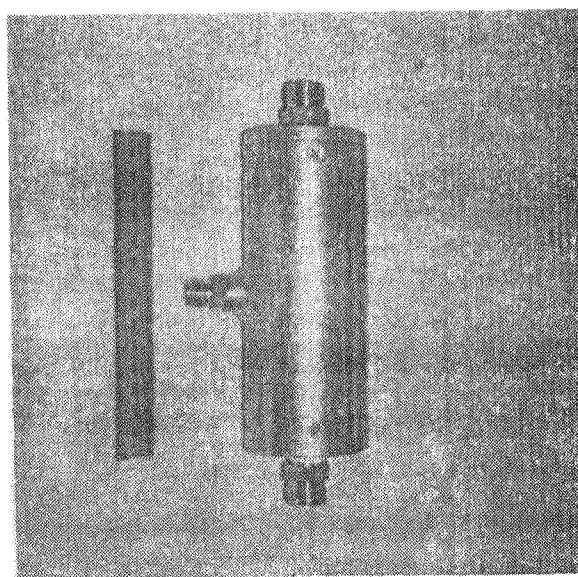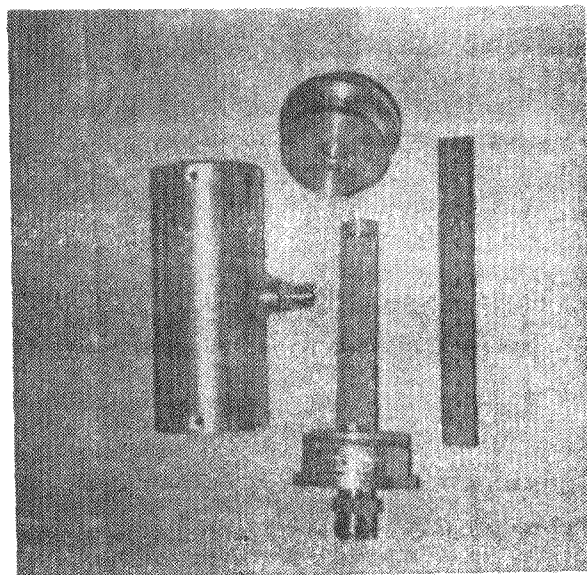
Figure 4.4.7 Photographs of the assembled and disassembled flow diluter used in the SURC-2 tests showing the diluter body, sintered inner tube and end caps

two numbers and when those numbers are close, the error in the difference can become large. For example, if the uncertainty in the flows QT and QD is ± 5% for each, the resulting uncertainty in dilution ratio is ± 36% for a nominal dilution ratio of 5. This magnification of the flow uncertainties in the calculation of the dilution ratio places a practical upper limit on dilution ratio of about 5. For this test, nominal dilution ratios were about three for each of the two diluters.

Because the system pressure in the SEDS is the same as that of the experimental apparatus, the SEDS can become pressurized (at higher gas evolution rates, the evolution gas flow train causes some back pressure in the apparatus). Each orifice controlling the dilution gas flow delivers a fixed molar flow of dilution gas by virtue of its fixed upstream temperature and pressure. The orifices controlling the sample flow draw at a fixed volumetric flow rate. The fixed volumetric flow rate yields a molar flow rate directly proportional to the system pressure. Consequently, if the dilution flow is unchanged, the dilution ratio will decrease with increasing system pressure. To maintain a consistent level of dilution in the face of a pressurizing system, the molar flow of dilution gas must be increased in proportion to the increase in molar flow of the sample produced by the increase in system pressure. This increase in dilution molar flow was accomplished in diluter 1 by selecting combinations of three orifices as shown in Figure 4.4.3. These orifices were switched in and out by actuating remotely controlled valves controlling each orifice. This feature was not included in diluter 2.

Figure 4.4.8 is a photograph of the filter bank of 12 filter samples on the SEDS. The flow through each filter was controlled by a remotely actuated valve. The 12 valves were plumbed to a single critical orifice giving a nominal filter sample flow rate of 10 liters per minute. The filter bank consists of 12 Gelman in-line stainless steel filter holders. These stainless steel, 5.9 cm

diameter, 5.7 cm long filter holders (Gelman catalog number 2220) are designed for pressure applications of up to 200 psig. They use 47 mm diameter Durapore Membrane filtration media from Millipore (catalog designation HVLP 047). The effective filtration area is 9.67 cm^2 for each filter sample. Figure 4.4.9 shows photographs of one Gelman high pressure filter holder.

The inlet to the filter sample section was connected to a preseparator which removes particles larger than 10 to 15 micrometers aerodynamic equivalent diameter. This pre-separator is manufactured by Andersen and is of stainless steel construction, 8.2 cm in diameter and 12.8 cm long. The preseparator collects coarse material in an impaction cup, passing on the finer aerosol to the filter sample section.

Each filter sample provides a collected mass of aerosol with aerodynamic equivalent particle diameter less than 10 to 15 micrometers. This sample allows calculation of the aerosol mass concentration of these smaller particles. The collected material can also be chemically analyzed. The filter sample is the principal measurement in determining aerosol mass source rate and elemental composition.

The filter sample section was mounted in an insulated box and electrically heated to avoid water condensation. The heaters were controlled by an Omega Model 920 temperature controller with a type K thermocouple.

Figure 4.4.10 is a photograph of the impactor sample section. Andersen Mark III cascade impactors were used. An Andersen Mark III cascade impactor intertially classifies aerosol particles into nine size bins. This inertial classification is accomplished by accelerating the particles through successively smaller holes (and higher velocity jets) in a stack of orifice plates. Under the jets of each plate is a glass fiber collection substrate. Particles are collected by impaction on the substrates. Those small enough to follow the gas stream lines in one stage pass
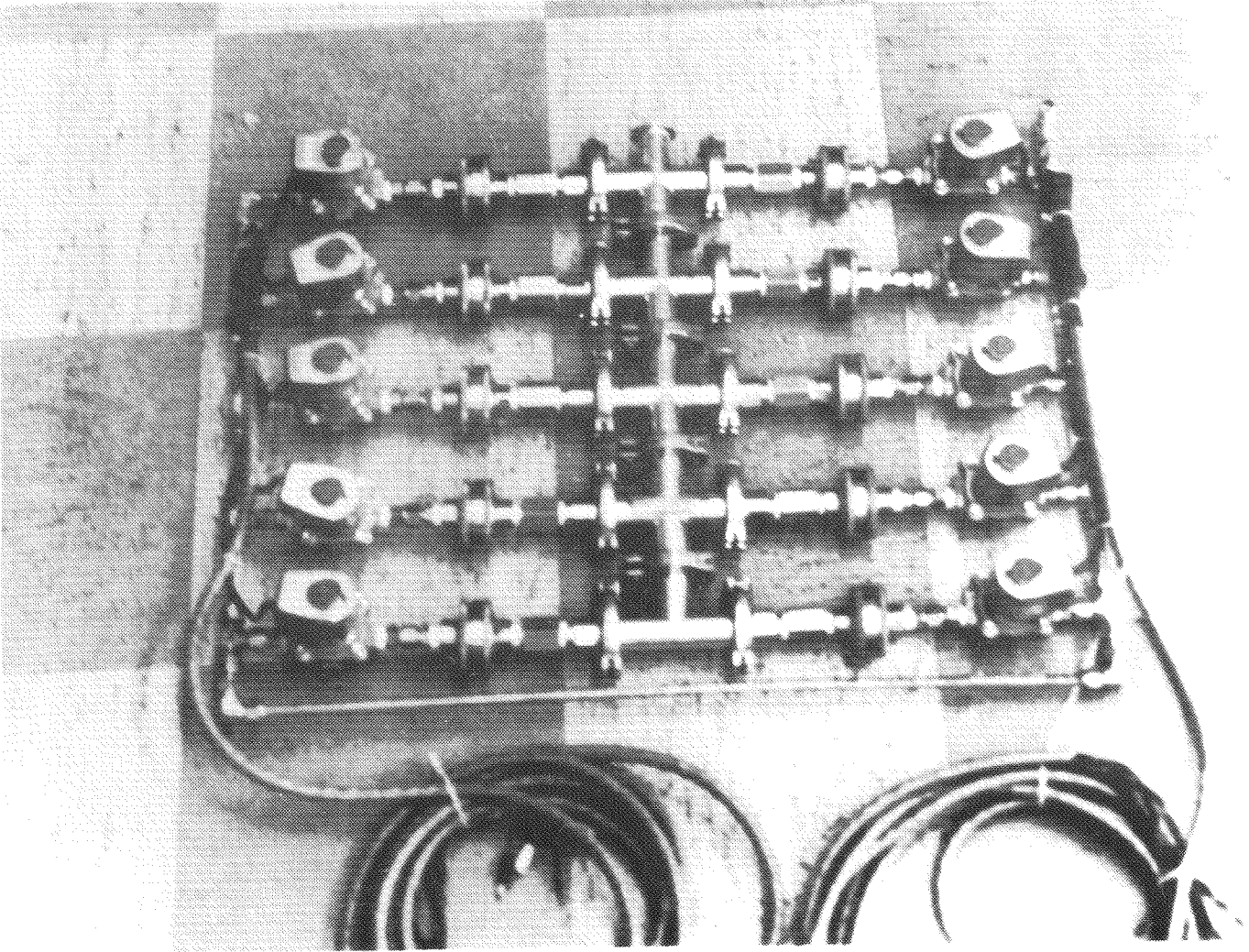
65

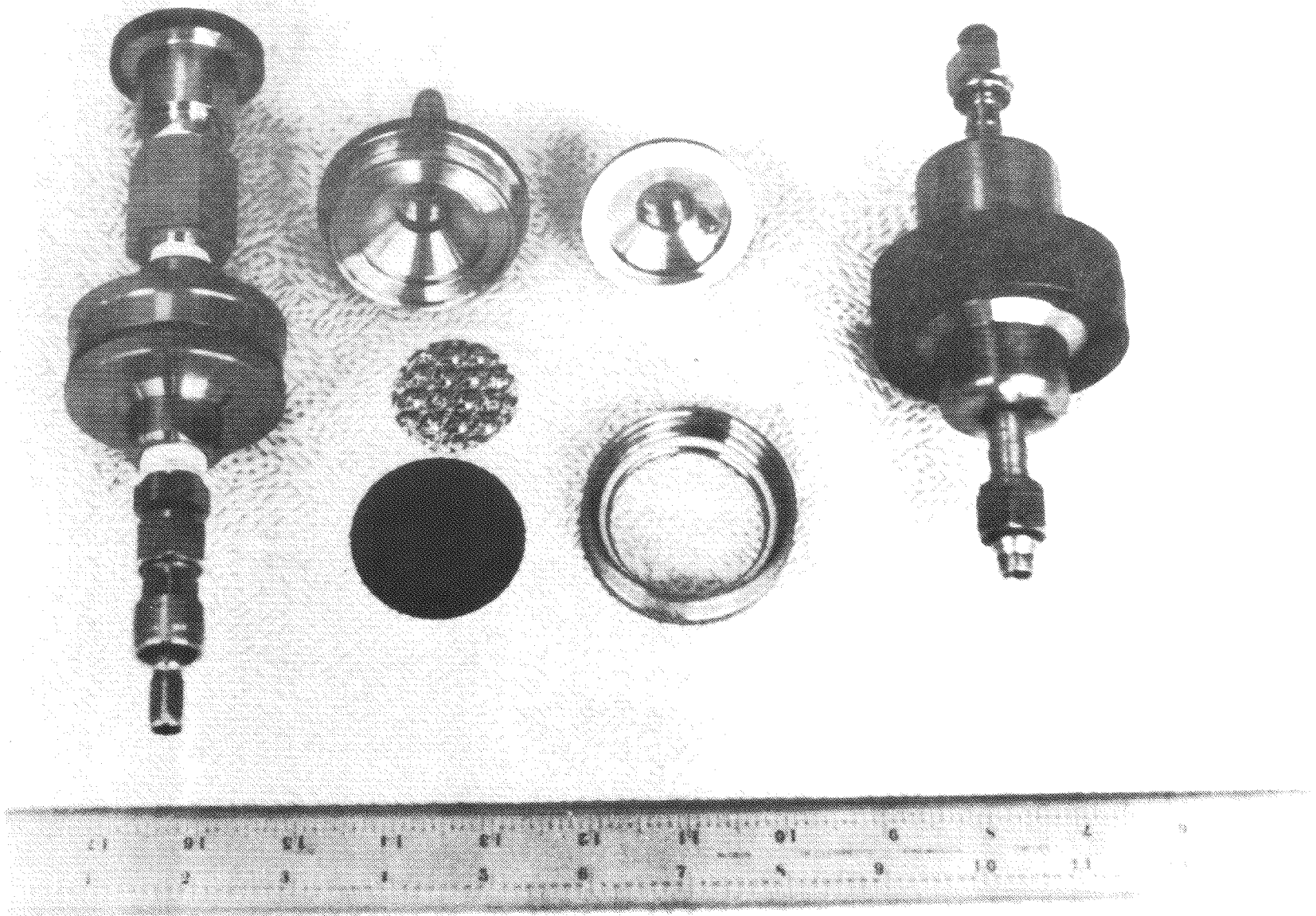Figure 4.4.8 Photograph of the filter bank

Figure 4.4.9 The Gelman high pressure filter holder shown disassembled with filter substrate support (left) and filter substrate and supports in place (right)
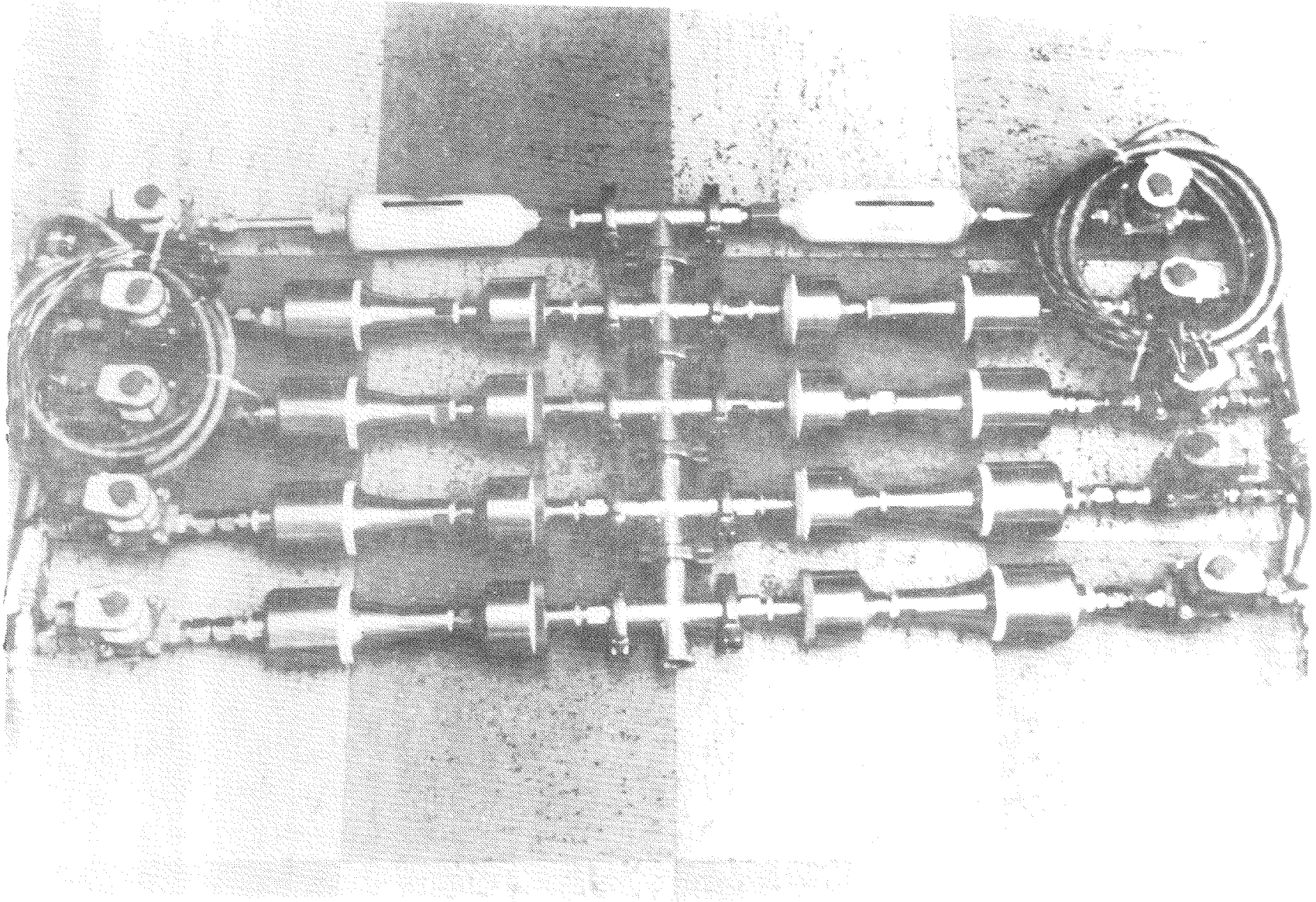
Figure 4.4.10 Schematic diagram of the impactor bank showing the impactors and by-pass filter

on to subsequent orifice plates or stages where they may be collected. The impactor consists of eight stages and a backup filter to collect any unimpacted particles. It yields a mass distribution of aerosol with respect to aerodynamic equivalent particle diameter. The Andersen Mark III cascade impactor is 8.2 cm in diameter and 18 cm long and is constructed of stainless steel.

A preseparator (shown in Figure 4.4.11), which removes particles nominally larger than 10 to 15 micrometers aerodynamic diameter, was used to avoid overloading (more than ~25 mg of material on any one stage) of the impactor by these larger particles. It effectively collects material which would otherwise be collected on the first two stages of the impactor. The preseparator collects material in an impaction cup, which is brushed out to retrieve the collected sample. The preseparator is of stainless steel construction, 8.2 cm in diameter and 12.8 cm long. It threads into the front of the impactor. The assembled preseparator-impactor is 8.2 cm in diameter and 29.8 cm long.

Two impactor samples were taken simultaneously, one at a nominal 10 liters per minute and the other at a nominal 15 liters per minute. This provides a more detailed measurement of the aerosol size distribution and will be discussed further in the section on impactor calibration. The box containing the impactor bank is heated in the same way as the filter sample box.

Figure 4.4.11 shows photographs of the assembled and disassembled Andersen Mark III impactor and preseparator. Also shown are the jet plates and glass fiber collection substrates.

Figure 4.4.12 shows photographs of the Sierra cascade cyclone.

Figure 4.4.13 shows the disassembled cascade cyclone. Sample flow was controlled by two Millipore critical orifices in parallel to give a nominal sample flow of 24 liters per minute. A remotely actuated valve manufactured by ASCO was used to take the sample.

The cascade cyclone intertially classifies aerosol particles and yields a mass distribution with respect to aerodynamic equivalent particle diameter. This classification is accomplished by flowing the aerosol sample through a succession of smaller cyclones. The flow is introduced tangentially into the circular body of the cyclone where the circulating swirling flow causes larger particles to move by centrifugal force to the walls where they are collected. The smaller particles are withdrawn through the center and passed on to subsequent cyclones where they may be collected. Particles too small to be collected by the cyclones are collected by a backup filter. A cyclone is capable of collecting much more material than an impactor and can be used to collect size classified material for bulk analyses.

The Sierra cascade cyclone is a series of six cyclones of increasing capability to collect smaller particles followed by a glass fiber backup filter. The aerosol sample was brushed out of the collection cup of each cyclone for weighing. The cascade cyclone is of stainless steel construction and when assembled is 12.7 cm in diameter at the widest point and about 60 cm in length.

Figures 4.4.12 and 4.4.13 shows two views of the Sierra cascade cyclone: assembled and disassembled into its component six cyclones and the backup filter. The assembled unit is actually more compact than shown in the photograph because the cyclones were rotated about their connection points to nest together in a more compact cylindrical configuration.

Figure 4.4.14 is a schematic diagram of the Dynatron Model 301 opacity meter placed in the exhaust line from the containment vessel upstream of the gravel filter and flow measurement devices. This device measures the attenuation of a light beam as it travels through an aerosol. Light attenuation correlates with aerosol mass concentration. Correlation of the opacity meter

69
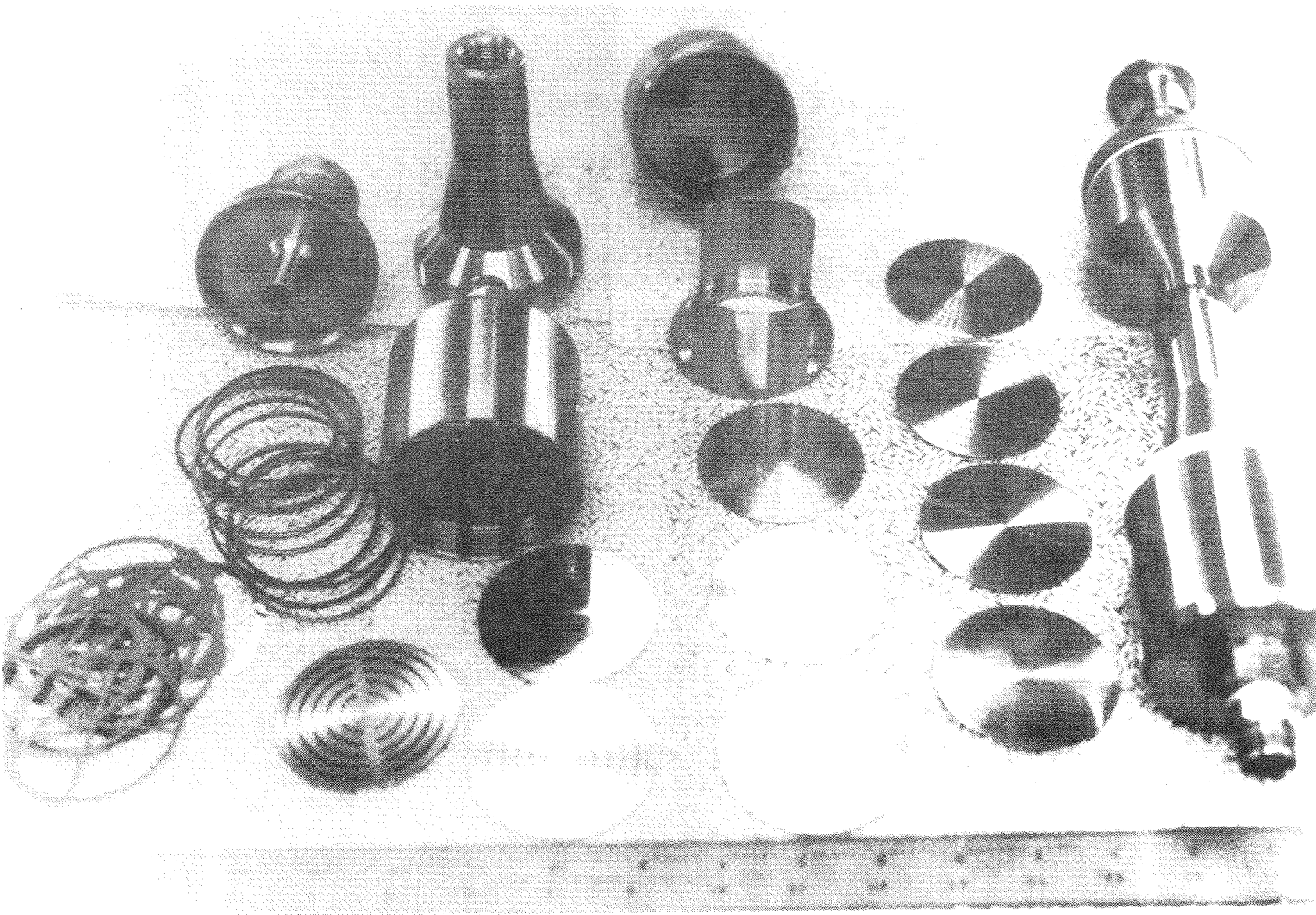
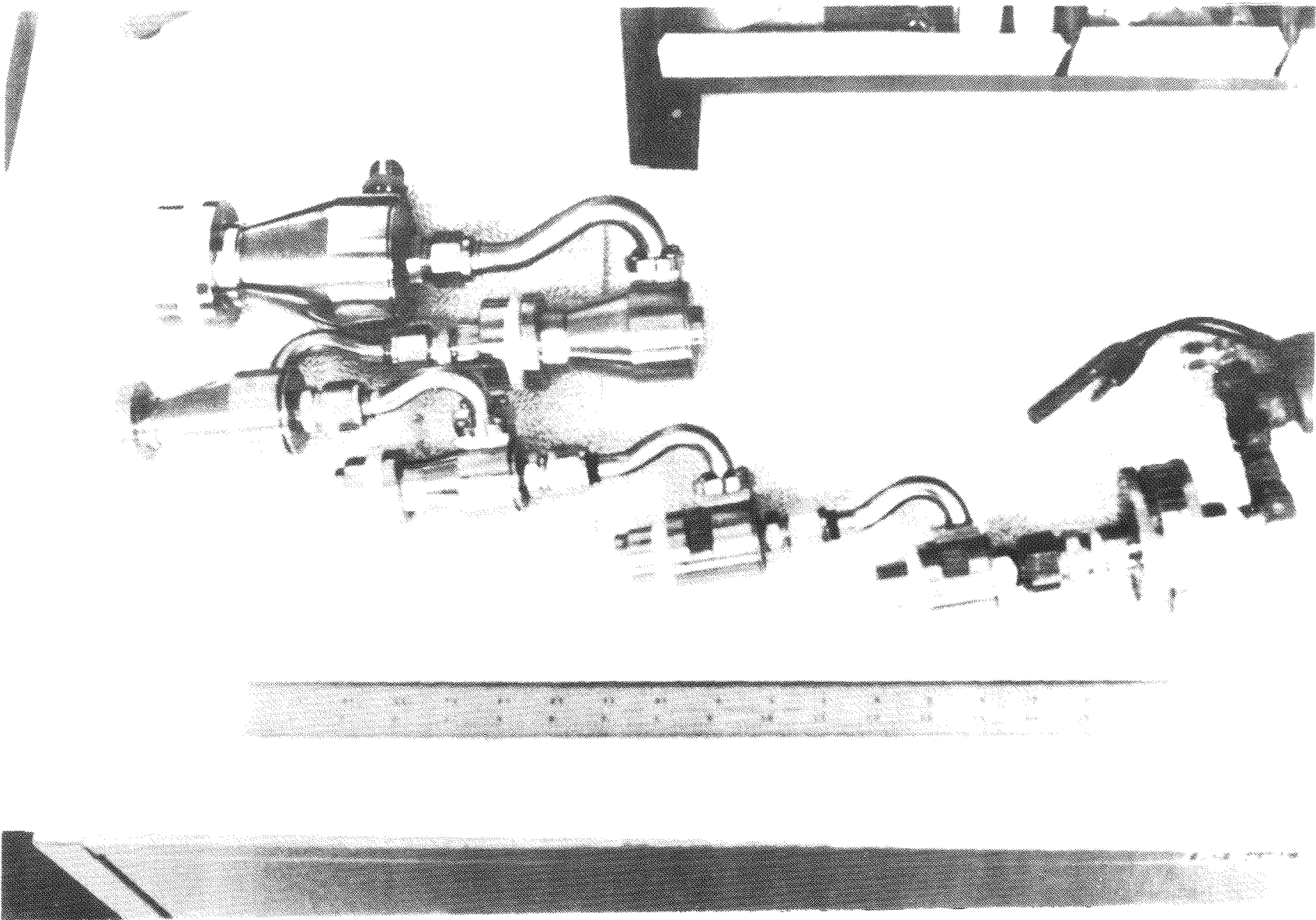Figure 4.4.11 Photographs showing the assembled Andersen Mark III impactor

70

Figure 4.4.12 Sierra cascade cyclone shown assembled with its six constituent cyclones and backup filter
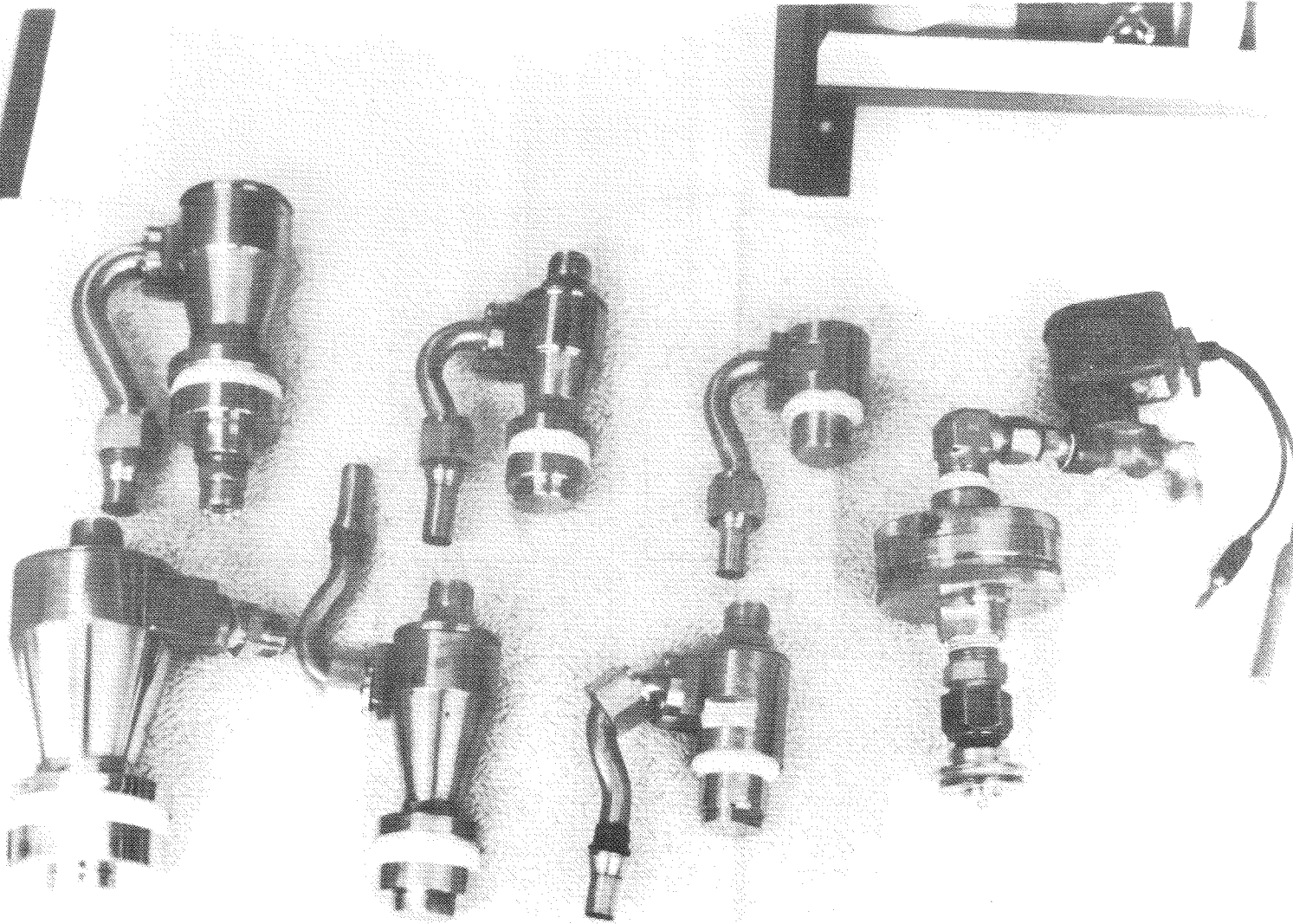
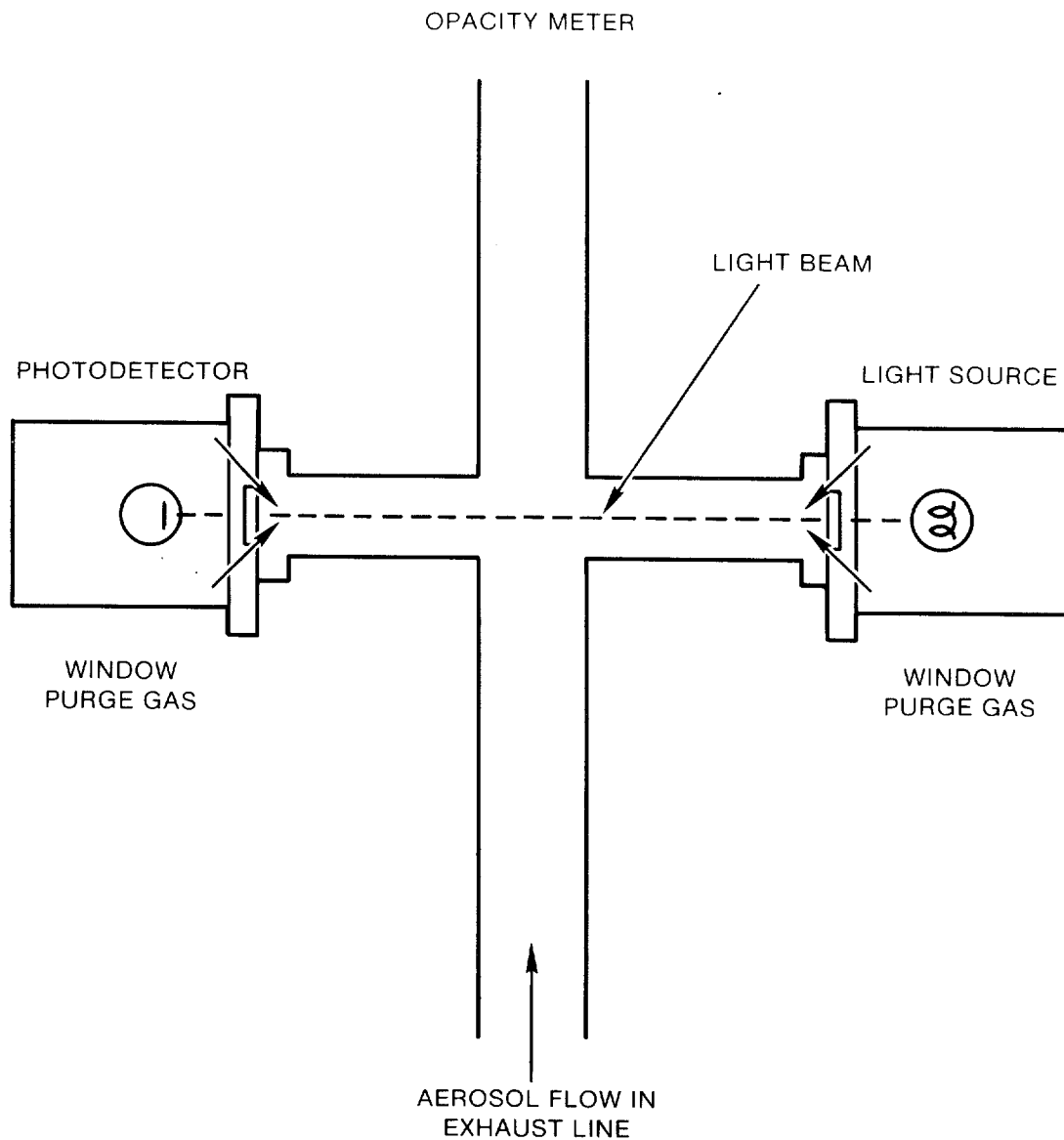Figure 4.4.13 Sierra cascade cyclone shown disassembled into its six constituent cyclones and backup filter

OPACITY METER

LIGHT BEAM

PHOTODETECTOR

LIGHT SOURCE

WINDOW
PURGE GAS

WINDOW
PURGE GAS

AEROSOL FLOW IN
EXHAUST LINE

Figure 4.4.14 Schematic diagram of the opacity meter used on the SURC-2 test showing how it
was installed behind gas purged windows in the exhaust gas line

output with the mass measured by the filter samples provided a continuous record of mass concentration in the pipe exhausting gas and aerosol from the interaction crucible in the SURC-2 test. The windows allowing light transmission were kept clean and free of aerosol deposition by a purge gas flow.

Figure 4.4.15 shows the light source module, the photo detector module and the on-line output of the Dynatron Opacity Monitor.

Pressure Transducer Calibration

Kulite 0 to 100 psia pressure transducers were used to monitor the pressure of the gas upstream of the orifices in the diluters and the pressures in the sample extraction-dilution system. The calibration data for the pressure transducers are given in Table 4.4.1. The locations of the pressure transducers and the flow controlling critical orifices in the SEDS are shown in Figure 4.4.3.

From the pressure transducers located upstream and downstream of the flow controlling orifices, critical flow determination is made.

Orifice Calibration

The sample flows are controlled by critical orifices from Millipore. These orifices have been calibrated in Sandia Laboratories' primary standards lab. The orifice calibration flow rates are given in Table 4.4.2. The orifice location and designation are shown in Figure 4.4.3 of the SEDS.

Impactor Calibration

The Andersen Mark III cascade impactor has been calibrated by Cushing et al. [1976]. We have employed their experimentally determined calibration in the reduction of data taken with the Andersen Mark III impactors.

Each impactor stage is assumed to collect all particles larger than some characteristic size and pass along all particles smaller than that size. This characteristic size is called the cut point. Thus, in a cascade impactor (an impactor composed of a series of stages with successively smaller cut points) each stage collects particles of a size between the cut point of that stage and that of the previous stage. The impactor yields a distribution of aerosol mass as mass between successive cut points.

The cut point of an impactor can be expressed as a Stokes number:

$$Stk = \frac{\rho_o D_{ae}^2 U}{18 L \mu}$$

where ρ_0 is the reference density of 1 g/cm^3, D_{ae} is the aerodynamic equivalent diameter, U is the velocity through the orifice, μ is the absolute viscosity of the gas, and L is the diameter of the orifice. Impactor theory holds that for a given stage, the characteristic Stokes number is constant [Marple and Willeke, 1979]. Thus, changing the flow (or U) through the impactor changes the cut point for that stage. The aerodynamic equivalent diameter corresponding to the cut point for each stage for impactors operating at 10 and 15 liters per minute are given in Table 4.4.3.

The preseparator used on the impactors has been calibrated by McFarland et al. [1978] and their calibration is used in the work presented here. Table 4.4.3 gives the cut points for the preseparator-impactor combination at the two nominal flow rates of 10 and 15 liters per minute.

The cut points for the two flow rates were staggered. A simultaneous sample taken by two such impactors will give the same distribution but with different cut points. Combination of the two distribution measurements gives a distribution
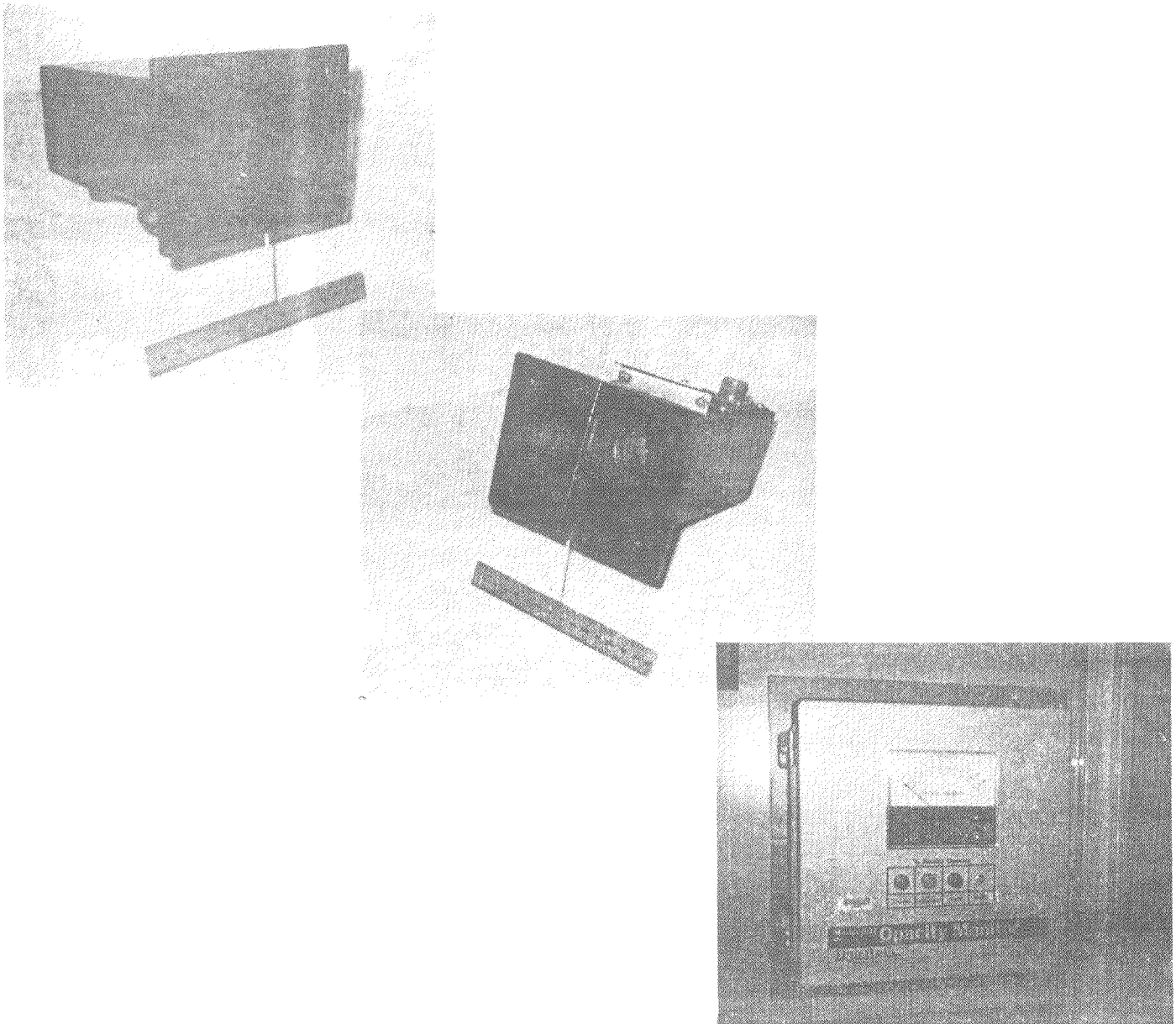
Figure 4.4.15 Photographs of the light source (left) and photodetector (center) modules and the on-line output of the dynatron opacity meter (right)

Table 4.4.1 Pressure transducer calibrations

	Transducer ID, Range (psia), and output in volts						
Pressure	11-2 0-100 (V)	11-3 0-100 (V)	P104 0-30 (V)	P105 0-30 (V)	P106 0-30 (V)	P107 0-30 (V)	P109 0-30 (V)
12.15	0.814	0.806	2.552	2.520	2.508	2.370	2.035
15.00	0.950	0.945	3.103	3.077	3.056	2.985	2.611
20.00	1.193	1.193	4.080	4.061	4.046	4.063	3.639
30.00	1.672	1.675	5.916	5.910	5.870	6.070	5.550
40.00	2.154	2.159					
50.00	2.614	2.644					
60.00	3.104	3.120					
70.00	3.565	3.603					
80.00	4.053	4.080					
90.00	4.514	4.560					
100.00	4.992	5.030					

with a finer definition than either measurement alone.

Cyclone Calibration

The cyclone exhibits the same general cut point behavior as an impactor, but there is no corresponding theory of cyclones as there is for impactors. The cyclone must be calibrated and operated at the same conditions. The manufacturer's calibration (Table 4.4.4) is used in the work presented here. Since the cyclone was used to collect bulk aerosol material over an extended period of the test, this calibration is reasonably accurate.

Aerosol Transport Calibration

The relationship between the sampled aerosol and the aerosol actually evolved from the test crucible must be understood. This relationship is defined by the efficiencies of aerosol extraction and transport. These efficiencies are calculated with an aerosol sampling efficiency model and an aerosol penetration model of the sampling system.

The extraction of the aerosol sample from the exhaust line through the gooseneck sampling probe is subject to the inefficiencies of anisokinetic sampling. Models describing the sampling efficiency exist in the literature [Davies and Subari, 1982; Jayasekera and Davies, 1980] and are used to calculate the probe performance.

The aerosol penetration model employed is described more fully in Gronager et al. [1986]. In this model, particle losses have been estimated for inertial deposition, diffusive deposition, and particle settling. The source term at the sampling point and sampling times can be adjusted for estimated loss and delay time.

Aerosol transport through the sample extraction and dilution system (SEDS) is not universally efficient. It is dependent upon particle size and flow conditions. Transport data for the SEDS system have been taken to test the transport model. These data are highly limited comprising only a portion of the desired calibration work. Exacting test schedules and limited resources prevented the in-depth testing desired. Further calibration of the system is under way.

Instrumentation

Table 4.4.2 Critical orifice calibration

Orifice I.D.	Critical Calibration Flow (cc/sec)
10B	178.0
14F	240.8
10G	181.3
25	379.3
D51	69.8
D52	83.8

The aerosol mass source rates are calculated by multiplying the measured aerosol concentration by the exhaust gas flow rates. Delay times for the aerosol to flow from the crucible volume to the sampling point are taken into account by calculating the time to flow through the intervening volume.

Experimental measurements of penetration through a series of 90° bends and through the SEDS plumbing from inlet to filter sample point and to impactor sample point have been made. The calibration aerosol was monodisperse oleic acid particles generated with the vibrating orifice generator manufactured by TSI, Inc. [Berglund and Liu, 1973]. Measurements of the aerosol concentration were made with a TSI aerodynamic particle sizer (APS-33). Aerosol concentration measurements were made upstream and downstream of the test section to obtain the penetration efficiency. Table 4.4.5 gives the results for the 90° bend and Figure 4.4.16 shows these results as penetration efficiency plotted against Stokes number along with the theoretical curve. For these high levels of penetration, the theory and data match well; however, for larger particles or higher flows resulting in lower penetration, the theory may be in some error.

Figure 4.4.17 is the room temperature penetration of a 4.56 micrometer diameter particle through the SEDS plumbing to the filter sample point. The curve is the theoretical penetration

calculated by the model discussed above. Figure 4.4.18 is the penetration of a 4.56 micrometer particle through the plumbing to the impactor sample point along with the theoretical penetration.

In both cases, the experiment gave lower penetration than the model calculated: about 30% low for the filters and 15% low for the impactors. The cause of these differences is not known and further calibration and verification of models are required.

Aerosol data from previous tests [Brockmann, 1987] have indicated that aerosols produced during melt interactions with concrete are typically on the order of one micrometer aerodynamic equivalent diameter. Penetration of this size to the samplers is seen from Figures 4.4.17 and 4.4.18 to be high.

4.5 Induction Power Instrumentation

The 203.9 kg of UO_2-ZrO_2-Zr core debris was melted and sustained using an Inductotherm 250 kW, 1 kHz induction power supply, shown in Figure 4.5.1. Power was delivered to the coils via remote control using a pair of No. 16 high current, water-cooled, flexible leads. During the melting process, the induction power supply automatically controlled voltage and frequency to deliver the desired power. Maximum efficiency was maintained throughout

Table 4.4.3 Andersen Mark III impactor cut points

| Stage | 50% Cut Points (Particle Diameter in Micrometers for Two Flow Rates) | |
	10 LPM	15 LPM
Preseparato r	10.5	10.0
1	-	-
2	-	-
3	7.6	6.3
4	5.1	4.3
5	2.8	2.4
6	1.3	1.1
7	.84	.70
8	.49	.41

Table 4.4.4 Sierra cascade cyclone cut points supplied by manufacturer. Flow Nominally at 0.8 SDFM and Temperature at 23RC

Cyclone Stage	Cut Point (μm)
1	Not supplied at these conditions
2	6.2
3	2.65
4	1.55
5	0.84
6	0.54

Table 4.4.5 Particle penetration through a 90° Bend

Dp (μm)	Q (cm^3/sec)	Tube I.D. (cm)	Stk	Experimental Penetration	Model Predicted Penetration
4.56	136	1.092	$8.3 \bullet 10^{-3}$	.978-.987	.987
4.56	208	1.092	$1.26 \bullet 10^{-2}$	.961-.972	.980
4.56	136	1.727		.972-1.00	.997
4.56	208	1.727	$2.1 \bullet 10^{-3}$	.981-1.00	.995
7.24	136	1.727	$3.2 \bullet 10^{-3}$	.945-.985	.992
9.12	136	1.727	$5.2 \bullet 10^{-3}$	.942-.967	.987
			$8.3 \bullet 10^{-3}$		

the experiment without the need to switch capacitors or voltage taps. The power at the buss bars was measured using a power transducer manufactured by Research Incorporated. This device converted the current and voltage measured at the buss bars inside the power supply into a voltage equivalent of power.

In order to conduct a posttest power balance, the flow rate and differential temperature of the cooling fluid across the power supply and coil were both measured during the experiment. The cooling fluid was a mixture of 30% ethylene glycol/70% water. The flow rate of the cooling fluid flowing through the coil and power supply (separate circuits) was measured using a turbine flow meter installed in line. The meter was manufactured by Signet Scientific and included a power supply and signal conditioner. Net power to the tungsten susceptors was calculated to be 50% of the gross power. This ratio is determined using calorimetric methods and is detailed in Appendix A.

The differential temperature across the power supply was measured across the inlet and exit using two Omega ON-970-44008, 33,000 ohm thermisters arranged in a half bridge circuit. The differential temperature across the coil was measured using a differential temperature transducer manufactured by Delta-T Co. Type K

thermocouples were installed at the inlet and exit of both the power supply and coil for redundant temperature measurement.

4.6 Data Acquisition System

An HP 1000 data acquisition system is used to sample and record the experimental results. Two-hundred-ten channels of data may be acquired during an experiment. Of the 210 channels, 150 are for type K thermocouples, 20 are for either type S or type C thermocouples and the remaining 40 are DC voltage channels. A patch panel routes all the analog data channels from the test location to the Hewlett-Packard Model 2250 Measurement and Control Unit. This unit houses an analog to digital converter capable of multiplexing the 210 data channels. The voltage range of the data acquisition unit is ± 10 volts DC, with a programmable gain to increase sensitivity if the expected signal is small. A Hewlett-Packard Model 1000 series A-600 minicomputer is used to control all remote devices and manipulate the data received from the Measurement and Control Unit. Data are stored on a Hewlett-Packard Model 7946, 15 Megabyte hard disk. A Hewlett-Packard Model 2623 terminal is used to command the minicomputer during test and to display real-time data in a tabular format as data acquisition progresses. A desktop terminal Hewlett-Packard Model 9836 is

PENETRATION THROUGH A 90° BEND

$(1 - stk \cdot \theta)$

PENETRATION (%)
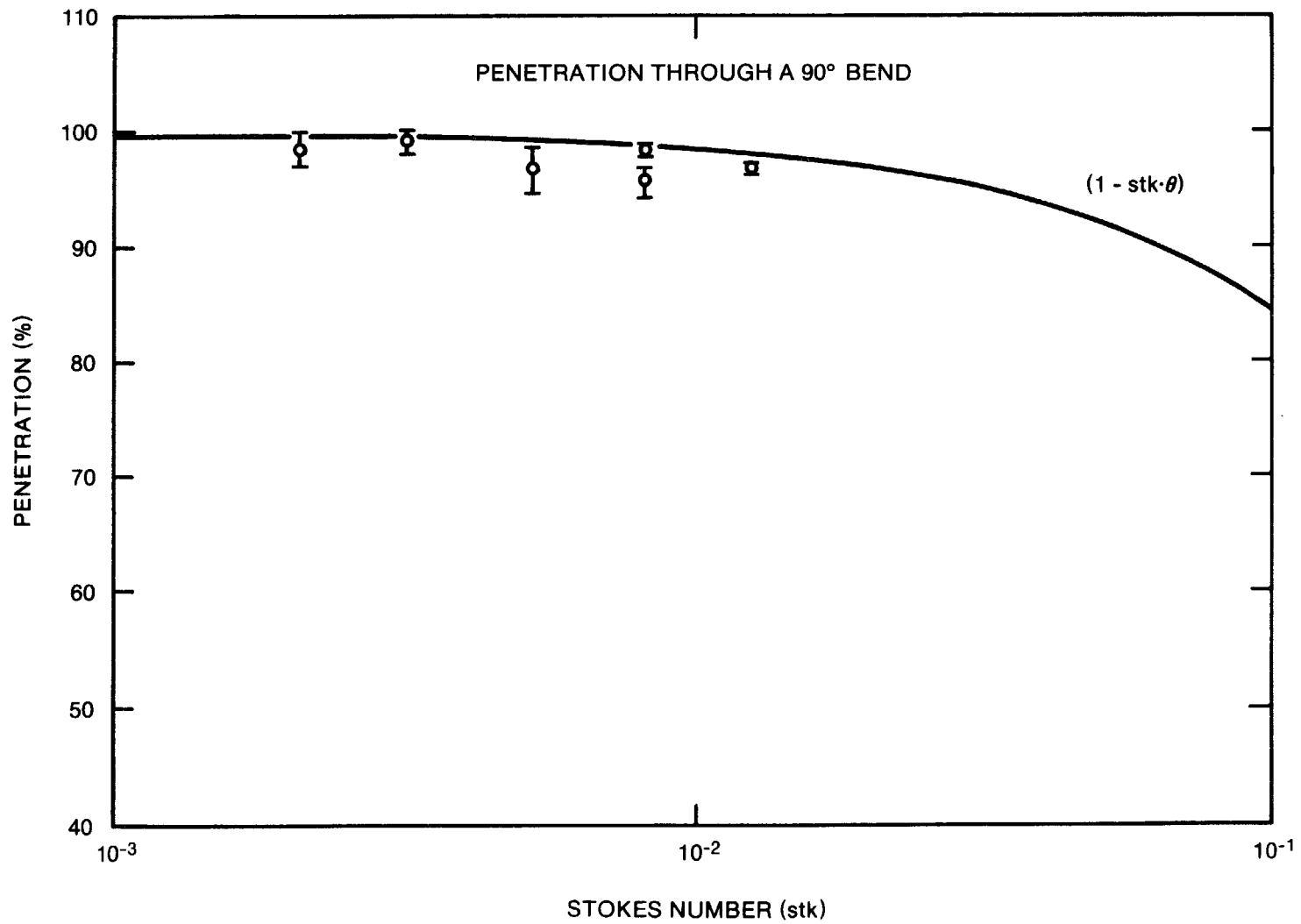
STOKES NUMBER (stk)

Figure 4.4.16 Experimental results and theory for particle penetration through a 90° bend as a function of Stokes Number

MEASURED AND PREDICTED PENETRATION
TO FILTER SAMPLES

PARTICLE DIAMETER (μm)
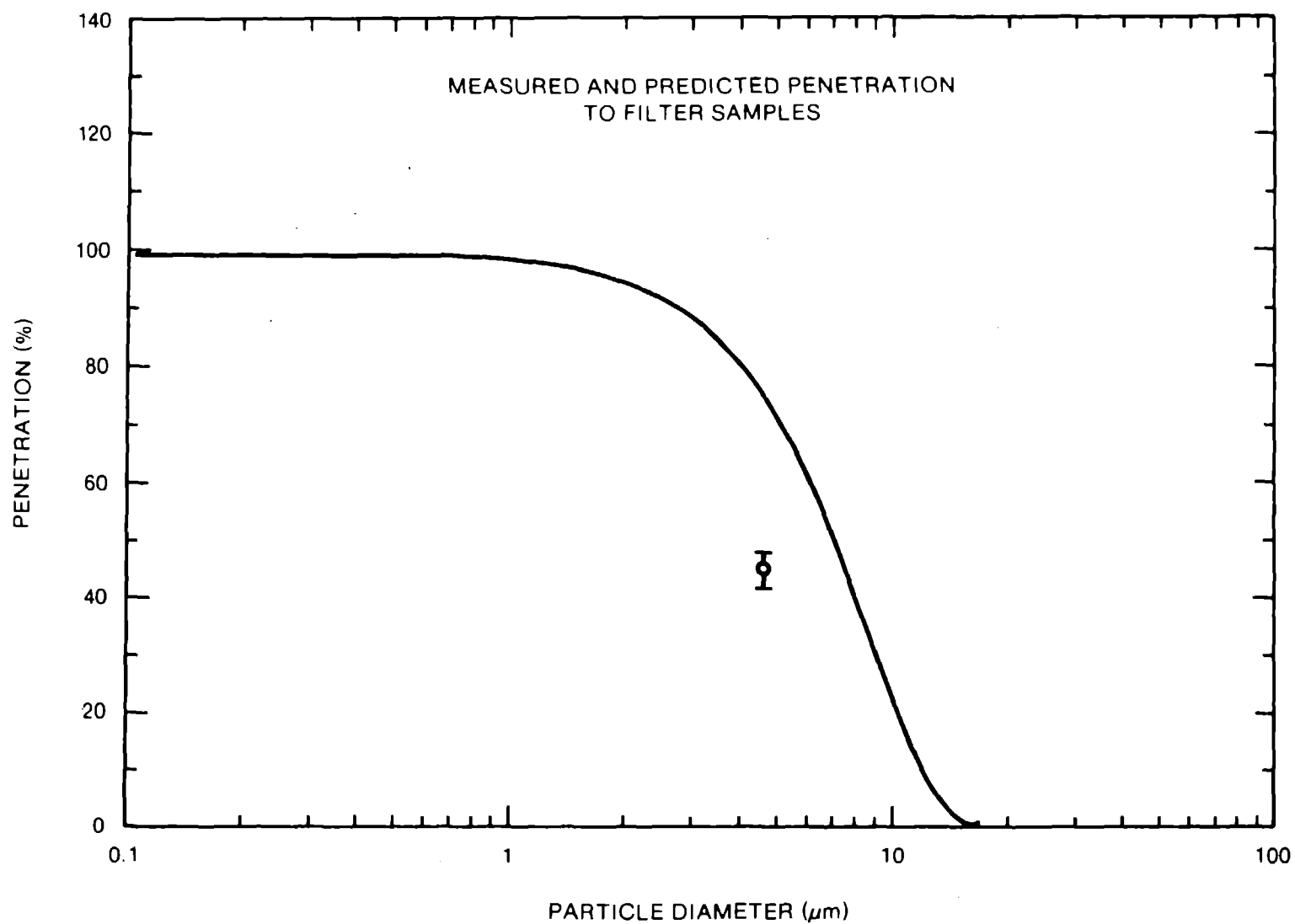
PENETRATION (%)

Figure 4.4.17   Penetration efficiency as a function of particle aerodynamic diameter predicted by theory and measured for a 4.56 μm particle from the SEDS inlet at diluter 1 to the filter sample point
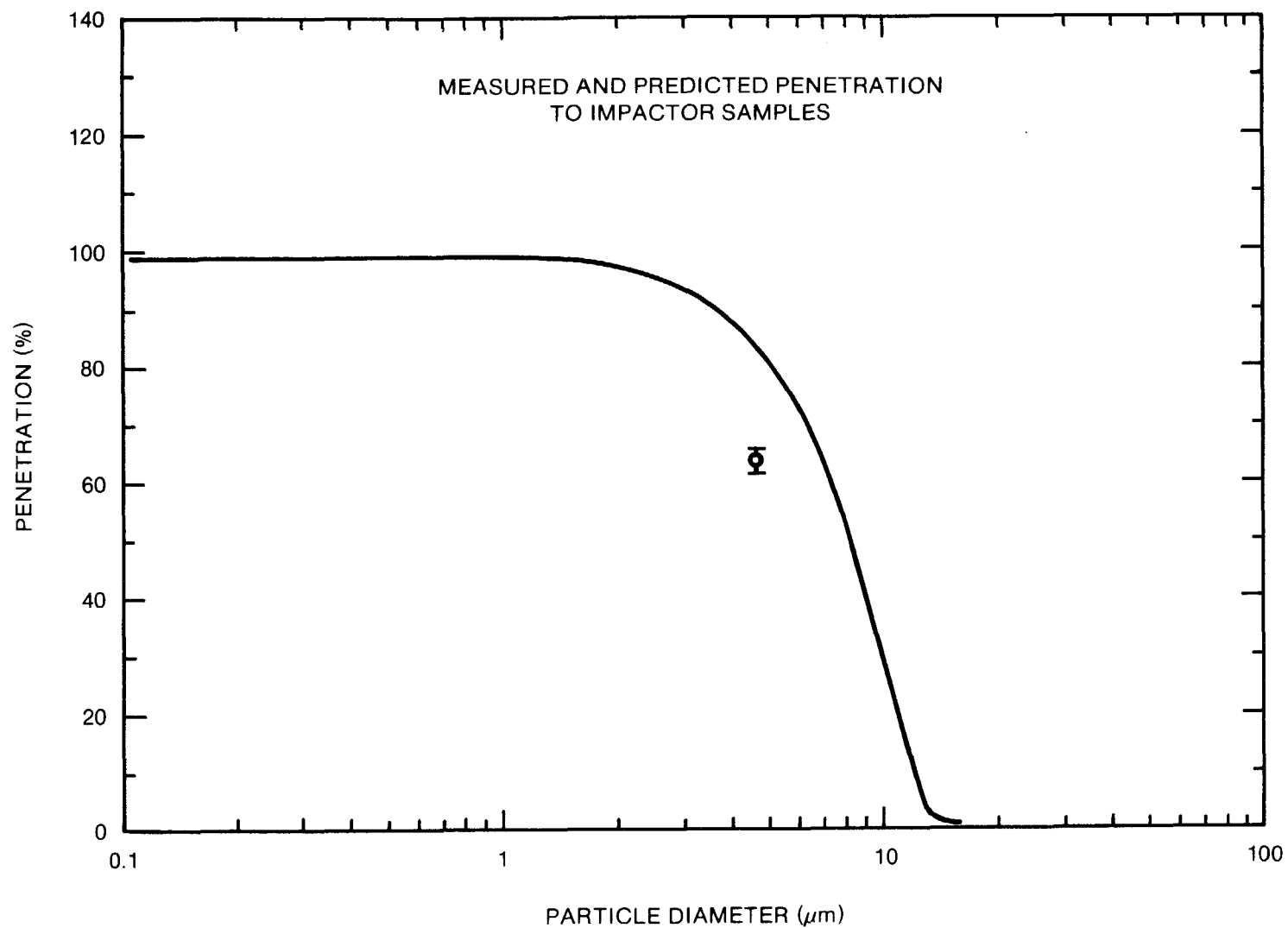
Figure 4.4.18 **Penetration efficiency as a function of particle aerodynamic diameter predicted by theory and measured for a 4.56 μm particle from the SEDS inlet at diluter 1 to the impactor sample point**
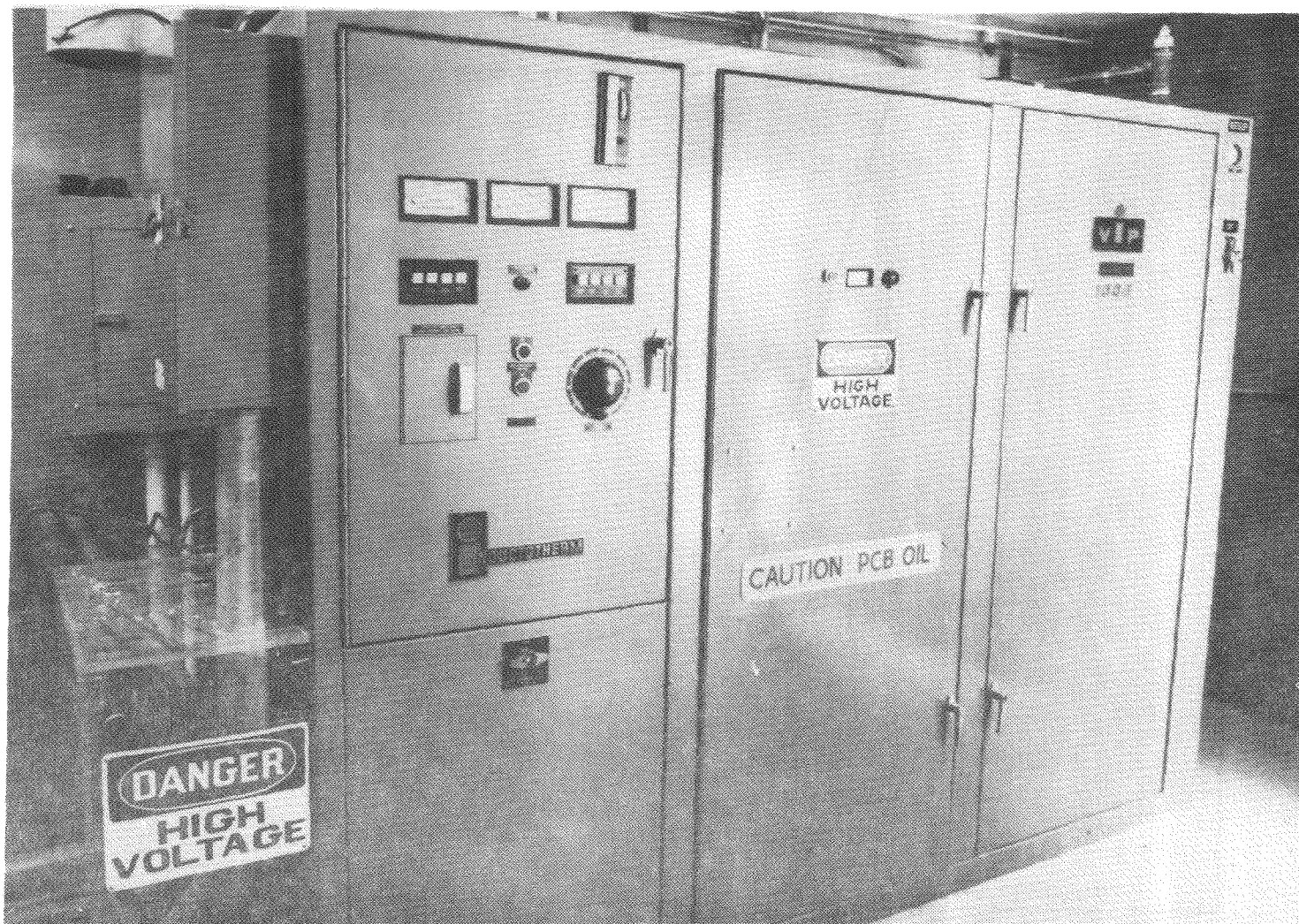
Figure 4.5.1 Inductotherm power supply

Instrumentation

used to display real-time data in both graphic and numeric format as well as to provide interrupt control over the mini-computer during a test. A Hewlett-Packard Model 9872 four color plotter and nine track magnetic tape are used for posttest data plotting and transfer.

The measurement accuracy of the 14-bit analog to digital converter is 1.56 microvolts in the most sensitive range and 1.25 millivolts at the highest range (-10 to +10 volts). With the appropriate range setting, the resolution for a type K thermocouple is ± 1°C, and for a type S or a type C thermocouple, the resolution is ± 1.1°C.

The data acquisition speed can be selected upward from 1.25 seconds per point upward for

210 channels. The sample rate can be increased by reducing the number of channels sampled. For the SURC-2 test, data for the channels were sampled initially at 15 second intervals.

4.7 Video Monitoring Instrumentation

The experiment was monitored remotely using a Sony Beta Model HVC 2200 video camera connected to a Sony Model SL 2000 portable Beta recorder and Model TT 2000 Tuner/Timer. The real-time camera image was displayed on a 19-in. Sony model CVM 1900 color monitor. The image was passed between the video recorder and color monitor via a RG-59 coax cable.

83 NUREG/CR-5564

5.0 Test Procedure and Posttest Observations

5.1 Operational Procedure

On the day of the test the SURC-2 assembly was leak-tested. Results of the leak tests using argon gas as the flow medium indicated a cold leak rate of 12 alpm at an inlet flow rate of 165 alpm (7% losses) and an overpressure of 1 psig in the SURC-2 containment vessel. After final calibration and pretest checkouts were performed, the data acquisition system was started. This marks the beginning of the SURC-2 test and is the time, t = 0, to which all other times are referenced. Power was then applied to the coil at a rate of 50 kW at time = 10 minutes. Net power to the charge was calculated to be 42% of the gross power. This ratio is determined using calorimetric methods and is detailed in Appendix A.

A summary of the events in the SURC-2 test is presented in Table 5.1. The power history shown in Figures 5.1 and 5.2 was monitored in order to closely duplicate the power history from the SURC-1 experiment. Consequently, power increases were affected to a level of 100 kW after 30 minutes (vs. 30 minutes for SURC-1), to a level of 150 kW after 100 minutes (vs. 90 minutes for SURC-1), and to a level of 200 kW after 210 minutes (vs. 200 minutes in SURC-1). The charge became molten 2700 K after 120 minutes and concrete attack began at 130 minutes when the zirconia insulator board at the bottom of the charge was dissolved into the melt. Aerosol samples were taken at 132 minutes as the optical pyrometer started to indicate large amounts of aerosol production. Gas composition grab samples were also taken at this time.

There were two points in the heatup phase of the test where the power supply tripped off due to a systems failure. The first was at 55 minutes due to a coolant flow blockage. This was corrected in 7 minutes and power was restored to 100 kW. The second was at 120 minutes due to a coolant line temperature fault. Auxiliary cooling was

provided and power was restored in 3 minutes. No other unusual conditions arose during the remainder of the test.

Additional gas samples were taken at 140, 175, 190, and 202 minutes and supplementary aerosol samples were taken at regular intervals between 140 and 175 minutes. The data acquisition system, which was initially set to take data every 15 seconds, was reprogrammed at 130 minutes to take data every 5 seconds and then changed back to 15 second scans at 216 minutes. A large pressure excursion was noted in the containment vessel at 280 minutes and the power supply was turned off, thus terminating the test.

5.2 Posttest Observations

The flow system was leak tested and no extraordinary leakage was found. The SURC-2 containment vessel was then opened in order to inspect the interaction crucible. This inspection showed that the MgO sidewalls were intact and that there was no evidence of melt pool-sidewall interaction other than thermal dehydration. The molten oxide charge had completely penetrated the bottom of the interaction crucible through a gap between the MgO annulus and the remainder of the concrete basemat. The remainder of the basemat was not cracked and showed no signs of asymmetric erosion. Further inspection of the oxide charge and the slag material remaining in the crucible showed that 100% of the zirconium metal had been oxidized into the melt.

A posttest x-ray was taken prior to disassembly of the test article. A sketch of this x-ray is shown in Figure 5.3. The x-ray showed several cracks were present in the MgO sidewalls of the inner crucible. There were traces of unmelted charge materials at locations above the original concrete surface and three of the five tungsten rings appeared to be intact. Both the charge materials and the tungsten rings had collapsed downward. The concrete interface was easily

Table 5.1 Events of test SURC-2

Time (min)	Event
0.0	Start of data acquisition system sampling 197 channels of data at 15 second intervals 11:18 MDT
10.0	Power supply turned on; power meter reading 50 kW
11.35	C type thermocouples noisy; installed filter to reduce induction feedback
40.0	Power increased to 100 kW
48.0	Installed filter on C type thermocouple installed in pyrotube
55.0	Power supply shut off due to low pressure limit on cabinet coolant flow. Changed coolant filter to correct problem
61.0	Power supply restarted, power meter reading 100 kW
110.0	Power increased to 150 kW
120.	Power supply shut off due to trip of a limit switch on the inlet temperature. This incident was corrected by starting cooling towers
123	Power supply restarted at 150 kW
130	Axial array thermocouples C1 (z = 0.0 cm) and C2 (z = -1.0 cm) failed Change computer sample rate to 5 sec/scan photometer pegged
130.0	Grab sample #1 taken
130.5	Cascade Cyclone sample started, sample duration 5 min
132.0	Filter Sample #1 taken, sample duration 30 sec
132.5	Filter Sample #2 taken, sample duration 30 sec Impactor sample "E" taken, sample duration 30 sec Impactor sample "F" taken, sample duration 30 sec
133.0	Filter sample #3 taken, sample duration 30 sec
133.4	Significant flow of aerosol indicated by photometer
133.5	Filter sample #4 taken, sample duration 30 sec
134.0	Filter sample #5 taken, sample duration 30 sec Impactor sample "G" taken, sample duration 30 sec Impactor sample "H" taken
134.5	Filter sample #6 taken
135.5	Cascade Cyclone Sample Terminated
139.5	Filter sample #A taken, sample duration 30 sec
140.0	Filter sample #B taken, sample duration 30 sec Grab sample #2 and #3 taken
140.5	Filter sample "C" taken, sample duration 30 sec
141.0	Filter sample "D" taken, sample duration 30 sec
143	Filter sample #7 taken, sample duration 30 sec
143.5	Filter sample #8 taken, sample duration 30 sec Impactor sample "J" taken, sample duration 30 sec Impactor sample "K" taken, sample duration 30 sec
144.0	Filter sample #9 taken, sample duration 30 sec
151.	Output of photometer has decreased somewhat
154.0	Filter sample E taken, sample duration 30 sec
154.5	Filter sample F taken

Table 5.1 Events of test SURC-2 (concluded)

Time (min)	Event
155	Filter sample G taken, sample duration 30 sec
	Gas grab sample #4 taken
155.5	Filter sample H taken, sample duration 30 sec
163.5	Filter sample #10 taken, sample duration 30 sec
164.0	Filter sample #11 taken, sample duration 30 sec
	Impactor sample N taken, sample duration 30 sec
	Impactor sample O taken, sample duration 30 sec
164.5	Filter sample #12 taken, sample duration 30 sec
174.5	Filter sample I taken, sample duration 30 sec
175.0	Filter sample J taken, sample duration 30 sec
	Gas grab sample #5 taken
190.	Gas grab sample #6 taken
202	Gas grab sample #7 taken
216	Change computer sample rate to 15 sec/scan
220	Power increased to 200 kW
280.21	Power supply turned off, test terminated erosion depth 35 cm total
281	Large pressure excursion in the containment vessel
303	Data acquisition system turned off

87
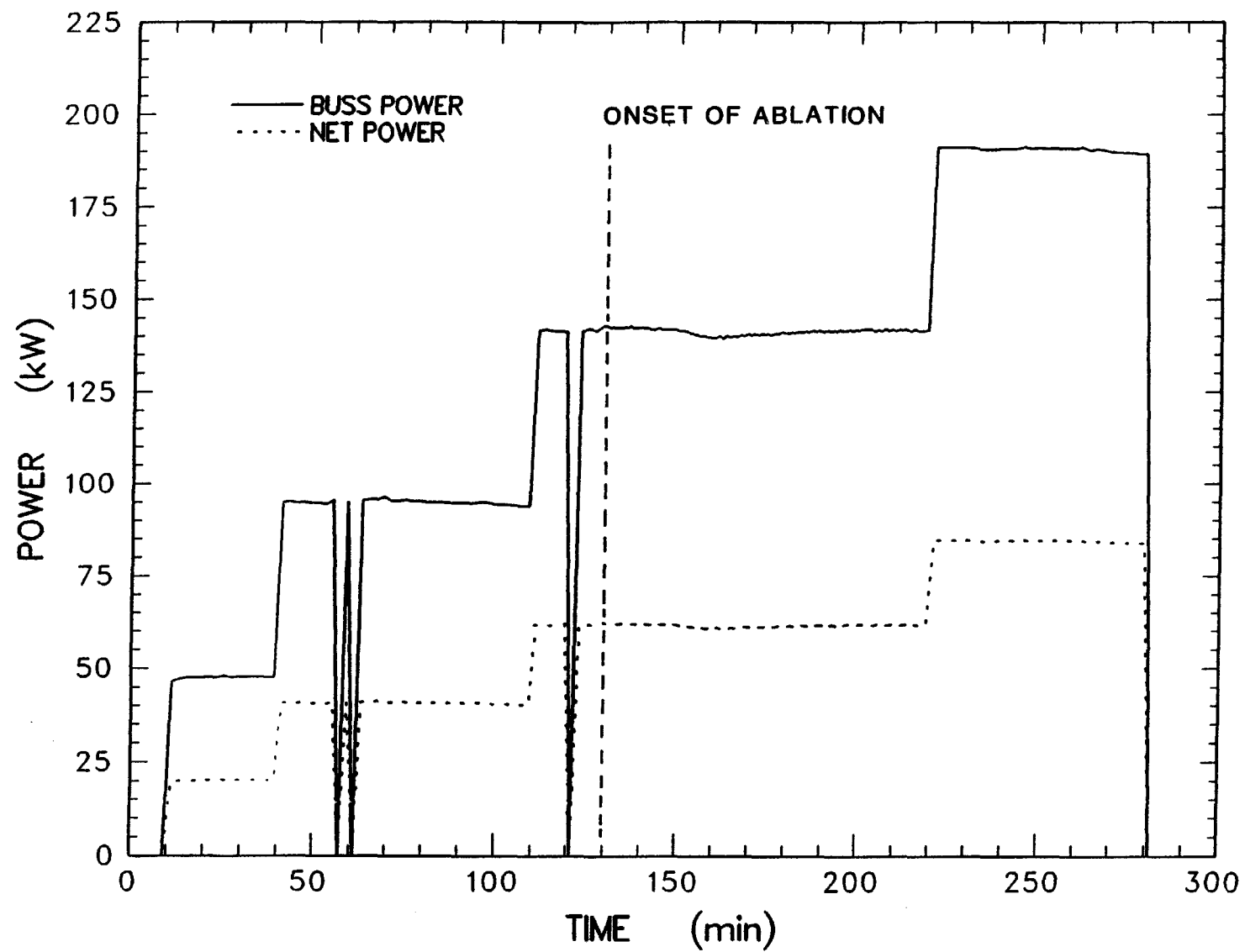
Figure 5.1 Power history for SURC-2

POWER MEASURED AT THE BUSS BARS, TEST SURC-1

INDUCTION POWER , TEST SURC-2
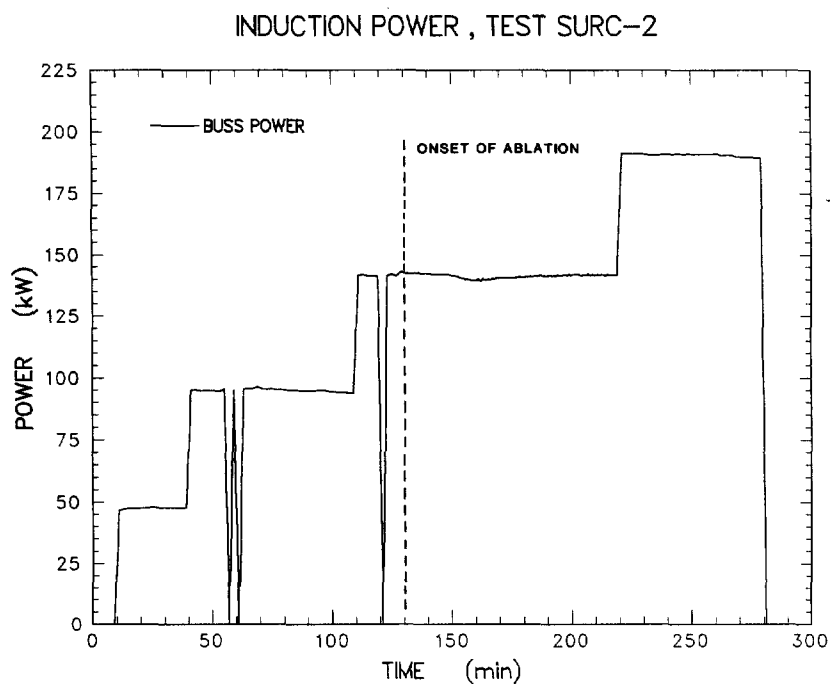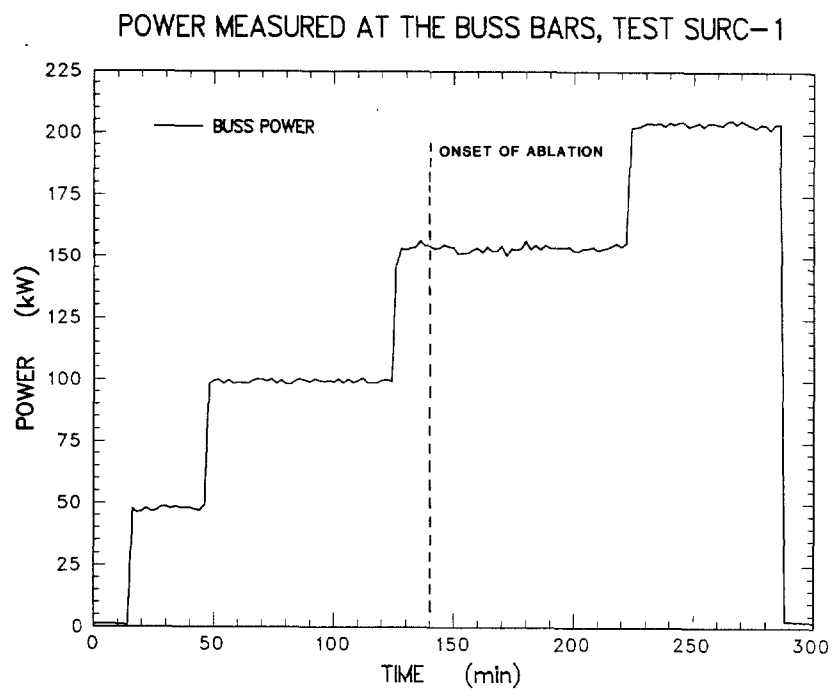
Figure 5.2 Comparison of SURC-1 and SURC-2 power histories
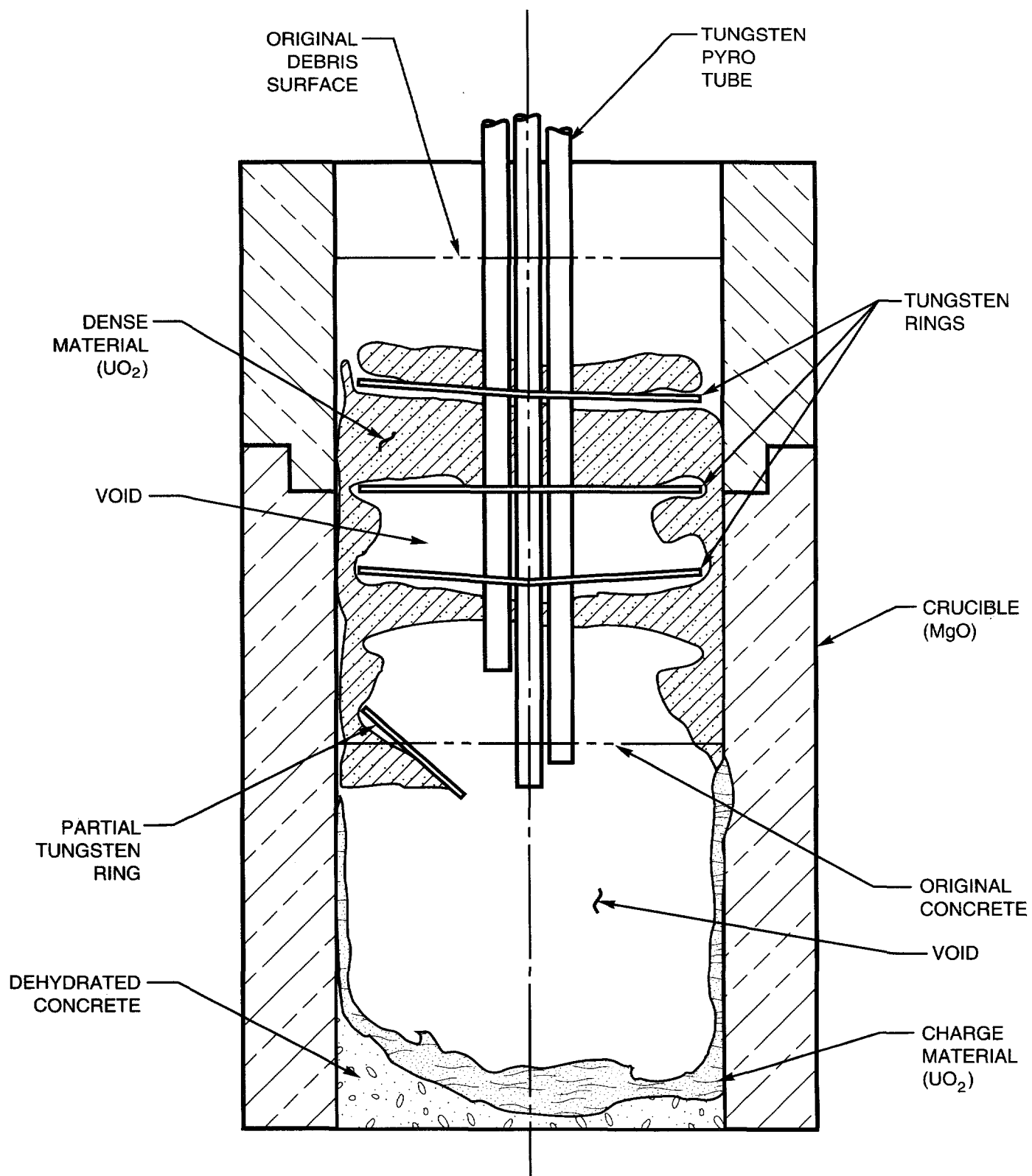
Figure 5.3 Drawing of posttest x-ray of SURC-2

crack in the MgO sidewall appeared at the top of the crucible and extended roughly 20 cm downward. Another crack appeared at a distance 40 cm from the top of the crucible which extended at least 150° around the circumference. Aside from these cracks (~0.5 cm wide) there was no evidence of mechanical or chemical decomposition of the MgO sidewalls.

When the crucible bottom was examined it showed that molten material had penetrated the remaining 5 cm of concrete in the SURC-2 interaction crucible and run out into the bottom of the containment vessel. Examination of the crucible and vessel indicated that a 4-cm hole penetrated the bottom of the concrete basemat. Some remains of the tungsten ring assembly were seen through this hole but there were no signs of solidified melt material in the crucible. All of the melt had spread evenly across the bottom of the 120 cm diameter aluminum containment vessel to a thickness of 5 cm. Neither the MgO

bricks nor aluminum vessel material appeared to have been attacked during the runout and subsequent freezing process. Photographs of the runout material are shown in Figures 5.4-5.6. Figure 5.4 shows the bottom of the crucible and the hole through which the melt materials escaped after the test was concluded. The runout materials flowed uniformly between the crucible and the aluminum containment vessel wall as seen in Figure 5.5. Figure 5.6 shows the cross section of the runout depth as compared to an adjacent MgO brick. A density measurement was made on several samples showing the material to be 3.5-4.0 g/cm^3. It was black in appearance, lava-like, and had some retained porosity in the form of 1 mm voids. Elemental analysis was performed on the SURC-2 runout materials by Coors Analytical Laboratory using inductively coupled plasma spectroscopy. This analysis of the material indicated high concentrations of uranium, calcium, silicon, zirconium, and tungsten. A table of elemental analysis for the runout material is given in Table 5.2.
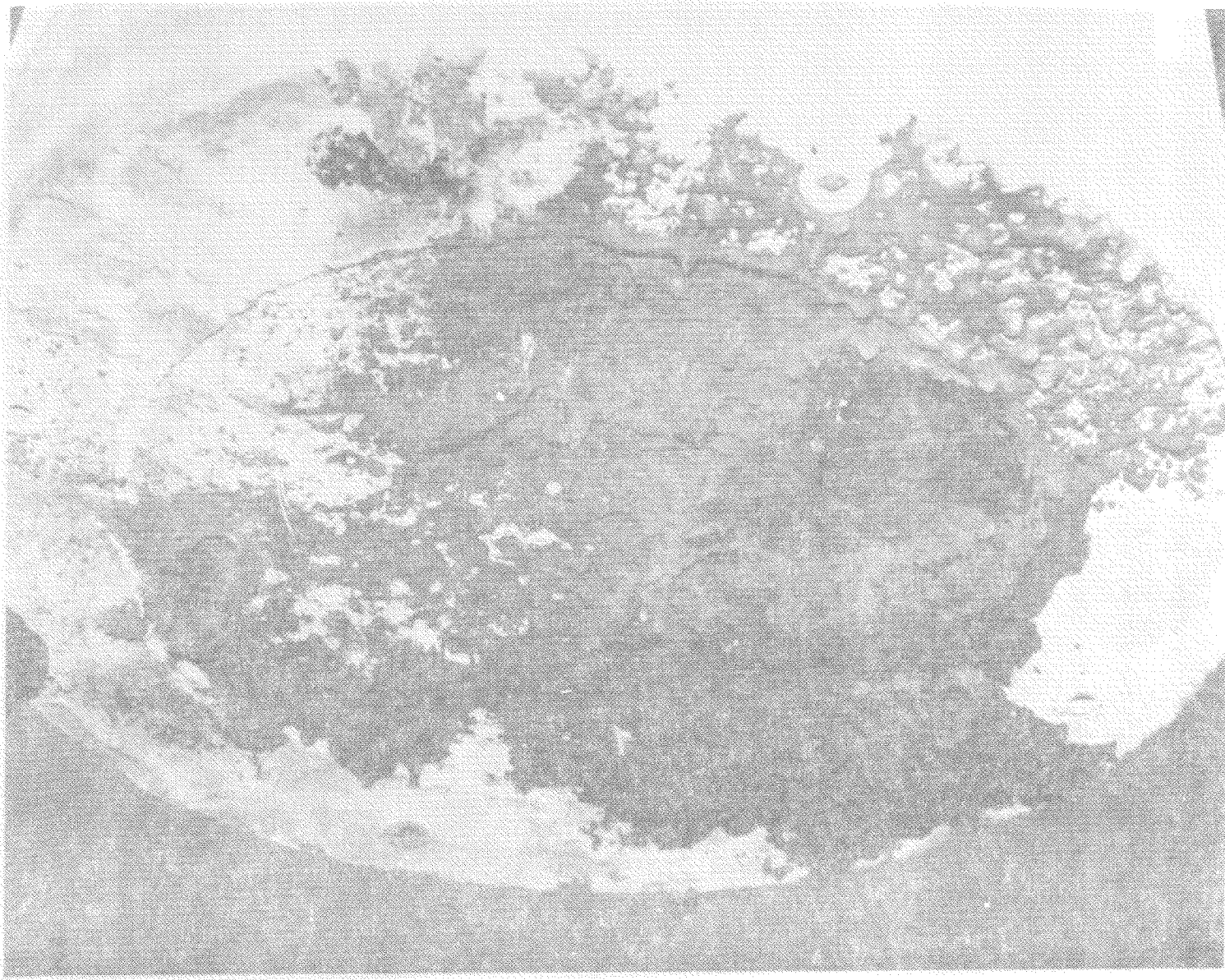
Figure 5.4 Posttest runout material - SURC-2

106

Figure 5.5 Posttest photograph - SURC-2

Figure 5.6 Posttest photograph - SURC-2

Table 5.2 SURC-2 posttest materials analysis

Description	Ba	Ca	Ce	Cl	K	La	Mg	Mo	Na	Nb	Si	U	W	Zr	Moisture
Runout - Top	.15	4.98	.23	.0017	.37	.086	3.42	.080	6.42	.17	15.2	9.26	4.72	9.75	-
Runout - Center	.15	3.61	.081	.0011	.48	.032	2.86	.076	6.95	.16	11.9	8.21	4.00	9.82	-
Runout - Bottom	.14	3.84	.20	.0022	.39	.078	2.71	.078	9.42	.15	14.9	9.48	4.39	9.75	-

Elemental analysis in weight percent

6.0 Data Presentation and Results

The 204 kg charge of UO_2-Zr_2-Zr material was heated for 130 minutes prior to the onset of concrete erosion. Interactions then proceeded in three stages. First came rapid erosion enhanced by Zr oxidation lasting 30 minutes. Then came slower erosion at lower temperatures for 60 minutes. There was an increased erosion period when power was increased by 33%. At 280 minutes and 35 cm of erosion melt escaped the crucible terminating the test.

6.1 Temperature Data

The temperature data from SURC-2 are used to determine concrete erosion and the crucible thermal response. Three regions of the melt/concrete interaction are shown in Figure 6.1.1 [Cole et al., 1984]. The pool consists primarily of uranium dioxide, but it may also contain zirconium metal and zirconium oxide as well as condensed products of concrete decomposition and fission product compounds. The "dry" region consists of the concrete that is dehydrated, decomposing, and beginning to melt. The "wet" region is the concrete that still contains water of hydration and water in the concrete pores. The transition between the "wet" and the "dry" region is taken here to be the point at which hydration and pore water undergo the phase change to vapor.

Surrounding the three important regions of the melt/concrete interaction in the SURC-2 test, is the magnesium oxide annulus. In an ideal circumstance, the confining annulus of the test would be totally inert. That is, it would neither conduct heat nor mechanically degrade or chemically interact. Clearly, no such totally inert material exists and it is necessary to record how the magnesia annulus affects the thermal response of melt/concrete interaction.

In this section, the temperature data obtained in the SURC-2 experiment will be used to describe the thermal response of melt/concrete

interactions, the magnesium oxide annulus and the crucible cover.

Concrete Response

The dehydration front of the concrete defined by the 400 K isotherm began to propagate through the concrete slug at approximately t = 65 min. Concrete ablation began at t = 129 min. The ablation front was defined by the failure of the type K thermocouples embedded in the concrete. The failure temperature for type K thermocouples is approximately 1645 K. Thirty-five centimeters of concrete were eroded over a period of 151.2 minutes. Melt temperatures as high as 2650 K were measured by the fiber optic pyrometers. Sidewall heat fluxes calculated from thermocouple data adjacent to the melt ranged between 6×10^4 and 1×10^5 W/m^2. The peak upward heat flux imparted to the crucible cover was calculated to be 6×10^5 W/m^2.

Figure 6.1.2 shows a typical temperature versus time profile indicated by thermocouples embedded in the concrete slug during a period of steady state ablation. The figure shows the response of five thermocouples located in the axial array at depths between z = -15 and -19 cm. The temperature histories for other thermocouples cast into the concrete slug in various arrays are presented in Appendix C. Temperatures rise slowly between 300 and 400 K as the concrete dehydrates. This is followed by a rapid increase in temperature to failure caused by contact with the melt pool.

The axial centerline array has been chosen to characterize the position of the dehydration front with respect to time. This is shown by the solid line connecting the circles in Figure 6.1.3. There are three periods of interest: The initial heating period prior to the onset of concrete ablation between t = 65 and 129 minutes; the period during the onset of concrete ablation
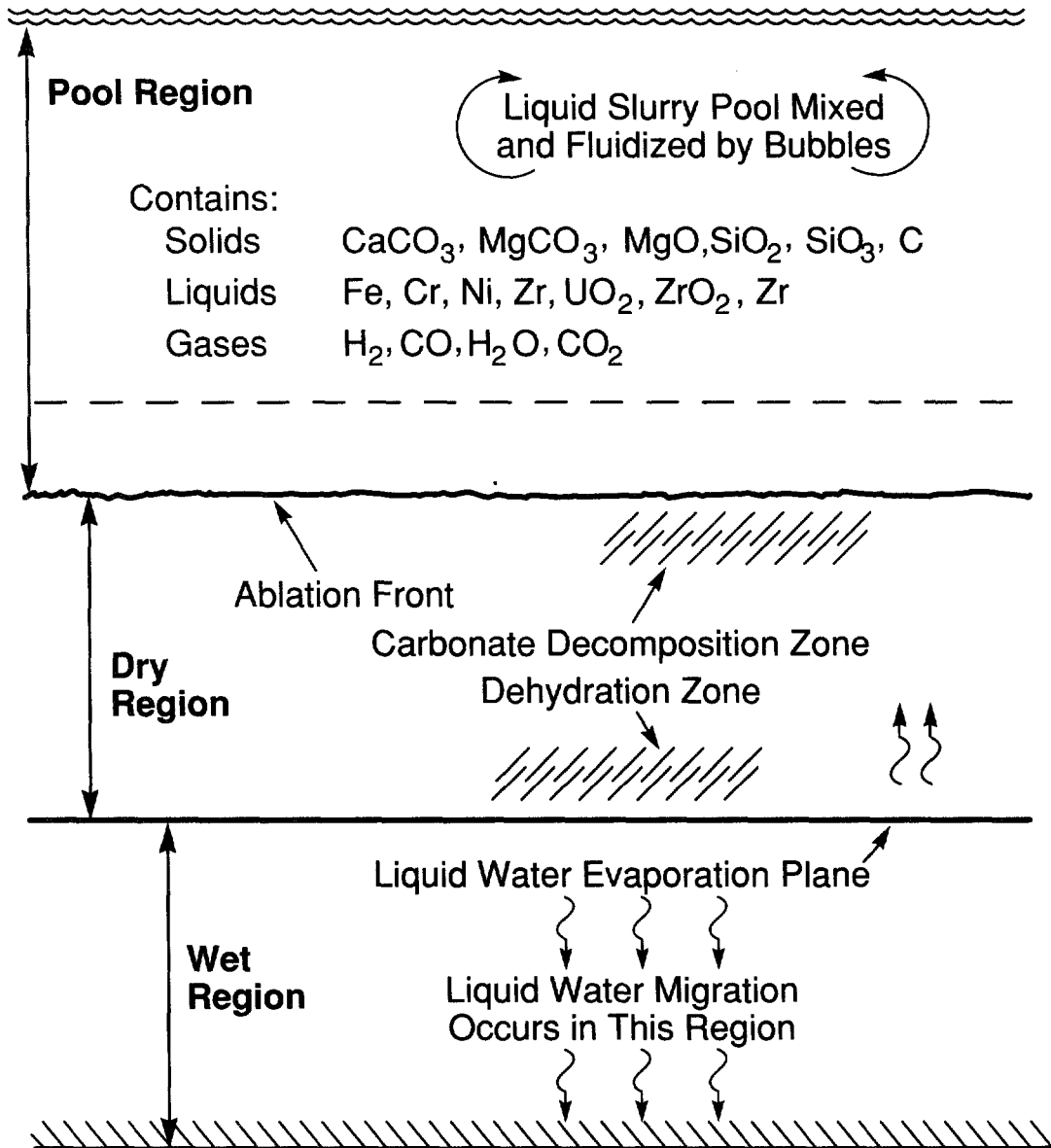
Figure 6.1.1 Three regions for analyzing melt concrete interactions
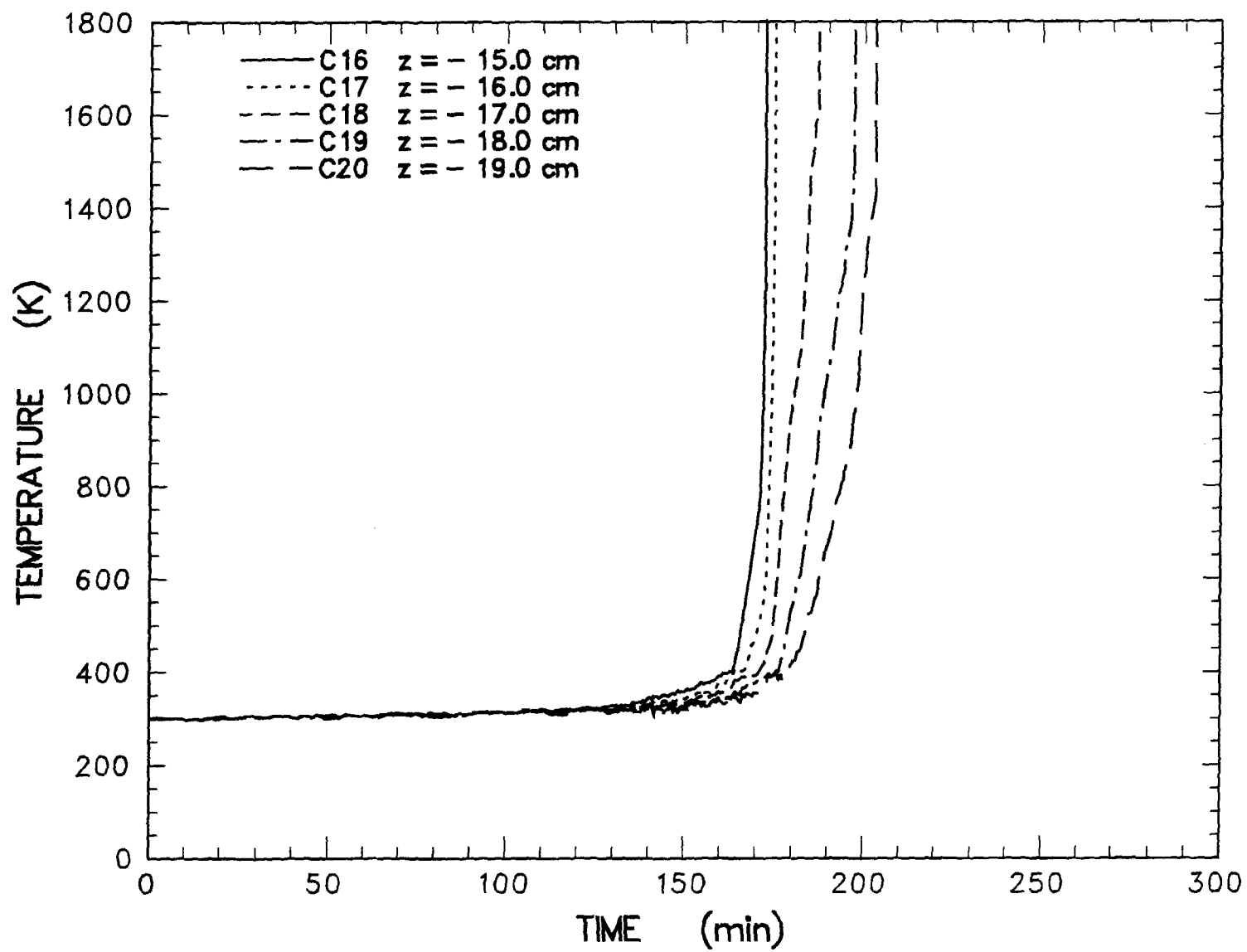
Figure 6.1.2 Typical thermal response of the concrete for the SURC experiment

Figure 6.1.3 Location of the SURC-2 400 K isotherm
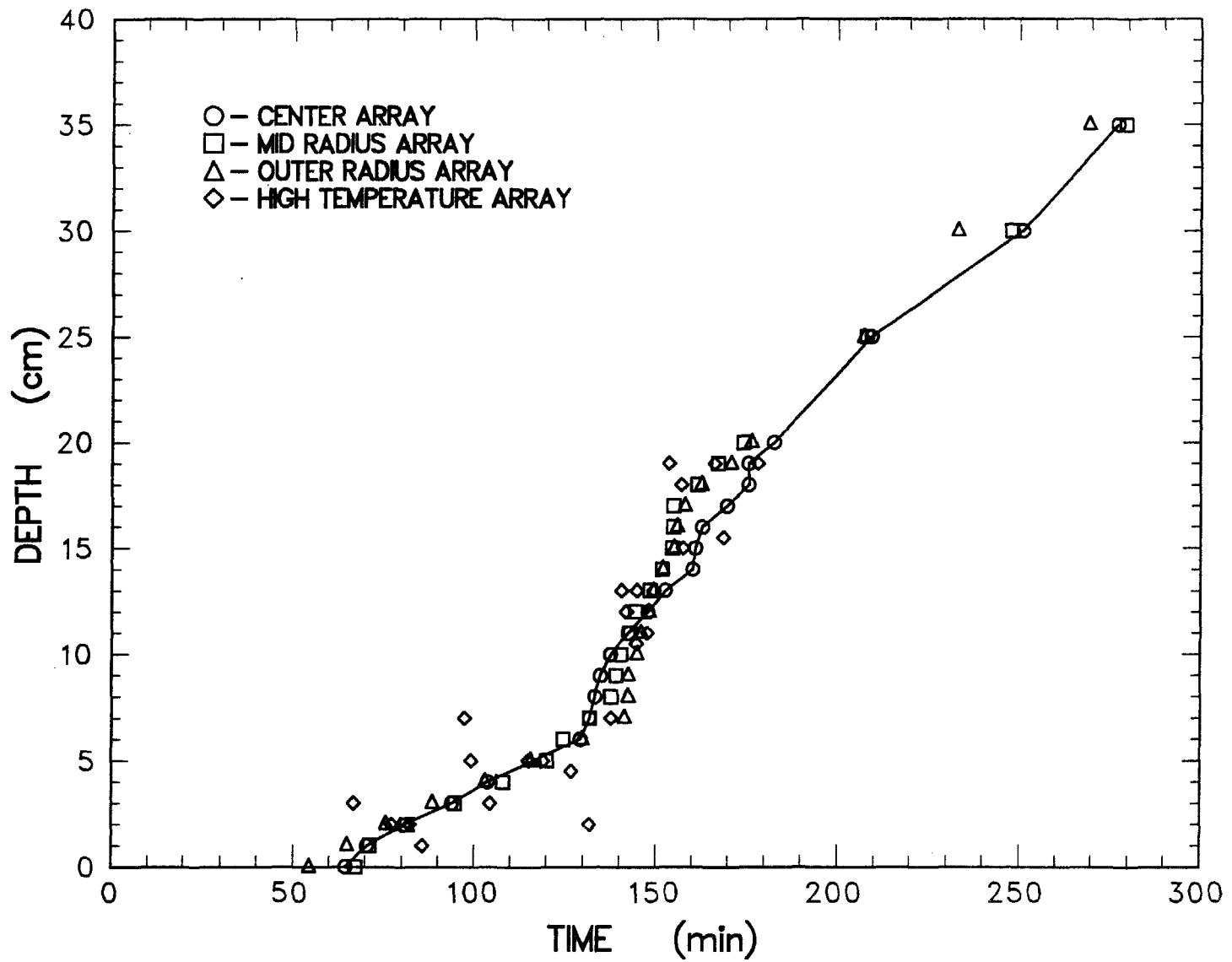
between t = 129 and 183 minutes; and late in the test between t = 183 and 277 minutes. A linear regression routine was used to calculate the velocity of the dehydration front for various time periods. During the initial heating period of the UO_2-ZrO_2-Zr charge material the velocity of the 400 K isotherm was calculated to be 5.4 ± 0.23 cm/hr. At the onset of concrete ablation at 129 through 183 minutes the propagation rate of the wet/dry front was calculated to be 14.9 ± 0.61 cm/hr. This was nearly three times greater than the initial rate. Late in the test between 183 and 277 minutes the rate was calculated to be 9.1 ± 0.73 cm/hr. This is 1.7 times greater than the initial rate and 61% of the rate calculated for the period of concrete erosion between 129 and 183 minutes.

The power supply was tripped off between 120 and 123 minutes due to exceeding a temperature limit on the inlet cooling water to the power supply. This period of power loss did not appear to have any observable effect on the propagation rate of the 400 K isotherm.

The basaltic concrete used in the SURC-2 experiment melts over the temperature range of 1350 to 1650 K. The temperature at which physical ablation of the melting concrete occurs is not precisely known. Here it is assumed ablation occurs at 1600 K for the purpose of measuring the propagation of the erosion front. The position of the 1600 K isotherm plotted as a function of time is shown in Figure 6.1.4. Based on the data shown in the figure, concrete ablation began at approximately 129 min. and continued until the melt escaped the crucible terminating the test at 281 minutes.

After the melt penetrated the zirconia insulating board, it eroded 6 cm of concrete in 2.3 minutes. This equates to an erosion rate of 150 cm/hr. Figure 6.1.5 shows the temperature profiles for the first five thermocouples in the axial array embedded in the concrete at depths between z = 0.0 and -4 cm. The figure shows that the thermocouples, located at z = -1, -2, -3, and -4 cm fail at nearly the same time. The data in Figure 6.1.4 shows an offset when comparing individual arrays during the early period of erosion. This is due to the insulating effect of the zirconia board separating the melt from the concrete. In an ideal case the melt would uniformly take the zirconia board into solution and spread over the concrete surface uniformly. This was not the case. However, late in the test the position of the erosion front comparing the three arrays almost coincide with each other. This indicates that the erosion front was planar for the last 15 cm of concrete. The greatest difference in the location of the erosion front measured between arrays was 5 cm. This difference decreased as the test continued. Taking the axial array as being representative of the position of the erosion front in the concrete, linear calculations were conducted to determine erosion rates during specific time periods.

Ablation during the initial melt attack was quite rapid and 15 cm of concrete were eroded during the period from 130 minutes to 160 minutes at an average rate of 30 cm/hr. After 160 minutes, the concrete erosion slows to 5 cm/hr for the period from 160 minutes to 220 minutes. The power to the tungsten susceptors was then increased at 218 minutes, resulting in an increased ablation rate. During times between 220 minutes and 280 minutes an additional 15 cm of concrete was eroded at an average rate of 15 cm/hr.

The depth to which the concrete was dehydrated (Note that the dehydration temperature increases as the test proceeds) can be determined by comparing the position of the 400 K (wet/dry interface) and 1600 K (ablation front) isotherm at a specific time. Figure 6.1.6 shows a plot comparing data representing the 400 and 1600 K isotherms. The depth of the dehydrated concrete at the onset of ablation is initially 6 cm at t = 129 minutes. The 1600 K isotherm converges to within 2 cm of the 400 K isotherm near t = 140 minutes. After this time the 400 K isotherm precedes the ablation front by approximately 2 to 5 cm for the remainder of the test.
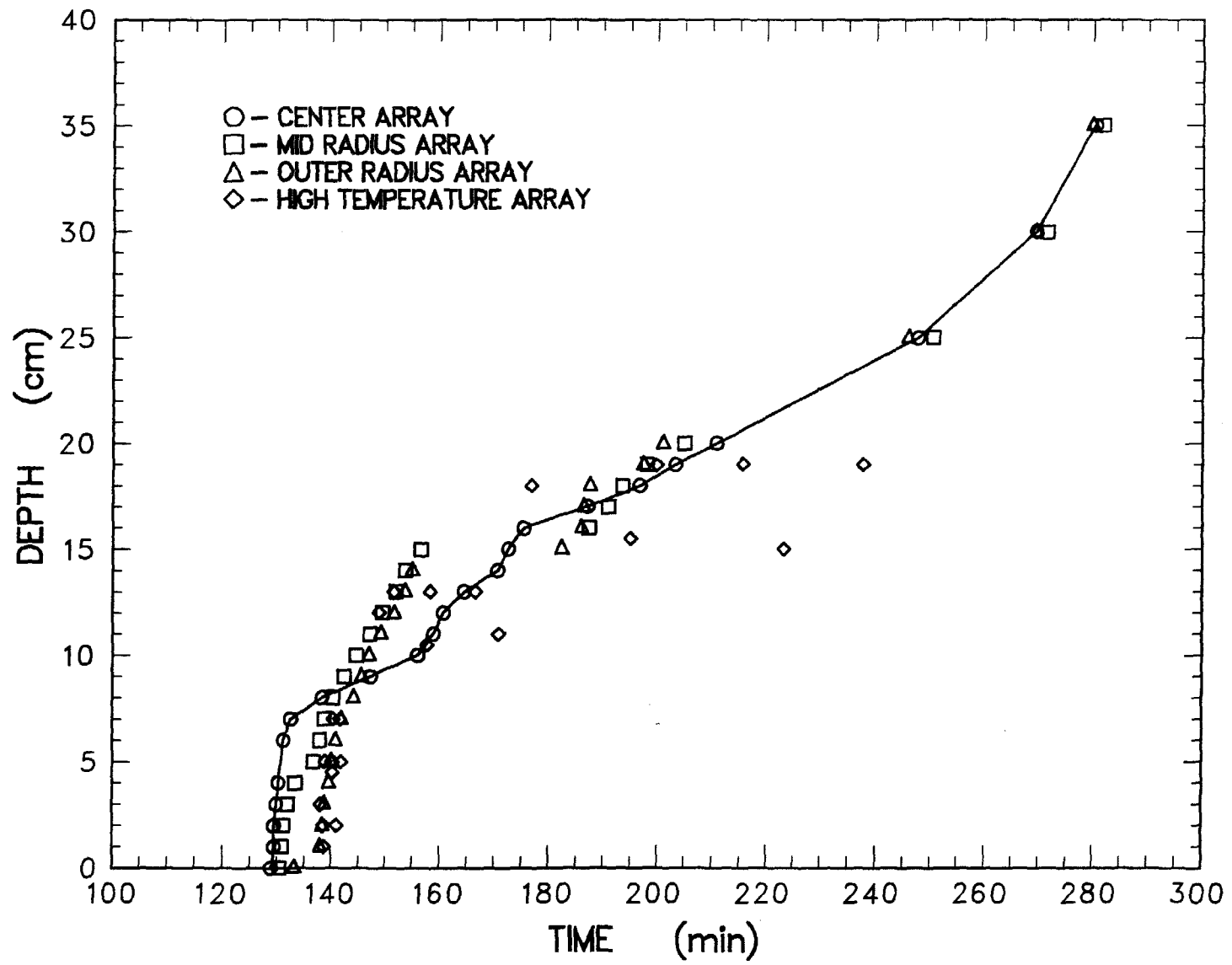
Figure 6.1.4   Location of the SURC-2 erosion front
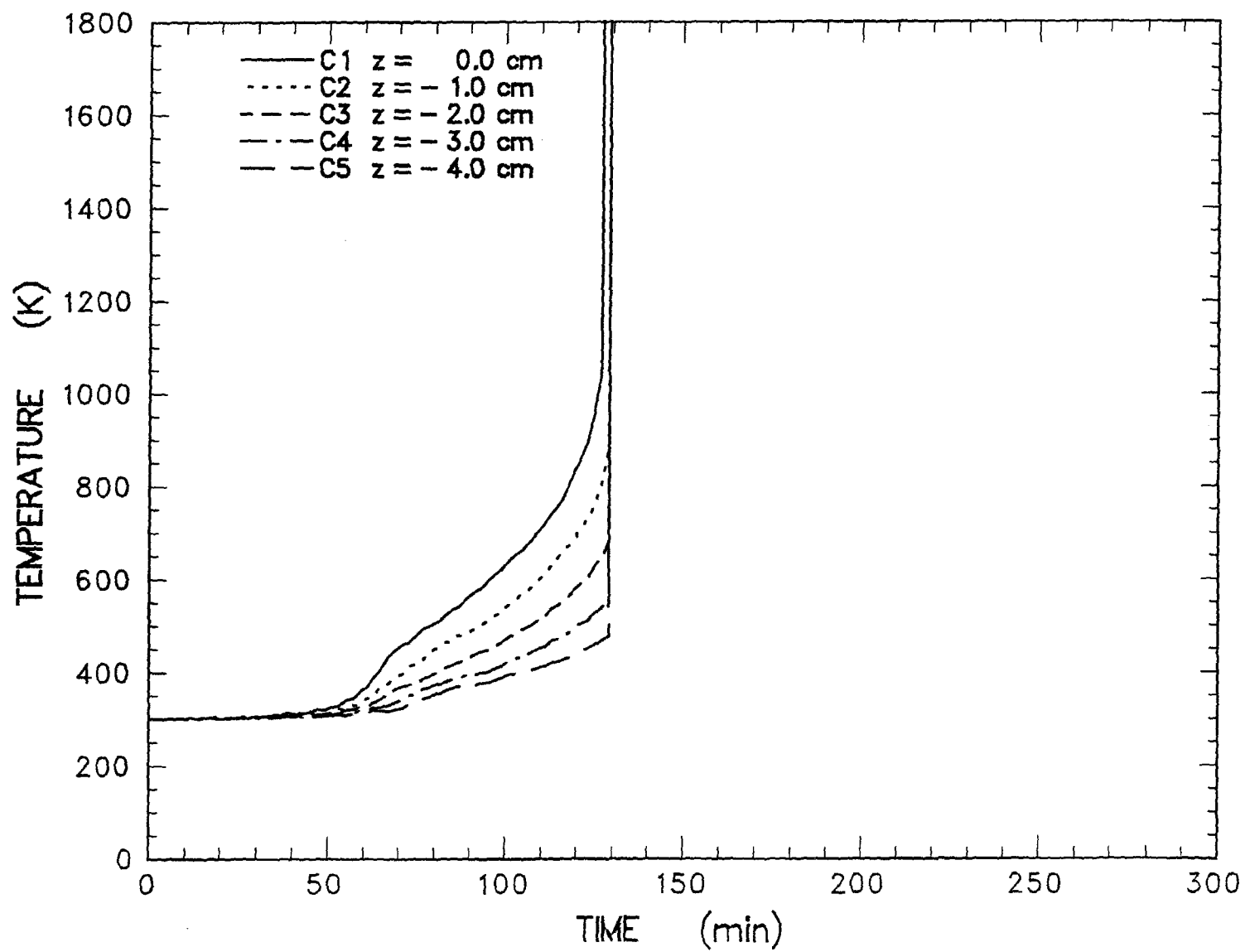
Figure 6.1.5 Initial thermal response of the concrete during the onset of ablation
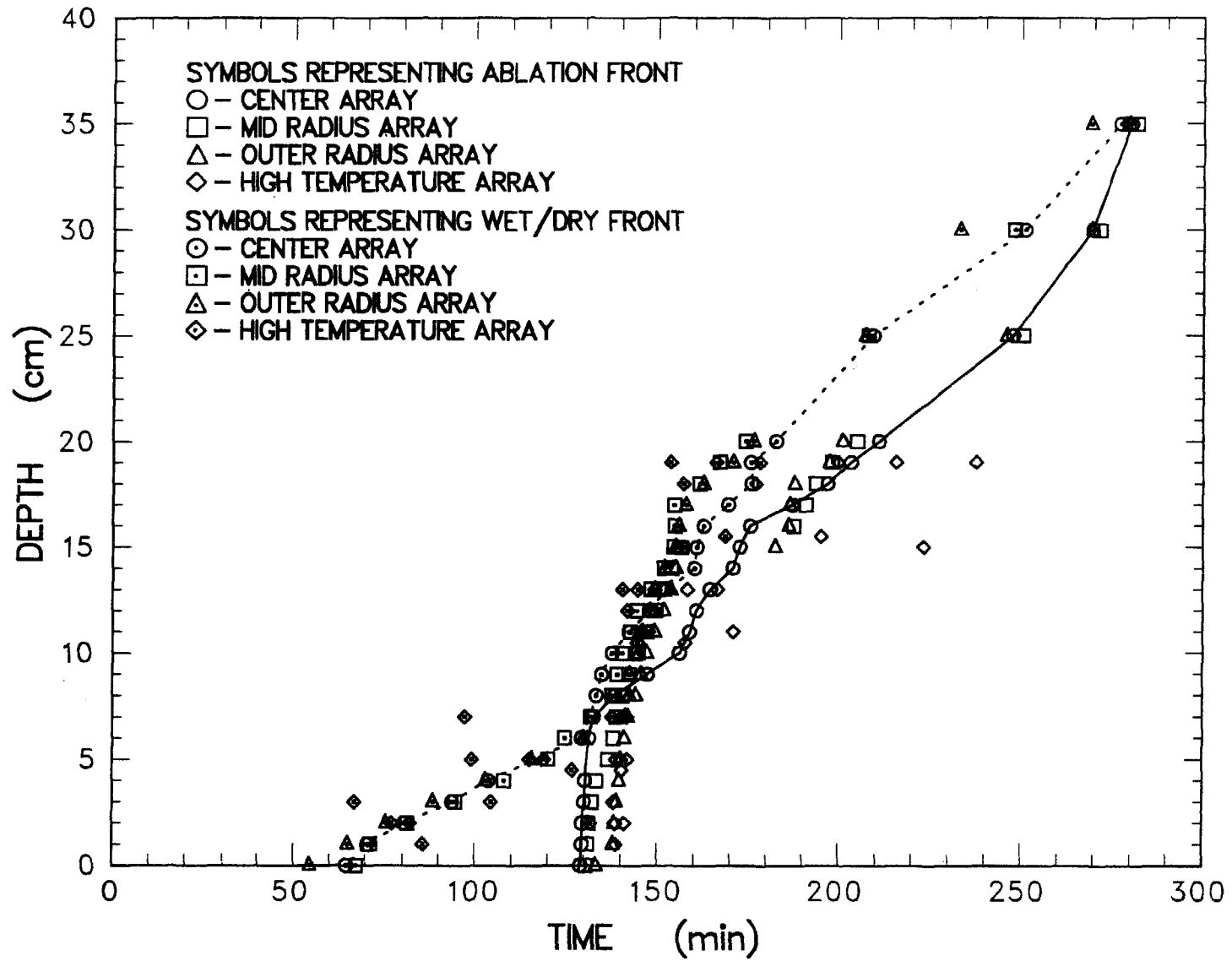
Figure 6.1.6 Comparison of the 400 K and 1600 K isotherms in SURC-2

Meltpool Temperature

Melt temperatures were measured during the experiment with 12 type C and 12 type S thermocouples installed in alumina tubes and cast into the concrete at various depths within the concrete slug. The debris temperature was also measured using three fiber optic pyrometers focused at the base of a thick walled closed end tungsten tube embedded into the melt charge. In addition to the pyrometers a type C thermocouple was installed in the base of each tungsten pyrotube to measure temperatures.

Figures 6.1.7-10 show an expansion of melt temperature data measured by the C and S type thermocouples installed in alumina tube T1. The figures indicate a rapid rise in temperature upon contact with the melt front. This is followed by a plateau usually lasting several minutes. These plateaus closely match the failure times of the type C and S thermocouples. The peak melt temperature measured by type C thermocouple T1-1 located at a depth of z = -2.0 cm was 2550 K. The melt temperature decreases as the erosion depth increases and concrete is added to the melt. The peak temperature measured by the type S thermocouple located at z = -15.5 cm is 1950 K. This is 600 K less than the initial melt temperature measured at z = -2.0 cm. The melt temperature ranged between 1850 and 2550 K. Other individual plots of melt temperature can be found in Appendix D.

Figure 6.1.11 shows a plot of the peak melt temperature as a function of time for all the thermocouples cast into the alumina tubes. The failure temperature of the type C and S thermocouples in a non-oxidizing atmosphere is 2589 and 2041 K respectively. The type S thermocouples were installed into the alumina tubes at the lower depths between z = -11 to 19 cm. It is obvious that the melt temperatures indicated by these thermocouples are not in fact the actual melt temperature of the debris but the failure temperature of the thermocouple itself. The melt temperature is several hundred degrees greater

than the temperature measured by these thermocouples. This will be shown to be true in the presentation of the pyrometer data that follows.

In addition to the thermocouples described above, three fiber optic pyrometers focused at the bottom of a thick wall, closed end, tungsten tube embedded in the center of the oxidic debris were also used. To compare the temperatures measured by the pyrometers a type C thermocouple was installed at the base of each of the three tubes. Figure 6.1.12 shows a plot of the temperatures indicated by the type C thermocouple plotted as a function of time. Two of the three failed within the first 82 minutes of the test. The third located at the bottom of pyrotube No. 1 initially located 15 cm above the zirconia board placed on the concrete survived during the entire test. It measured temperatures as high as 2625 K. For the period between t = 140 and 220 minutes this thermocouple indicated a nominal melt temperature of 2400 K. The increase in temperature indicated at 218 minutes was due to increasing the power from 142 kW to 190 kW. The decrease in temperature at t = 136 minutes will be discussed later. The power supply is turned off at t = 280.2 minutes. Forty-five seconds later molten UO_2 breached the crucible and flowed onto the MgO bricks lining the base of the aluminum containment vessel. This is the reason for the sudden drop in temperature at t = 281 minutes from 2150 to 1400 K.

Figure 6.1.13 shows the temperatures histories measured by the three fiber optic pyrometers. Also included for comparison is the temperature profile for the type C thermocouple installed in pyrotube No. 1.

The temperatures between the three pyrometers agree to within 200 K. They are not presumed to be identical since they are located at different elevations within the melt. The type C thermocouple agrees with pyrometer No. 1 within 75 K. The pyrometer and type C thermocouple temperatures decrease significantly at approximately
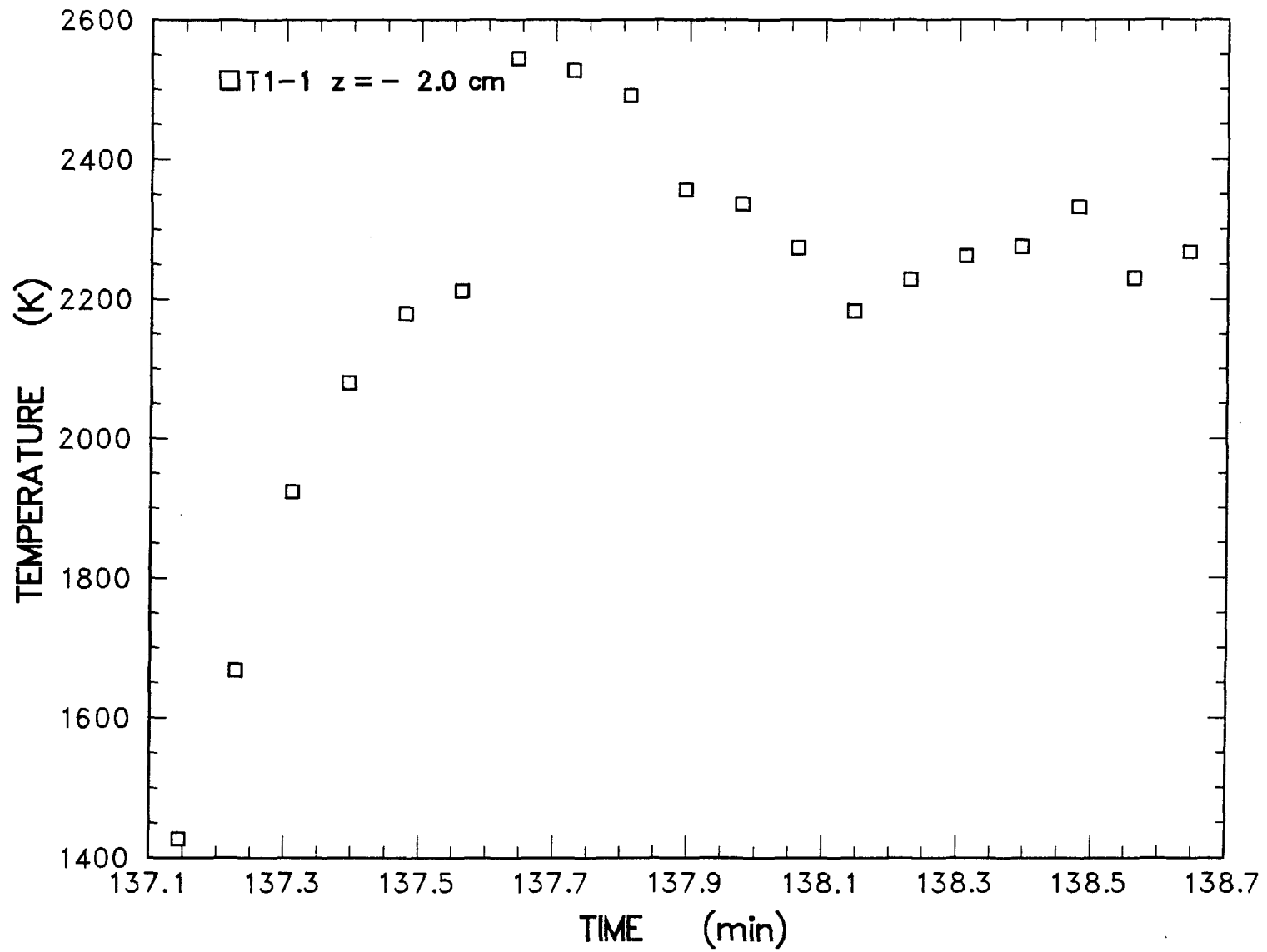
Figure 6.1.7 Type C thermocouple response to contact with the melt front at z = -2.0 cm

105
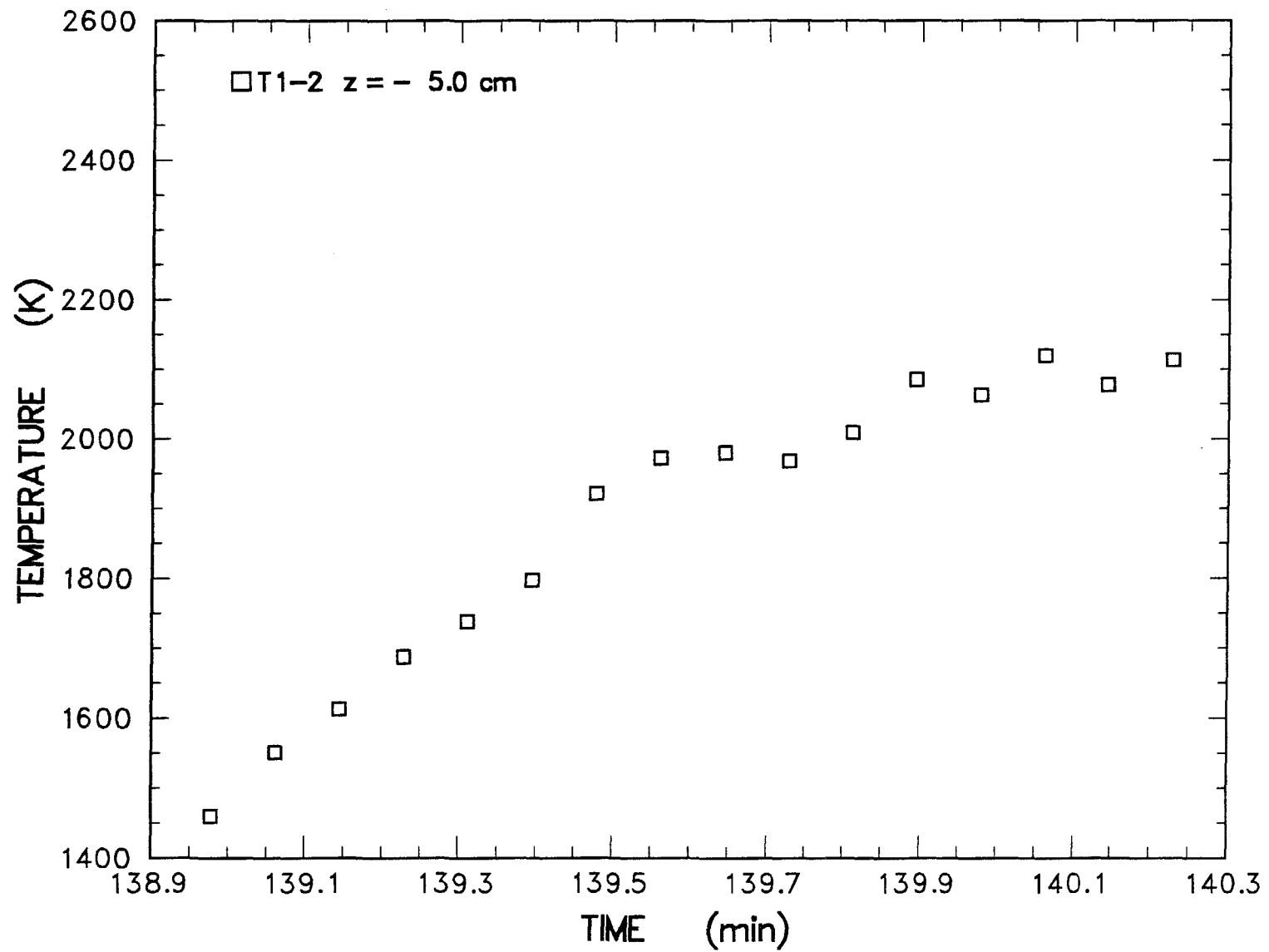
Figure 6.1.8 Type C thermocouple response to contact with the melt front at z = -5.0 cm
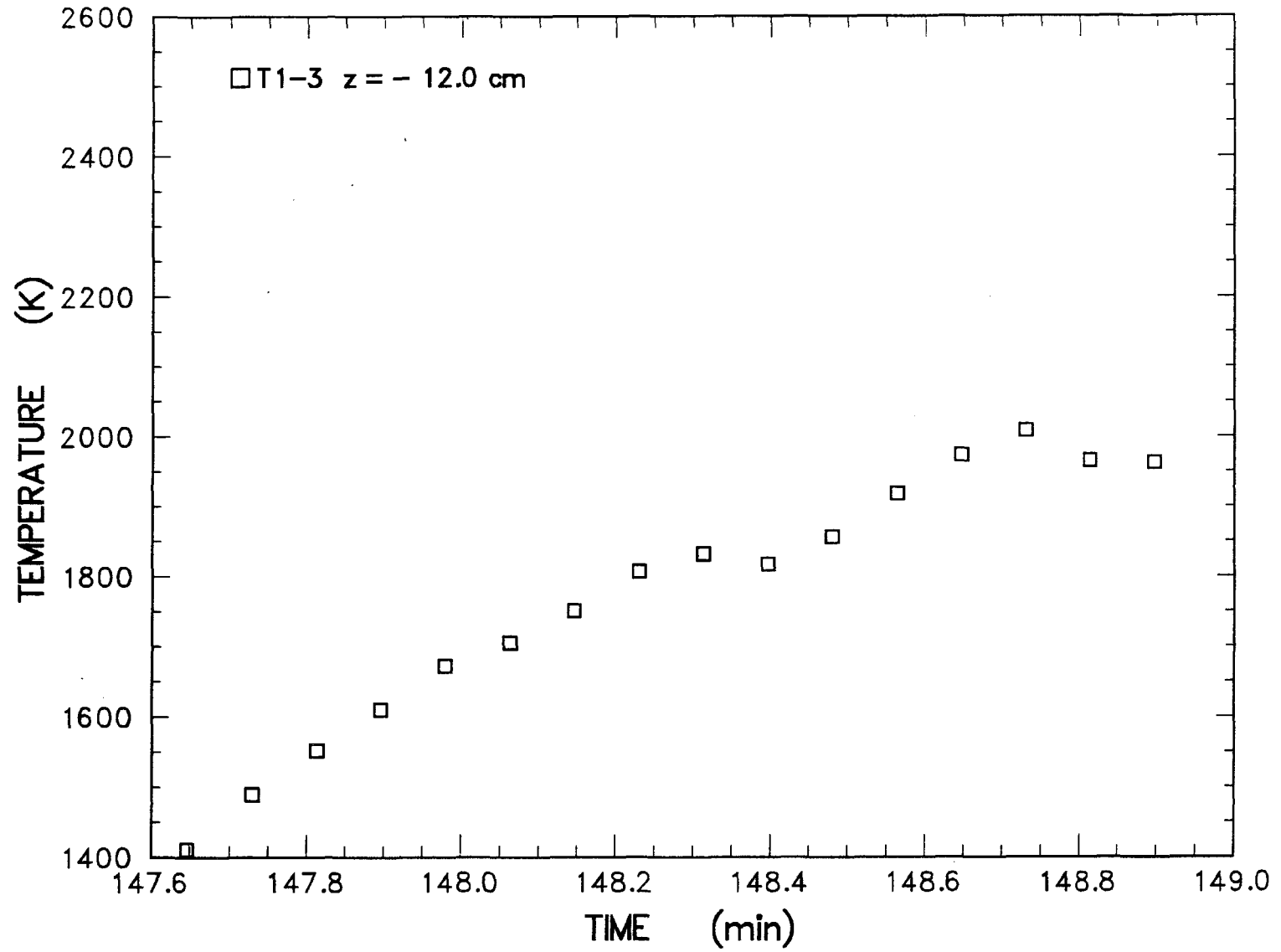
Figure 6.1.9 Type S thermocouple response to contact with the melt front at z = -12.0 cm
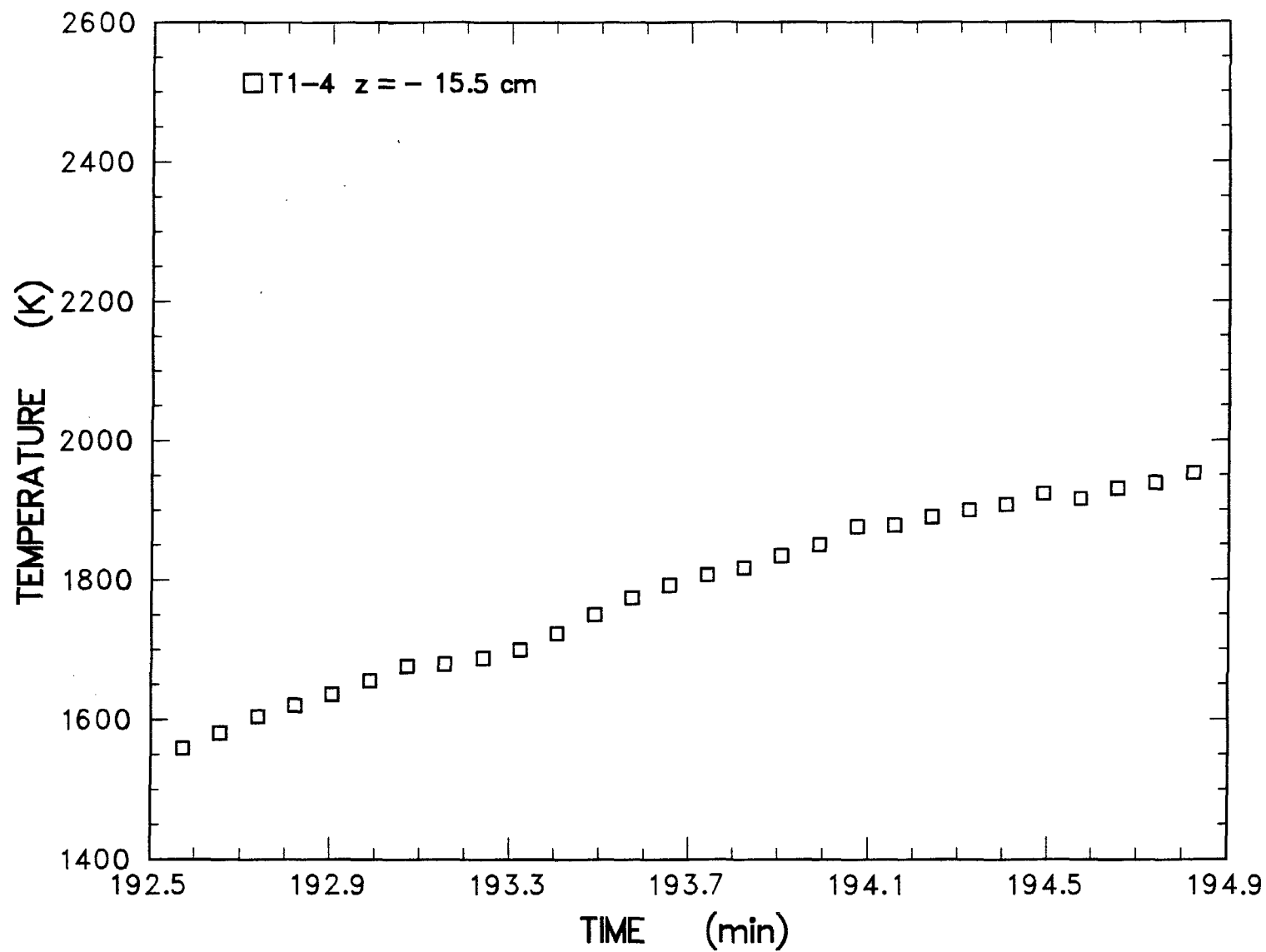
Figure 6.1.10 Type S thermocouple response to contact with the melt front at z = -15.5 cm
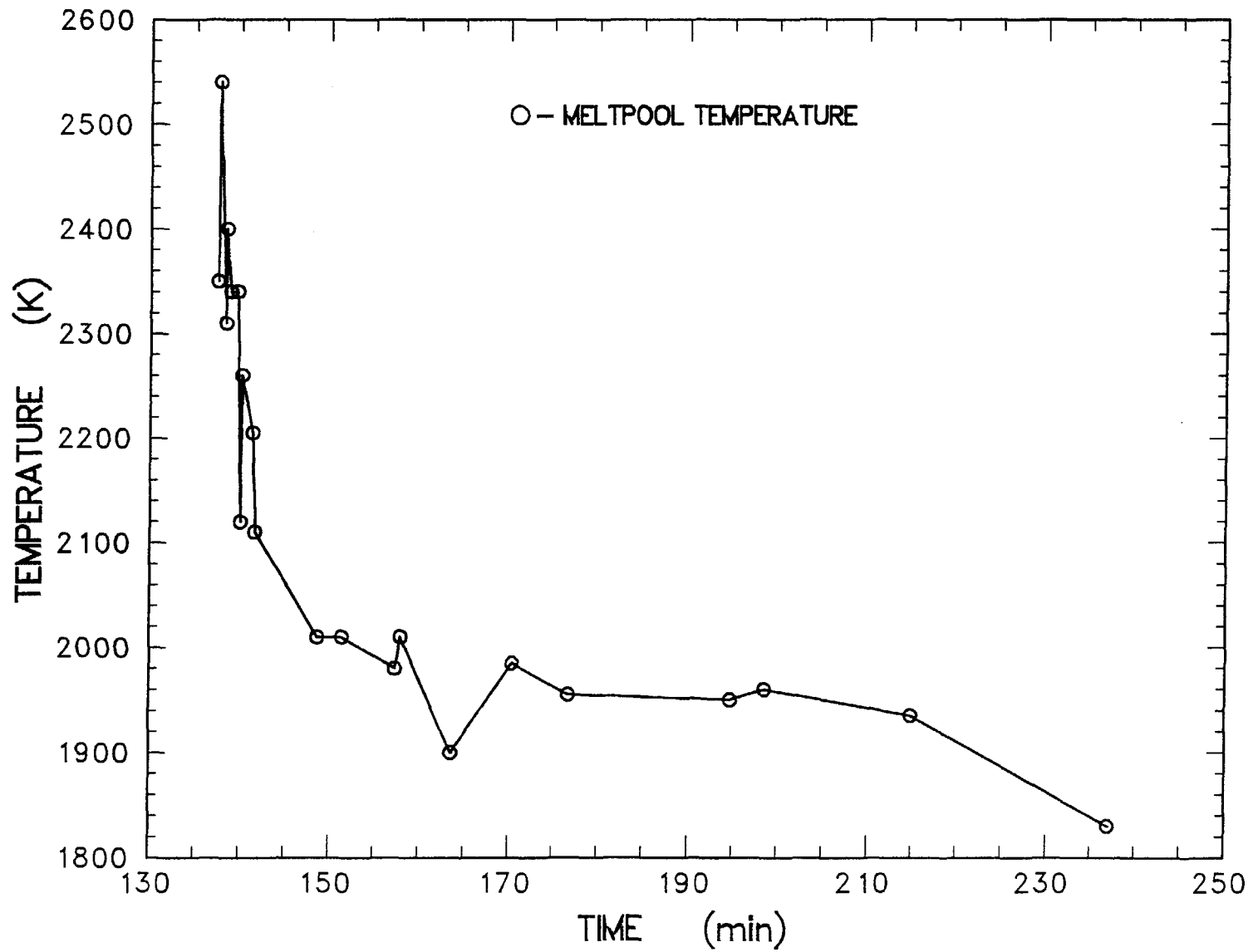
Figure 6.1.11 Meltpool temperature measured as a function of time for the alumina tube array thermocouples
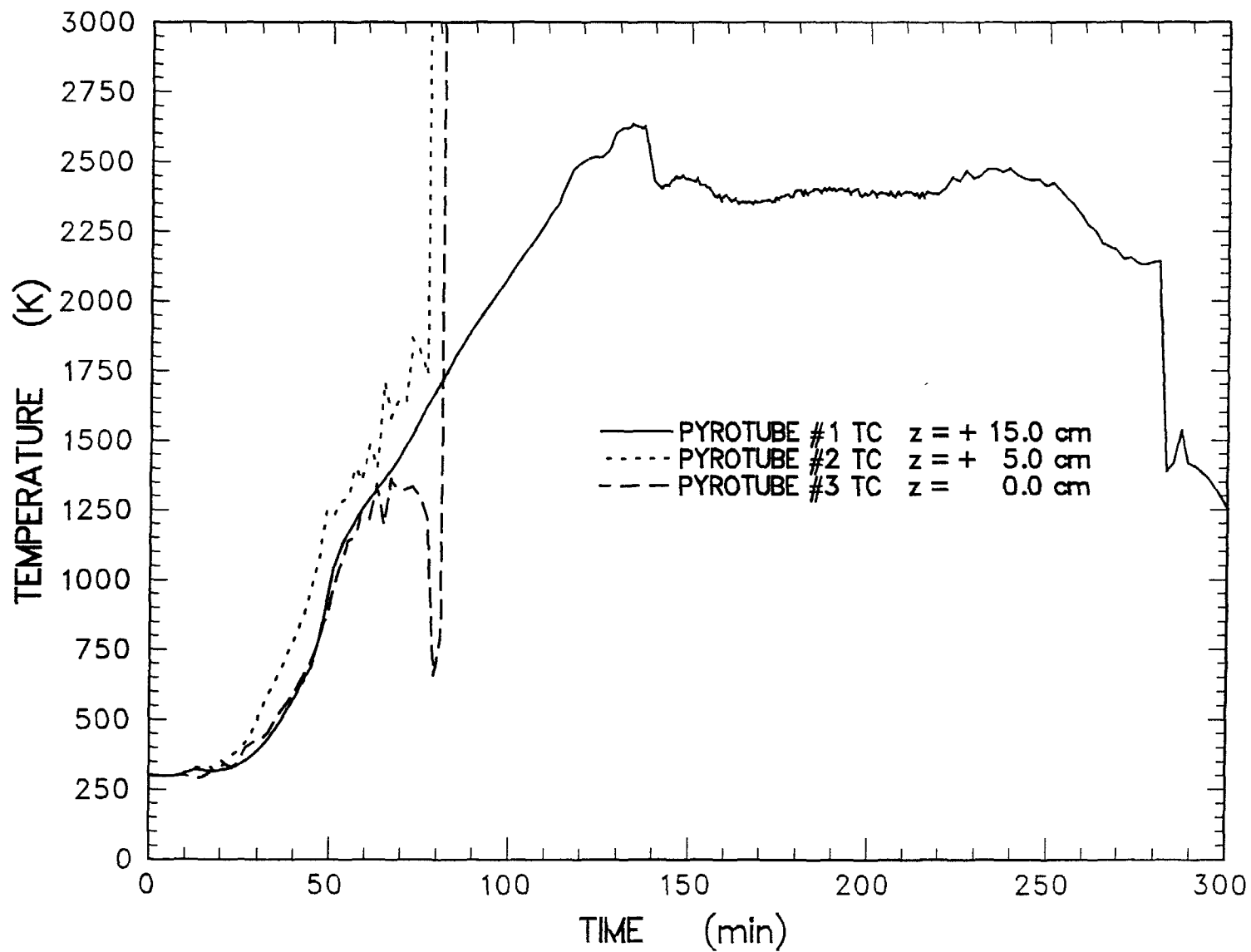
Figure 6.1.12 Thermal response of Type C thermocouples installed in the tungsten pyrotubes
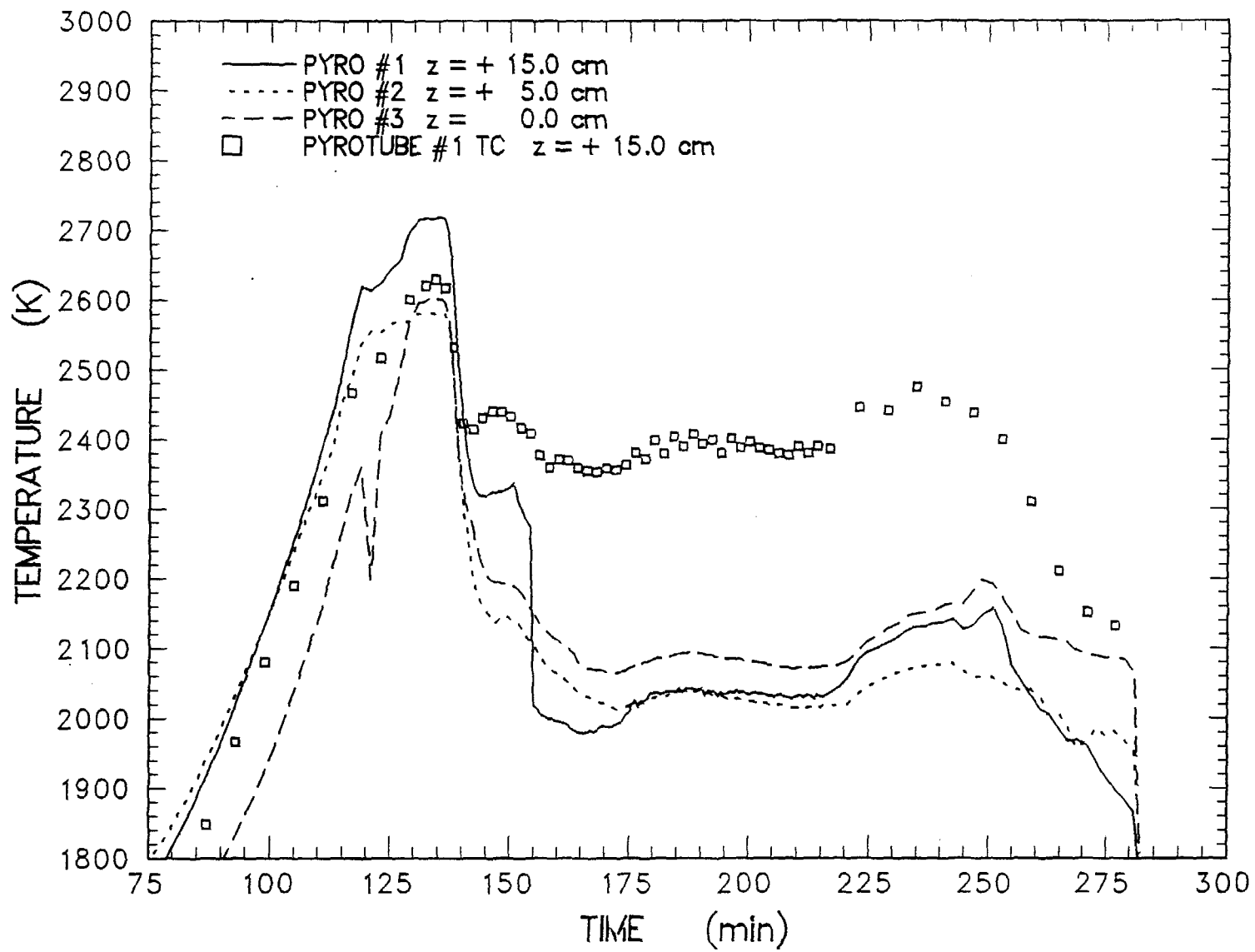
Figure 6.1.13 Temperature profiles produced by the fiber optic pyrometers

136 minutes. At about this same time the pressures in the containment increases about 2 psig. Upon posttest examination, it was observed that the pyrotubes pulled away from the stainless steel Swageloc adapter. They dropped about 5 cm. Even though they appeared to be aligned with the pyrometer, the optical focal point was now focused on the inside diameter of each pyrotube rather than the base. This resulted in dissolving the focal point causing the spot to be integrated over a larger temperature gradient, thus reducing the measured temperature. Even though the type C thermocouple dropped 200 K during the pressure excursion in the vessel, the temperature it measured agreed very well with the melt temperatures indicated by type C thermocouples cast into the concrete between t = 137.5 and 141.7 minutes.

MgO Sidewalls

The heat transfer to the MgO sidewalls during the interaction has a global effect on the energy balance and affects the heat transfer to the concrete. As discussed in Section 3.2 thermocouple arrays were installed at various locations within the MgO annulus to determine the thermal response of the sidewalls. A typical temperature history is shown in Figure 6.1.14 for the sidewall array located adjacent to the melt at an elevation of z = +10 cm.

The temperatures indicated by thermocouples located at depths of 0.5, 1.5, 2.5, and 9.0 cm rise gradually peaking at t = 140 minutes and declining approximately 100 K. This is most likely due to settling and repositioning of the melt within the crucible. The temperatures continue to rise until melt breached the crucible at t = 281 minutes and melted the stainless steel sheaths located on the floor of the aluminum containment vessel. The temperature difference in the MgO wall at this location at the time of failure was 550 K. The temperature histories measured by thermocouples in other arrays, cast into the MgO sidewall, are presented in Appendix E.

The calculation of heat flux to the MgO walls is a classic example of an "inverse" heat conduction problem (IHCP) where the boundary condition (e.g., heat flux) is determined from known interior temperatures. Of the available methods for solving the IHCP, one that appears to be successful for a wide variety of applications is a nonlinear estimation technique. In this method, the value of the calculated heat flux minimizes the square of the difference between the calculated and the experimental temperatures. A computer code, IHCP, has been written by Bradley based on Beck's methods [Beck et al., 1985]. The code was tested using a variety of exact solution problems. In general, it was found that the greater the number of thermocouples utilized in the analysis, the greater the accuracy of the solution. However, Bradley found that beyond three thermocouples, the improvement in accuracy was not sufficient to justify additional instrumentation. The experimental data utilized in the IHCP consisted of at least two thermocouples at depths from the surface of 0.5 to 2.5 cm into the MgO sidewall. A typical IHCP solution was calculated for each array of the thermocouples that was embedded in the MgO sidewall at various locations above and below 0 cm. Here the 0 cm location is taken as the original location of the concrete surface.

The thermal property data for the MgO castable used to calculate the sidewall heat fluxes are presented in Section 2.1.

Shown in Figure 6.1.15, 6.1.16, and 6.1.17 are the heat flux histories for the sidewall arrays initially below the melt, adjacent to the melt, and above the melt, respectively. Heat flux histories for other sidewall arrays are shown in Appendix E. Figure 6.1.15 shows the heat flux at z = -20.0 cm. The heat flux shown slowly increases from a value of 1×10^3 W/m^2 at 95 minutes to 1.2×10^5 W/m^2 at 255 min when the melt becomes adjacent to the thermocouple array.
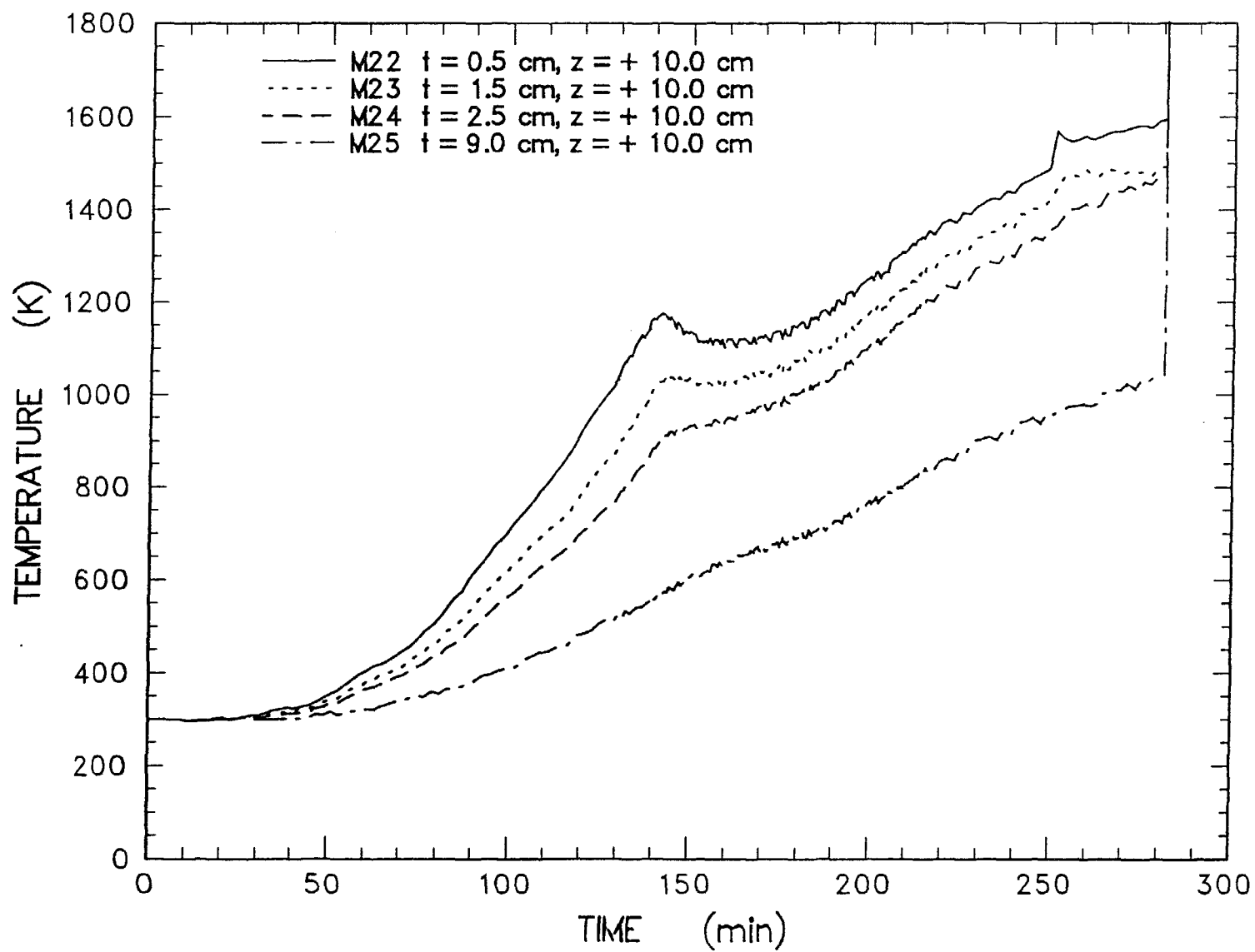
Figure 6.1.14 Typical SURC-2 MgO thermocouple response
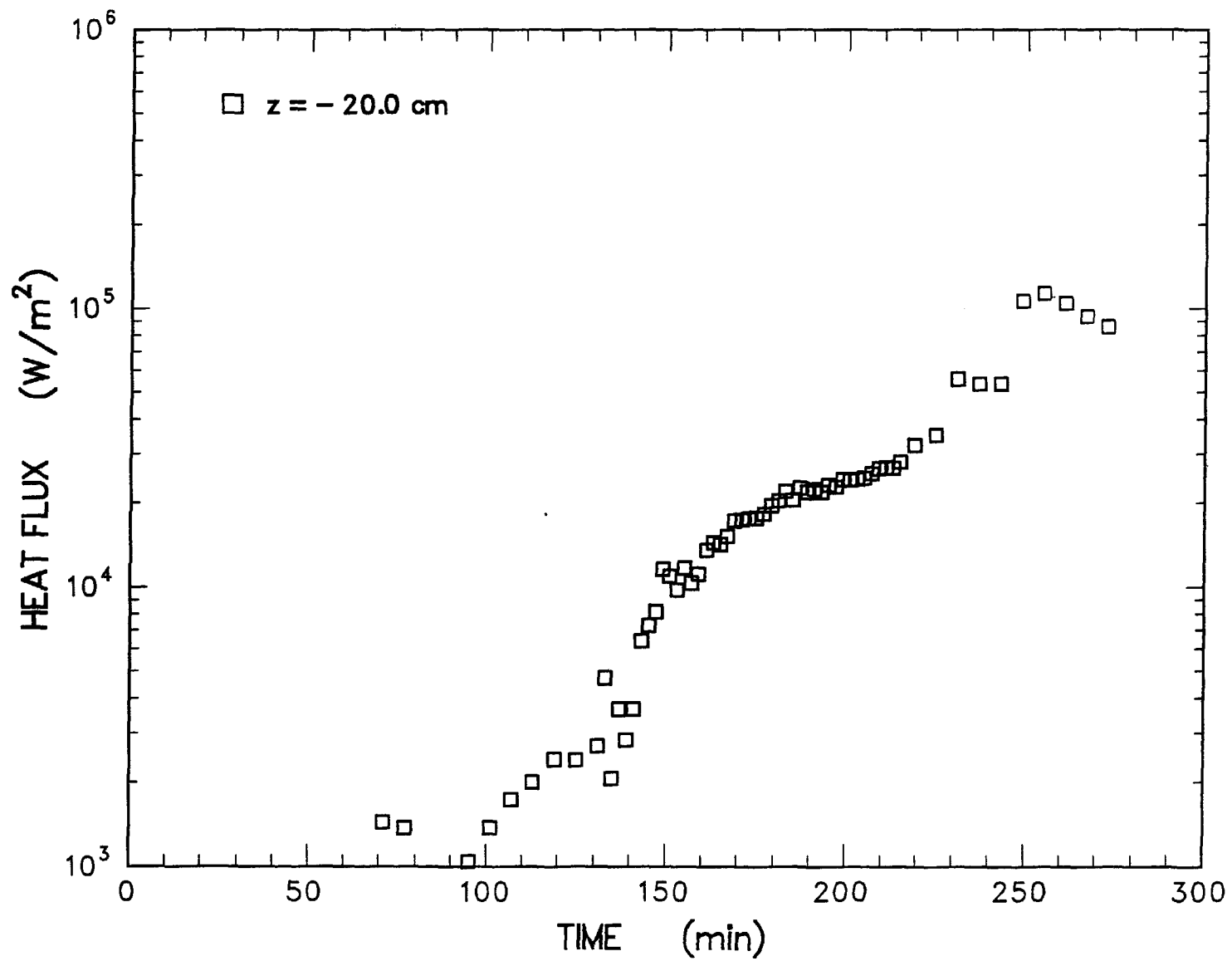
Figure 6.1.15 SURC-2 sidewall heat flux - initially below the melt
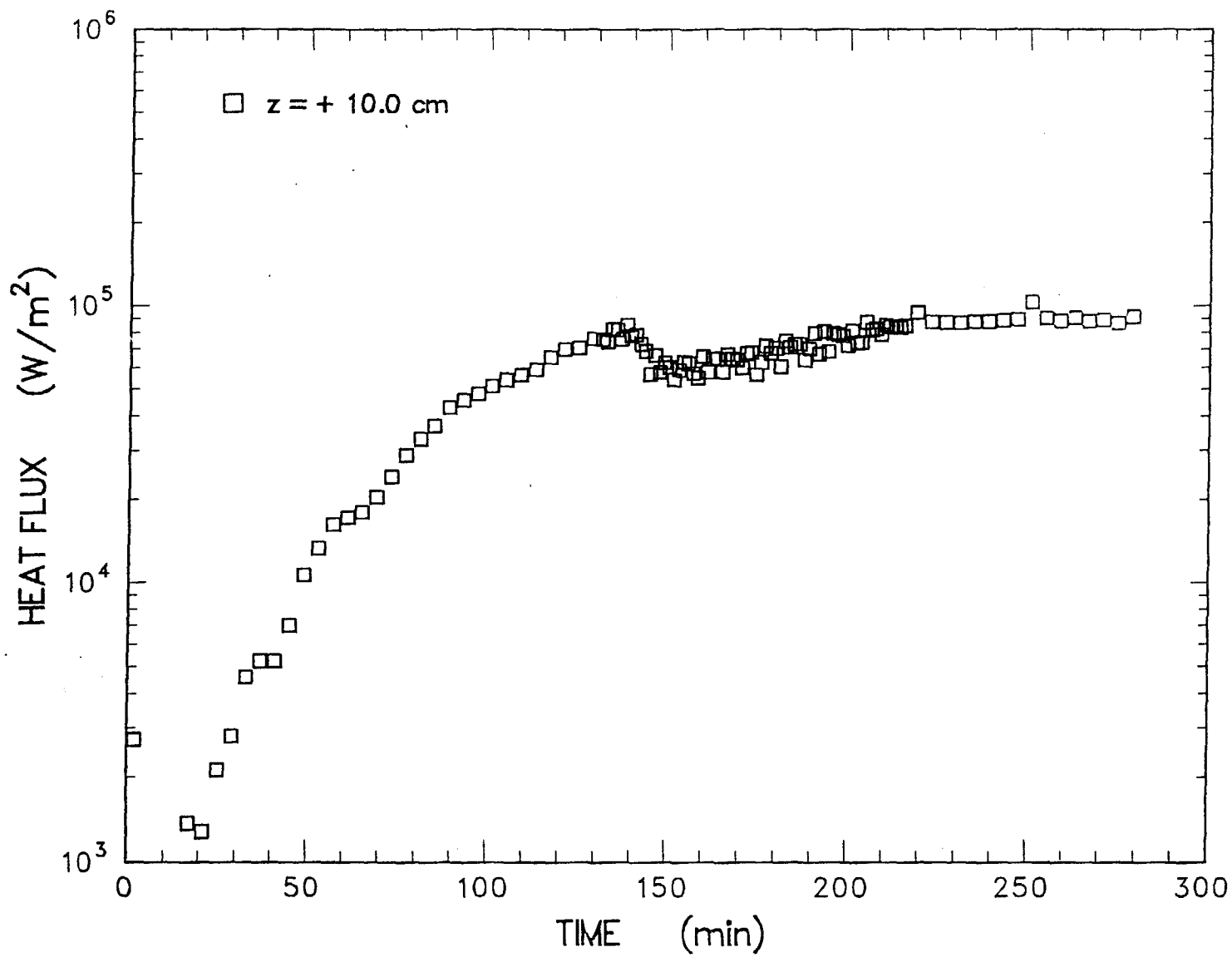
Figure 6.1.16 SURC-2 sidewall heat flux - initially adjacent to the melt
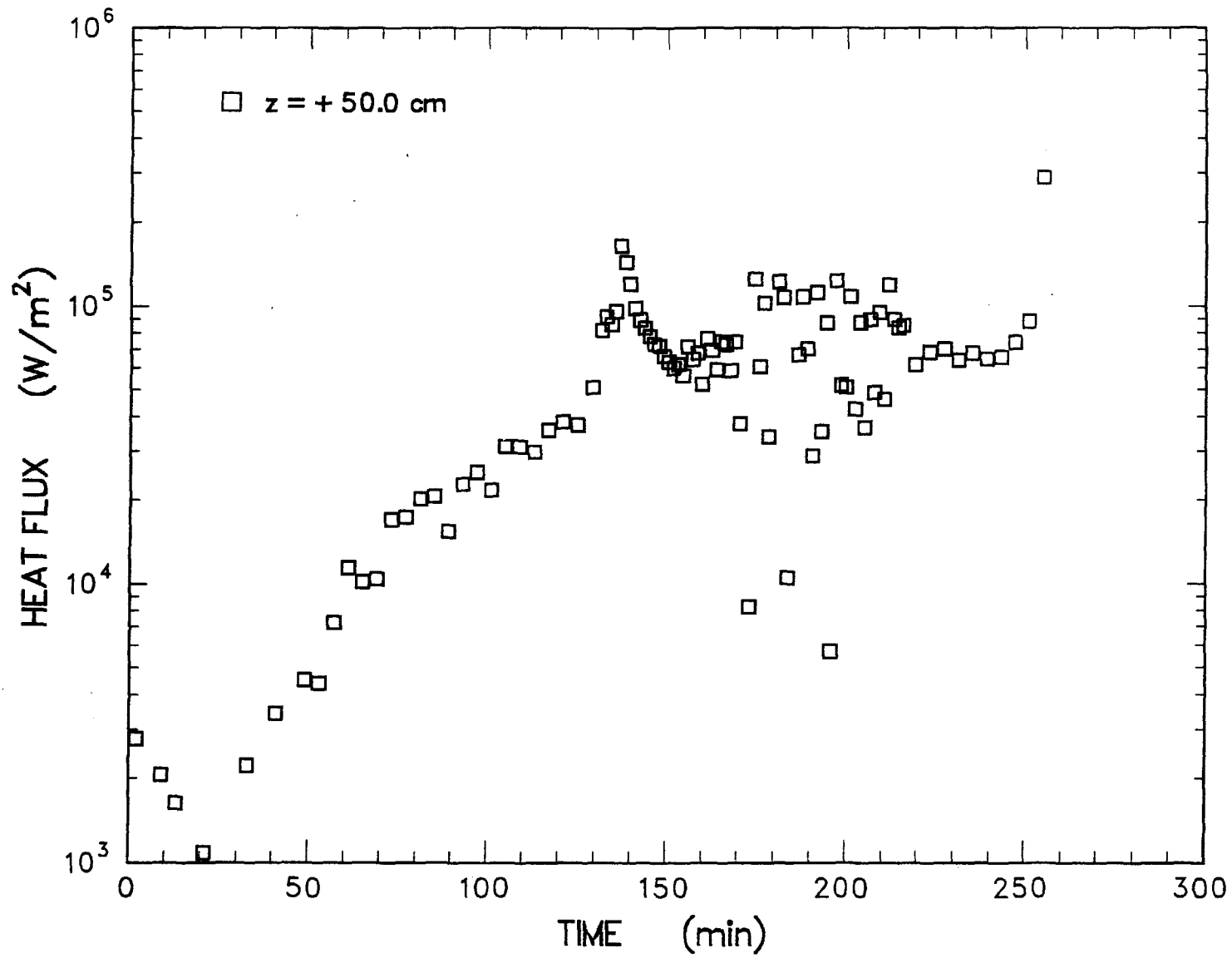
Figure 6.1.17 SURC-2 sidewall heat flux - above the melt

The thermocouples in the array located at $z = +10.0$ cm (Figure 6.1.16) were directly adjacent to the charge during initial heating, melting and the early period of erosion. The heat flux increases as the melt temperature increases and reaches a maximum of 9×10^4 W/m^2 at $t = 140$ minutes, 10 minutes after concrete erosion began. This corresponds to the peak temperatures seen in Figure 6.1.14. The heat flux maintains a value between 6×10^4 and 1×10^5 W/m^2 for the remainder of the test.

Thermocouples in the sidewall array at $z = +50.0$ cm (Figure 6.1.17) were above the melt after the debris became molten and became redistributed in the crucible. The heat flux reaches a peak value at this elevation of 1.07×10^5 W/m^2 at $t = 137$ min. The heat flux then decreases to a value of $6.5 \pm 1 \times 104$ W/m^2 after steady erosion began. Again this value occurs minutes after the onset of erosion.

In summary, the heat flux when the melt was adjacent to the MgO sidewall arrays was calculated to average 1.02×10^5 W/m^2. The array located above the melt inferred heat fluxes in the range of 6.0×10^4 to 1.07×10^5 W/m^2. Heat fluxes indicated by the array embedded in the sidewalls below the concrete surface increased to a value near 1.02×10^5 W/m^2 when the melt was directly adjacent to the array. This value decreased to a value 8.5×10^4 W/m^2 as the melt continued to penetrate the concrete and pass the array.

Crucible Cover

Two duplicate arrays of three thermocouples each were cast into the MgO cover to infer upward heat flux. The temperatures indicated by type K thermocouples cast in one of the arrays is shown in Figure 6.1.18. The temperature response of the second array is nearly identical as seen in Appendix E. The specific location of these thermocouples with respect to the crucible geometry can be found in Table 3.4. At the onset of erosion, the temperature indicated by the

thermocouples increases rapidly at $t = 130$ min. The temperature then steadily increases until failure by melt runout at $t = 281$ min.

Figure 6.1.19 shows the heat flux calculated from the temperatures measured by the thermocouples. The figure indicates that the heat flux steadily increased, peaking at a value of 1.9×10^5 W/m^2 at $t = 138$ min. The heat flux then declines to a value of 5×10^4 W/m^2 at $t = 150$ min. The heat flux increases steadily from this period to $t = 263$ min where the value of 1.01×10^5 W/m^2 is calculated.

6.2 Gas Composition Data Presentation

Gas sampling for the SURC-2 test was done using three techniques: an Infocon Model IQ200 mass spectrometer, an Infrared Industries Model 700 CO/CO$_2$ detector, and integral grab samples. The first two techniques yield real-time data that is viewed on-line and stored on computer disks. The grab samples are stored and analyzed posttest using both gas chromatography and mass spectrometry.

Additional information on these systems is detailed in Section 4.2.

Test Procedures

Operational procedures for the gas analysis equipment and support components were accomplished in the following manner:

The output from the type K thermocouples installed in the flow stream 3 meters downstream from the crucible was continuously monitored and recorded by the data acquisition system as was the output from the other type K thermocouple mounted at the actual sampling location. Although the temperature in the flow line ranged from 300 to 600 K, the conditions at the actual sampling point were very constant at 300 ± 3 K throughout the test.
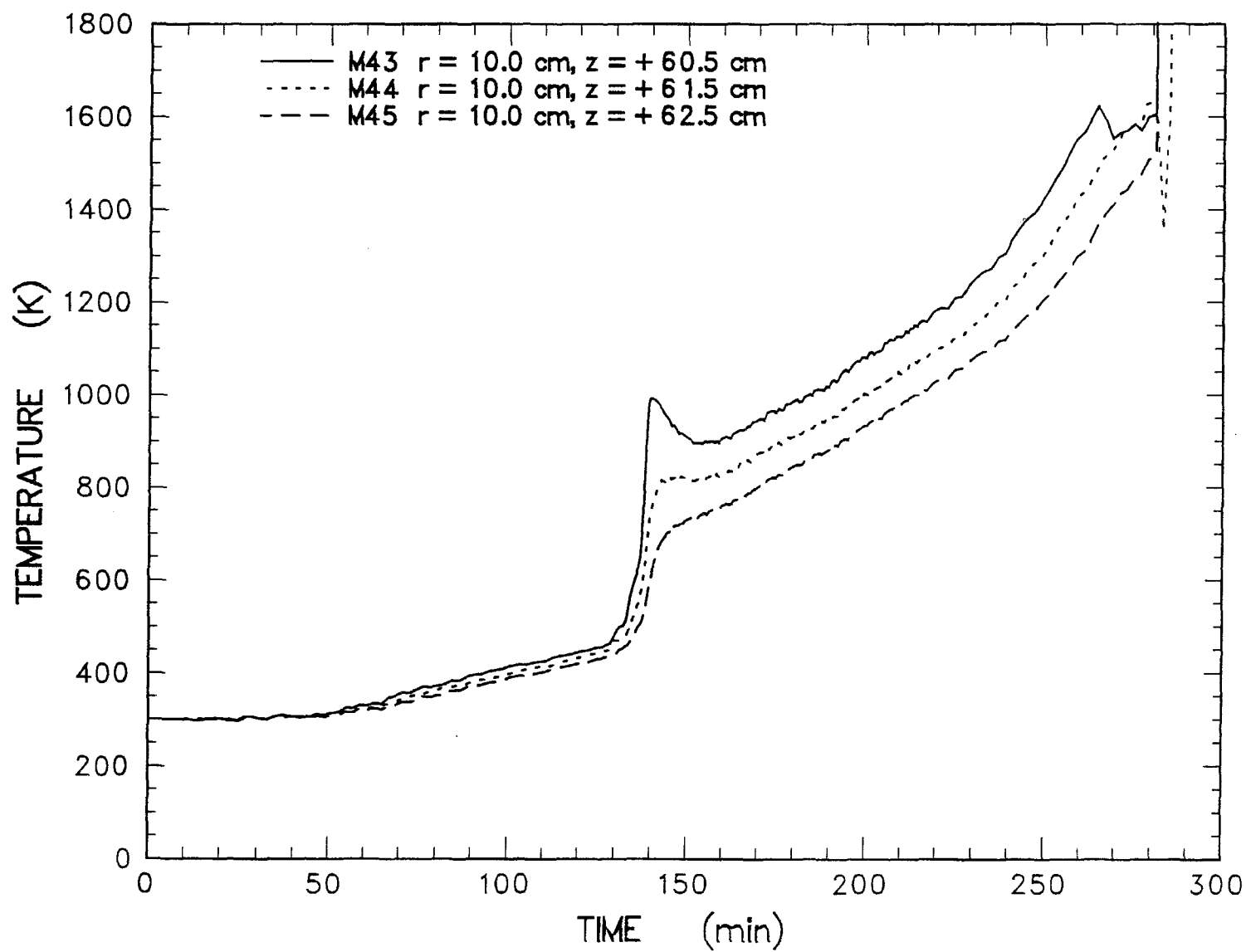
Figure 6.1.18 Typical SURC-2 MgO thermocouple response located in the cover
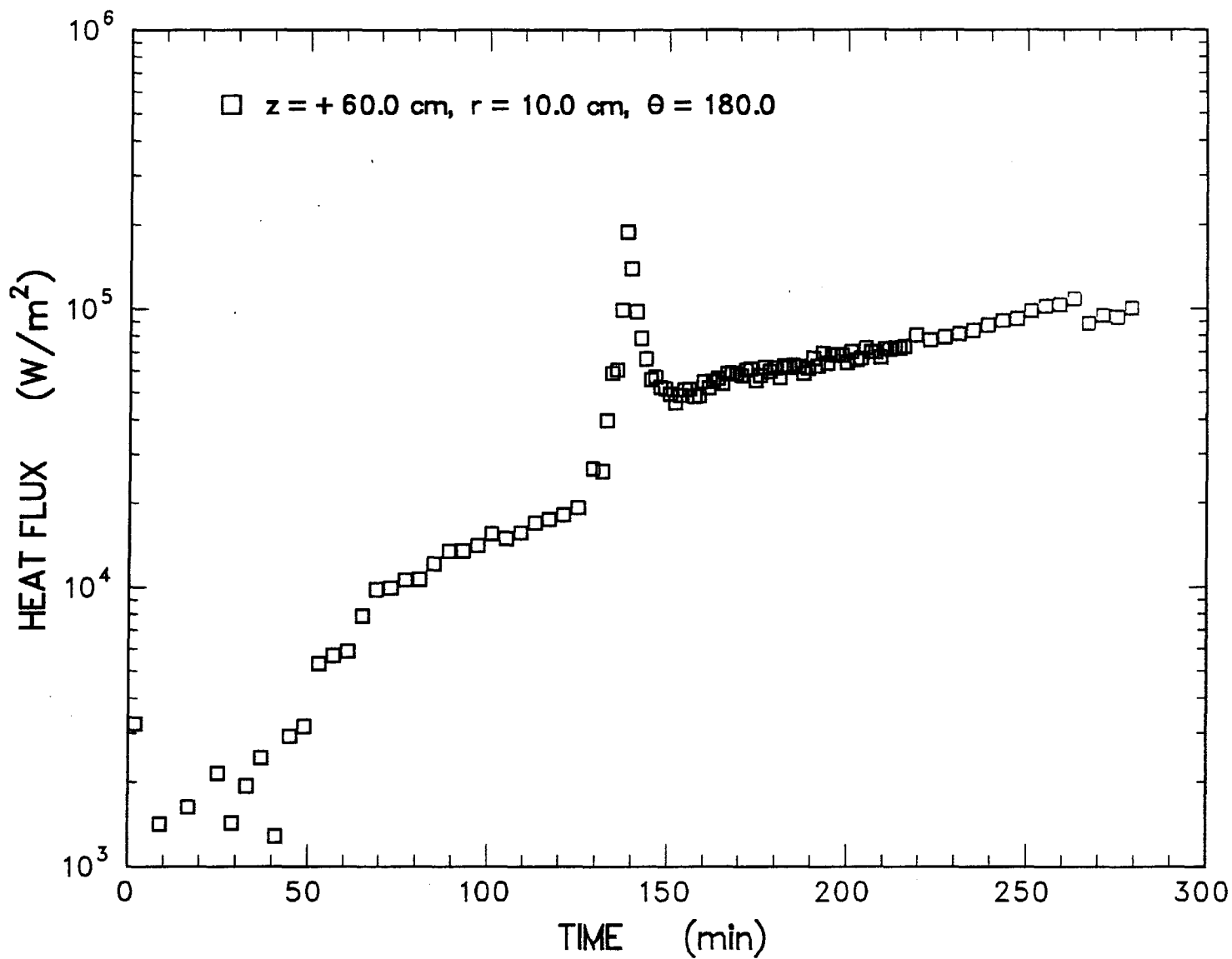
Figure 6.1.19 Upward heat flux calculated from thermocouple data located in the MgO çover

Gas flow through the sample line was established 30 minutes before the test by energizing the diaphragm pump. The flow was manually regulated to provide a 3 lpm flow rate. Monitoring of the sample line flow rate was done continuously. No substantial fluctuations were indicated.

The grab sample bottles were evacuated before the test and then individually subjected to vacuum. Six samples were taken manually. Times for the samples were recorded by the computer as pressure spikes. One grab sample bottle was utilized at each sampling event and each bottle was filled in approximately 1 second.

The CO/CO_2 monitor was warmed up at least 30 minutes before the test. A pretest calibration was performed prior to start-up of the data acquisition system and no irregularities were noted. The CO/CO_2 data were automatically recorded by the data acquisition system throughout the test. In addition, a visible readout was monitored locally at the instrument and remotely in the control room. Following the test, another calibration run was performed, again indicating no irregularities.

The mass spectrometer system was in operation under a low vacuum of 100 m torr for one week prior to establishing a vacuum of 10^{-6} torr for three days before the test date. The analysis display was continuously monitored and several hundred discrete samples were recorded during the test. On-line data were recorded every 10 to 20 seconds throughout the test.

Results

Four periods of time are of interest for the SURC-2 gas composition data: the onset of gas production between 50 and 130 minutes, the rapid initial erosion between 130 and 160 minutes, the slowed erosion period after Zr depletion between 160 and 220 minutes, and the increased erosion following the power increase from 140 kW to 190 kW at 220 minutes which

lasted until the termination of the test at 280 minutes. Notable events which affected the gas composition data were the blockage of sample port No. 3 (containment) at 145 minutes due to aerosol trapping and switching to sample port No. 2 (flow line) at 153 minutes until test termination at 280 minutes.

Although water vapor is present in the reaction gas, it cannot be measured in large amounts by the gas analysis system without ruining the equipment. Consequently, water vapor traps are installed in the gas analysis flow lines. A total of 7 ml of water was recovered from the ice-cooled cold trap. This would have added 8.7 liters of H_2O vapor to the 240 liters of collected H_2, CO, and CO_2 yielding an estimated water content of 3-5% in addition to the reported gas compositions for H_2, CO, and CO_2.

The results from the mass spectrometer are shown in Table 6.2.1 and in Appendix G. The table lists the raw data as volume (mole) percent along with the time for the sampled gas species. The mass spectrometer data from Appendix G indicate the onset of gas release at 52 minutes followed by the onset of rapid erosion between 130 and 160 minutes. The change in gas composition after the depletion of Zr metal at times after 160 minutes is marked by lower percentages of H_2 gas production. This trend is reversed at later times when the power is increased. The reaction gas (H_2, CO, H_2O, and CO_2) data is separated from the argon carrier gas data and normalized in Table 6.2.2. Here the H_2O content can be assumed to have somewhat greater average values because of the volume of water collected in the condensate traps.

An examination of the normalized data from the mass spectrometer shows that the onset of gas production between times 52 and 130 minutes is characterized by a gas composition which is 70 to 80% H_2, 5 to 15% H_2O, and 10-20% CO. When concrete erosion began at around 130 minutes, the hydrogen concentration in the effluent gas increased and the H_2O concentration

Data

Table 6.2.1 SURC-2 mass spectrometer raw data - volume percent

Run Time (min)	H_2	H_2O	CO	O_2	Ar	CO_2	Notes
Before 50	-	2	2	-	95	1	Background
76	10	3	3	-	83	1	Initial
93	10	3	3	-	83	1	Dehydration
116	15	4	5	-	75	1	
134	20	5	10	-	63	2	Rapid Erosion
141	47	5	13	-	33	2	w/Zr
155	38	5	10	1	42	4	
166	34	4	8	1	49	4	Erosion rate
175	28	4	6	2	56	4	Slows
194	19	3	5	2	66	5	
202	18	3	5	1	69	4	
211	15	3	5	1	70	4	
219	12	3	5	1	76	3	
230	11	3	5	-	78	3	Increased
250	11	3	5	-	78	3	Power
263	19	3	5	-	70	3	and Erosion
272	23	3	7	-	64	3	
276	28	3	8	-	68	3	

Table 6.2.2 SURC-2 mass spectrometer normalized
data - volume percent

Run Time (min)	H_2	H_2O	CO	CO_2	Notes
Before 50	--	--	--	--	Ar only
76	83	8	8	-	Initial dehydration
93	83	8	8	-	
116	75	10	15	-	
134	63	9	25	3	Rapid Erosion
141	76	5	18	2	w/Zr
155	73	6	15	6	
166	76	4	13	7	Erosion Rate
175	76	5	11	8	Slows
194	70	4	11	15	
202	72	4	12	12	
211	68	5	14	14	
219	67	6	17	11	
230	65	6	18	12	Increased Power
250	65	6	18	12	and Erosion
263	76	4	12	8	
272	74	3	16	6	
276	76	3	16	5	

decreased. A typical composition during this period (130-160 minutes) is 75% H_2-5% H_2O, 15% CO-5% CO_2. After the depletion of Zr metal at times after 160 minutes, the gas composition changed to a mixture richer in H_2O and CO_2. This composition averaged 70% H_2-5% H_2O-15% CO-10% CO_2. The final period of activity resulted in increased hydrogen and CO production relative to H_2O and CO_2. An average composition is 75% H_2-5% H_2O-15% CO-5% CO_2.

The results from the CO/CO_2 monitor are shown in Figure 6.2.1. The raw data, shown here as percent CO and percent CO_2 in the sampling flowline, indicate the onset of gas release between 55-60 minutes into the test. Both CO and CO_2 content rise from the onset of gas release until erosion begins at around 130 minutes with the CO content being lower than the CO_2 content. When concrete erosion begins at time = 130 minutes, the CO concentration increases and the CO_2 concentration decreases so that between times 130 and 160 minutes the CO/CO_2 ratio steadily decreases from 5:1 to 3:2. After Zr metal was depleted at times after 160 minutes the concentration of CO dropped and the CO_2 concentration recovered to a level above the value indicated before Zr depletion. CO/CO_2 ratios during this period of slow erosion averaged 2:3. The $CO/CO2$ ratio for the remaining period (60 minutes) of interaction averaged 3:2, indicating a relative increase in CO.

The grab sample results for SURC-2 are shown in Table 6.2.3. These results agree qualitatively with the more complete and more accurate results from the mass spectrometer. The carrier gas for these samples included argon in total amounts ranging from 15-50%. A total of 6 samples were taken in which no other gases besides H_2, O_2, CO_2, N_2, CO, or Ar were detected. Normalized results for the samples taken during the erosion phase of the test between times 130 and 202 minutes are also shown in Table 6.2.3. These samples have an average H_2 concentration of 80% with 15% CO and 5% CO_2. As with the

mass spectrometer results, these concentrations do not include H_2O vapor, which averaged 3-5% over the entire test.

6.3 Flow Data Presentation

Four different devices were used to measure the reaction gas flow rate in SURC-2: A 1.02 cm orifice plate, a laminar flow element, a Rockwell 450 gas clock, and a Rockwell 750 gas clock. A flow train schematic for these devices is shown in Figure 4.3.1 and information regarding the description, operation, and calibration of the flow equipment is detailed in Section 4.3.

Procedures

All of the flow devices were operated continuously throughout the test. Data from the devices in the form of voltage outputs from either pressure transducers or a summing transmitter were initially recorded at 15 second intervals using the HP1000 data acquisition system. Initial flow for the system was established and maintained using argon carrier gas. Argon was introduced into the apparatus at two locations. The first location was into the water cooled aluminum containment vessel. The flow rate of argon at this position was monitored using a turbine meter. Argon was also used to purge a window protecting the opacity meter. The opacity meter was located in the flow tube approximately 3 meters downstream from the crucible. The flow of argon at this position was monitored using a Kulite 100 psi pressure transducer upstream of a Milipore 1.1 mm (5 lpm) diameter critical orifice. The turbine meter registered a flow rate of 16 $\pm$ 1 liters per minute throughout the test. The pressure transducer recorded a constant gauge pressure of 16 $\pm$ 1 psi. The flow rate at this location based on the pressure and orifice calibration was calculated to be 16 $\pm$ 1 liters per minute. The combined flow rate of argon into the experimental apparatus considering both locations was 32 $\pm$ 2 slpm.
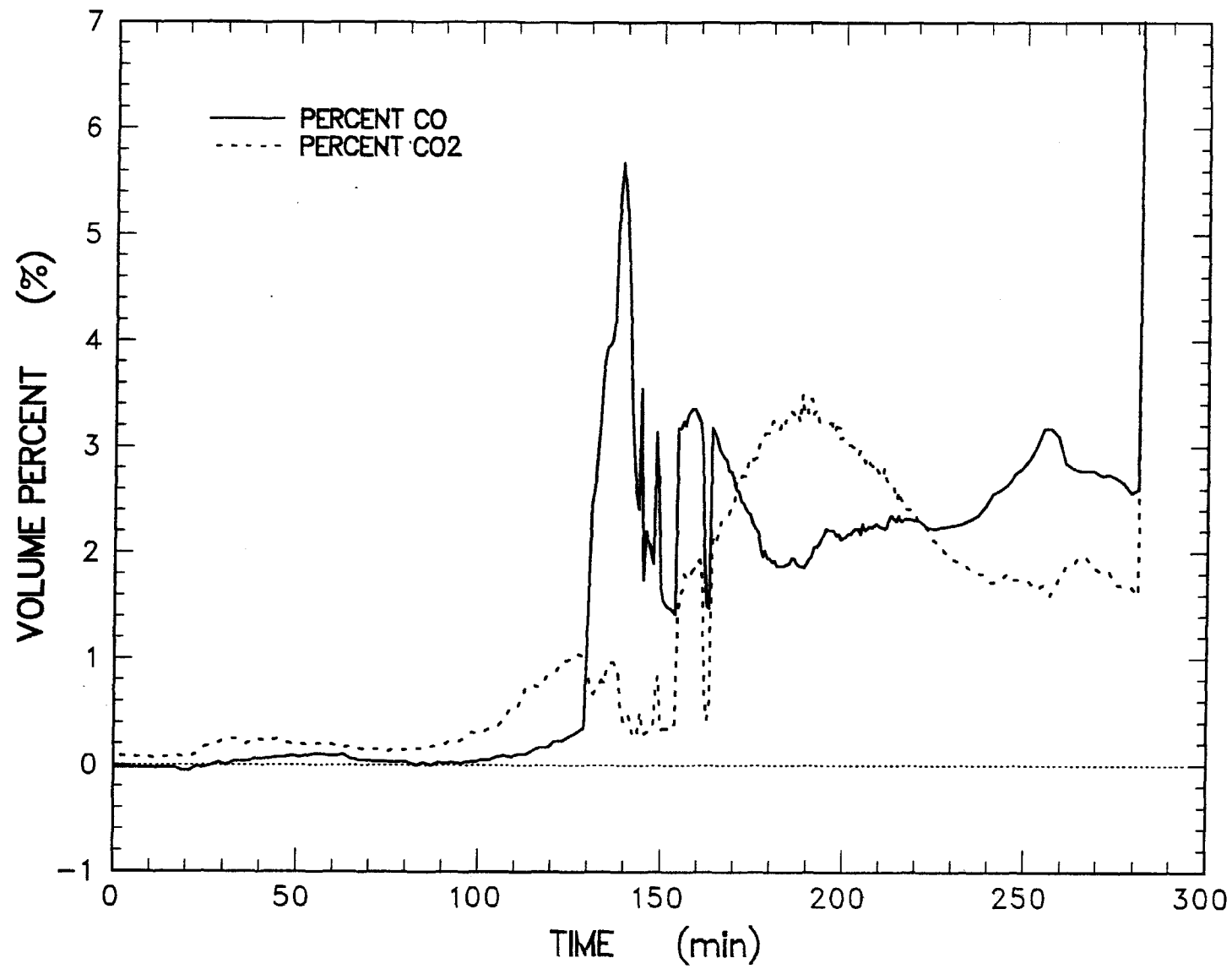
Figure 6.2.1 SURC-2 CO/CO$_2$ monitor data

Data

Table 6.2.3 SURC-2 grab sample analysis
raw data in volume (mole) percent

Run Time (min)	H_2	CO	O_2	Ar	CO_2
130	40.9	8.8	1.7	47.9	.7
140	71.4	12.0	1.9	14.3	.4
155	65.8	12.0	2.4	18.3	1.4
175	53.8	9.0	2.8	32.0	2.4
190	42.0	8.2	3.6	43.3	2.5
202	38.3	8.9	3.1	47.3	2.5

Normalized Data in Volume (Mole) Percent

Run Time (min)	H_2	CO	CO_2
130	81.1	17.5	1.4
140	85.2	14.3	0.5
155	83.1	15.2	1.8
175	82.5	13.8	3.7
190	79.1	15.4	5.5
202	77.1	17.9	5.0

The temperature of the gas in the flow system was measured at two locations: 1 meter from the crucible in the containment vessel and 7 meters downstream from the crucible at the flow system exhaust. A plot of the flow system temperatures at these locations is shown in Figure 6.3.1. Although the reaction gases generated in the crucible can have initial temperatures in excess of 2000 K, these gases cool quickly and were mixed with argon at ambient conditions so that the temperatures at the flow measurement devices were generally less than 400 K. The system pressure was also monitored and is shown in Figure 6.3.2. This pressure was recorded in the containment vessel and 10 cm upstream from the orifice flow meter. This location represents the highest pressures achieved in the flow system during the SURC-2 test at which the measured values were very modest and ranged from 0.1 to 2.5 psi.

Results

As with the crucible temperature and gas composition data, four time periods are of interest for the SURC-2 flow data. These are the onset of gas release from concrete between 50 to 130 minutes, the gas release associated with initial rapid concrete erosion between 130 and 160 minutes, and the decrease in gas evolution due to the cessation of Zr interactions at times after 160 minutes, and the increased gas flow resulting from a power increase at 220 minutes and lasting until crucible failure at 280 minutes. Events during the SURC-2 test which caused fluctuations in the data are after 200 minutes when the orifice plate became partially blocked by aerosol.

The raw data for the gas clocks are shown in Figure 6.3.3. Here the total volume is in actual cubic meters of gas collected at the ambient conditions of 12.2 psia and 295 K. As seen by Figure 6.3.3, the two gas clocks measured virtually identical volumes of gas throughout the experiment. A total of 18,100 standard liters of gas were collected before the crucible failed in

SURC-2. Based on a constant argon input flow of 32 slpm and the temperature profiles for the crucible materials, approximately 9000 liters of this total were due to the argon carrier gas, 3000 liters were due to the dehydration of the MgO, and 6100 liters were due to the decomposition of the basaltic concrete basemat. Average flow rates for discrete periods of time during the test have been calculated using the gas clock data and are presented in Table 6.3.1.

Table 6.3.1 SURC-2 flow rates from gas clock data

Time (min)	Total Flow (Actual Liters)	Avg. Flow Rate (alpm)	Corrected Flow Rate (slpm)
0-50	1,920	38	32
100	5,070	63	53
130	7,500	81	68
160	12,650	172	145
190	15,850	107	90
220	17,630	59	50
250	19,330	56	47
280	21,850	84	71

The actual flow rate has been corrected in the final column of Table 6.3.1 to account for leakage from the system (5%) and non-STP conditions. These data indicate that the initial argon flow was 32 slpm. When the initial argon flow of 32 slpm is subtracted from the values shown in the final column of Table 6.3.1, it can been seen that significant offgassing of the concrete basemat began between 50 and 100 minutes at an average rate of 21 slpm. During the period from 100 to 130 minutes, the reaction gas flow rate averaged 36 slpm. This is the characteristic flow rate for the period prior to the onset of ablation. After ablation began at 130 minutes the flow rate increased to 113 slpm between 130 and 160 minutes and gradually
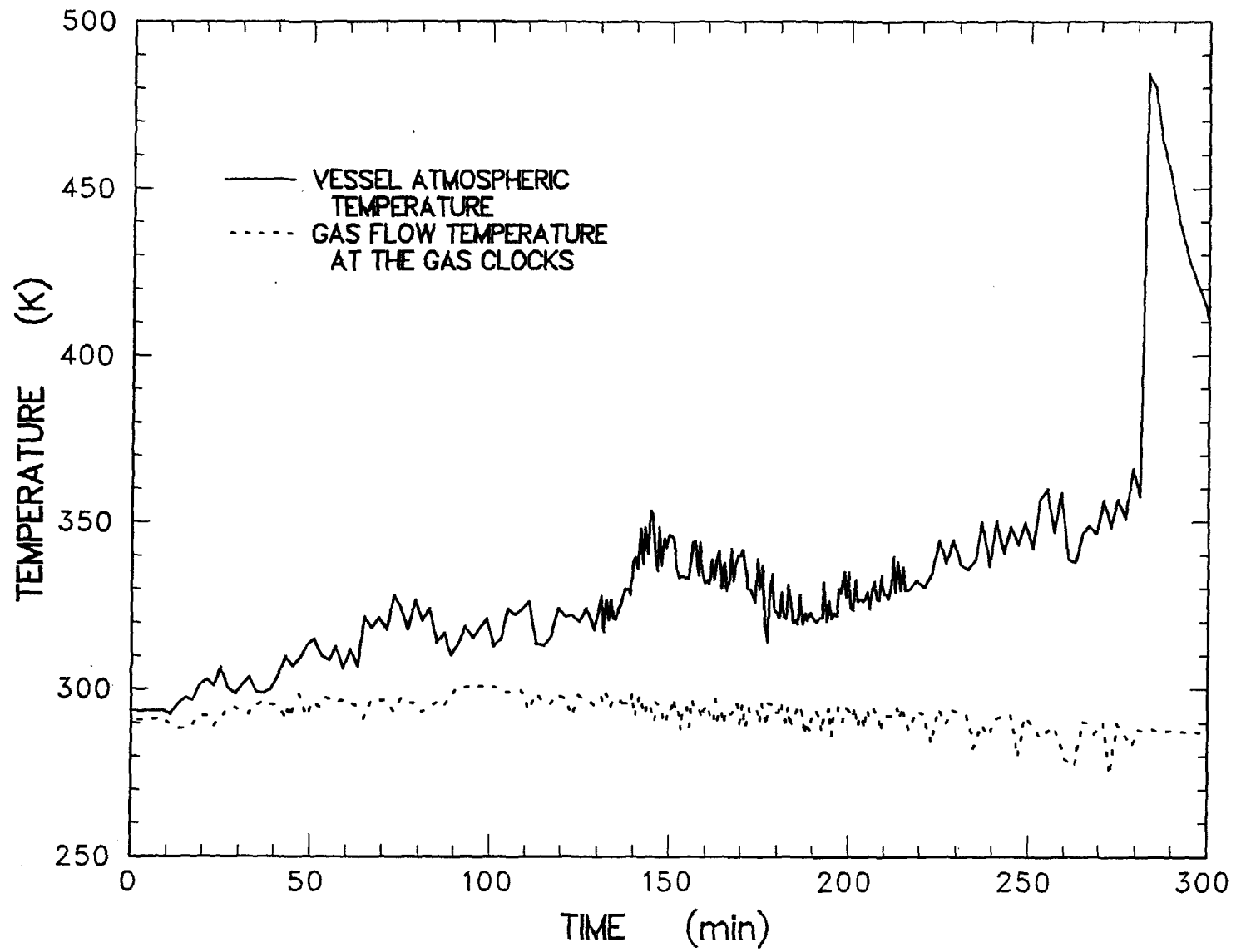
Figure 6.3.1 Temperature distribution in the SURC-2 flow system
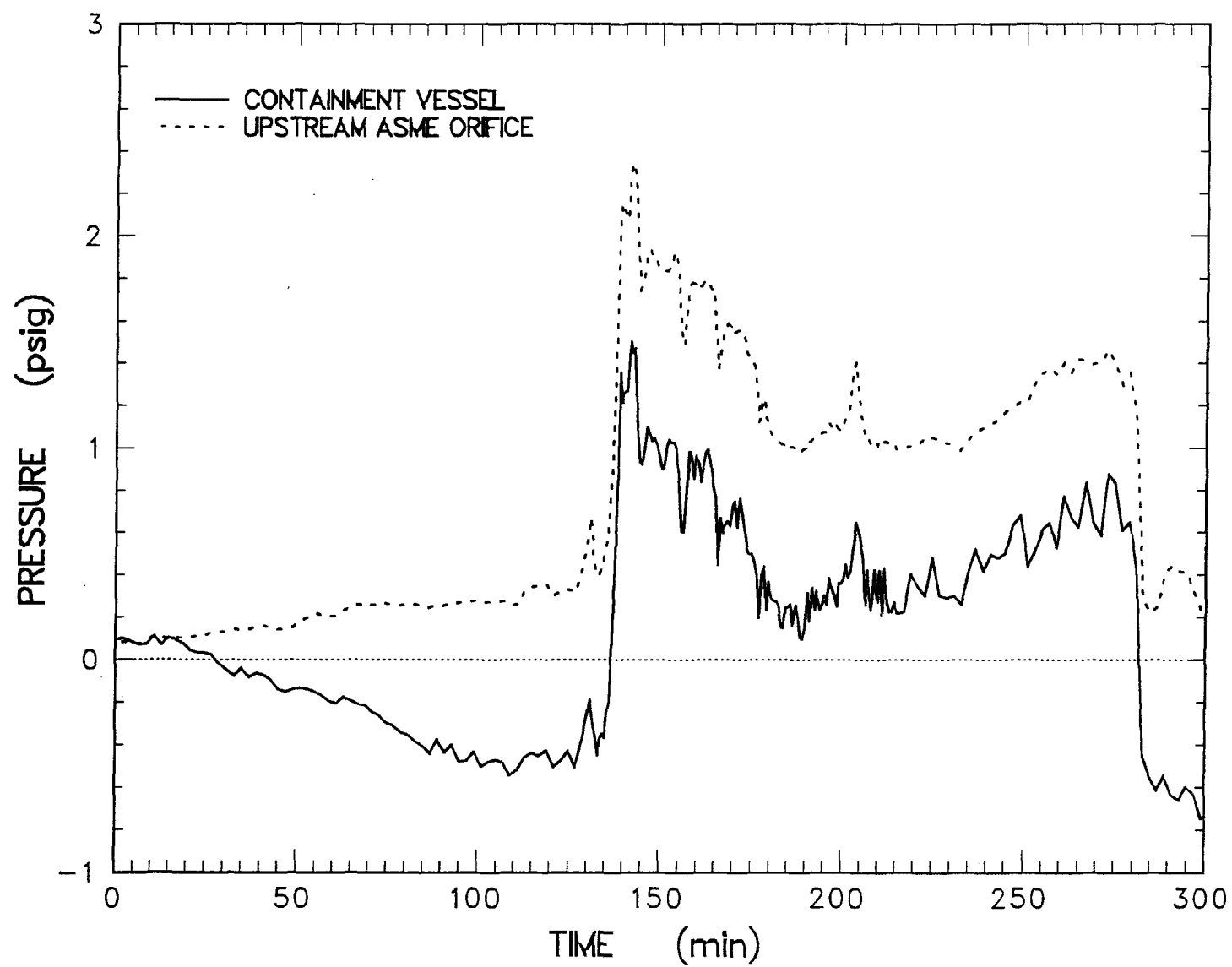
Figure 6.3.2 Pressure history in the SURC-2 flow system

127
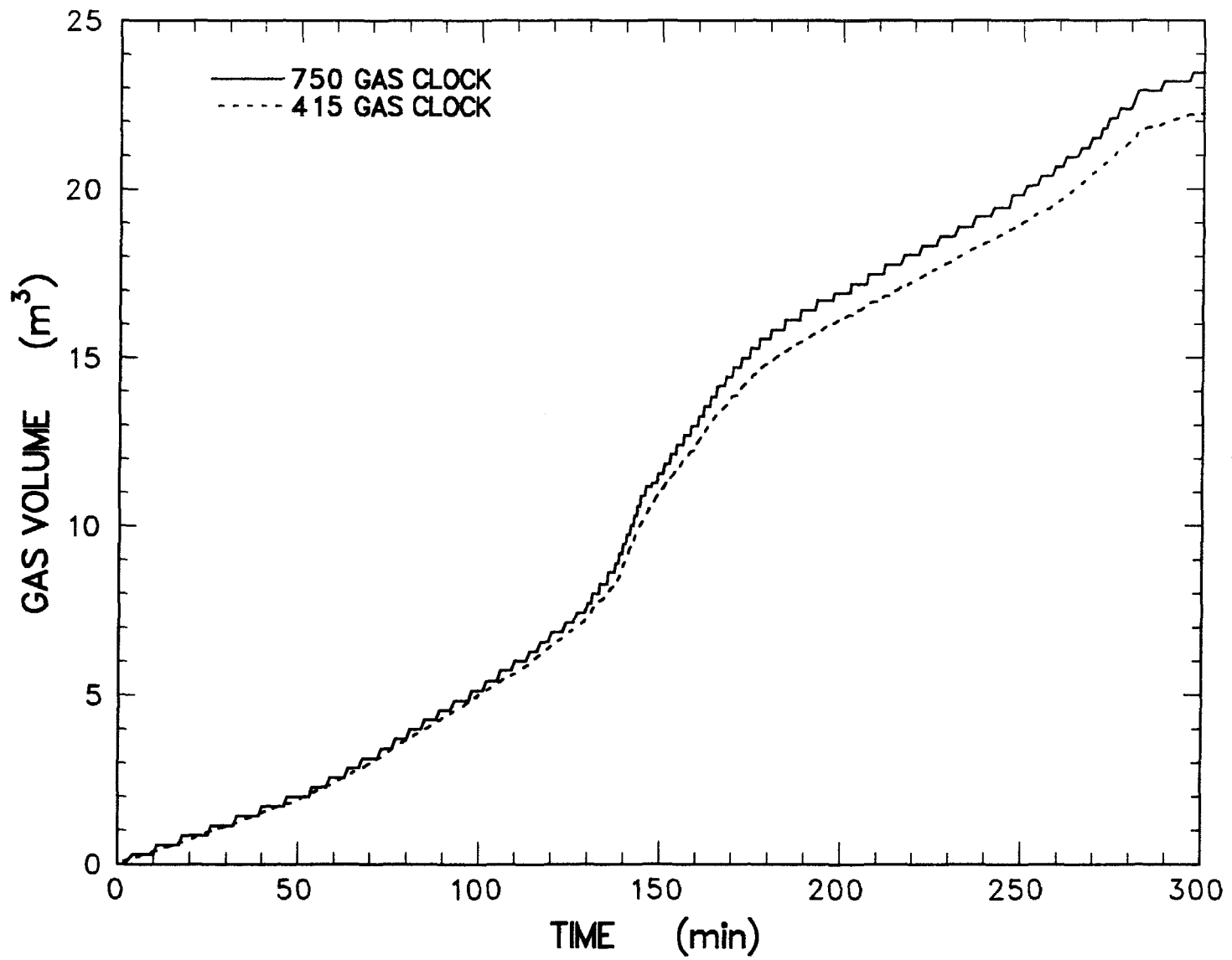
Data

Figure 6.3.3 SURC-2 total flow - gas clock data

decreased to a rate of 15 slpm at 250 minutes, followed by an increase to 39 slpm.

The reduced data for the orifice plate flowmeter are shown in Figure 6.3.4. Figure 6.3.4 is a plot of the total flow rate including the argon inlet flow for the period identical to that for the gas clocks. Examination of the total flow rate at the orifice plate from Figure 6.3.4 shows that the initial argon input flow was 15 alpm. Initial offgassing began between 50-60 minutes and the total flow rate increased to a plateau of 70-80 alpm during the period before ablation began. After 130 minutes, the total flow jumped to 200-240 alpm then decreased to 120 alpm for the middle portion of the test. During the final period of the test between 240-280 minutes the flow rate was observed to rise again to a peak of 190 alpm.

Figure 6.3.5 shows the flow rate data for the outlet turbine. These results show that the initial offgassing started at 44 minutes with low flow rates. Significant offgassing began after 60 minutes as the flow rate increased from 30 alpm to 70-80 alpm at 88 minutes. After concrete erosion began at 130 minutes, the flow rate increased to 175-200 alpm. After 160 minutes the reaction gas flow rate decreased to 50-60 alpm and averaged 60-80 alpm for the remainder of the test. Similar results are shown in Figure 6.3.6 and 6.3.7 for the laminar flow element. Figure 6.3.6 illustrates that the total flow rate during the SURC-2 test for the period was identical to that for the orifice plate and the gas clocks. The argon inlet flow was established at 40 alpm between 0 and 40 minutes. Off-gassing began between 40 and 50 minutes and the flow rate increased to a plateau of 70 alpm between 85 and 100 minutes. After concrete erosion began at 130 minutes, the flow rate increased to a rate of 145-180 alpm. Flow then decreased to 50 alpm followed by an increase to 75-80 alpm.

Figure 6.3.7 shows the reaction gas flow rate after corrections were made for leakage, temperature, pressure, and the argon carrier gas flow. The initial flow began at 45 minutes, and increased gradually to 25-30 slpm at 85 minutes. When concrete ablation began at 130 minutes the flow rate increased to 185-200 slpm. After ablation slowed, the reaction gas flow rate decreased to 5 slpm followed by an increase to 50 slpm for the duration of the test.

The results from the orifice plate, turbine, and laminar flow element compare well with the results of the gas clocks with regard to the timing and relative magnitudes of the initial gas release, the gas release associated with steady state concrete erosion, and the increased release associated with the Zr metal in the initial melt. The absolute flow rates for these events, however, are most accurately represented by the gas clocks (Table 6.3.1) since no corrections are required to account for significant flow blockage or fluctuations in gas density or gas viscosity as are required for the turbine, orifice plate, and laminar flow element. A detailed listing of the gas clock results is included in Appendix G.

6.4 Aerosol Data

A total of 2-4 kg of aerosol material was produced during the SURC-2 experiment with 1/3 to 1/2 of that material being accounted for by the aerosol measurement techniques. A large quantity of material was deposited in the containment vessel and was never transported to the measurement system. In addition, large diameter materials which can account for a large fraction of the aerosol mass cannot be sampled efficiently.

Aerosols were collected and measured using Gelman filters, Anderson Impactors, cyclones, and an opacity meter. These instruments are described in Section 4.4. The SURC-2 aerosol
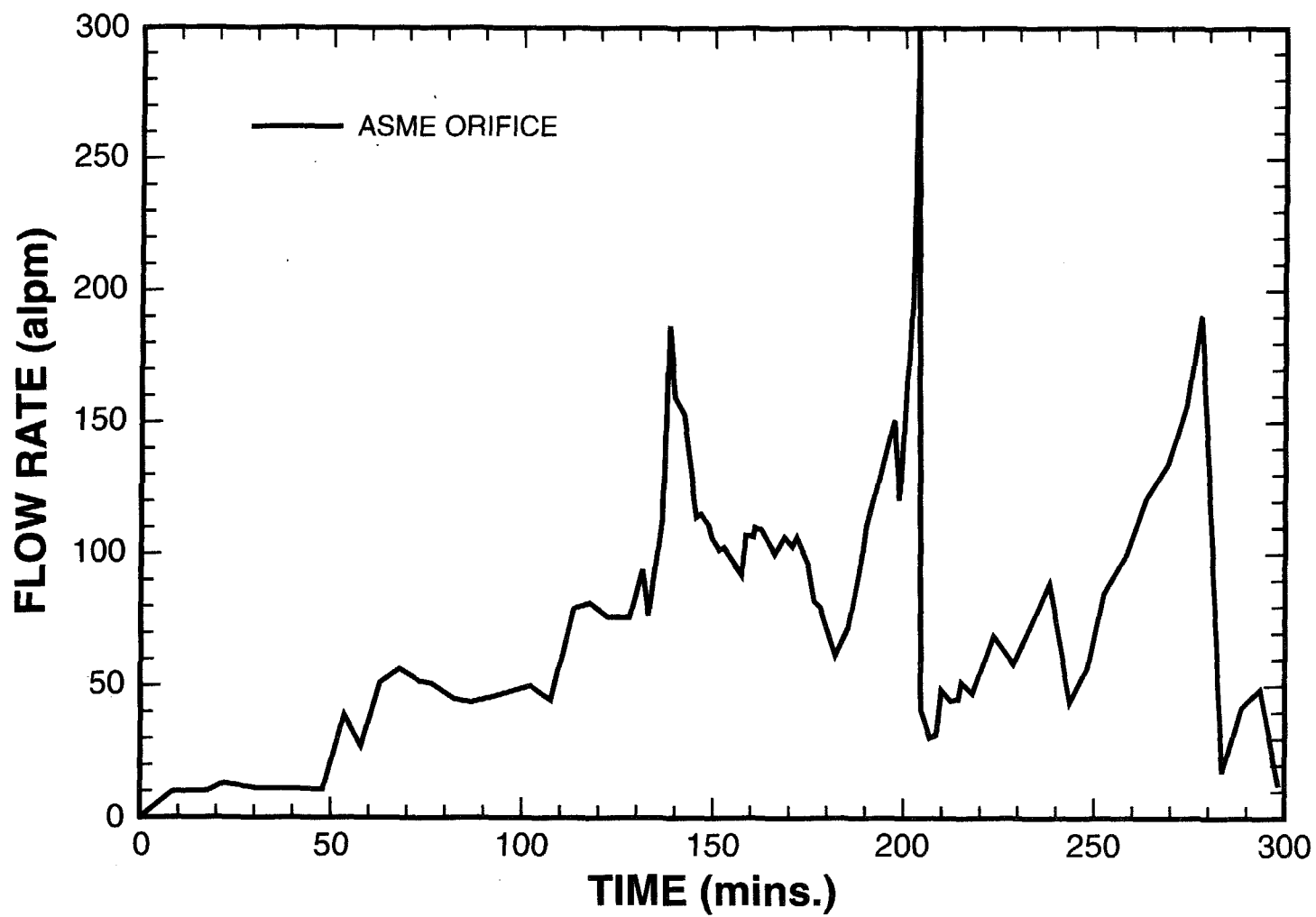
Figure 6.3.4 SURC-2 total flow - orifice plate data

131
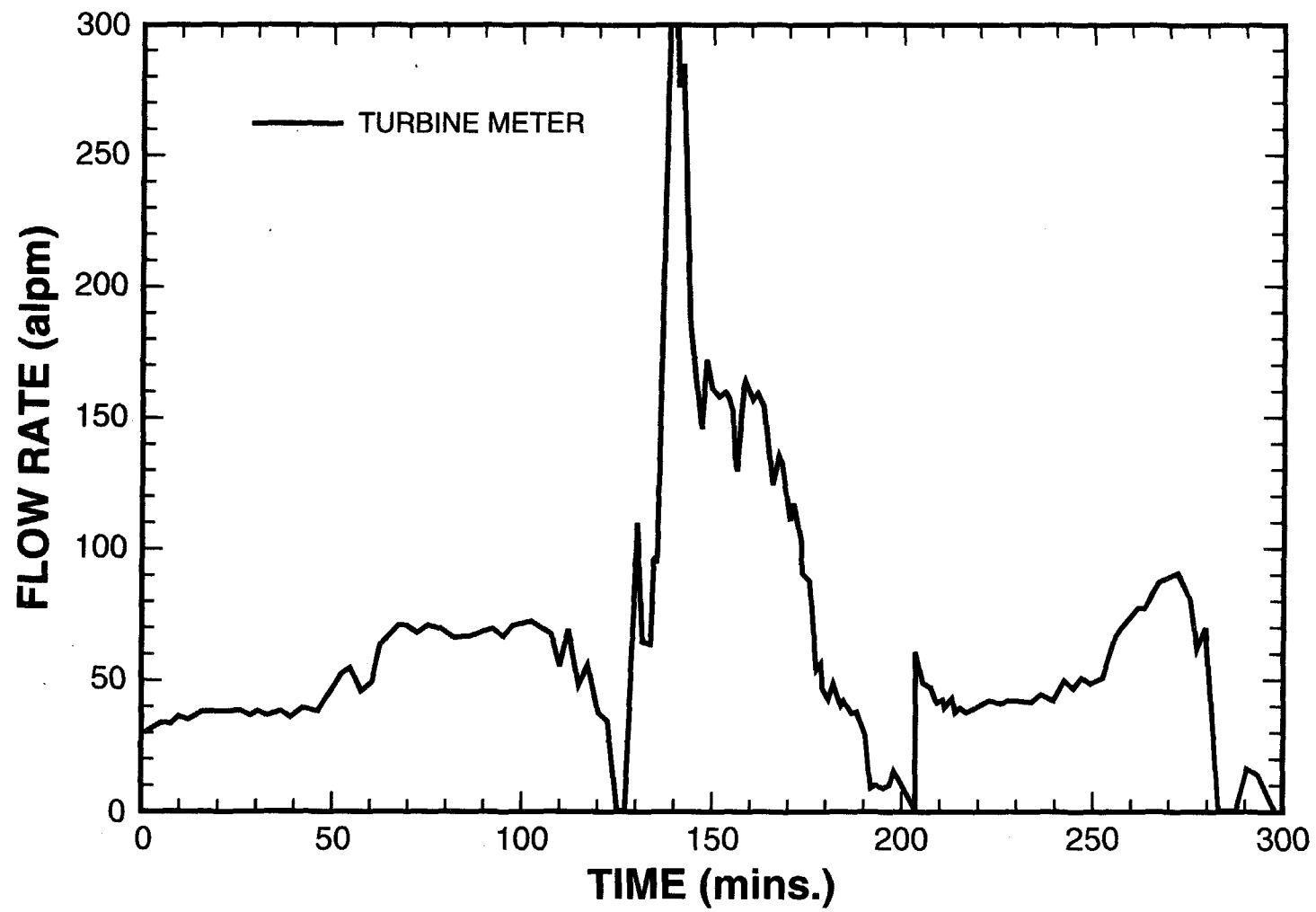
Figure 6.3.5 SURC-2 reaction gas flow - turbine meter
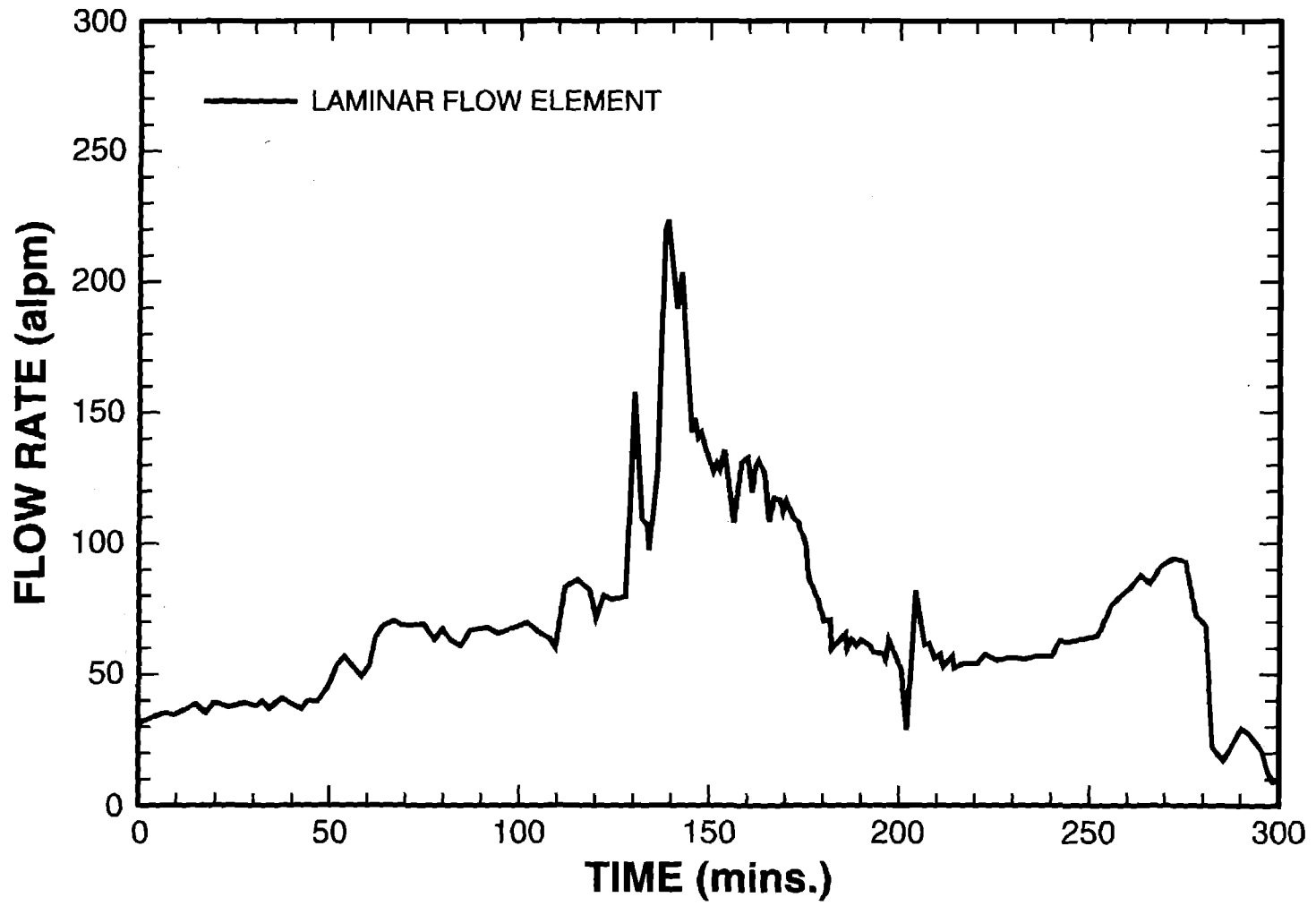
Figure 6.3.6 SURC-2 total flow - laminar flow element
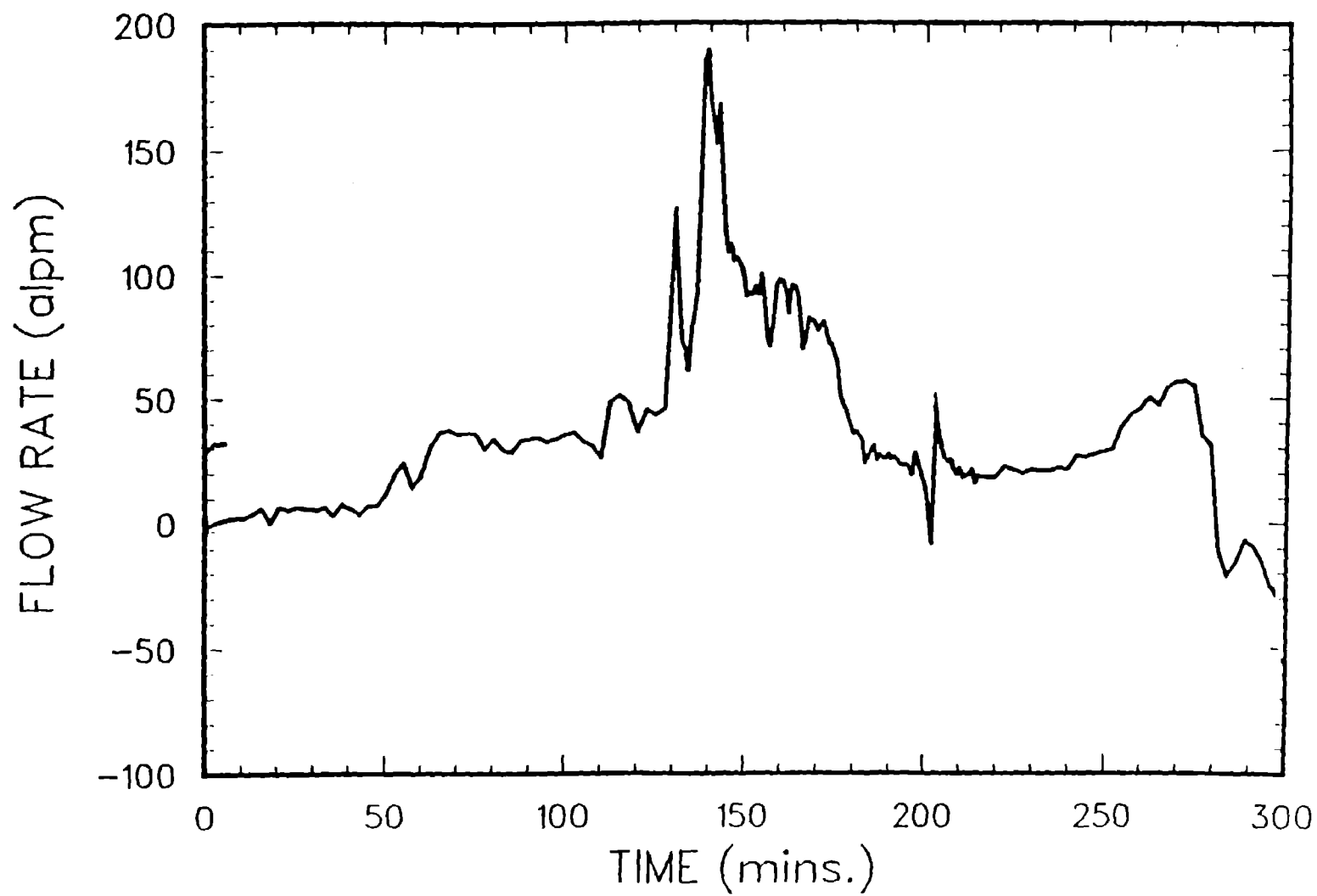
Figure 6.3.7 SURC-2 reaction gas flow - LFE

Data

Data

was found to be broadly distributed between about 0.5 to 20 micrometers aerodynamic particle diameter with a peak ranging from .2 to 4 micrometer. Its composition was dominated by sodium, potassium, and silicon from the concrete along with barium, molybdenum, and uranium from the charge materials. The aerosol concentrations measured during SURC-2 ranged from on the order of 15 to 300 g/m^3 STP.

Procedure

Sample gangs were initiated manually with the Modicon controller during the onset of erosion at 132 and 134 minutes, during the initial attack phase at 143 minutes, and during the reduced erosion period at 164 minutes. Each sample gang consisted of three sequential 30-second filter samples along with two 30-second impactor samples. Additional 30-second filter samples were taken between 139 to 141 minutes, 154 to 156 minutes, and 174 to 175 minutes. The pressure transducers giving flow indication were monitored at the control site and recorded on the data acquisition system. A cyclone sample was taken for a total of 5 minutes between 130 and 135 minutes.

The opacity meter operated for the duration of the test. Its output was monitored on the meter at the control site and recorded on the data acquisition system.

Pressure transducer outputs and thermocouple readings were recorded on the data acquisition system. The instrumentation and its calibration and operation has been discussed in Section 4.4. The aerosol mass was collected on filters, on impactor collection surfaces and in the cyclone. These masses were recovered and weighed after the test using procedures described in Section 4.4. Selected filter, impactor, and cyclone samples were submitted for elemental analysis using inductively coupled plasma spectroscopy.

Results

The sample times, sample flows, collected masses, dilution rates and calculated concentrations for the filter samples are given in Table 6.4.1. The same information for the impactors is given in Table 6.4.2. This information for the cyclone is given in Table 6.4.3. The flow was calculated from the system temperature and pressure and the flow control orifice calibration.

The voltage output from the opacity meter is plotted as a function of time in Figure 6.4.1 and Figure 6.4.2. Here voltage is used as an indicator of relative aerosol density. The higher the voltage, the greater the opacity and the higher the aerosol concentration.

The filter samples 1, 2, and 3 give good agreement on an aerosol concentration between 57 and 65 g/m^3 STP. The impactor samples taken at this time (E and F, 132.5 minutes) indicate higher aerosol concentrations of 202 to 245 g/m^3 with a substantial fraction of aerosol in a size range greater than 20 microns. This size distribution is shown in Figure 6.4.3. Particle diameters range from 0.5 to 25 microns and fall into two groups, one with a mean of 2.0 microns and the other with a mean of 20 microns.

Filter samples 4, 5, and 6 (134 minutes) show similar results at slightly higher concentrations. These filters indicate concentrations ranging from 59 to 69 g/m^3 STP. The concentrations indicated by the impactor samples (G and H, 134 minutes) are 179 and 315 g/m^3. The sizes of these aerosols (Figure 6.4.4) again range from 0.5 to 25 microns with a mean at 2.0 and at 20 microns.

Filter samples A, B, C, and D were taken at 139.5 to 141 minutes. These samples indicate higher concentrations of material which range from 75 to 124 g/m^3 STP. An average

Table 6.4.1 SURC-2 filter data

Filter Sample	On Time (min)	Duration (min)	Orifice Pressure (PSIA)	Orifice Flow (ALPM)	System Pressure (PSIA)	Diluter Gas Flow (ALPM)	Dilution Ratio	Total Mass (gm)	System Actual Mass conc (g/m³)	System Mass conc STP (g/m³)	Exhaust Actual Mass conc (g/m³)
1	132.0	0.5	12.00	11.28	12.50	13.78	2.87	0.09347	47.50	64.90	32.60
2	132.5	0.5	12.00	11.28	12.50	13.78	2.87	0.08270	42.03	57.50	28.80
3	133.0	0.5	12.00	11.28	12.50	13.78	2.87	0.09074	46.11	63.00	31.60
4	133.5	0.5	12.00	11.28	12.50	13.78	2.87	0.08433	42.86	58.60	29.40
5	134.0	0.5	12.00	11.28	12.50	13.78	2.87	0.08928	45.37	62.00	31.10
6	134.5	0.5	12.00	11.28	12.50	13.78	2.87	0.09565	48.61	66.50	33.30
A	139.5	0.5	12.00	11.80	13.50	12.72	2.26	0.25499	97.68	123.70	67.00
B	140.0	0.5	12.00	11.83	14.00	12.31	2.11	0.17456	62.18	75.90	42.70
C	140.5	0.5	12.50	11.83	14.00	12.31	2.11	0.17695	63.03	77.00	43.20
D	141.0	0.5	12.50	11.83	14.00	12.31	2.11	0.20865	74.32	90.70	51.00
7	143.0	0.5	12.50	11.86	14.50	11.92	1.99	0.19013	63.69	75.10	43.70
8	143.5	0.5	12.50	11.86	14.50	11.92	1.99	0.15148	50.74	59.80	34.80
9	144.0	0.5	12.50	11.83	14.00	12.31	2.11	0.16836	60.06	73.30	41.20
E	154.0	0.5	12.50	11.76	13.00	13.30	2.55	0.09999	43.31	56.90	29.70
F	154.5	0.5	12.50	11.76	13.00	13.30	2.55	0.08968	38.85	51.10	26.70
G	155.0	0.5	12.50	11.76	13.00	13.30	2.55	0.09000	38.98	51.20	26.70
H	155.5	0.5	12.50	11.76	13.00	13.30	2.55	0.08563	37.09	48.80	25.40
10	163.5	0.5	12.50	11.76	13.00	13.30	2.55	0.08775	38.01	50.00	26.20
11	164.0	0.5	12.50	11.76	13.00	13.30	2.55	0.07384	31.98	42.00	21.90
12	164.5	0.5	12.50	11.76	13.00	13.30	2.55	0.07673	33.24	43.70	22.80
I	174.5	0.5	12.50	11.76	13.00	13.30	2.55	0.02632	11.40	15.00	7.80
J	175.0	0.5	12.50	11.76	13.00	13.30	2.55	0.04520	19.58	25.70	13.40

Presep   0.11650

Total Mass (gm)

Dilution Gas   N2

System Temp   343 K
Exhaust Temp   500 K
Orifice Temp   298 K

Table 6.4.2 SURC Test 2 impactor data

	Stage	IMPACTOR E mass (gm)	IMPACTOR F mass (gm)	IMPACTOR G mass (gm)	IMPACTOR H mass (gm)	IMPACTOR J mass (gm)	IMPACTOR K mass (gm)	IMPACTOR N mass (gm)	IMPACTOR O mass (gm)
	Presep	0.04955	0.05418	0.01147	0.07933	0.08322	0.02030	0.02143	0.00097
	1	0.00183	0.00165	0.00072	0.01770	0.00953	0.00173	0.00144	0.00061
	2	0.00353	0.00143	0.00107	0.00605	0.00456	0.00245	0.00101	0.00080
	3	0.00413	0.00235	0.00195	0.01309	0.00876	0.00991	0.00183	0.00199
	4	0.00330	0.00459	0.00419	0.01682	0.01342	0.02280	0.00344	0.00698
	5	0.01208	0.01759	0.01294	0.03716	0.02833	0.03843	0.01289	0.03204
	6	0.04059	0.05116	0.04319	0.05452	0.04500	0.05061	0.02172	0.02456
	7	0.02833	0.04525	0.02292	0.03744	0.03134	0.02039	0.01693	0.00427
	8	0.01637	0.00020	0.01693	0.01844	0.01662	0.00778	0.00901	0.00090
	backup	0.01208	0.01313	0.01011	0.01790	0.01637	0.00143	0.02434	0.00150
	Total	0.17179	0.19153	0.12549	0.29845	0.25715	0.17583	0.11404	0.07462
Sample Time (on)		132.5 min	132.5 min	134.0 min	134.0 min	143.5 min	143.5 min	164.0 min	164.0 min
Sample Duration (min)		0.50	0.50	0.50	0.50	0.50	0.50	0.50	0.50
Orifice Temp (K)		298	298	298	298	298	298	298	298
System Pressure (PSIA)		12.5	12.5	12.5	12.5	14.5	14.5	13.0	13.0
Orifice Flowrate (ALPM)		11.51	15.57	11.51	15.57	15.76	11.65	15.62	11.54
Diluter 1 Orifice Pressure (PSIA)		30.50	30.50	30.50	30.50	30.50	30.50	30.50	30.50
Diluter 2 Orifice Pressure (PSIA)		32.50	32.50	32.50	32.50	32.50	32.50	32.50	32.50
Diluter 1 Gas Flow (ALPM)		13.78	13.78	13.78	13.78	11.92	11.92	13.30	13.30
Diluter 2 Gas Flow (ALPM)		17.63	17.63	17.63	17.63	15.25	15.25	17.02	17.02
Dilution Ratio Total		8.212	8.212	8.212	8.212	4.481	4.481	6.821	6.821
Dilution Gas Composition		N2	N2	N2	N2	N2	N2	N2	N2
Mass Conc Acutal (g/m^3)		245.13	202.01	179.07	314.78	146.23	135.26	99.60	88.21

Table 6.4.3 SURC Test 2 cascade cyclone data

Cyclone Type	Cyclade Six Stage
Orifice Temp (K)	298.0
Orifice Pressure	12.0
Sampler	PSIA
Flow Rate	22.8
Sample Duration	LPM
Sample Time	5.0
(ON)	MIN
	130.5
	MIN

STAGE	MASS (gm)
1	0.40767
2	2.29835
3	2.24979
4	0.31270
5	0.33428
6	0.23793
Backup Filter	0.00000
TOTAL	5.84072
Mass Concentration	51.32443 gm/m^3
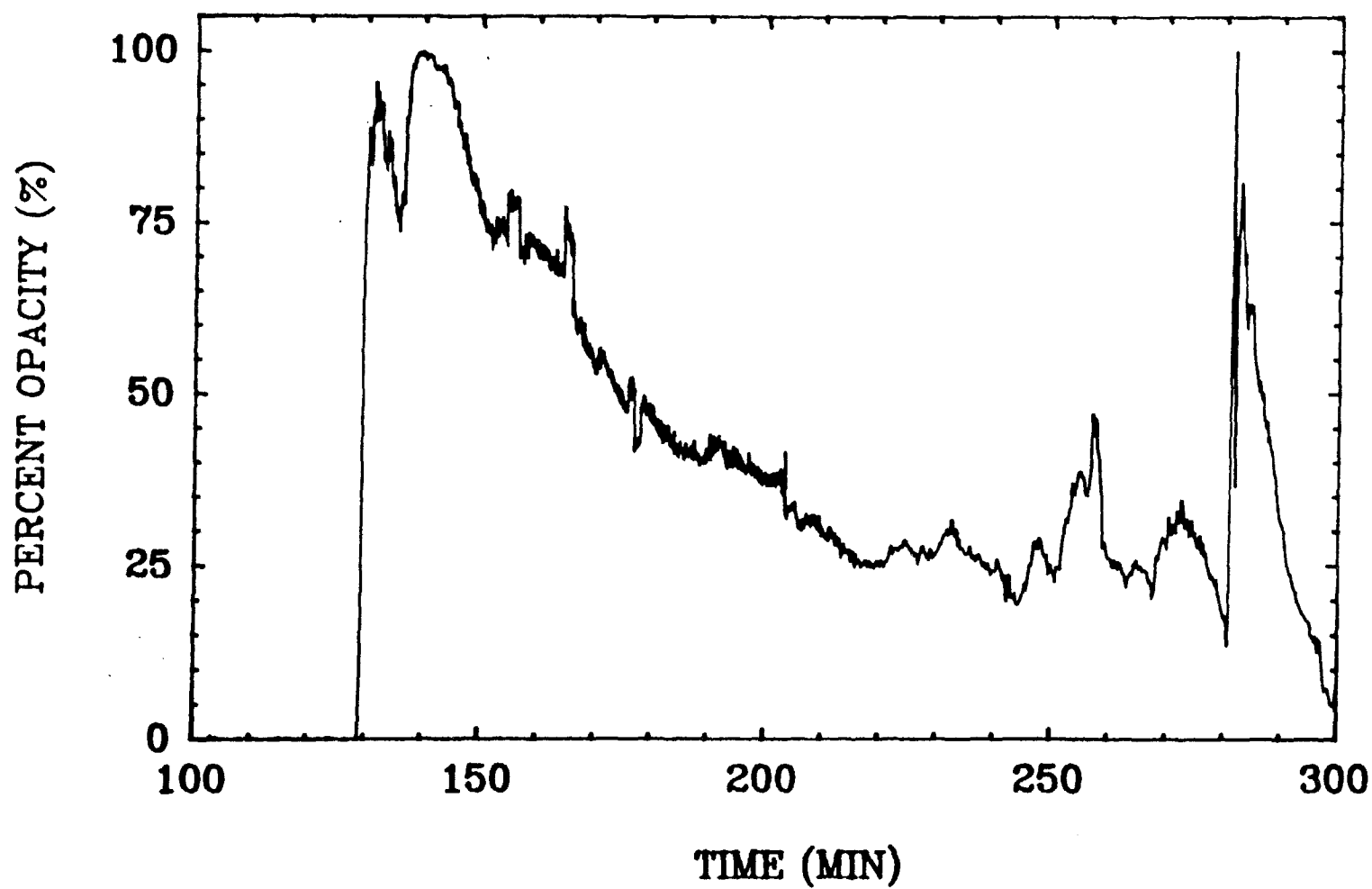
Figure 6.4.1 Opacity meter output for SURC-2 test. Voltage level is directly proportional to aerosol concentration.
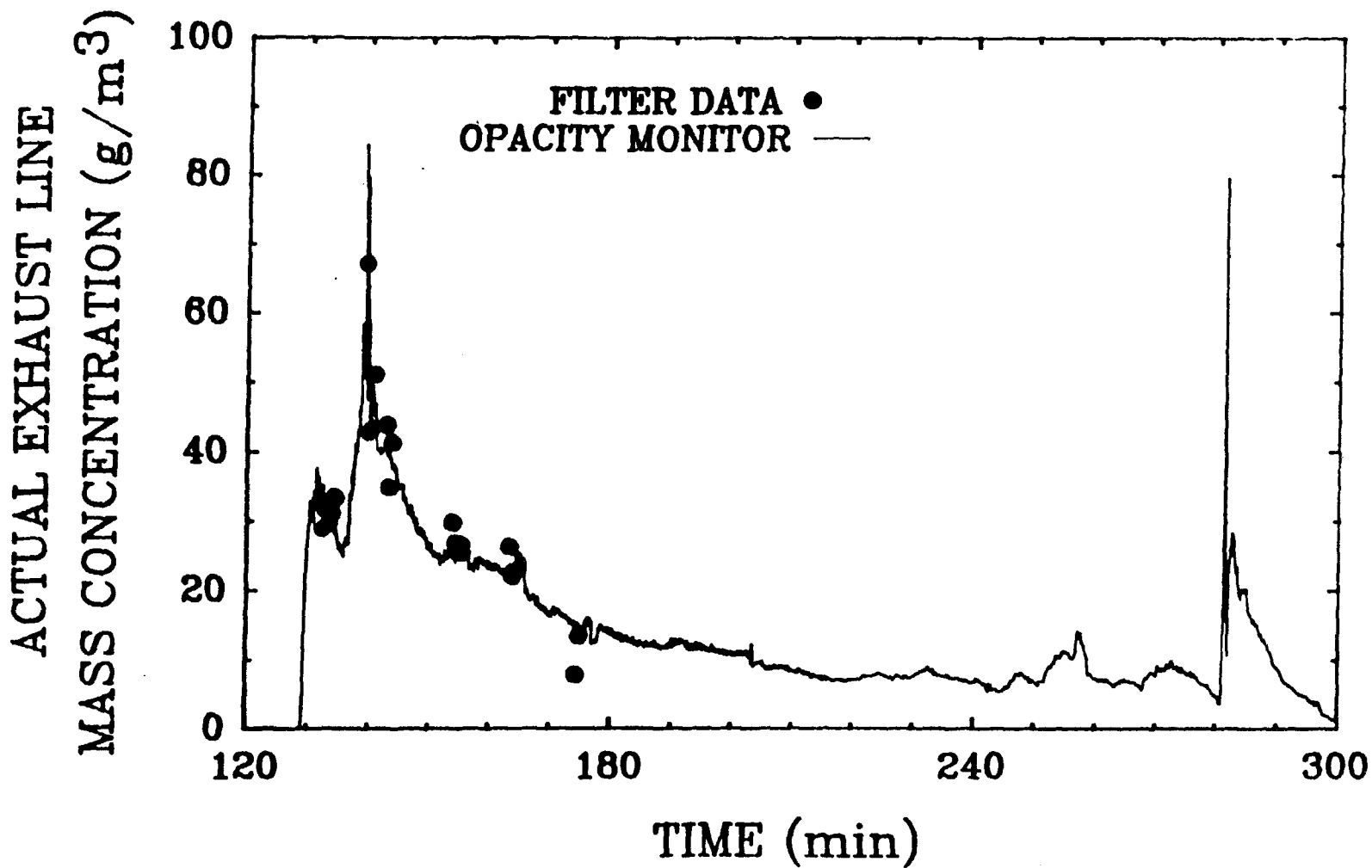
Figure 6.4.2 Measured aerosol concentrations for SURC-2 test. These are compared to opacity meter output as a function of time.
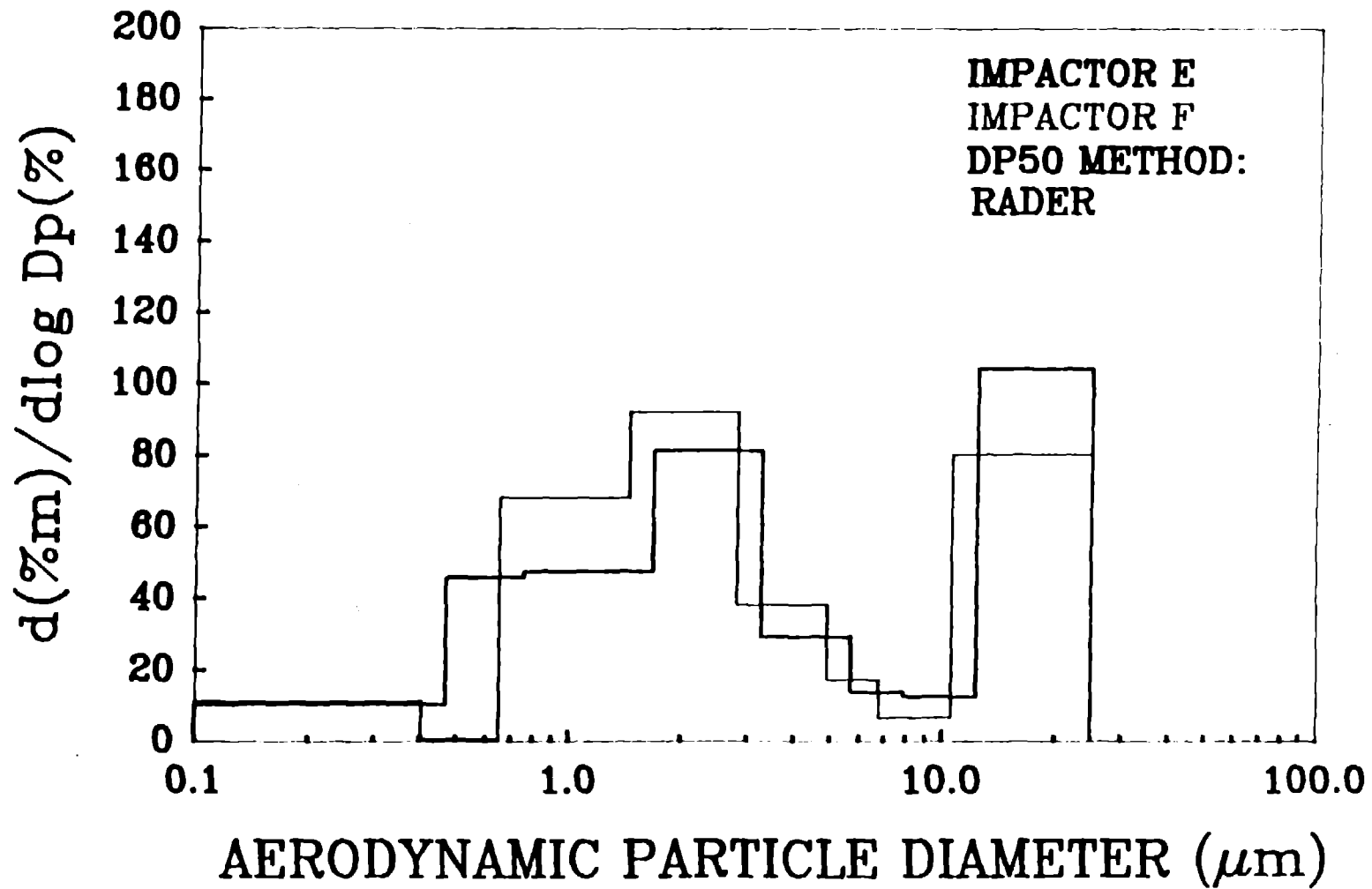
Figure 6.4.3   SURC-2 aerosol size distribution.   Normalized aerosol mass distributions from impactors E and F taken at 132.5 minutes.
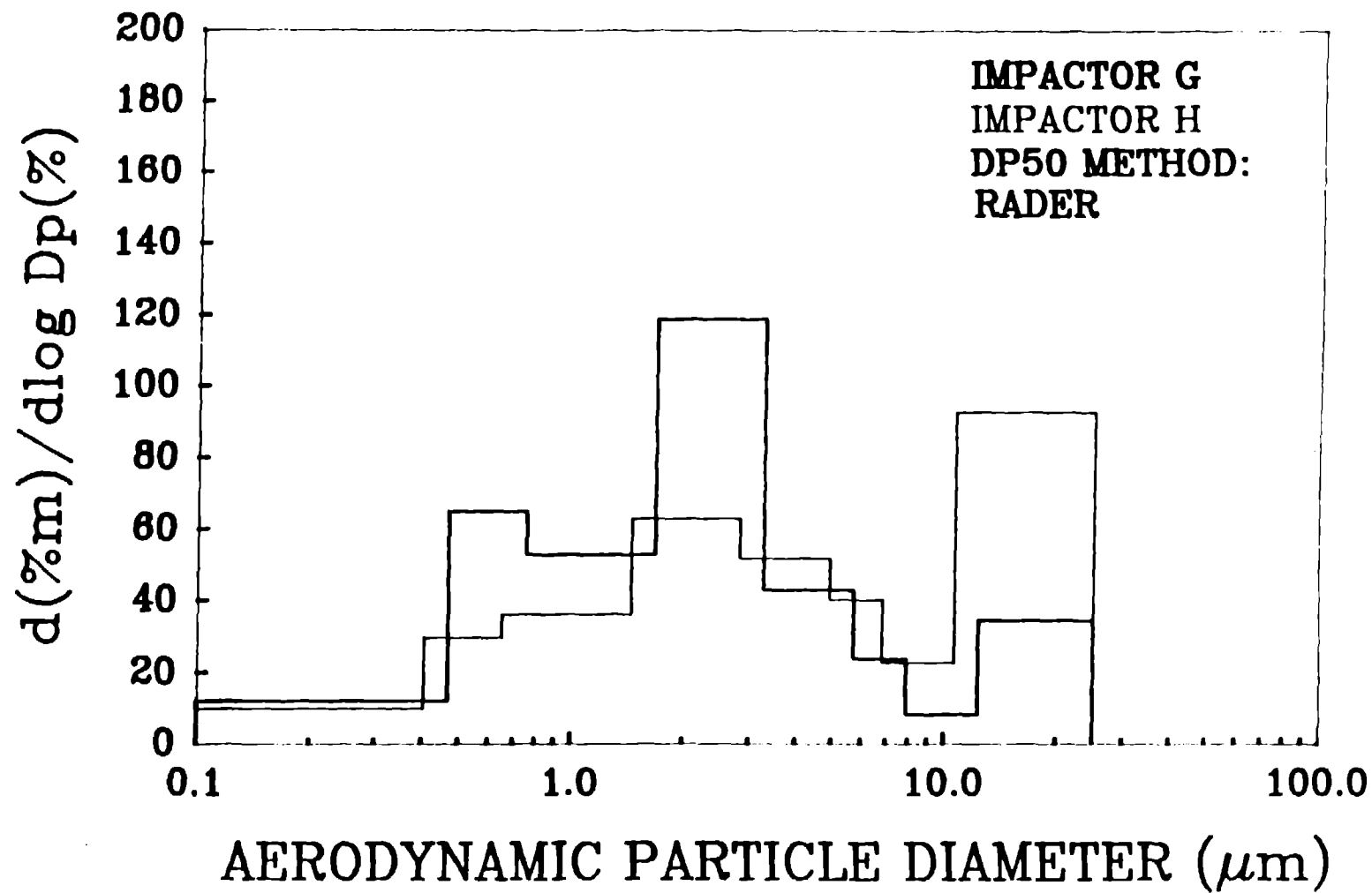
Figure 6.4.4   SURC-2 aerosol size distribution.   Normalized aerosol mass distributions from impactors G and H taken at 134 minutes.

concentration of 92 g/m^3 STP with a standard deviation of 15 g/m^3 STP is calculated using all four results.

Filter samples 7, 8, and 9 (143-144 minutes) show lower concentrations ranging from 60 to 73 g/m^3 STP. The impactors J and K (143.5 minutes) indicate concentrations of 135 to 146 g/m^3. The opacity meter (Figure 6.4.1) shows that the peak concentration aerosols were released at around 140 minutes and that the source term declines at times after 140 minutes. This observation is consistent with the filter and impactor data. The size distribution (Figure 6.4.5) for the aerosols measured at 143 minutes ranged from 0.5 to 25 microns with a mean at about 5 microns.

Filter samples E, F, G, and H were taken at 154 to 155 minutes. These samples indicate a declining aerosol concentration of 48 to 56 g/m^3 STP.

The filter samples 10, 11, and 12 (164 minutes) range from 42 to 50 g/m^3 STP. Impactor samples N and O were taken at the same time and indicate concentrations of 88 to 100 g/m^3. The size distribution is shown in Figure 6.4.6. The fraction of aerosols in the larger particle diameters is lower in these later aerosol samples. The mean diameter is now shown at 3 microns and there appears to be only one mode of primary response.

The last filter samples, I and J, were taken at 175 minutes. Concentrations at this time have dropped to 15 to 26 g/m^3. Figure 6.4.2 compares the opacity meter output to the filter sample results. Aerosol release is seen to be continuous throughout the time of concrete ablation with the peak concentrations being at earlier times when both melt temperatures and gas release rates were at their highest levels.

The cyclone sample was taken for five minutes between 130 to 135 minutes. An average concentration of 51 g/m^3 was recorded for the six collection stages. The size distribution for aerosols collected in the cyclone are presented in Figure 6.4.7. This shows a large amount of material in the 2 to 25 micron size range with a mean at 3.5 microns which is generally consistent with the impactor results.

Elemental analysis using inductively coupled plasma spectroscopy was performed on the six cyclone stages and on selected filter samples. The results are given in Table 6.4.4. All of the samples show large amounts of Na, K, Si, and Mg from the concrete and crucible materials. The fission product materials of Ba and Mo are also present in significant quantities as are W and U from the meltpool. Little or no traces of Nb and La were found and Ce was barely detectable. Where no element was detected, the result is given as less than the detectable threshold for the element on that sample. An elemental distribution with respect to time for the combined aerosol source term is given in Figures 6.4.8 and 6.4.9.
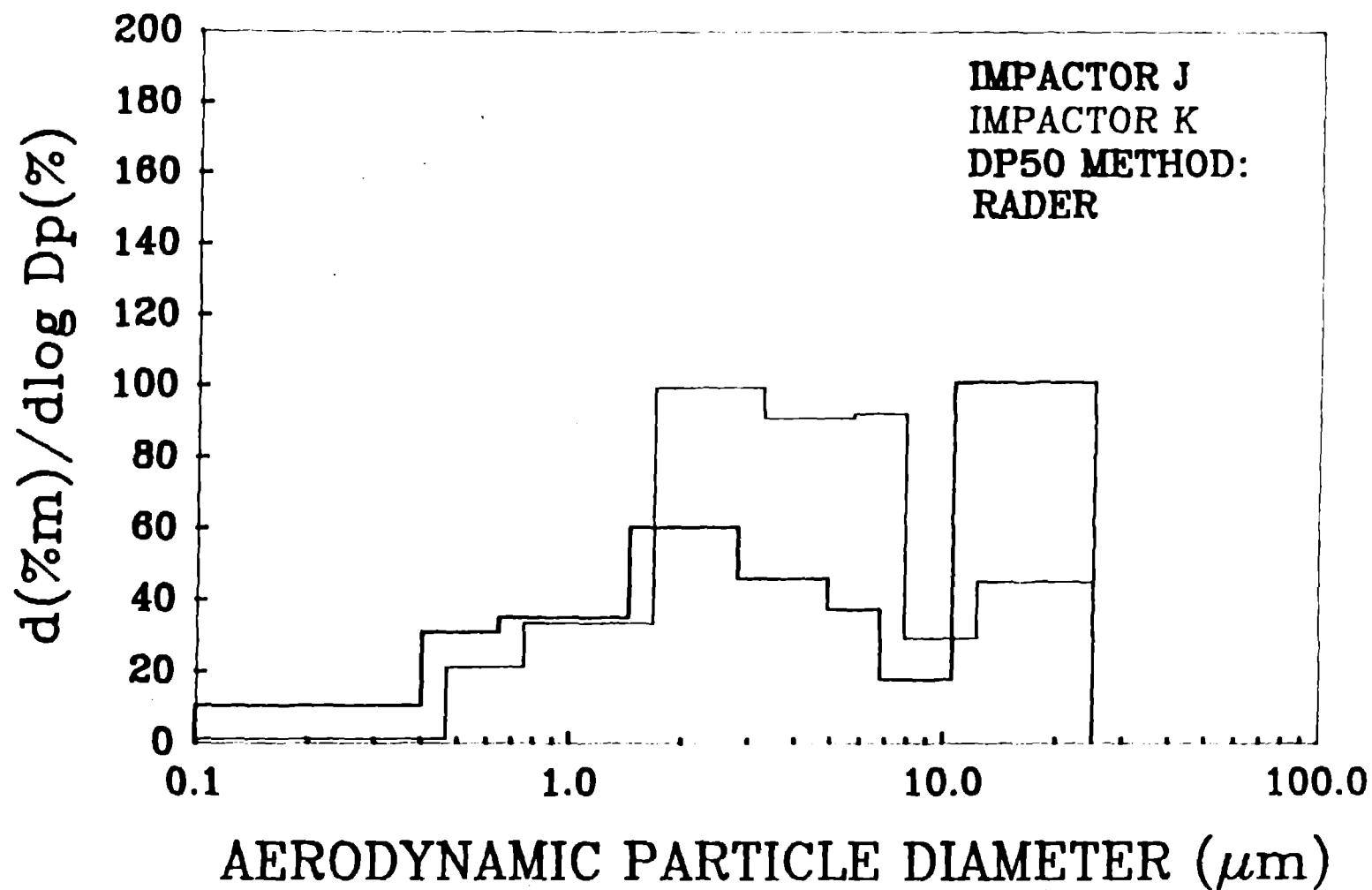
Figure 6.4.5 SURC-2 aerosol size distribution. Normalized aerosol mass distributions from impactors J and K taken at 143.5 minutes.
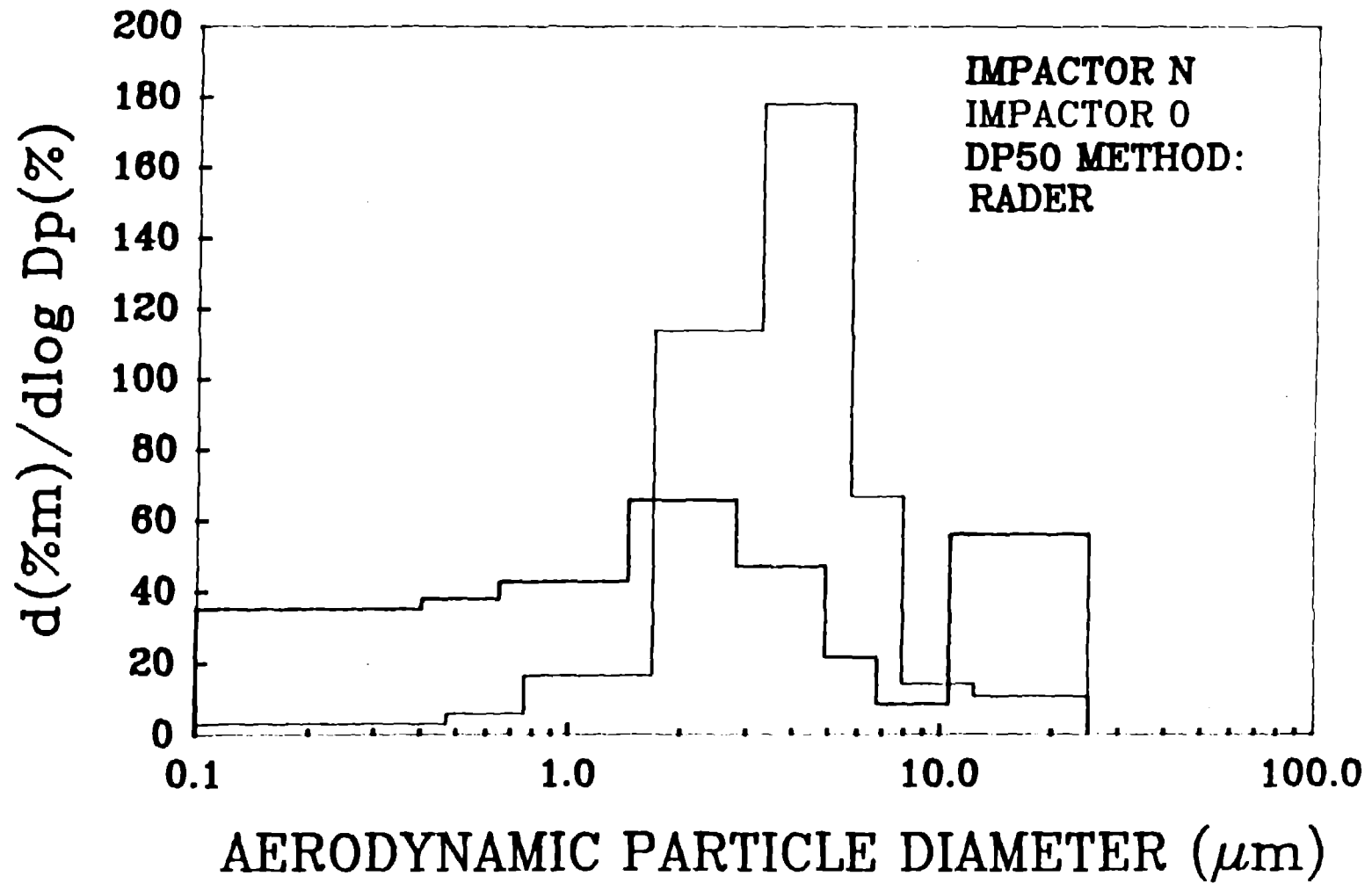
Figure 6.4.6   SURC-2 aerosol size distribution. Normalized aerosol mass distributions from impactors N and O taken at 164 minutes.
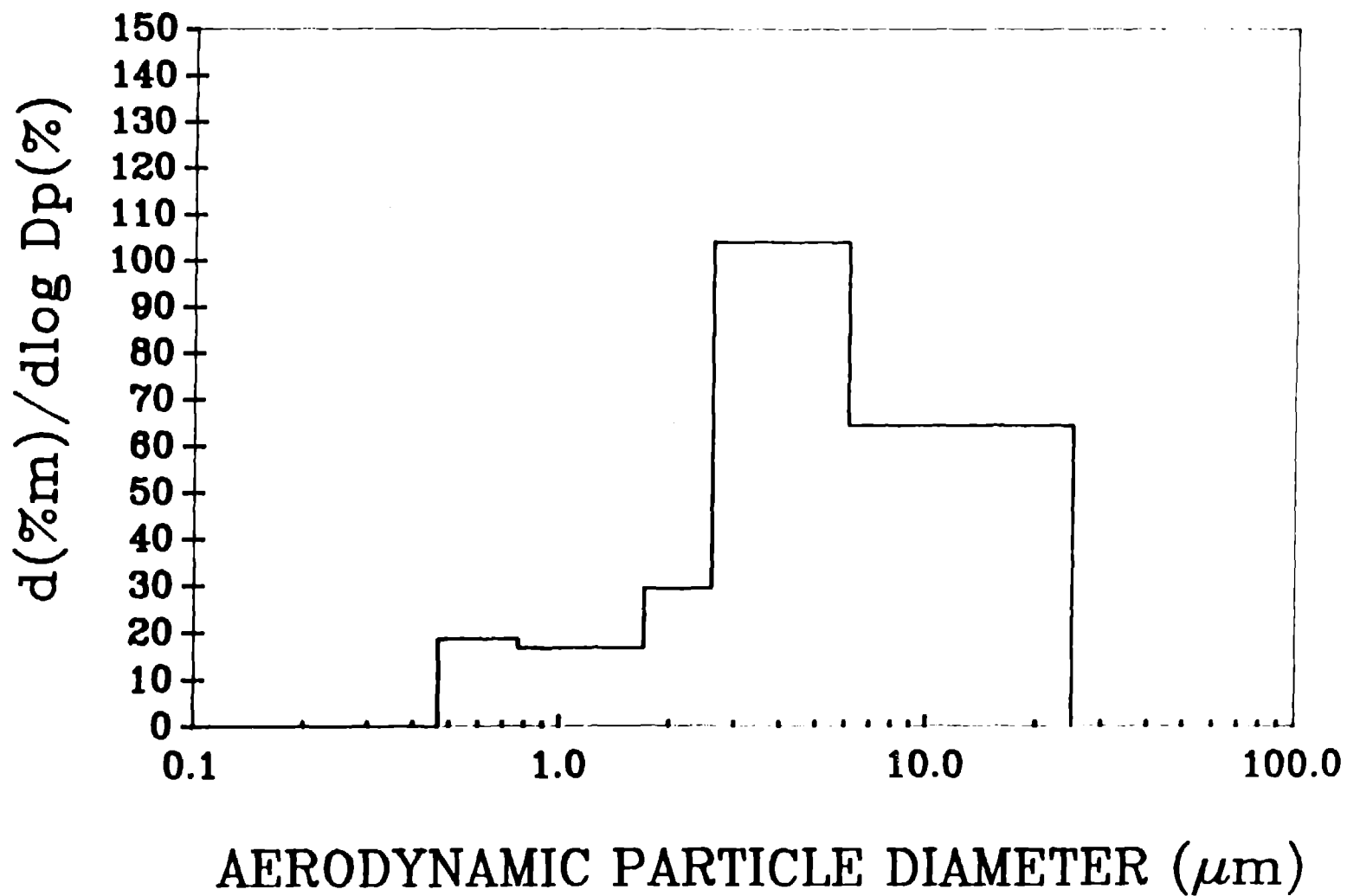
Figure 6.4.7   SURC-2 aerosol size distribution.   Normalized aerosol mass distribution from cyclone taken from 130 to 135 minutes.

Table 6.4.4 Elemental analysis of SURC-2 aerosol. Weight percent of element in sample.

Sample	Ba	Ca	Ce	Cl	K	La	Mg	Mo	Na	Nb	Si	U	W	Zr
Cyclone 1	.035	.010	.001	.88	9.00	.009	.47	.054	33.3	<.001	5.91	.18	4.88	.010
Cyclone 2	.050	<.005	.002	.96	7.60	.012	2.11	.020	31.0	<.001	23.7	.15	2.36	.011
Cyclone 3	.048	<.005	.001	.81	5.76	.001	1.58	.008	27.0	<.001	16.2	.14	.08	.007
Cyclone 4	.041	<.005	.003	.90	10.9	<.001	2.00	.004	14.6	<.001	37.6	.13	.02	.004
Cyclone 5	.037	<.005	.002	.76	6.73	<.001	1.94	.004	14.5	<.001	30.7	.13	.03	<.001
Cyclone 6	.033	.033	.001	.72	5.07	<.001	1.61	.004	44.9	<.001	15.9	.09	.02	<.001
Filter 2	.058	<.005	.003	1.56	5.00	<.001	2.10	.005	25.3	<.001	23.9	.17	.058	.022
Filter 4	.057	<.005	.002	1.62	4.81	<.001	2.10	.004	25.9	<.001	24.0	.16	.046	.016
Filter 6	.045	<.005	.001	1.98	3.35	.012	1.89	.007	25.1	<.001	19.2	.10	.070	.001
Filter 9	.029	<.005	<.001	.95	4.30	.007	1.92	.021	27.2	<.001	21.8	.31	2.41	<.001
Filter 11	.009	<.005	<.001	1.60	7.24	.002	.72	.36	10.3	<.001	9.39	.26	26.3	<.001
Filter H	.016	<.005	<.001	.90	29.1	.003	1.18	.10	11.8	<.001	14.5	.22	13.5	<.001
Filter J	.002	1.35	<.001	1.74	1.25	<.001	.01	.37	6.29	<.001	21.0	.26	31.5	<.001
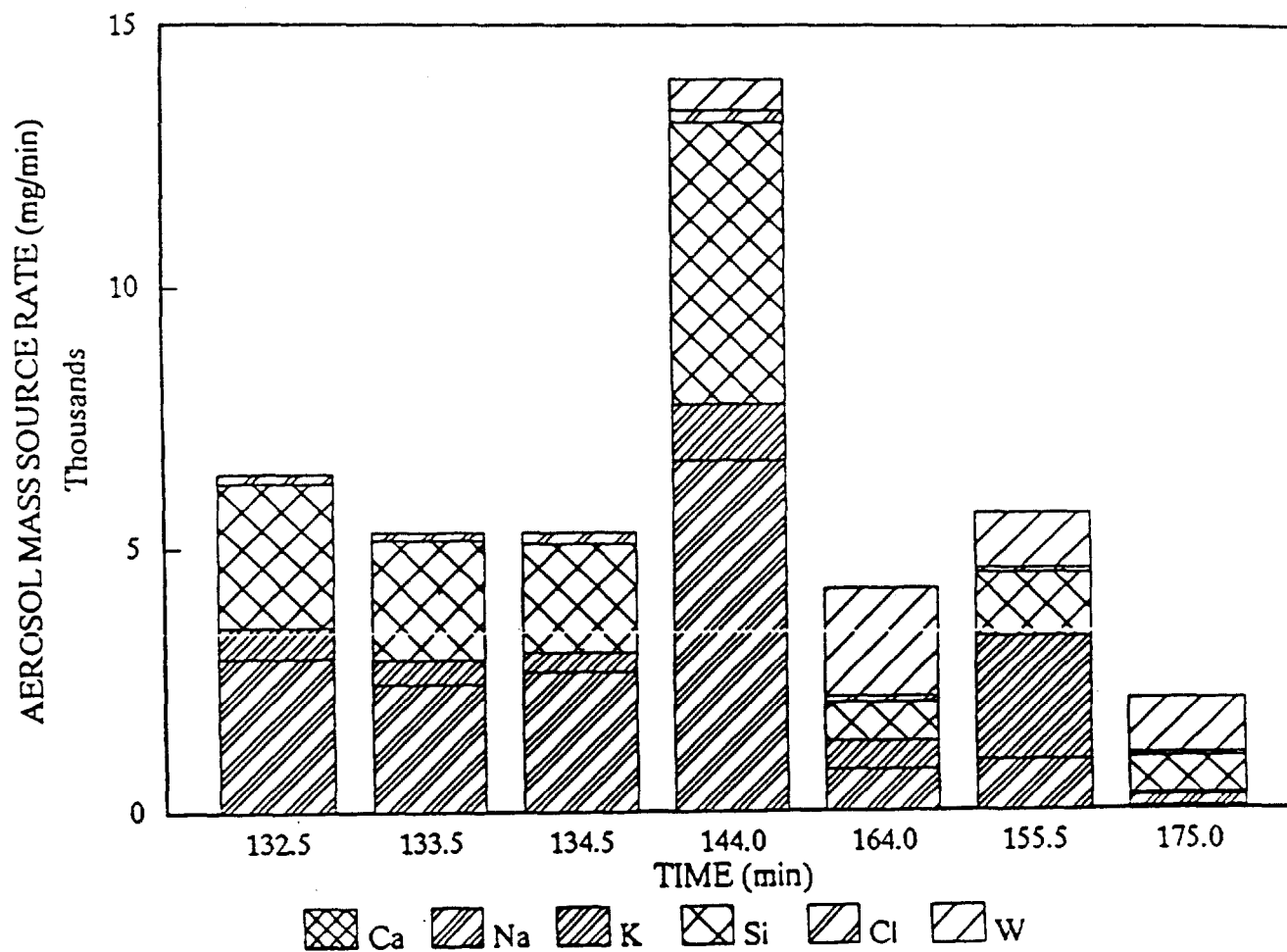
Figure 6.4.8 SURC-2 elemental source term distribution

Data
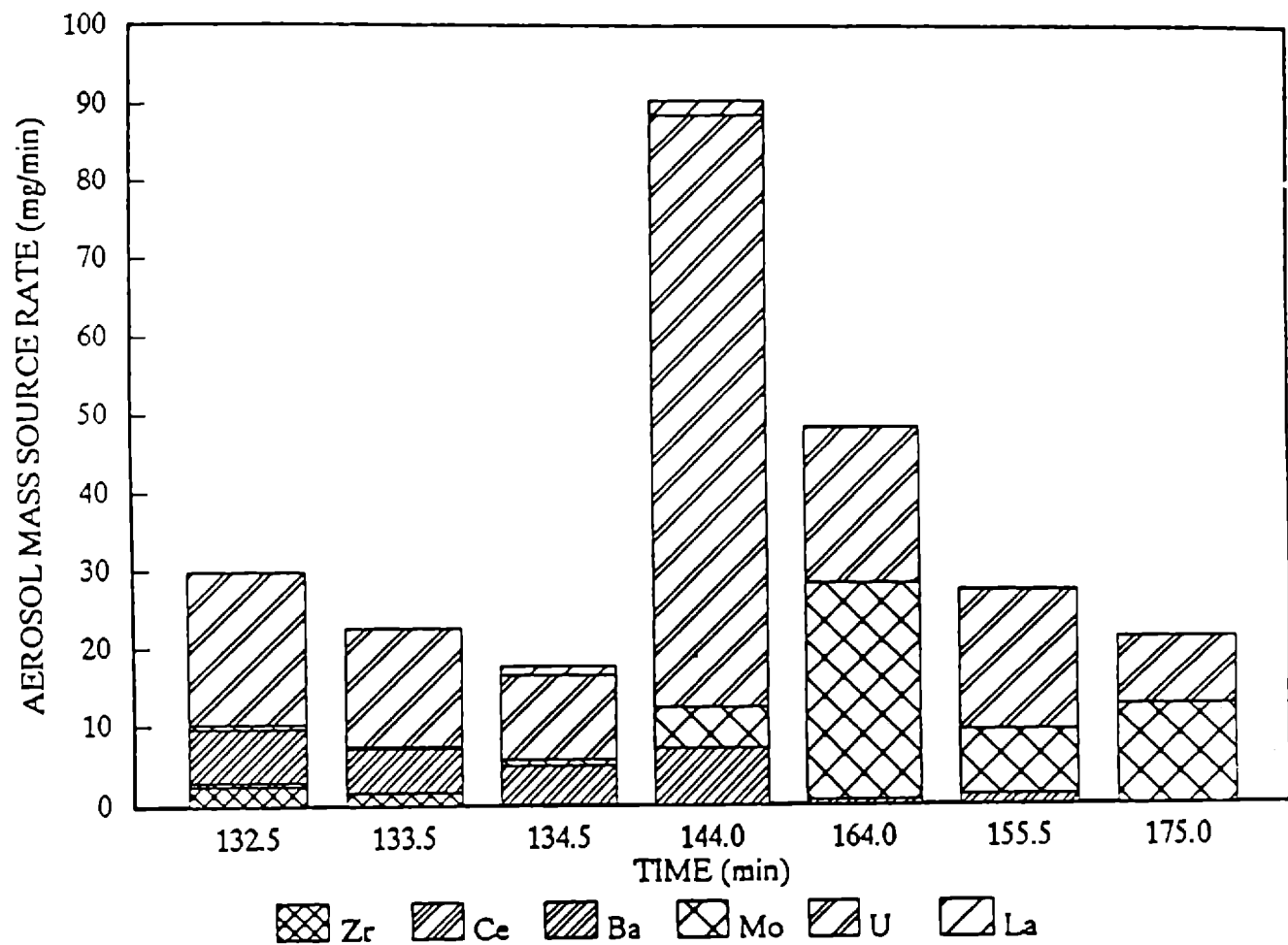
Figure 6.4.9 SURC-2 elemental source term distribution

7.0 Test Summary and Conclusions

The SURC-2 experiment was a molten material/concrete interaction test designed to sustain a melt of 203.9 kg of depleted uranium oxide, zirconium metal and zirconium oxide in a magnesium oxide crucible with a basaltic concrete bottom. The goals of the experiment were to measure in detail the gas evolution, aerosol generation, and erosion characteristics associated with molten oxide-concrete interactions.

The charge material in SURC-2 was a mixture of 69 w/o UO_2-22 w/o ZrO_2 - 9 w/o Zr. Additionally, 3.4 kg of fission product stimulants were added to the melt to study fission product release. The SURC-2 experiment was conducted in a 60 cm diameter interaction crucible constructed with a 40 cm basaltic concrete cylinder in the base of a magnesium oxide (MgO) annulus. A 10-cm-thick cover of MgO was placed on top of the crucible. The interaction crucible and an induction coil were housed in a sealed, water cooled, aluminum containment vessel which was 180 cm high and 120 cm in diameter. Exhaust ports in the crucible and in the containment vessel directed the reaction products through flow and aerosol sampling instrumentation. The interaction crucible was instrumented with thermocouple arrays cast into the concrete cylinder, MgO annulus, and MgO cover. A 280 kW induction power supply was used to heat tungsten rings placed in the charge which in turn heated, melted, and sustained the oxide-concrete interaction. Flow rates of generated gases were measured using a sharp-edged orifice, a laminar flow element, a turbine meter, and two dry gas clocks. Gaseous effluents produced during the experiment were monitored and sampled using an infrared gas analyzer, a mass spectrometer, and by an integral grab sample technique. Aerosols were captured on filters, cascade impactors, and a cascade cyclone. Concrete erosion characteristics were measured using type K, S, and C thermocouples. Three tungsten thermowells containing optical pyrometers were embedded in the charge in order to define the meltpool temperature. The apparatus was purged with argon gas in order to direct the majority of the reaction gas and aerosol effluents through a 5 cm diameter flow pipe. The SURC-2 test was run at local atmospheric pressure (.83 atm) and at an ambient temperature of 25°C.

The SURC-2 test ran for a total of 280 minutes. A data summary is given in Table 7.1. A total of 35 cm of basaltic concrete was eroded during the final 150 minutes of the experiment. Figure 7.1 shows a net power of 61 kW was applied to the tungsten susceptors to sustain the initial interaction between 120-220 min. This was increased to a net power of 84 kW for the final portion (220-280 min) of the test.

Four time periods during the test are of particular interest. These are the onset of gas release from the concrete between 50 to 130 minutes, the initial rapid erosion period between 130 and 160 minutes, the slowed erosion period after Zr depletion between 160 and 220 minutes, and the increased erosion following the power increase from 140 kW (gross) to 190 kW at 220 minutes, which lasted until the termination of the test at 280 minutes.

During the initial heatup period between 50 and 130 minutes, the temperature of the oxide charge, as shown in Figure 7.2, increased from 750 K to 2500 K and it began to melt. Figure 7.3 shows that the concrete basemat started to dehydrate during this time at an average rate of 5.4 cm/hr. This produced a reaction gas flow rate of 26 slpm (31 alpm) as shown in Figure 7.4. The composition of this initial effluent gas was 70 to 80% H_2-5 to 15% H_2O-10 to 20% CO. No aerosol samples were taken during this period and the opacity meter did not register an aerosol density above its threshold of 10 g/m^3.

Concrete erosion began after 130 minutes when the oxide charge became completely molten. The ZrO_2 insulator board separating the UO_2-ZrO_2-Zr material from the concrete was incorporated into the melt between 120-130 minutes, thus initiating the attack. The meltpool

Table 7.1 SURC-2 data summary

	Early (with Zr)	Mid (without Zr)	Late (without Zr)
Time	130-160 min	160-220 min	220-280 min
Power setting	Total 140 kW Charge 61 kW	Total 190 kW Charge 84 kW	Total 190 kW Charge 84 kW
Melt temperature	2700-2100 K	2100-2050 K	2050-2150 K
Erosion rate	30 cm/hr	5 cm/hr	15 cm/hr
Gas flow	110 slpm	20 slpm	50 splm
Gas composition	75% H_2-5% H_2O 15% CO-50% CO_2	70% H_2-5% H_2O 15% CO-10% CO_2	75% H_2-5% H_2O 15% CO-5% CO_2
Aerosol density	90 g/m^3	50 g/m^3	40 g/m^3

temperatures at 130 minutes were 2650 to 2720 K (Figure 7.5). These temperatures decreased to 2100 K, at 160 minutes when 15 cm of concrete were eroded at a rate of 20-40 cm/hr as shown in Figure 7.6. The reaction gas flow rate between 130 and 160 minutes averaged 113 slpm (136 alpm)(Figure 7.4) and had a typical composition of 75% H_2-5% H_2O - 15% CO-5% CO_2 (Table 6.2.2). Seventeen aerosol filter samples (Table 6.4.1), six impactor samples (Table 6.4.2), and a cyclone sample (Table 6.4.3) were taken during this period. These samples indicated aerosol densities ranging from 50-300 g/m^3 and were rich in silicon, sodium, potassium, barium, molybdenum, and uranium (Table 6.4.4). The size distribution of these aerosols ranged from .5 to 20 microns with a mass mean diameter at 3 microns as shown in Figures 6.4.3 through 6.4.5 and 6.4.7.

Between 160 and 220 minutes the erosion rate dropped from 20-40 cm/hr to 5 cm/hr (Figure 7.6) after all of the Zr metal had been oxidized. The meltpool temperatures during this period ranged from 2050 to 2100 K (Figure 7.5) as an additional 5 cm of concrete were eroded. The

reaction gas flow rate decreased to 20 slpm (24 alpm) (Figure 7.4) and had a typical composition of 70% H_2-5% H_2O-15% CO-10% CO_2 (Table 6.2.2). Two aerosol impactor samples and five filter samples were taken during this period yielding aerosol densities ranging from 90 to 15 g/m^3. These aerosols were predominantly in the 1-10 micron range and had a mass mean diameter of 4 microns as shown in Figure 6.4.6. Traces of calcium and tungsten were found in these later samples in addition to abundant amounts of uranium, molybdenum, silicon, sodium, and potassium (Table 6.4.4).

At 220 minutes, the gross power to the charge was increased from 140 kW to 190 kW (Figure 7.1). This resulted in higher erosion rates, higher gas release rates, and higher pool temperatures. The meltpool temperature increased from 2050 K to 2150 K (Figure 7.5) during the final 60 minutes of the test. The erosion rate increased from 5 cm/hr to 15 cm/hr (Figure 7.6) as an additional 15 cm of concrete were eroded bringing the total erosion to 35 cm. The reaction gas flow rate went from 15 to 39 slpm (18 to 41 alpm) and the gas composition

151
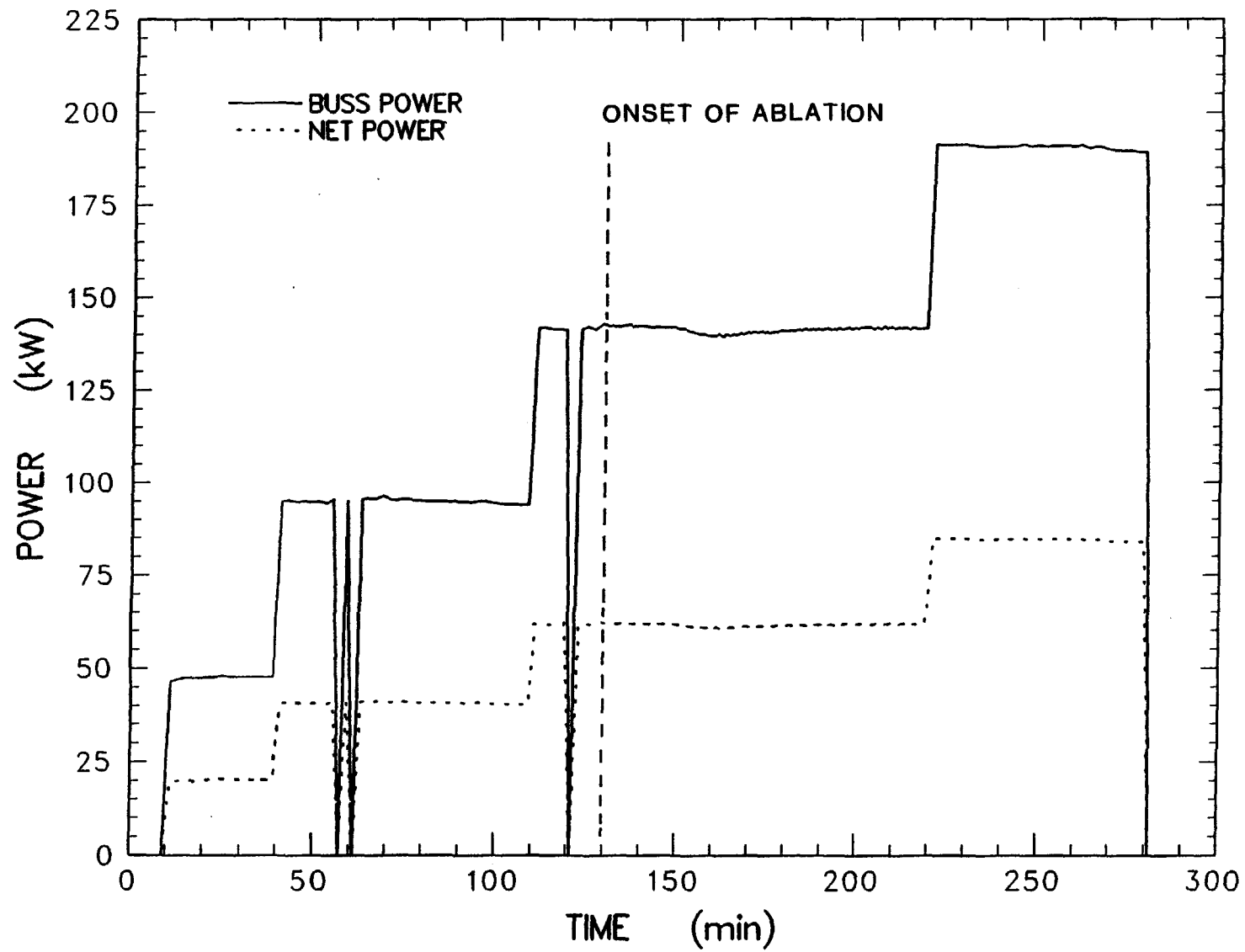
Figure 7.1 Total and net power histories for SURC-2
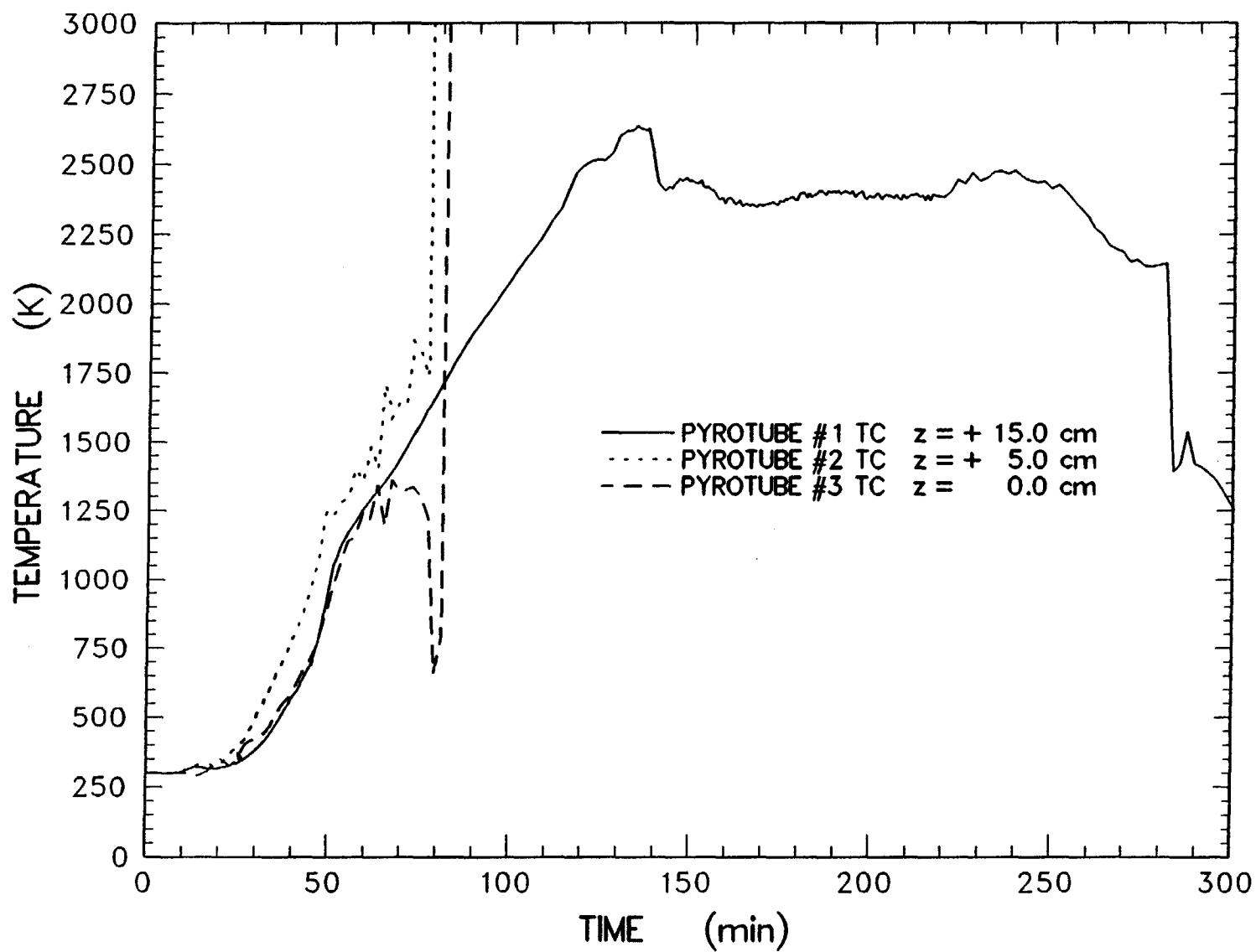
Figure 7.2   Thermal response of the charge measured by type C thermocouples installed in the tungsten pyrotubes
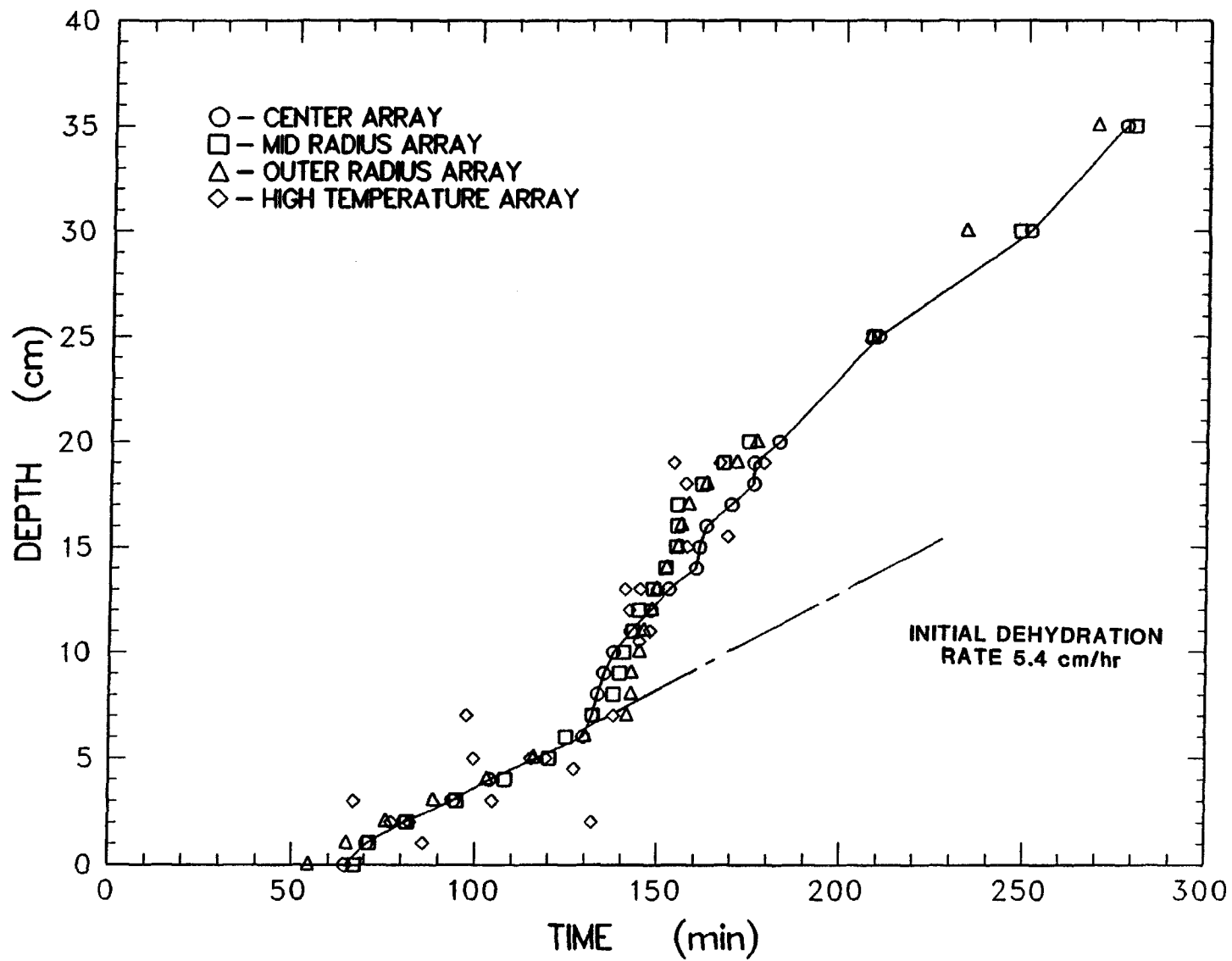
Figure 7.3 Location of the dehydration front for SURC-2
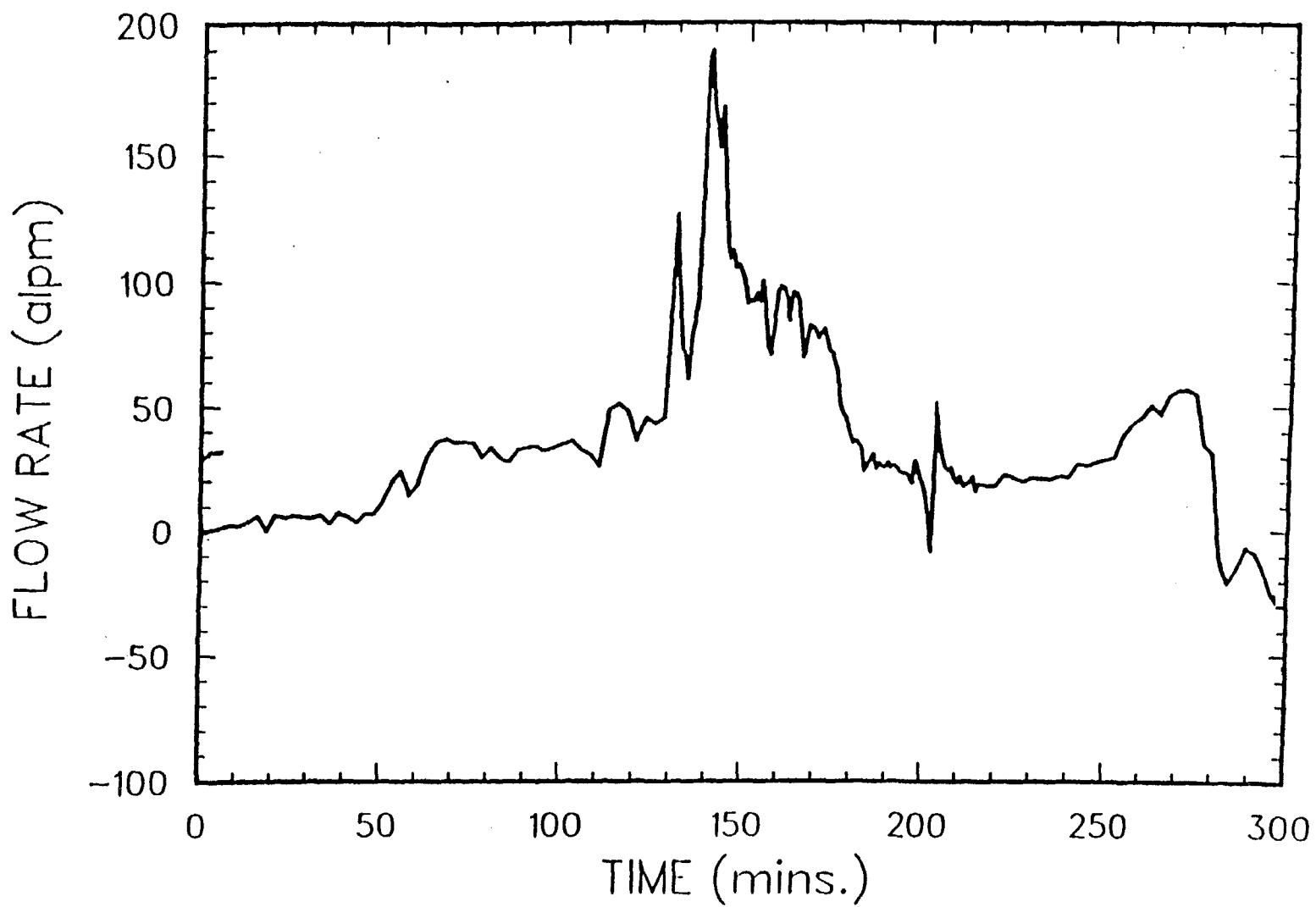
Figure 7.4 Reaction gas flow rate taken from LFE data
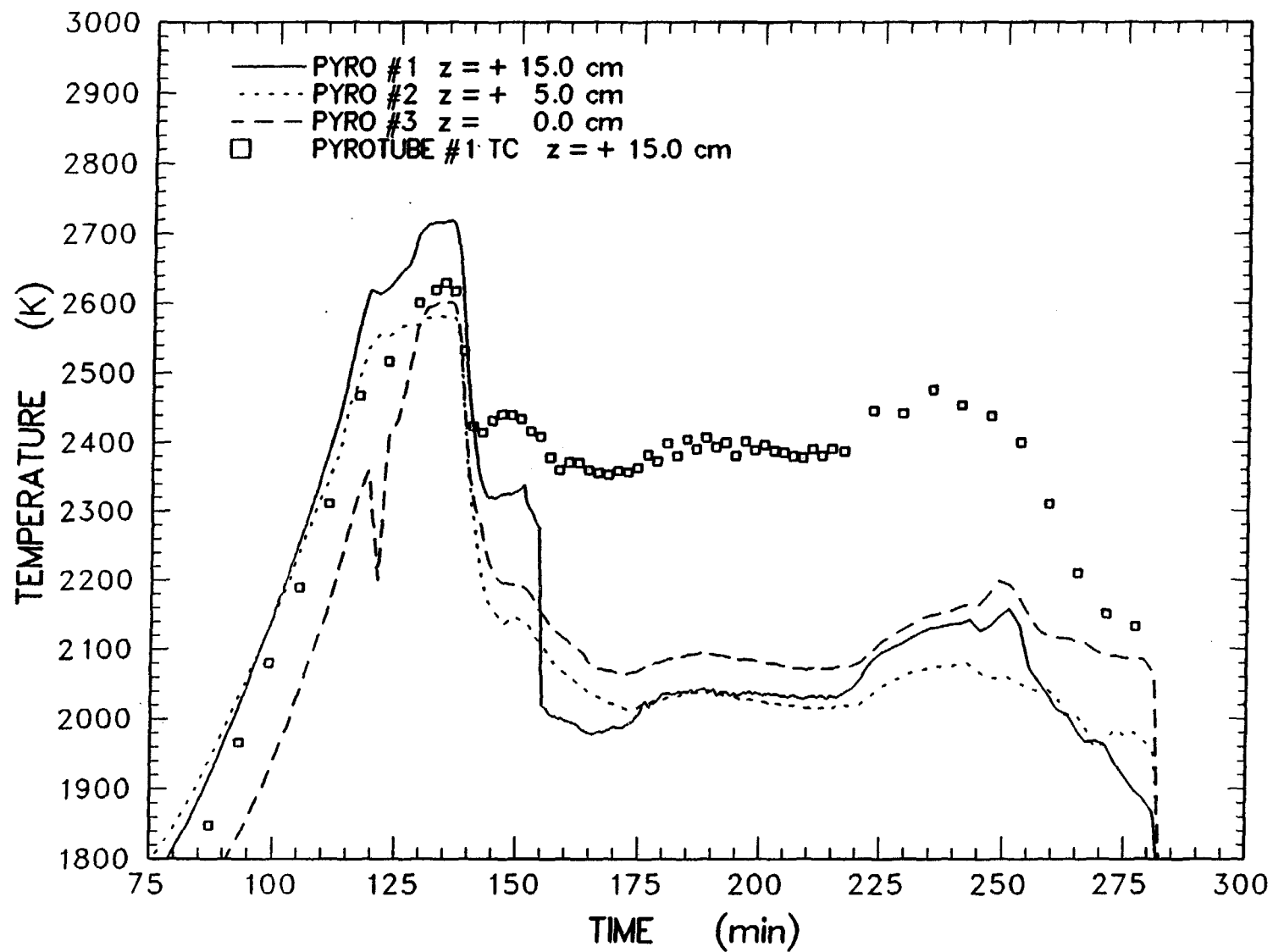
Figure 7.5 Melt pool temperatures indicated by the fiber optic pyrometers
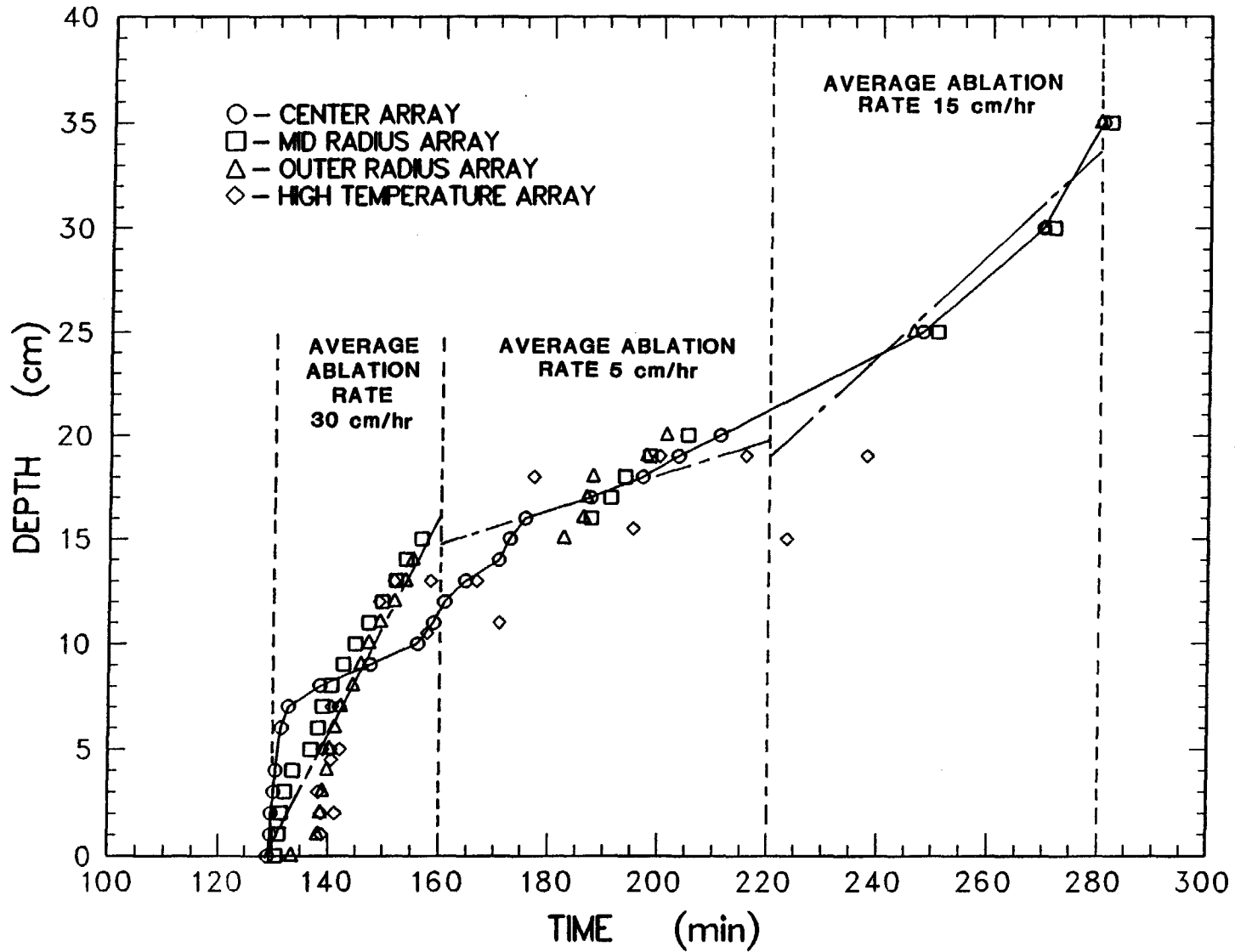
Figure 7.6 Location of the ablation front and average ablation rates during different phases of the experiment

was 75% H_2-5% H_2O-15% CO-5% CO_2 (Table 6.2.2). Although no aerosol samples were taken during this period, the optical photometer registered constant levels of aerosol production at about 10 g/m^3 as shown in Figure 7.7.

After 280 minutes of heating and 150 minutes of concrete erosion, the SURC-2 melt penetrated the remaining 5 cm of concrete and ran out into the bottom of the containment vessel. Posttest examination of the crucible and vessel indicated that the escaping melt created a large hole 4 cm in diameter in the bottom of the interaction crucible. The melt runout completely covered the MgO bricks in the bottom of the 120 cm diameter containment vessel to a depth of 5 cm. Neither the MgO brick nor the aluminum vessel appeared to have been attacked during the runout and subsequent freezing process. Analysis of the runout material indicated high concentrations of uranium, calcium, silicon, zirconium, and tungsten. This material had a density of 3.5-4.0 g/cm^3 and had a blackish, lava-like appearance with some retained porosity. The runout at 280 minutes effectively terminated the SURC-2 test.

The initial temperatures in the SURC-2 test were in excess of 2500 K and erosion rates were as high as 150 cm/hr during the first 2.3 min of concrete ablation. Both chemical energy and decay heat power appear to contribute to these observed phenomena. As the Zr content of the melt is depleted by oxidation and concrete byproducts are incorporated into the melt pool, both temperatures and erosion rates decrease.

The sustained temperatures of 2050 to 2150 K are observed for over 100 minutes following the initial rapid erosion period. This is well above the liquids temperature of basaltic concrete (1350-1650 K) and implies that there is a significant thermal resistance between the molten oxide pool and the concrete. An increase in power to the oxide pool also increases the oxide pool temperature as well as the erosion rate.

Aerosols are continuously released in concentrations ranging from 15 to 300 g/m^3. Although the composition of these aerosols is mostly concrete materials, significant amounts of barium, molybdenum, and uranium, along with some cerium, are also found. These amounts are orders of magnitude higher than would be predicted from mechanical release mechanisms. This implies that the aerosol release is predominantly vaporization-driven and would be expected to continue as long as the melt temperature remained high and significant amounts of gas generation continued.

The aerosols changed in composition and release rate over the course of the test. Generally, high melt temperatures and high gas evolution rates produce high aerosol releases. The melt chemistry will influence the type of materials released. Early in the test, there was zirconium metal present which produced a chemically reducing environment in the melt. Later after the zirconium has been oxidized, the melt was an oxidizing environment. This is seen in Figure 6.4.9 by the early barium release. Barium oxide was reduced to more volatile barium during the initial part of the test. During the later part of the test, the molybdenum is oxidized to its more volatile oxide and substantial molybdenum release is observed. Higher silicon release is observed during the early stages of the test as shown in Figure 6.4.8. This demonstrates the importance of melt chemistry on release.

The results of the SURC-2 test generally confirm the observations made in the SURC-1 test with limestone concrete. Both tests had very similar charge compositions and nearly identical power histories.

The key observations made during the tests were (1) high initial temperatures and erosion rates, (2) sustained interaction temperatures in excess of 2000 K, and (3) continuous release of aerosols in large amounts.
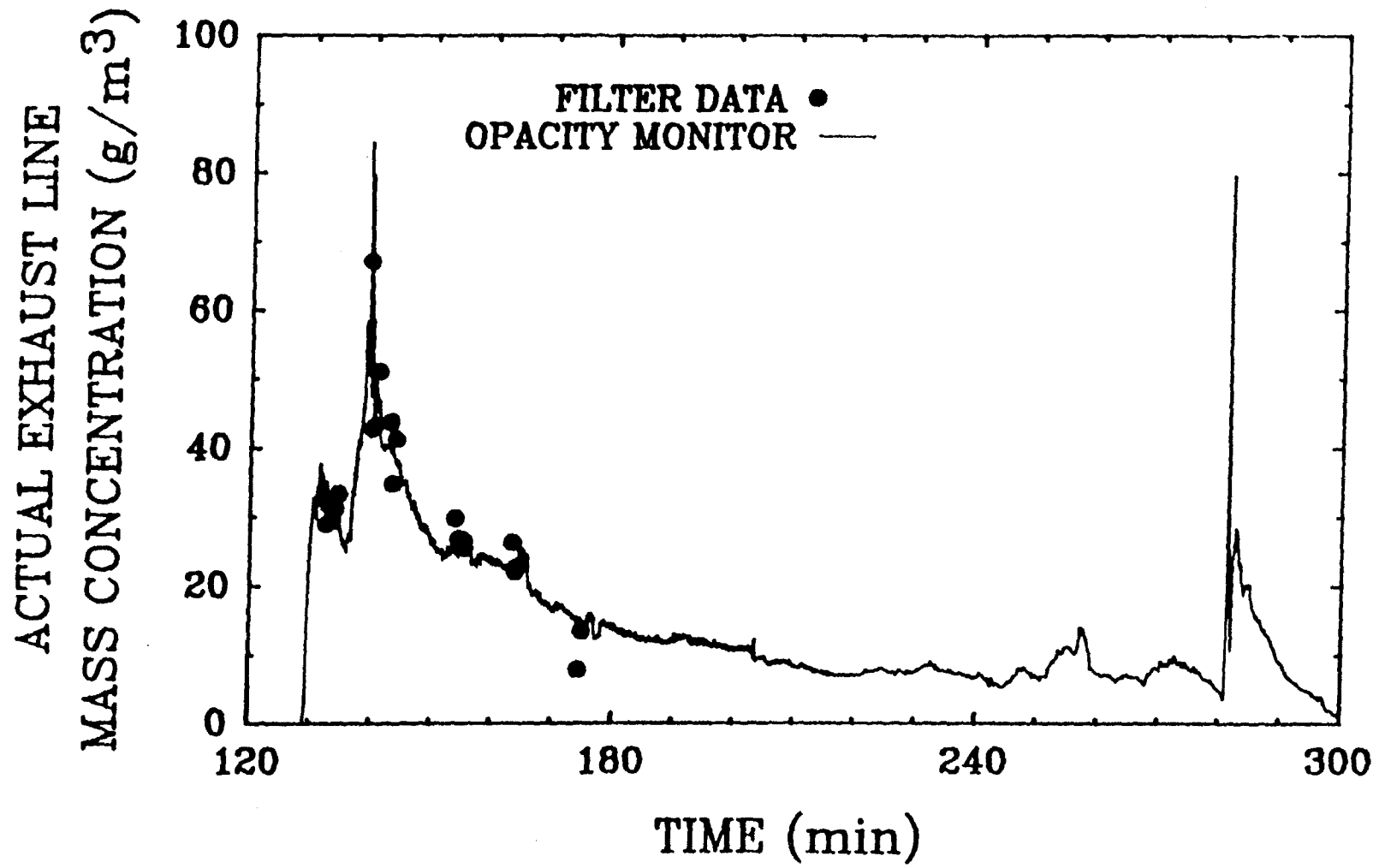
Figure 7.7 Measured aerosol concentrations for SURC-2 filter data compared to opacity meter output as a function of time

The concrete dehydration history for each experiment was very similar when comparing dehydration depth with time. The basalt concrete in SURC-2 began dehydrating at about 55 minutes and the limestone concrete in SURC-1 began near 75 minutes.

The onset of ablation occurred at about 135 minutes in SURC-2 and 150 minutes in SURC-1. The ablation rate for the two experiments was initially high for the first 2 to 5 minutes calculating to be 150 cm/hr for SURC-2 and 110 cm/hr for SURC-1. This was followed by an order of magnitude decrease in ablation for the remainder of the experiment in both cases.

The melt pool temperatures increased and peaked at about 2720K for SURC-2 and 2650K for SURC-1. The melt pool temperatures then declined as concrete was taken into solution with the UO_2.

A comparison of sidewall heat flux profiles calculated at various elevations, for the two experiments, were very similar. The steady state values calculated for each of the locations at the end of the experiment (300 minutes) ranged between 4.5×10^4 W/m^2 and $1. \times 10^5$ W/m^2 in both experiments.

The gas flow rates measured in SURC-2 were generally lower than in SURC-1 because of the composition of the concrete. During the high ablation period, gas flow rates averaged 110 slpm for SURC-2 and 150 slpm for SURC-1. In the mid to later stages of the experiments, gas flow rates averaged between 20 - 60 slpm and 40 - 80 slpm for SURC-2 and SURC-1 respectively.

Aerosol concentrations in the early and middle stages of SURC-2 were higher then for the same period in SURC-1. In the later stage the opposite was true. The aerosol concentration in SURC-2 was lower than SURC-1. For SURC-2, the initial and middle stage concentrations measured 90 g/m^3 and 50 g/m^3 respectively. For the same period in SURC-2 concentrations measured 50 g/m^3 and 30 g/m^3. In the later stages of the experiments SURC-2 averaged a slightly lower concentration which measured 40 g/m^3 when compared to SURC-1 which measured 60 g/m^3.

The aerosol particulate size is nearly the same for both experiments with each exhibiting particle diameters ranging form 0.4 to 25 microns. Both experiments indicated a mean particle size of 2 - 3 microns with a peak between 10 and 25 microns.

The SURC-2 test was excellent in all respects and successfully met all of the test goals. This test should provide comprehensive, redundant, and well-characterized information on molten oxide interactions with basaltic concrete which is well-suited for code validation efforts.

8.0 References

Baker, W. C., and J. F. Pouchot, "The Measurement of Gas Flow," Control Technology News, Vol. 33, No. 1, 1983.

Beck, J. V., B. Blackwell, and C. R. St. Clair, Jr., Inverse Heat Conduction, New York, NY, Wiley Interscience, 1985.

Berglund, R. N., and B. Y. H. Liu, "Generation of Monodisperse Aerosol Standards," Environmental Science Technology, Vol. 7, p. 147-153, 1973.

Blose, R. E., J. E. Gronager, A. J. Suo-Antilla, and J. E. Brockmann, SWISS: Sustained Heated Metallic Melt/Concrete Interactions with Overlying Water Pools, NUREG/CR-4727, SAND85-1546, Sandia National Laboratories, Albuquerque, NM, 1987.

Bradley, D. R., and E. R. Copus, Interaction of Hot Solid Core Debris with Concrete, NUREG/CR-4558, SAND85-1739, Sandia National Laboratories, Albuquerque, NM, 1986.

Brockmann, J. E., "Ex-Vessel Releases: Aerosol Source Terms in Reactor Accidents," Progress in Nuclear Energy, Vol. 19, p. 17-68, 1987.

Brockmann, J. E., B. Y. H. Liu, and P. H. McMurry, "A Sample Extraction Diluter for Ultra Fine Aerosol Sampling," Aerosol Science and Technology, Vol. 3, Number 4, pp. 441-451, 1984.

Cole, R. K., Jr., D. P. Kelly, and M. A. Ellis, CORCON-MOD2: A Computer Program for Analysis of Molten-Core Concrete Interactions, NUREG/CR-3920, SAND84-1246, Sandia National Laboratories, Albuquerque, NM, 1984.

Copus, E. R., Development of the Inductive Ring Susceptor Technique for Sustaining Oxide Melts, NUREG/CR-3043, SAND82-2546, Sandia National Laboratories, Albuquerque, NM 1983.

Copus, E. R., R. E. Blose, J. E. Brockmann, R. B. Simpson, and D. A. Lucero, Core-Concrete Interactions Using Molten UO_2 with Zirconium on a Limestone Basemat: The SURC-1 Experiment, NUREG/CR-5443, SAND90-0087, Sandia National Laboratories, Albuquerque, NM, 1992.

Copus, E. R., R. E. Blose et al., Core-Concrete Interactions Using Molten Steel with Zirconium on a Basaltic Basemat: The SURC-4 Experiment, NUREG/CR-4994, SAND87-2008, Sandia National Laboratories, Albuquerque, NM, 1989.

Cushing, K. E., G. E. Lacey, J. D. McCain, and W. B. Smith, Particulate Sizing Techniques for Control Device Evaluation: Cascade Impactor Calibrations, EPA-600/2-76-280, U.S. Environmental Protection Agency, 1976.

Davies, C. N., and M. Subari, "Aspiration Above Wind Velocity of Aerosols with Thin-Walled Nozzles Facing and at Right Angles to the Wind Direction," J. Aerosol Sci., Vol. 13, Number 1, pp. 59-71, 1982.

Gronager, J. E., A. J. Suo-Antilla, and J. E. Brockmann, TURC2 and 3: Large Scale UO2/ZrO2/Zr Melt-Concrete Interaction Experiments and Analysis, NUREG/CR-4521, SAND86-0318, Sandia National Laboratories, Albuquerque, NM, 1986.

Holman, J. P., Experimental Methods for Engineers, New York, NY, McGraw-Hill, Inc., 1966.

Jayasekera, P. N., and C. N. Davies, "Aspiration Below Wind Velocity of Aerosols with Sharp Edged Nozzles Facing the Wind," J. Aerosol Sci., Vol. 11, pp. 535-547, 1980.

Marple, V. A., and Willeke, K., Inertial Impactors in Aerosol Measurement, Gainesville, FL, University Presses of Florida, pp. 90-107, 1979.

McFarland, A. R., C. A. Ortiz, and R. W. Bertch Jr., "A High Capacity Preseparator for Collecting Large Particles," AIHA Paper No. 80, Texas A&M University, Civil Engineering Department, Air Quality Lab Publication 3718/04/78/ARM, 1978.

Powers, D. A., J. E. Brockmann, and A. W. Shiver, VANESA: A Mechanistic Model of Radionuclide Release and Aerosol Generation During Core Debris Interactions with Concrete, NUREG/CR-4308, SAND85-1370, Sandia National Laboratories, Albuquerque, NM, 1986.

Powers, D. A., and Arellano, F. E., Large-Scale, Transient Tests of the Interaction of Molten Steel with Concrete, NUREG/CR-2282, SAND81-1753, Sandia National Laboratories, Albuquerque, NM, 1982.

The Temperature Handbook, Volume 28, Omega Engineering Inc., P.O. Box 2284, Stamford, CT, 1992.

Appendix A: Calorimetric Test Data and Equations

Experimental Apparatus

Data obtained in the calorimetric tests of the induction power supply are shown in this appendix. Calorimetric tests were conducted to quantify the coupling efficiency of the inductive ring susceptors. During the experiment tungsten susceptor plates placed in the charge are heated inductively. These plates transfer heat to the oxide debris surrounding it by conduction melting the debris and sustaining the interaction. For the calorimeter test five stainless steel plates were fabricated with the same hole patterns as the tungsten susceptor rings used in the experiments. The coupling efficiency of the power supply to the charge is a function of the materials resistivity. 304 stainless steel at near ambient temperature (300 K) has nearly the same resistivity of tungsten at 2400 K. Since the stainless was easier to work with, a ring assembly was prepared modeling the spacing of the tungsten rings in the charge. The test apparatus for conducting the calorimetric test is shown in Figure A-1. The stainless plates were spaced equidistant apart using five stainless steel tubes.

This assembly was placed into the cavity of a crucible fabricated from MgO castable. The crucible contained an outlet for water flow. The copper induction coil was placed around the crucible and centered vertically with the plate assembly. Cooling water was supplied to the plates using a 1.9 cm diameter copper tubing placed at approximately mid height of the water pool. A large 7.6 cm hole in the center of the stainless susceptor plates made this possible. Water flow into the crucible was measured by a positive displacement flow meter. The inlet and exit temperature of the water was measured during the test with type K thermocouples. Type K thermocouples were also mounted on the second and third plate from the top. This was done to ensure that the

plates did not get so hot that the water surrounding the plate went into film boiling. It was desired to keep enough water flowing so that all the heat generated in the plate was transferred to the water in the nuclear boiling regime. This whole assembly was placed inside the water cooled aluminum containment vessel to duplicate the actual experimental conditions.

Power Based on Calorimetry Calculations

Three calibration tests were performed at input powers of 100, 175, and 300 kW, based on power meter readings on the control console of the power supply. The output of the power transducer connected to the buss bars, the thermocouples and flow meter were connected to a Hewlett-Packard HP-1000 data acquisition system for collection and posttest plotting and analysis.

The calorimetric test was initiated by starting the data acquisition system, establishing base line data for the instrumentation. The water was turned on and the flow was regulated by a gate valve. After a few minutes of base line data was taken, the induction power supply was started and a constant input power was applied to the stainless steel rings. The power supply was run until the differential temperature in the water pool and in the aluminum containment vessel reached a steady state condition.

The power imparted to the stainless steel susceptor plates was calculated using the common energy equation

$$P_{susceptor} = \dot{m} \, C_p \, (T_{out} - T_{in}) \qquad (A-1)$$

where

$P_{susceptor}$ = Power deposited into the susceptor plates j/sec
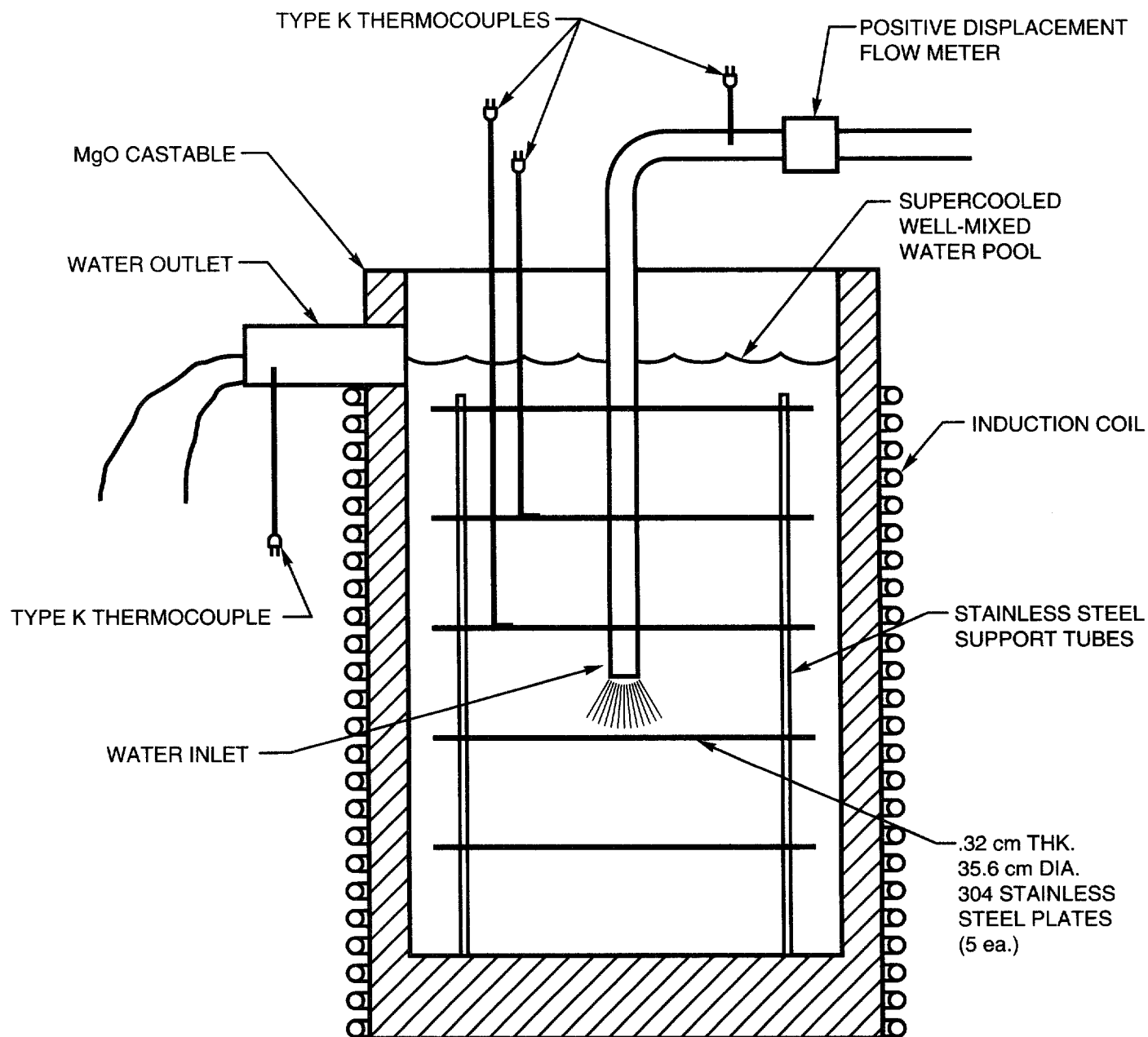
Figure A-1 Test apparatus for conducting calorimetric tests for the SURC-2 experiment

C_p = specific heat of water $(j/kg \cdot K)$

T_{out} = temperature of the water flowing out of the crucible (K)

T_{in} = temperature of the water flowing into the crucible (K)

The specific heat for water is taken at the mean temperature of the water pool $((T_{out} - Tin)/2)$.

The fraction of power deposited in the aluminum containment vessel is found similarly. The only difference is that the cooling fluid was a 50/50 mixture of ethylene glycol and water.

For the initial test the input power was 101.7 kW. The output from the power transducer is shown in Figure A-2. The flow rate of water and ethylene glycol/water mixture is shown in Figure A-3 plotted as a function of time. The flow rate of water to the crucible and through the containment vessel was 3.6 and 8.8 gallons/minute respectively. The steady state differential temperature measured for the crucible pool and containment vessel was 45.8°C and 5.1°C, respectively. The plot of differential temperature for the crucible pool and aluminum containment vessel is shown in Figures A-4 and A-5, respectively.

Converting units and substituting the appropriate values into Equation (A-1) for the water pool and containment vessel yields 43.5 kW of power imparted to the UO_2-ZrO_2 susceptor plates and 10.2 kW to the aluminum containment vessel.

The coupling efficiency is then defined by the ratio of the power imparted to the plate

divided by the total power measured by the power transducer at the buss bars.

$$\% \ eff = P_{plates} / P_{total} \ x \ 100 \qquad (A-2)$$

The coupling efficiency of the containment vessel is found likewise.

Power, differential temperature, and flow rate profiles plotted as a function of time for the 175 and 300 kW calorimetry are shown in Figures A-6 through A-9.

Based on these data, the coupling efficiency for the 175 and 300 kW power levels were calculated as well as the coupling to the containment vessel. The results of all three calorimetry tests for the susceptor assembly are presented in Table A-1. The power imparted to the aluminum containment is presented in Table A-2. Included in this table is a calculation of the power applied to the vessel with the power supply operating without the susceptor assembly in place. The power supply essentially operated in a no-load condition.

The calculated coupling efficiencies for the susceptor plate assembly ranged between 42.8 and 45.8% for buss power between 101.7 and 301 kW. The efficiency increases slightly with the increase of buss power.

The fraction of total power coupled to the containment vessel ranged between 10.0 and 4.8% for the same buss powers described above. As the buss power is increased the power to the vessel remains about the same thus reducing the coupling efficiency. The power coupled to the containment vessel for the no load case is about 3.2% higher than the loaded case when the induction power supply operated at essentially the same peak power.
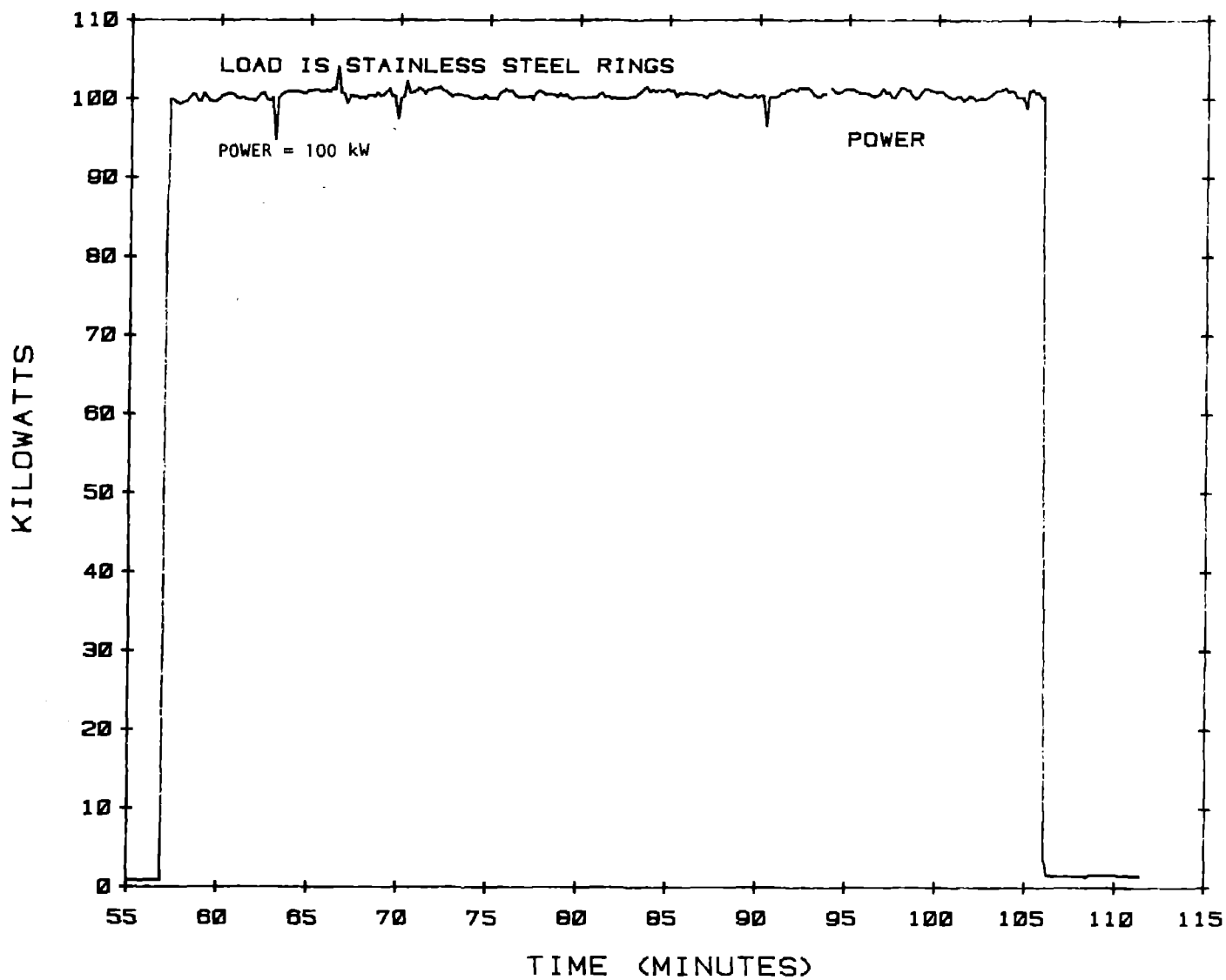
Figure A-2 Plot of effective power plotted as a function of time, 100 kW calorimetric test
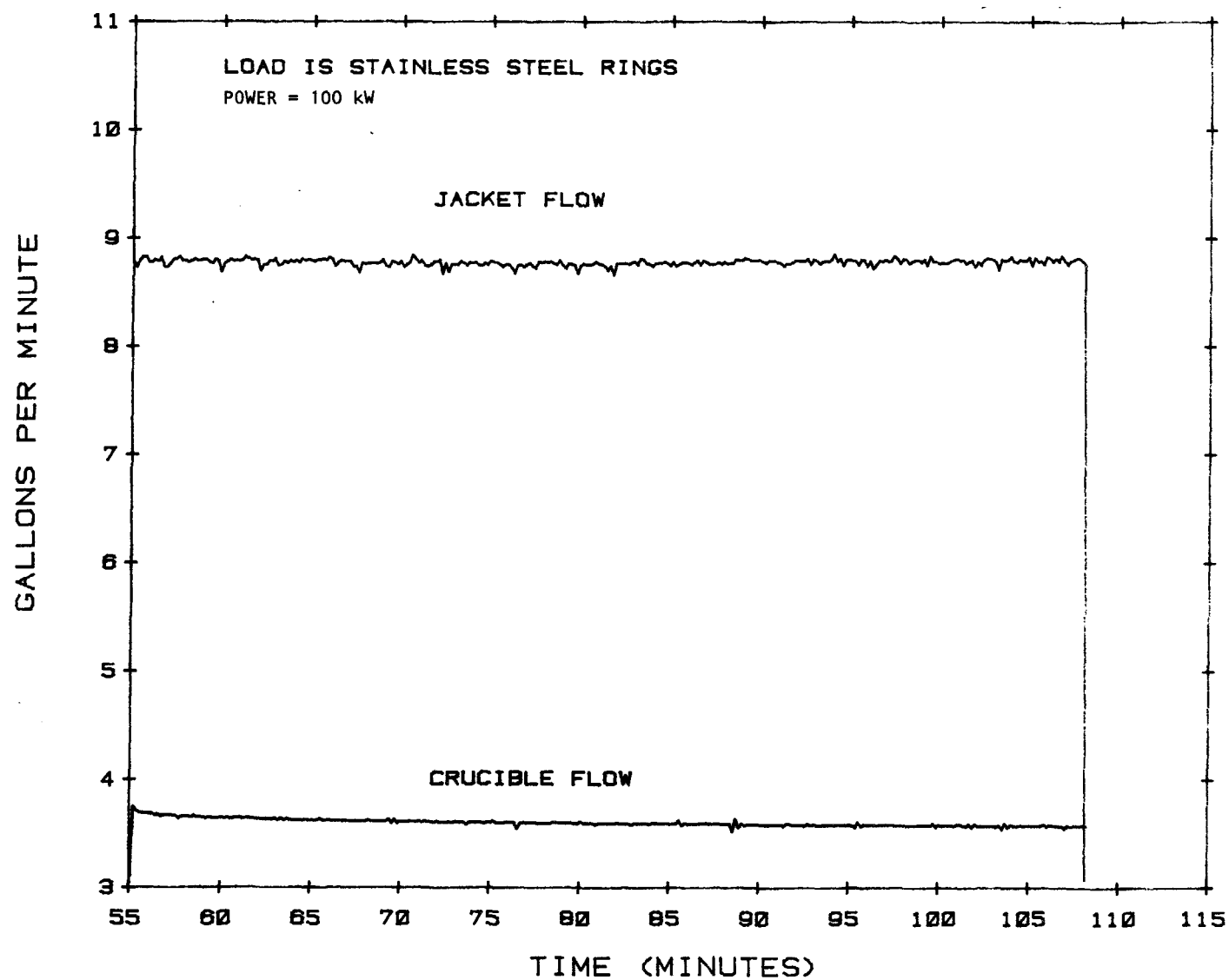
Figure A-3 Flow rate of cooling fluid through the crucible and containment vessel, 100 kW calorimetric test
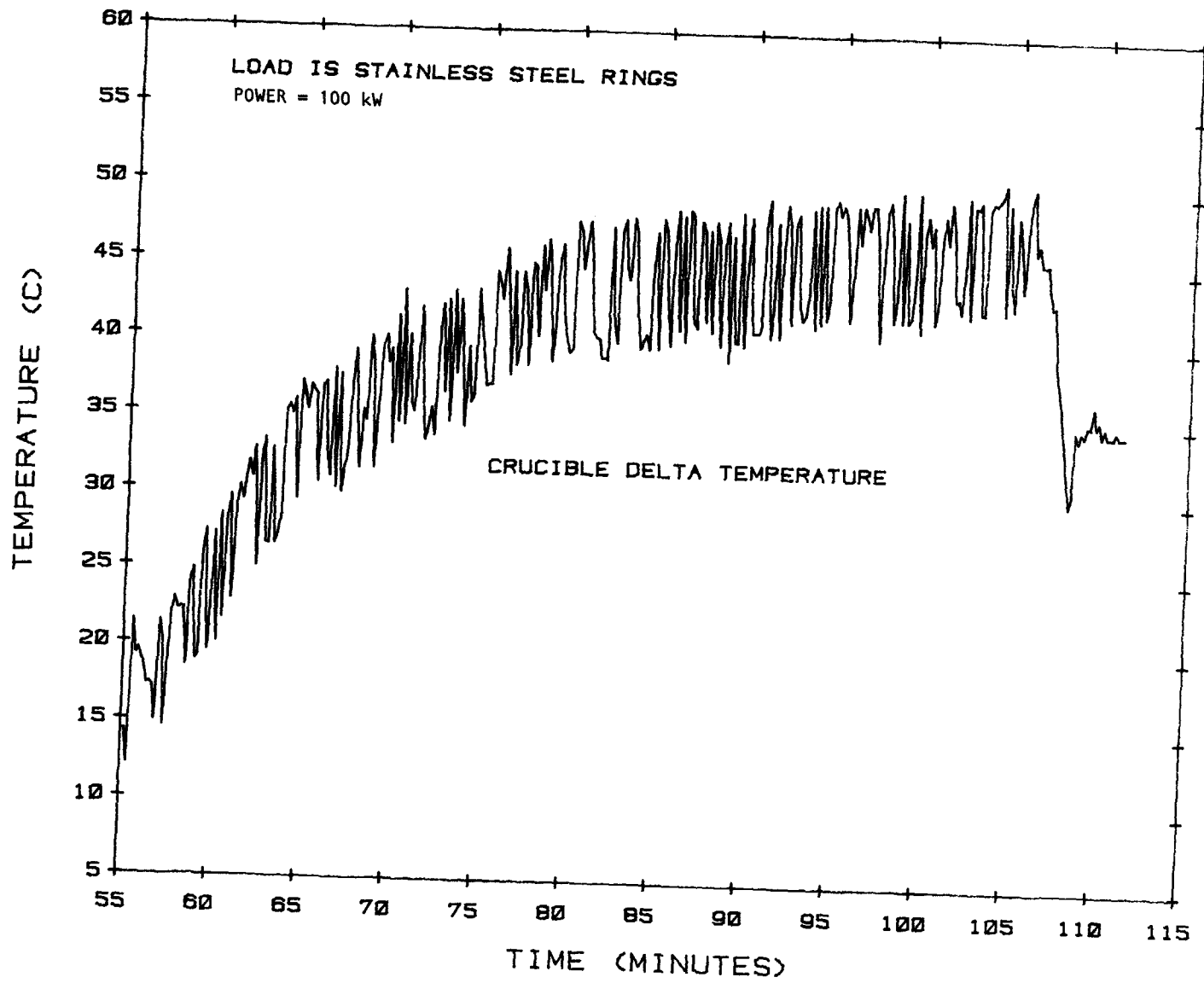
Figure A-4 Differential temperature of the water flowing through the crucible, 100 kW calorimetric test
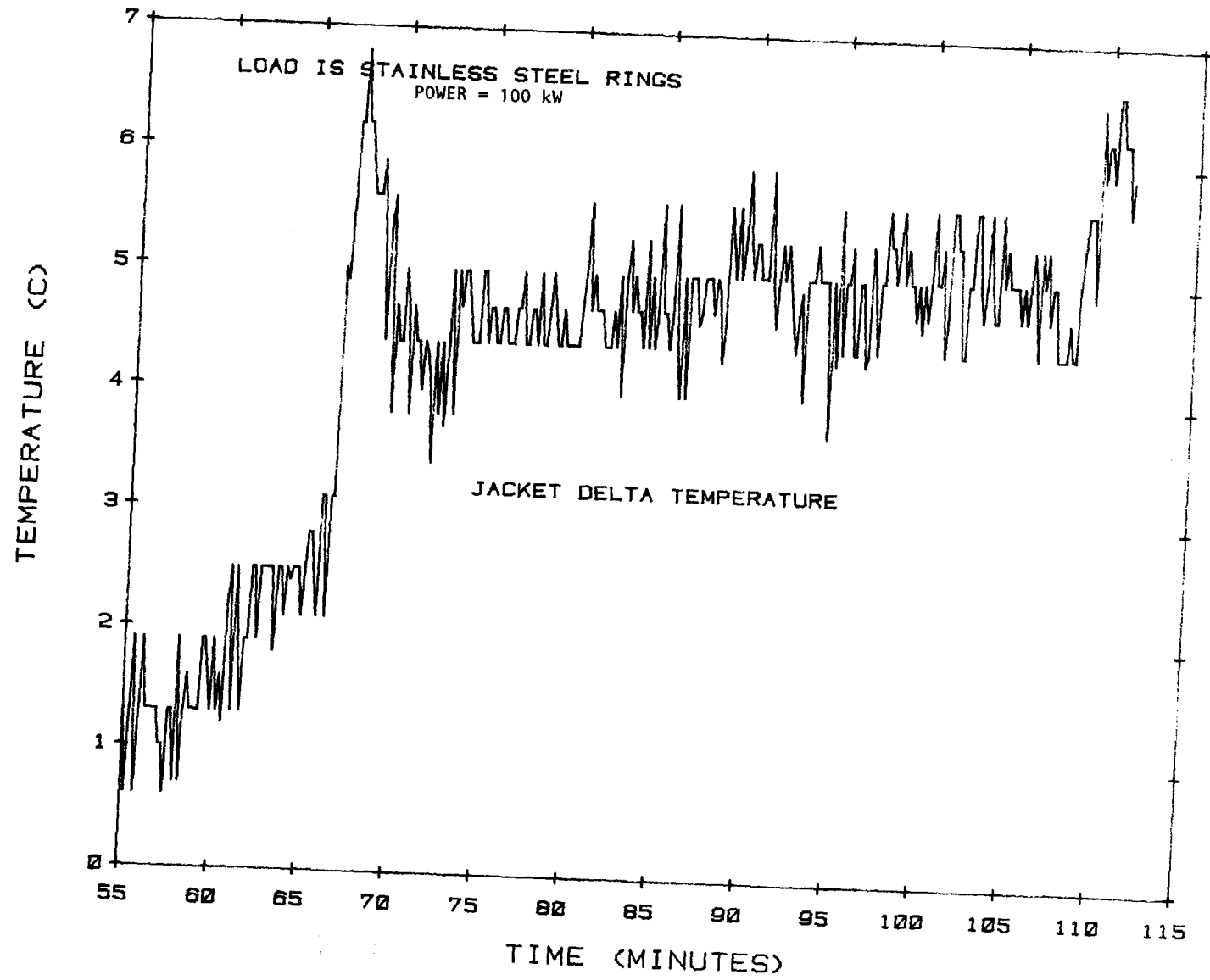
Figure A-5 Differential temperature of the cooling fluid flowing through the aluminum containment vessel, 100 kW calorimetric test
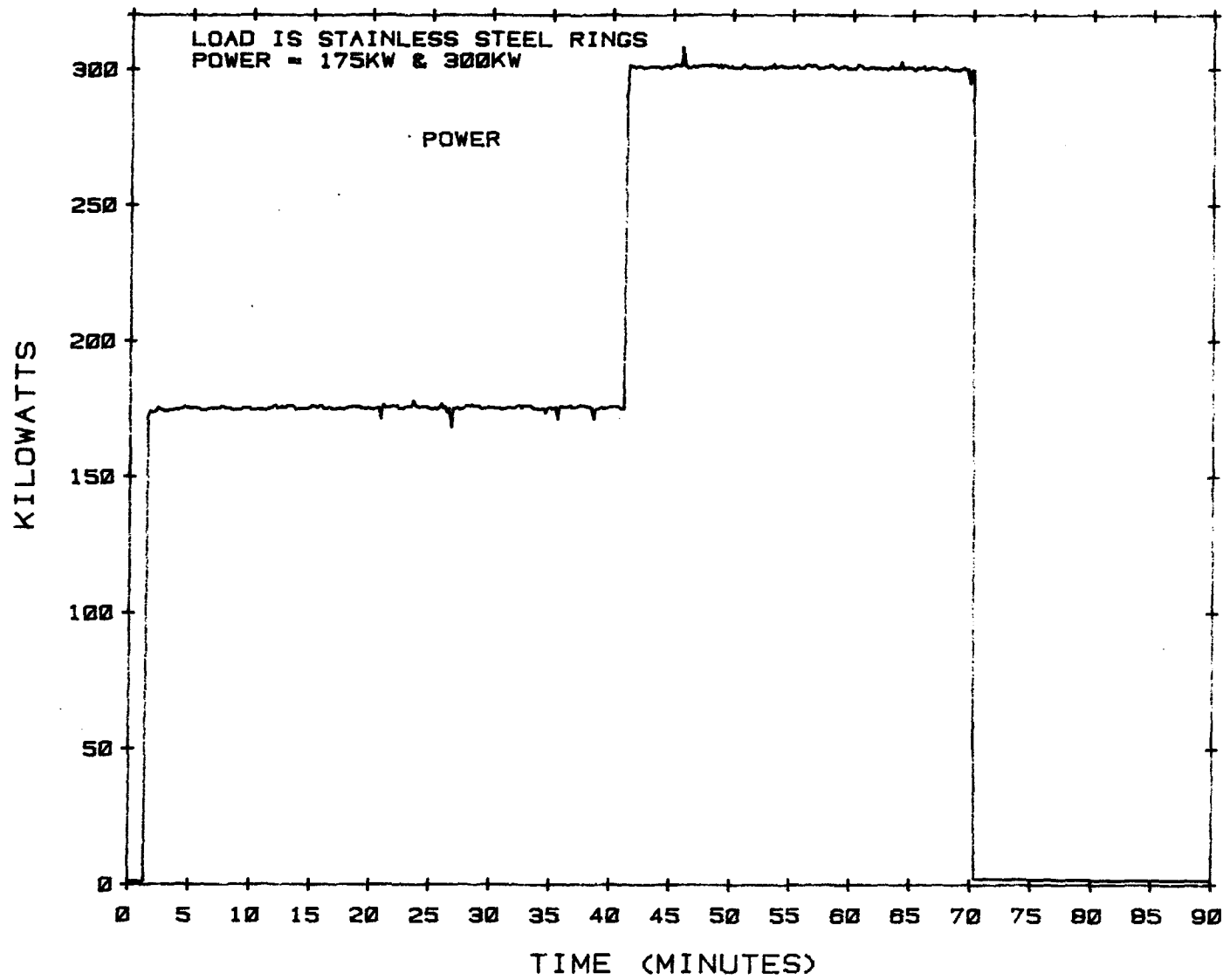
Figure A-6 Plot of effective power plotted as a function of time, 175 and 300 kW calorimetric test
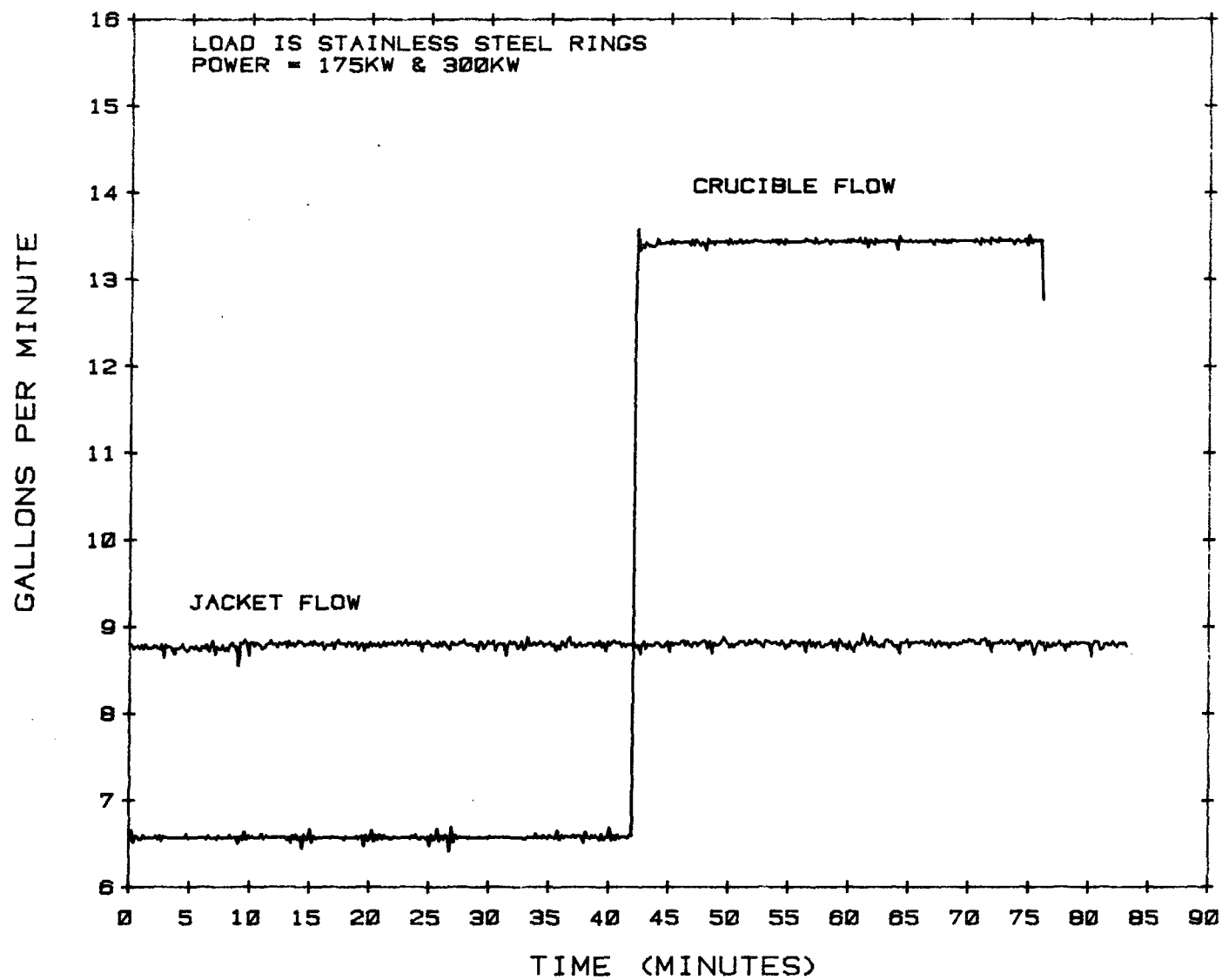
Figure A-7 Flow rate of cooling fluid through the crucible and containment vessel, 175 and 300 kW calorimetric tests
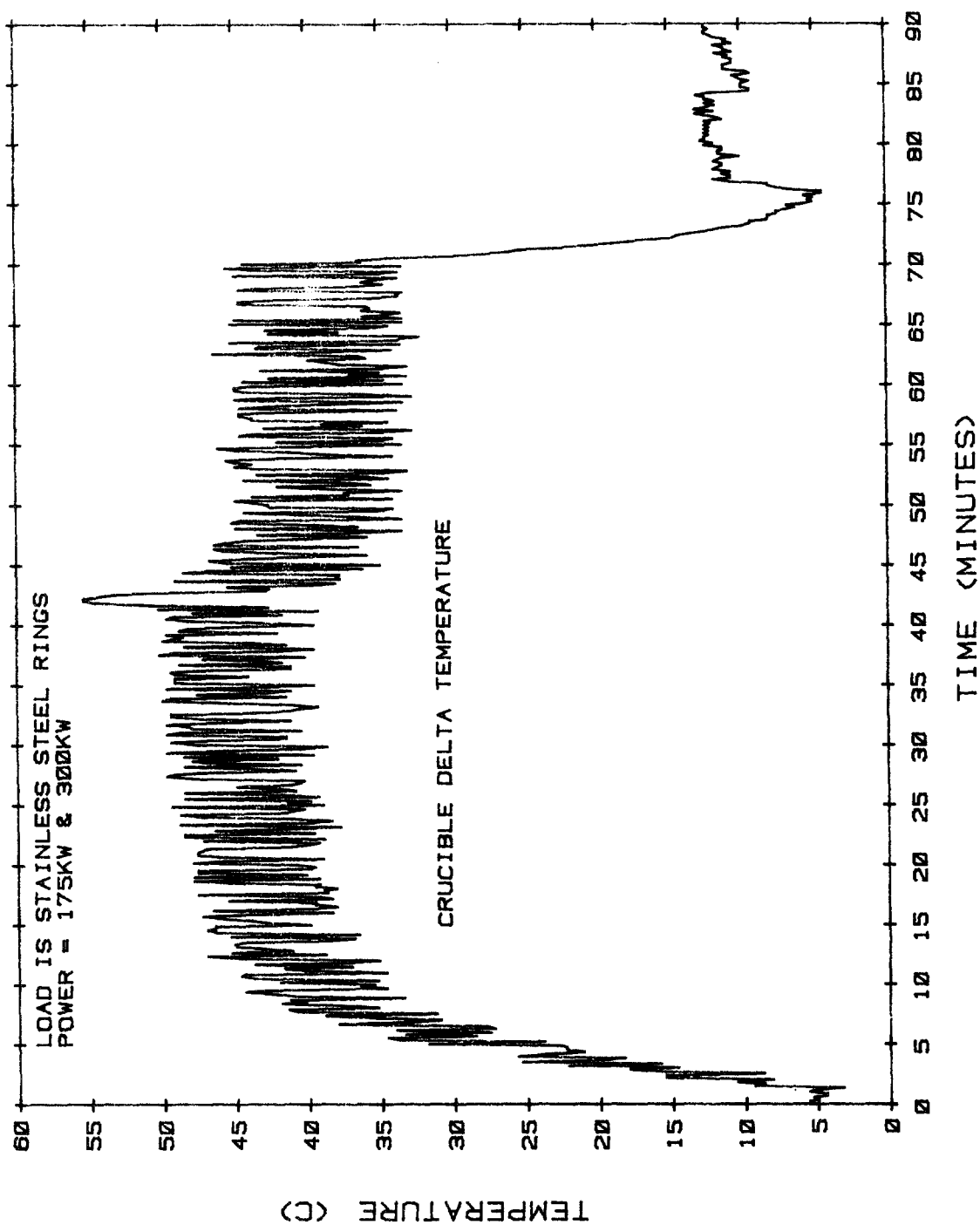
Figure A-8 Differential temperature of the water flowing through the crucible, 175 and 300 kW calorimetric tests
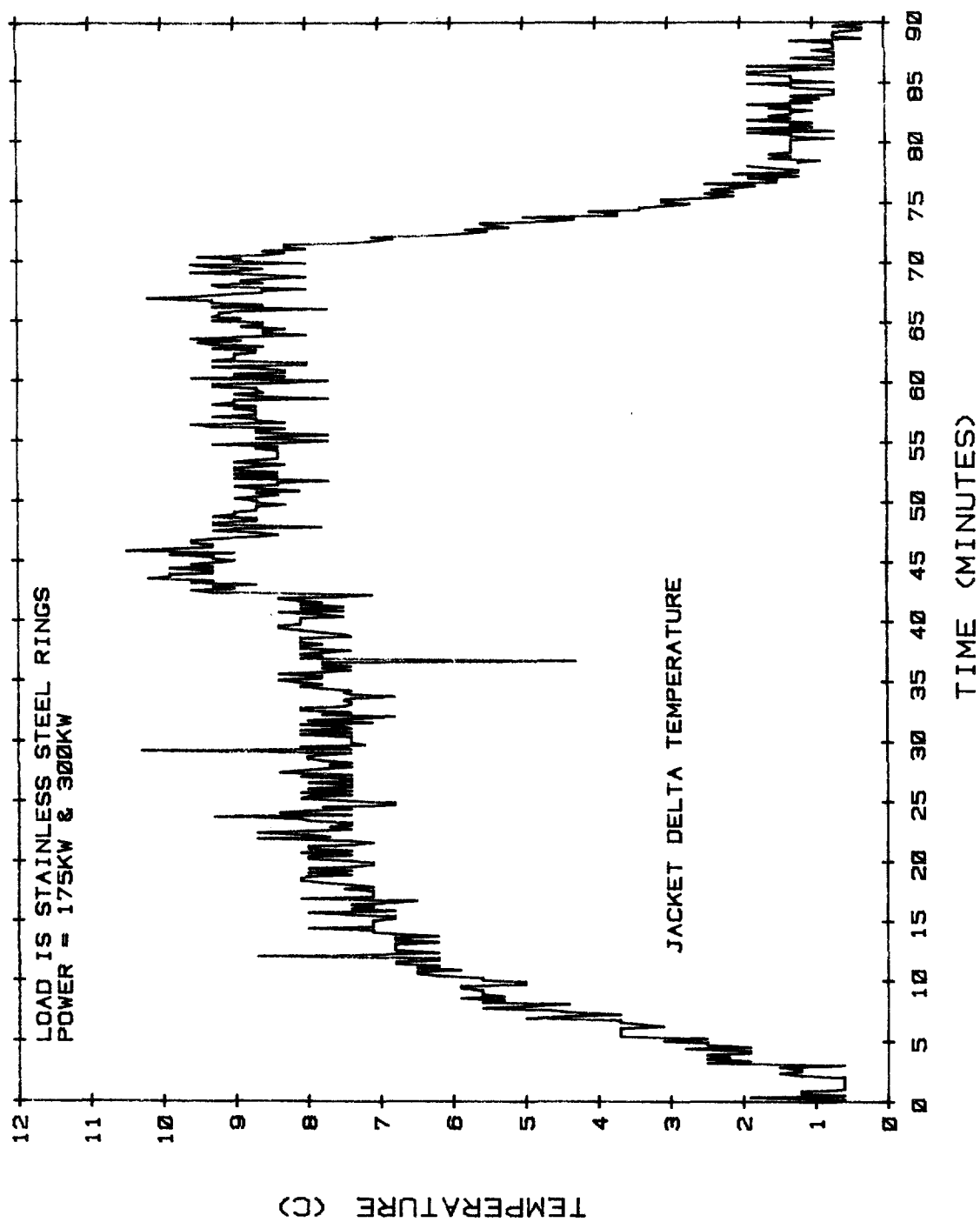
Figure A-9 Differential temperature of the cooling fluid flowing through the containment vessel, 175 and 300 kW calorimetric tests

Table A-1 Susceptor assembly coupling efficiency

Input Power Console Power Meter (kW)	Power Measured at Buss Bars (kW)	Power Deposited in Susceptor Plates (kW)	Coupling Efficiency
100	101.7	43.5	42.8%
175	175.5	77.5	44.2
300	301.0	137.9	45.8%

Table A-2 Aluminum containment vessel coupling efficiency

Input Power Console Power Meter (kW)	Power Measured at Buss Bars (kW)	Power Deposited in Susceptor Plates (kW)	Coupling Efficiency
100	101.7	10.2	10.0%
175	175.5	15.5	8.8%
300	301.0	14.4	4.8%
170 No Load Configuration	166.3	19.9	12.0%

Appendix B: Power Supply Operational Data

In this appendix data is presented related to the operation of the power supply. This data includes buss power, flow rate and temperature data for the cooling fluid flowing through the power supply, induction coil and containment vessel.

Figure B-1 Power applied at the Buss bars during the SURC-2 experiment
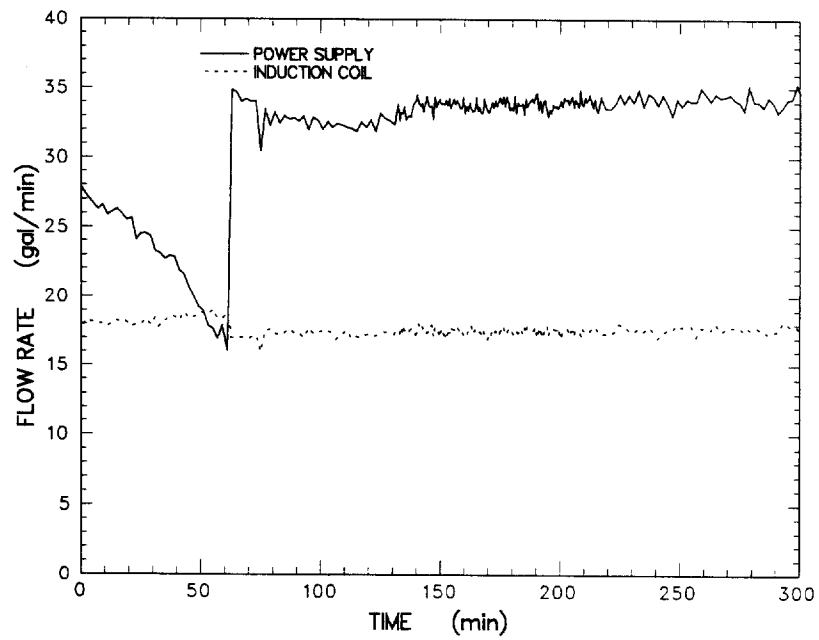
Figure B-2 Flow rate of cooling fluid flowing through the power supply and induction coil
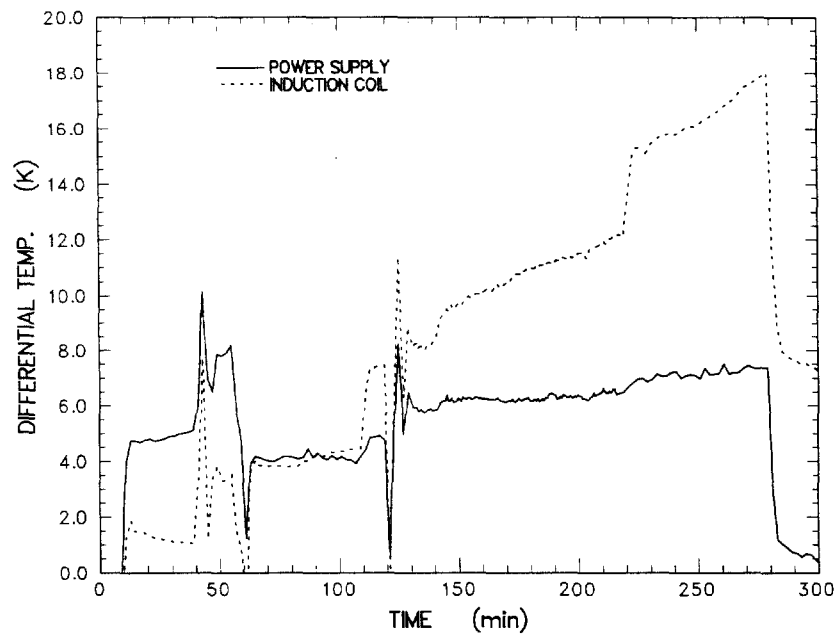
Figure B-3 **Differential temperature of the cooling fluid flowing through the power supply and induction coil**
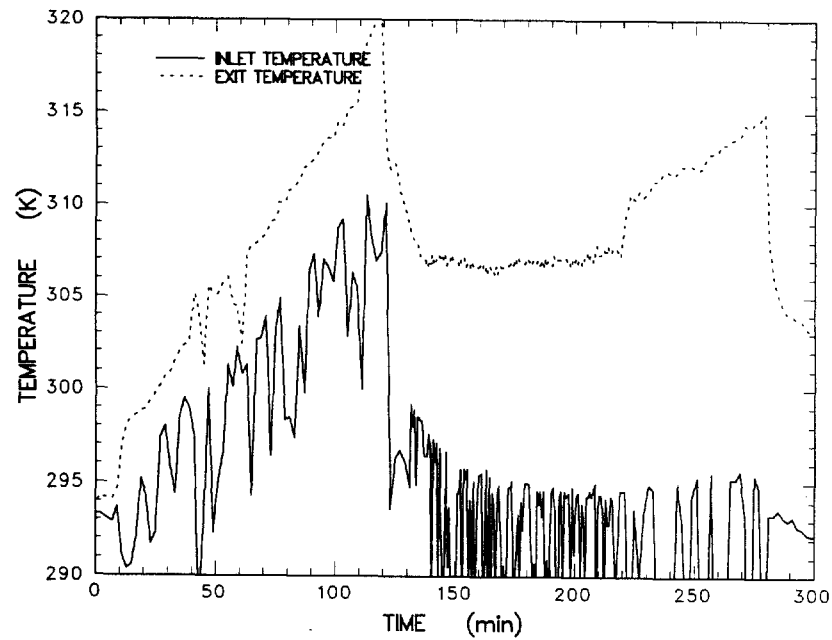
Figure B-4 Inlet/exit temperature of the cooling fluid flowing through the coil
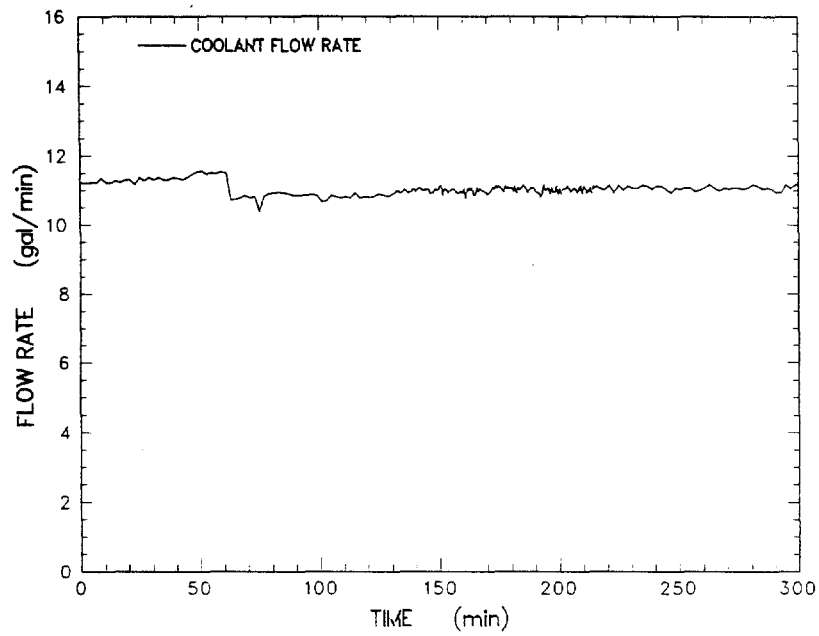
Figure B-5 Flow rate of cooling fluid flowing through the containment vessel
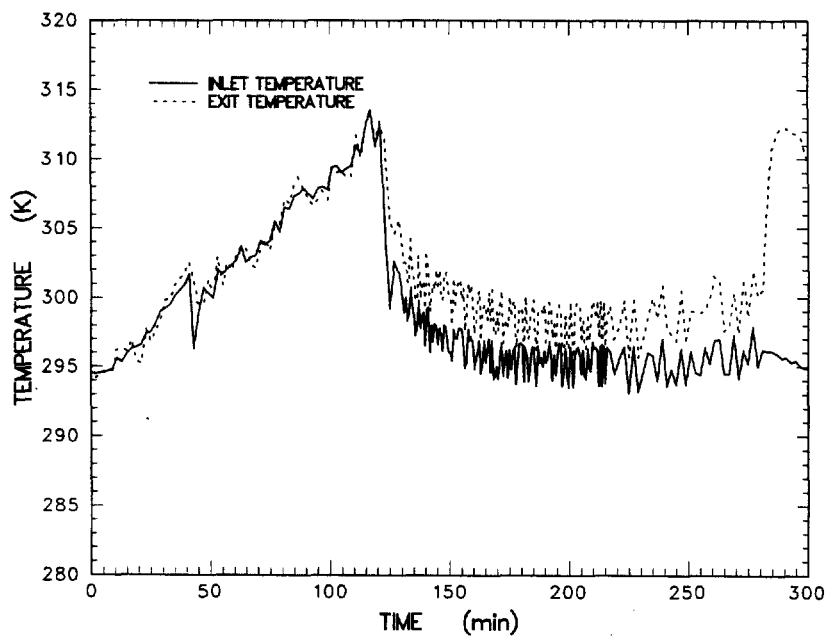
Figure B-6 Inlet/exit temperature of the cooling fluid flowing through the containment vessel

Appendix C: Crucible Thermocouple Profiles

resented in this appendix are the temperature rofiles produced from type K and S thermocouples imbedded in the concrete, MgO castable sidewall and MgO cover.

Appendix C
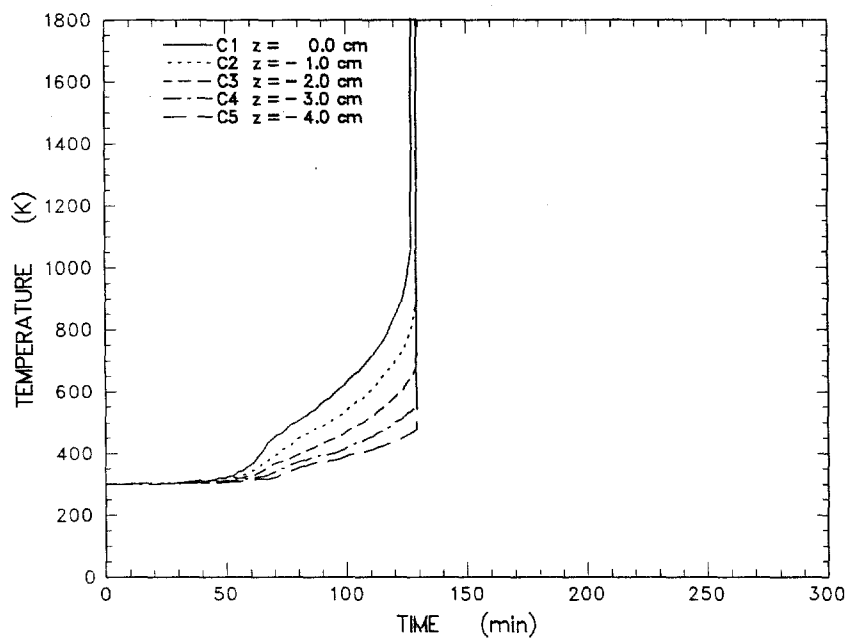
Figure C-1   Concrete temperature data measured by thermocouples located in the axial centerline array between z = 0.0 and -4.0 cm
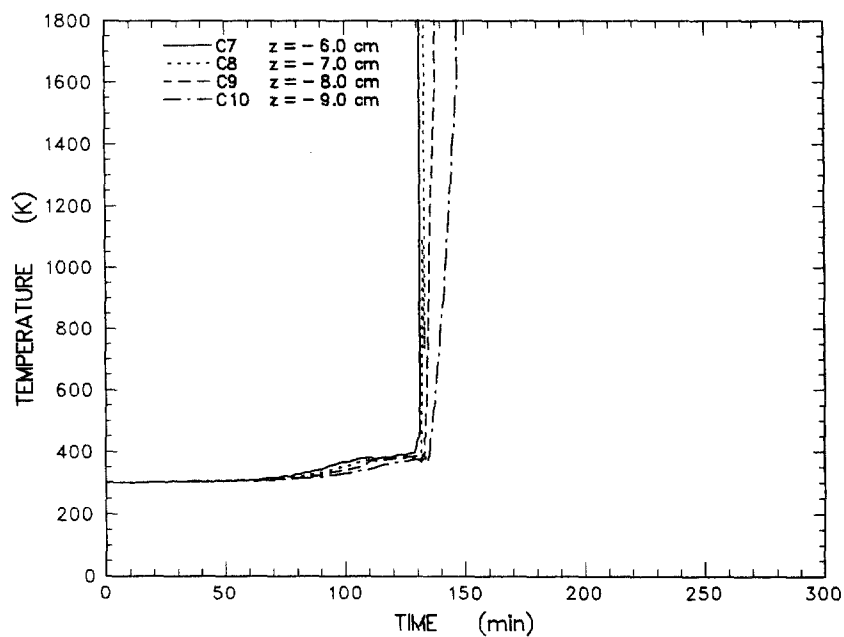
Figure C-2   Concrete temperature data measured by thermocouples located in the axial centerline array between z = -6.0 and -9.0 cm.
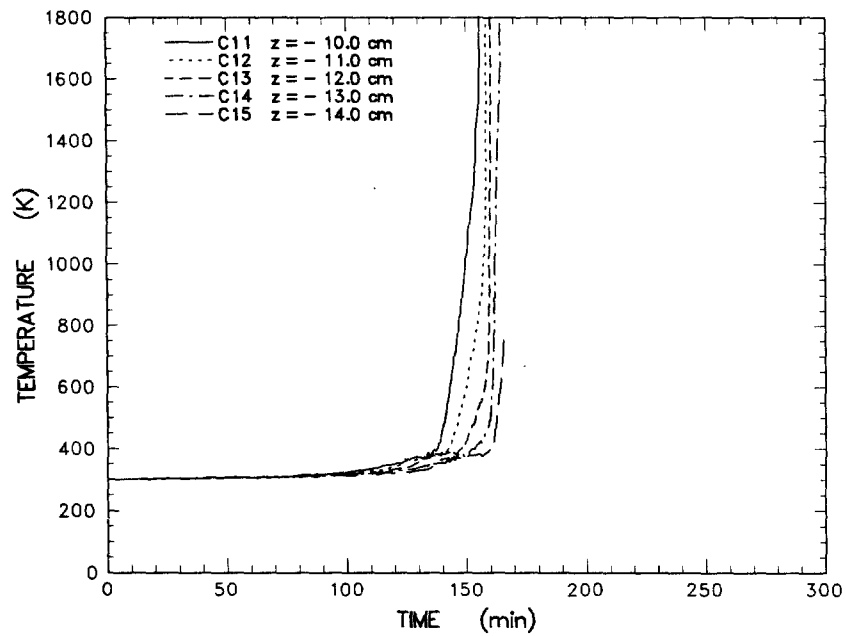
Figure C-3 Concrete temperature data measured by thermocouples located in the axial centerline array between z = -10.0 and -14.0 cm
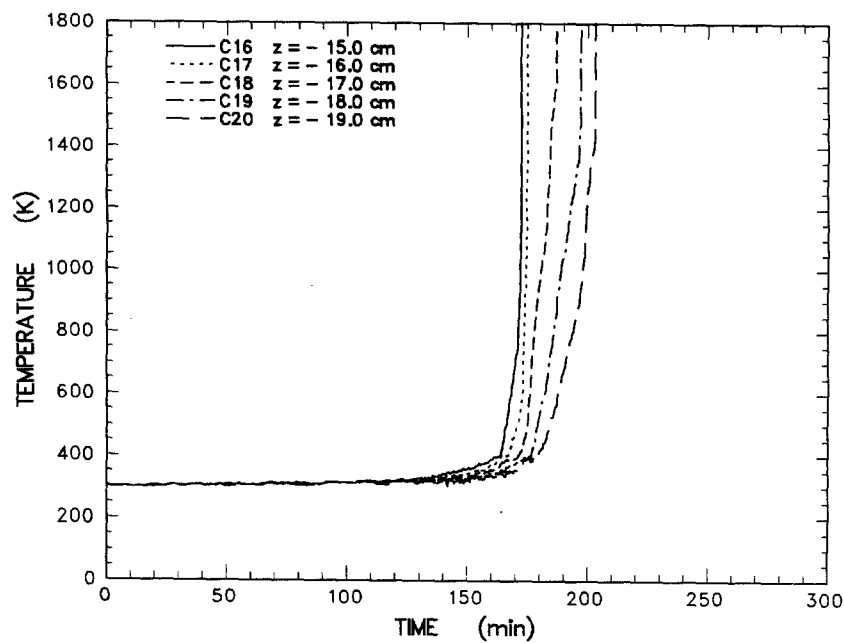
Figure C-4 Concrete temperature data measured by thermocouples located in the axial centerline array between z = -15.0 and -19.0 cm

Appendix C
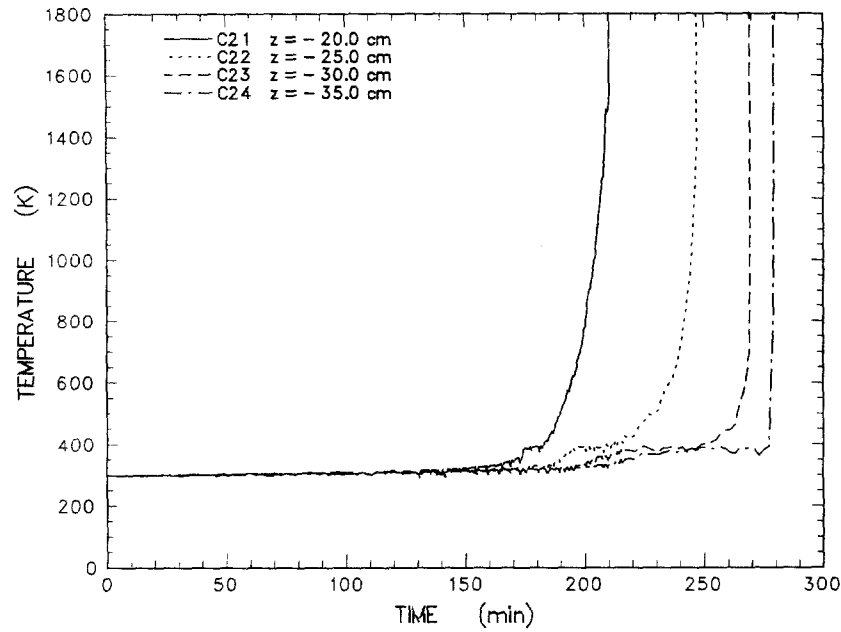
Figure C-5 Concrete temperature data measured by thermocouples located in the axial centerline array between z = -20.0 and -35.0 cm
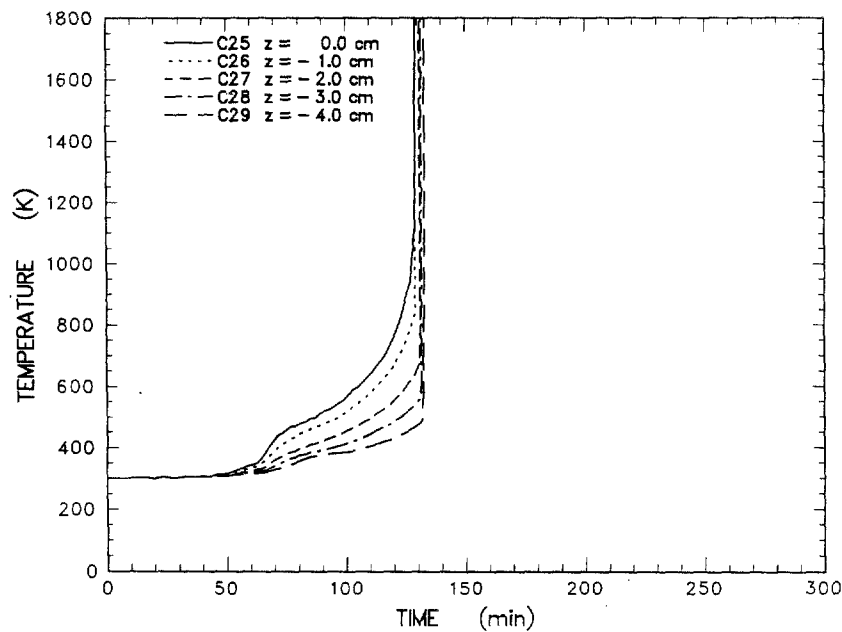
Figure C-6 Concrete temperature data measured by thermocouples located in the midradius array between z = 0.0 and -4.0 cm
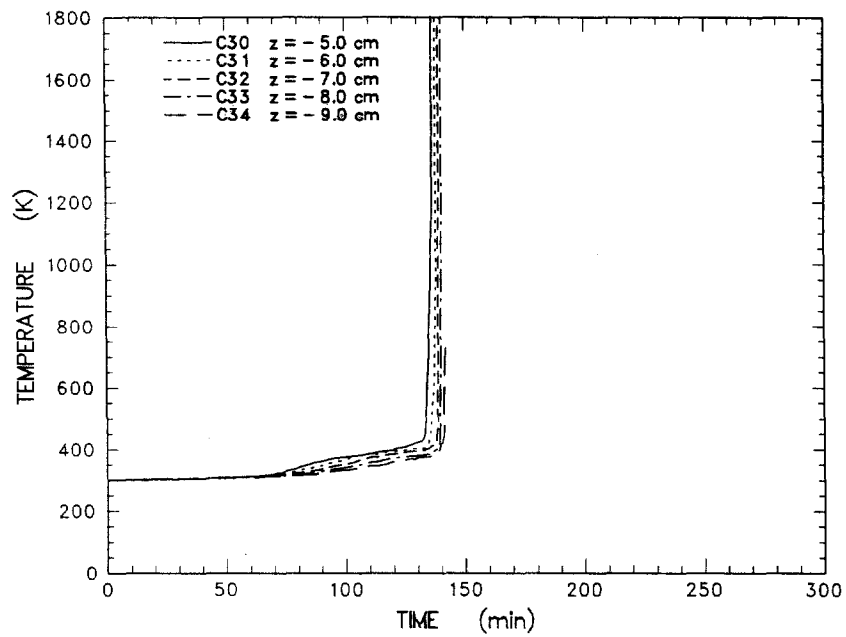
Figure C-7   Concrete temperature data measured by thermocouples located in the midradius array between z = -5.0 and -9.0 cm
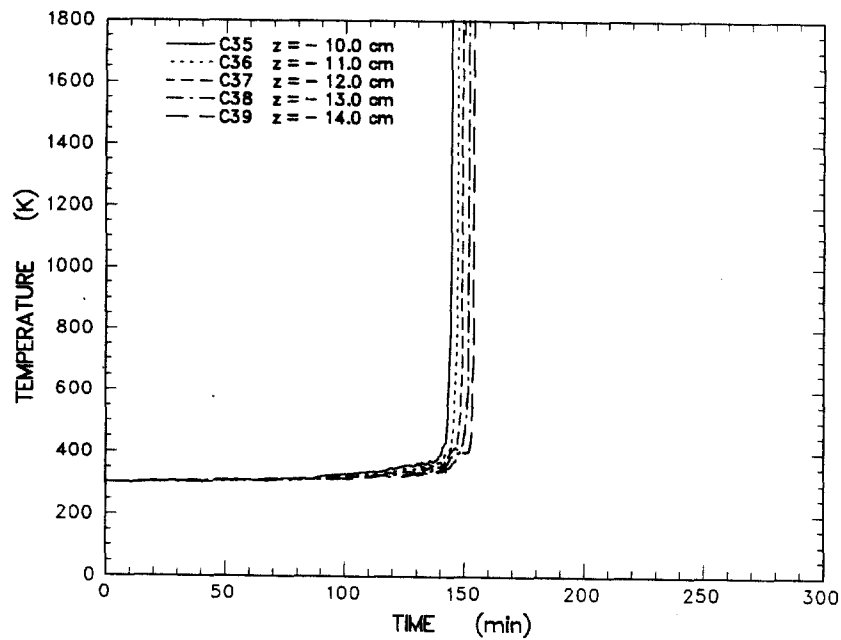
Figure C-8   Concrete temperature data measured by thermocouples located in the midradius array between z = -10.0 and -14.0 cm
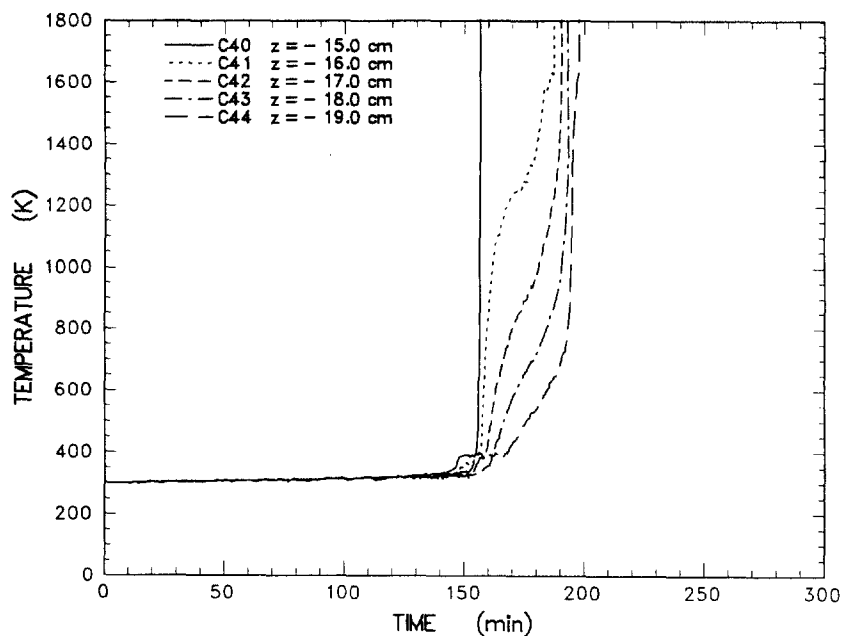
Figure C-9 Concrete temperature data measured by thermocouples located in the midradius array between z = -15.0 and -19.0 cm
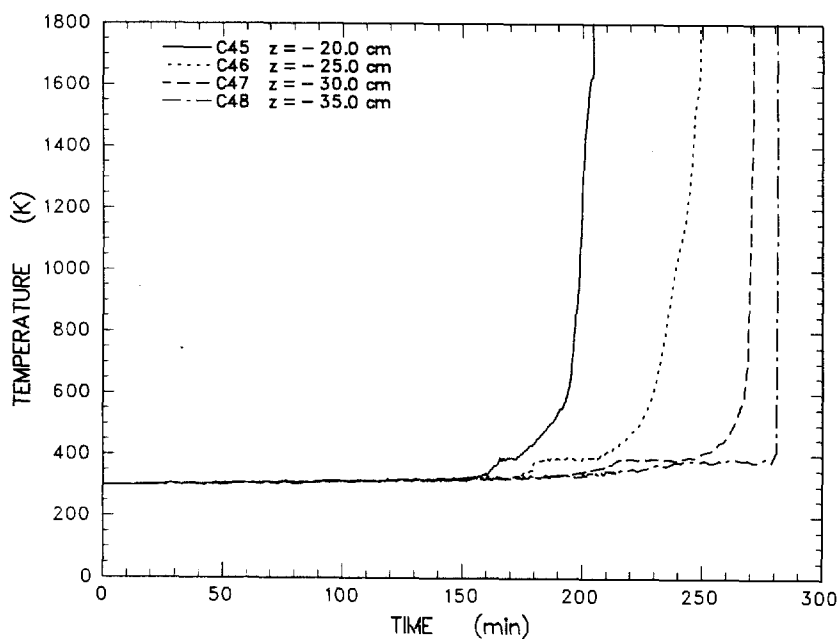
Figure C-10 Concrete temperature data measured by thermocouples located in the midradius array between z = -20.0 and -35.0 cm
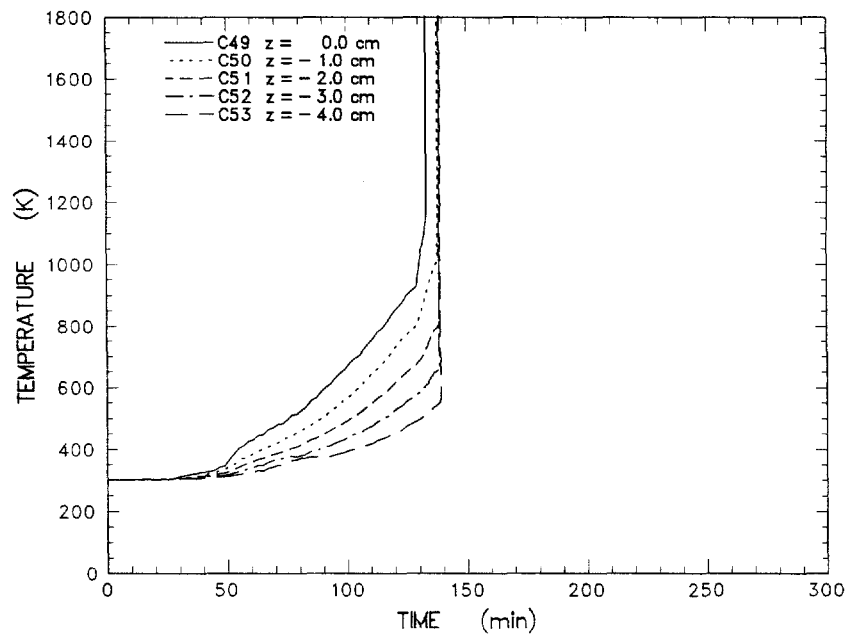
Figure C-11   Concrete temperature data measured by thermocouples located in the perimeter array between z = 0.0 and -4.0 cm
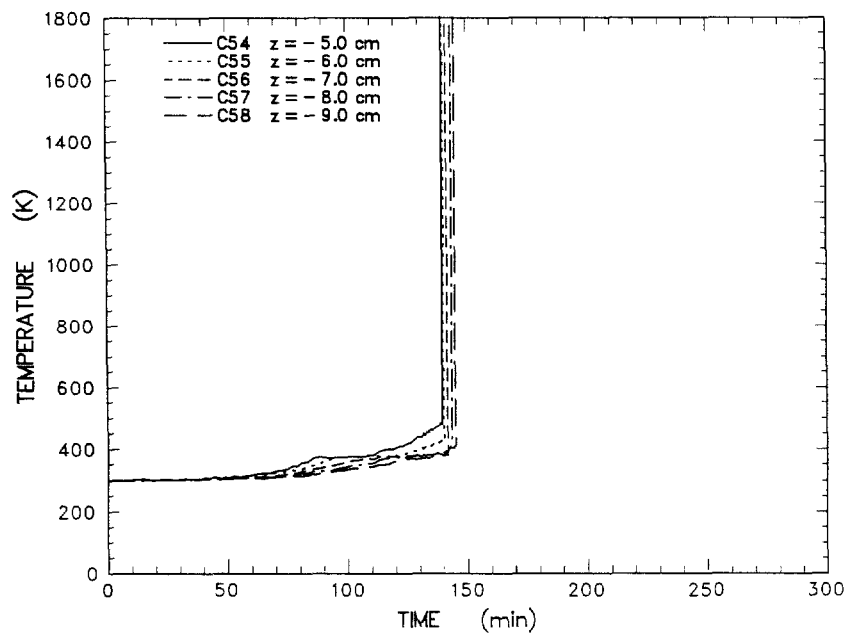
Figure C-12   Concrete temperature data measured by thermocouples located in the perimeter array between z = -5.0 and -9.0 cm
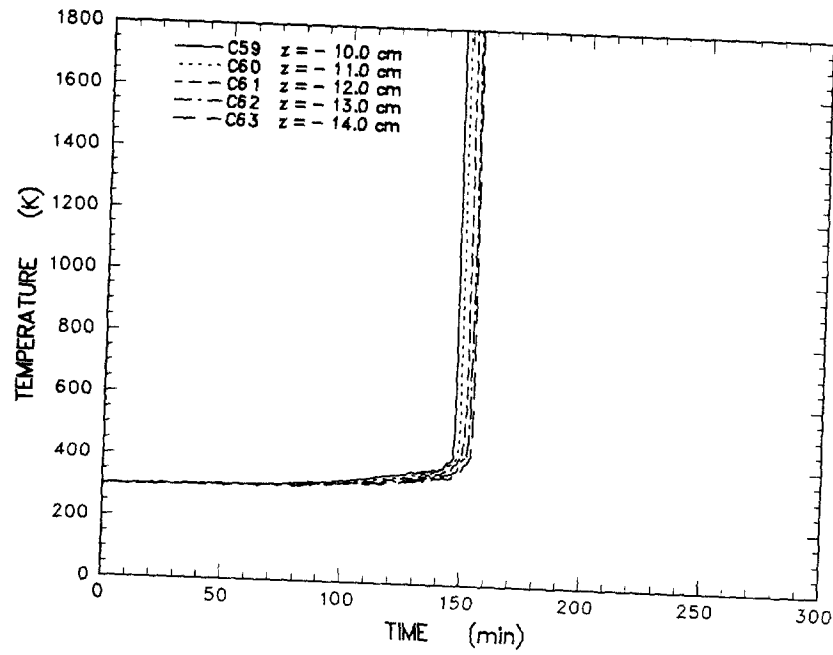
Figure C-13 Concrete temperature data measured by thermocouples located in the perimeter array between z = -10.0 and -14.0 cm
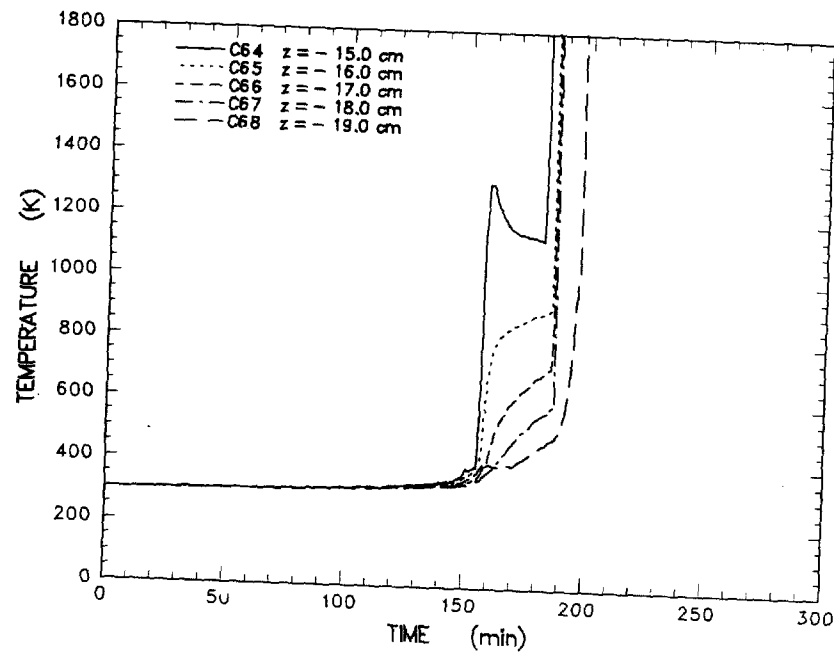
Figure C-14 Concrete temperature data measured by thermocouples located in the perimeter array between -15.0 and -19.0 cm
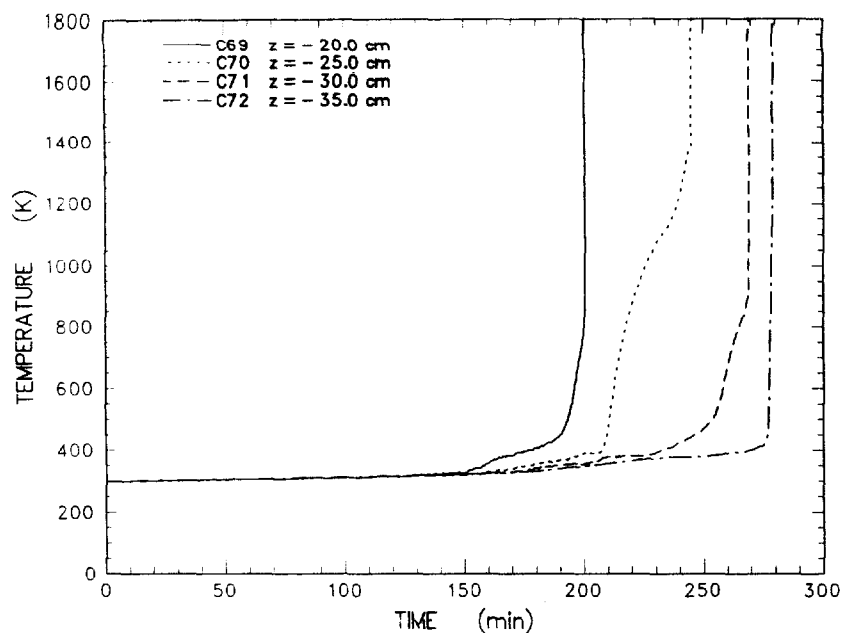
Figure C-15 Concrete temperature data measured by thermocouples in the perimeter array between z = -20.0 and -35.0 cm
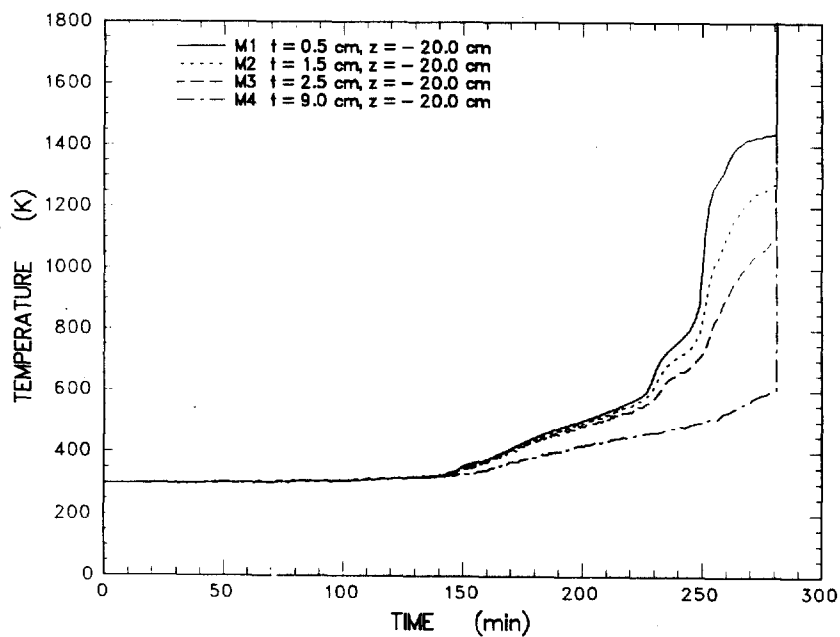
Figure C-16 MgO sidewall temperature data measured by thermocouples in the array located at z = -20.0 cm
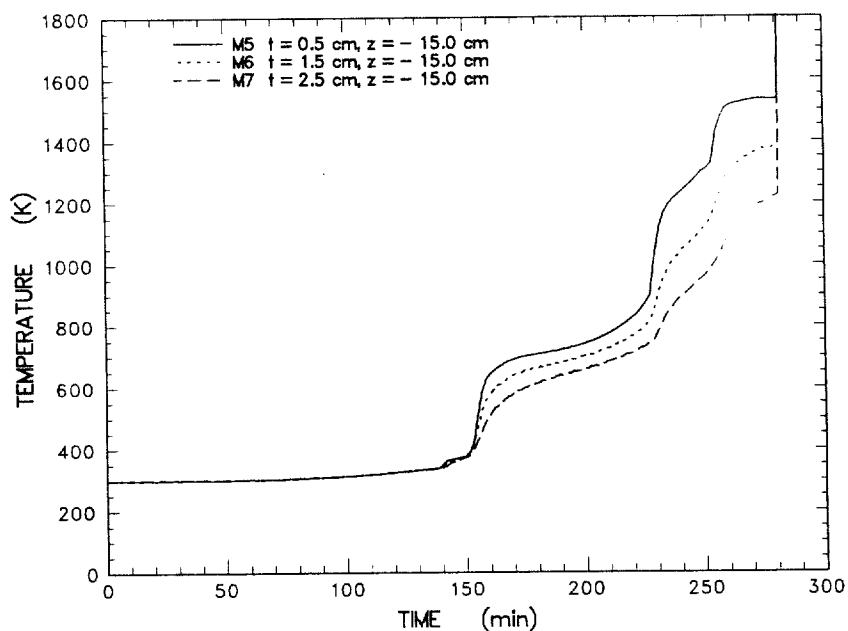
Figure C-17 MgO sidewall temperature data measured by thermocouples in the array located at z = -15.0 cm
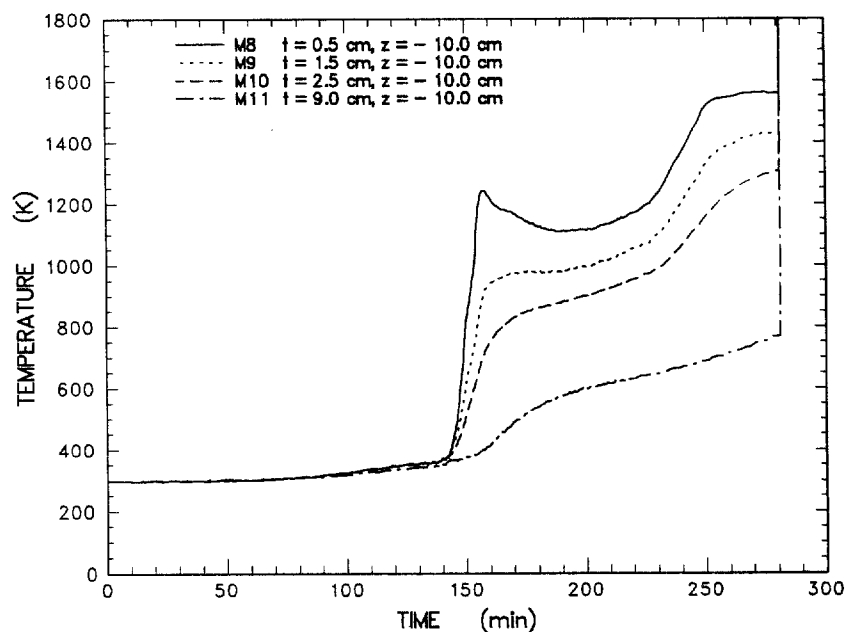
Figure C-18 MgO sidewall temperature data measured by thermocouples in the array located at z = -10.0 cm
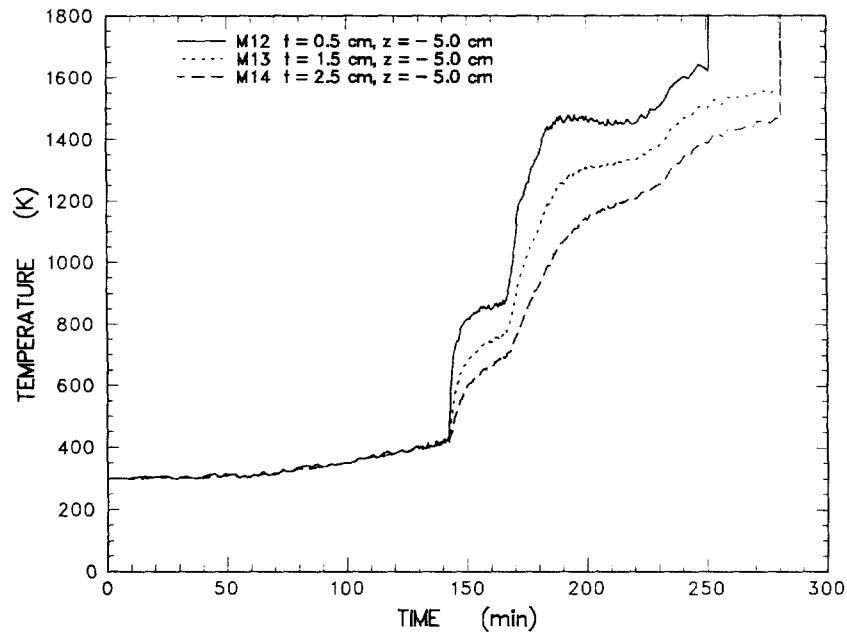
Figure C-19 MgO sidewall temperature data measured by thermocouples in the array located at z = -5.0 cm
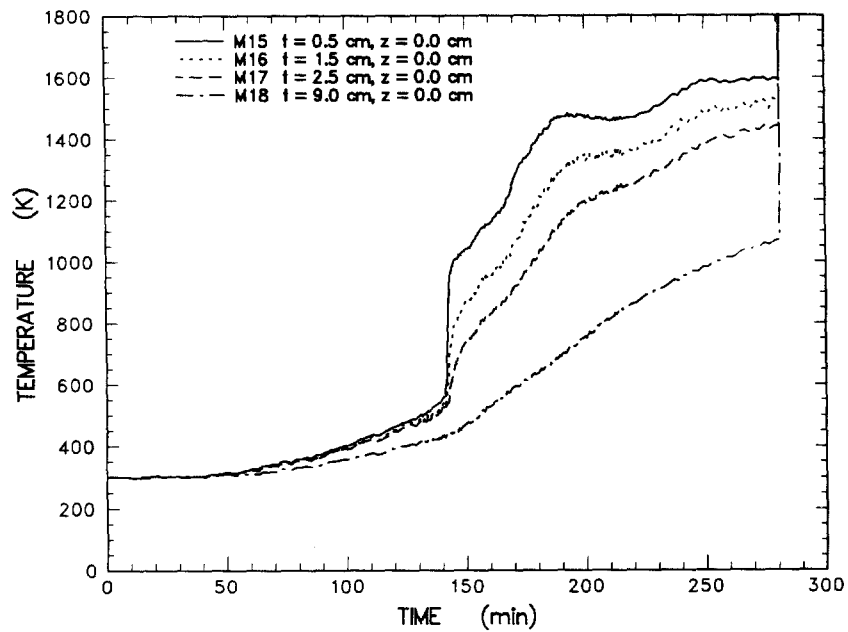
Figure C-20 MgO sidewall temperature data measured by thermocouples in the array located at z = 0.0 cm
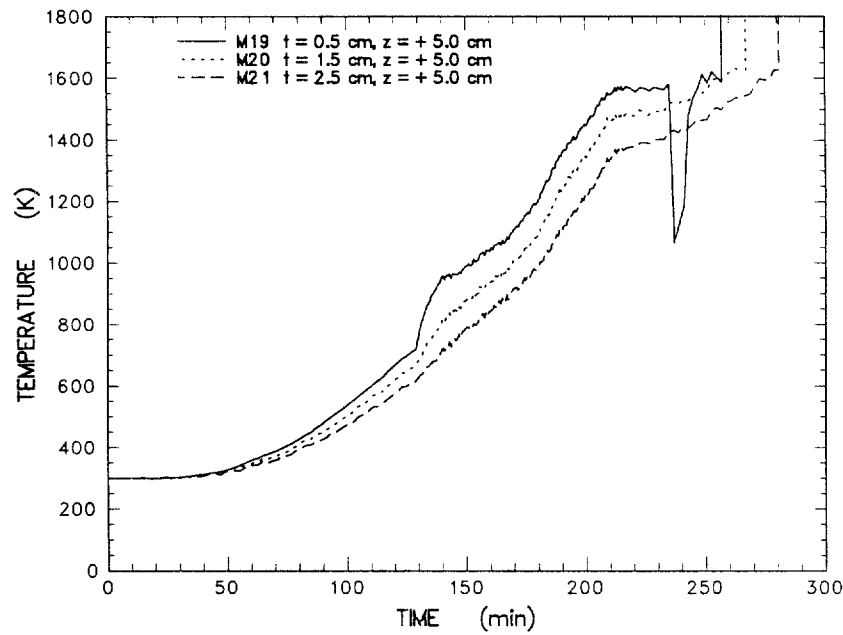
Figure C-21 MgO sidewall temperature data measured by thermocouples in the array located at z = +5.0 cm
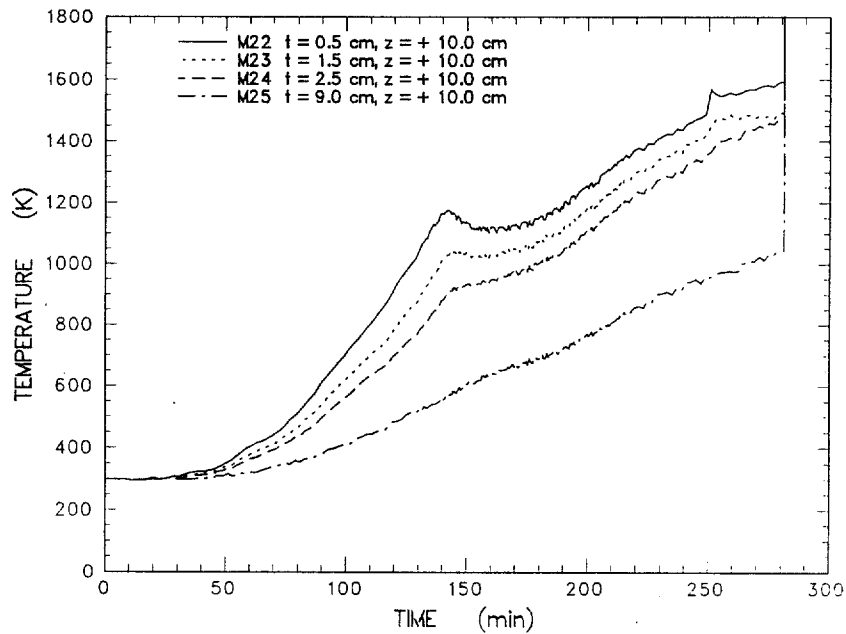
Figure C-22 MgO sidewall temperature data measured by thermocouples in the array located at z = +10.0 cm
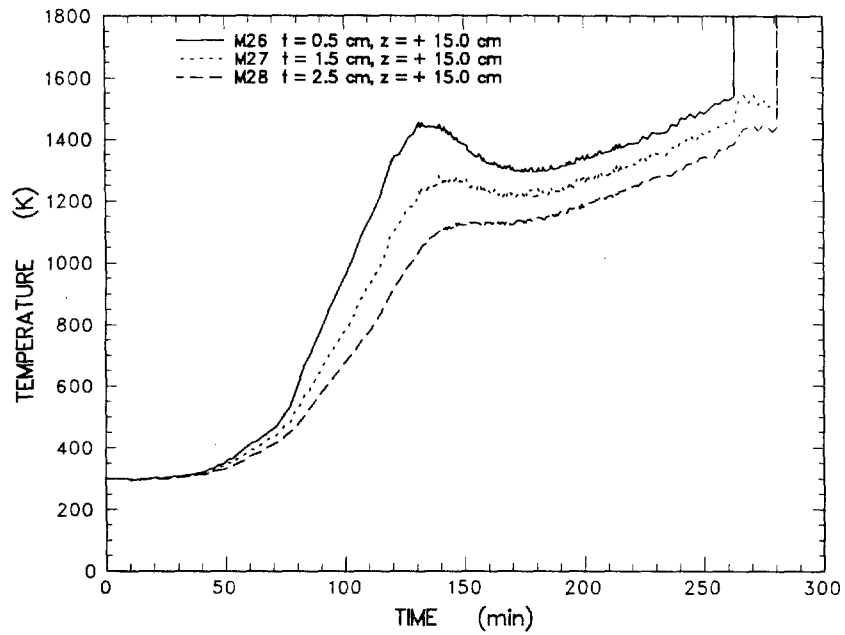
Figure C-23 **MgO sidewall temperature data measured by thermocouples in the array located at z = +15.0 cm**
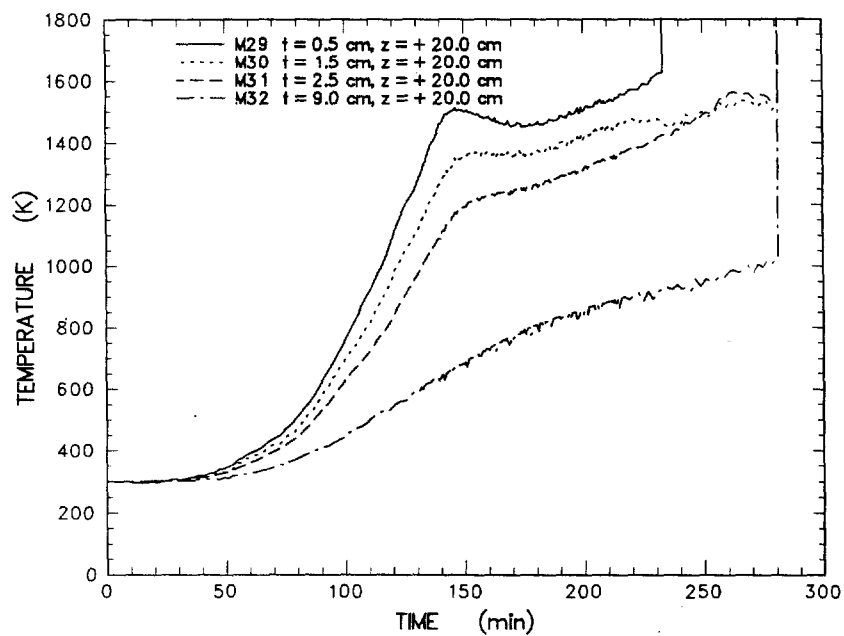
Figure C-24 **MgO sidewall temperature data measured by thermocouples in the array located at z = +20.0 cm**
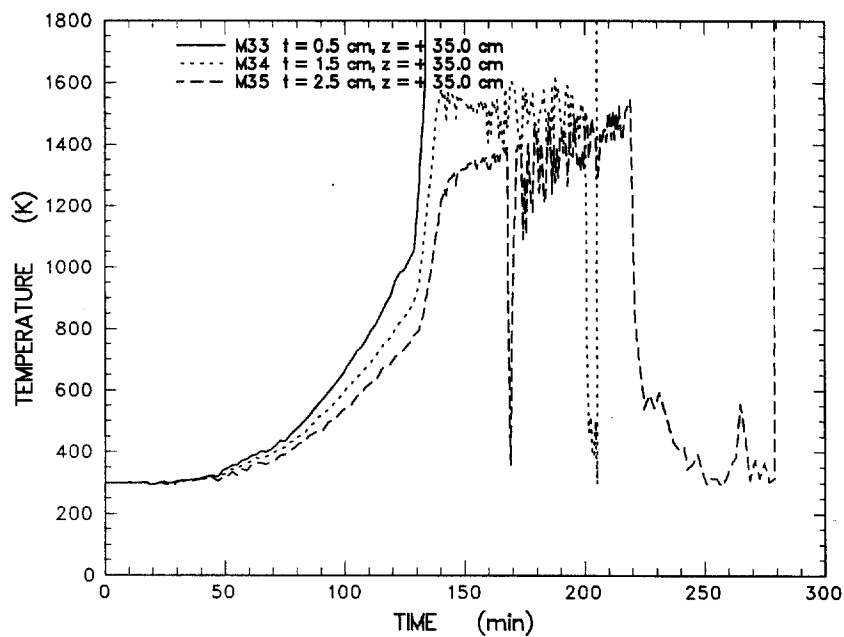
Figure C-25 **MgO sidewall temperature data measured by thermocouples in the array located at z = +35.0 cm**
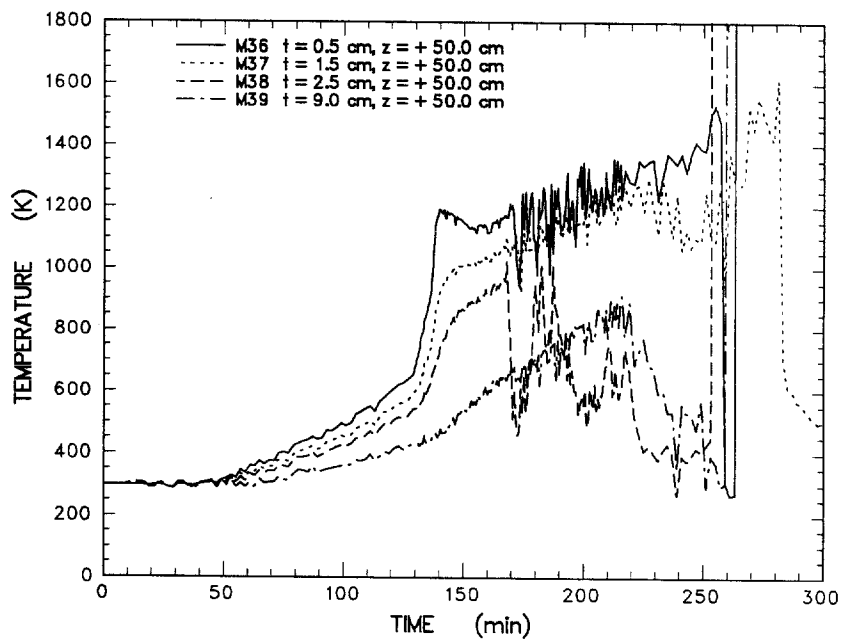
Figure C-26 **MgO sidewall temperature data measured by thermocouples in the array located at z = +50.0 cm**
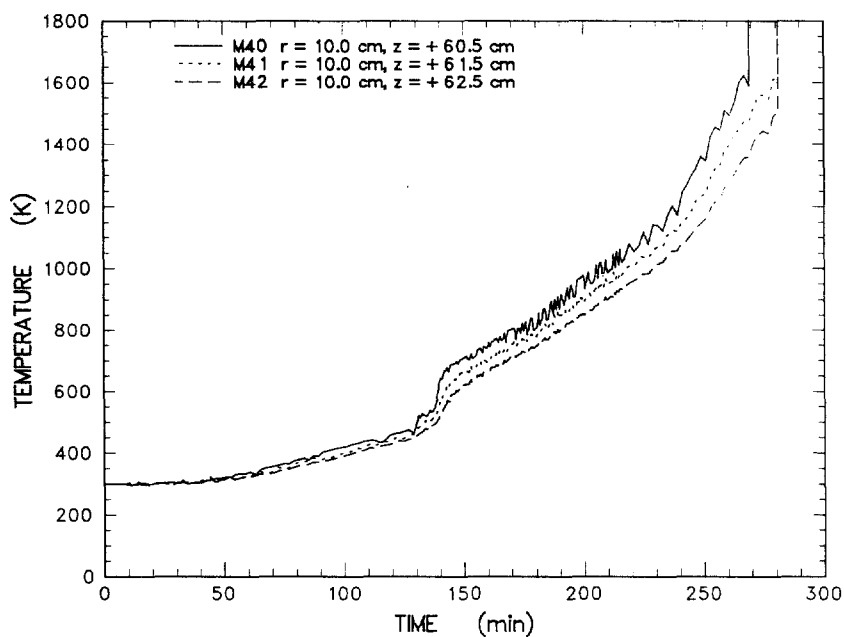
Figure C-27 MgO sidewall temperature data measured by thermocouples in the array located at r = +10.0 cm, θ = 0, and z = +60.0 cm
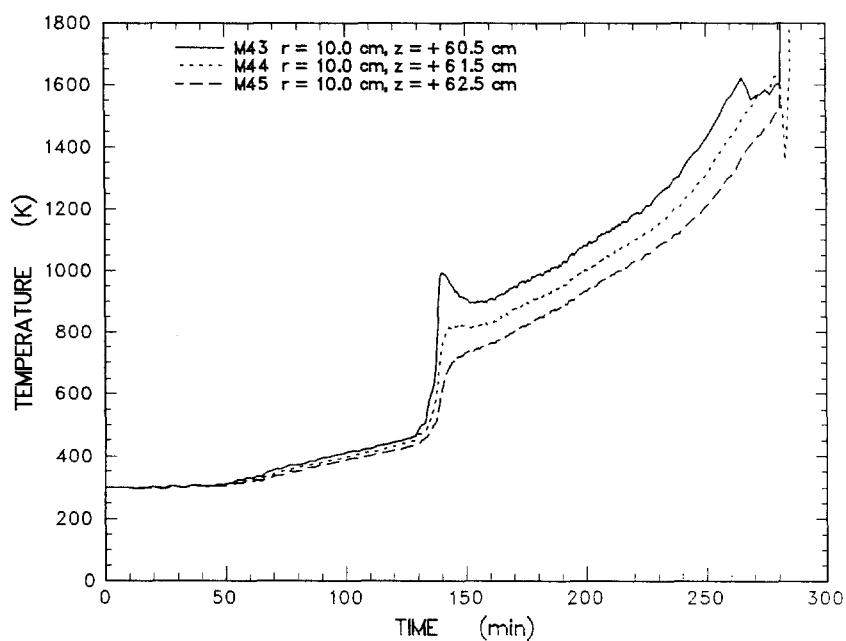
Figure C-28 Alumina sidewall temperature data measured by thermocouples in the array located at r = 10.0 cm, θ = 180, and z = +60.0 cm
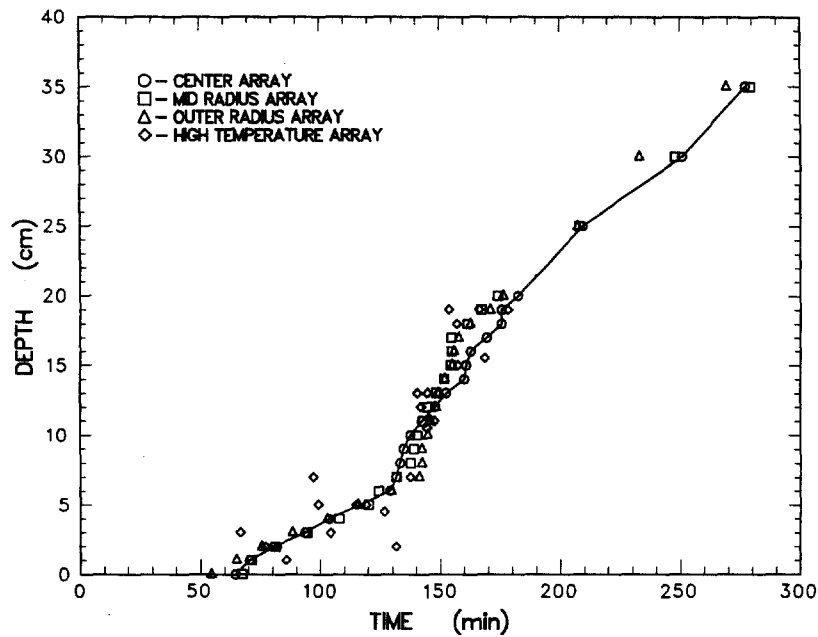
Figure C-29 Position of the 400 K isotherm plotted as a function of time
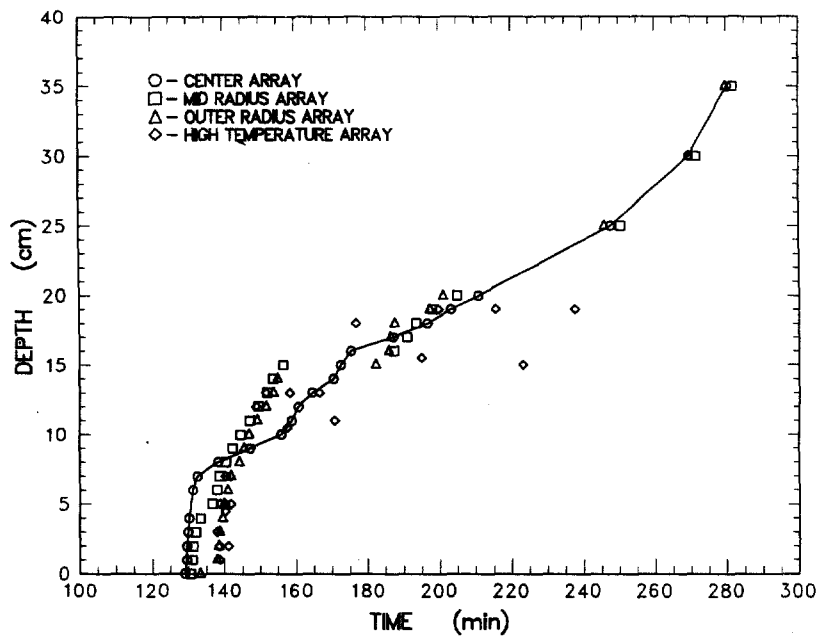
Figure C-30 Position of the concrete erosion plotted as a function of time
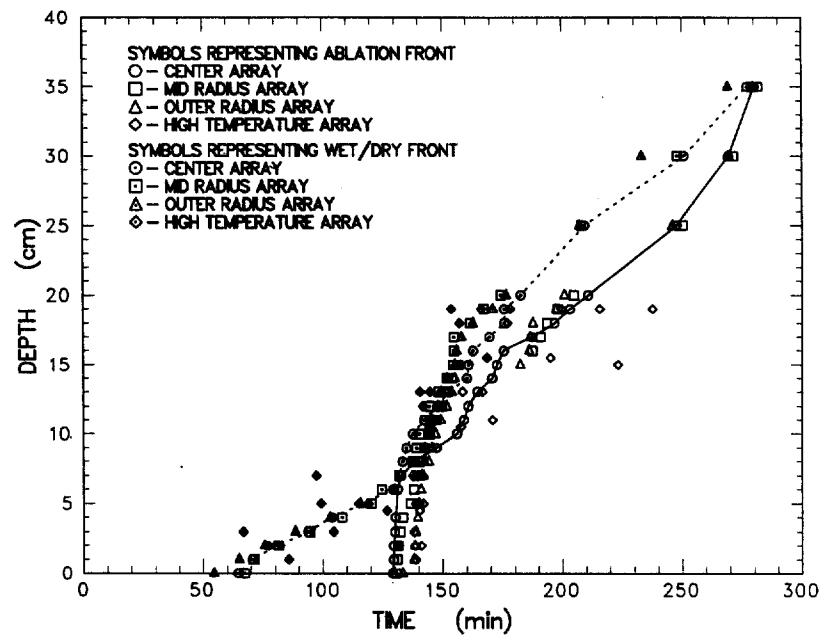
Figure C-31 Comparison of the position of the 400 K isotherm and the concrete erosion front

Appendix D: Melt Temperature and Pyrometer Data

In this appendix charge temperature data is presented for type C and S thermocouples installed in alumina tubes and cast into the concrete cylinder. Pyrometer data is presented for three fiber optic pyrometers each focused at the base of a thick walled, closed end tungsten tube. Also presented, are the temperature profiles for the C type thermocouples installed at the base of each of the tungsten tubes. The tubes were purged with argon to minimize oxidation.
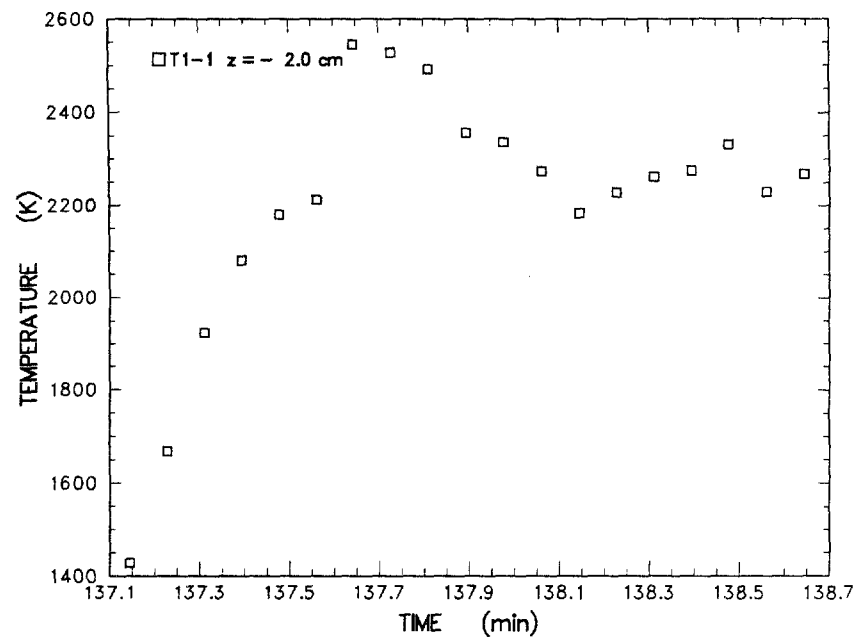
Figure D-1 Expansion of meltpool temperature data measured by a C type thermocouple installed in an alumina tube cast into the concrete at z = -2.0 cm
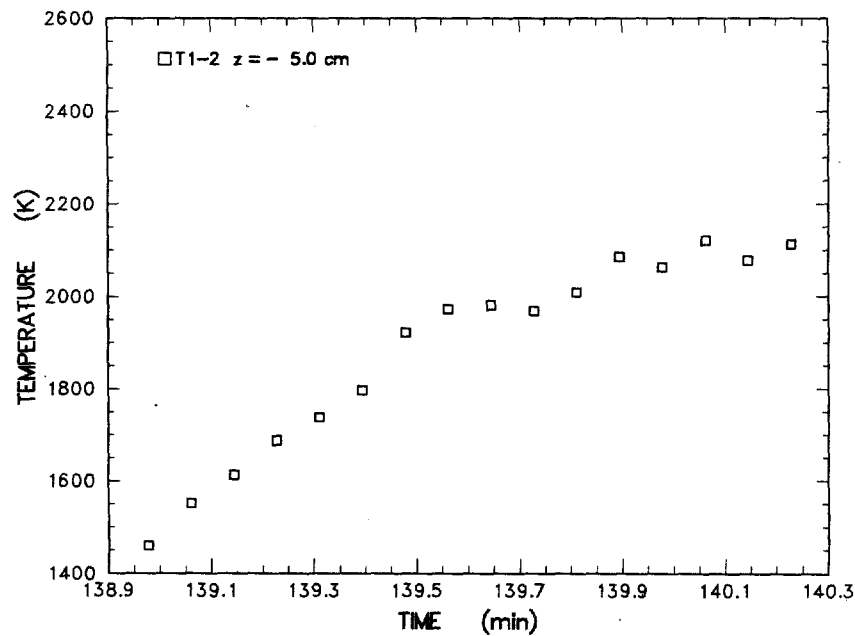
Figure D-2 Expansion of meltpool temperature data measured by a C type thermocouple installed in an alumina tube cast into the concrete at z = -5.0 cm
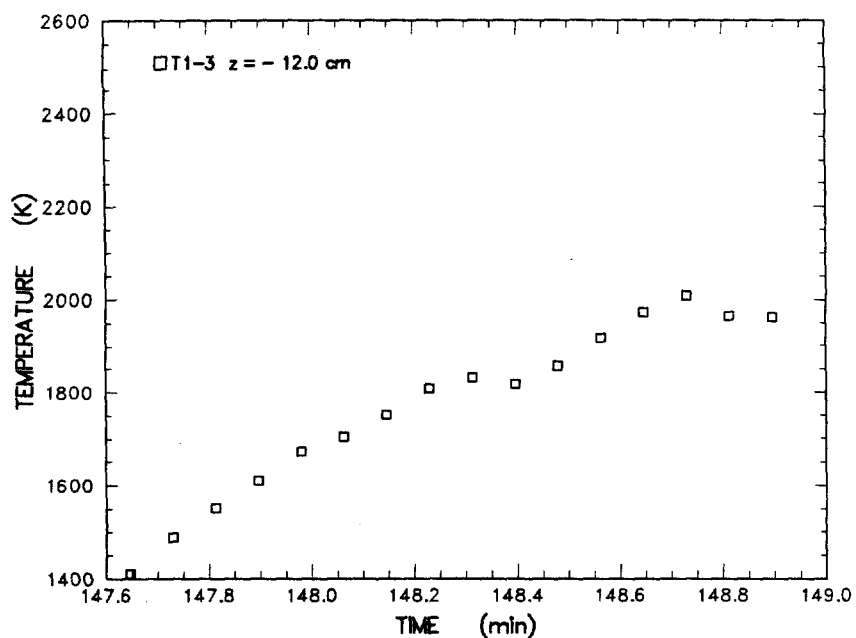
Figure D-3   Expansion of meltpool temperature data measured by a S type thermocouple installed in an alumina tube cast into the concrete at z = -12.0 cm
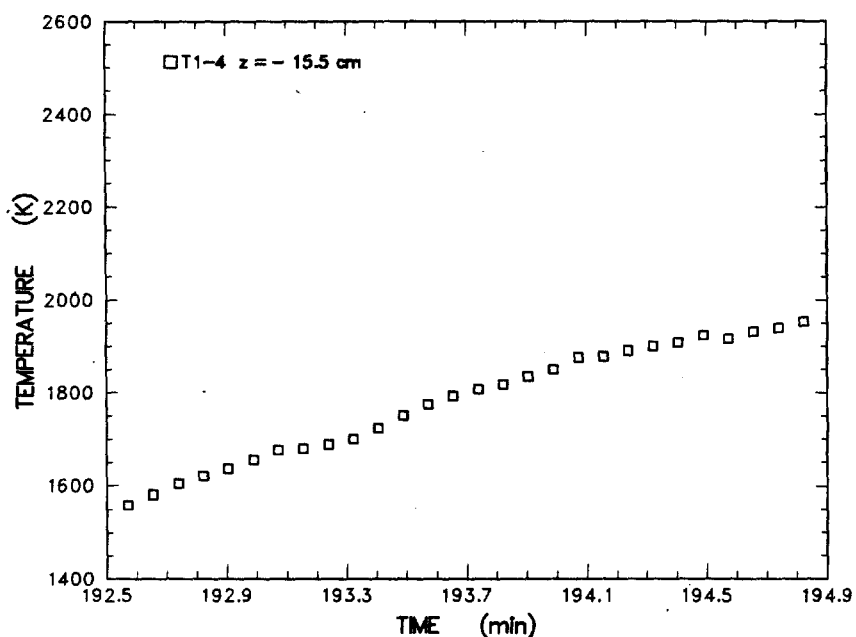
Figure D-4   Expansion of meltpool temperature data measured by a S type thermocouple installed in an alumina tube cast into the concrete at z = -15.0 cm
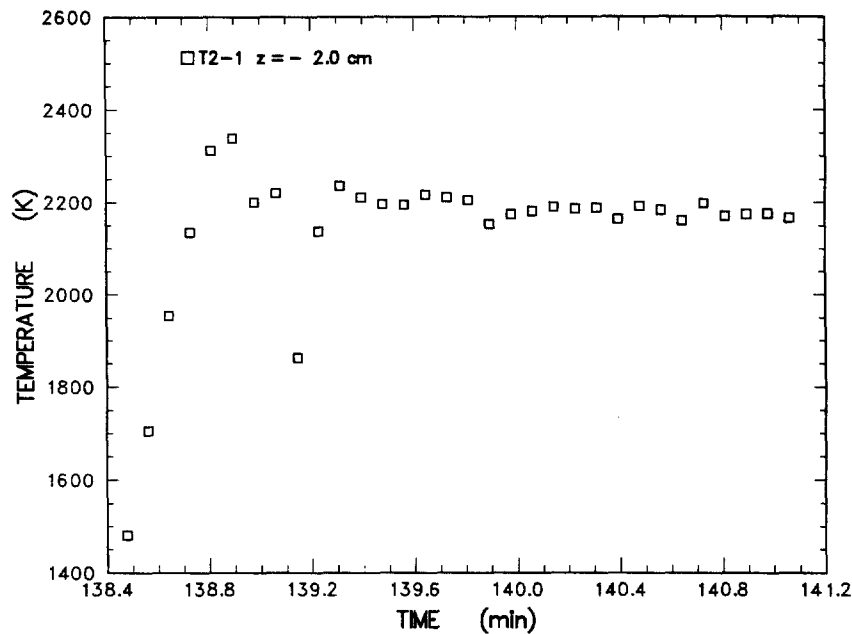
Figure D-5 Expansion of meltpool temperature data measured by a C type thermocouple installed in an alumina tube cast into the concrete at z = -2.0 cm
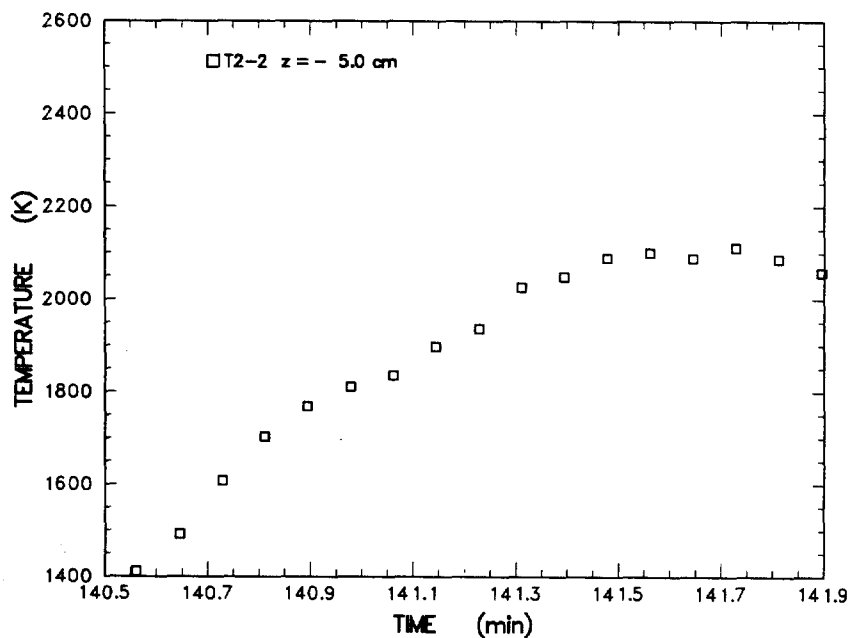
Figure D-6 Expansion of meltpool temperature data measured by a C type thermocouple installed in an alumina tube cast into the concrete at z = -5.0 cm
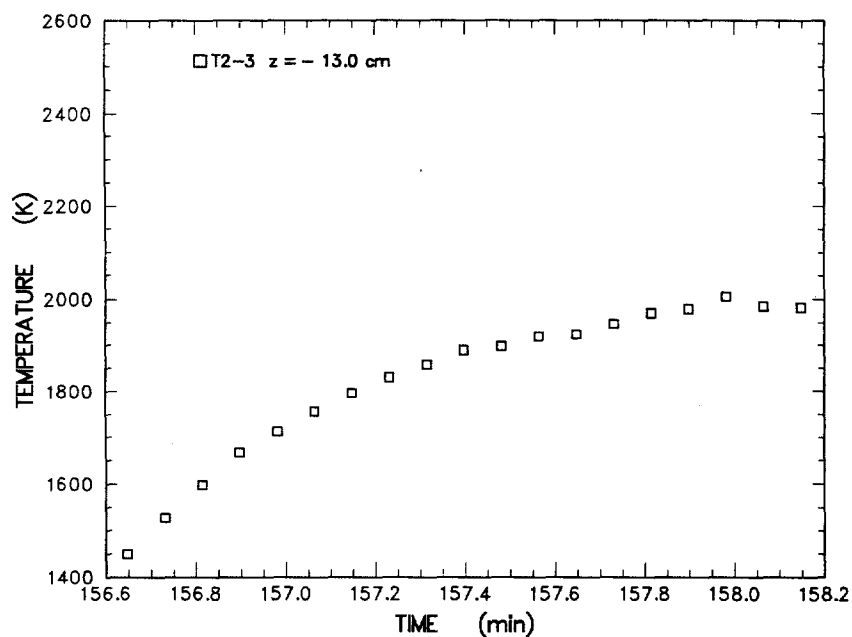
Figure D-7 Expansion of meltpool temperature data measured by a S type thermocouple installed in an alumina tube cast into the concrete at z = -13.0 cm
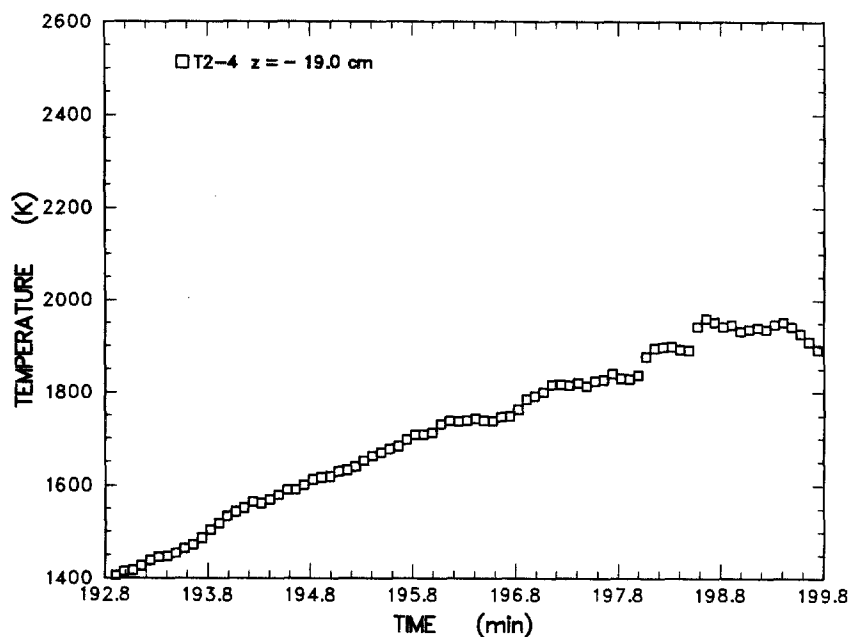
Figure D-8 Expansion of meltpool temperature data measured by a S type thermocouple installed in an alumina tube cast into the concrete at z = -19.0 cm
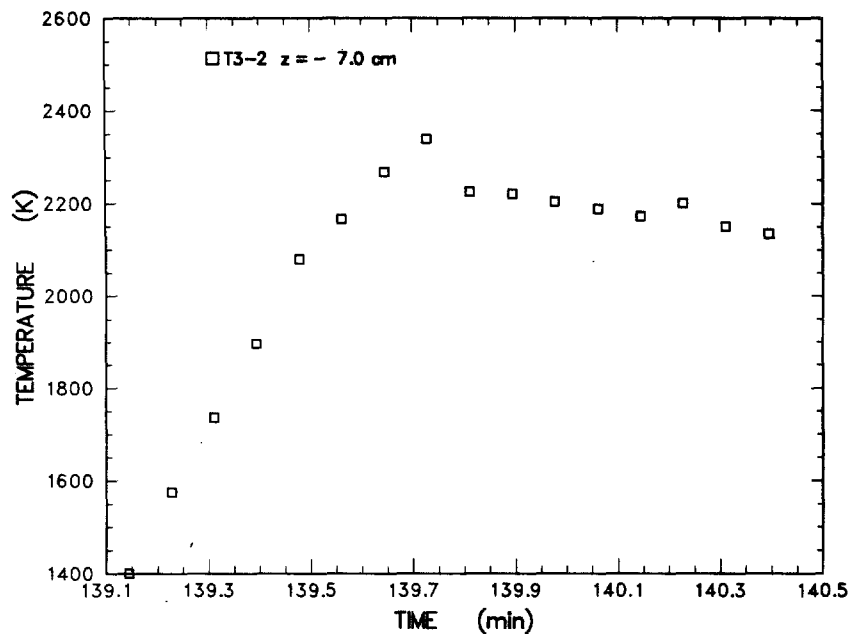
Figure D-9 Expansion of meltpool temperature data measured by a C type thermocouple installed in an alumina tube cast into the concrete at z = -7.0 cm
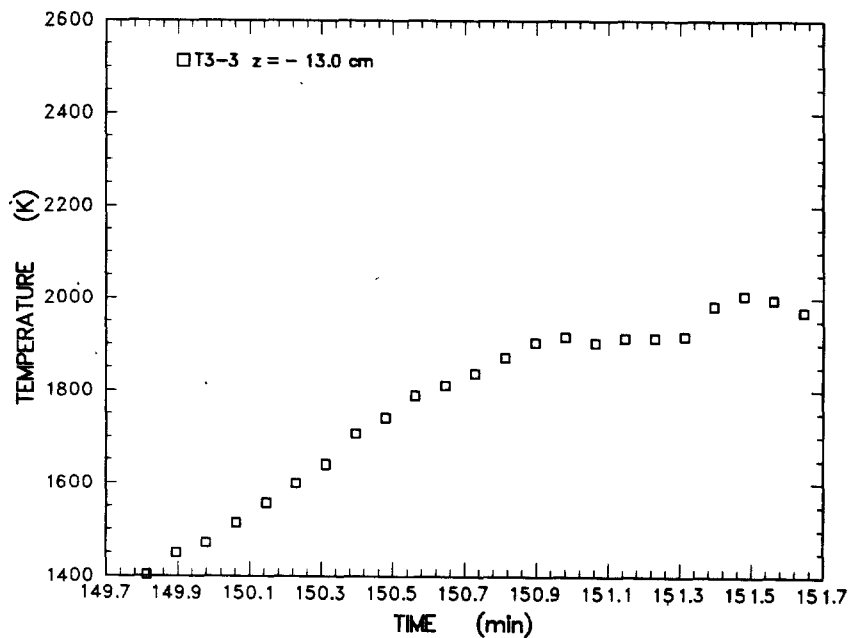
Figure D-10 Expansion of meltpool temperature data measured by a S type thermocouple installed in an alumina tube cast into the concrete at z = -13.0 cm
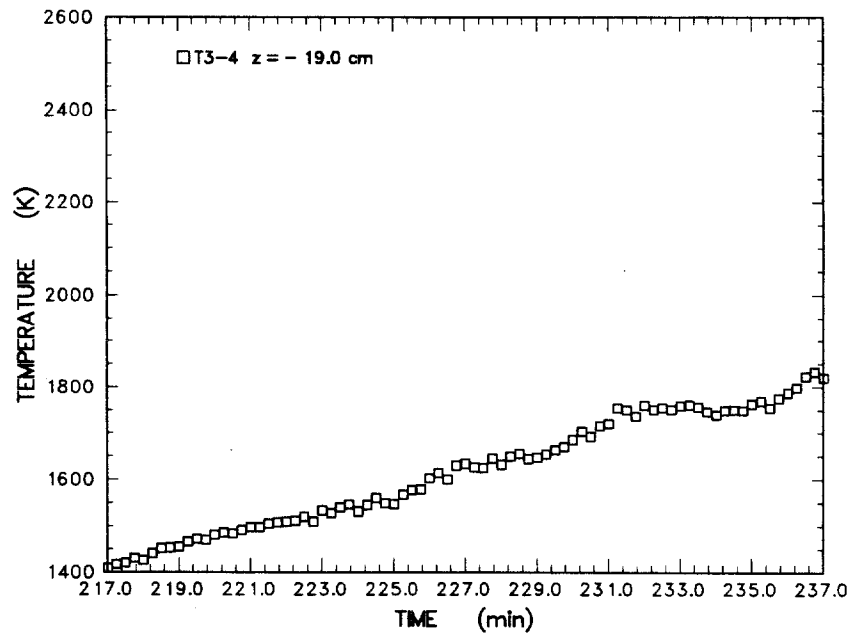
Figure D-11 Expansion of meltpool temperature data measured by a S type thermocouple installed in an alumina tube cast into the concrete at z = -19.0 cm
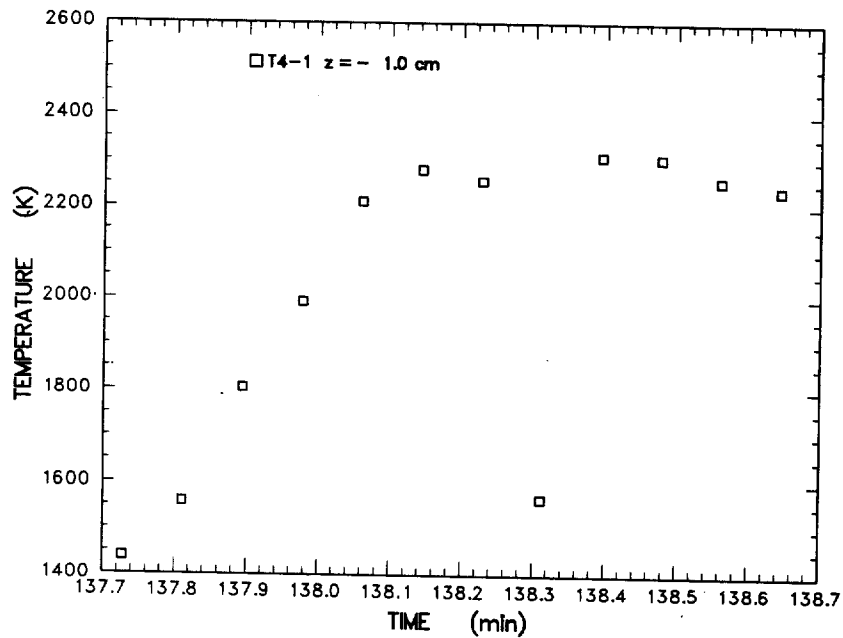
Figure D-12 Expansion of meltpool temperature data measured by a C type thermocouple installed in an alumina tube cast into the concrete at z = -1.0 cm
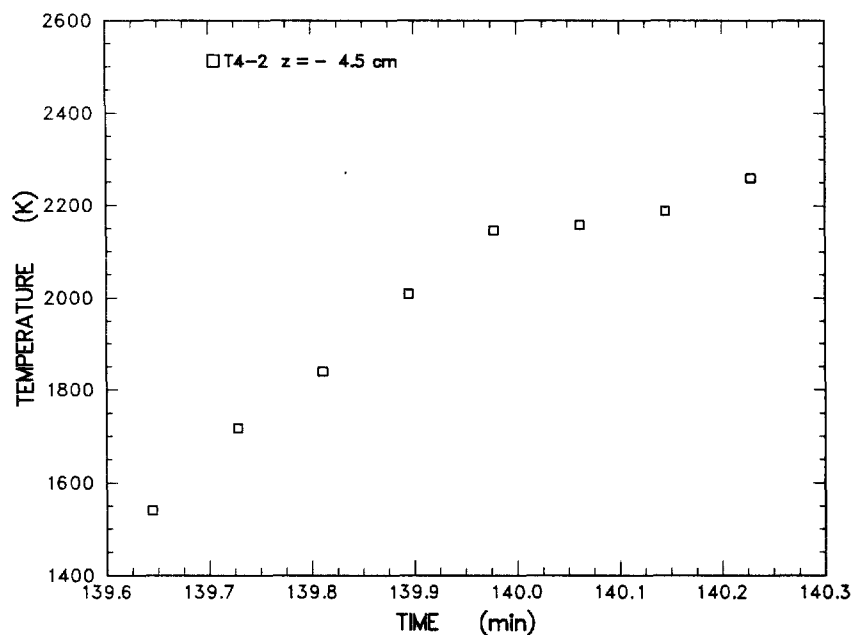
Figure D-13 Expansion of meltpool temperature data measured by a C type thermocouple installed in an alumina tube cast into the concrete at z = -4.5 cm
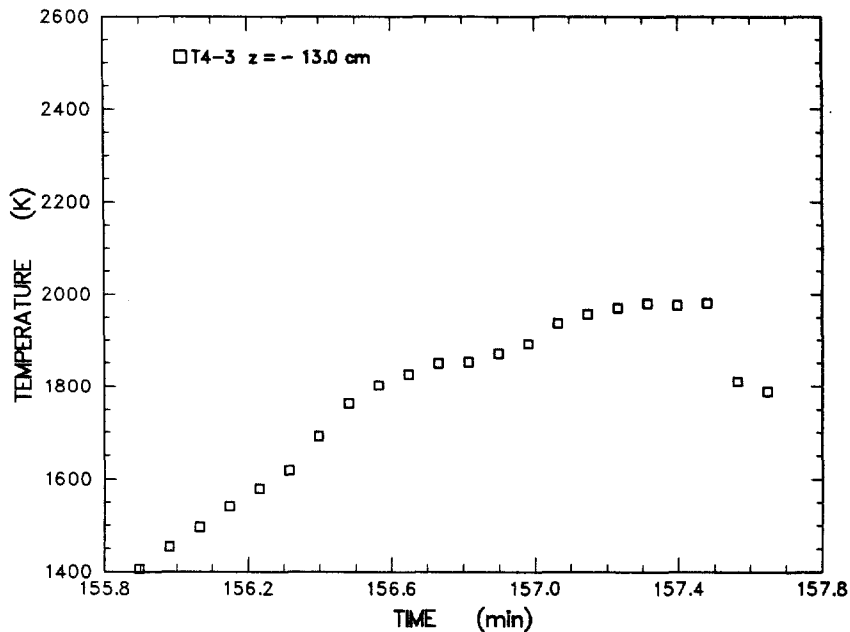
Figure D-14 Expansion of meltpool temperature data measured by a S type thermocouple installed in an alumina tube cast into the concrete at z = -13.0 cm
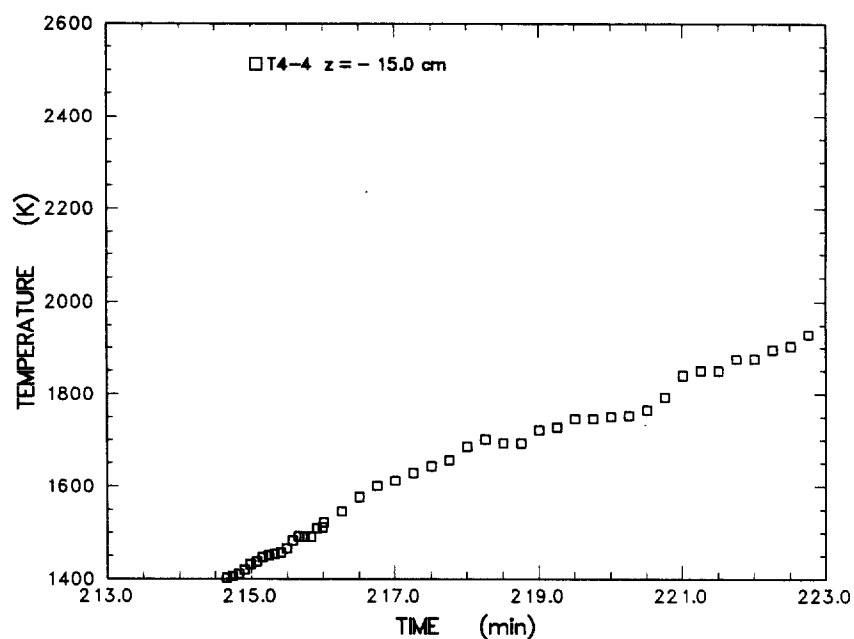
Figure D-15 Expansion of meltpool temperature data measured by a S type thermocouple installed in an alumina tube cast into the concrete at z = -15.0 cm
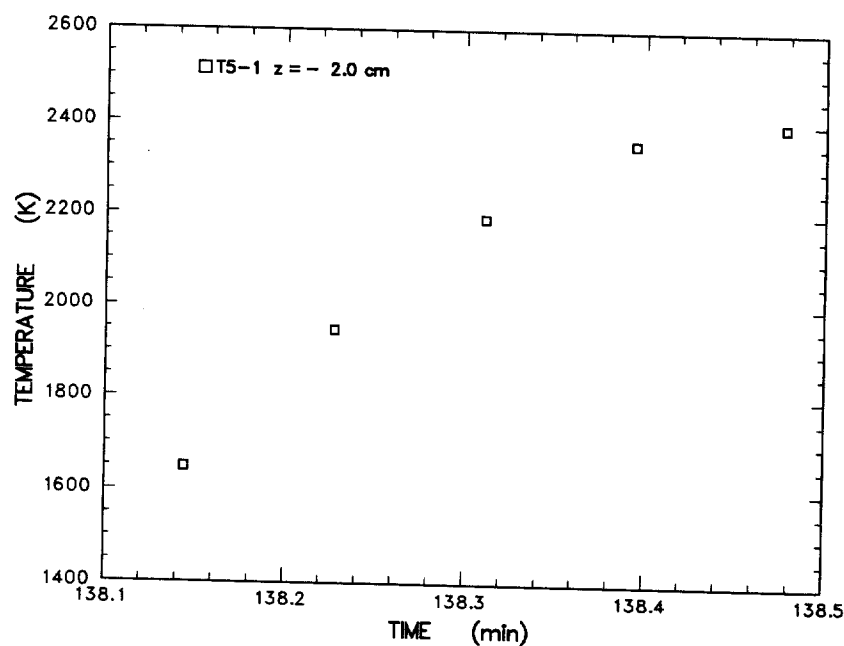
Figure D-16 Expansion of meltpool temperature data measured by a C type thermocouple installed in an alumina tube cast into the concrete at z = -2.0 cm
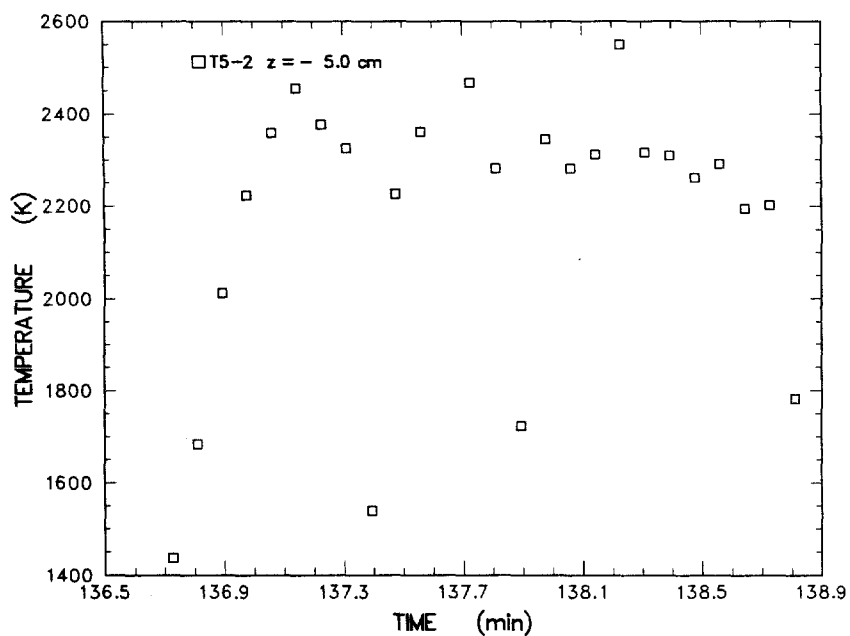
Figure D-17 **Expansion of meltpool temperature data measured by a C type thermocouple installed in an alumina tube cast into the concrete at z = -5.0 cm**
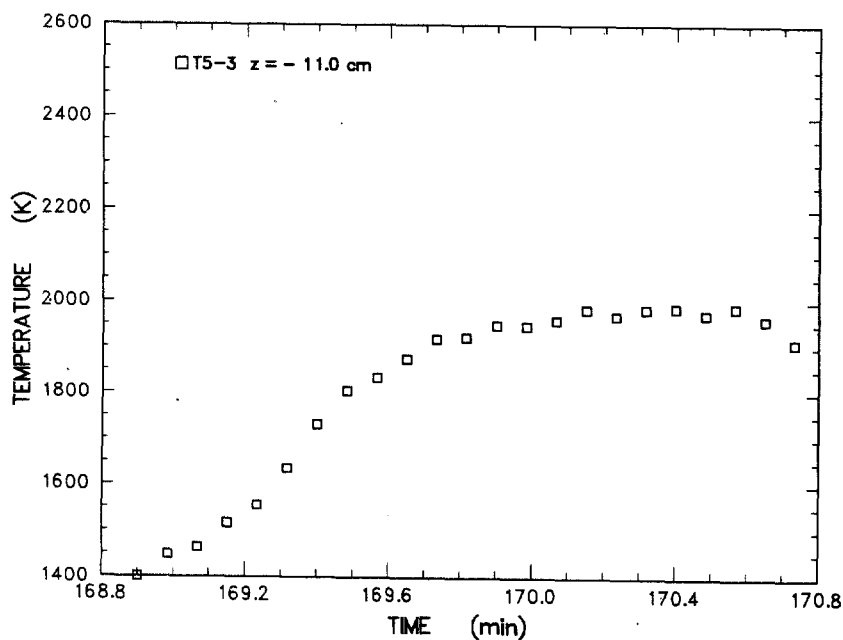
Figure D-18 **Expansion of meltpool temperature data measured by a S type thermocouple installed in an alumina tube cast into the concrete at z = -11.0 cm**
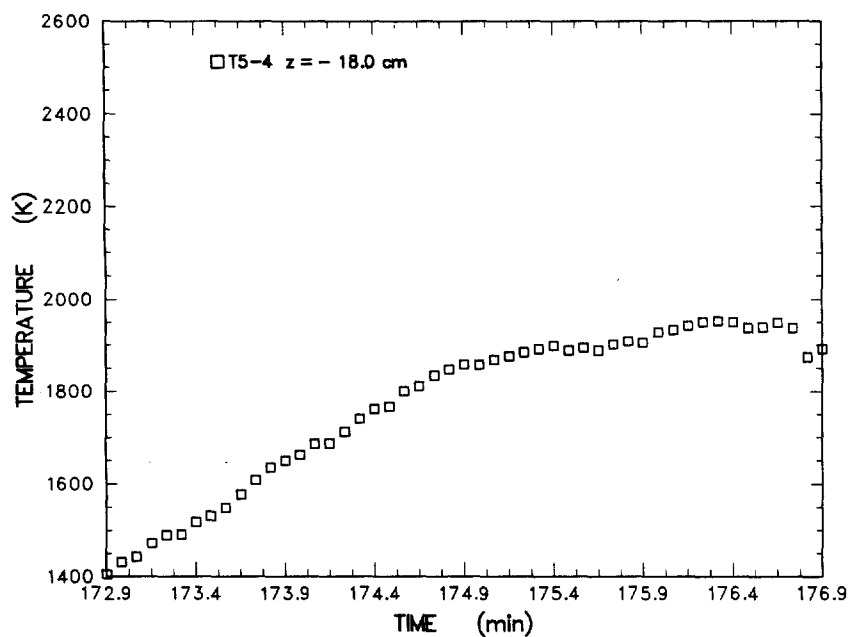
Figure D-19 Expansion of meltpool temperature data measured by a S type thermocouple installed in an alumina tube cast into the concrete at z = -18.0 cm
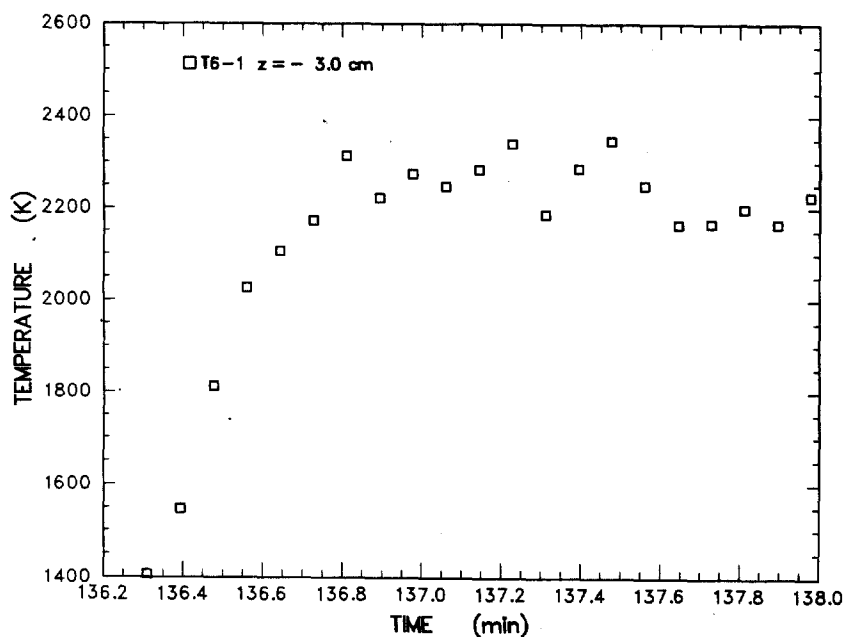
Figure D-20 Expansion of meltpool temperature data measured by a C type thermocouple installed in an alumina tube cast into the concrete at z = -3.0 cm
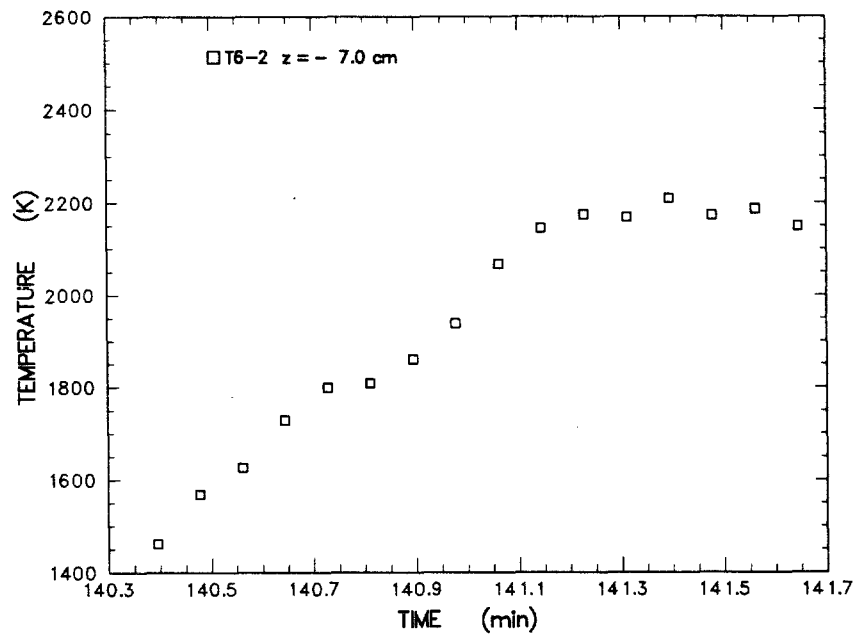
Figure D-21 Expansion of meltpool temperature data measured by a C type thermocouple installed in an alumina tube cast into the concrete at z = -7.0 cm
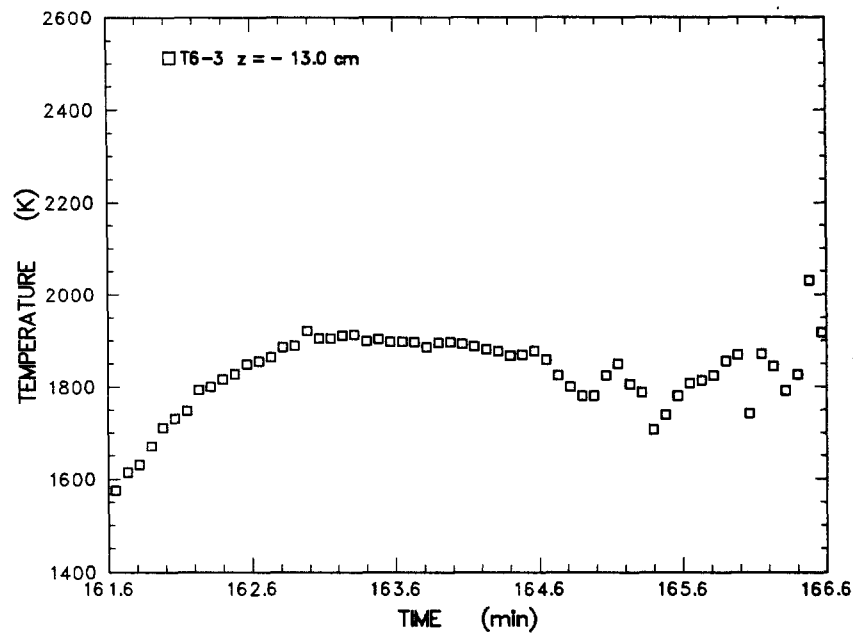
Figure D-22 Expansion of meltpool temperature data measured by a S type thermocouple installed in an alumina tube cast into the concrete at z = -13.0 cm
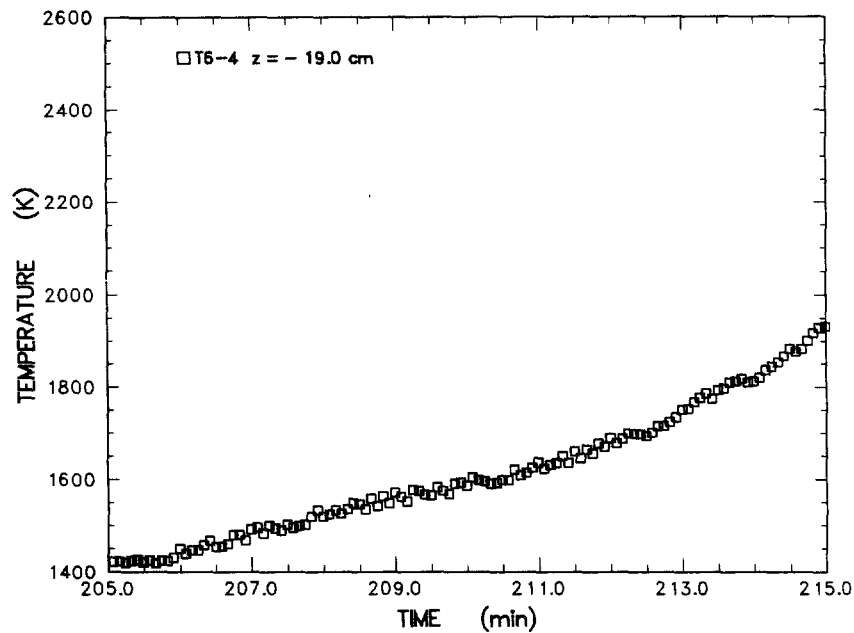
Figure D-23 Expansion of meltpool temperature data measured by a S type thermocouple installed in an Alumina tube cast into the concrete at z = -19.0 cm
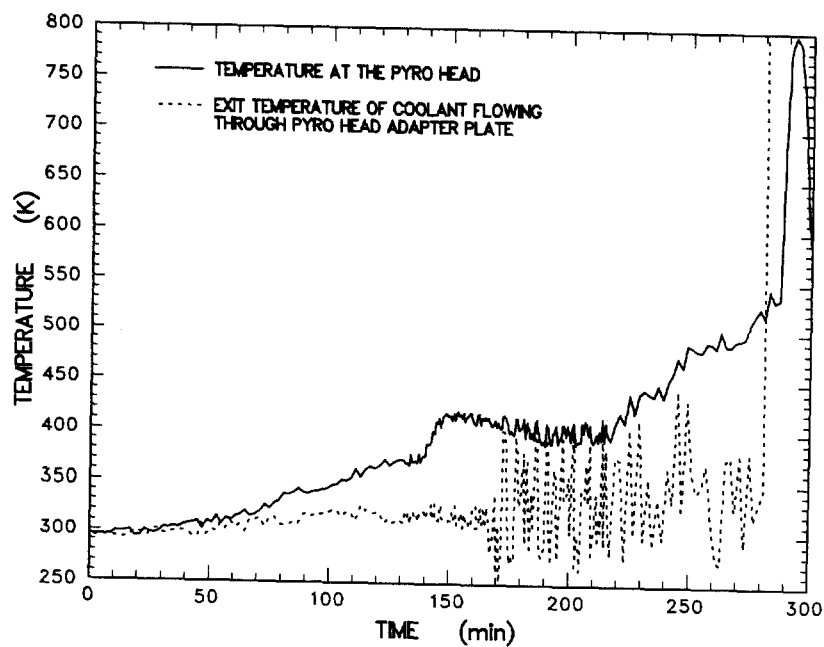
Figure D-24 Temperature at the pyrometer head and exit temperature of the cooling fluid flowing through the pyrometer adapter/support plate
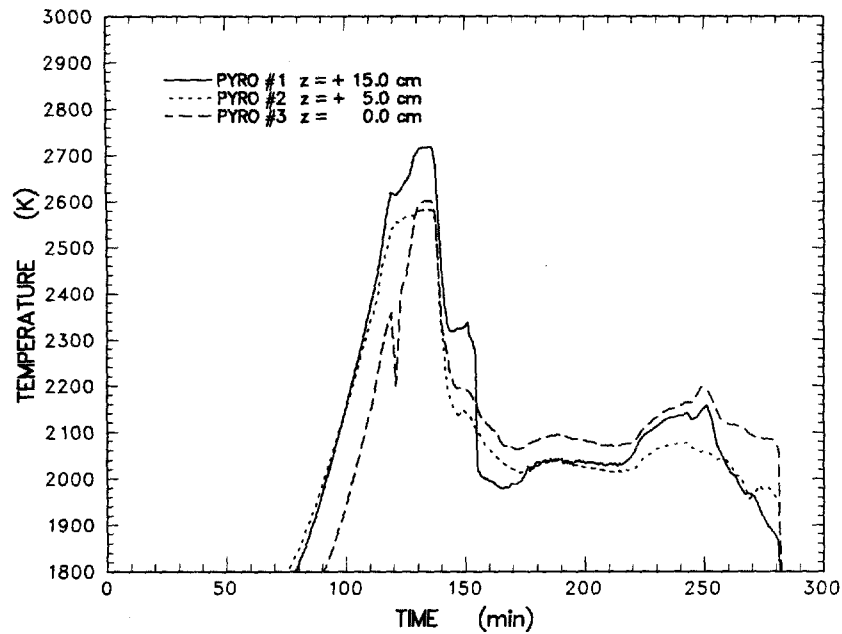
Figure D-25 Temperatures measured by the micron fiber optic pyrometers
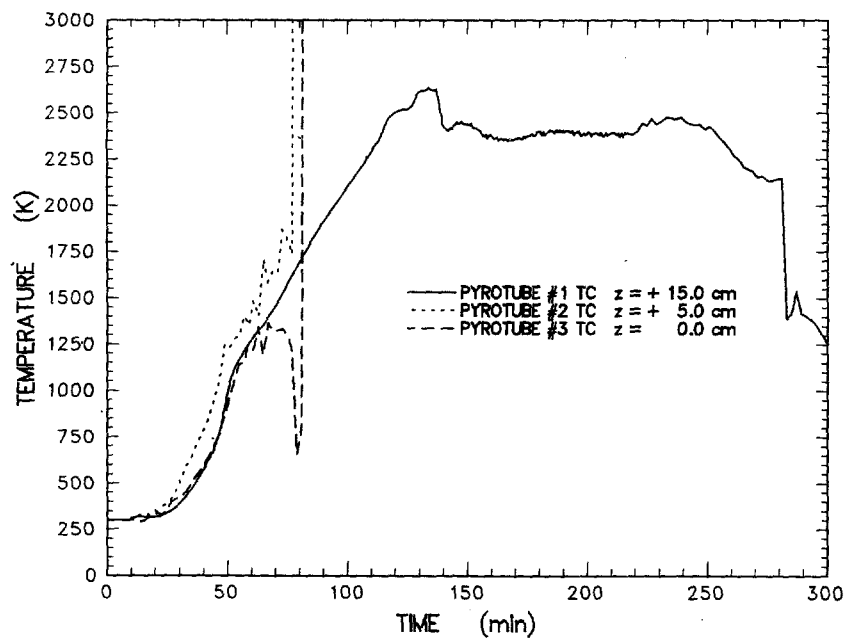
Figure D-26 Temperatures measured by the Type C thermocouples installed at the base of the tungsten pyrotubes
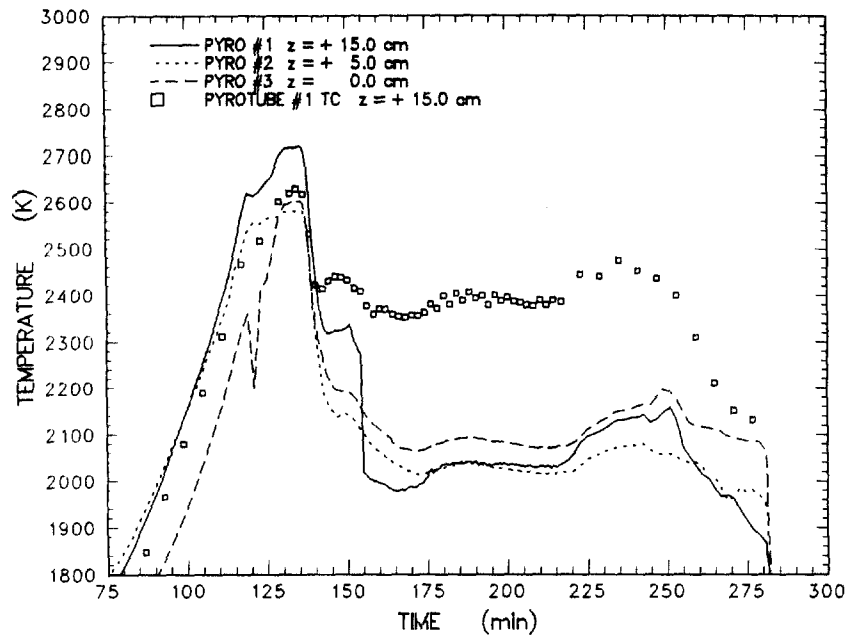
Figure D-27 Comparison of temperatures measured by the pyrometers and the type C thermocouple installed in the tungsten pyrotube located at z = +15.0 cm
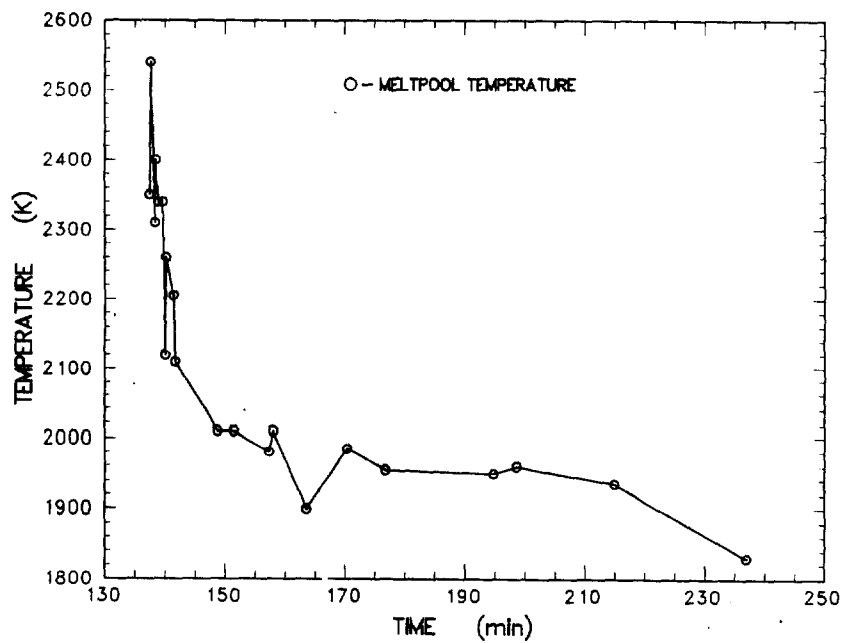
Figure D-28 Meltpool temperature summary

Appendix E: Calculated Sidewall Heat Flux Data

Presented in this appendix are the sidewall and upward heat fluxes calculated using an inverse heat conduction code. Calculations were made based on temperature data produced from type K thermocouple arrays imbedded in the alumina annulus and crucible cover. Additionally, plots are presented comparing sidewall temperatures measured during the experiment and calculated from the inverse heat conduction code.
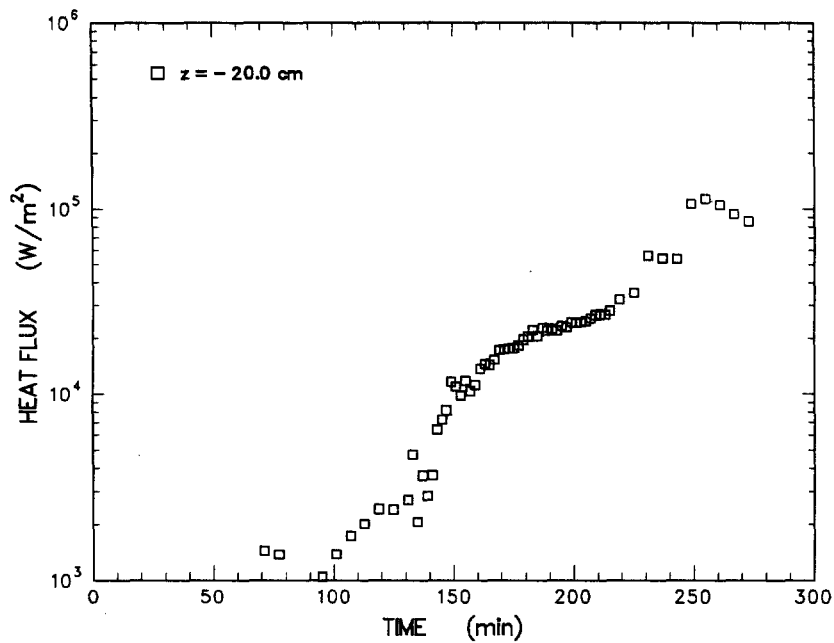
Figure E-1 MgO sidewall heat flux calculated from thermocouple data for the array located at z = -20.0 cm
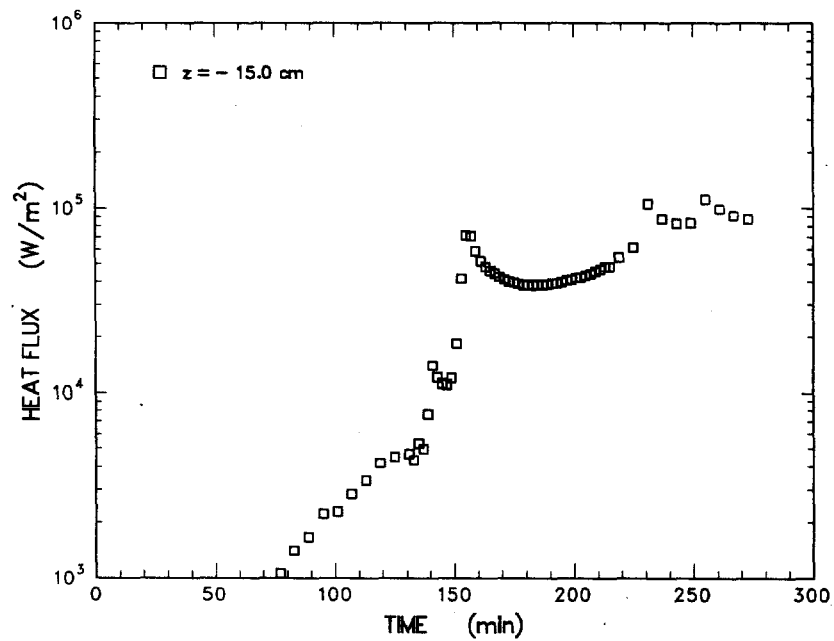
Figure E-2 MgO sidewall heat flux calculated from thermocouple data for the array located at z = -15.0 cm
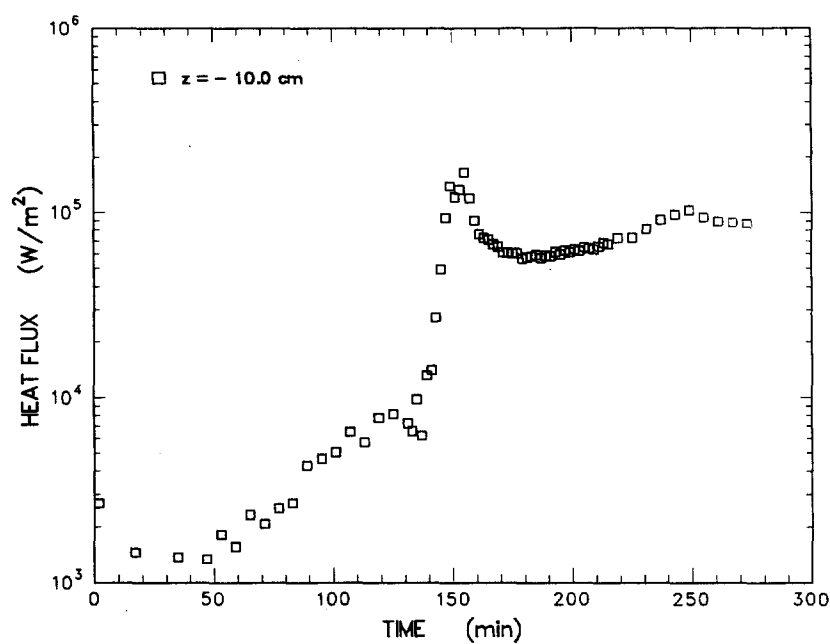
Figure E-3 MgO sidewall heat flux calculated from thermocouple data for the array located at z = -10.0 cm
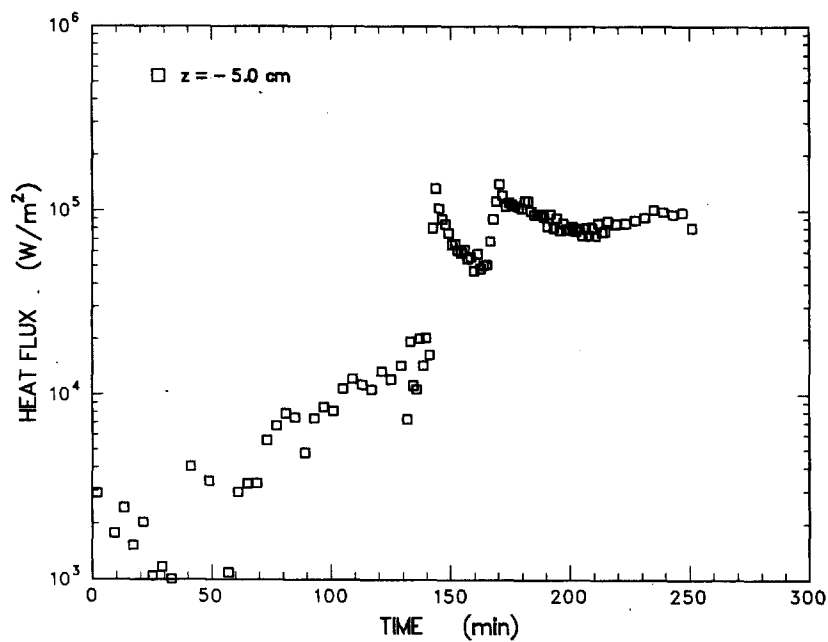
Figure E-4 MgO sidewall heat flux calculated from thermocouple data for the array located at z = -5.0 cm

Appendix E
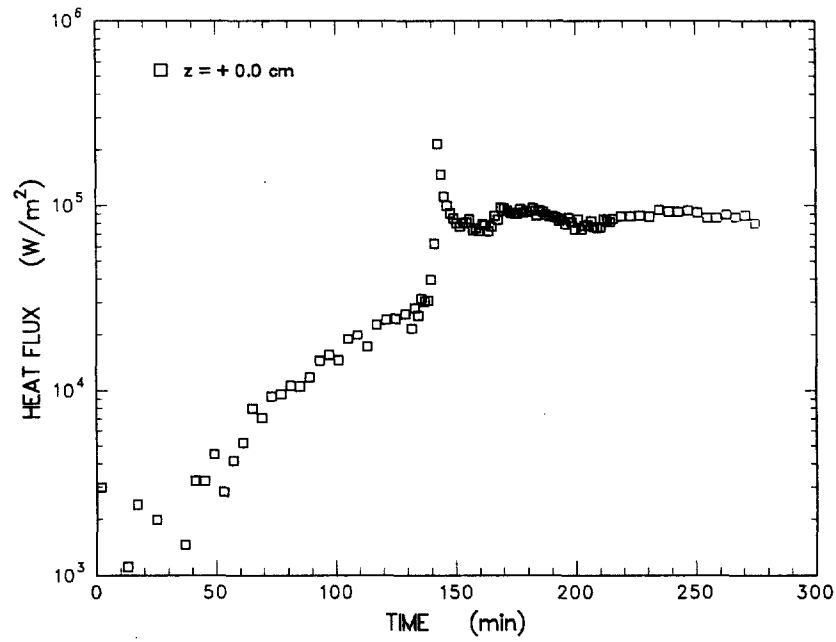
Figure E-5   **MgO sidewall heat flux calculated from thermocouple data for the array located at z = 0.0 cm**
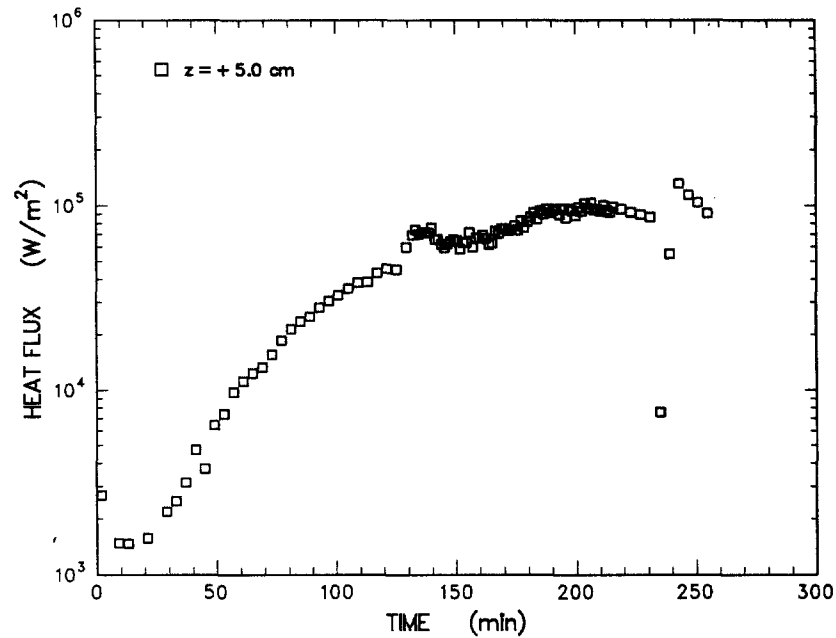
Figure E-6   **MgO sidewall heat flux calculated from thermocouple data for the array located at z = +5.0 cm**
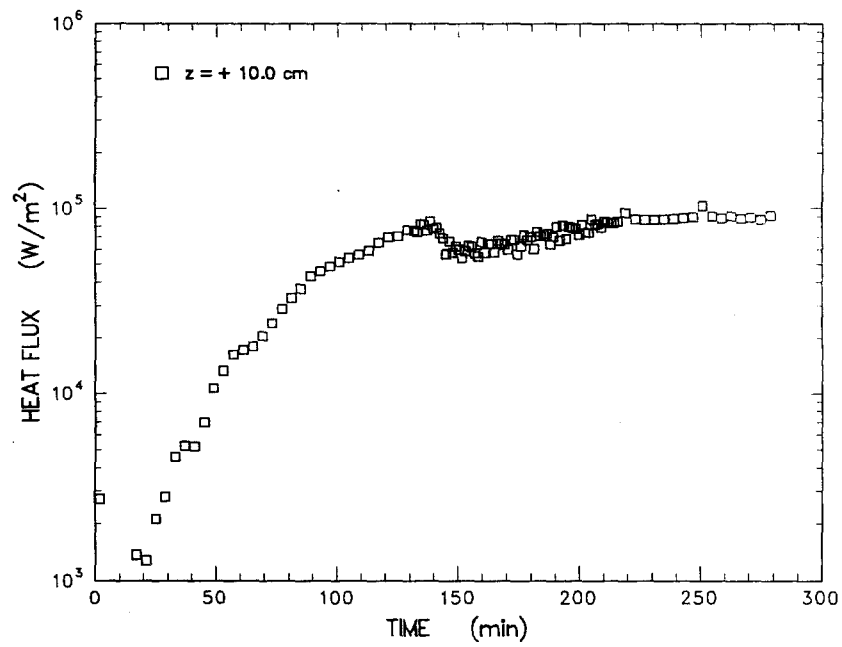
Figure E-7 MgO sidewall heat flux calculated from thermocouple data for the array located at z = +10.0 cm
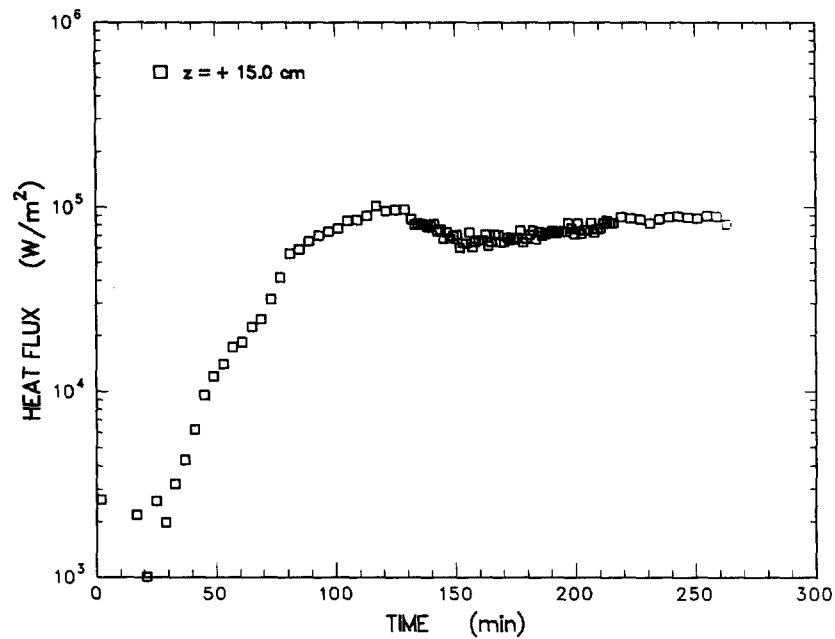
Figure E-8 MgO sidewall heat flux calculated from thermocouple data for the array located at z = +15.0 cm
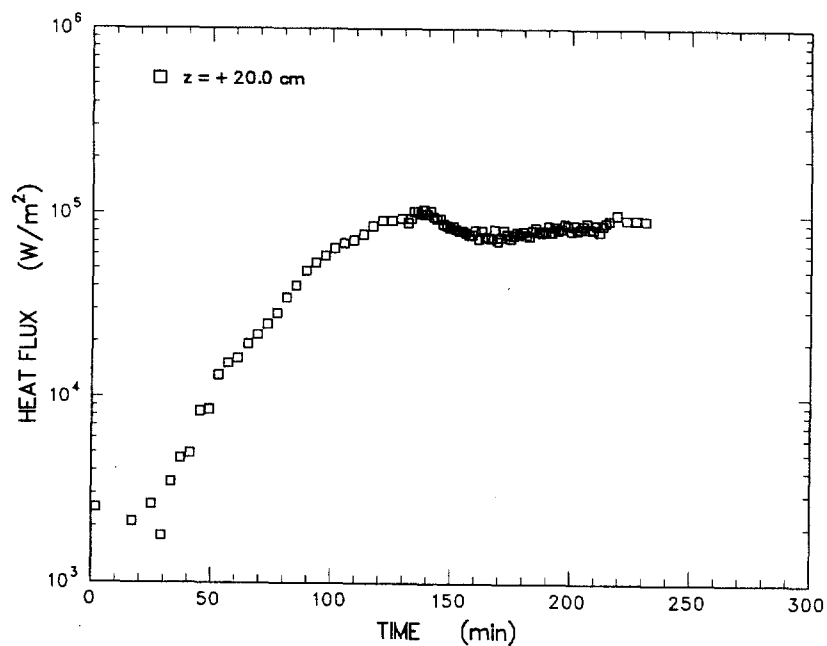
Figure E-9 MgO sidewall heat flux calculated from thermocouple data for the array located at z = +20.0 cm
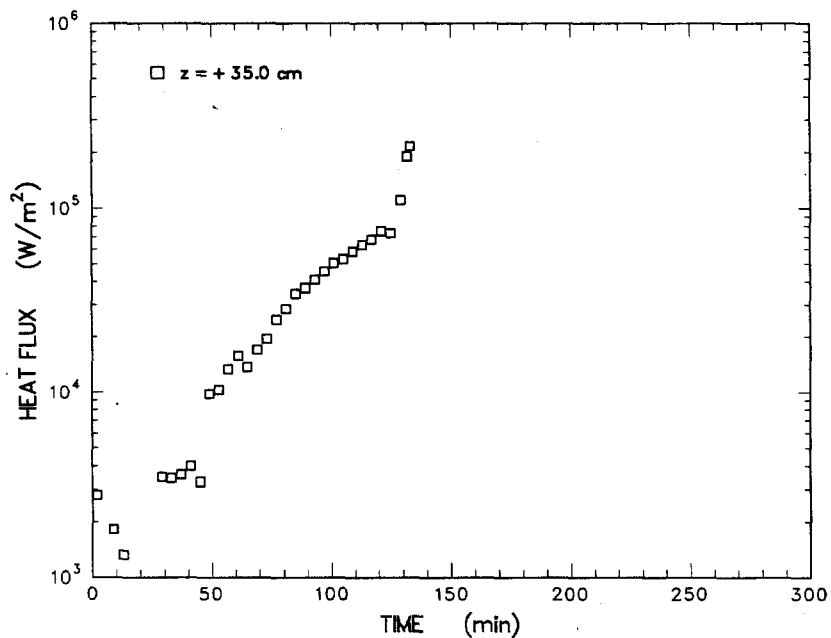
Figure E-10 MgO sidewall heat flux calculated from thermocouple data for the array located at z = +35.0 cm
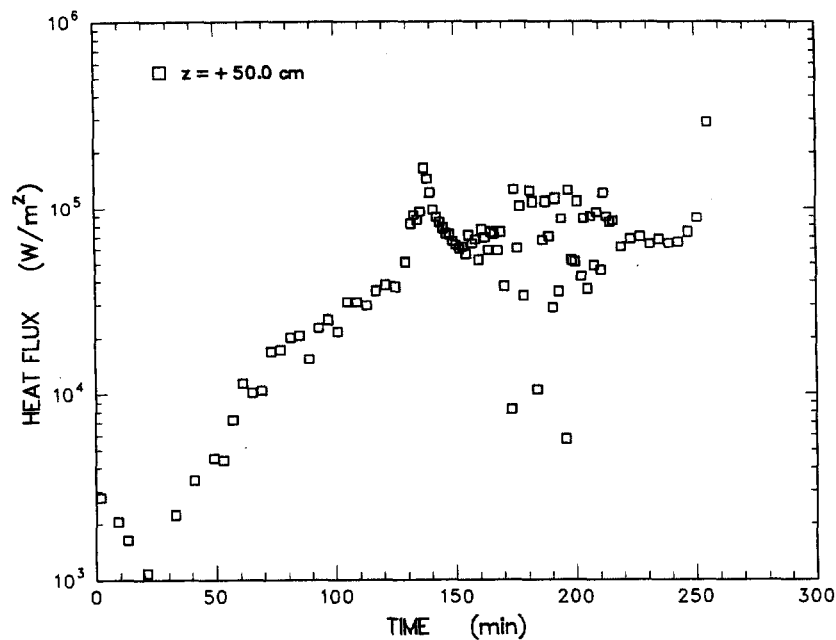
Figure E-11 **Alumina sidewall heat flux calculated from thermocouple data for the array located at z = +50.0 cm**
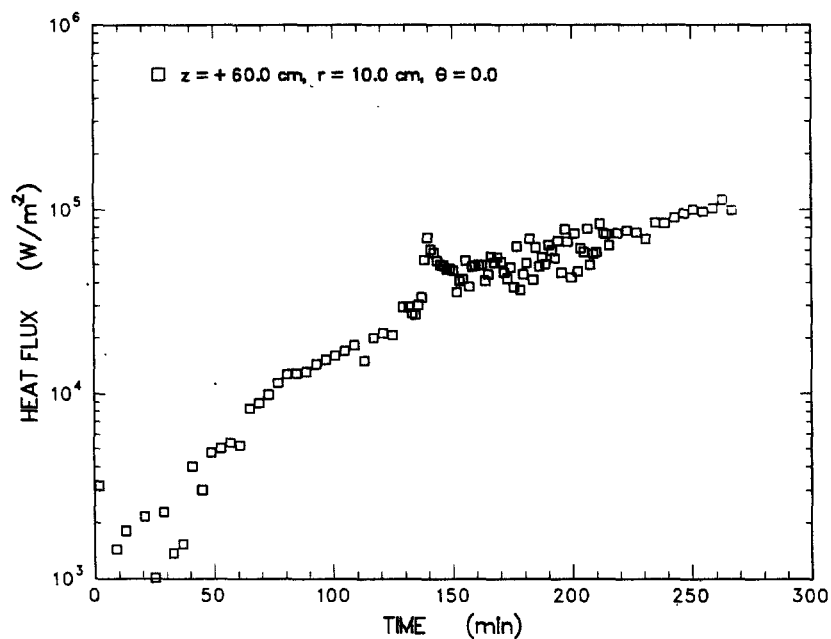
Figure E-12 **Alumina cover heat flux calculated from thermocouple data for the array located at r = 10.0 cm, θ = 0, and z = +60.0 cm**

Appendix E
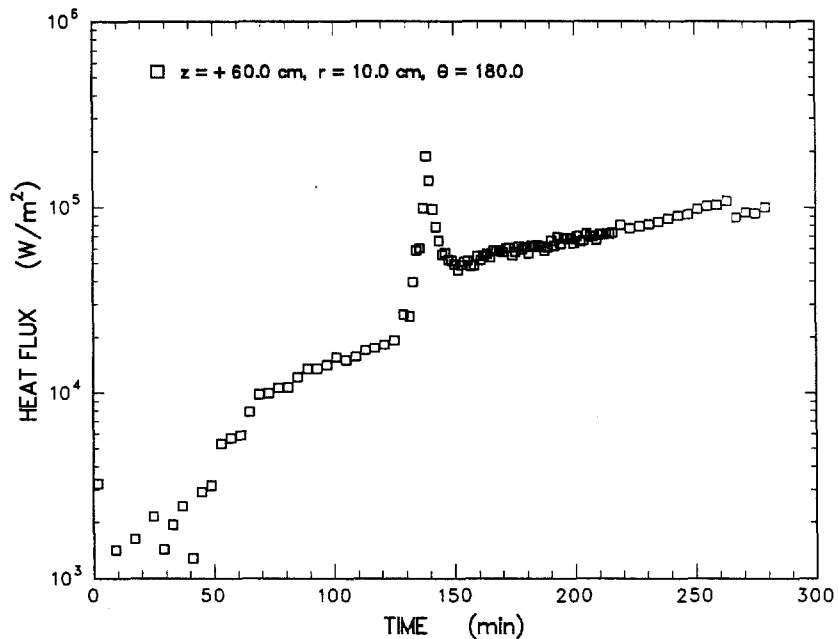
Figure E-13 Alumina cover heat flux calculated from thermocouple data for the array located at r = 10.0 cm, θ = 180, z = +60.0 cm
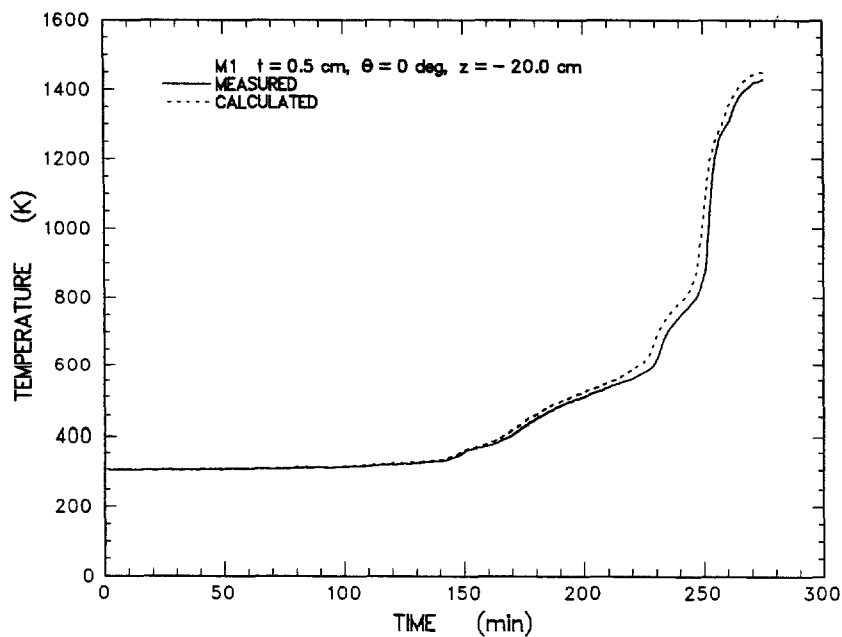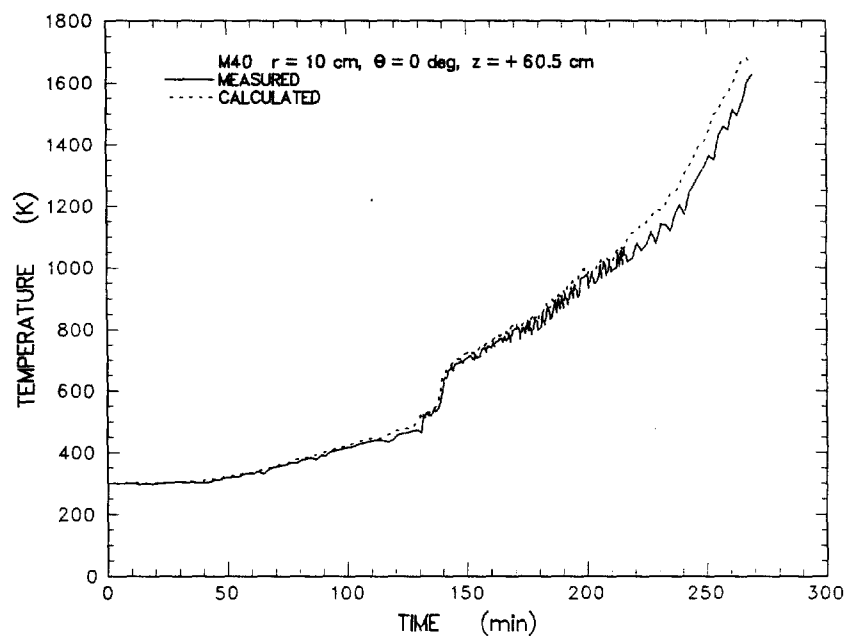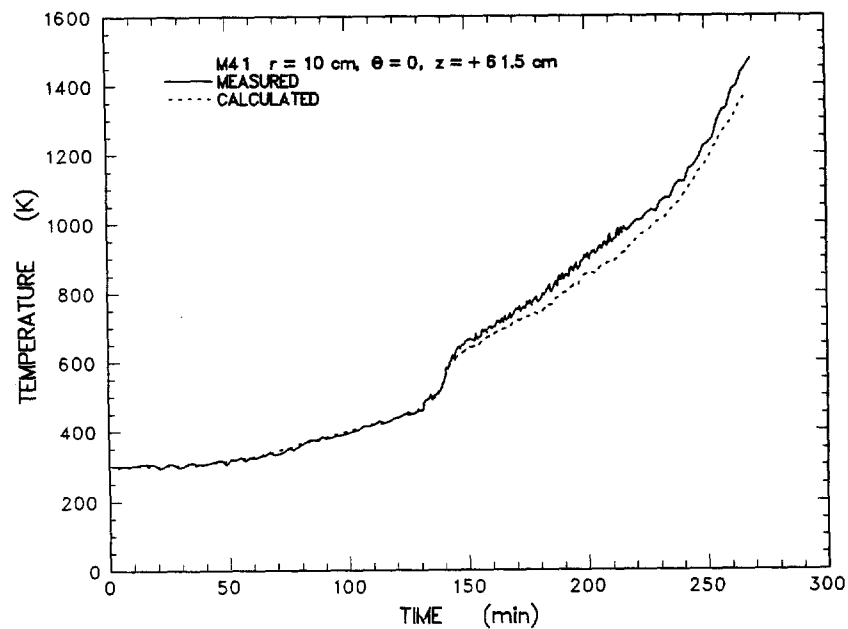

Figure E-14 Comparison of sidewall temperatures measured during the experiment and calculated from the heat flux code for the thermocouple located at z = -20.0 cm and t = 0.5 cm
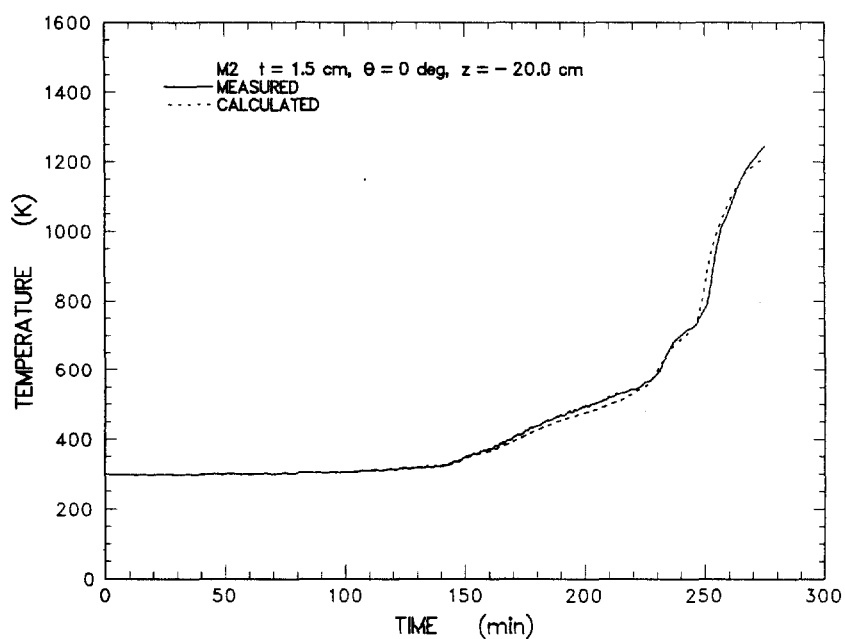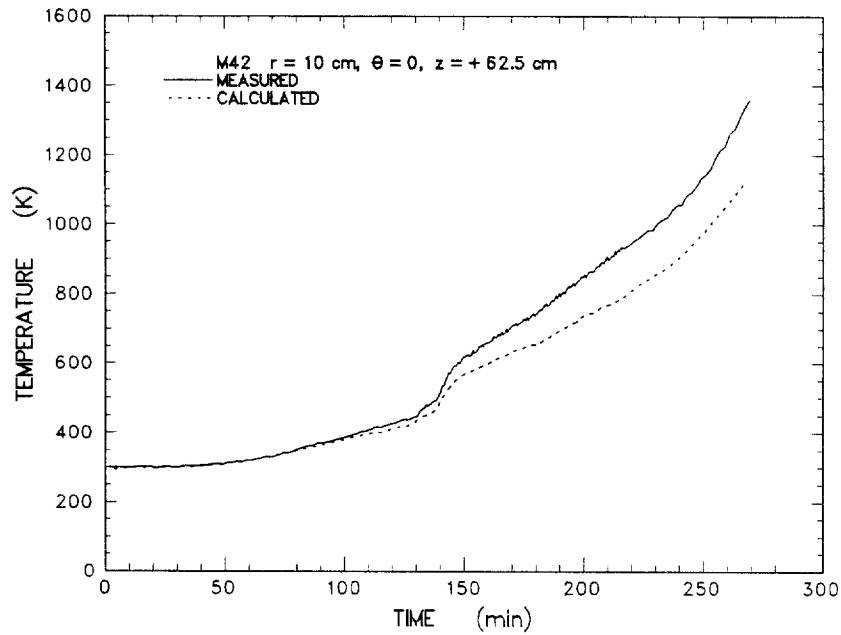
Figure E-15 Comparison of sidewall temperatures measured during the experiment and calculated from the heat flux code for thermocouple located at z = -20.0 cm and t = 1.5 cm
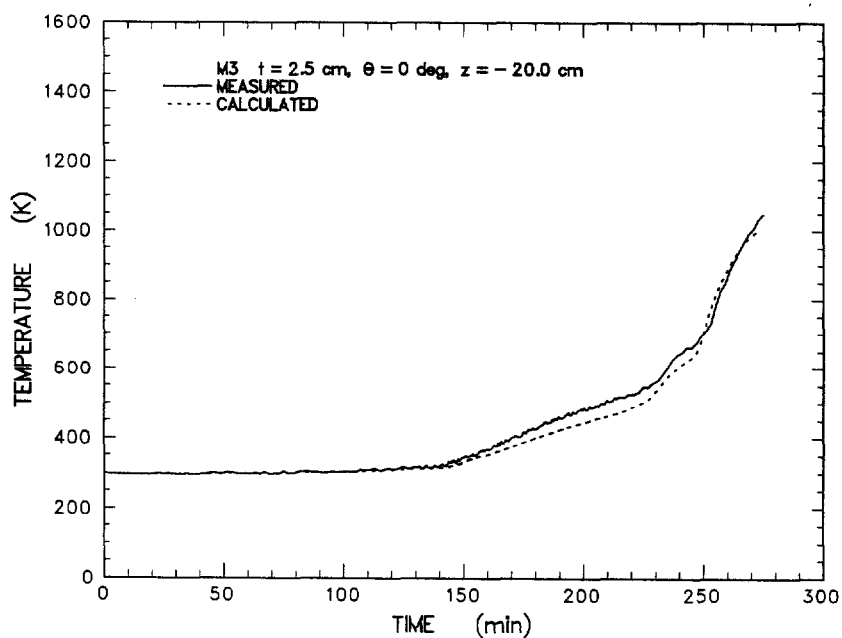
Figure E-16 Comparison of sidewall temperatures measured during the experiment and calculated from the heat flux code for the thermocouple located at z = -20.0 cm and t = 2.5 cm
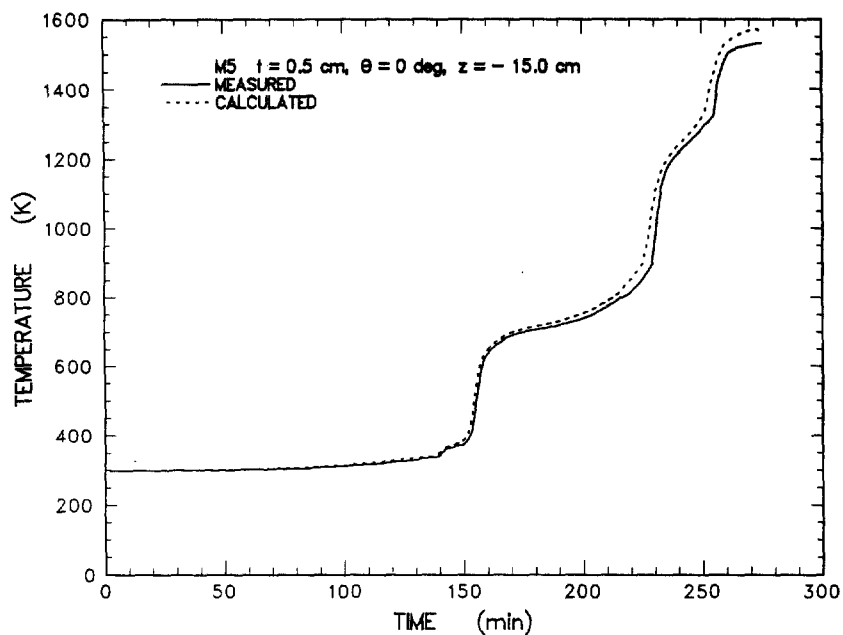
Figure E-17 Comparison of sidewall temperatures measured during the experiment and calculated from the heat flux code for thermocouple located at z = -15.0 cm and t = 0.5 cm
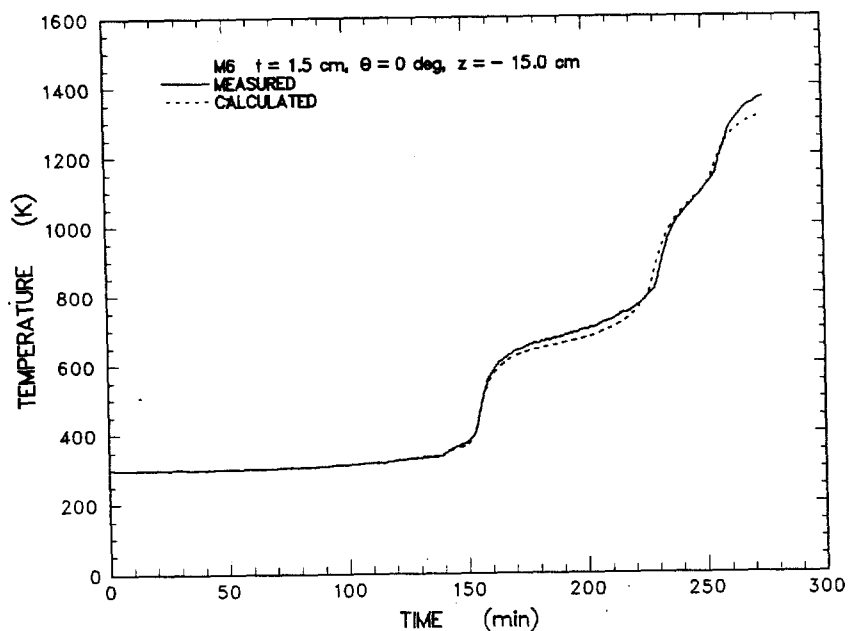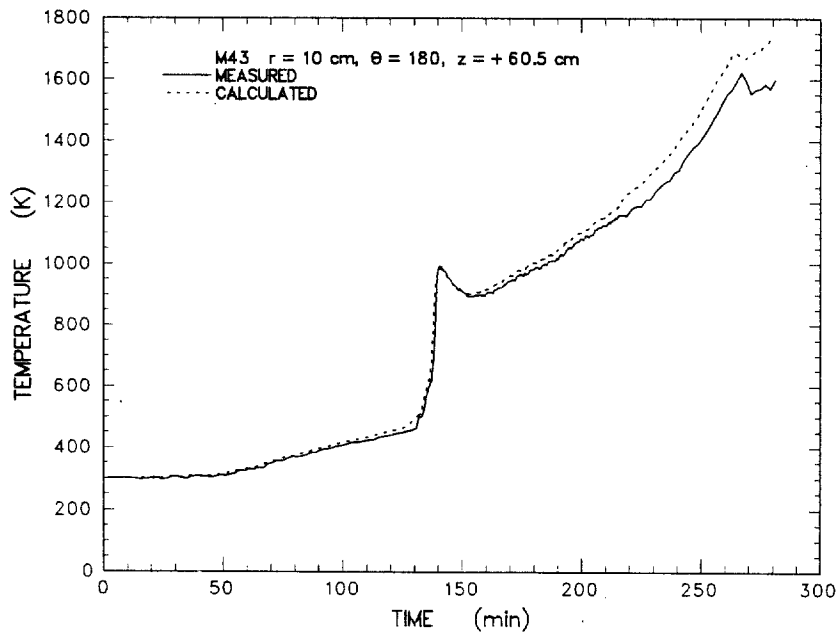

Figure E-18 Comparison of sidewall temperatures measured during the experiment and calculated from the heat flux code for the thermocouple located at z = -15.0 cm and t = 1.5 cm
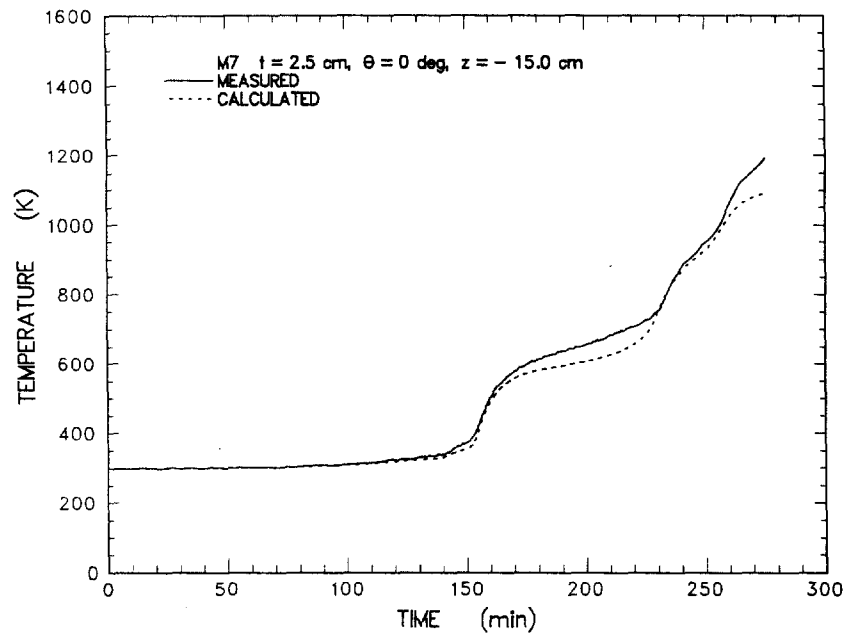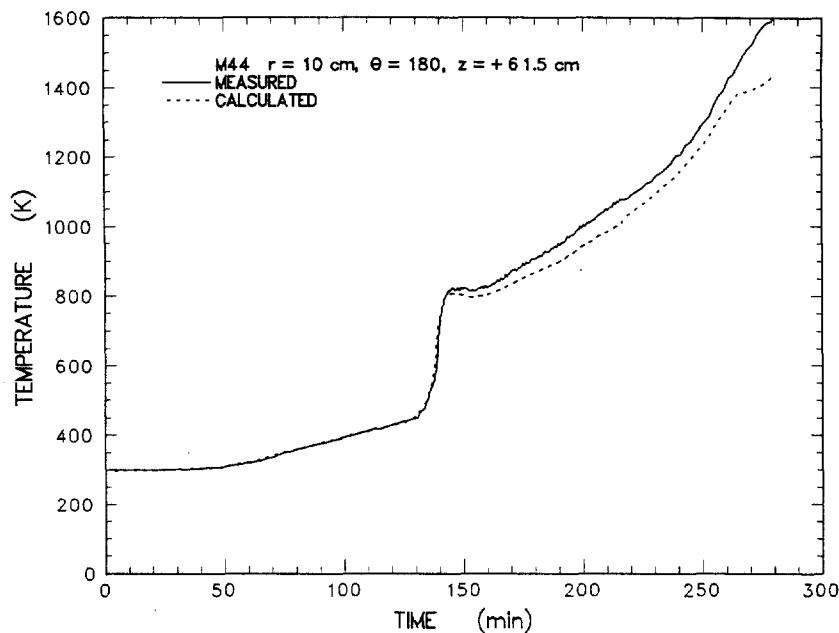
Figure E-19 Comparison of sidewall temperatures measured during the experiment and calculated from the heat flux code for thermocouple located at z = -15.0 cm and t= 2.5 cm
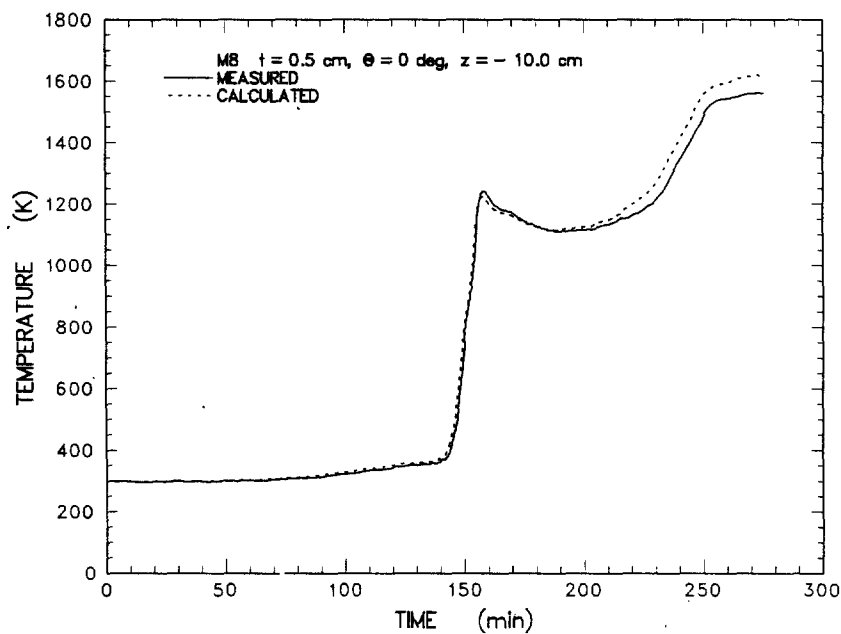
Figure E-20 Comparison of sidewall temperatures measured during the experiment and calculated from the heat flux code for the thermocouple located at z = -10.0 cm and t = 0.5 cm

Appendix E
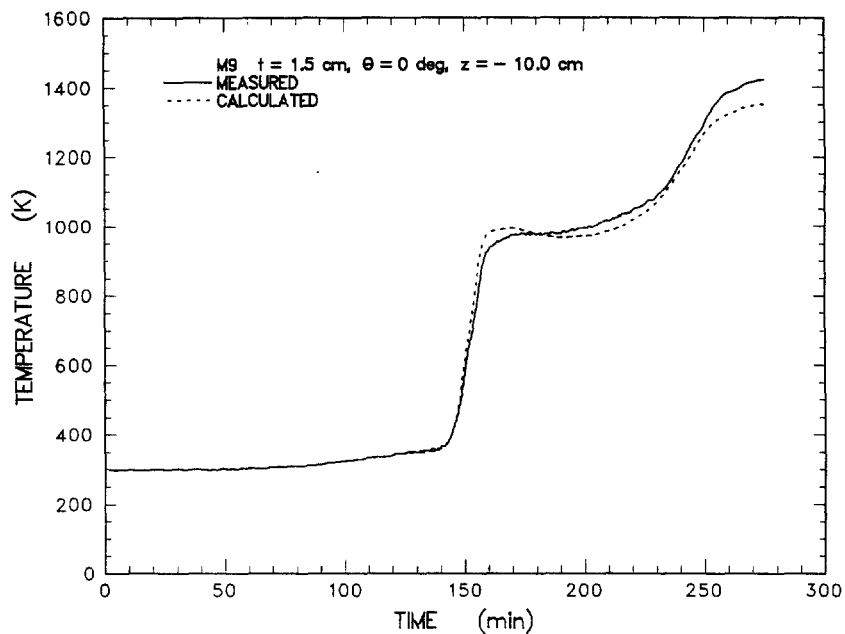
Figure E-21 Comparison of sidewall temperatures measured during the experiment and calculated from the heat flux code for thermocouple located at z = -10.0 cm and t = 1.5 cm
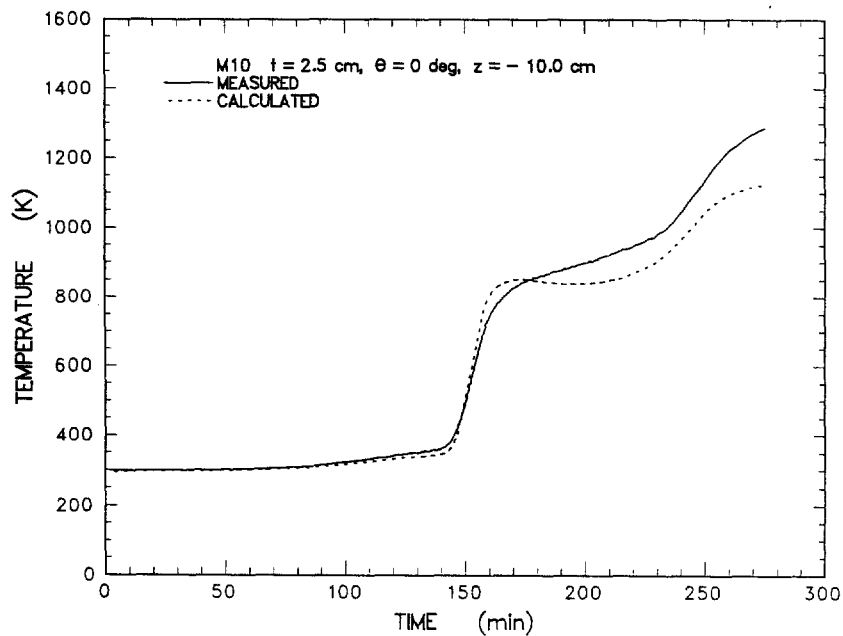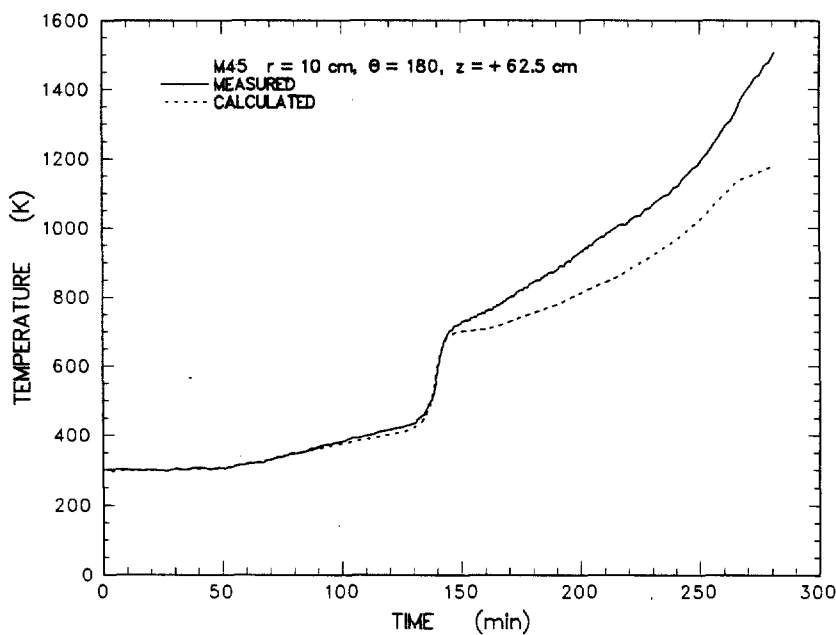

Figure E-22 Comparison of sidewall temperatures measured during the experiment and calculated from the heat flux code for the thermocouple located at z = -10.0 cm and t = 2.5 cm
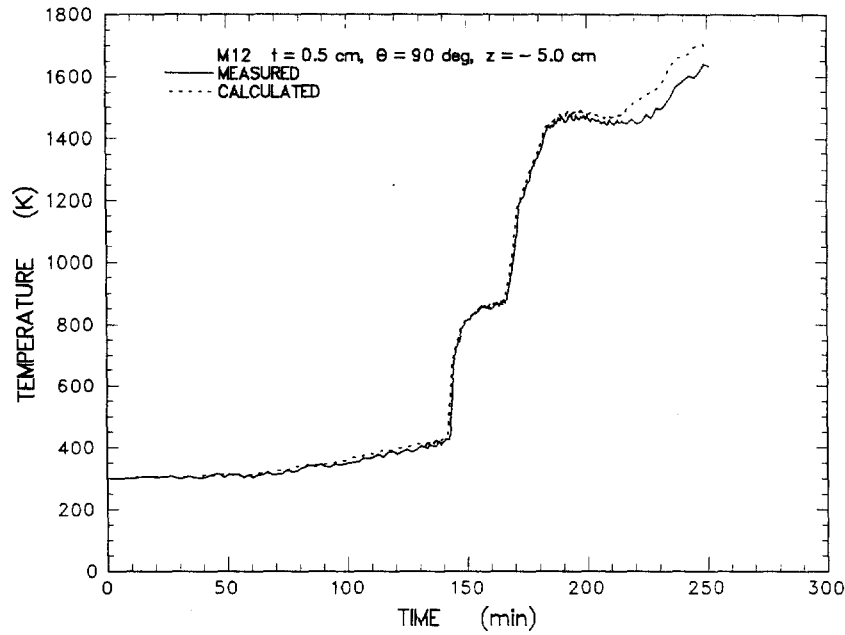
Figure E-23 **Comparison of sidewall temperatures measured during the experiment and calculated from the heat flux code for thermocouple located at z = -5.0 cm and t = 0.5 cm**
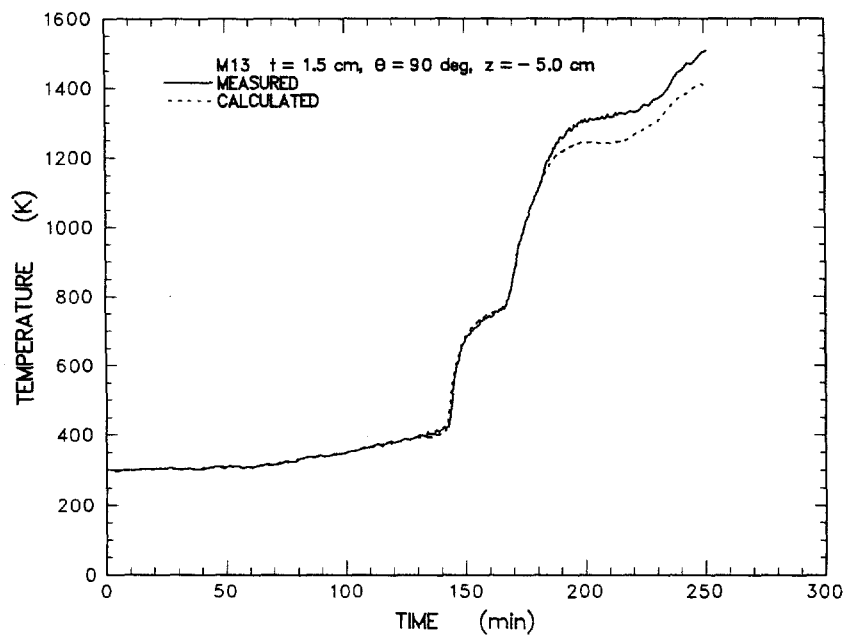
Figure E-24 **Comparison of sidewall temperatures measured during the experiment and calculated from the heat flux code for the thermocouple located at z = -5.0 cm and t = 1.5 cm**
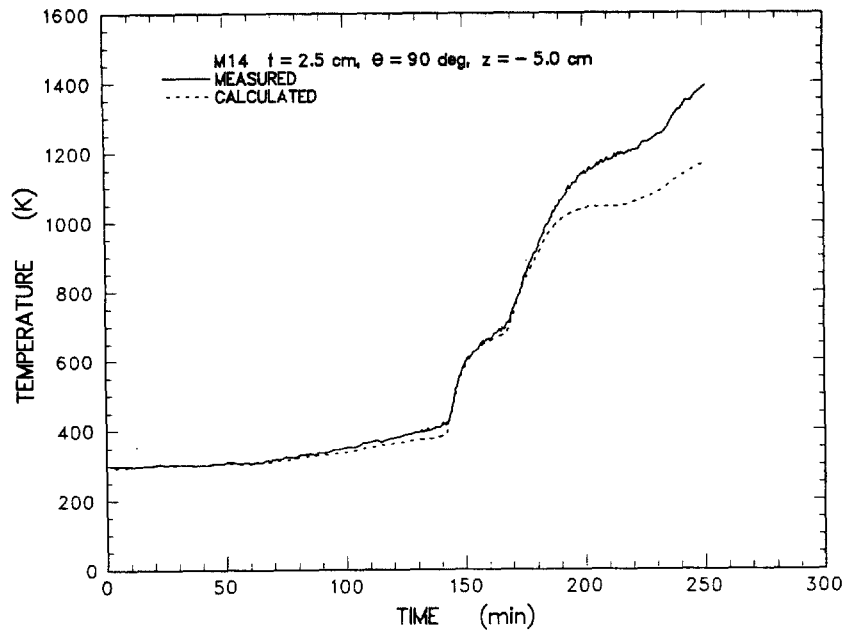
Figure E-25 Comparison of sidewall temperatures measured during the experiment and calculated from the heat flux code for thermocouple located at z = -5.0 cm and t = 2.5 cm
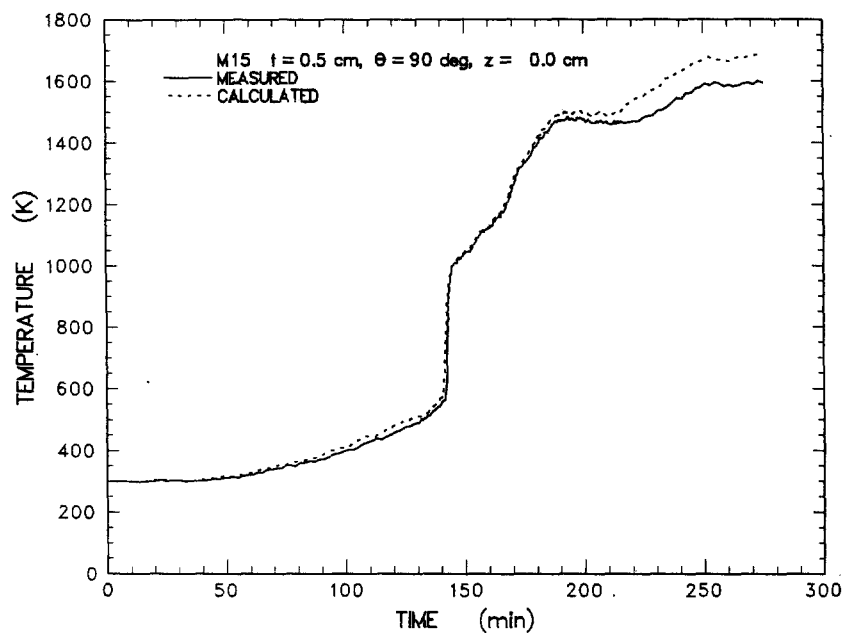
Figure E-26 Comparison of sidewall temperatures measured during the experiment and calculated from the heat flux code for the thermocouple located at z = 0.0 cm and t = 0.5 cm
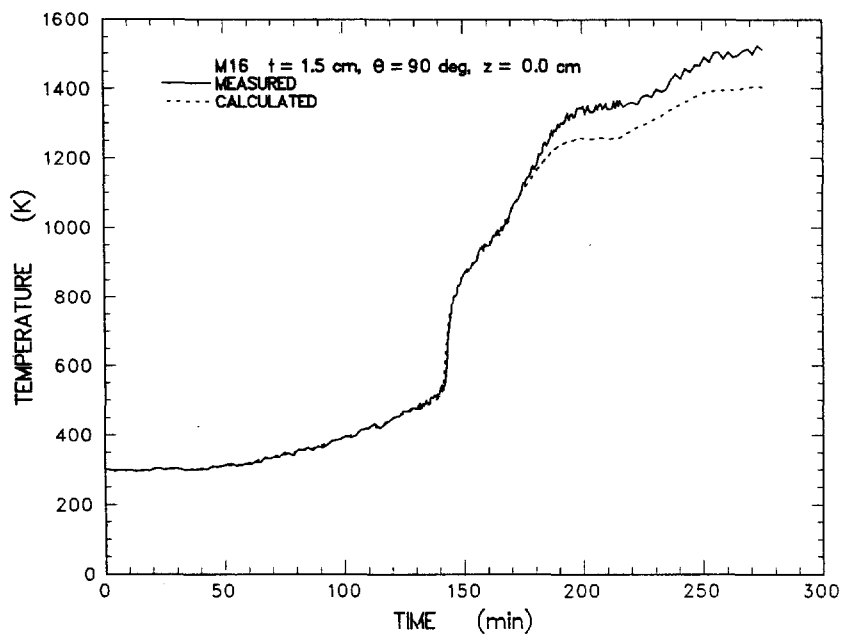
Figure E-27 Comparison of sidewall temperatures measured during the experiment and calculated from the heat flux code for thermocouple located at z = 0.0 cm and t = 1.5 cm
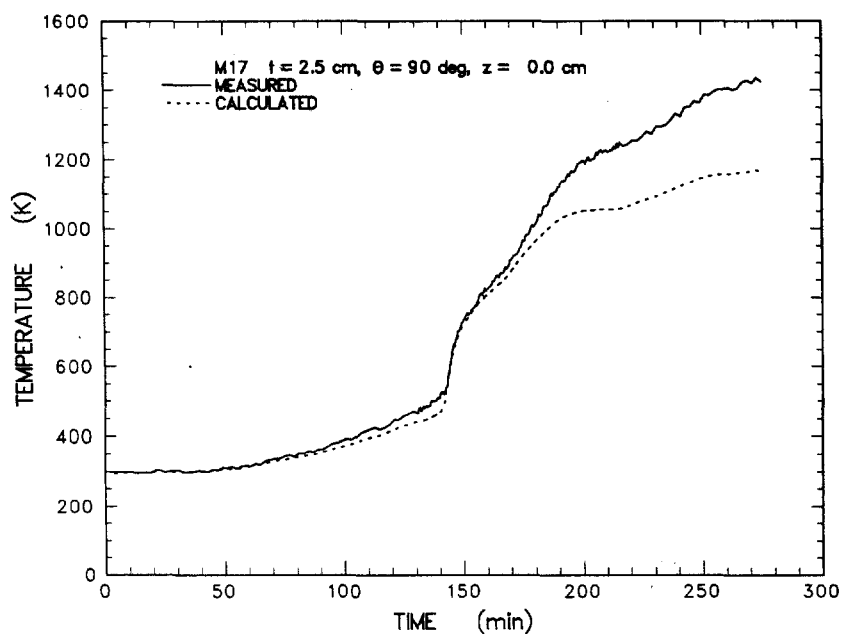
Figure E-28 Comparison of sidewall temperatures measured during the experiment and calculated from the heat flux code for the thermocouple located at z = 0.0 cm and t = 2.5 cm
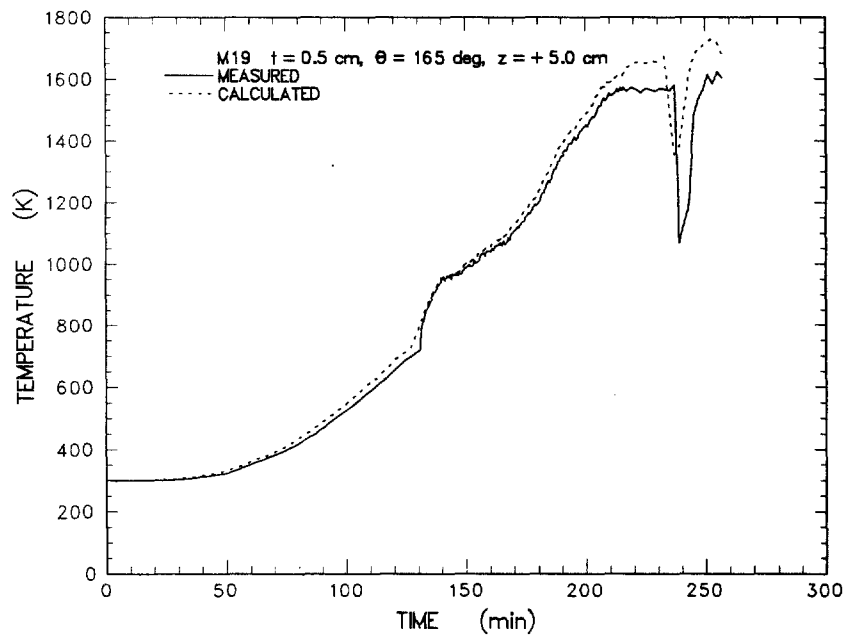
Figure E-29 Comparison of sidewall temperatures measured during the experiment and calculated from the heat flux code for thermocouple located at z = +5.0 cm and t = 0.5 cm
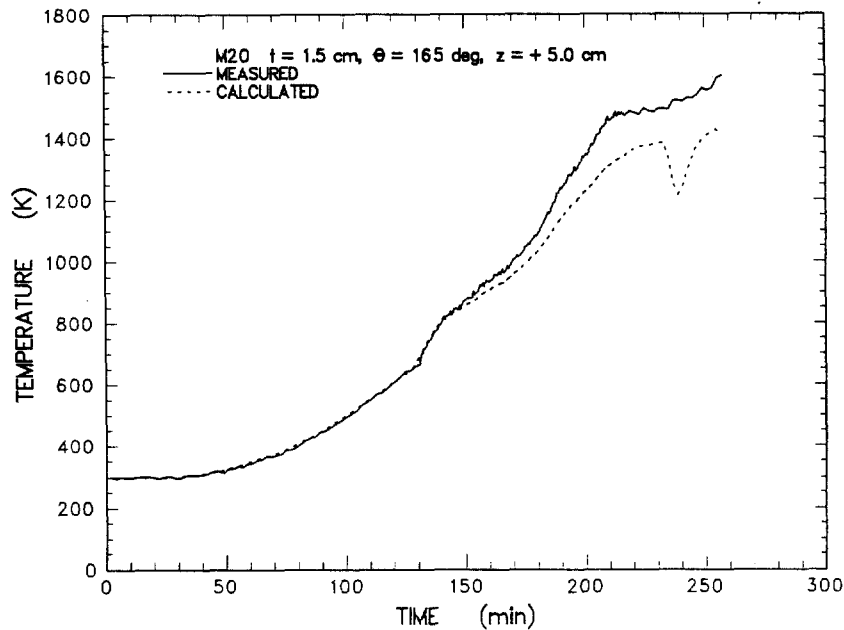
Figure E-30 Comparison of sidewall temperatures measured during the experiment and calculated from the heat flux code for the thermocouple located at z = +5.0 cm and t = 1.5 cm
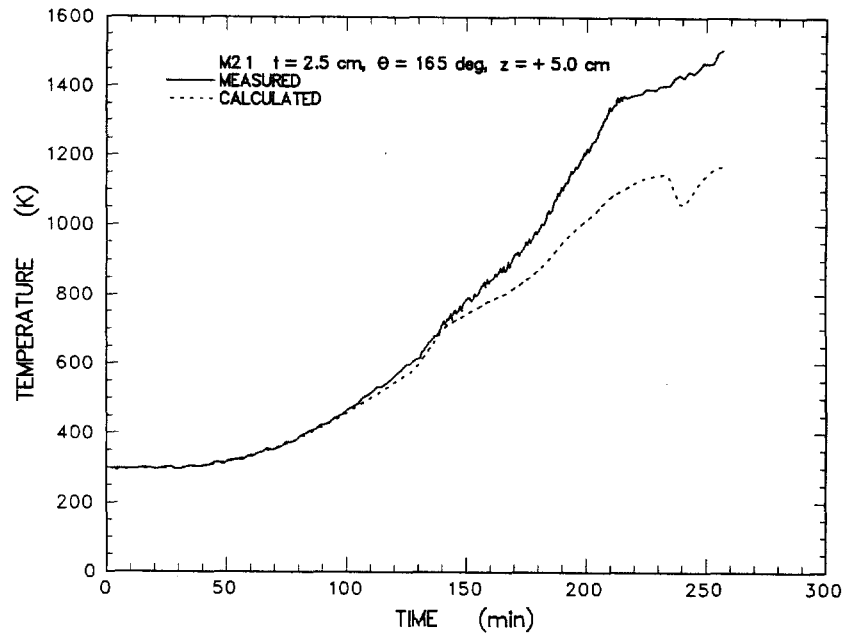
Figure E-31 **Comparison of sidewall temperatures measured during the experiment and calculated from the heat flux code for thermocouple located at z = +5.0 cm and t = 2.5 cm**
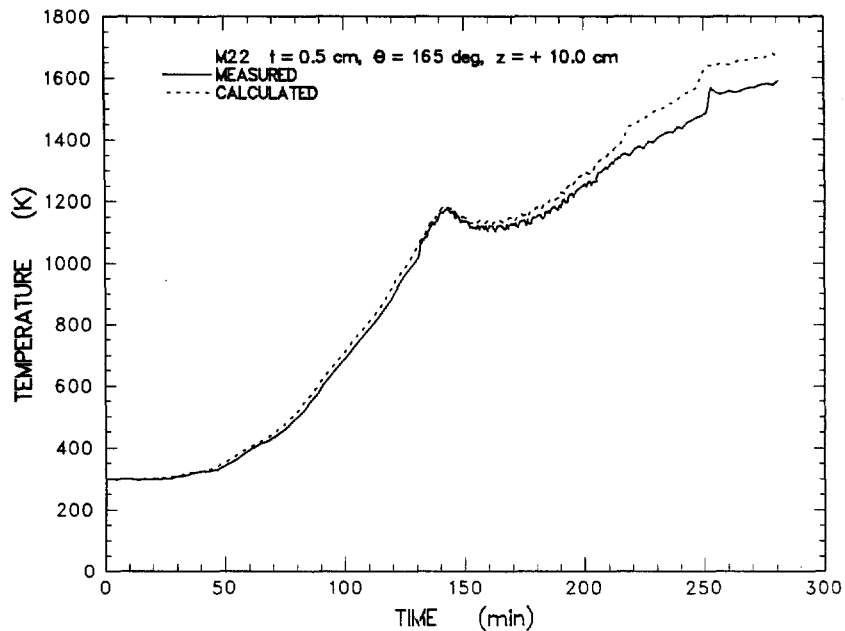
Figure E-32 **Comparison of sidewall temperatures measured during the experiment and calculated from the heat flux code for the thermocouple located at z = +10.0 cm and t = 0.5 cm**
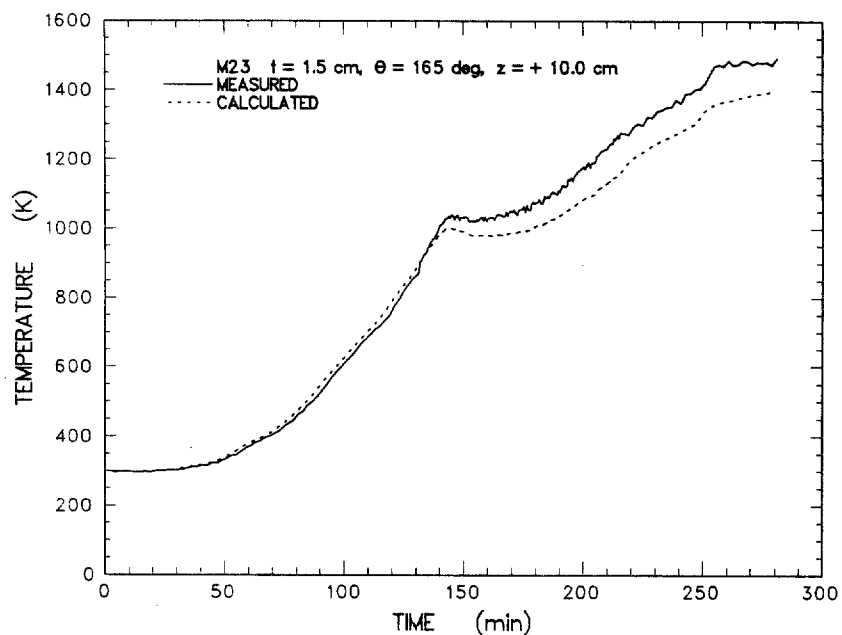
Figure E-33 **Comparison of sidewall temperatures measured during the experiment and calculated from the heat flux code for thermocouple located at z = +10.0 cm and t = 1.5 cm**
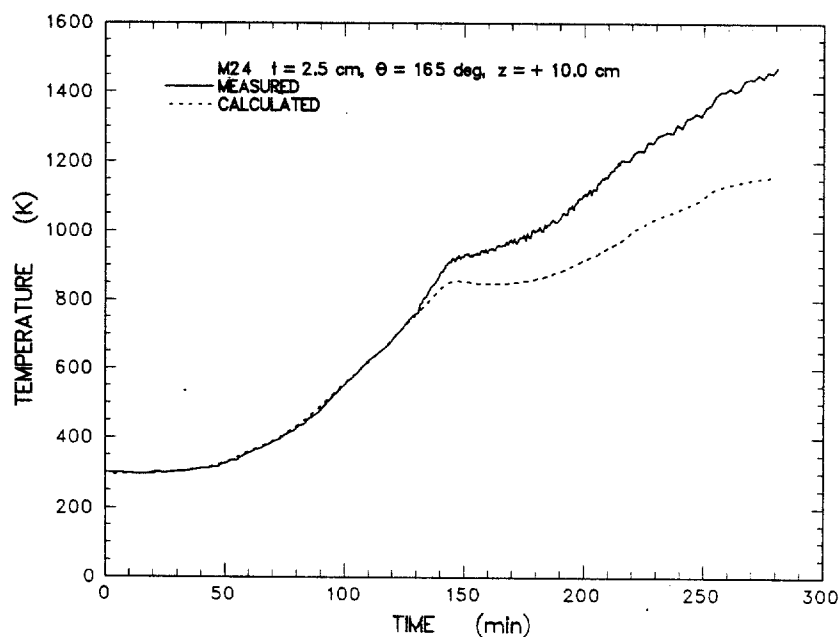
Figure E-34 **Comparison of sidewall temperatures measured during the experiment and calculated from the heat flux code for the thermocouple located at z = +10.0 cm and t = 2.5 cm**
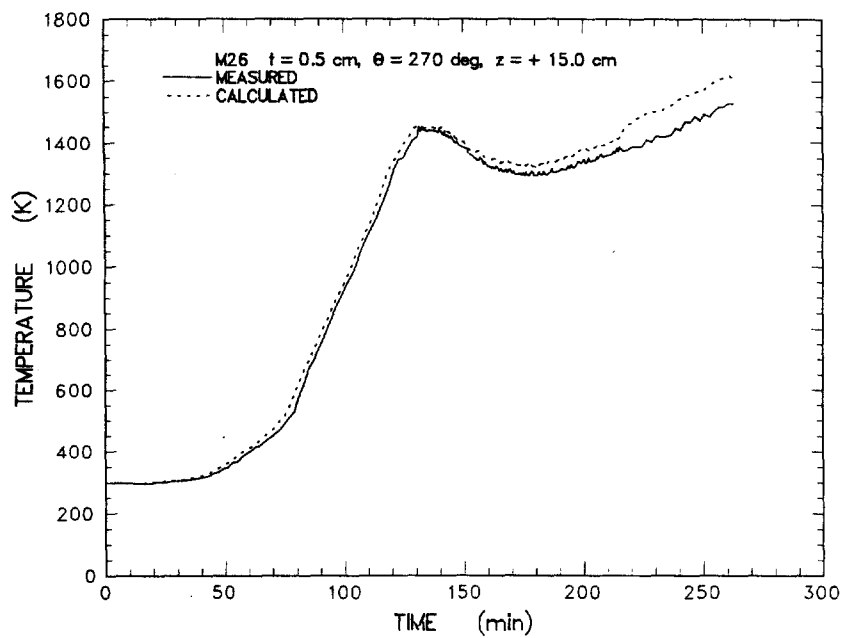
Figure E-35 Comparison of sidewall temperatures measured during the experiment and calculated from the heat flux code for thermocouple located at z = +15.0 cm and t = 0.5 cm
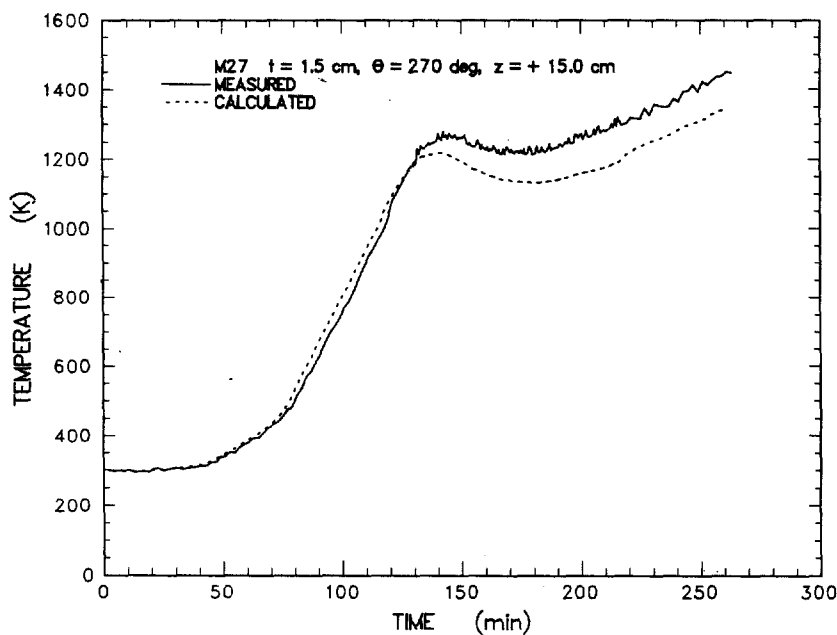
Figure E-36 Comparison of sidewall temperatures measured during the experiment and calculated from the heat flux code for the thermocouple located at z = +15.0 cm and t = 1.5 cm
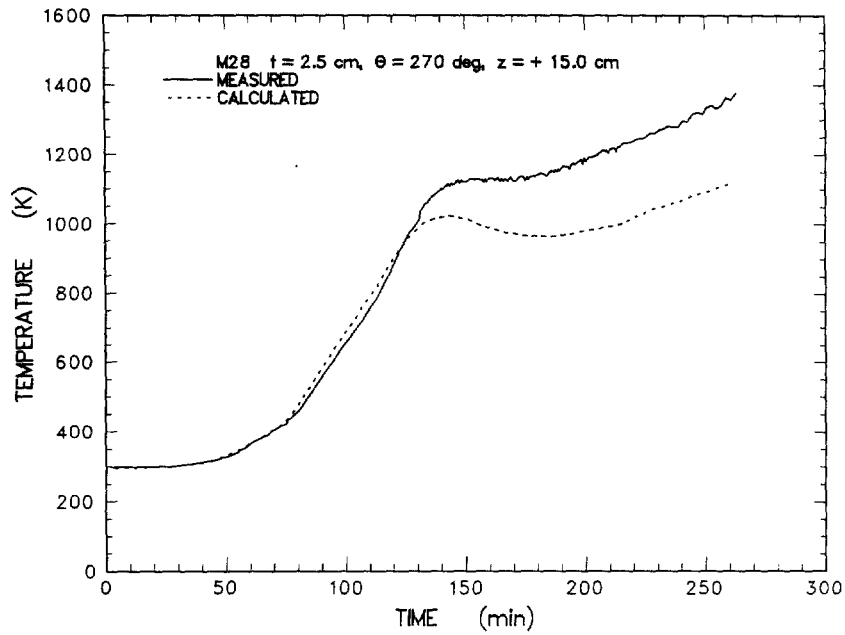
Figure E-37 **Comparison of sidewall temperatures measured during the experiment and calculated from the heat flux code for thermocouple located at z = +15.0 cm and t = 2.5 cm**
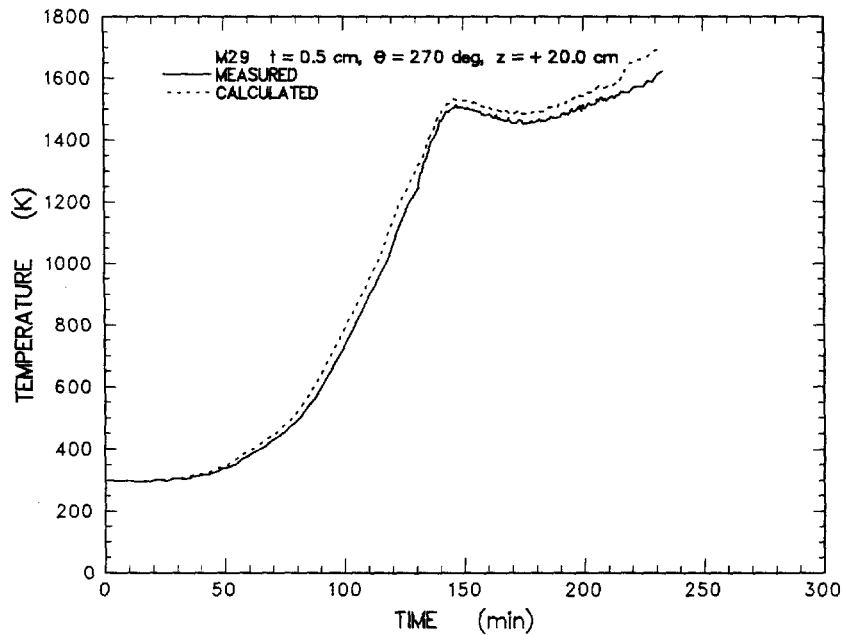
Figure E-38 **Comparison of sidewall temperatures measured during the experiment and calculated from the heat flux code for the thermocouple located at z = +20.0 cm and t = 0.5 cm**
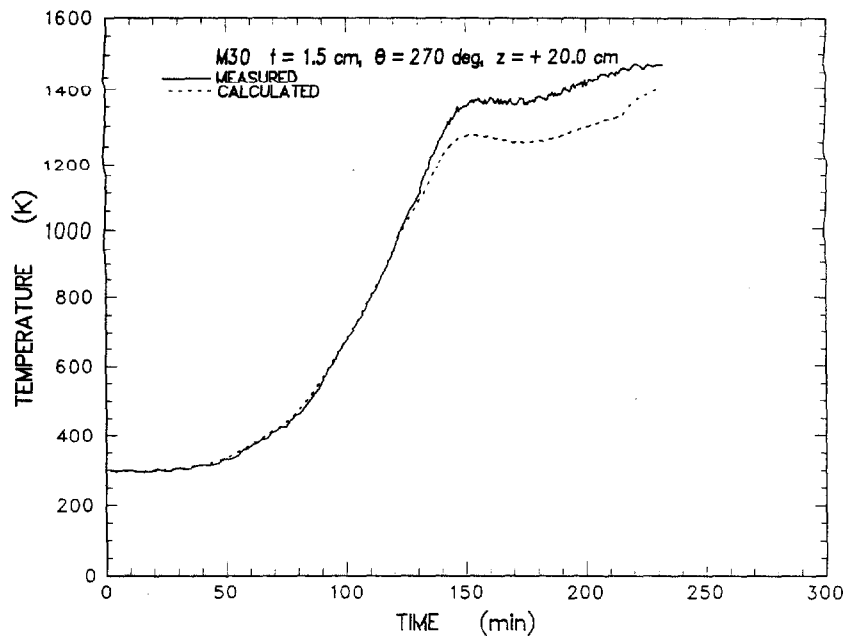
Figure E-39 Comparison of sidewall temperatures measured during the experiment and calculated from the heat flux code for thermocouple located at z = +20.0 cm and t = 1.5 cm
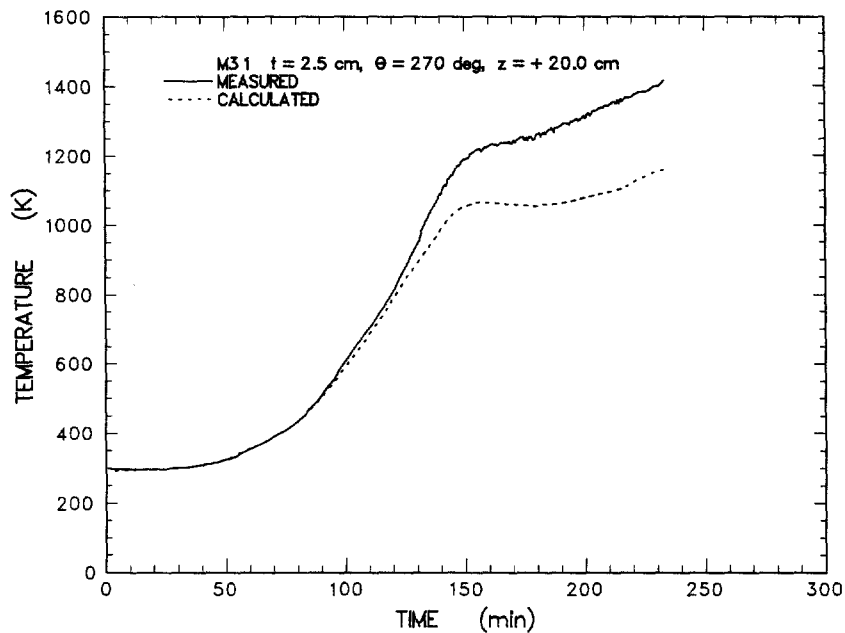
Figure E-40 Comparison of sidewall temperatures measured during the experiment and calculated from the heat flux code for the thermocouple located at z = +20.0 cm and t = 2.5 cm

Appendix E
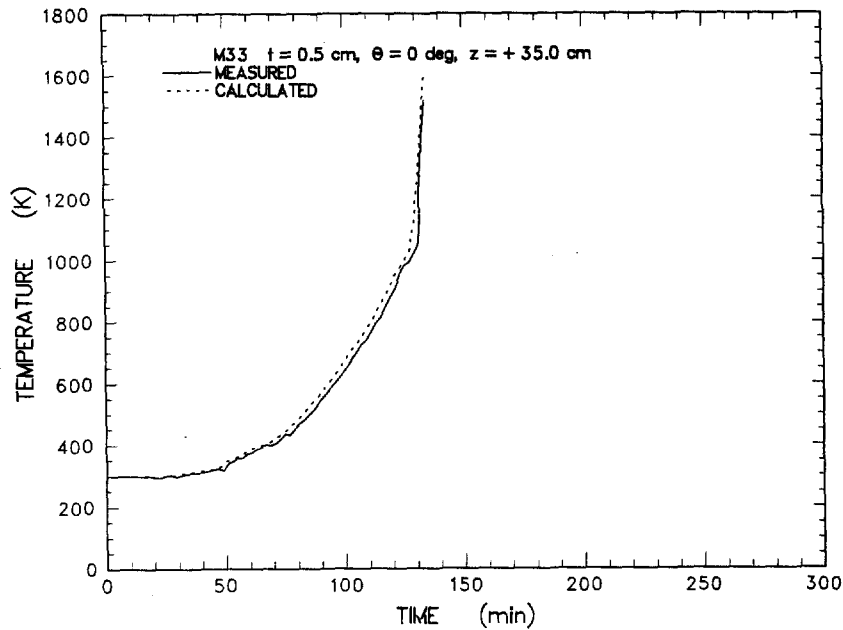
Figure E-41 **Comparison of sidewall temperatures measured during the experiment and calculated from the heat flux code for thermocouple located at z = +35.0 cm and t = 0.5 cm**
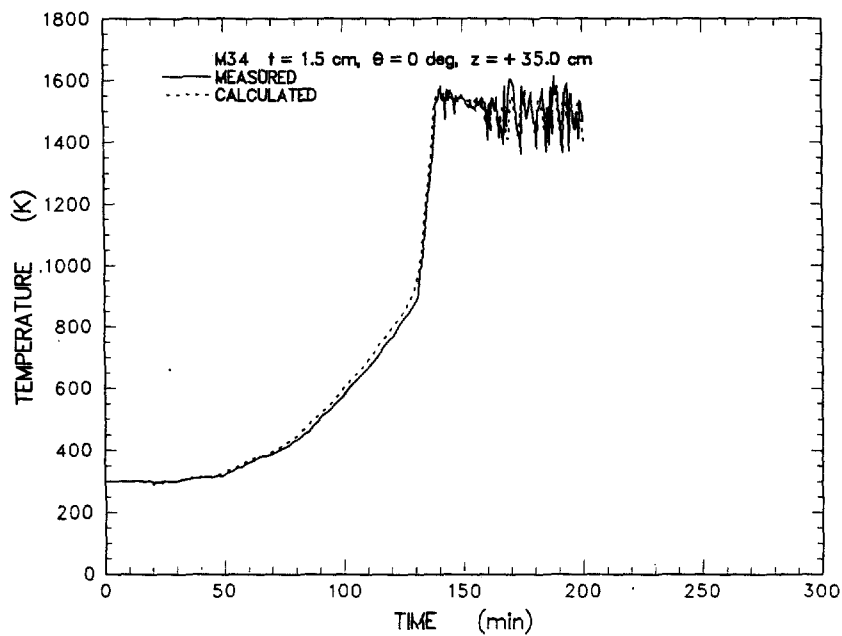
Figure E-42 **Comparison of sidewall temperatures measured during the experiment and calculated from the heat flux code for the thermocouple located at z = +35.0 cm and t = 1.5 cm**
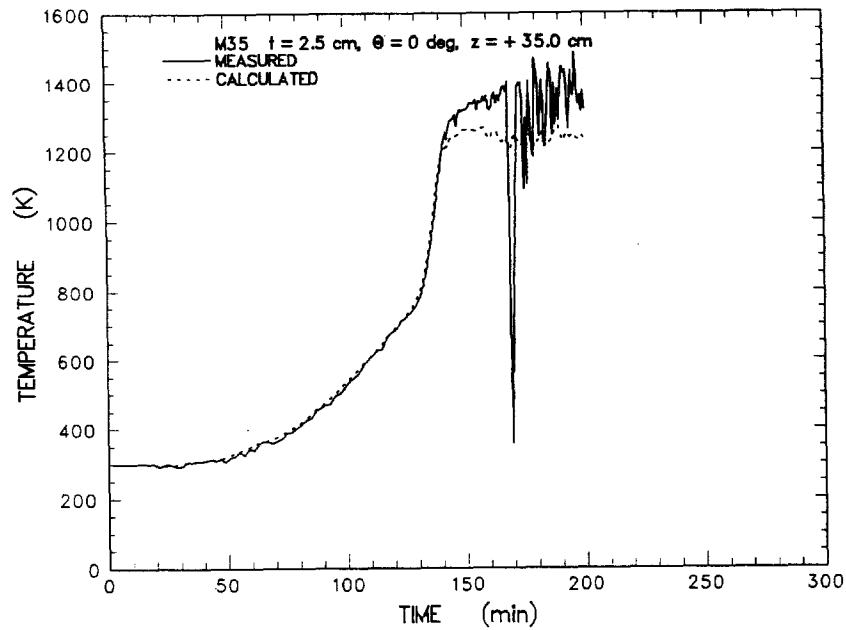
Figure E-43 Comparison of sidewall temperatures measured during the experiment and calculated from the heat flux code for thermocouple located at z = +35.0 cm and t = 2.5 cm
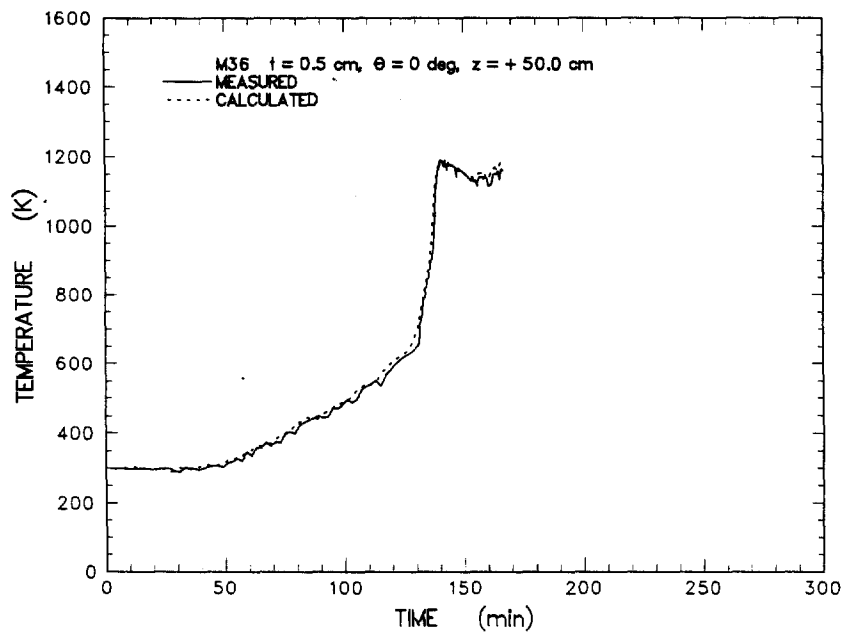
Figure E-44 Comparison of sidewall temperatures measured during the experiment and calculated from the heat flux code for the thermocouple located at z = +50.0 cm and t = 0.5 cm
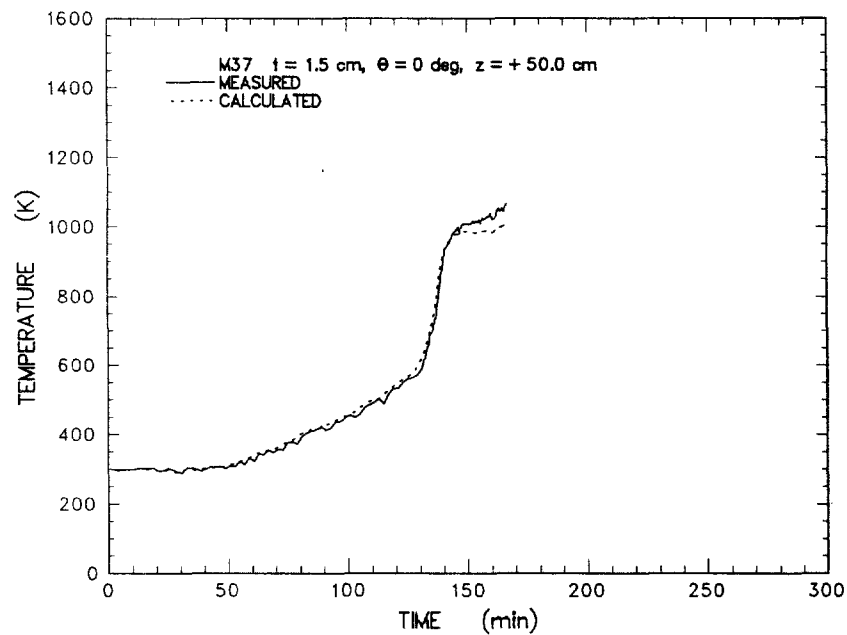
Figure E-45 Comparison of sidewall temperatures measured during the experiment and calculated from the heat flux code for thermocouple located at z = +50.0 cm and t = 1.5 cm
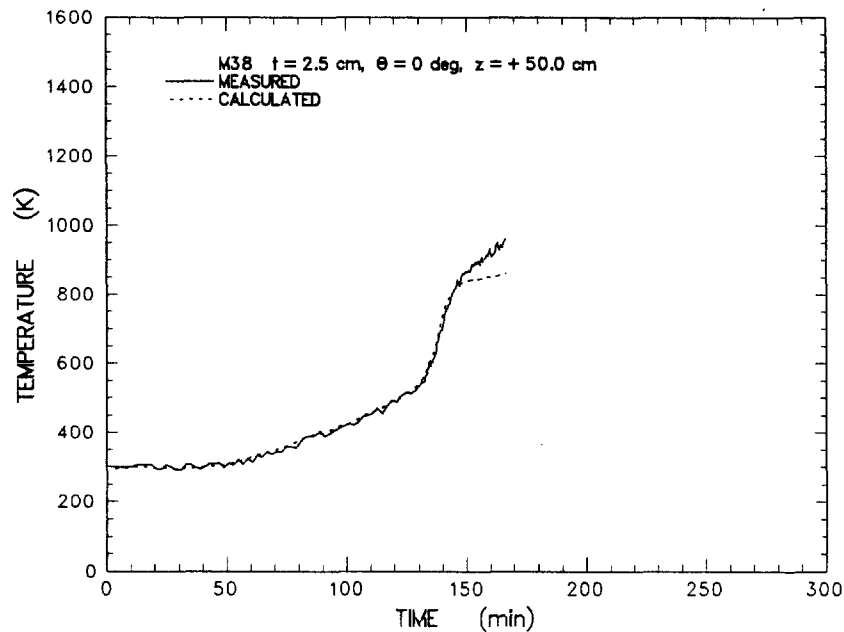
Figure E-46 Comparison of sidewall temperatures measured during the experiment and calculated from the heat flux code for the thermocouple located at z = +50.0 cm and t = 2.5 cm

Figure E-47 Comparison of sidewall temperatures measured during the experiment and calculated from the heat flux code for thermocouple located at r = 10.0 cm, θ = 0, z = +60.0 cm and t = 0.5 cm

Figure E-48 Comparison of sidewall temperatures measured during the experiment and calculated from the heat flux code for the thermocouple located at r = 10.0 cm, θ = 0, z = +60.0 cm and t = 1.5 cm

Figure E-49 Comparison of sidewall temperatures measured during the experiment and calculated from the heat flux code for thermocouple located at r = 10.0 cm, θ = 0, z = +60.0 cm and t = 2.5 cm

Figure E-50 Comparison of sidewall temperatures measured during the experiment and calculated from the heat flux code for the thermocouple located at r = 10.0 cm, θ = 180, z = +60.0 cm and t = 0.5 cm

Figure E-51 **Comparison of sidewall temperatures measured during the experiment and calculated from the heat flux code for thermocouple located at r = 10.0 cm, θ = 180, z = +60.0 cm and t = 1.5 cm**

Figure E-52 **Comparison of sidewall temperatures measured during the experiment and calculated from the heat flux code for the thermocouple located at r = 10.0 cm, θ = 180, z = +60.0 cm and t = 2.5 cm**

Appendix F: Pressure Transducer and Flow Device Calibration Data

Enclosed in this appendix are the calibration data for the pressure transducers used in the flow system and calibration plots of the flow devices used in the experiment.
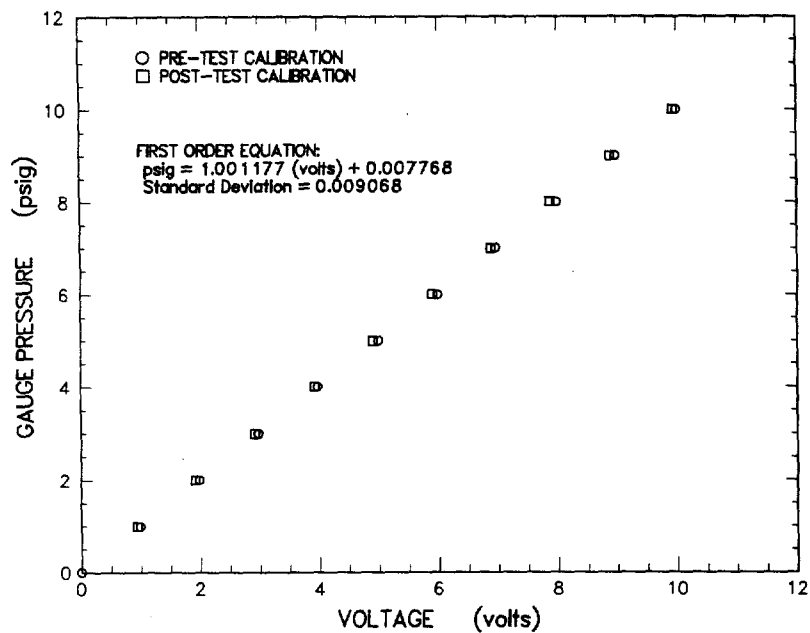
Figure F-1 Gauge pressure transducer (10 psig) calibration installed on the containment vessel
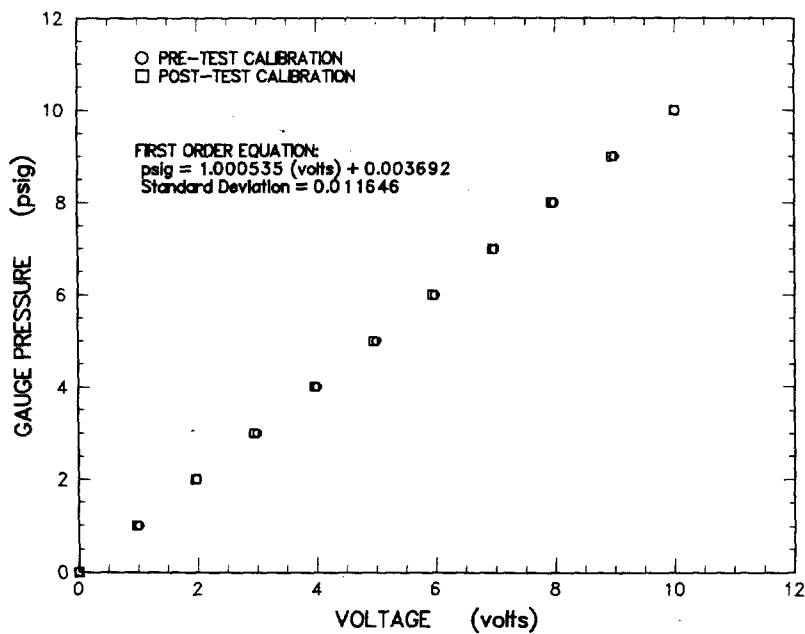
Figure F-2   Gauge pressure transducer (10 psid) calibration installed upstream of the ASME orifice
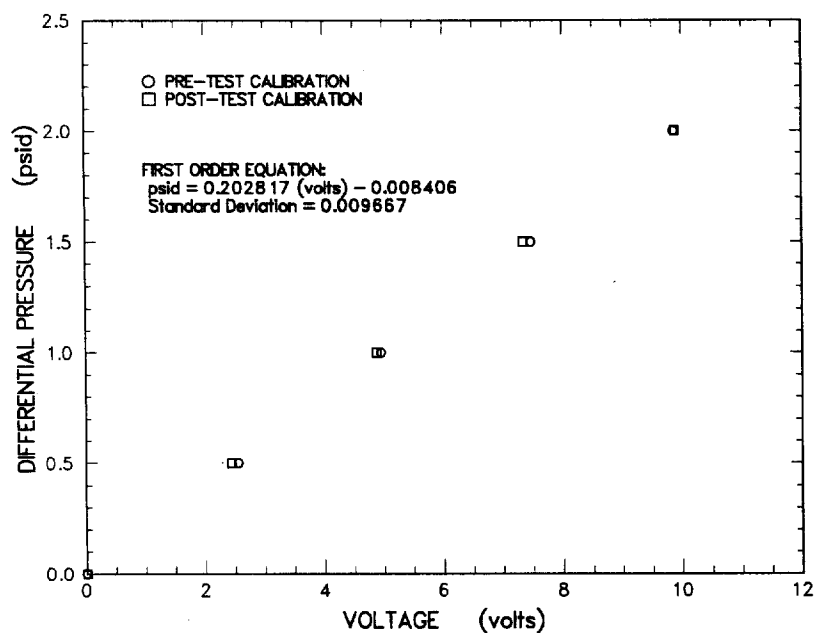
Figure F-3 Differential pressure transducer (2 psid) calibration installed across the ASME sharp edge orifice
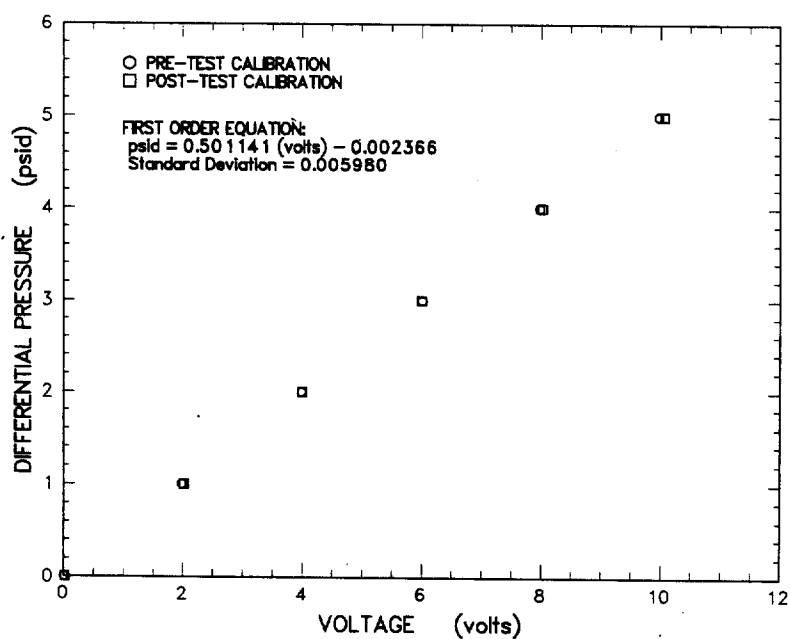
Figure F-4 Differential pressure transducer (5 psid) calibration installed across the ASME sharp edge orifice
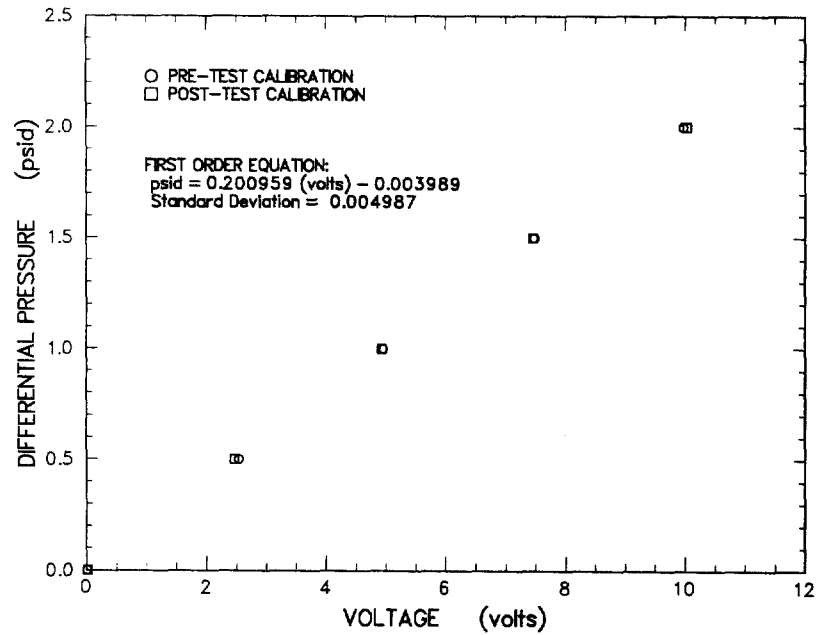
Figure F-5   Differential pressure transducer (2 psid) calibration installed across the laminar flow element
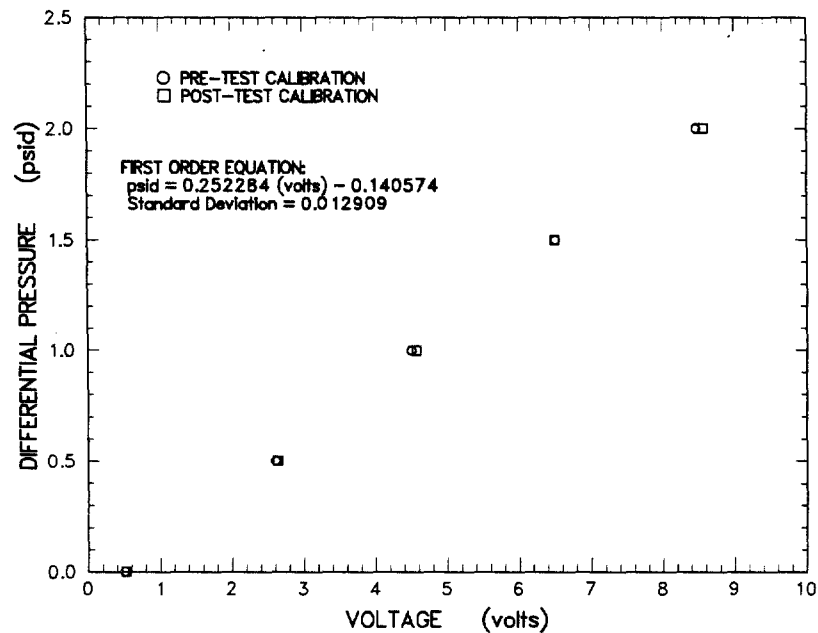
Figure F-6   Differential pressure magnahelic transducer (2 psid) calibration installed across the ASME sharp edge orifice
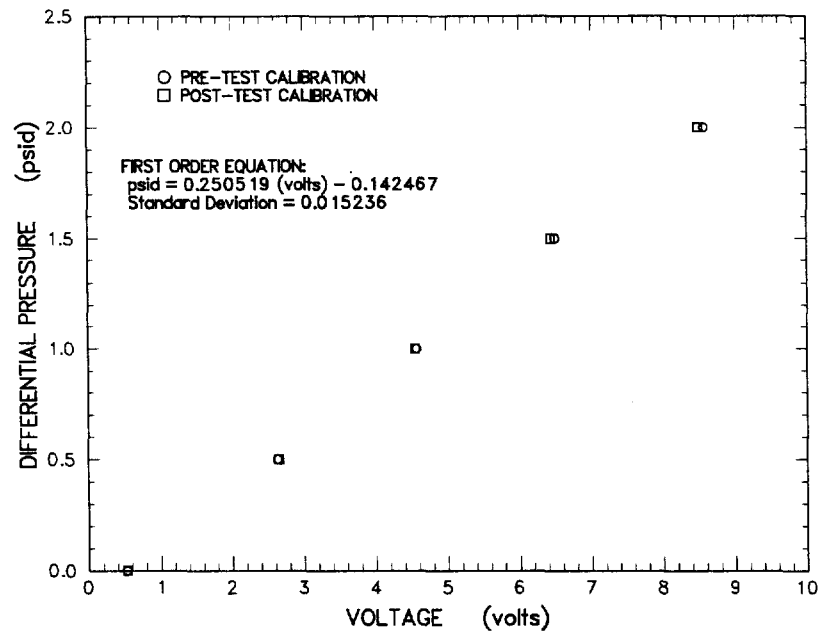
Figure F-7   **Differential pressure magnahelic transducer (2 psid) calibration installed across the laminar flow element**
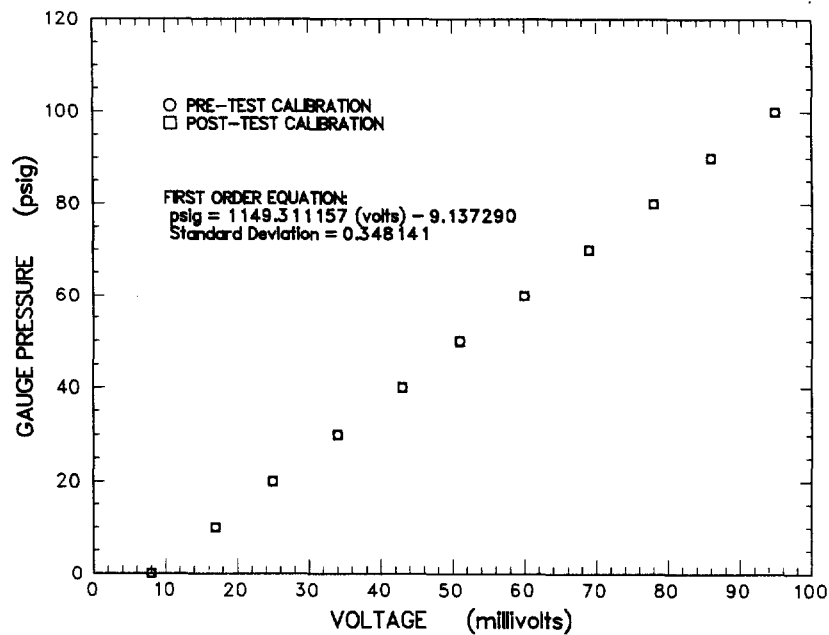
Figure F-8   **Gauge pressure transducer (100 psig) calibration installed upstream of the 14 lpm critical orifice to meter the flow of Argon purge gas flowing into the containment vessel**
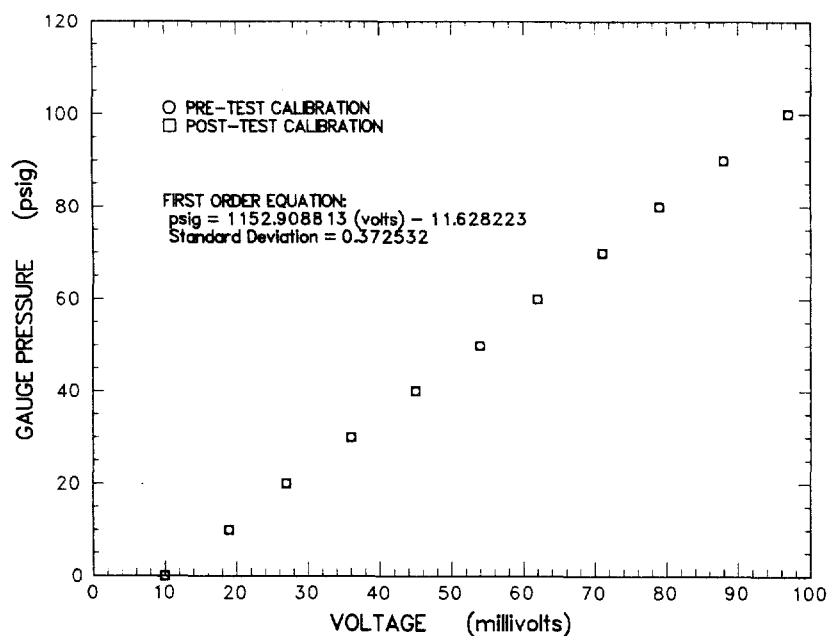
Figure F-9   Gauge pressure transducer (100 psig) calibration installed upstream of the 3 lpm critical orifice to meter the flow of argon used to purge the tungsten pyrotubes
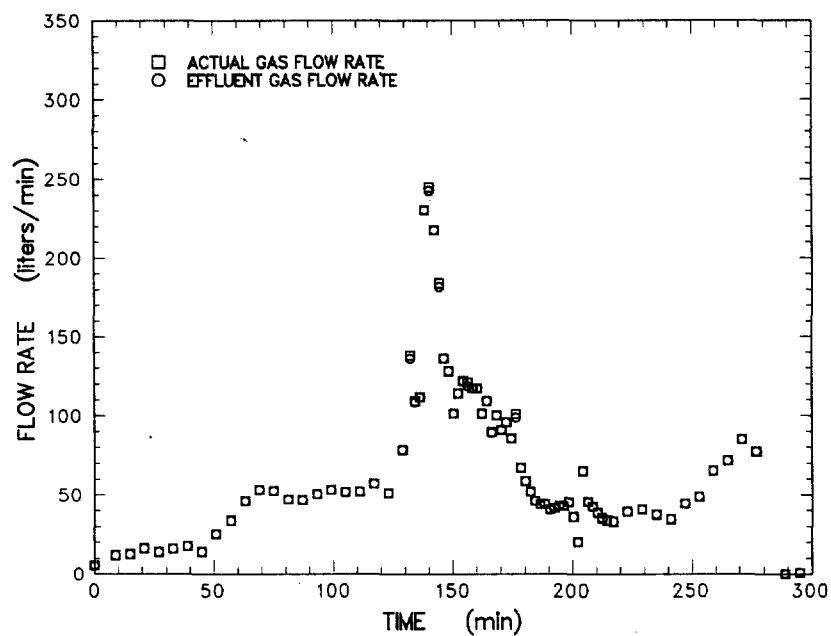
Figure F-10   Flow rate summary from LFE using argon calibration
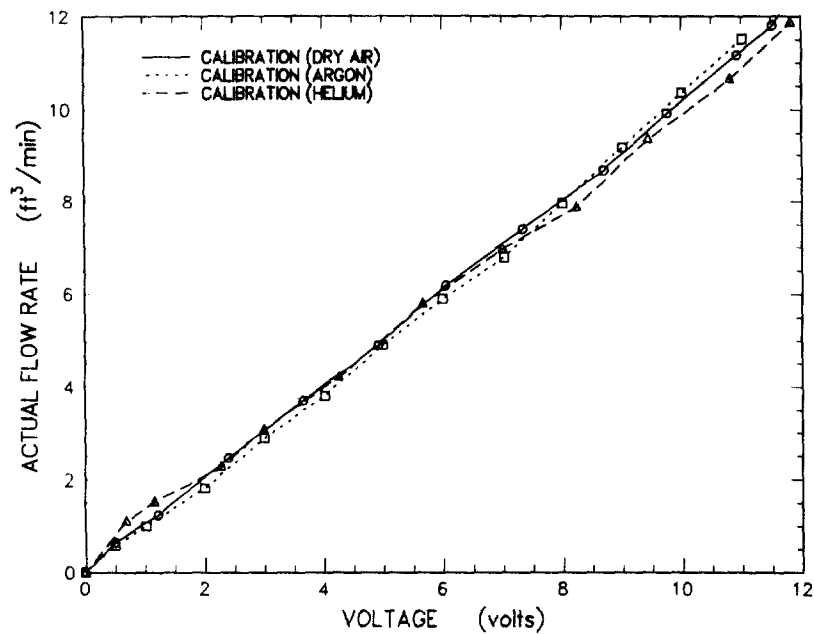
Figure F-11 Turbine meter calibration installed at the inlet of the argon purge to the containment vessel
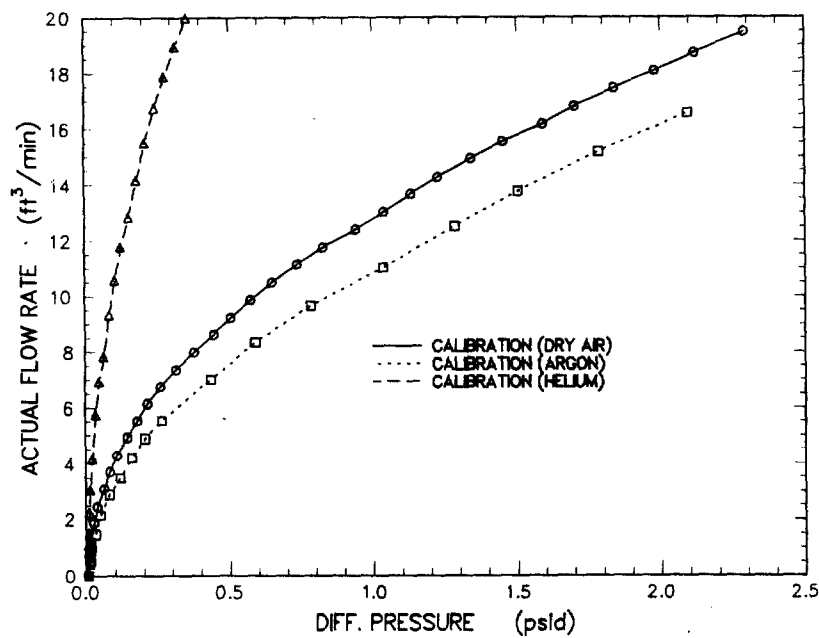
Figure F-12 Calibration of the ASME sharp edge orifice installed in the flow circuit

Figure F-13 Calibration of the laminar flow element installed downstream of the gravel filter and near the exit of the flow circuit
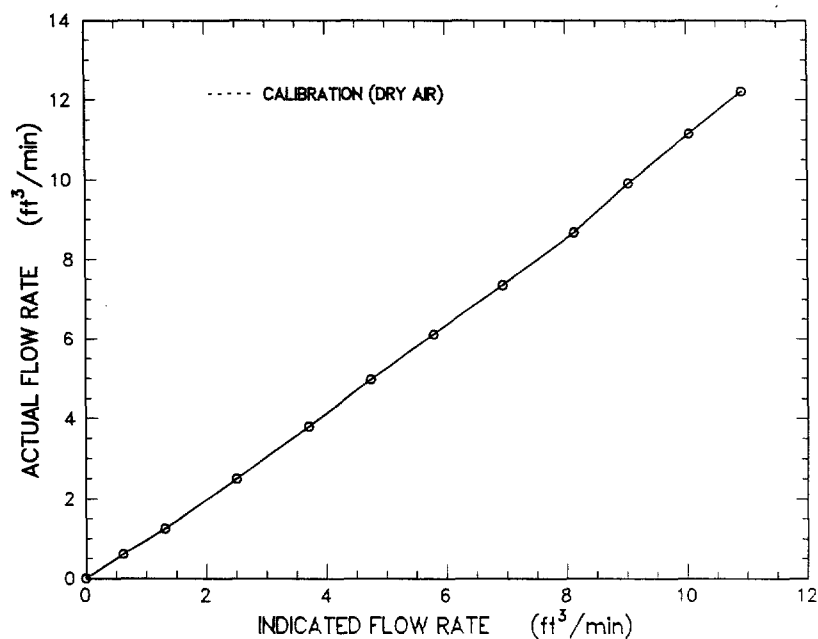
Figure F-14 Calibration of the Rockwell 415 positive displacement gas clock (meter)
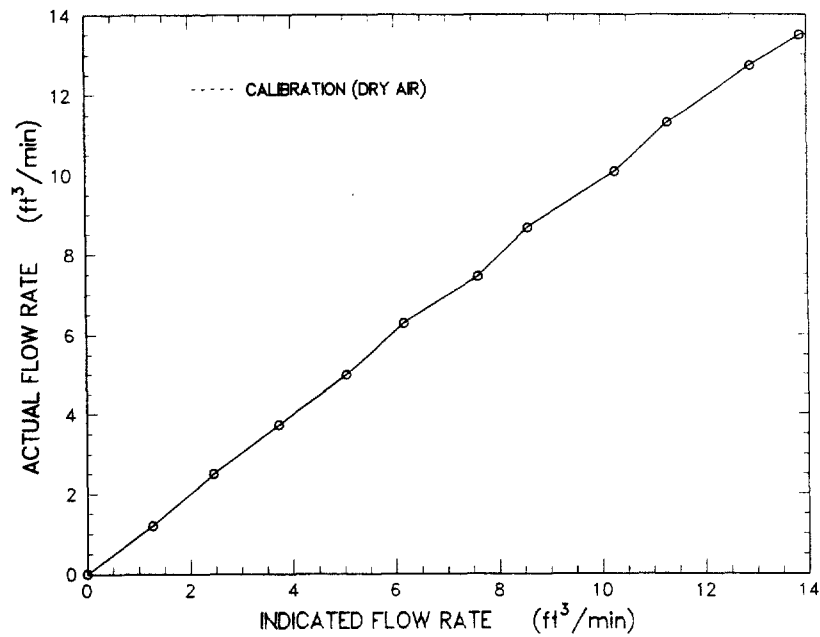
Figure F-15 Calibration of the Rockwell 750 positive displacement gas clock (meter)
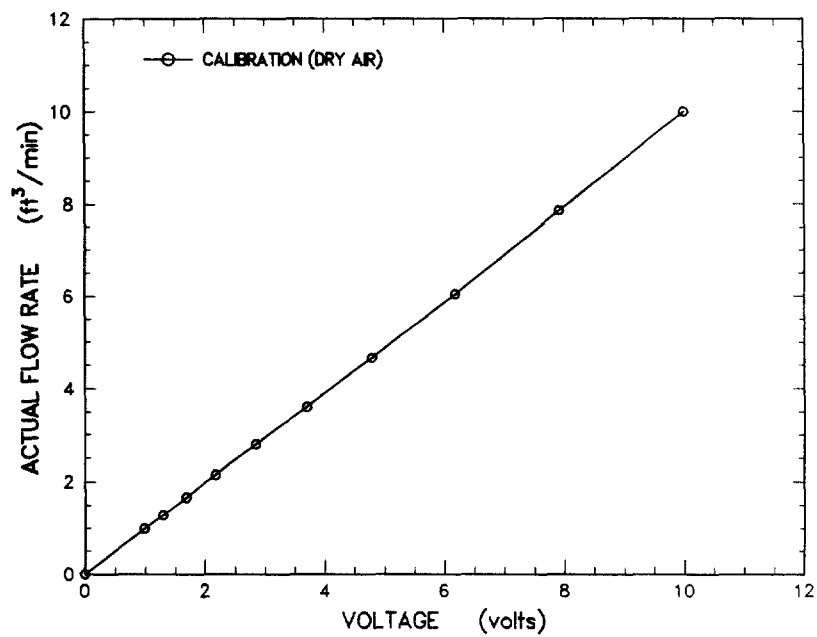
Figure F-16   Turbine meter calibration installed downstream of the laminar flow element near the exit of the flow circuit

Appendix G: Flow Circuit Pressures, Gas Composition, Flow Rate and Aerosol Data

In this appendix data is presented for system and flow pressures, gas composition, gas flow rate and aerosols sampled during the experiment.
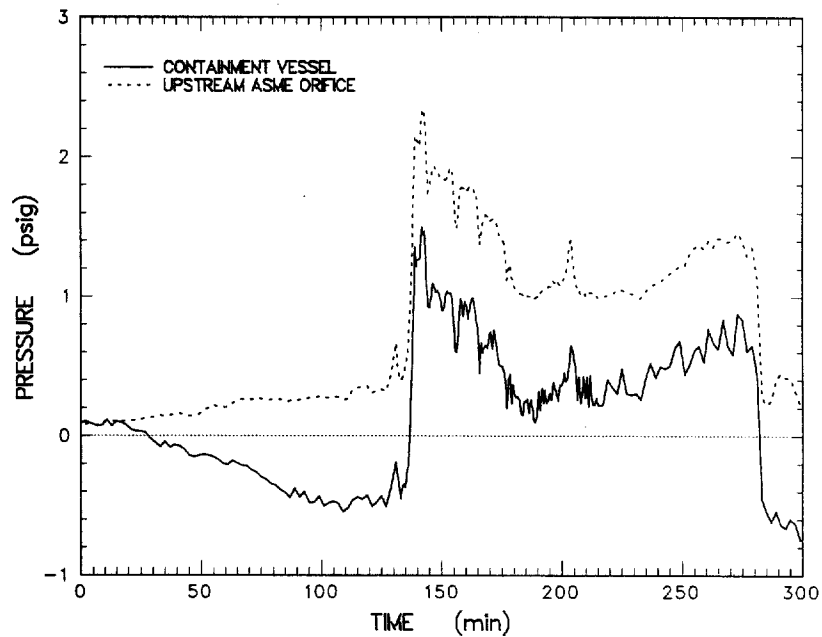
Figure G-1   Gauge pressure measured in the containment vessel and upstream of the ASME sharp edge orifice
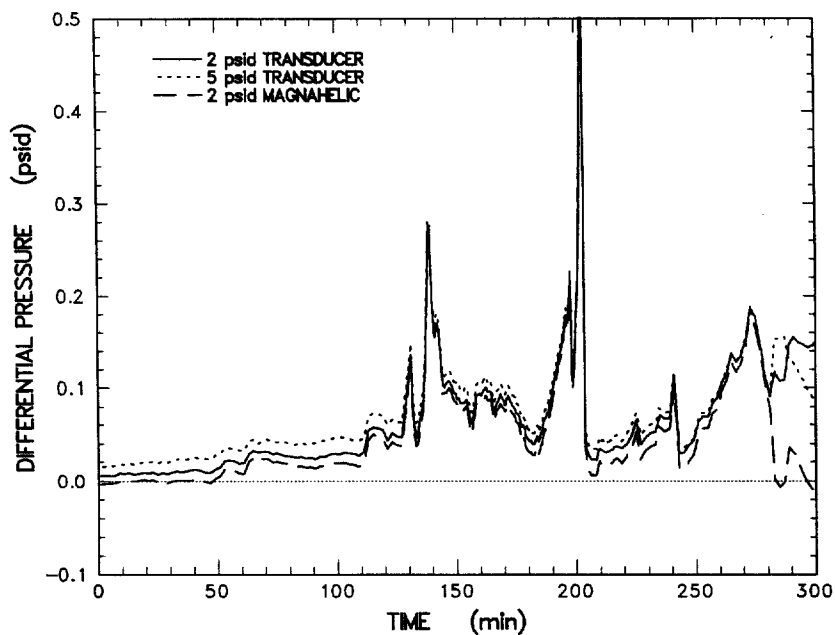
Figure G-2   Differential pressure measured by transducers installed across the ASME sharp edge orifice
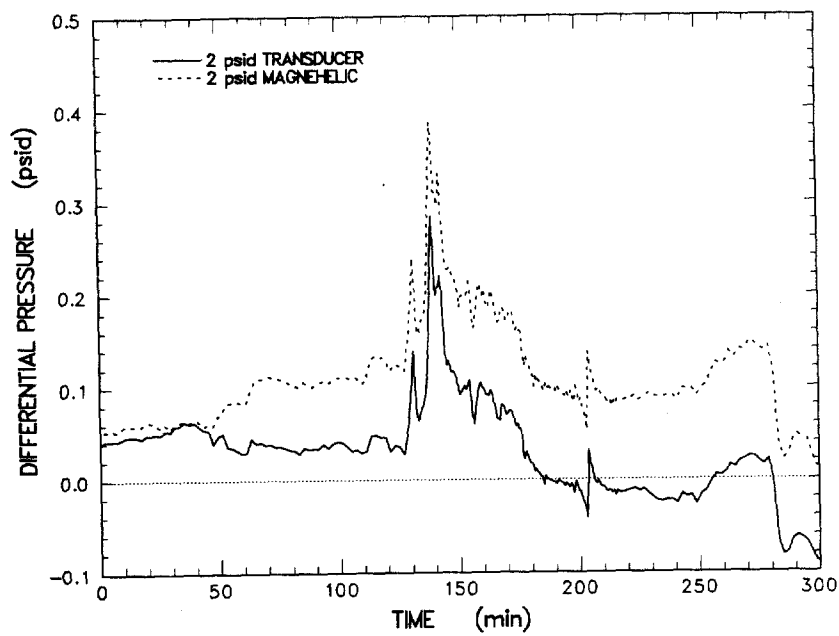
Figure G-3 Differential pressure measured by two transducers installed across the laminar flow device
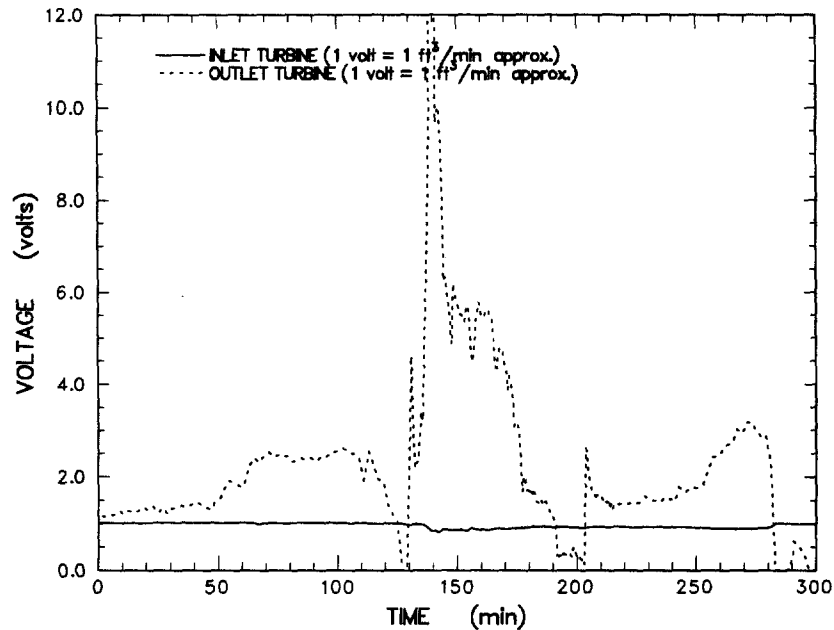
Figure G-4 Flow rate indicated by the turbine meters installed at the inlet of the argon purge and downstream of the laminar flow device near the exit of the flow circuit

Figure G-5 Total volume of gas measured during the experiment by the Rockwell 415 and 750 positive displacement gas clocks (meters)
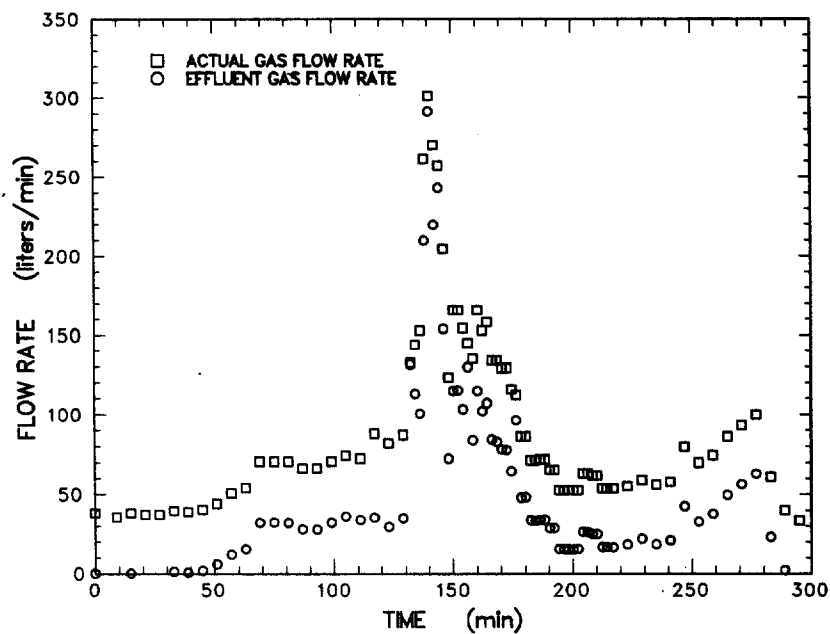
Figure G-6 Total Actual and net flow rate of gas calculated using data acquired from the Rock well 750 positive displacement gas clock (meter) and other flow devices
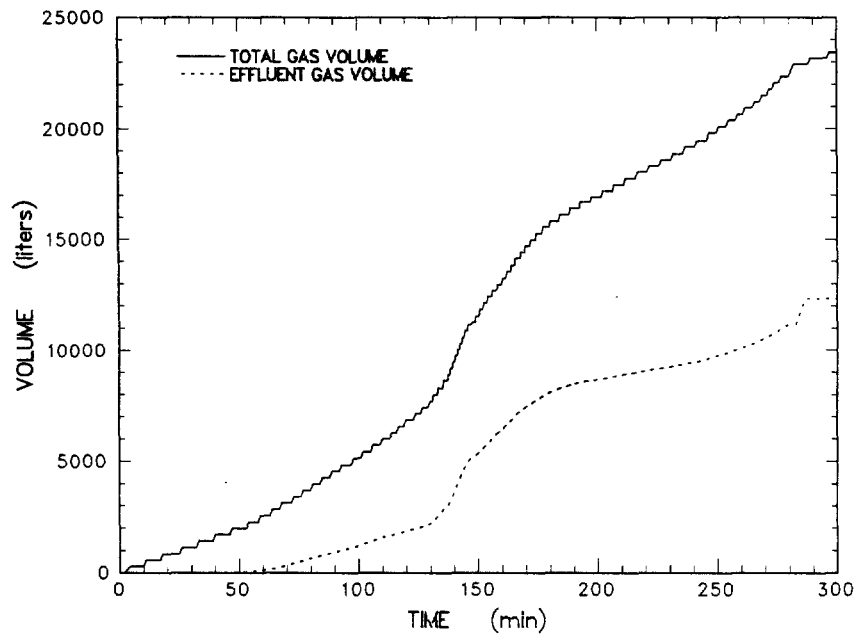
Figure G-7 Comparison of total gas volume measured by the Rockwell 750 gas meter and the reaction gas volume calculated from flow device data
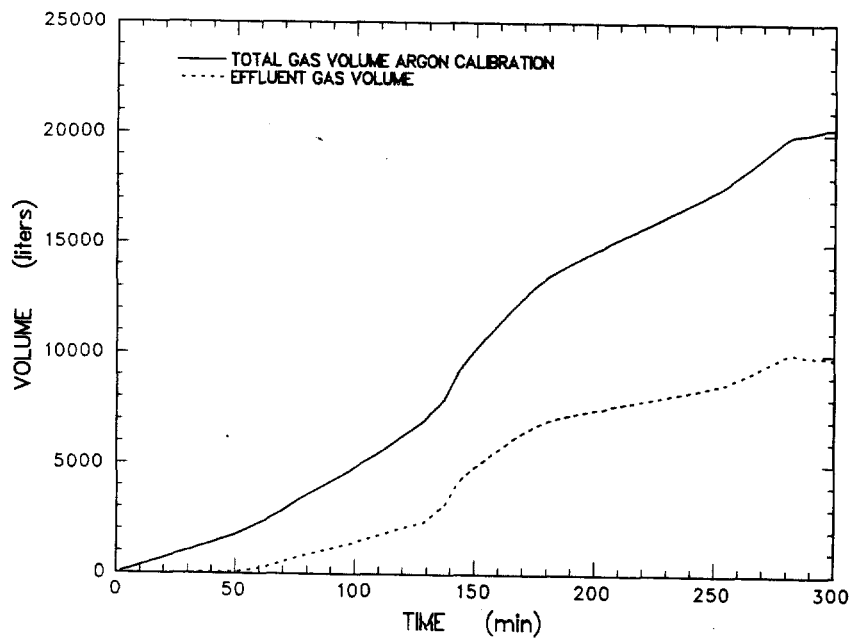
Figure G-8 Comparison of total gas volume calculated using laminar flow device data (argon cal.) and the reaction gas volume calculated from flow device data
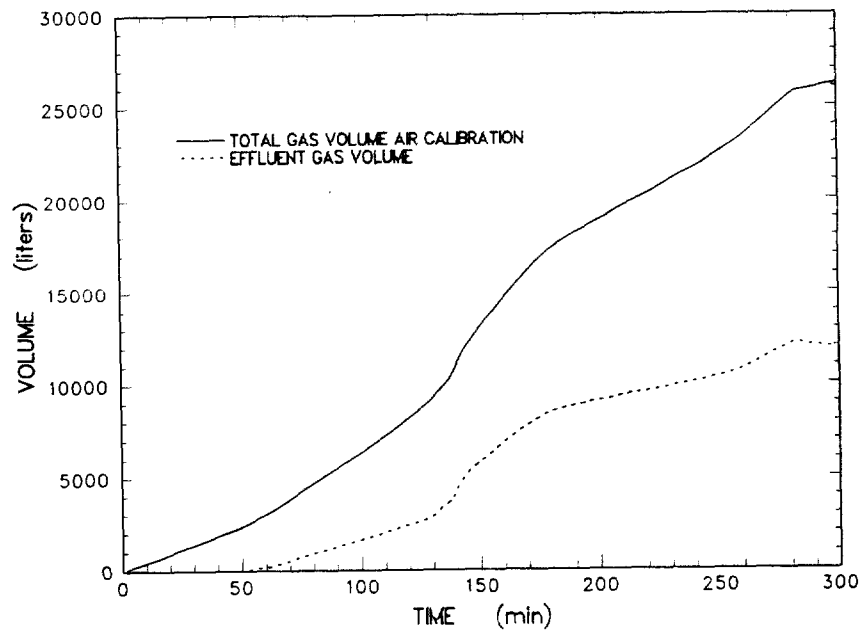
Figure G-9 Comparison of total gas volume calculated using laminar flow device data (air cal.) and the reaction gas volume calculated from flow device data
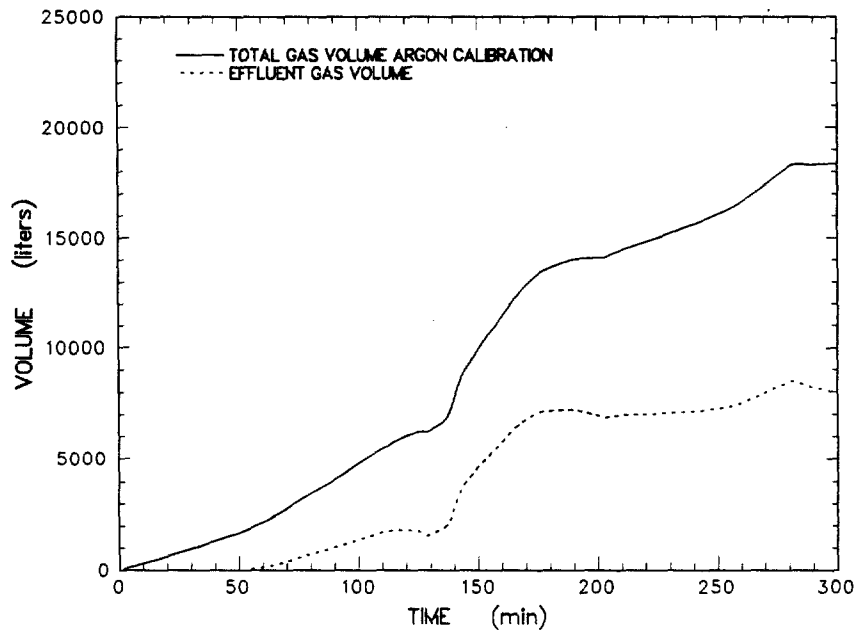
Figure G-10 Comparison of total gas volume calculated from the outlet turbine meter data (argon cal.) and the reaction gas volume calculated from flow device data
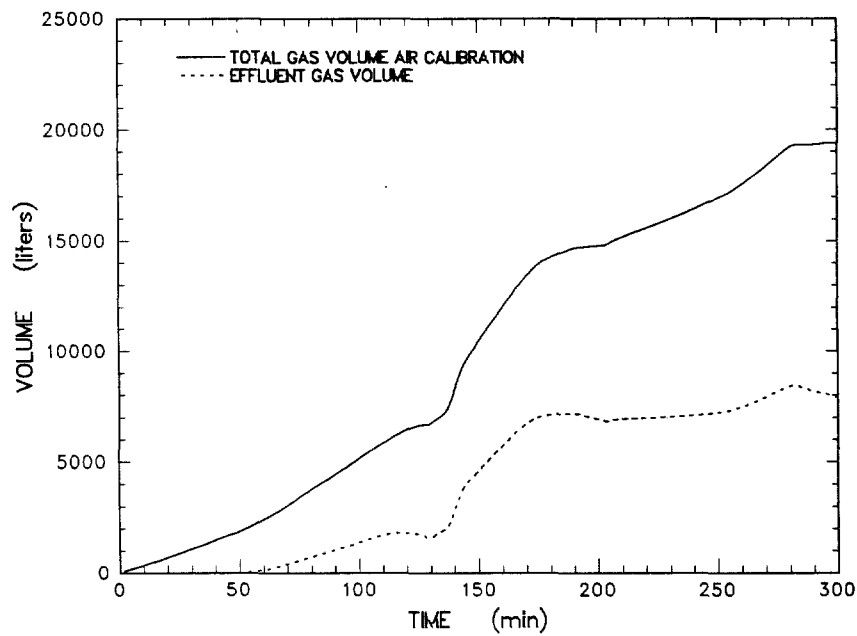
Figure G-11 Comparison of total gas volume calculated from the outlet turbine meter data (air cal.) and the reaction gas volume calculated from flow device data
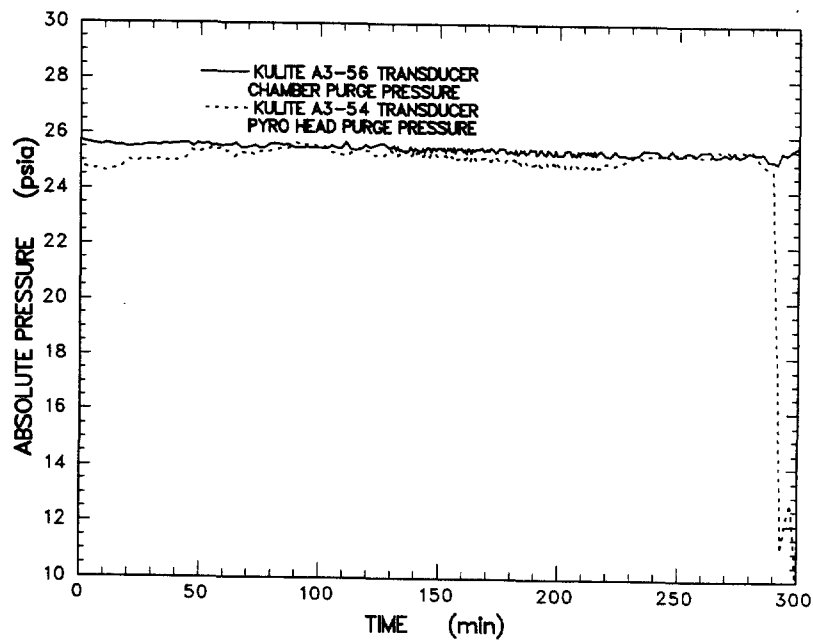
Figure G-12 Absolute pressure measured upstream of the 14 and 3 lpm critical orifice metering argon purge gas flowing into the containment vessel and tungsten pyrotubes
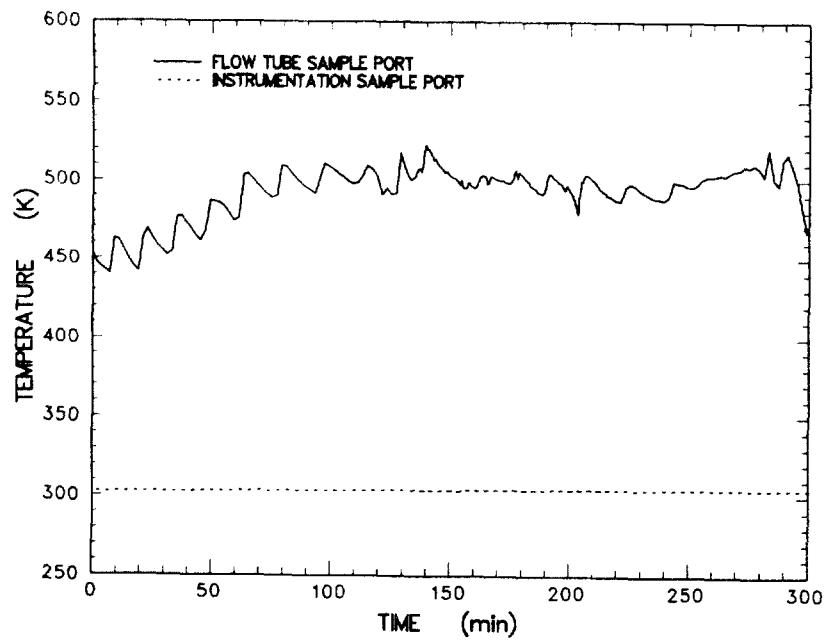
Figure G-13 Gas sample port temperatures
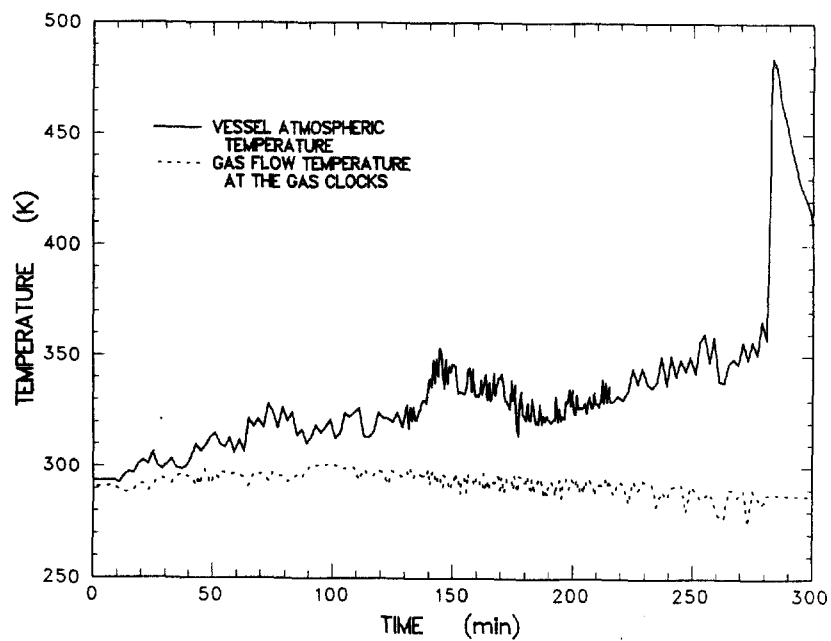
Figure G-14 Atmospheric temperature measured in the containment and in the flow circuit at the 415 positive displacement gas meter
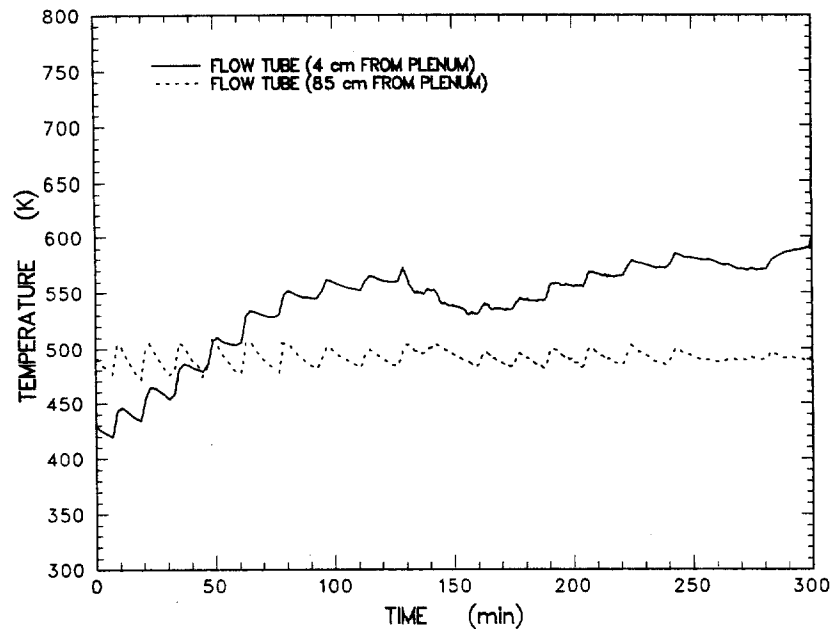
Figure G-15 **Temperature of the flow tube exiting the containment vessel wrapped with heater tapes to eliminate condensation of gases and aerosols prior to sampling**
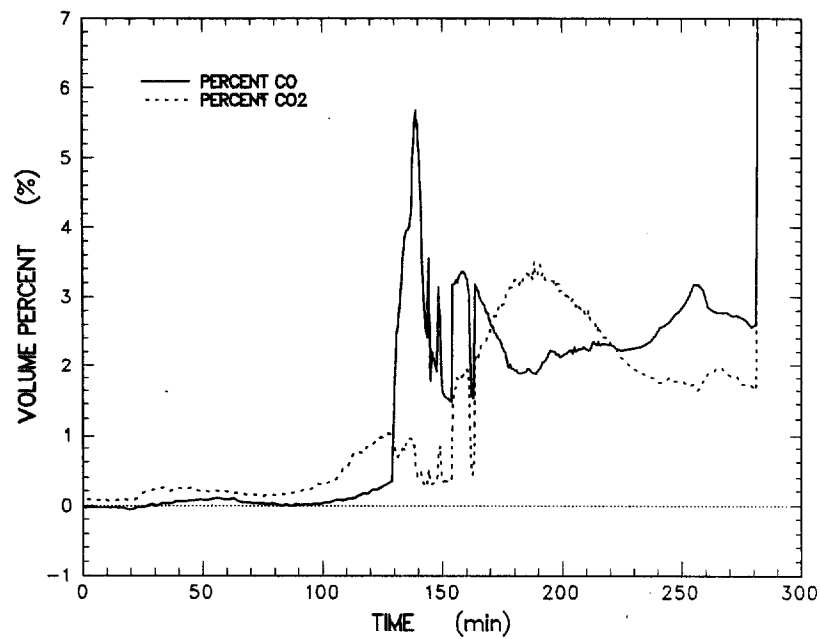
Figure G-16 **Volume percent CO and CO_2 measured using the infrared gas monitor**
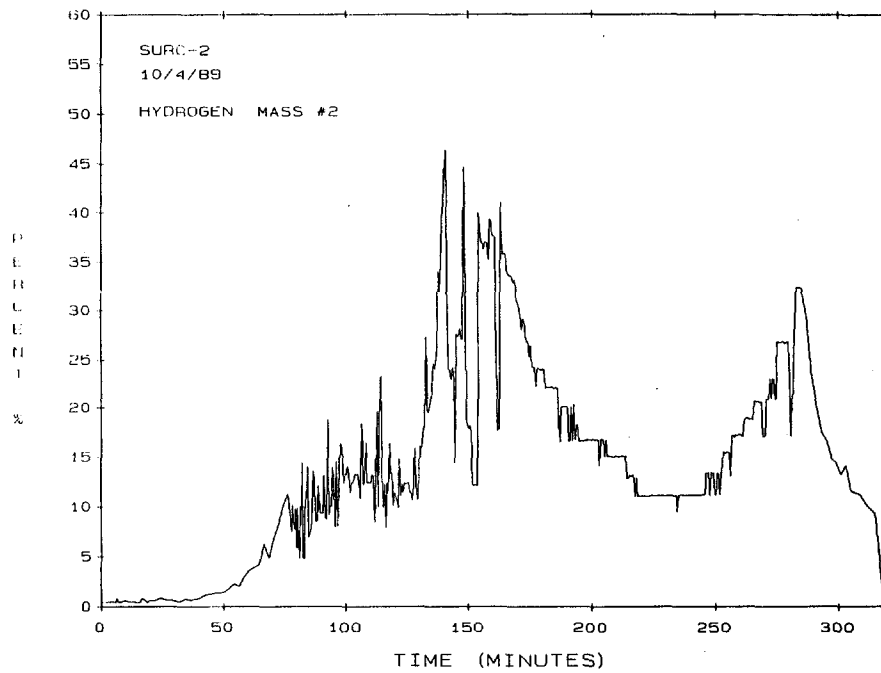
Figure G-17 Volume percent of hydrogen measured by the mass spectrometer
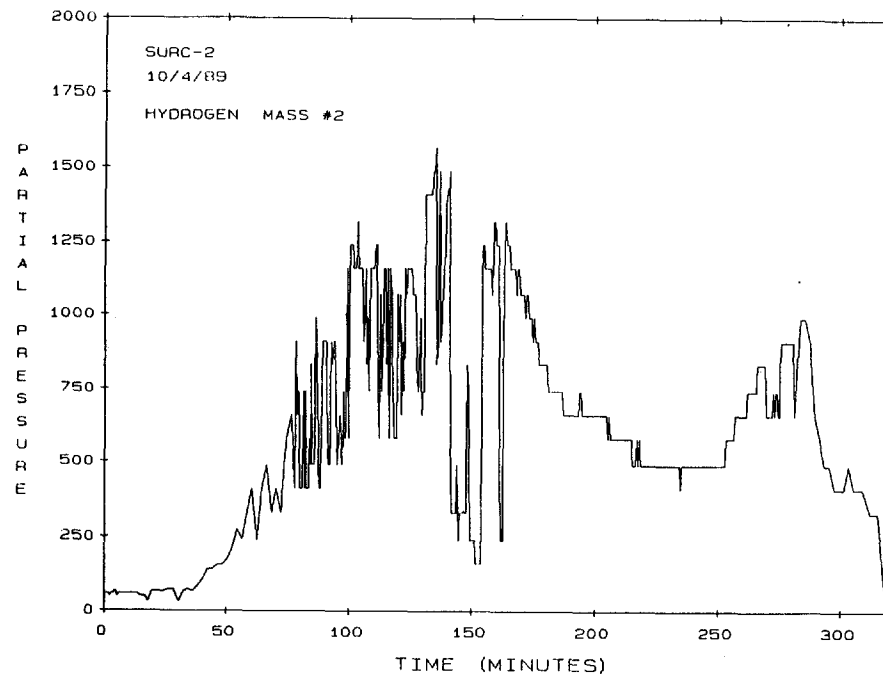
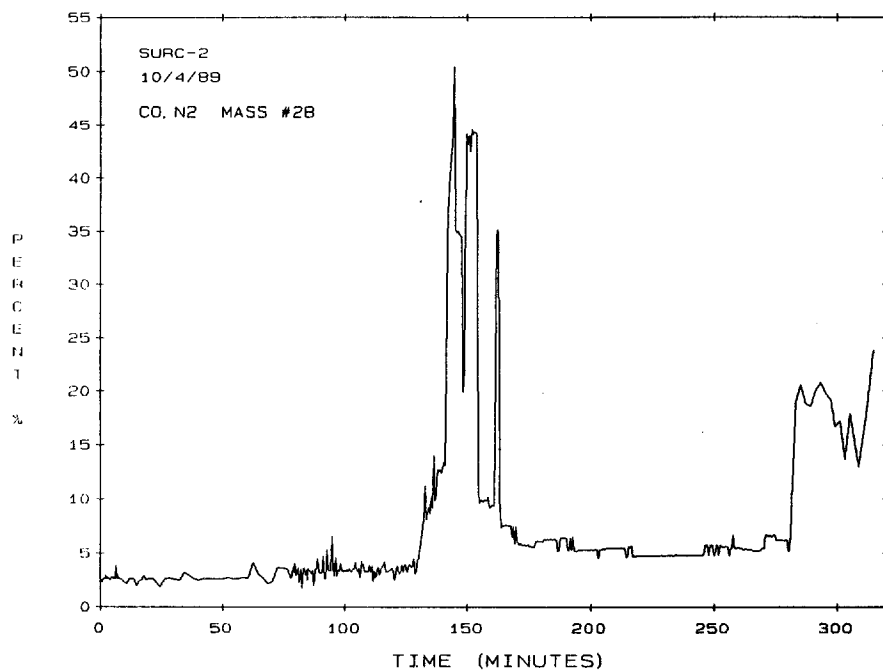**Figure G-18 Partial pressure of hydrogen sampled by the mass spectrometer**
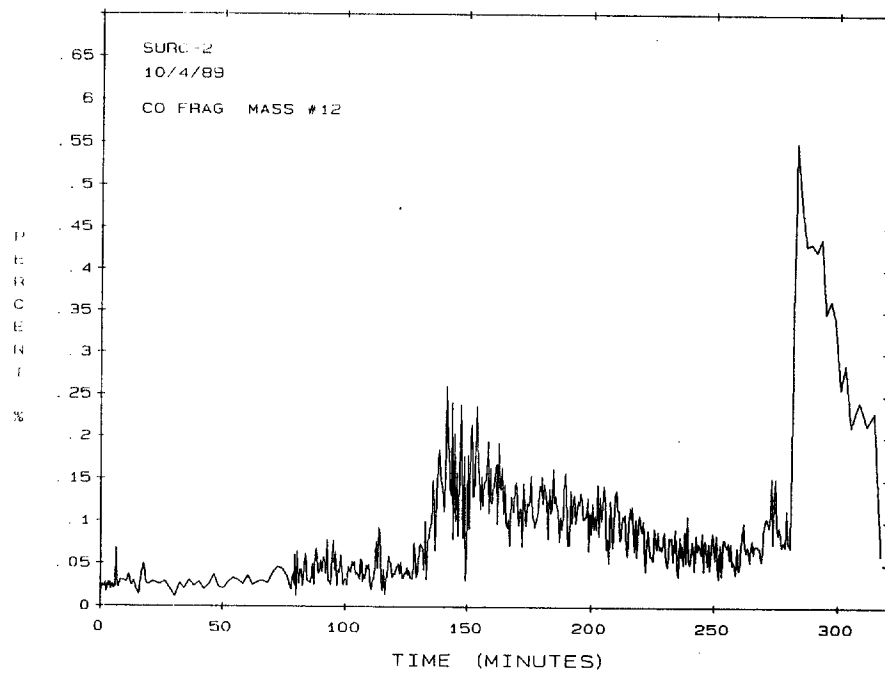
Figure G-19 Volume fragment of carbon monoxide measured by the mass spectrometer
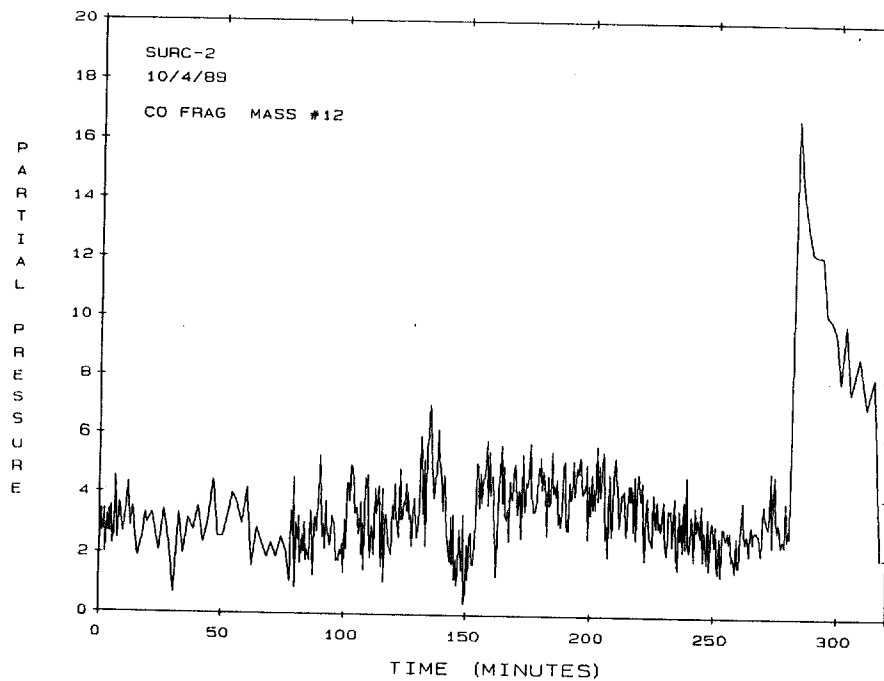
Figure G-20 Partial pressure of carbon monoxide fragment measured by the mass spectrometer
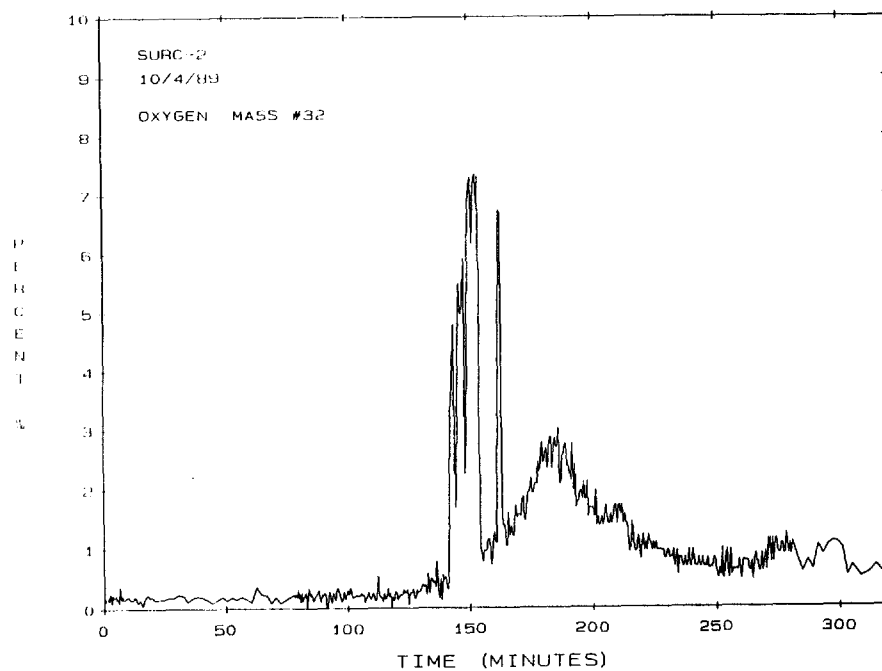
Appendix G
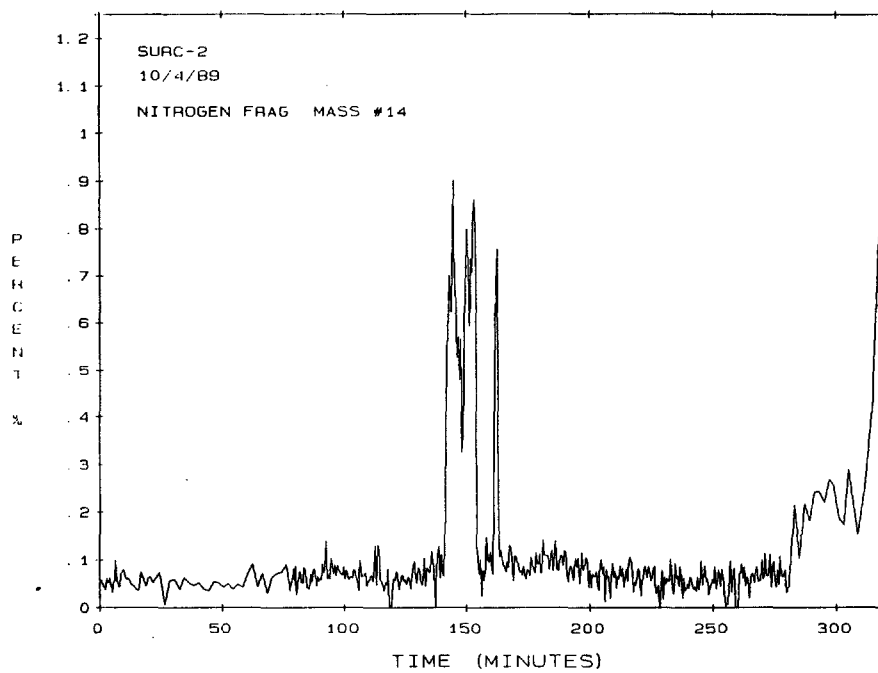
Figure G-21 Volume fragment of the nitrogen measured by the mass spectrometer
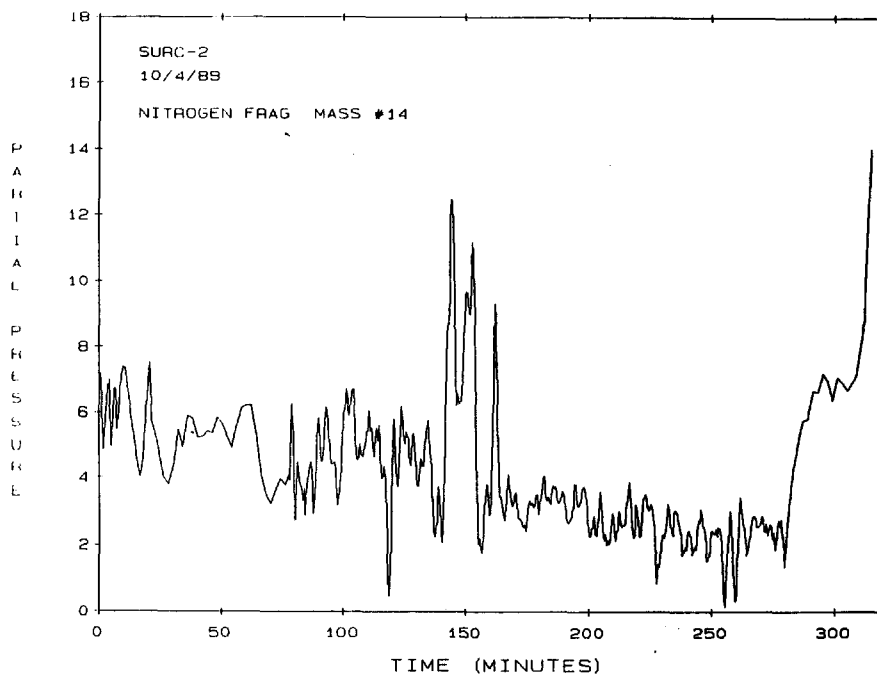
Figure G-22 Partial pressure of nitrogen fragment measured by the mass spectrometer
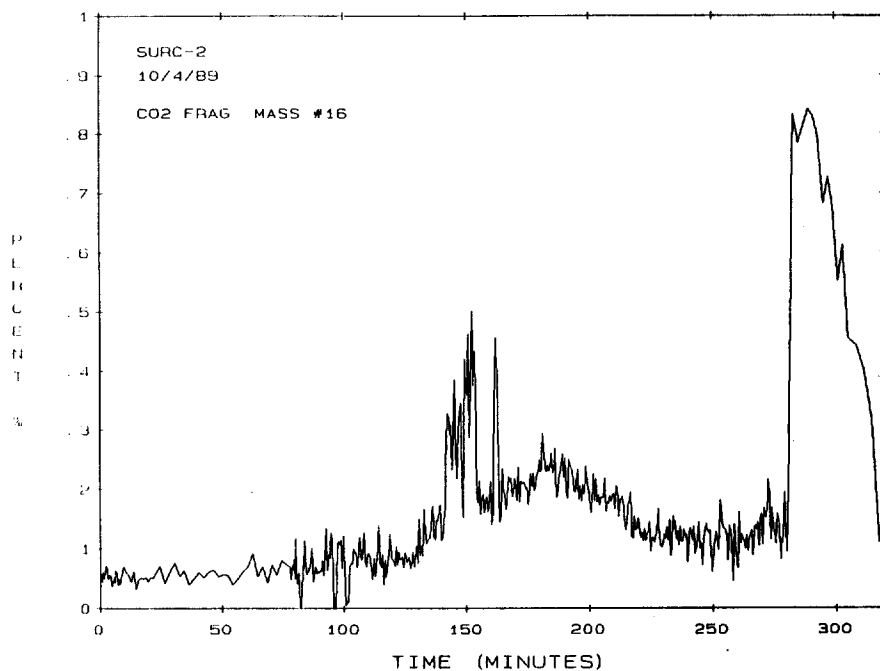
Figure G-23 Volume fragment of carbon dioxide measured by the mass spectrometer
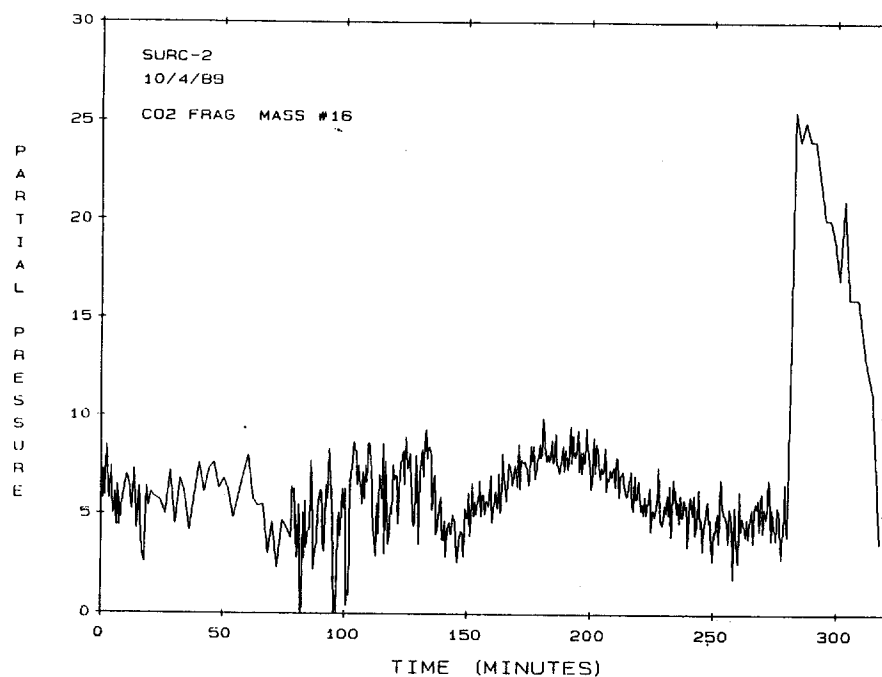
Figure G-24 Partial pressure of carbon dioxide fragment measured by the mass spectrometer
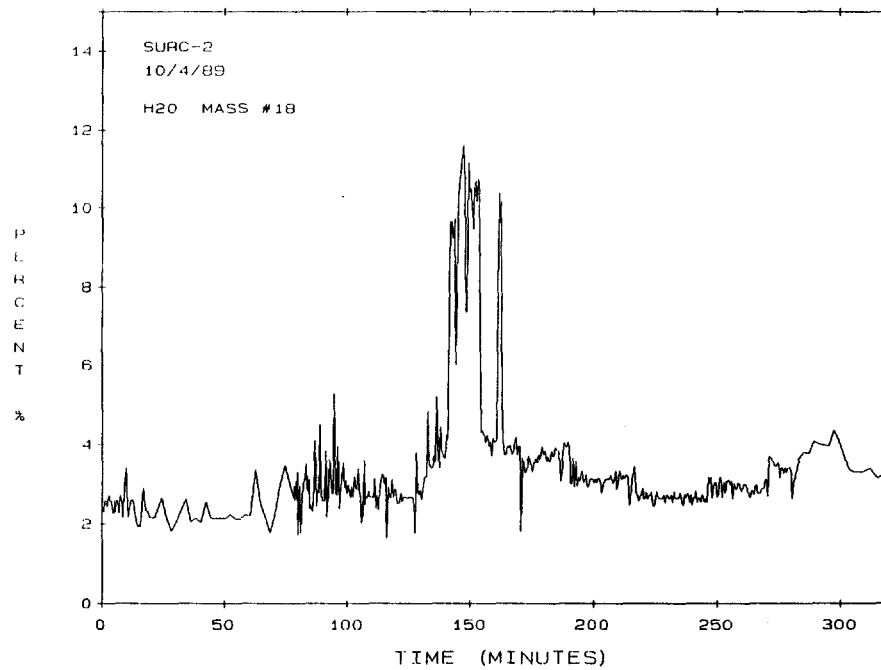
Figure G-25 Volume percent of water vapor measured by the mass spectrometer
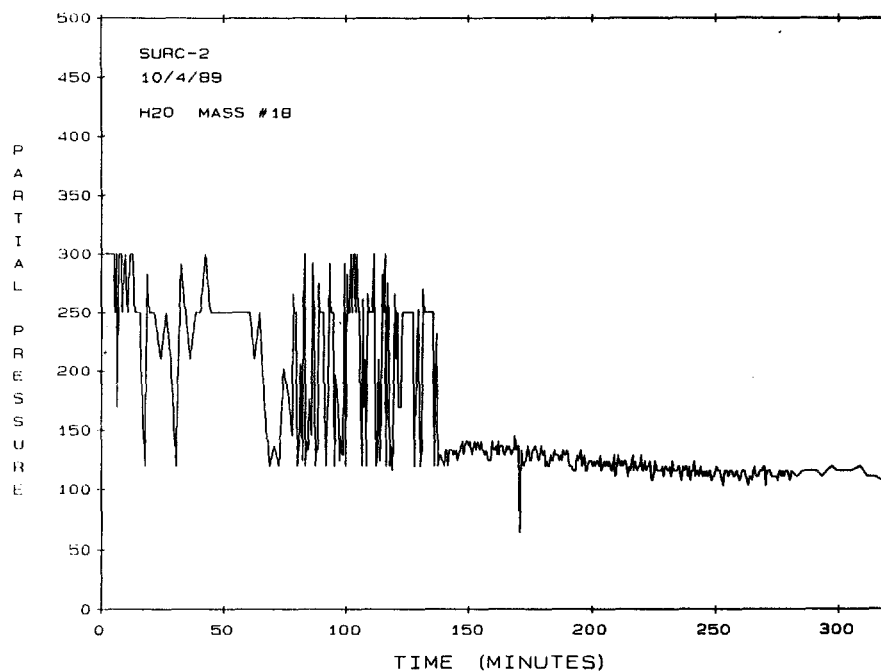
Figure G-26 Partial pressure of water vapor measured by the mass spectrometer

Figure G-27 Volume percent of carbon monoxide and nitrogen measured by the mass spectrometer
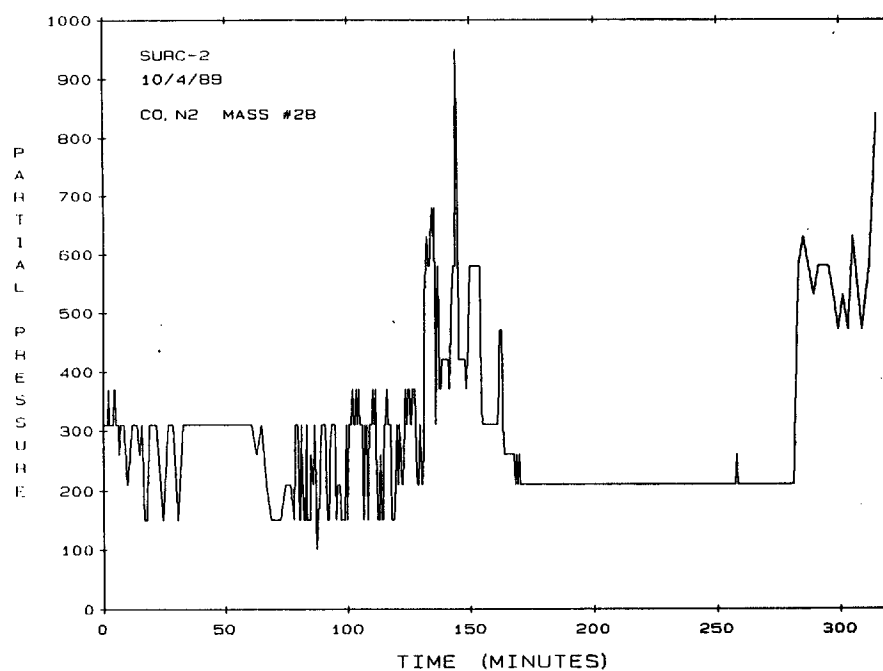
Figure G-28 Partial pressure of carbon monoxide and nitrogen measured by the mass spectrometer

Figure G-29 Volume percent of oxygen measured by the mass spectrometer
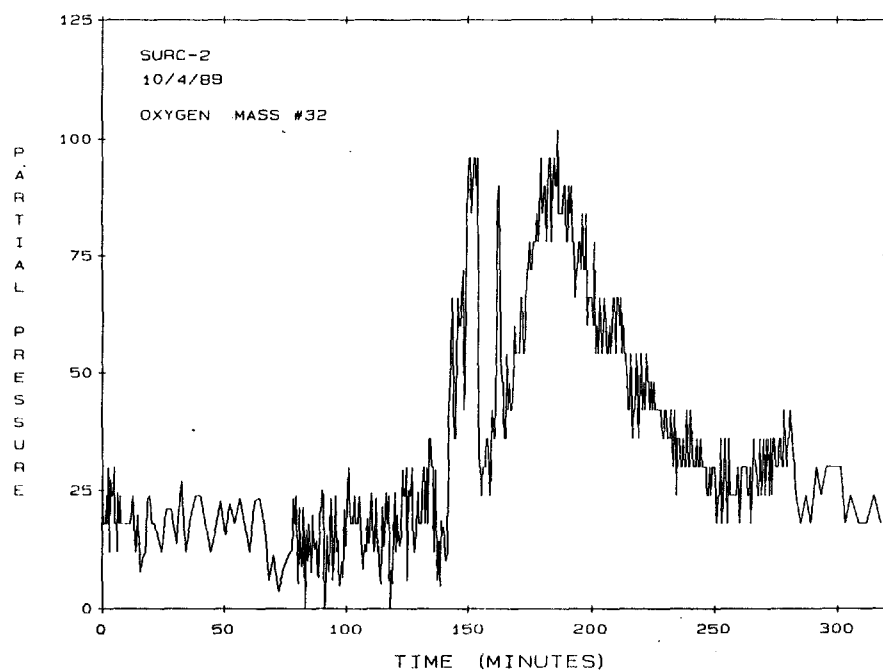
Figure G-30 Partial pressure of oxygen measured by the mass spectrometer
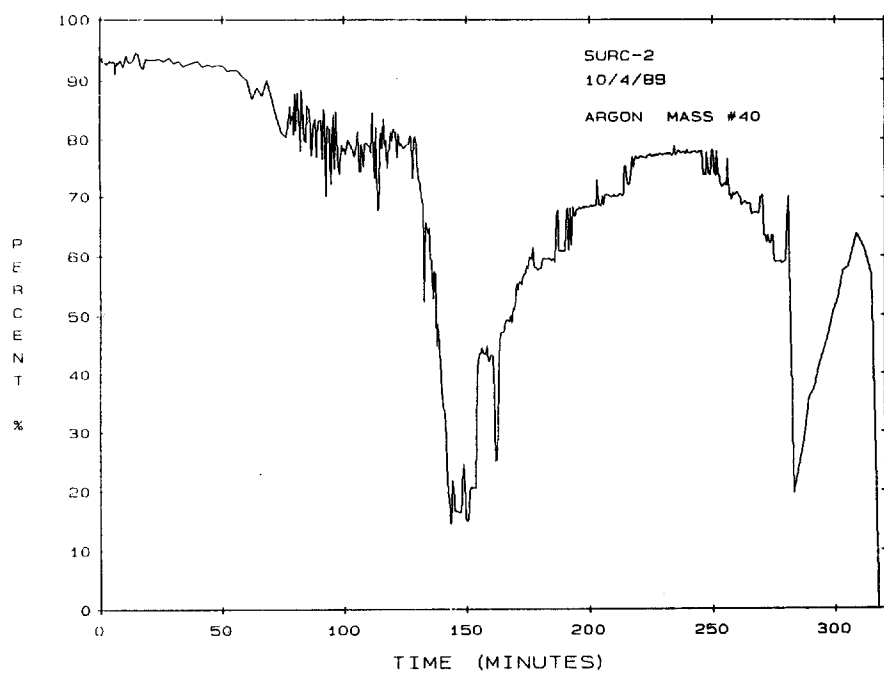
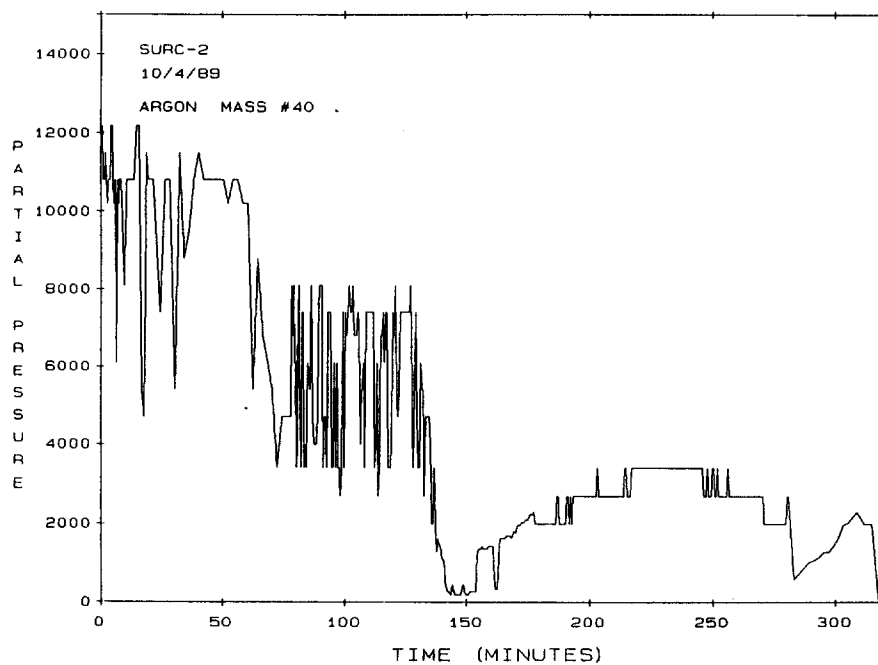**Figure G-31 Volume percent of argon measured by the mass spectrometer**

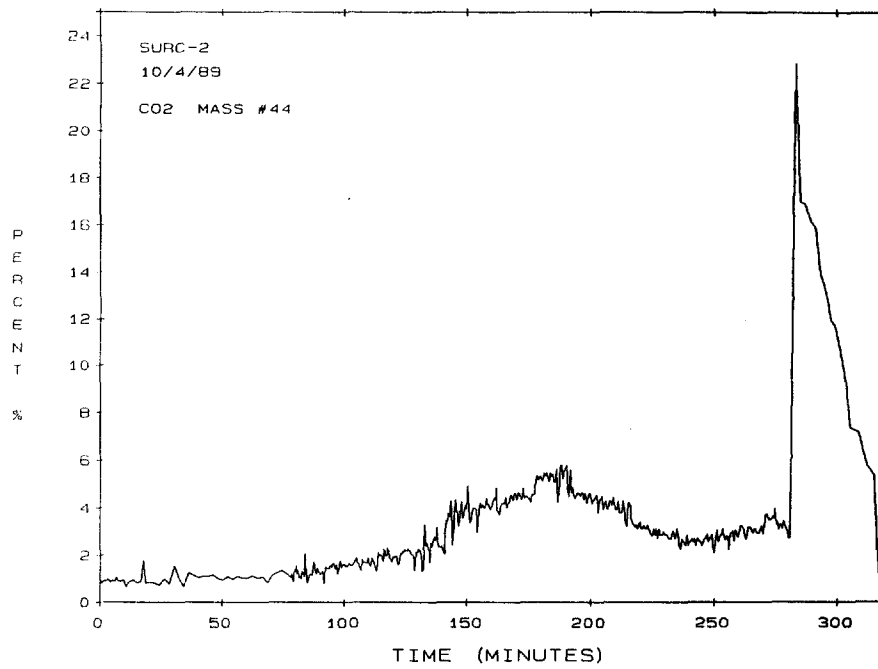**Figure G-32 Partial pressure of argon measured by the mass spectrometer**

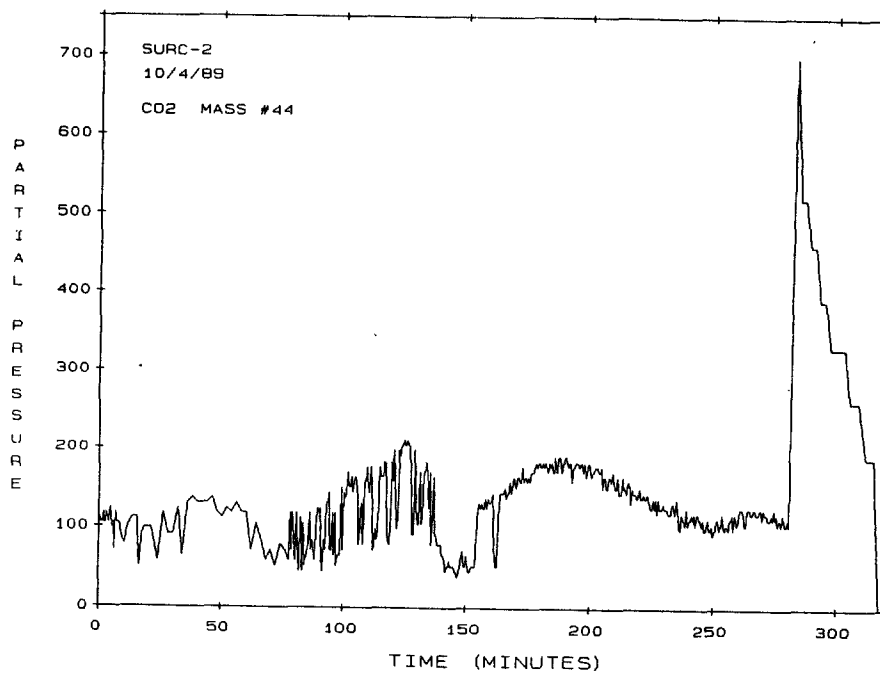**Figure G-33 Volume percent of carbon dioxide measured by the mass spectrometer**

Figure G-34 Partial pressure of carbon monoxide measured by the mass spectrometer
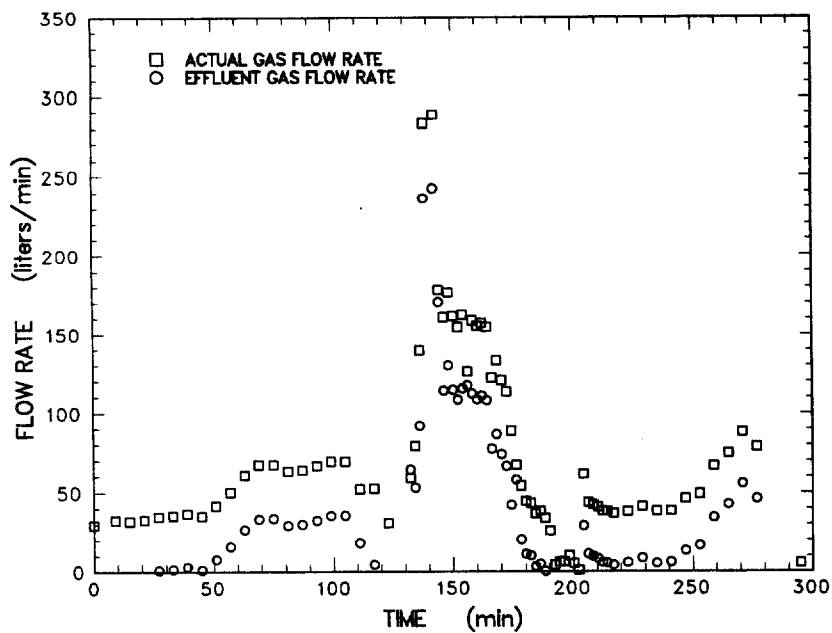
Figure G-35 Gas flow rate summary for turbine meter

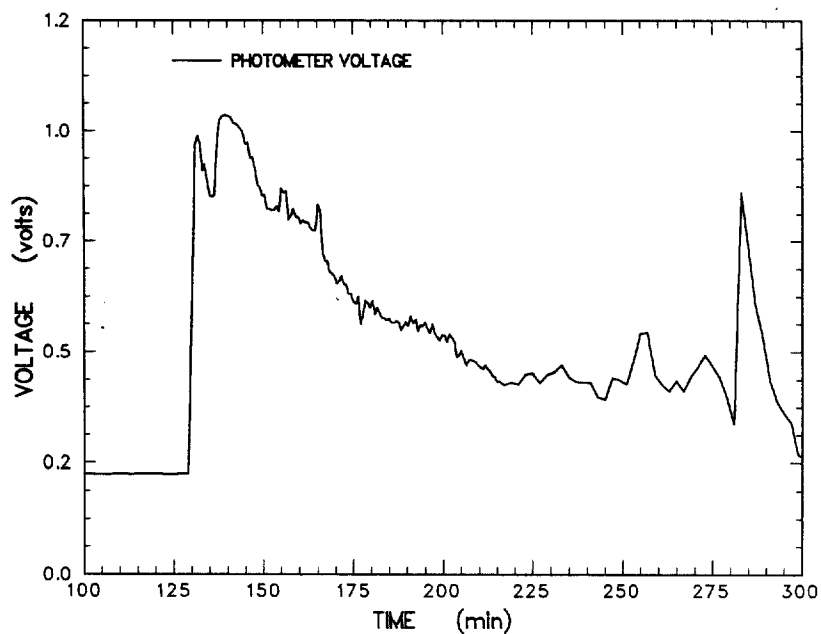**Figure G-36 Opacity meter output. Voltage level is directly proportional to aerosol concentration.**
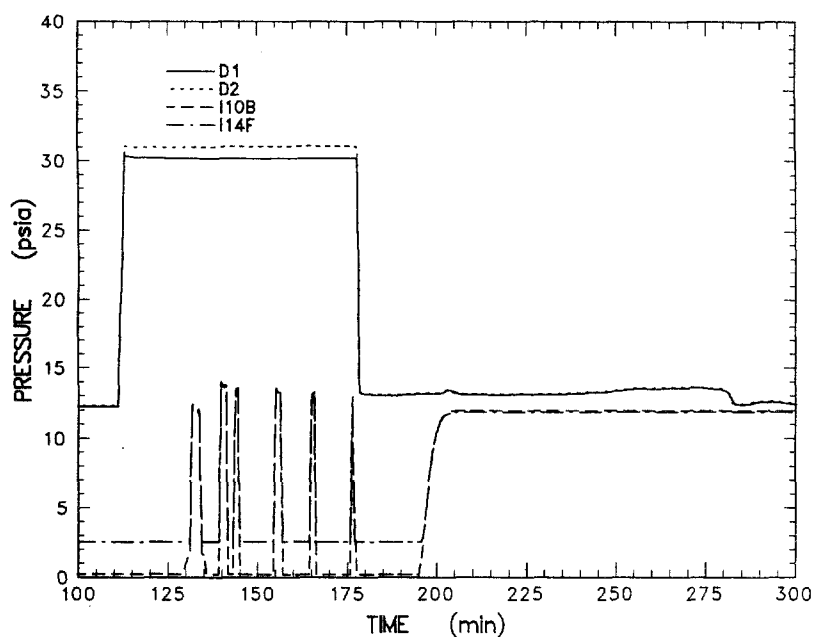
Figure G-37 Absolute pressure measured upstream of critical orifices installed in the aerosol sample line for the diluters and impactors
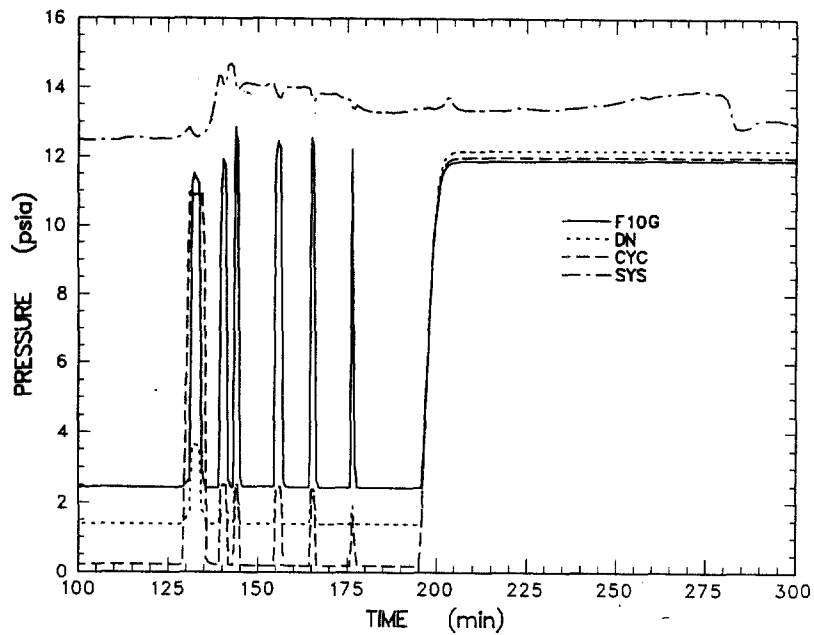

Figure G-38 Absolute pressure measured upstream of critical orifices installed in the aerosol sample line for the filters and cyclone
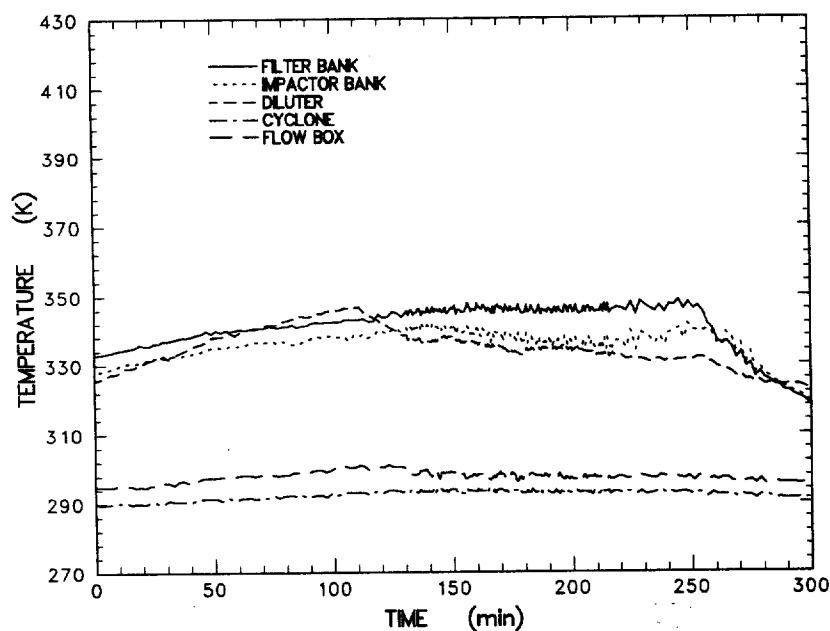
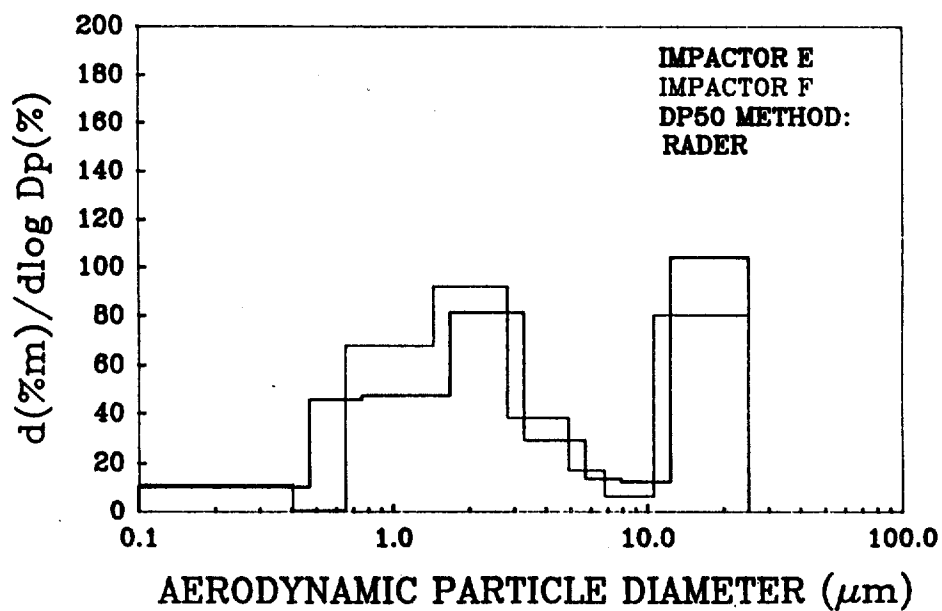**Figure G-39 Temperature measured at different locations in the aerosol sampling system**

Figure G-40 Normalized aerosol mass distribution from impactors E and F taken between 132.5 and 133.0 minutes

Figure G-41 Normalized aerosol mass distribution from impactors G and H taken between 134.0 and 134.5 minutes

Figure G-42 Normalized aerosol mass distribution from impactors J and K taken between 143.5 and 144.0 minutes
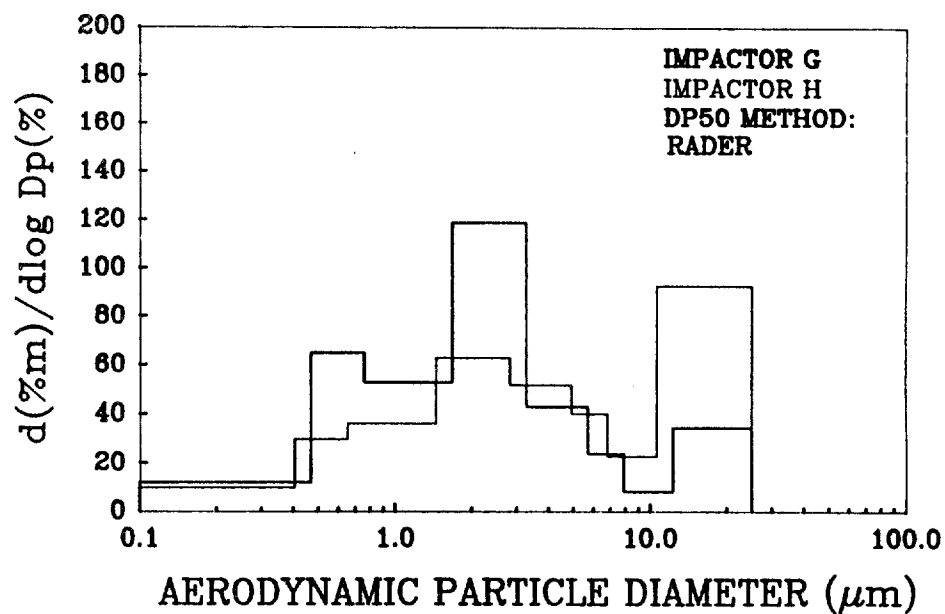
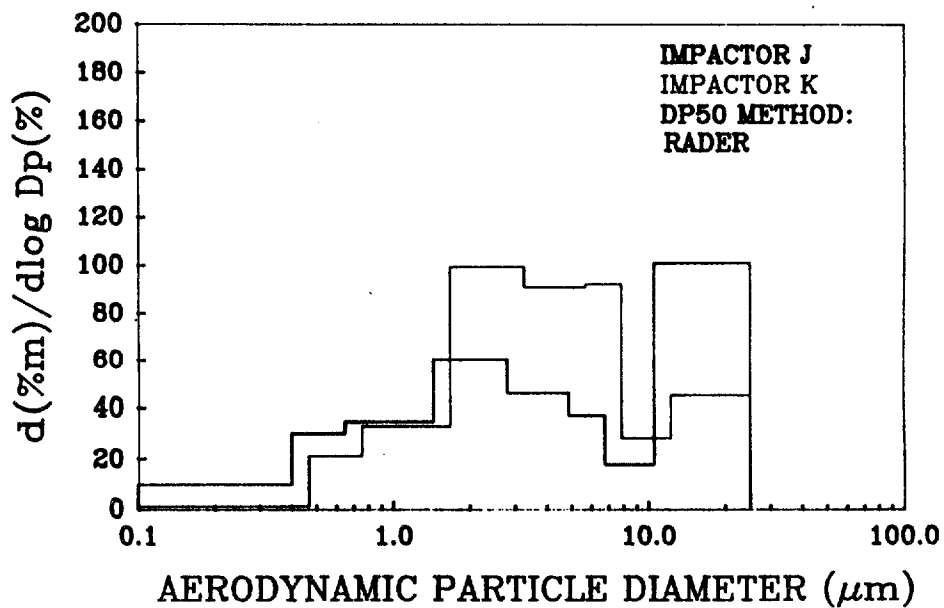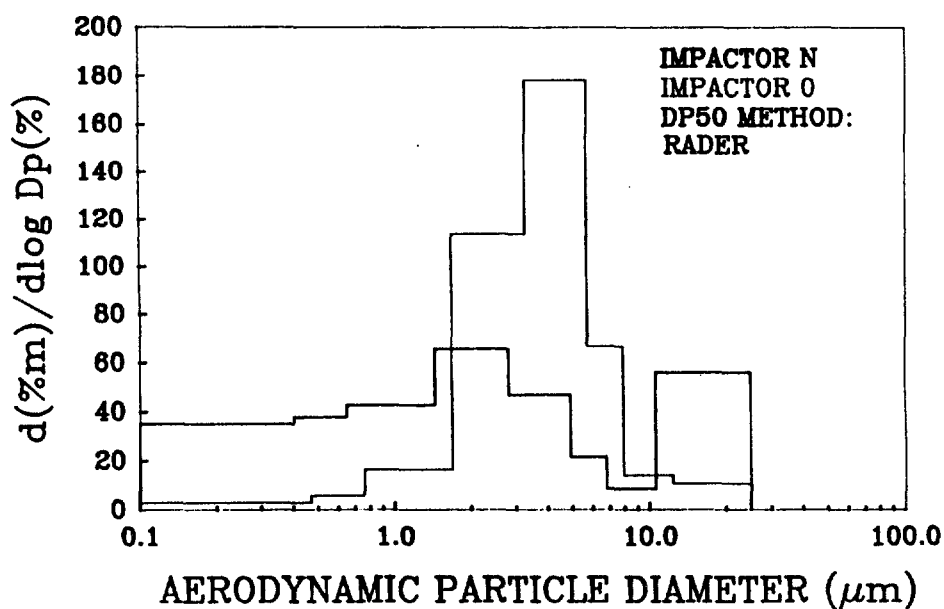**Figure G-43** Normalized aerosol mass distribution from impactors N and O taken between 164.0 and 164.5 minutes
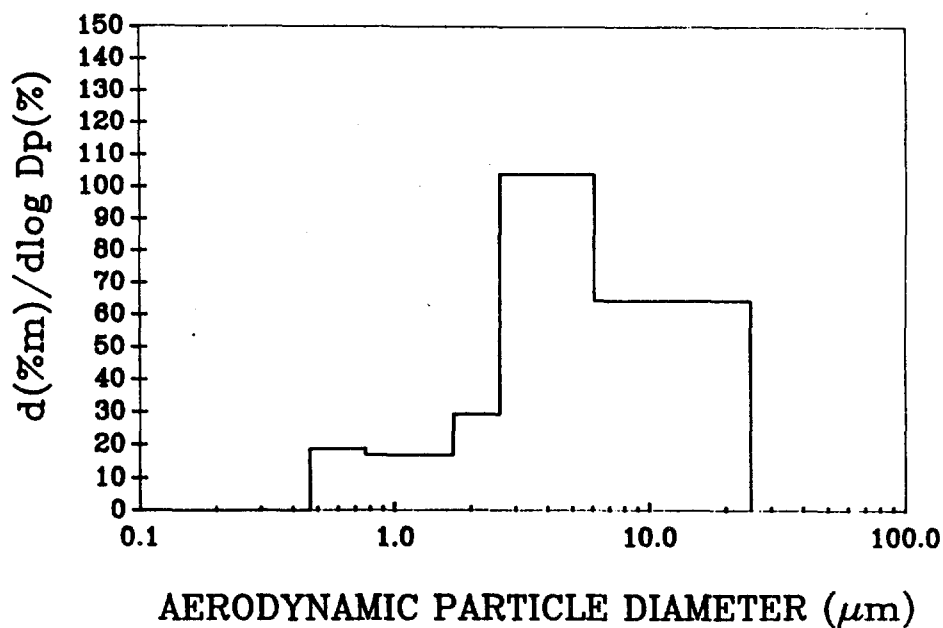
Figure G-44 Normalized aerosol mass distribution from Cascade cyclone taken between 130.5 and 135.5 minutes
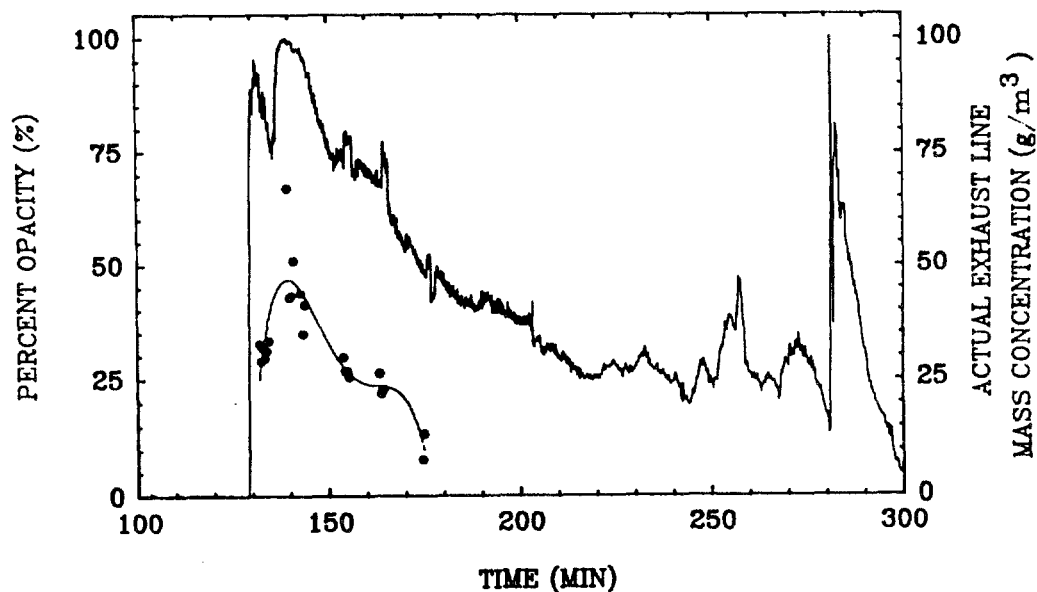
Figure G-45 Comparison of percent opacity with actual exhaust line mass concentrations
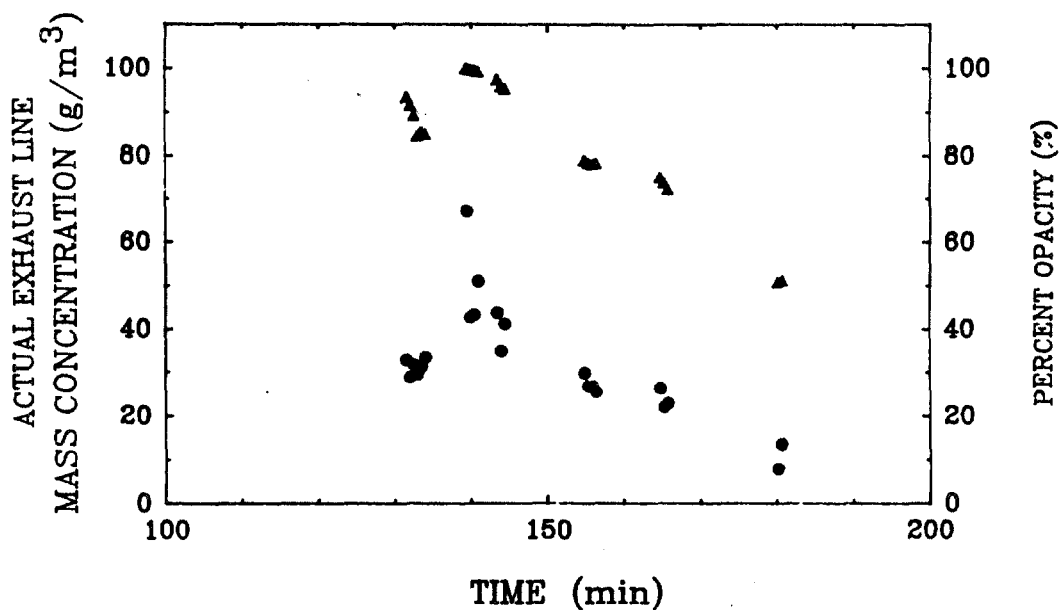
Figure G-46 Filter data comparing percent opacity with actual exhaust line mass concentration
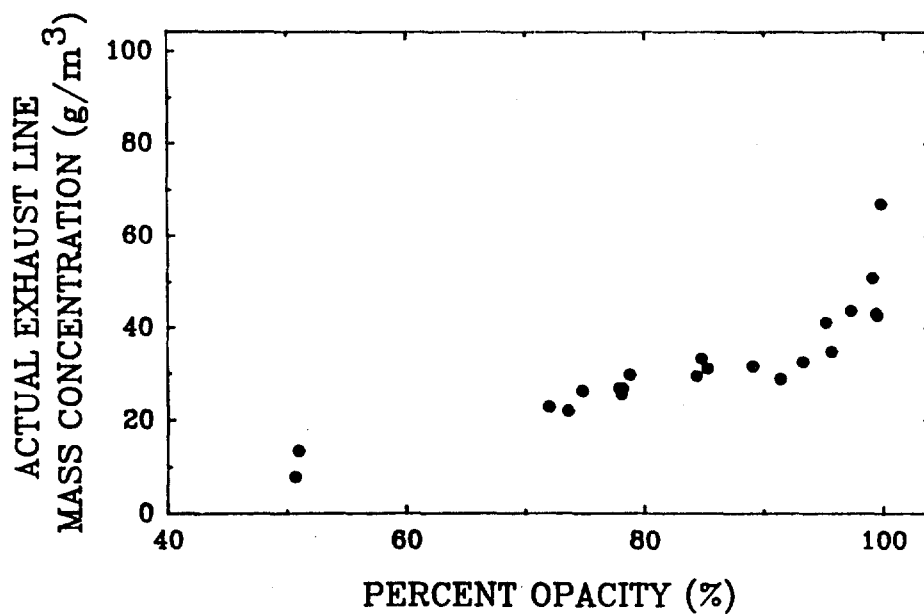
Figure G-47 Plot of mass concentration as a function of percent opacity calculated from filter data
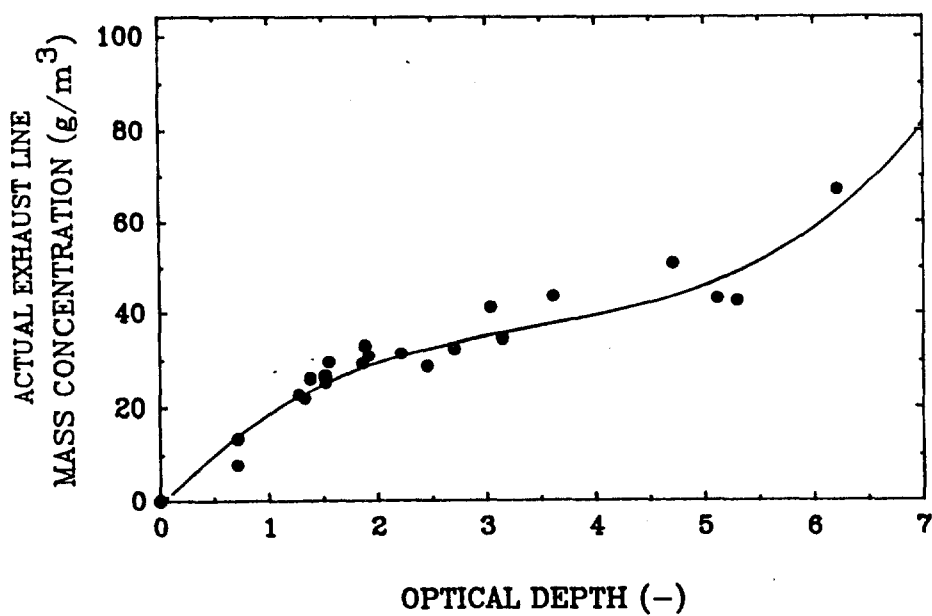
Figure G-48 Plot of mass concentration as a function of optical depth calculated from filter data
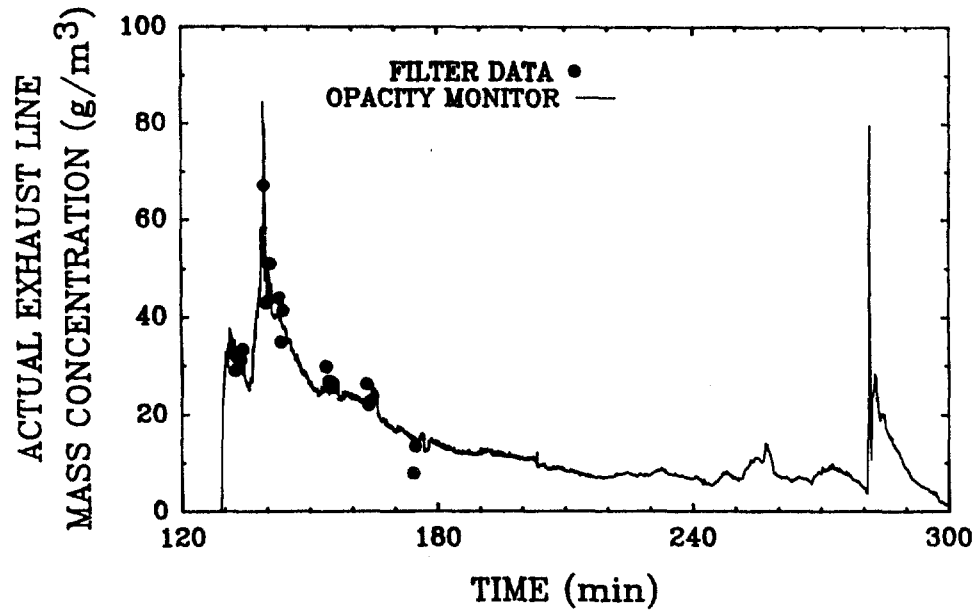
Figure G-49 Comparison of mass concentrations to opacity monitor fit using filter data
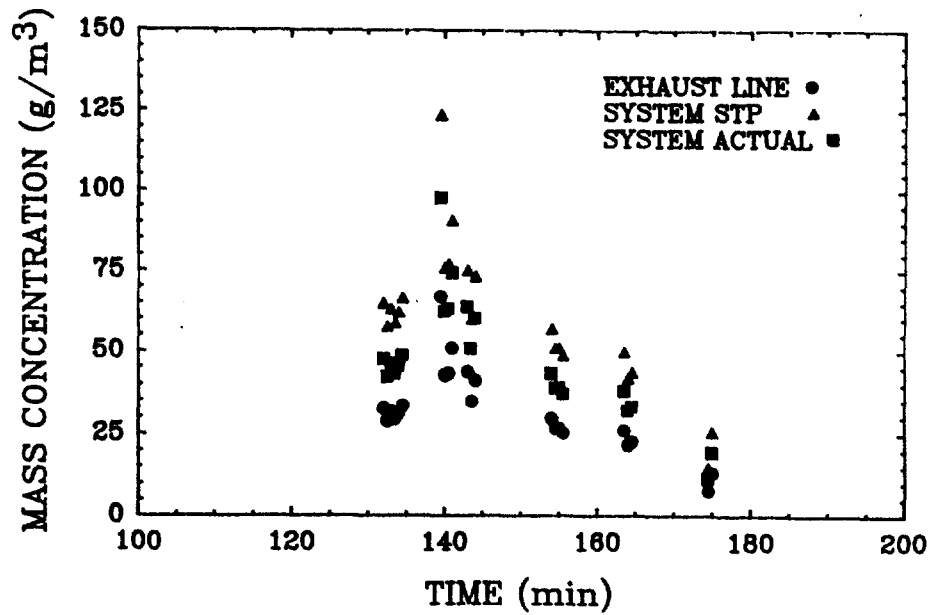
Figure G-50 Aerosol mass concentration plotted as a function of time

DISTRIBUTION LIST

No. of
Copies

No. of
Copies

25   U.S. Nuclear Regulatory Commission
Office of Nuclear Regulatory Research
Washington, DC 20555
Attn: B. W. Sheron, NLS007
        C.G. Tinkler, Jr, NLN344
        G.R. Marino, NLS007
        A.M. Rubin, NLN344
        R.B. Foulds, NLN344
        J.A. Murphy, NLS007
        S. Basu, NLN344 (15)
        E.S. Beckjord, NLS007
        F. Eltawila, NLN 344
        Z. Rosztoczy, NLS169
        T.P. Speis, NLS007

5   U.S. Nuclear Regulatory Commission
Office of Nuclear Reactor Regulation
Washington, DC 20555
Attn: T.C. Murley, 12G18
        F.P. Gillespie, 12G18
        A.C. Thadani, 8E2 (3)

2   U.S. Department of Energy
Albuquerque Operations Office
P.O. Box 5400
Albuquerque, NM 87185
Attn: C.E. Garcia, Director

2   Electric Power Research Institute
3412 Hillview Avenue
Palo Alto, CA 94303
Attn: A. Machiels

3   Brookhaven National Laboratory
130 BNL
Upton, NY 11973
Attn: T. Pratt

3   Oak Ridge National Laboratory
P.O. Box Y
Oak Ridge, TN 37830
Attn: T. Kress

3   Argonne National Laboratory
9700 S. Cass Avenue
Argonne, IL 60439
Attn: B. Spencer

1   Nuclear Safety Oversight Commission
1133 15th Street, NW
Room 307
Washington, D.C. 20005
Attn: Cathy Anderson

1   Battelle Columbus Laboratory
505 King Avenue
Columbus, OH 43201
Attn: P. Cybulskis

1   Los Alamos National Laboratories
P.O. Box 1663
Los Alamos, NM 87545
Attn: M. Stevenson

1   UCLA
Nuclear Energy Laboratory
405 Hilgaard Avenue
Los Angeles, CA 90024
Attn: I. Catton

Dist

DISTRIBUTION LIST (Continued)

No of
Copies

No of
Copies

1   University of Wisconsin
Nuclear Engineering Department
1500 Johnson Drive
Madison, WI 53706
Attn: M.L. Corradini

1   EG&G Idaho
Willo Creek Building, W-3
P.O. Box 1625
Idaho Falls, ID 83415
Attn: R. Hobbins

1   Battelle Pacific Northwest Laboratory
P.O. Box 999
Richland, WA 99352
Attn: M. Freshley

1   Department of Energy
Scientific and Tech. Info. Center
P.O. Box 62
Oak Ridge, TN 37831

1   Fauske and Associates, Inc.
16W070 West 83rd Street
Burr Ridge, IL 60952
Attn: R. Henry

1   IAEA
Division of Nuclear Reactor Safety
Wagranesrstrasse 5
P.O. Box 100
A/1400 Vienna
Austria
Attn: M. Jankowski

1   Department LWR Fuel
Belgonucleaire
Rue de Champde Mars. 25
B-1050 Brussels
Belgium
Attn: Mr. H. Bairiot, Chief

1   U.S. Nuclear Regulatory Commission
Advisory Comm. on Reactor Safeguarde
Washington, D.C. 20555
Attn: M.D. Houston, P-315

2   Atomic Energy Canada, Ltd.
Chalk River, Ontario
Canada KOJ IJO
Attn: R.D. MacDonald

1   Institute of Nuclear Energy Research
P.O. Box 3
Lungtan
Taiwan 325
Republic of China
Attn: Sen-I Chang

1   Department of Nuclear Safety
Finnish Center for Radiation
and Nuclear Safety
P.O. Box 268
SF-00181 Helsinki
Finland
Attn: Jorma V. Sandberg

1   CEN Cadarache
18108 Saint Paul Lez Durance
France
Attn: A. Meyer-Heine

DISTRIBUTION LIST (Continued)

No of
Copies

No of
Copies

1   Centre d'Estudes Nuclearies (IPSN-DAS)
Commisariat a l'Energie Atomique
Boite Postale No. 6
F-92265 Fontenay-aux-Roses Cedex
France
Attn: Jacques Duco

1   Gesellschaft fur Reaktorsicherheit (GRS)
Postfach 101650
Glockengrasse 2
5000 Koeln 1
Federal Rebulic of Germany

1   Kraftwerk Union
Hammerbacher Strasse 1214
Postfach 3220
D-8520 Erlangen 2
Federal Rebulic of Germany
Attn: Dr. M. Peeks

2   Kernforschungszentrum Karlsruhe
Postfach 3640
75 Karlsruhe
Federal Republic of Germany
Attn: S. Hagen

1   Nucleare e della Protezione
    Sanitaria (DISP)
Ente Nazionnle Energie
    Alternative 7(ENEA)
Viale Regina Margherita, 125
Casella Postale M. 2358
I-00100 Roma A.D.
Italy
Attn: Mr. G. Petrangeli

1   Thermodynamics & Rad. Physics
CEC Joint Research Center, ISPRA
I-21020 Ispra (Varese)
Italy
Attn: Alan V. Jones

2   Japan Atomic Energy Research Institute
Tokai-Mura, Naka-Gun
Ibaraki-Ken 319-11
Japan
Attn: K. Soda

1   Reactor Centrum Nederland
1755 ZG Petten
The Netherlands
Attn: Dr. K.J. Brinkman

1   I.V. Kurchatov Institute of Atomic Energy
Nuclear Safety Department
Moscow, 123182
Russia
Attn: V. Asmalov

1   Sub. Emplazamientos y Programas
Consejo de Seguridad Nuclear
Justo Dorado II
28040 Madrid
Spain
Attn: Jose Angel Martinez

1   Consejo de Seguridad Nuclear
SOR Angela de la Cruz No. 3
Madrid
Spain
Attn: Juan Bagues

1   E.T.S. Ingenieros Industriales
28006 Madrid
Spain
Attn: Professor Agustin Alonso

1   Department of Nuclear Power Safety
Royal Institute of Technology
S-100 44 Stockholm
Sweden
Attn: B. Raj Sehgal

Dist

DISTRIBUTION LIST (Concluded)

No of
Copies

No of
Copies

2   Statens Karnkraftinspektion
P.O. Box 27106
S-10252 Stockholm
Sweden
Attn: W. Frid

1   Light Water Reactor Safety Program
Paul Scherrer Institute
CH-5232 Villigen PSI
Switerzerland
Attn: J. Peter Hosemann

1   Swiss Federal Nuclear Safety Directorate
CH-5303 Wurenlingen
Switzerland
Attn: S. Chakraborty

1   Korea Atomic Energy Research Inst.
Korea Adv Energy Research Inst.
PO Box 7
Daeduk-Danji
Taejan 305-353
Attn: C.K. Park

2   UKAEA
Winfrith, Dorchester
Dorset DT2 8DH
United Kingdom
Attn: A. Nichols 102/A50
S. Kinnersly 204/A32

1   UKAEA Culham Laboratory
Abingdon
Oxfordshire OX14 3DB
United Kingdom
Attn: B.D. Turland E5.157

40   Sandia National Laboratories
P.O. Box 5800
Albuquerque, NM 87185
Attn: D.W. Schaeffer/1810
S.A. Landenberger/3141 (5)
Document Processing for
DOE-OSTI/3145 (8)
G.C. Claycomb/3151(3)
N.R. Ortiz/6400
D.A. Powers/6404
M.D. Allen/6422 (5)
F.E. Arellano/6422
N. Bixler/6422
T.K. Blanchat/6422
R.E. Blose/6422
J.E. Brockmann/6422
R.M. Elrick/6422
T. Heames/6422
M. Pilch/6422
K.O. Reil/6423
K.E. Washington/6429
E.R. Copus/7725
Central Technical Files/8523-2

NUREG/CR-5564   DIST-4

1. REPORT NUMBER (Assigned by NRC. Add Vol., Supp., Rev., and Addendum Numbers, if any.)
NUREG/CR-5564
SAND90-1022

2. TITLE AND SUBTITLE

Core-Concrete Interactions Using Molten UO$_2$ With Zirconium on A Basaltic Basemat

The SURC-2 Experiment

3. DATE REPORT PUBLISHED	
MONTH	YEAR
August	1992

4. FIN OR GRANT NUMBER

A1218

5. AUTHOR(S)

E. R. Copus, R. E. Blose*, J. E. Brockmann,
R. B. Simpson, D. A. Lucero

6. TYPE OF REPORT

Technical

7. PERIOD COVERED (Inclusive Dates)

8. PERFORMING ORGANIZATION – NAME AND ADDRESS (If NRC, provide Division, Office or Region, U.S. Nuclear Regulatory Commission, and mailing address; if contractor, provide name and mailing address.)

Sandia National Laboratories
Albuquerque, NM 87185

*Ktech Corporation
Albuquerque, NM 87110

9. SPONSORING ORGANIZATION – NAME AND ADDRESS (If NRC, type "Same as above"; if contractor, provide NRC Division, Office or Region, U.S. Nuclear Regulatory Commission, and mailing address.)

Division of Systems Research
Office of Nuclear Regulatory Research
U.S. Nuclear Regulatory Commission
Washington, DC 20555

10. SUPPLEMENTARY NOTES

11. ABSTRACT (200 words or less)

An inductively heated experiment, SURC-2, was executed as part of the Integral Core-Concrete Interactions Experiments Program. The purpose of this experiment was to measure and assess the variety of source terms produced during core debris/concrete interactions. These source terms include thermal energy released to both the reactor basemat and the containment environment, as well as flammable gas, condensable vapor and toxic or radioactive aerosols generated during the course of a severe reactor accident.

The SURC-2 experiment used 200 kg of prototypic UO$_2$-ZrO$_2$ materials to study the interactions between core debris and a basaltic basement. The experiment eroded 35 cm of concrete during 160 minutes of sustained interaction at temperatures which ranged from 2700 to 2200 K. Comprehensive gas flow rates, gas compositions, and aerosol release rates from the interaction were also measured.

12. KEY WORDS/DESCRIPTORS (List words or phrases that will assist researchers in locating the report.)

Molten core interactions, ex-vessel interactions, reactor containment safety studies, melt-concrete heat transfer, core debris-concrete interactions, ex-vessel aerosol source terms, zirconium oxidation.

13. AVAILABILITY STATEMENT

Unlimited

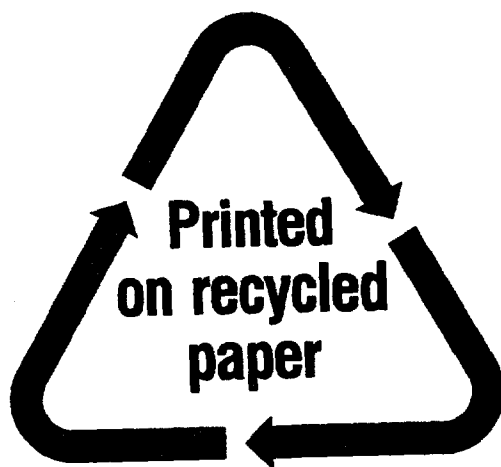14. SECURITY CLASSIFICATION

(This Page)

Unclassified

(This Report)

Unclassified

15. NUMBER OF PAGES

16. PRICE

Printed
on recycled
paper

Federal Recycling Program

UNITED STATES
NUCLEAR REGULATORY COMMISSION
WASHINGTON, D.C. 20555-0001

OFFICIAL BUSINESS
PENALTY FOR PRIVATE USE, $300